



Experimental Study of Hypersonic Inflatable Aerodynamic Decelerator (HIAD) Aeroshell with Axisymmetric Surface Deflection Patterns

Brian R. Hollis
Langley Research Center, Hampton, Virginia

Kevin E. Hollingsworth
Jacobs Technology Inc., Hampton, Virginia

NASA STI Program . . . in Profile

Since its founding, NASA has been dedicated to the advancement of aeronautics and space science. The NASA scientific and technical information (STI) program plays a key part in helping NASA maintain this important role.

The NASA STI program operates under the auspices of the Agency Chief Information Officer. It collects, organizes, provides for archiving, and disseminates NASA's STI. The NASA STI program provides access to the NTRS Registered and its public interface, the NASA Technical Reports Server, thus providing one of the largest collections of aeronautical and space science STI in the world. Results are published in both non-NASA channels and by NASA in the NASA STI Report Series, which includes the following report types:

- **TECHNICAL PUBLICATION.** Reports of completed research or a major significant phase of research that present the results of NASA Programs and include extensive data or theoretical analysis. Includes compilations of significant scientific and technical data and information deemed to be of continuing reference value. NASA counter-part of peer-reviewed formal professional papers but has less stringent limitations on manuscript length and extent of graphic presentations.
- **TECHNICAL MEMORANDUM.** Scientific and technical findings that are preliminary or of specialized interest, e.g., quick release reports, working papers, and bibliographies that contain minimal annotation. Does not contain extensive analysis.
- **CONTRACTOR REPORT.** Scientific and technical findings by NASA-sponsored contractors and grantees.

- **CONFERENCE PUBLICATION.** Collected papers from scientific and technical conferences, symposia, seminars, or other meetings sponsored or co-sponsored by NASA.
- **SPECIAL PUBLICATION.** Scientific, technical, or historical information from NASA programs, projects, and missions, often concerned with subjects having substantial public interest.
- **TECHNICAL TRANSLATION.** English-language translations of foreign scientific and technical material pertinent to NASA's mission.

Specialized services also include organizing and publishing research results, distributing specialized research announcements and feeds, providing information desk and personal search support, and enabling data exchange services.

For more information about the NASA STI program, see the following:

- Access the NASA STI program home page at <http://www.sti.nasa.gov>
- E-mail your question to help@sti.nasa.gov
- Phone the NASA STI Information Desk at 757-864-9658
- Write to:
NASA STI Information Desk
Mail Stop 148
NASA Langley Research Center
Hampton, VA 23681-2199

NASA/TM-2017-219585



Experimental Aeroheating Study of Hypersonic Inflatable Aerodynamic Decelerator (HIAD) Aeroshells with Axisymmetric Surface Deflection Patterns

Brian R. Hollis
Langley Research Center, Hampton, Virginia

Kevin E. Hollingsworth
Jacobs Technology Inc., Hampton, Virginia

National Aeronautics and
Space Administration

Langley Research Center
Hampton, Virginia 23681-2199

March 2017

The use of trademarks or names of manufacturers in this report is for accurate reporting and does not constitute an official endorsement, either expressed or implied, of such products or manufacturers by the National Aeronautics and Space Administration.

Available from:

NASA STI Program / Mail Stop 148
NASA Langley Research Center
Hampton, VA 23681-2199
Fax: 757-864-6500

Table of Contents

Abstract	1
Nomenclature	2
Symbols	2
Subscripts	3
Acronyms	3
Introduction	3
HIAD Background and History	4
Experimental Tools and Methods	5
Model Design and Fabrication	5
Model Fabrication	5
Baseline Smooth Model Geometry	5
Engineering Demonstration Unit Deflected OML Geometry	5
Parametric Deflection Models	6
Test Facility and Conditions	7
Wind Tunnel Test Conditions	7
Data Acquisition, Reduction, Uncertainty and Presentation	8
Data Acquisition	8
Data Reduction	9
Data Uncertainty	9
Data Presentation	9
Computational Method	10
Results and Analysis	10
Overview	10
Flow Field Schlieren Imagery	10
Smooth OML Model Data	11
Deflected OML Model Data	11
Parametric OML Deflection Models Data	12
Correlation of Wind Tunnel Data and Extrapolation to Flight	13
Scallop Heating Bump Factors	13
Simple Transition Onset Model	16
Detailed Transition Onset Model	17
Application of Correlations to Wind Tunnel Conditions	22
Application of Correlations to Flight Condition Predictions	23
Summary and Conclusions	24
References	25
Appendix A. Global Heating Images	136

List of Tables

Table 1. Geometry Information.	28
Table 2. Parametric Model Information.....	28
Table 3. Test 6979, 20-Inch Mach 6 Air Tunnel Conditions.....	29
Table 4. Curve Fit Information for Scallop Parameter Correlation Form.	32
Table 5. Curve Fit Information for Wind Tunnel Roughness Correlation Form.....	32
Table 6. Curve Fit Information for Multiple Parameter Correlation Form.....	32
Table 7. IRVE-3 trajectory parameters.....	33

List of Figures

Figure 1. IRVE-3 Flight Vehicle Cross Section.	34
Figure 2. IRVE-3 Flight Vehicle Geometry.	34
Figure 3. Underlying Structure of IRVE EDU Test Article without F-TPS.	35
Figure 4. Inflated IRVE EDU Test Article at Static Atmospheric Conditions.	35
Figure 5. Inflated IRVE EDU Test Article Under Pressure Loading.	35
Figure 6. Parametric Scallop Model Outer Mold Line Dimensions.	36
Figure 7. Parametric Scallop Details.	36
Figure 8. Renderings of IRVE Parametric Scallop Model Surfaces.	37
Figure 9. Schematic of LaRC 20-Inch Mach 6 Air Tunnel.	38
Figure 10. Camera View Direction and Coordinate System Nomenclature.	38
Figure 11. Schlieren Images, $\alpha = 0$ -deg.	39
Figure 12. Schlieren Images, $\alpha = 6$ -deg.	40
Figure 13. Schlieren Images, $\alpha = 12$ -deg.	41
Figure 14. Schlieren Images, $\alpha = 18$ -deg.	42
Figure 15. Comparison of Scallop Heights and Smooth-Wall Boundary Layer Heights.	43
Figure 16. IRVE Scallop-0 Model, Reynolds Number Effects at $\alpha = 0$ deg.	44
Figure 17. IRVE Scallop-0 Model, Reynolds Number Effects at $\alpha = 6$ deg.	45
Figure 18. IRVE Scallop-0 Model, Reynolds Number Effects at $\alpha = 12$ deg.	46
Figure 19. IRVE Scallop-0 Model, Reynolds Number Effects at $\alpha = 18$ deg.	47
Figure 20. IRVE EDU Model, Reynolds Number Effects at $\alpha = 0$ deg.	48
Figure 21. IRVE EDU Model, Reynolds Number Effects at $\alpha = 6$ deg.	49
Figure 22. IRVE EDU Model, Reynolds Number Effects at $\alpha = 12$ deg.	50
Figure 23. IRVE EDU Model, Reynolds Number Effects at $\alpha = 18$ deg.	51
Figure 24. IRVE Scallop-2.5 Model, Reynolds Number Effects at $\alpha = 0$ deg.	52
Figure 25. IRVE Scallop-2.5 Model, Reynolds Number Effects at $\alpha = 6$ deg.	53
Figure 26. IRVE Scallop-2.5 Model, Reynolds Number Effects at $\alpha = 12$ deg.	54
Figure 27. IRVE Scallop-2.5 Model, Reynolds Number Effects at $\alpha = 18$ deg.	55
Figure 28. IRVE Scallop-5 Model, Reynolds Number Effects at $\alpha = 0$ deg.	56
Figure 29. IRVE Scallop-5 Model, Reynolds Number Effects at $\alpha = 6$ deg.	57
Figure 30. IRVE Scallop-5 Model, Reynolds Number Effects at $\alpha = 12$ deg.	58
Figure 31. IRVE Scallop-5 Model, Reynolds Number Effects at $\alpha = 18$ deg.	59
Figure 32. IRVE Scallop-10 Model, Reynolds Number Effects at $\alpha = 0$ deg.	60
Figure 33. IRVE Scallop-10 Model, Reynolds Number Effects at $\alpha = 6$ deg.	61
Figure 34. IRVE Scallop-10 Model, Reynolds Number Effects at $\alpha = 12$ deg.	62
Figure 35. IRVE Scallop-10 Model, Reynolds Number Effects at $\alpha = 18$ deg.	63
Figure 36. IRVE Scallop-15 Model, Reynolds Number Effects at $\alpha = 0$ deg.	64
Figure 37. IRVE Scallop-15 Model, Reynolds Number Effects at $\alpha = 6$ deg.	65
Figure 38. IRVE Scallop-15 Model, Reynolds Number Effects at $\alpha = 12$ deg.	66
Figure 39. IRVE Scallop-15 Model, Reynolds Number Effects at $\alpha = 18$ deg.	67
Figure 40. IRVE Scallop-20 Model, Reynolds Number Effects at $\alpha = 0$ deg.	68
Figure 41. IRVE Scallop-20 Model, Reynolds Number Effects at $\alpha = 6$ deg.	69
Figure 42. IRVE Scallop-20 Model, Reynolds Number Effects at $\alpha = 12$ deg.	70
Figure 43. IRVE Scallop-20 Model, Reynolds Number Effects at $\alpha = 18$ deg.	71

Figure 44. Configuration Effects at $Re_\infty = 2.10 \times 10^6/\text{ft}$, $\alpha = 0$ deg.	72
Figure 45. Configuration Effects at $Re_\infty = 3.03 \times 10^6/\text{ft}$, $\alpha = 0$ deg.	73
Figure 46. Configuration Effects at $Re_\infty = 3.88 \times 10^6/\text{ft}$, $\alpha = 0$ deg.	74
Figure 47. Configuration Effects at $Re_\infty = 6.63 \times 10^6/\text{ft}$, $\alpha = 0$ deg.	75
Figure 48. Configuration Effects at $Re_\infty = 8.34 \times 10^6/\text{ft}$, $\alpha = 0$ deg.	76
Figure 49. Configuration Effects at $Re_\infty = 2.10 \times 10^6/\text{ft}$, $\alpha = 6$ deg.	77
Figure 50. Configuration Effects at $Re_\infty = 3.03 \times 10^6/\text{ft}$, $\alpha = 6$ deg.	78
Figure 51. Configuration Effects at $Re_\infty = 3.88 \times 10^6/\text{ft}$, $\alpha = 6$ deg.	79
Figure 52. Configuration Effects at $Re_\infty = 6.63 \times 10^6/\text{ft}$, $\alpha = 6$ deg.	80
Figure 53. Configuration Effects at $Re_\infty = 8.34 \times 10^6/\text{ft}$, $\alpha = 6$ deg.	81
Figure 54. Configuration Effects at $Re_\infty = 2.10 \times 10^6/\text{ft}$, $\alpha = 12$ deg.	82
Figure 55. Configuration Effects at $Re_\infty = 3.03 \times 10^6/\text{ft}$, $\alpha = 12$ deg.	83
Figure 56. Configuration Effects at $Re_\infty = 3.88 \times 10^6/\text{ft}$, $\alpha = 12$ deg.	84
Figure 57. Configuration Effects at $Re_\infty = 6.63 \times 10^6/\text{ft}$, $\alpha = 12$ deg.	85
Figure 58. Configuration Effects at $Re_\infty = 8.34 \times 10^6/\text{ft}$, $\alpha = 12$ deg.	86
Figure 59. Configuration Effects at $Re_\infty = 2.10 \times 10^6/\text{ft}$, $\alpha = 18$ deg.	87
Figure 60. Configuration Effects at $Re_\infty = 3.03 \times 10^6/\text{ft}$, $\alpha = 18$ deg.	88
Figure 61. Configuration Effects at $Re_\infty = 3.88 \times 10^6/\text{ft}$, $\alpha = 18$ deg.	89
Figure 62. Configuration Effects at $Re_\infty = 6.63 \times 10^6/\text{ft}$, $\alpha = 18$ deg.	90
Figure 63. Configuration Effects at $Re_\infty = 8.34 \times 10^6/\text{ft}$, $\alpha = 18$ deg.	91
Figure 64. Illustration of Scallop Peak Heating Data used for Correlation.	92
Figure 65. Turbulent Correlation for IRVE Scallop-2.5 Data.	92
Figure 66. Turbulent Correlation for IRVE Scallop-5 Data.	93
Figure 67. Turbulent Correlation for IRVE Scallop-10 Data.	93
Figure 68. Turbulent Correlation for IRVE Scallop-15 Data.	94
Figure 69. Turbulent Correlation for IRVE Scallop-20 Data.	94
Figure 70. Curve Fit for Laminar Augmentation.	95
Figure 71. Curve Fit for Turbulent Slope.	95
Figure 72. Transition Intermittency Function.	96
Figure 73. Curve Fit for Simple Transition Onset Model.	96
Figure 74. Curve Fit for Transition Length.	97
Figure 75. Transitional Correlation for IRVE Scallop-2.5 Data.	97
Figure 76. Transitional Correlation for IRVE Scallop-5 Data.	98
Figure 77. Transitional Correlation for IRVE Scallop-10 Data.	98
Figure 78. Transitional Correlation for IRVE Scallop-15 Data.	99
Figure 79. Transitional Correlation for IRVE Scallop-20 Data.	99
Figure 80. Transition Correlation Form.	100
Figure 81. Tangent-Slope-Intercept Identification of Transition Onset.	100
Figure 82. Scallop-Parameter Correlation Variations.	101
Figure 83. Wind-Tunnel-Roughness Correlation Variations.	102
Figure 84. Multiple-Parameter Correlation Variations.	103
Figure 85. Scallop-Parameter-4 Combined Correlation with Uncertainties.	104
Figure 86. Wind-Tunnel-Roughness-4 Combined Correlation with Uncertainties.	105
Figure 87. Multiple-Parameter-5 Combined Correlation with Uncertainties.	106
Figure 88. Correlation Comparison with IRVE Scallop-2.5 Model Data, $\alpha = 0$ deg.	107

Figure 89. Correlation Comparison with IRVE Scallop-2.5 Model Data, $\alpha = 6$ deg.	108
Figure 90. Correlation Comparison with IRVE Scallop-2.5 Model Data, $\alpha = 12$ deg.	109
Figure 91. Correlation Comparison with IRVE Scallop-2.5 Model Data, $\alpha = 18$ deg.	110
Figure 92. Correlation Comparison with IRVE Scallop-5 Model Data, $\alpha = 0$ deg.	111
Figure 93. Correlation Comparison with IRVE Scallop-5 Model Data, $\alpha = 6$ deg.	112
Figure 94. Correlation Comparison with IRVE Scallop-5 Model Data, $\alpha = 12$ deg.	113
Figure 95. Correlation Comparison with IRVE Scallop-5 Model Data, $\alpha = 18$ deg.	114
Figure 96. Correlation Comparison with IRVE Scallop-10 Model Data, $\alpha = 0$ deg.	115
Figure 97. Correlation Comparison with IRVE Scallop-10 Model Data, $\alpha = 6$ deg.	116
Figure 98. Correlation Comparison with IRVE Scallop-10 Model Data, $\alpha = 12$ deg.	117
Figure 99. Correlation Comparison with IRVE Scallop-10 Model Data, $\alpha = 18$ deg.	118
Figure 100. Correlation Comparison with IRVE Scallop-15 Model Data, $\alpha = 0$ deg.	119
Figure 101. Correlation Comparison with IRVE Scallop-15 Model Data, $\alpha = 6$ deg.	120
Figure 102. Correlation Comparison with IRVE Scallop-15 Model Data, $\alpha = 12$ deg.	121
Figure 103. Correlation Comparison with IRVE Scallop-15 Model Data, $\alpha = 18$ deg.	122
Figure 104. Correlation Comparison with IRVE Scallop-20 Model Data, $\alpha = 0$ deg.	123
Figure 105. Correlation Comparison with IRVE Scallop-20 Model Data, $\alpha = 6$ deg.	124
Figure 106. Correlation Comparison with IRVE Scallop-20 Model Data, $\alpha = 12$ deg.	125
Figure 107. Correlation Comparison with IRVE Scallop-20 Model Data, $\alpha = 18$ deg.	126
Figure 108. Correlation Comparison with IRVE EDU Model Data, $\alpha = 0$ deg.	127
Figure 109. Correlation Comparison with IRVE EDU Model Data, $\alpha = 6$ deg.	128
Figure 110. Correlation Comparison with IRVE EDU Model Data, $\alpha = 12$ deg.	129
Figure 111. Correlation Comparison with IRVE EDU Model Data, $\alpha = 18$ deg.	130
Figure 112. IRVE-3 Flight Trajectory Heating and Pressure.	131
Figure 113. Correlation Applied to IRVE-3 Flight Trajectory – $t = 664.85$ sec – 673.50 sec. ..	132
Figure 114. Correlation Applied to IRVE-3 Flight Trajectory – $t = 674.55$ sec – 679.95 sec. ..	133
Figure 115. Correlation Applied to IRVE-3 Flight Trajectory – $t = 681.05$ sec – 687.50 sec. ..	134
Figure 116. Correlation Applied to IRVE-3 Flight Trajectory – $t = 689.70$ sec – 691.85 sec. ..	135
Figure 117. IRVE Scallop-0 Model, Run 80: $\alpha = 0$ deg, $Re_{\infty} = 2.10 \times 10^6/\text{ft}$	137
Figure 118. IRVE Scallop-0 Model, Run 81: $\alpha = 0$ deg, $Re_{\infty} = 3.03 \times 10^6/\text{ft}$	137
Figure 119. IRVE Scallop-0 Model, Run 82: $\alpha = 0$ deg, $Re_{\infty} = 3.88 \times 10^6/\text{ft}$	138
Figure 120. IRVE Scallop-0 Model, Run 83: $\alpha = 0$ deg, $Re_{\infty} = 6.63 \times 10^6/\text{ft}$	138
Figure 121. IRVE Scallop-0 Model, Run 84: $\alpha = 0$ deg, $Re_{\infty} = 8.33 \times 10^6/\text{ft}$	139
Figure 122. IRVE Scallop-0 Model, Run 70: $\alpha = 6$ deg, $Re_{\infty} = 2.10 \times 10^6/\text{ft}$	139
Figure 123. IRVE Scallop-0 Model, Run 72: $\alpha = 6$ deg, $Re_{\infty} = 3.03 \times 10^6/\text{ft}$	140
Figure 124. IRVE Scallop-0 Model, Run 71: $\alpha = 6$ deg, $Re_{\infty} = 3.88 \times 10^6/\text{ft}$	140
Figure 125. IRVE Scallop-0 Model, Run 73: $\alpha = 6$ deg, $Re_{\infty} = 6.63 \times 10^6/\text{ft}$	141
Figure 126. IRVE Scallop-0 Model, Run 74: $\alpha = 6$ deg, $Re_{\infty} = 8.33 \times 10^6/\text{ft}$	141
Figure 127. IRVE Scallop-0 Model, Run 103: $\alpha = 12$ deg, $Re_{\infty} = 2.10 \times 10^6/\text{ft}$	142
Figure 128. IRVE Scallop-0 Model, Run 104: $\alpha = 12$ deg, $Re_{\infty} = 3.03 \times 10^6/\text{ft}$	142
Figure 129. IRVE Scallop-0 Model, Run 105: $\alpha = 12$ deg, $Re_{\infty} = 3.88 \times 10^6/\text{ft}$	143
Figure 130. IRVE Scallop-0 Model, Run 106: $\alpha = 12$ deg, $Re_{\infty} = 6.63 \times 10^6/\text{ft}$	143
Figure 131. IRVE Scallop-0 Model, Run 107: $\alpha = 12$ deg, $Re_{\infty} = 8.33 \times 10^6/\text{ft}$	144
Figure 132. IRVE Scallop-0 Model, Run 161: $\alpha = 18$ deg, $Re_{\infty} = 2.10 \times 10^6/\text{ft}$	144
Figure 133. IRVE Scallop-0 Model, Run 162: $\alpha = 18$ deg, $Re_{\infty} = 3.03 \times 10^6/\text{ft}$	145

Figure 134. IRVE Scallop-0 Model, Run 163: $\alpha = 18$ deg, $Re_\infty = 3.88 \times 10^6/\text{ft}$	145
Figure 135. IRVE Scallop-0 Model, Run 164: $\alpha = 18$ deg, $Re_\infty = 6.63 \times 10^6/\text{ft}$	146
Figure 136. IRVE Scallop-0 Model, Run 165: $\alpha = 18$ deg, $Re_\infty = 8.33 \times 10^6/\text{ft}$	146
Figure 137. IRVE EDU Model, Run 36: $\alpha = 0$ deg, $Re_\infty = 2.10 \times 10^6/\text{ft}$	147
Figure 138. IRVE EDU Model, Run 39: $\alpha = 0$ deg, $Re_\infty = 3.03 \times 10^6/\text{ft}$	147
Figure 139. IRVE EDU Model, Run 40: $\alpha = 0$ deg, $Re_\infty = 3.88 \times 10^6/\text{ft}$	148
Figure 140. IRVE EDU Model, Run 41: $\alpha = 0$ deg, $Re_\infty = 6.63 \times 10^6/\text{ft}$	148
Figure 141. IRVE EDU Model, Run 42: $\alpha = 0$ deg, $Re_\infty = 8.33 \times 10^6/\text{ft}$	149
Figure 142. IRVE EDU Model, Run 122: $\alpha = 6$ deg, $Re_\infty = 2.10 \times 10^6/\text{ft}$	149
Figure 143. IRVE EDU Model, Run 120: $\alpha = 6$ deg, $Re_\infty = 3.03 \times 10^6/\text{ft}$	150
Figure 144. IRVE EDU Model, Run 119: $\alpha = 6$ deg, $Re_\infty = 3.88 \times 10^6/\text{ft}$	150
Figure 145. IRVE EDU Model, Run 123: $\alpha = 6$ deg, $Re_\infty = 6.63 \times 10^6/\text{ft}$	151
Figure 146. IRVE EDU Model, Run 125: $\alpha = 6$ deg, $Re_\infty = 8.33 \times 10^6/\text{ft}$	151
Figure 147. IRVE EDU Model, Run 113: $\alpha = 12$ deg, $Re_\infty = 2.10 \times 10^6/\text{ft}$	152
Figure 148. IRVE EDU Model, Run 114: $\alpha = 12$ deg, $Re_\infty = 3.03 \times 10^6/\text{ft}$	152
Figure 149. IRVE EDU Model, Run 115: $\alpha = 12$ deg, $Re_\infty = 3.88 \times 10^6/\text{ft}$	153
Figure 150. IRVE EDU Model, Run 117: $\alpha = 12$ deg, $Re_\infty = 6.63 \times 10^6/\text{ft}$	153
Figure 151. IRVE EDU Model, Run 118: $\alpha = 12$ deg, $Re_\infty = 8.33 \times 10^6/\text{ft}$	154
Figure 152. IRVE EDU Model, Run 137: $\alpha = 18$ deg, $Re_\infty = 2.10 \times 10^6/\text{ft}$	154
Figure 153. IRVE EDU Model, Run 138: $\alpha = 18$ deg, $Re_\infty = 3.03 \times 10^6/\text{ft}$	155
Figure 154. IRVE EDU Model, Run 136: $\alpha = 18$ deg, $Re_\infty = 3.88 \times 10^6/\text{ft}$	155
Figure 155. IRVE EDU Model, Run 139: $\alpha = 18$ deg, $Re_\infty = 6.33 \times 10^6/\text{ft}$	156
Figure 156. IRVE EDU Model, Run 140: $\alpha = 18$ deg, $Re_\infty = 8.34 \times 10^6/\text{ft}$	156
Figure 157. IRVE Scallop-2.5 Model, Run 8: $\alpha = 0$ deg, $Re_\infty = 2.10 \times 10^6/\text{ft}$	157
Figure 158. IRVE Scallop-2.5 Model, Run 7: $\alpha = 0$ deg, $Re_\infty = 3.03 \times 10^6/\text{ft}$	157
Figure 159. IRVE Scallop-2.5 Model, Run 6: $\alpha = 0$ deg, $Re_\infty = 3.88 \times 10^6/\text{ft}$	158
Figure 160. IRVE Scallop-2.5 Model, Run 9: $\alpha = 0$ deg, $Re_\infty = 6.63 \times 10^6/\text{ft}$	158
Figure 161. IRVE Scallop-2.5 Model, Run 10: $\alpha = 0$ deg, $Re_\infty = 8.33 \times 10^6/\text{ft}$	159
Figure 162. IRVE Scallop-2.5 Model, Run 56: $\alpha = 6$ deg, $Re_\infty = 2.10 \times 10^6/\text{ft}$	159
Figure 163. IRVE Scallop-2.5 Model, Run 57: $\alpha = 6$ deg, $Re_\infty = 3.03 \times 10^6/\text{ft}$	160
Figure 164. IRVE Scallop-2.5 Model, Run 55: $\alpha = 6$ deg, $Re_\infty = 3.88 \times 10^6/\text{ft}$	160
Figure 165. IRVE Scallop-2.5 Model, Run 58: $\alpha = 6$ deg, $Re_\infty = 6.63 \times 10^6/\text{ft}$	161
Figure 166. IRVE Scallop-2.5 Model, Run 59: $\alpha = 6$ deg, $Re_\infty = 8.33 \times 10^6/\text{ft}$	161
Figure 167. IRVE Scallop-2.5 Model, Run 93: $\alpha = 12$ deg, $Re_\infty = 2.10 \times 10^6/\text{ft}$	162
Figure 168. IRVE Scallop-2.5 Model, Run 94: $\alpha = 12$ deg, $Re_\infty = 3.03 \times 10^6/\text{ft}$	162
Figure 169. IRVE Scallop-2.5 Model, Run 92: $\alpha = 12$ deg, $Re_\infty = 3.88 \times 10^6/\text{ft}$	163
Figure 170. IRVE Scallop-2.5 Model, Run 95: $\alpha = 12$ deg, $Re_\infty = 6.63 \times 10^6/\text{ft}$	163
Figure 171. IRVE Scallop-2.5 Model, Run 96: $\alpha = 12$ deg, $Re_\infty = 8.33 \times 10^6/\text{ft}$	164
Figure 172. IRVE Scallop-2.5 Model, Run 157: $\alpha = 18$ deg, $Re_\infty = 2.10 \times 10^6/\text{ft}$	164
Figure 173. IRVE Scallop-2.5 Model, Run 158: $\alpha = 18$ deg, $Re_\infty = 3.03 \times 10^6/\text{ft}$	165
Figure 174. IRVE Scallop-2.5 Model, Run 156: $\alpha = 18$ deg, $Re_\infty = 3.88 \times 10^6/\text{ft}$	165
Figure 175. IRVE Scallop-2.5 Model, Run 159: $\alpha = 18$ deg, $Re_\infty = 6.63 \times 10^6/\text{ft}$	166
Figure 176. IRVE Scallop-2.5 Model, Run 160: $\alpha = 18$ deg, $Re_\infty = 8.33 \times 10^6/\text{ft}$	166
Figure 177. IRVE Scallop-5 Model, Run 13: $\alpha = 0$ deg, $Re_\infty = 2.10 \times 10^6/\text{ft}$	167
Figure 178. IRVE Scallop-5 Model, Run 12: $\alpha = 0$ deg, $Re_\infty = 3.03 \times 10^6/\text{ft}$	167
Figure 179. IRVE Scallop-5 Model, Run 11: $\alpha = 0$ deg, $Re_\infty = 3.88 \times 10^6/\text{ft}$	168

Figure 180. IRVE Scallop-5 Model, Run 14: $\alpha = 0$ deg, $Re_\infty = 6.63 \times 10^6/\text{ft}$	168
Figure 181. IRVE Scallop-5 Model, Run 15: $\alpha = 0$ deg, $Re_\infty = 8.33 \times 10^6/\text{ft}$	169
Figure 182. IRVE Scallop-5 Model, Run 65: $\alpha = 6$ deg, $Re_\infty = 2.10 \times 10^6/\text{ft}$	169
Figure 183. IRVE Scallop-5 Model, Run 66: $\alpha = 6$ deg, $Re_\infty = 3.03 \times 10^6/\text{ft}$	170
Figure 184. IRVE Scallop-5 Model, Run 67: $\alpha = 6$ deg, $Re_\infty = 3.88 \times 10^6/\text{ft}$	170
Figure 185. IRVE Scallop-5 Model, Run 68: $\alpha = 6$ deg, $Re_\infty = 6.63 \times 10^6/\text{ft}$	171
Figure 186. IRVE Scallop-5 Model, Run 69: $\alpha = 6$ deg, $Re_\infty = 8.33 \times 10^6/\text{ft}$	171
Figure 187. IRVE Scallop-5 Model, Run 185: $\alpha = 12$ deg, $Re_\infty = 2.10 \times 10^6/\text{ft}$	172
Figure 188. IRVE Scallop-5 Model, Run 186: $\alpha = 12$ deg, $Re_\infty = 3.03 \times 10^6/\text{ft}$	172
Figure 189. IRVE Scallop-5 Model, Run 187: $\alpha = 12$ deg, $Re_\infty = 3.88 \times 10^6/\text{ft}$	173
Figure 190. IRVE Scallop-5 Model, Run 188: $\alpha = 12$ deg, $Re_\infty = 6.63 \times 10^6/\text{ft}$	173
Figure 191. IRVE Scallop-5 Model, Run 189: $\alpha = 12$ deg, $Re_\infty = 8.33 \times 10^6/\text{ft}$	174
Figure 192. IRVE Scallop-5 Model, Run 152: $\alpha = 18$ deg, $Re_\infty = 2.10 \times 10^6/\text{ft}$	174
Figure 193. IRVE Scallop-5 Model, Run 153: $\alpha = 18$ deg, $Re_\infty = 3.03 \times 10^6/\text{ft}$	175
Figure 194. IRVE Scallop-5 Model, Run 151: $\alpha = 18$ deg, $Re_\infty = 3.88 \times 10^6/\text{ft}$	175
Figure 195. IRVE Scallop-5 Model, Run 154: $\alpha = 18$ deg, $Re_\infty = 6.63 \times 10^6/\text{ft}$	176
Figure 196. IRVE Scallop-5 Model, Run 155: $\alpha = 18$ deg, $Re_\infty = 8.33 \times 10^6/\text{ft}$	176
Figure 197. IRVE Scallop-10 Model, Run 16: $\alpha = 0$ deg, $Re_\infty = 2.10 \times 10^6/\text{ft}$	177
Figure 198. IRVE Scallop-10 Model, Run 17: $\alpha = 0$ deg, $Re_\infty = 3.03 \times 10^6/\text{ft}$	177
Figure 199. IRVE Scallop-10 Model, Run 18: $\alpha = 0$ deg, $Re_\infty = 3.88 \times 10^6/\text{ft}$	178
Figure 200. IRVE Scallop-10 Model, Run 19: $\alpha = 0$ deg, $Re_\infty = 6.63 \times 10^6/\text{ft}$	178
Figure 201. IRVE Scallop-10 Model, Run 20: $\alpha = 0$ deg, $Re_\infty = 8.33 \times 10^6/\text{ft}$	179
Figure 202. IRVE Scallop-10 Model, Run 50: $\alpha = 6$ deg, $Re_\infty = 2.10 \times 10^6/\text{ft}$	179
Figure 203. IRVE Scallop-10 Model, Run 51: $\alpha = 6$ deg, $Re_\infty = 3.03 \times 10^6/\text{ft}$	180
Figure 204. IRVE Scallop-10 Model, Run 52: $\alpha = 6$ deg, $Re_\infty = 3.88 \times 10^6/\text{ft}$	180
Figure 205. IRVE Scallop-10 Model, Run 53: $\alpha = 6$ deg, $Re_\infty = 6.63 \times 10^6/\text{ft}$	181
Figure 206. IRVE Scallop-10 Model, Run 54: $\alpha = 6$ deg, $Re_\infty = 8.33 \times 10^6/\text{ft}$	181
Figure 207. IRVE Scallop-10 Model, Run 98: $\alpha = 12$ deg, $Re_\infty = 2.10 \times 10^6/\text{ft}$	182
Figure 208. IRVE Scallop-10 Model, Run 99: $\alpha = 12$ deg, $Re_\infty = 3.03 \times 10^6/\text{ft}$	182
Figure 209. IRVE Scallop-10 Model, Run 100: $\alpha = 12$ deg, $Re_\infty = 3.88 \times 10^6/\text{ft}$	183
Figure 210. IRVE Scallop-10 Model, Run 101: $\alpha = 12$ deg, $Re_\infty = 6.63 \times 10^6/\text{ft}$	183
Figure 211. IRVE Scallop-10 Model, Run 102: $\alpha = 12$ deg, $Re_\infty = 8.33 \times 10^6/\text{ft}$	184
Figure 212. IRVE Scallop-10 Model, Run 146: $\alpha = 18$ deg, $Re_\infty = 2.10 \times 10^6/\text{ft}$	184
Figure 213. IRVE Scallop-10 Model, Run 147: $\alpha = 18$ deg, $Re_\infty = 3.03 \times 10^6/\text{ft}$	185
Figure 214. IRVE Scallop-10 Model, Run 148: $\alpha = 18$ deg, $Re_\infty = 3.88 \times 10^6/\text{ft}$	185
Figure 215. IRVE Scallop-10 Model, Run 149: $\alpha = 18$ deg, $Re_\infty = 6.63 \times 10^6/\text{ft}$	186
Figure 216. IRVE Scallop-10 Model, Run 150: $\alpha = 18$ deg, $Re_\infty = 8.33 \times 10^6/\text{ft}$	186
Figure 217. IRVE Scallop-15 Model, Run 22: $\alpha = 0$ deg, $Re_\infty = 2.10 \times 10^6/\text{ft}$	187
Figure 218. IRVE Scallop-15 Model, Run 23: $\alpha = 0$ deg, $Re_\infty = 3.03 \times 10^6/\text{ft}$	187
Figure 219. IRVE Scallop-15 Model, Run 21: $\alpha = 0$ deg, $Re_\infty = 3.88 \times 10^6/\text{ft}$	188
Figure 220. IRVE Scallop-15 Model, Run 24: $\alpha = 0$ deg, $Re_\infty = 6.63 \times 10^6/\text{ft}$	188
Figure 221. IRVE Scallop-15 Model, Run 25: $\alpha = 0$ deg, $Re_\infty = 8.33 \times 10^6/\text{ft}$	189
Figure 222. IRVE Scallop-15 Model, Run 126: $\alpha = 6$ deg, $Re_\infty = 2.10 \times 10^6/\text{ft}$	189
Figure 223. IRVE Scallop-15 Model, Run 127: $\alpha = 6$ deg, $Re_\infty = 3.03 \times 10^6/\text{ft}$	190
Figure 224. IRVE Scallop-15 Model, Run 128: $\alpha = 6$ deg, $Re_\infty = 3.88 \times 10^6/\text{ft}$	190
Figure 225. IRVE Scallop-15 Model, Run 129: $\alpha = 6$ deg, $Re_\infty = 6.63 \times 10^6/\text{ft}$	191

Figure 226. IRVE Scallop-15 Model, Run 130: $\alpha = 6$ deg, $Re_\infty = 8.33 \times 10^6/\text{ft}$	191
Figure 227. IRVE Scallop-15 Model, Run 166: $\alpha = 12$ deg, $Re_\infty = 2.10 \times 10^6/\text{ft}$	192
Figure 228. IRVE Scallop-15 Model, Run 167: $\alpha = 12$ deg, $Re_\infty = 3.03 \times 10^6/\text{ft}$	192
Figure 229. IRVE Scallop-15 Model, Run 168: $\alpha = 12$ deg, $Re_\infty = 3.88 \times 10^6/\text{ft}$	193
Figure 230. IRVE Scallop-15 Model, Run 169: $\alpha = 12$ deg, $Re_\infty = 6.63 \times 10^6/\text{ft}$	193
Figure 231. IRVE Scallop-15 Model, Run 170: $\alpha = 12$ deg, $Re_\infty = 8.33 \times 10^6/\text{ft}$	194
Figure 232. IRVE Scallop-15 Model, Run 131: $\alpha = 18$ deg, $Re_\infty = 2.10 \times 10^6/\text{ft}$	194
Figure 233. IRVE Scallop-15 Model, Run 132: $\alpha = 18$ deg, $Re_\infty = 3.03 \times 10^6/\text{ft}$	195
Figure 234. IRVE Scallop-15 Model, Run 133: $\alpha = 18$ deg, $Re_\infty = 3.88 \times 10^6/\text{ft}$	195
Figure 235. IRVE Scallop-15 Model, Run 134: $\alpha = 18$ deg, $Re_\infty = 6.63 \times 10^6/\text{ft}$	196
Figure 236. IRVE Scallop-15 Model, Run 135: $\alpha = 18$ deg, $Re_\infty = 8.33 \times 10^6/\text{ft}$	196
Figure 237. IRVE Scallop-20 Model, Run 26: $\alpha = 0$ deg, $Re_\infty = 2.10 \times 10^6/\text{ft}$	197
Figure 238. IRVE Scallop-20 Model, Run 27: $\alpha = 0$ deg, $Re_\infty = 3.03 \times 10^6/\text{ft}$	197
Figure 239. IRVE Scallop-20 Model, Run 28: $\alpha = 0$ deg, $Re_\infty = 3.88 \times 10^6/\text{ft}$	198
Figure 240. IRVE Scallop-20 Model, Run 29: $\alpha = 0$ deg, $Re_\infty = 6.63 \times 10^6/\text{ft}$	198
Figure 241. IRVE Scallop-20 Model, Run 30: $\alpha = 0$ deg, $Re_\infty = 8.33 \times 10^6/\text{ft}$	199
Figure 242. IRVE Scallop-20 Model, Run 45: $\alpha = 6$ deg, $Re_\infty = 2.10 \times 10^6/\text{ft}$	199
Figure 243. IRVE Scallop-20 Model, Run 46: $\alpha = 6$ deg, $Re_\infty = 3.03 \times 10^6/\text{ft}$	200
Figure 244. IRVE Scallop-20 Model, Run 47: $\alpha = 6$ deg, $Re_\infty = 3.88 \times 10^6/\text{ft}$	200
Figure 245. IRVE Scallop-20 Model, Run 48: $\alpha = 6$ deg, $Re_\infty = 6.63 \times 10^6/\text{ft}$	201
Figure 246. IRVE Scallop-20 Model, Run 49: $\alpha = 6$ deg, $Re_\infty = 8.33 \times 10^6/\text{ft}$	201
Figure 247. IRVE Scallop-20 Model, Run 87: $\alpha = 12$ deg, $Re_\infty = 2.10 \times 10^6/\text{ft}$	202
Figure 248. IRVE Scallop-20 Model, Run 89: $\alpha = 12$ deg, $Re_\infty = 3.03 \times 10^6/\text{ft}$	202
Figure 249. IRVE Scallop-20 Model, Run 88: $\alpha = 12$ deg, $Re_\infty = 3.88 \times 10^6/\text{ft}$	203
Figure 250. IRVE Scallop-20 Model, Run 90: $\alpha = 12$ deg, $Re_\infty = 6.63 \times 10^6/\text{ft}$	203
Figure 251. IRVE Scallop-20 Model, Run 91: $\alpha = 12$ deg, $Re_\infty = 8.33 \times 10^6/\text{ft}$	204
Figure 252. IRVE Scallop-20 Model, Run 141: $\alpha = 18$ deg, $Re_\infty = 2.10 \times 10^6/\text{ft}$	204
Figure 253. IRVE Scallop-20 Model, Run 142: $\alpha = 18$ deg, $Re_\infty = 3.03 \times 10^6/\text{ft}$	205
Figure 254. IRVE Scallop-20 Model, Run 143: $\alpha = 18$ deg, $Re_\infty = 3.88 \times 10^6/\text{ft}$	205
Figure 255. IRVE Scallop-20 Model, Run 144: $\alpha = 18$ deg, $Re_\infty = 6.63 \times 10^6/\text{ft}$	206
Figure 256. IRVE Scallop-20 Model, Run 145: $\alpha = 18$ deg, $Re_\infty = 8.33 \times 10^6/\text{ft}$	206

Abstract

A wind tunnel test program was conducted to obtain aeroheating environment data on Hypersonic Inflatable Aerodynamic Decelerator aeroshells with flexible thermal protection systems. Data were obtained on a set of rigid wind tunnel models with surface deflection patterns of various heights that simulated a range of potential in-flight aeroshell deformations. Wind tunnel testing was conducted at Mach 6 at unit Reynolds numbers from $2.1 \times 10^6/\text{ft}$ to $8.3 \times 10^6/\text{ft}$ and angles of attack from 0 deg to 18 deg. Boundary-layer transition onset and global surface heating distribution measurements were performed using phosphor thermography and flow field images were obtained through schlieren photography. Surface deflections were found to both promote early transition of the boundary layer and to augment heating levels for both laminar and turbulent flows. A complimentary computational flow field study was also performed to provide heating predictions for comparison with the measurements as well as boundary layer flow field properties for use in correlating the data. Correlations of the wind tunnel data were developed to predict deflection effects on boundary layer transition and surface heating and were applied to both the wind tunnel test conditions and to the trajectory of NASA's successful IRVE-3 flight test. In general, the correlations produced at least qualitative agreement with the wind tunnel data, although the heating levels were underpredicted for some of the larger surface deflections. For the flight conditions, the correlations suggested that peak heating levels on the leeward side conical flank of the IRVE-3 vehicle may have exceeded those at nose for times late in the trajectory after the peak heating time point. However, the flight estimates were based on a conservative assumption of surface deflection magnitude (i.e., larger) than likely was produced in flight.

Nomenclature

Symbols

A_k	laminar heating augmentation curve-fit coefficient
B_k	turbulent heating augmentation curve-fit coefficient
BF_{LAM}	laminar heating bump-factor multiplier
BF_{TURB}	turbulent heating bump-factor multiplier
C_{TR}	transition onset curve-fit coefficient
D_{TR}	transition onset curve-fit exponent
h	heat-transfer film coefficient ($\text{kg/m}^2 \cdot \text{s}$)
h_{FR}	heat-transfer film coefficient based on Fay-Riddell theory ($\text{kg/m}^2 \cdot \text{s}$)
h_k	heat-transfer film coefficient on scalloped geometry ($\text{kg/m}^2 \cdot \text{s}$)
h_{lam}	laminar component of heat-transfer film coefficient ($\text{kg/m}^2 \cdot \text{s}$)
h_{ref}	heat-transfer film coefficient reference value ($\text{kg/m}^2 \cdot \text{s}$)
h_{turb}	turbulent component of heat-transfer film coefficient ($\text{kg/m}^2 \cdot \text{s}$)
H_0	wind tunnel total enthalpy (J/kg)
H_{AW}	adiabatic wall enthalpy (J/kg)
H_w	wall enthalpy (J/kg)
$H_{300\text{K}}$	enthalpy at 300 K temperature (J/kg)
I_{TR}	transition intermittency function
k_{SC}	scallop height (mil)
L_{SC}	scallop length (mil)
M_e	boundary layer edge Mach number
M_∞	free stream Mach number
p_∞	free stream pressure (Pa)
q	heat-transfer rate (W/cm^2)
q_∞	dynamic pressure (Pa)
R_A	aftbody base radius (in or m)
R_B	maximum body radius (in or m)
R_P	payload radius (in or m)
R_N	nose radius (in or m)
R_{SC}	scallop radius (in or m)
R_S	shoulder radius (in or m)
R_T	toroid radius (in or m)
Re_∞	free stream unit Reynolds number (1/ft or 1/m)
Re_θ	boundary layer momentum thickness Reynolds number
T_e	boundary layer edge temperature (K)
T_w	wall temperature (K)
T_∞	free stream temperature (K)
t	time (sec)
U_∞	free stream velocity (m/s)
U_e	boundary-layer edge velocity (m/s)
x, y, z	Cartesian coordinates (in or m)
α	angle of attack (deg)
β_{SC}	toroid/scallop tangency angle
ρ_∞	free stream density (kg/m^3)
ρ_e	boundary-layer edge density (kg/m^3)
θ	boundary layer momentum thickness (m)

μ_{∞}	free stream viscosity (kg/m · s)
μ_e	boundary layer edge viscosity (kg/m · s)
μ_w	wall viscosity (kg/m · s)

Subscripts

∞	free stream condition
0	reservoir condition
B	aeroshell base
e	edge condition
FR	Fay-Riddell
lam	laminar condition
N	aeroshell nose
S	aeroshell shoulder
SC	aeroshell scallop
T	aeroshell toroid
turb	turbulent condition
TR	transition
w	wall condition

Acronyms

CFD	Computational Fluid Dynamics
F-TPS	flexible thermal protection system
HIAD	Hypersonic Inflatable Aerodynamic Decelerator
IHEAT	Imaging for Hypersonic Experimental Aerothermodynamic Testing
IRVE	Inflatable Reentry Vehicle Experiment
LAL	Langley Aerothermodynamic Laboratory
LAURA	Langley Aerothermodynamic Upwind Relaxation Algorithm
SLA	Stereo-Lithographic Apparatus

Introduction

An experimental study has been conducted to define the aeroheating environment of a Hypersonic Inflatable Aerodynamic Decelerator (HIAD) with a flexible thermal protection system (F-TPS). The goal of this study was to determine the effects of surface deflections on boundary-layer transition and convective heating levels. Hypersonic wind tunnel testing was conducted using aeroshell models with rigid, nonsmooth surfaces that simulated the deformation under flight pressure loads, referred to as “scalloping”, that could be experienced during the flight of a HIAD with an F-TPS. Boundary-layer transition and convective heating data were obtained on these deflected outer mold line (OML) models using global phosphor thermography. Computational simulations were also performed for comparisons with the measurements and to provide boundary layer parameters for use in correlation of the data.

The basis of this study was a vehicle geometry similar to that of NASA’s Inflatable Reentry Vehicle Experiment (IRVE) flight test project. However, the ground test conditions were more severe and the F-TPS deflections were greater than expected for the IRVE flight tests, thus providing a conservative basis for analysis. These data may be more relevant to potential future HIAD flights that could experience more challenging environments than those of the flight test

project. Correlations for deflected-OML transition onset and heating augmentation were generated from the wind tunnel data for this purpose.

In addition to the relevance of this study to the IRVE flight test project, the data from this study are also intended for use in the future development and/or validation of numerical methods for simulation of flow fields over blunt bodies with an F-TPS. The accuracy of these tools in the prediction of boundary-layer transition and surface heating will need to be determined before application to future HIAD systems.

HIAD Background and History

HIAD technology offers an effective, mass-saving alternative to conventional aerodynamic decelerators. Relative to a rigid TPS aeroshell, a HIAD F-TPS aeroshell has lower mass and a smaller packaging volume, but when deployed and inflated it provides a large surface area for drag production, resulting in a lower ballistic coefficient than a rigid aeroshell of equivalent surface area. The lower ballistic coefficient of the HIAD results in lower heat fluxes and integrated heat loads, thus reducing the performance demands on the F-TPS material.

The inflatable aeroshell concept was first proposed in the 1960s and was then referred to as a “ballute”, from “balloon” + “parachute”. Since then, various inflatable configurations have been proposed and studied (e.g., Ref. 1), such as attached, trailing, tension cone, ram-inflated, etc. However, no successful hypersonic flight test had ever been conducted with an inflatable system until NASA initiated the Inflatable Reentry Vehicle Experiment Flight Project to mature and validate this technology (Ref. 2).

The first IRVE flight test (Ref. 3) in 2007 failed to exit the launch vehicle due to a launch vehicle anomaly that was unrelated to HIAD technology. A duplicate of this vehicle was commissioned and in 2009 the IRVE-II launch resulted in the first successful flight of a HIAD (Ref. 4). The IRVE-II flight test demonstrated exo-atmospheric inflation of the aeroshell and stable flight from hypersonic through subsonic speeds. However, because the IRVE-II vehicle was launched from a small sounding rocket, the aeroheating environment was quite benign. The maximum Mach number was ~ 5 , which produced peak heat fluxes of only $\sim 2 \text{ W/cm}^2$. Nevertheless, the success of IRVE-II provided the foundation for the next step in HIAD technology development, the IRVE-3 flight test¹ and the HIAD Project (Ref. 2).

The successful IRVE-3 flight test in 2012 was a direct follow-up to IRVE-II, with the overall goal of demonstrating HIAD performance and gathering flight data in a mission-relevant environment (Ref. 5). The primary requirement for IRVE-3 was to demonstrate F-TPS survivability during the hypersonic segment of the flight at heating levels an order-of-magnitude higher than IRVE-II, and so it was launched on a larger, three-stage sounding rocket to obtain greater entry velocity (maximum Mach ~ 10). This objective was achieved with the vehicle reaching a peak heating rate of $\sim 15 \text{ W/cm}^2$ at a Mach number of 7.

¹ Although the nomenclature for the flight test numbers differs, i.e., IRVE, IRVE-II and IRVE-3, these are the official designations.

Experimental Tools and Methods

Model Design and Fabrication

Model Fabrication

Ceramic wind tunnel models for this study were fabricated following the process discussed in Ref. 6. First, a pattern is generated using a rapid-prototyping stereo-lithography apparatus (SLA). An investment mold is then constructed from the SLA pattern and cured. Next, a silica-ceramic slip casting is made from the mold and sintered at high temperature. Finally, the slip-cast ceramic model is fired at high temperature and coated with a thermographic phosphor compound. The ceramic model is then mounted on a stainless steel sting through the aft end of the payload section. The geometries of the wind tunnel models are discussed in the following sections and the OML dimensions for all models are listed in Table 1. As will be discussed below, the model surface geometries were defined to simulate those of aeroshells with deflected F-TPS surfaces, but in all cases the actual wind tunnel models had rigid surfaces.

Baseline Smooth Model Geometry

Wind tunnel models for the test program were derived from the aeroshell of the IRVE-3 flight test vehicle. As shown in Figure 1, the flight vehicle had two components: a solid centerbody and an inflatable aeroshell. The centerbody carried the inflation system, an attitude control system, and cameras to record the inflation of the aeroshell. The aeroshell, which was mounted to the spherical nose-cap of the centerbody, consisted of a series of inflatable toroids over which the flexible thermal protection system was attached. As shown in Figure 2, the aeroshell geometry was a 60 deg sphere-cone geometry with a maximum radius (R_B) of 1.500 m, a nose radius (R_N) of 0.1905 m, and a shoulder radius (R_S) of 0.0508 m. The baseline wind tunnel model was a 3.000-in. radius, 0.0508-scale representation of this IRVE-3 flight test geometry. For the baseline model, the outer mold line was fabricated as though the TPS was smooth and rigid, as opposed to flexible. For consistency with parametric model nomenclature discussed below, the smooth OML model will be referred to as IRVE Scallop-0

A noteworthy aspect of this geometry was the ratio of the nose radius to the vehicle base radius, $R_N/R_B = 0.1270$, which was relatively small in comparison to, for example, the value of 0.500 for the Mars Science Laboratory Aeroshell. The nose radius of the IRVE-3 was designed to be as small as possible in order to increase the convective heating at the nose of the vehicle. This design choice was obviously contrary to the normal process followed in designing an operational vehicle. However, the purpose of this flight test was to generate the highest possible heating levels to demonstrate the survivability of the F-TPS at high heating fluxes. Given the relatively low entry velocity produced by the sounding rocket that carried the IRVE-3 vehicle, high heating levels could only be obtained by sharpening the nose.

Engineering Demonstration Unit Deflected OML Geometry

In contrast to the smooth-OML IRVE Scallop-0 baseline wind tunnel model, the OML of the actual IRVE-3 aeroshell experienced deflections of the F-TPS around the supporting structural elements during flight due to aerodynamic loads. As shown in Figure 3, the underlying structure

of the aeroshell consisted of a solid nose cap surrounded by a series of stacked toroids held together by tension straps. The flexible TPS (which had not yet been attached to the vehicle in this image) deflects around these structural elements under flight pressure loads (except at the solid nose cap) creating a nonsmooth surface. Additional information on the design of the IRVE-3 structure and F-TPS can be found in Refs. 7 - 8.

There were no structural modeling capabilities available prior to launch that could be used to predict the extent of the F-TPS deflections and the shape of the resulting nonsmooth OML. Some experimental information on F-TPS deflections was obtained during structural testing of a test article (Ref. 8). This Engineering Demonstration Unit (EDU) consisted of a full-scale replica of the IRVE-3 flight vehicle, including the F-TPS, as shown in Figure 4. This EDU was wrapped in a vacuum bag and subjected to a differential pressure load approximately equivalent to the expected peak flight dynamic pressure load. As shown in Figure 5, the pressure load caused the F-TPS to be pulled into the gaps between the structural toroids and tension straps to form scalloping patterns.

This static ground test did not provide an exact duplication of flight conditions due to both the uniform pressure loading across the aeroshell and the presence of the vacuum bag, which was thought to accentuate scalloping of the F-TPS around the structural elements. Nevertheless, this test provided the only information available for estimation of the in-flight OML deflections and was thus used as the basis for the design of a deflected-OML wind tunnel model.

A 3.000-in radius wind tunnel model of the IRVE EDU was designed using surface laser scan measurements of the test article obtained during the static pressure testing. This solid model incorporated the smooth nose section and the complex, three-dimensional scalloping between the toroids and structural straps.

Parametric Deflection Models

The deflected-OML IRVE EDU model discussed above provided the most “flight-like” geometry for the wind tunnel test program. However, additional parametric deflection models were fabricated in order to undertake a more comprehensive examination of F-TPS scalloping on aeroheating environments. In contrast to the IRVE EDU geometry, which represents the OML scalloping resulting from a single pressure load case (roughly equivalent to flight peak dynamic pressure), the parametric OML models were designed to provide data across a wide range of scalloping levels. These parametric models also provide a simplified and easily reproducible geometric representation of OML scalloping that can be used for further testing or for computational studies, whereas the IRVE EDU geometry, while more realistic, was based on a point-cloud database that cannot easily be archived or represented in print.

The parametric geometries were based on a simplified representation of the support structure and F-TPS of the IRVE-3 vehicle. The OML dimensions of the parametric models are shown in Figure 6. Like the IRVE-3 geometry, the parametric models were 3.000-in. radius, 60 deg sphere-cones with a relatively sharp nose. For convenience in wind tunnel model design, the nose and shoulder radii ratios were changed slightly from those of the flight vehicle, resulting in a nose to max-radius ratio of $R_N/R_B = 0.125$ and a shoulder to max-radius ratio of $R_S/R_B = 0.03125$, as opposed to the flight vehicle ratios of 0.127 and 0.03390, respectively. The parametric models (and also the baseline and EDU models) differed from the flight article in

having a closed base, rather than an open base. The closed base provided a more solid structural element into which to mount the wind tunnel support sting than an open base and in no way affected the aeroshell forebody heating measurements that were the point of this study.

The scalloping of the parametric models was based on specified deflections over a series of, regularly-spaced, perfectly-circular cross-section toroids. As shown in the close-up section of Figure 6, five parametric scalloping levels were considered. The wind tunnel models based on these scalloping levels were designated as “IRVE Scallop- β_{SC} ”, where the larger the value of β_{SC} , the greater the resulting scalloping heights.

The exact geometry of the parametric scalloping is shown in Figure 7. The relevant parameters are the toroid radius (R_T), the scallop radius (R_{SC}), and the scallop angle (β_{SC}). This angle represents the tangency point of the toroid and the scallop circular cross-sections. A solid surface was defined by joining together the surfaces of the toroids at this tangency point with circular arc-sections based on the scallop radius. The resulting OML deflection then has a maximum height (k_{SC}) defined by the vertical distance from the baseline smooth OML and a length (L_{SC}) equal to twice the toroid radius. These parameters (which are also listed in Figure 7) provide the information to define five identical scallops between the six toroids. The parametric models also included scallops between the solid nose and the first toroid and between the last toroid and the shoulder. These two scallops were defined by scaling the length of a regular scallop to fit the spanwise distance between the nose and the first toroid, and between the last toroid and the shoulder, respectively, but maintaining the original scallop height. The scallop parameters for these models are listed in Table 2. Average and maximum values for the height of the three-dimensional IRVE EDU scallop features (which were nonuniform) based on data from multiple surface locations are also listed in this table.

Side-view renderings of the models of the IRVE Scallop- β_{SC} geometries are shown in Figure 8 along with a rendering of the IRVE EDU model. The smallest parametric scalloping model, IRVE Scallop-2.5, had an OML approaching that of the smooth baseline model (not shown), while the larger parametric scalloping models (IRVE Scallop-15 and IRVE Scallop-20), had heights that were much larger than any practical flight vehicle design likely would have. The height of the IRVE EDU deflections appears to be bounded by that of the IRVE Scallop-10 and IRVE Scallop-15 models. However, the IRVE EDU geometry had a complex, irregular, three-dimensional scalloping pattern, whereas the parametric models all had a simple and consistent axisymmetric scalloping pattern. Thus, it is unlikely that a simple equivalency in height scales between the axisymmetric and 3D scalloping would produce exact equivalency in flow field effects.

Test Facility and Conditions

Wind Tunnel Test Conditions

Testing of the IRVE models was performed in NASA’s Langley Aerothermodynamics Laboratory (LAL) 20-Inch Mach 6 Air Tunnel. This facility is described in brief below, and more detailed information on the LAL can be found in Refs. 9 - 10.

The NASA LaRC 20-Inch Mach 6 Air Tunnel (Figure 9) is a blow-down facility in which heated, dried, and filtered air is used as the test gas. The tunnel has a two-dimensional contoured

nozzle that opens into a 20.5×20.0 in test section. The tunnel is equipped with a bottom-mounted injection system with a −5 deg to +55 deg pitch range and ±5 deg yaw range that can transfer a model from a sheltered model box to the tunnel centerline in less than 0.5 sec. Run times of up to 15 minutes are possible in this facility, although for the current aeroheating study run times of only a few seconds were required. The nominal reservoir conditions of this facility produce perfect-gas free stream flows with Mach numbers between 5.8 and 6.1 and unit Reynolds numbers of $0.5 \times 10^6/\text{ft}$ to $8.3 \times 10^6/\text{ft}$. With the wide Reynolds number operating range capable of producing laminar, transitional, or turbulent flow on most vehicle geometries, this tunnel is primarily used for heat-transfer and boundary-layer transition studies.

Data were obtained in Test Series 6979 on each model at five unit Reynolds numbers from $2.01 \times 10^6/\text{ft}$ to $8.34 \times 10^6/\text{ft}$. Angle of attack was varied from 0 deg to +18 deg, in 6 deg increments, at each Reynolds number. Free stream conditions for the test are listed in Table 3. Entries in these tables are sorted first by model, then by angle of attack, and then by free stream unit Reynolds number. The heat-transfer film coefficient (h_{FR}) values listed in these tables were based on Fay-Riddell (Ref. 11) calculations for the 0.375 in nose radius of the models² at cold-wall (300 K) conditions. The enthalpy term (ΔH_{tot}) was based on the difference between the free stream total enthalpy and the wall enthalpy at 300 K. The conditions listed in these tables are nominal values based on averages of all runs at a given condition. As the run-to-run variations were very slight (~1%), all supporting analyses were performed using these nominal values.

Data Acquisition, Reduction, Uncertainty and Presentation

Data Acquisition

Aeroheating data were obtained using the two-color, relative-intensity, global thermographic phosphor method (Ref. 12) and reduced using the Imaging for Hypersonic Experimental Aerothermodynamic Testing (IHEAT) code (Ref. 13). In this method, a model is illuminated by ultraviolet light sources that produce temperature-dependent fluorescence of the phosphor coating. Images of the model are taken in the tunnel before and during a run using a three-color, charge-coupled device camera and the images are processed to determine temperature and heat-transfer distributions. Flow-field schlieren images were also obtained for each model/angle-of-attack condition.

Although a global imaging technique was employed, it was not possible to obtain good imagery over the entire model forebody at the lower angles of attack owing to model geometry and optical access limitations. As shown in Figure 10, the camera view direction was from above and ahead of the models. For the 0 deg case, and to lesser extent the +6 deg case, the camera view was almost parallel to the bottom (windward side) of the models and thus the image quality for this region is poor, as will be seen in subsequent presentation of the data.

² Note that the IRVE EDU and IRVE Scallop-0 models actually had nose radii of 0.381. However the difference in Fay-Riddell coefficients due to nose radius was less than 1% and was ignored in the data analysis.

Data Reduction

The IHEAT code uses calibrations to convert the intensity data from each image pixel to temperatures. Heat-transfer film coefficients are then determined by assuming a step function in heat transfer beginning at injection of the model into the tunnel, which corresponds to a parabolic temperature-time history. Heat-transfer data from IHEAT are typically reported in terms of the ratio h/h_{FR} , where h_{FR} is the heat-transfer film coefficient resulting from a Fay-Riddell computation for a reference hemisphere of specified radius (in this case, the 0.375 in radius of the nose). The heat-transfer film coefficient is defined in terms of enthalpy as:

$$h = q/\Delta H_{tot} = q/(H_{AW} - H_w) = q/(H_0 - H_{300K}) \quad (1)$$

In the calculation of the heat-transfer film coefficient, it is assumed that, for a blunt body, the adiabatic wall enthalpy H_{AW} is equal to the free stream total enthalpy of the tunnel, H_0 and the wall temperature H_w is set to the assumed ambient temperature of 300K. This heat transfer coefficient definition provides a theoretically near-constant value over the course of a run since the decrease in time of the heat transfer rate in the numerator as the model surface becomes hotter is balanced by the decrease of the enthalpy term in the denominator.

The two-dimensional (2-D) image data obtained from IHEAT were corrected for optical perspective effects and mapped to a three-dimensional (3-D) surface representation of the model geometry. To accomplish this mapping, perspective, translational, and rotational transformations were first performed on the 3-D surface representation until its 2-D projection matched that of the 2-D image data. The image data were then assigned transformed (x, y, z) coordinates based on interpolation between the image and surface geometry and then the transformation was inverted to obtain an orthographic, 3-D heating distribution map.

Data Uncertainty

The experimental uncertainty for convective heat transfer measurements on blunt bodies in the LAL facilities has previously been quantified as a function of uncertainties resulting from: the data acquisition method ($\pm 10\%$); the flow quality and test-condition repeatability ($\pm 5\%$); and the accuracy of the 3D mapping process ($\pm 10\%$), which results in an overall root-sum-squared value of $\pm 15\%$. Experience with this technique indicates that these values are usually conservative and as will be shown later, the predicted and measured heating distributions were in close agreement (generally less than $\pm 5\%$) for laminar, smooth-wall cases.

Data Presentation

The heating data will be represented throughout in the usual manner for phosphor thermography studies in terms of h/h_{FR} , where h_{FR} is the film coefficient based on Fay-Riddell theory for the model nose radius. The heating data will be shown in both a qualitative format through global heating images and in a quantitative format through centerline heating plots.

In the body of this report, the global heating images were reduced in resolution and size in order to fit multiple images in each figure. However for reference, larger, higher resolution images for every run are shown in the Appendix.

Computational Method

Flow field predictions were performed using the Langley Aerothermodynamic Upwind Relaxation Algorithm (LAURA) code (Refs. 14 – 15) to generate heating values for comparisons with the experimental data as well as to provide boundary layer parameters for use in correlation of the heating and transition data. LAURA is a three-dimensional, finite-volume solver that includes perfect gas and nonequilibrium chemistry options, a variety of turbulence models, and ablation and radiative transport capabilities. In this study, the laminar, perfect gas air model was used for the wind tunnel predictions.

Solutions were generated using a structured grid of the ideal, smooth-OML geometry. Grid adaption to the solution features was performed to align the grid outer boundary with the shock and to cluster cells near the surface to produce wall cell Reynolds numbers on the order of 1 to 10. Free stream conditions were set to the nominal wind tunnel conditions listed in Table 3 and the wall temperature was set to a constant 300 K. The use of a constant wall temperature was acceptable because the heat-transfer film coefficient varies only very slightly over the range of wall temperatures produced in this facility. Computed film coefficients were normalized by the Fay-Riddell value for the test condition to determine h/h_{FR} .

As noted above, solutions were generated only for the smooth-OML geometry. While it would have been theoretically possible to generate solutions for the scalloped OML geometries, the level of effort would have been far greater due to the complex grids required to represent these surfaces. Furthermore, the validity of numerical models for turbulent flow fields over complex, irregular surfaces such as that of a scalloped F-TPS has not been established. In fact, obtaining data for the development and/or validation of such models was one of the purposes of this test program.

Results and Analysis

Overview

Data were obtained for each configuration / Reynolds number / angle-of-attack condition. The heating data provided information on both boundary-layer transition and heating augmentation effects due to OML scalloping and will be presented in detail. Correlations for these effects were generated from the wind tunnel data and their application to the IRVE-3 trajectory will be presented.

Flow Field Schlieren Imagery

Schlieren images for each model (except for the IRVE Scallop-0 smooth model) at angles of attack of 0 deg, 6 deg, 12 deg and 18 deg are presented in Figure 11 - Figure 14. These images reveal the complex nature of the flow fields created by the scalloping. For almost all angle-of-attack cases, the scallop peaks produced shock waves on the leeward side of the model (where the flow is supersonic at the edge of the boundary layer) that reflected off the main bow shock back toward the surface, creating a complicated pattern of shock reflections and interactions. The existence of these shock waves implies a cavity-like flow field between the peaks and valleys in which the peaks protrude above the subsonic boundary layer into the supersonic post-

shock flow. As shown in Figure 15, the scallop heights were indeed much larger than the boundary-layer height for the IRVE Scallop-10, -15 and -20 models at most conditions. These comparisons are approximate, in that the boundary-layer heights shown were determined from laminar, smooth-wall solutions. However, while the actual boundary-layer heights over the scalloped models may have differed from the smooth-OML computations, the schlieren images confirm that the peaks were higher than the boundary layer.

Smooth OML Model Data

The aeroheating data from the IRVE Scallop-0 smooth OML model are presented in Figure 16 - Figure 19. In each figure, data are shown for all of the Reynolds numbers ($2.01 \times 10^6/\text{ft}$ to $8.34 \times 10^6/\text{ft}$) at each of the respective angles of attack (0 deg to 18 deg). These data are mostly unremarkable and were obtained to provide a baseline for comparison with deflected-OML data, as well as to provide a validation data set for the smooth-wall CFD predictions. At each angle of attack, the centerline heating distributions were invariant with Reynolds number, which indicates that the boundary layer remained laminar except for the two highest Reynolds numbers at $\alpha = 18$ deg, for which conditions transition occurred on the leeward centerline.

As noted previously, the IRVE flight vehicle was intentionally designed with a very small nose radius in order to produce the higher heating rates needed to demonstrate the performance of the F-TPS. As seen in these plots, this design feature produced heating levels at the nose approximately 4 times greater than on the conical flank of the model.

Deflected OML Model Data

Data from the IRVE EDU deflected OML model are shown for all Reynolds numbers at each angle of attack in Figure 20 - Figure 23. As discussed earlier, the IRVE EDU model geometry was derived from laser scan data obtained during static pressure testing of a full-scale IRVE-3 test article at a pressure load approximately equal to the flight peak dynamic pressure.

Heating distributions on the IRVE EDU model differed substantially from those obtained on the IRVE Scallop-0 smooth OML baseline model. The model surface scalloping, which was based on the deflections of the F-TPS around the toroids and tension straps, produced a three-dimensional pattern of heating minima and maxima. The measured heating levels varied with Reynolds number over most of the vehicle (except near the smooth nose) for all conditions, indicating that the boundary-layer flow was transitional or turbulent.

It is noteworthy that for many of the higher Reynolds number cases, heating levels on the leeward conical flank approached or even exceeded those at the nose, because predicted, smooth-OML nose heating levels were used as the design condition for the entire IRVE-3 F-TPS. However, even though the IRVE EDU flank heating data exceeded the smooth-OML nose levels, this result did not affect the IRVE-3 mission planning for several reasons. First, was that the IRVE EDU surface deflections were based on the peak dynamic pressure condition, which occurs after the peak convective heating point on the trajectory, where the magnitude of the overall heating levels will be considerably lower. Second, is that the expected flight Reynolds numbers were almost an order-of-magnitude lower than those of the wind tunnel test conditions. Third, as discussed previously, was that the static pressure test from which the IRVE EDU data were obtained was thought to accentuate the OML deflections. Thus, while these substantial

levels of heating augmentation are factors that must be considered for future missions, they did not affect the design of the IRVE-3 vehicle.

In contrast to the IRVE flight test articles, a future operational vehicle would not have a sharpened nose and thus the levels of nose and conical flank heating would be closer. If substantial OML deflections were then to occur, the elevated turbulent heating levels on the conical flank of the aeroshell could exceed those at the nose and would then represent the critical F-TPS design condition, as opposed to those at the nose for the IRVE-3 flight test.

Parametric OML Deflection Models Data

The IRVE EDU model data presented in the previous section provide evidence that the effects of OML deflections need to be evaluated in the development of future flight vehicles. However, while the IRVE EDU data serve to illustrate the effects of OML scalloping, this model geometry is not an optimal basis for future study because it was derived from a point cloud of laser scan data that cannot easily be defined in an archival print format. Additionally, the IRVE EDU geometry represents a single OML deflection case that, while relevant to the IRVE-3 flight test, is not necessarily relevant to other potential missions. In contrast, the IRVE Scallop- β_{SC} models are based on a simple, and easily reproduced, parametric geometry definition and provide data for a wide range of scallop height effects.

The parametric model heating data are shown in Figure 24 - Figure 27 for the IRVE Scallop-2.5 model, Figure 28 - Figure 31 for the IRVE Scallop-5 model, Figure 32 - Figure 35 for the IRVE Scallop-10 model, Figure 36 - Figure 39 for the IRVE Scallop-15 model and Figure 40 - Figure 43 for the IRVE Scallop-20 model. In these figures, the data are shown for each Reynolds number at a given angle of attack. Smooth-OML, IRVE Scallop-0 centerline heating data are also shown in each figure for comparison with the parametric-OML data. Scalloping effects on heating were observed on all models for all angle-of-attack/Reynolds-number test points. These effects were seen for both laminar and transitional/turbulent boundary layer flows.

Laminar effects can be seen in the IRVE Scallop-2.5 and IRVE Scallop-5 model windward side data (Figure 24 - Figure 31) for all Reynolds numbers and also for small regions of the leeside data at lower Reynolds numbers. For these cases, there was little or no variation in heating levels with Reynolds number. However, the distributions revealed a small spanwise oscillation about the mean distribution (represented by the smooth OML data) that corresponds to the scallop peaks and valleys. Unfortunately, because of the shallow wind-side viewing angle noted previously, these oscillations were somewhat smeared on the windward side of the models. In contrast however, the oscillations were very well defined on the leeward side of the models.

Boundary-layer transition onset and augmented turbulent heating levels can be seen in the remainder of the data set (Figure 32 - Figure 43) from the IRVE Scallop-10, IRVE Scallop-15 and IRVE Scallop-20 models, as well as on IRVE Scallop-2.5 and IRVE Scallop-5 models at the higher Reynolds number. For these cases, the distributions showed a spanwise series of minima and maxima with mean levels that increased with Reynolds numbers, which was indicative of transitional/turbulent flow. Heating augmentation well above laminar levels can be seen on both the windward and leeward sides, with the maximum values approaching or slightly exceeding the nose heating levels for the larger scalloping, higher Reynolds numbers cases. Windward side

heating augmentation varied from 2-3 times the smooth laminar levels, while leeward side augmentation varied by a factor of 2-4.

The relative levels of scalloping effects as a function of scallop size are illustrated in the next series of figures, in which data from all of the parametric models are shown for each angle-of-attack / Reynolds number conditions. Data are shown for all Reynolds numbers at $\alpha = 0$ deg in Figure 44 - Figure 48, $\alpha = 6$ deg in Figure 49 - Figure 53, $\alpha = 12$ deg in Figure 54 - Figure 58 and $\alpha = 12$ deg in Figure 59 - Figure 63. These figures show the upstream movement in transition onset location and the increase in mean heating levels with increasing scallop height.

Correlation of Wind Tunnel Data and Extrapolation to Flight

In order to make use of the wind tunnel data for future HIAD missions, the effects of scalloping on boundary-layer transition and convective heating observed in the wind tunnel data must be extrapolated to flight conditions. The boundary-layer parameters and scallop dimensions are the independent variables used to correlate these effects, i.e.,

$$\text{transition, heating} = f(M_e, Re_\theta, k_{SC}, L_{SC}, \theta, \mu_e, \mu_w, etc) \quad (2)$$

Scallop Heating Bump Factors

The development of a correlation for scalloping effects on heating will be developed first. To begin, the smooth-wall turbulent heat-transfer film coefficient, h_{turb} , is defined as the sum of the laminar component plus an increment due to turbulence:

$$h_{\text{turb}} \equiv h_{\text{lam}} + (h_{\text{turb}} - h_{\text{lam}}) = h_{\text{lam}} + \Delta h_{\text{turb}} \quad (3)$$

These values can easily be obtained via computational methods for a smooth geometry. However, for a nonsmooth, scalloped geometry, the values cannot be easily predicted. For the deflected OML case, the scallop-augmented turbulent heat transfer film coefficient, $h_{k,\text{turb}}$, can be written similarly as:

$$h_{k,\text{turb}} \equiv h_{k,\text{lam}} + \Delta h_{k,\text{turb}} \quad (4)$$

This equation can be rewritten in terms of the smooth-wall components as:

$$h_{k,\text{turb}} = h_{\text{lam}} \left(\frac{h_{k,\text{lam}}}{h_{\text{lam}}} \right) + \Delta h_{\text{turb}} \left(\frac{\Delta h_{k,\text{turb}}}{\Delta h_{\text{turb}}} \right) \quad (5)$$

Now define the ratios of the scalloped-to-smooth terms for the laminar and turbulent components as:

$$BF_{\text{lam}} = (h_{k,\text{lam}} / h_{\text{lam}}) \quad (6)$$

and

$$BF_{\text{turb}} = (\Delta h_{k,\text{turb}} / \Delta h_{\text{turb}}) \quad (7)$$

Substitute these definitions into Eq. (5) to obtain:

$$h_{k,turb} = h_{lam} BF_{lam} + \Delta h_{turb} BF_{turb} \quad (8)$$

Finally, nondimensionalize by the smooth-wall, laminar term to obtain:

$$\frac{h_{k,turb}}{h_{lam}} = BF_{lam} + \left(\frac{\Delta h_{turb}}{h_{lam}} \right) BF_{turb} \quad (9)$$

For flight conditions, the effects of scalloping on heating can then be determined through Eq. (9) by applying these bump factors - that will be obtained from the wind tunnel data - to smooth-wall predictions for the laminar and turbulent components:

$$\frac{h_{k,turb}}{(h_{lam})_{CFD}} = (BF_{lam})_{WT} + \left(\frac{\Delta h_{turb}}{h_{lam}} \right)_{CFD} (BF_{turb})_{WT} \quad (10)$$

To determine these bump factors, heating levels on the scalloped models were extracted from the data set at the centerline scallop heating peaks (as illustrated by the example in Figure 64) for comparison with the predicted, smooth-wall values. Note that the data from the nose were not used because the wind tunnel models' noses were smooth, not scalloped, in order to properly represent the smooth, solid centerbody of an actual flight vehicle.

Following the approach from Ref. 16 the ratio of measured heating to the CFD prediction for smooth-wall laminar heating at the scallop peaks, $h_k/(h_{lam})_{CFD}$, was plotted against Re_θ . The results are presented in Figure 65 - Figure 69, where the individual plots show the data for all Reynolds numbers and angles of attack for the respective scallop height. Additionally, the smooth-wall turbulent limit - as determined from predictions - is also shown in each plot.

From these data, it can be seen that as Re_θ increases and the boundary-layer becomes fully-turbulent, the heating data for a given scallop height asymptotically approach a linear limit defined by:

$$\frac{(h_{k,turb})_{WT}}{(h_{lam})_{CFD}} = (A_k)_{WT} + (B_k)_{WT} (Re_{\theta,lam})_{CFD} \quad (11)$$

In Eq. (11), the first coefficient, A_k , defines the laminar component of heating augmentation due to scalloping and the second term, B_k , defines the turbulent heating increment slope due to scalloping. Also, note that the value of Re_θ used in this formulation was the predicted *laminar* value. The values of A_k and B_k for each scallop height determined by curve-fitting the data sets are also shown in the comparison figures.

In fitting these data, the values for the highest angle-of-attack, $\alpha = 18$ -deg, were excluded. As noted previously, the schlieren images showed that the shock waves generated by the larger scallops interacted with the bow shock to produce a complex system of waves and reflections. These wave structures increased in strength with scallop height and angle of attack. As a result, the flow fields for the $\alpha = 18$ -deg cases were so dissimilar from the other cases that the measured heating levels fell outside the acceptable limits of correlation. Although these cases were excluded from consideration, the heating levels for $\alpha = 18$ -deg were generally found to be lower

than the resulting fits, thus these fits provide a conservative estimate for heating effects at high angle of attack.

In order to generalize this correlation to arbitrary scallop heights, curve fits for the A_k and B_k coefficients were generated in terms of the independent variable k_{SC}/R_B (the ratio of scallop height to vehicle maximum radius). These fits are shown in Figure 70 - Figure 71. The curve fits were developed with the constraints on the smooth-wall ($k_{SC} = 0$) limits of $A_0 = 1$ and $B_0 = 0.006$. The A_0 constraint reflects the fact that there is no laminar augmentation for a smooth wall and the B_0 constraint is based on the smooth-wall limit for the turbulent heating increment. As the test Reynolds number range was insufficient to generate fully-turbulent flow over the smooth model, this value was based on a correlation of CFD predictions for the smooth wall turbulent component. The resulting curve fits for these coefficients are then given by:

$$(A_k)_{WT} = 1 + 7.3457(k_{SC}/R_B) \quad (12)$$

and

$$(B_k)_{WT} = 0.006 + 0.049294(k_{SC}/R_B)^{0.51841} \quad (13)$$

The bump factors can now be determined by comparing Eqs. (9) and (11), with the assumption that both the laminar, smooth-wall data and predictions and the turbulent, smooth-wall data and predictions are in agreement.

$$(BF_{lam})_{WT} + \left(\frac{\Delta h_{turb}}{h_{lam}} \right)_{CFD} (BF_{turb})_{WT} = (A_k)_{WT} + (B_k)_{WT} (Re_{\theta, lam})_{CFD} \quad (14)$$

From which the bump factors can be defined as:

$$(BF_{lam})_{WT} = (A_k)_{WT} \quad (15)$$

and

$$(BF_{turb})_{WT} = (B_k)_{WT} (Re_{\theta, lam})_{CFD} \left(\frac{h_{lam}}{\Delta h_{turb}} \right)_{CFD} \quad (16)$$

To complete the definition of the turbulent bump factor, note that in the limit of a smooth wall without scalloping ($k_{SC} = 0$), the bump factors must be equal to unity. For this case, Eq. (14) reduces to:

$$1 + \left(\frac{\Delta h_{turb}}{h_{lam}} \right)_{CFD} = (A_0)_{WT} + (B_0)_{WT} (Re_{\theta, lam})_{CFD} \quad (17)$$

Recalling that $A_0 = 1$, this equation can be rearranged as:

$$\frac{1}{(Re_{\theta, lam})_{CFD}} \left(\frac{\Delta h_{turb}}{h_{lam}} \right)_{CFD} = (B_0)_{WT} \quad (18)$$

Substituting Eq. (18) into Eq. (16) completes the definition of the turbulent bump factor

$$(BF_{\text{turb}})_{\text{WT}} = (B_k/B_0)_{\text{WT}} \quad (19)$$

where $B_0 = 0.006$ is the smooth-wall, $k_{\text{SC}} = 0$, limit from Eq. (13).

With these bump-factor definitions, the heating environments on a scalloped geometry can now be given by:

$$h_{k,\text{turb}} = (A_k)_{\text{WT}} (h_{\text{lam}})_{\text{CFD}} + (h_{\text{turb}} - h_{\text{lam}})_{\text{CFD}} (B_k/B_0)_{\text{WT}} \quad (20)$$

Equation (20) can now be used to estimate the effects of scalloping on heating at arbitrary conditions based on the computational predictions for smooth-wall heating at those conditions and the wind-tunnel derived bump factors.

Simple Transition Onset Model

The analysis of the previous section provides a conservative method for estimating scallop heating effects as it is based on the assumption of fully-turbulent flow. In order to provide a more accurate estimate for heating levels, boundary-layer transition effects can be included through the use of an intermittency multiplication factor, I_{TR} , on the turbulent heating component, as given by:

$$h_{k,\text{turb}} = (A_k)_{\text{WT}} (h_{\text{lam}})_{\text{CFD}} + (h_{\text{turb}} - h_{\text{lam}})_{\text{CFD}} (B_k/B_0)_{\text{WT}} (I_{\text{TR}})_{\text{WT}} \quad (21)$$

The intermittency is based on the wind tunnel data and is defined by the function:

$$I_{\text{TR}} = \frac{1}{2} \left\{ 1 + \tanh \left[\frac{(\text{Re}_{\theta} - \text{Re}_{\theta,\text{TR}})}{(\Delta \text{Re}_{\theta,\text{TR}}/4)} - 2 \right] \right\} = \frac{1}{2} \{ 1 + \tanh [\Psi - 2] \} \quad (22)$$

As shown in Figure 72, this hyperbolic tangent function provides a smooth, asymptotic transfer from fully-laminar conditions to fully-turbulent conditions. The effective blending length between laminar and turbulent flow, in terms of the nondimensional parameter Ψ , is $\Delta\Psi \approx 8$ with a center offset to $\Psi = 2$ (i.e., $\Psi \approx -2$ to 6). This offset is an empirical correction to account for the difference between the actual location at which fluctuations begin in the boundary layer and the value at which transition can first be detected through surface heat-transfer or temperature measurements.

From inspection of the heating-data ensembles for each scallop height in Figure 65 - Figure 69, the transition region in the Re_{θ} vs. $h_k/(h_{\text{lam}})_{\text{CFD}}$ parameter space was identified as the interval where the heating levels follow an “s-curve” like path between the laminar baseline and the fully-turbulent asymptote. The parameters $\text{Re}_{\theta,\text{TR}}$ and $\Delta \text{Re}_{\theta,\text{TR}}$ were then determined for each scallop height and general curve fits for these parameters were developed as shown in Figure 73 and Figure 74 with the fit equations given by:

$$\text{Re}_{\theta,\text{TR}} = 1.3424 (k_{\text{SC}}/R_B)^{-0.84163} \quad (23)$$

and

$$\Delta \text{Re}_{\theta,\text{TR}} = 0.80494 \text{Re}_{\theta,\text{TR}} \quad (24)$$

The Re_θ vs. $h_k/(h_{lam})_{CFD}$ correlations are shown again in Figure 75 - Figure 79, but with the transition model of Eqs. (22)-(24) added to the curve fits. In these figures, the grey shaded region denotes the transition zone. For the smaller scallop height cases, there was a great deal of scatter in the data and the fits represent an approximate average of the onset location. However, for the larger scallop cases (IRVE Scallop-10, -15, and -20), the transition onset locations from the data and the correlations were in good agreement.

This simplified transition onset model provides an acceptable engineering correlation that reproduces the wind tunnel data set. However, the approach of developing a correlation in the Re_θ vs. $h_k/(h_{lam})_{CFD}$ parameter space is somewhat different than the usual methodology and it is not clear how well these results would scale to different flow conditions and/or vehicle sizes. Therefore, the transition data were also correlated using a more detailed model.

Detailed Transition Onset Model

To develop a more detailed transition model based on geometric and boundary-layer parameters, the transition onset location for each individual run was determined from examination of the centerline heating comparisons between the deflected OML data and the laminar, smooth-wall predictions. Transition locations were determined for both the leeward side and the windward side centerline. Boundary-layer parameters were then extracted from the laminar, smooth-wall solutions at the onset locations for use in correlating the data. However, before the detailed model is presented, some discussion on the methodology of determining the onset location is required.

Identification of the transition onset was difficult and the resulting data set is somewhat approximate. From a flow physics standpoint, transition onset can be defined as the point where smooth, steady, laminar flow in the boundary layer begins to break down. This location could, in theory, be determined through flow-field imaging and/or diagnostics techniques (e.g. laser velocimetry, high-frequency surface pressure measurements). However in this study, the only measurements available were the surface heating distributions. For heat transfer (or temperature) measurements, the differences between levels for laminar flow and levels at the onset of transitional flow are generally too subtle to permit precise definition of the onset location, even for a simple flow field such as that generated over a flat plate. For a flow field with nonsimilar boundary layer characteristics, such as on the current sphere-cone geometry with a scalloped OML, identification of the onset location becomes even more difficult and subject to interpretation.

For the purposes of this work, the tangent-slope-intercept method was employed to identify an approximate onset location. As shown in Figure 81, the transition onset location was identified as the point where a line drawn tangent to the slope of the heat-transfer distribution curve (actually through the approximate average peak-valley value) in the transition region intercepts the nominal, smooth-wall laminar value. While the method does not provide the true transition location, but rather a point somewhat downstream of that point, it does provide a definition consistent with methods commonly employed in previous literature on boundary layer transition determination from surface heating data. The offset is then approximately accounted for in the intermittency model by the shift of $\Psi -2$ in Eq. (22) discussed previously.

Having identified transition onset locations for each condition, the next step was to correlate these data in terms of boundary-layer flow field parameters. Following the approach of Refs. 17-20, a correlation was sought between a *disturbance* parameter and a *flow-field* parameter as illustrated in Figure 80. Various definitions for the disturbance and flow-field parameters have been proposed and analyzed by different researchers based on different data sets and interpretations thereof. None of those definitions is strictly applicable to the current work, as they were based on discrete and/or distributed surface roughness elements with heights on the order of, or less than, the boundary-layer height. As shown previously in Figure 15, the scallop heights were greater than (and in some cases *much* greater than) the boundary layer height for almost all conditions. Nevertheless, this approach was followed in order to attempt to develop an engineering-level fidelity correlation.

The parameter set considered for the correlation is given in Eq. (25). These variables represent: the boundary-layer momentum thickness Reynolds number, $Re_\theta = \rho_e U_e \theta / \mu_e$; the boundary-layer edge Mach number, M_e ; the scallop aspect ratio (height-to-length), k_{SC}/L_{SC} ; the scallop height normalized by momentum thickness, k_{SC}/θ ; and the boundary-layer edge-to-wall viscosity ratio, μ_e/μ_w .

$$\text{Transition} = f \{ Re_\theta, M_e, (k_{SC}/L_{SC}), (k_{SC}/\theta), (\mu_e/\mu_w) \} \quad (25)$$

A few points concerning the use of these variables are noteworthy.

- With respect to the momentum thickness Reynolds number and edge Mach number, some previous studies have indicated that use of the variable Re_θ/M_e decorrelates transition data when applied to blunt-body flow fields. However, it will be shown that $(M_e)^\beta$, can - for the correct value of β - contribute to correlation of blunt-body transition effects (at least for the current set of data) by accounting for the differences in the windward side and leeward side boundary-layer conditions.
- The ratio k_{SC}/θ is a common factor in transition correlations that provides a nondimensionalization of the scallop height by the boundary-layer momentum thickness
- The scallop aspect ratio k_{SC}/L_{SC} is analogous to the cavity aspect ratio, H/L - or height to length - used in analyses of cavity transition data.
- The ratio μ_e/μ_w (or similarly T_e/T_w or H_e/H_w , all of which forms relate energy content at the boundary layer edge to that at the wall) is derived from literature that showed a wall temperature ratio effect on transition. For the current study, the viscosity ratio variation was too small within the data set to determine conclusively the influence of this parameter. While it will be included in the transition correlation formulation, it is recognized that further data are required to better define the effects of wall viscosity (or equivalently the wall temperature) on scallop-wall transition.

In order to correlate the current data set, which includes large variations in angle of attack (in addition to other parameters), it must be recognized that the flow fields on the leeward side and on the windward side of the nose differ drastically at high angles of attack. Any viable correlation must be relevant for both sides, so to ensure this, correlation curve fits were

generated for the windward side data and leeward side data separately, as well as for the combination of windward side and leeward side data. If the individual windward side and leeward side fits differed greatly for a given set of correlation variables then that correlation was not considered to be acceptable.

Various disturbance and flow field parameters were considered for use in correlation of the transition data through a power-law relationship as per Eq. (26). Three different sets of parameters are derived from this general form as given by Eqs. (27) - (29). For consistency, all correlations are formulated with Re_θ as the only variable on the left-hand side of the equation. However, any of these equations could be rewritten with other flow-field variables moved from the right-hand side to left-hand side. A discussion of the merits of each form follows below.

$$y = C_{TR} x^{D_{TR}} : \text{general correlation form, where } y \equiv Re_\theta \quad (26)$$

$$Re_\theta = C_{TR} \left\{ (M_e)^\beta \left(\frac{k_{SC}}{L_{SC}} \right) \right\}^{D_{TR}} : \text{scallop parameter correlation} \quad (27)$$

$$Re_\theta = C_{TR} \left\{ \left[\left(\frac{k_{SC}}{\theta} \right) \left(\frac{\mu_e}{\mu_w} \right) \right] (M_e)^\beta \right\}^{D_{TR}} : \text{wind tunnel roughness correlation} \quad (28)$$

$$Re_\theta = C_{TR} \left\{ \left[\left(\frac{k_{SC}}{\theta} \right) \left(\frac{\mu_e}{\mu_w} \right) \right]^\alpha (M_e)^\beta \left(\frac{k_{SC}}{L_{SC}} \right)^\gamma \right\}^{D_{TR}} : \text{multiple parameter correlation} \quad (29)$$

Scallop Parameter Correlations

The *scallop parameter* correlation form given by Eq. (27) was derived from the simplified transition onset correlation of the previous section and accounts for the edge Mach number and scallop aspect ratio. This general form can be related directly to Eq. (23) by specifying the edge Mach number exponent as $\beta = 0$ and substituting $R_B = 6 \times L_{SC}$ for the current wind tunnel geometries. *Scallop parameter* correlations are shown in Figure 82 with various exponents on the edge Mach number, β . The scallop correlation parameters are listed in Table 4.

In these figures, and in subsequent figures, the individual leeward side and windward side transition onset locations for each scallop height, as determined from the data at each test condition, are shown. Three power-law curve fits are also shown: one fit for all the leeward side data; one fit for all the windward side data; and one fit for the combined leeward and windward side data sets. The curve fit equations are shown in each plot along with the linear correlation coefficient, R , for each fit. The R -value of a correlation can vary from 0 to 1, with a value of 1 indicating a perfect fit to the data.

The *scallop-parameter-1* correlation produces curve fits through the average of all data for each scallop height on the leeward and windward sides, but the leeward side and windward side fits diverge from each other rendering this form unsatisfactory. The *scallop-parameter-2* correlation shows the decorrelating effect of a positive exponent β on the edge Mach number, which is higher on the leeward side than on the windward side. In contrast, a negative exponent on the edge Mach number provides a better fit as shown by the *scallop-parameter-3* and

scallop-parameter-4 correlations. Of these, the *scallop-parameter-4* correlation is considered to be slightly better because the R -values of the fits are higher and the difference between windward side and leeward side fits are smaller.

Despite a reasonably good fit to the data, the general *scallop parameter* form is unsatisfactory due to the degeneracy of the independent variable. Since the aspect ratio k_{SC}/L_{SC} variation was accomplished by changing the scallop height while maintaining a fixed scallop length, this variation also represents a change in the relative scallop height k_{SC}/θ . As the general correlation form explicitly accounts only for the aspect ratio, a very small height scallop would be equivalent to a very large height scallop as long as the scallop length was varied to maintain the same aspect ratio. Such a result is physically unrealistic even though the fit is relatively good within the domain of the current data set.

Wind Tunnel Roughness Correlations

The next set of correlations, shown in Figure 83, is derived on the independent variable definition of Ref. 17. This *wind tunnel roughness* formulation of Eq. (28) was developed to correlate wind tunnel transition data from hemispherical nose tips with distributed surface roughness. In the current analysis, the independent variable definition includes a viscosity ratio, rather than a temperature ratio as in the original work. However, these definitions can be shown to be approximately equivalent through use of the low-to-moderate temperature (~ 200 K – 2000 K) power-law expression for viscosity:

$$\mu/\mu_0 = (T/T_0)^n, \text{ where } n = 0.7 \text{ for air.} \quad (30)$$

The original formulation of Ref. 17 is reproduced by the *wind-tunnel-roughness-0* correlation, where the exponent on the independent variable is fixed at $D_{TR} = -0.7$ and the edge Mach number exponent β is set to 0. However, this formulation produces considerable scatter for the current data and the slopes of the fits do not match those of the data. For the remaining fits, both of these exponents were allowed to vary. Parameters for all these correlations are listed in Table 5.

As shown by the *wind-tunnel-roughness-1* correlation, the data can be better correlated by allowing the independent variable exponent to vary. However, there is still considerable difference between the two leeward and windward side fits. As with the scallop parameter correlations, introducing a positive exponent on the edge Mach number decorrelates the windward side and leeward side data as shown by the *wind-tunnel-roughness-2*. A negative exponent produces better agreement between windward side and leeward side fits as shown by the *wind-tunnel-roughness-3* and *wind-tunnel-roughness-4* correlations. Of these, the *wind-tunnel-roughness-4* formulation provides the best fit, with higher R -values and good agreement between the windward side and leeward side fits.

Multiple Parameter Correlations

The final set of correlations presented in Figure 84 is based on a combination of the *wind tunnel roughness* and *scallop parameter* formulations with parameters (as given in Table 6) that account for both the relative scallop height and the scallop aspect ratio as per Eq. (29). All of the parameter choices for these *multiple parameter* correlations provide reasonably good agreement with the data, but in general there is little improvement over that achieved with the *wind tunnel roughness* formulation. For some cases, the R -values are better than achieved using the best

wind tunnel roughness correlation, but in general, the differences between windward side and leeward side fits are slightly higher. The *multiple-parameter-5* correlation is deemed to provide the best of these fits with the highest R -values and the closest agreement between windward side and leeward side fits.

While the *multiple parameter* formulation does not provide much improvement over the *wind tunnel roughness* formulation for the current data set, the combined parameter formulation could potentially be of more use for correlating a wider range of data. The reason is the flexibility provided by incorporating both a relative scallop height term (k_{SC}/θ) and a scallop aspect ratio term (k_{SC}/L_{SC}). These two terms are linked in the current data set since only the k_{SC} parameter was varied, not the L_{SC} parameter. However, if future data become available in which the relative scallop height and scallop aspect ratio were independently varied, this formulation could allow for better correlation of such data.

Overall Assessment of Transition Correlations

Good correlations of the transition data were obtained through each of the three correlation methods presented, where the merit factors of the correlations were the linear correlation coefficient R and the agreement between separate fits for the windward side and leeward side data. The best combined windward side / leeward side fits to the data were obtained through the *scallop-4*, *wind-tunnel-roughness-4*, and *multiple-parameter-5* correlations, which are given in Eqs. (31) - (33). These functions are plotted in Figure 85 - Figure 87 with $\pm 20\%$ uncertainties on Re_θ , which serve to bound the majority of the experimental transition data. With respect to the transition length, the relationships developed for the simplified transition model for the transition length and intermittency, Eqs. (22) and (24), will also be used with the detailed transition onset models.

$$Re_\theta = 12.212 \left\{ (M_e)^{-1/2} \left(\frac{k_{SC}}{L_{SC}} \right) \right\}^{-0.66482} : \text{scallop - parameter - 4 correlation} \quad (31)$$

$$Re_\theta = 371.48 \left\{ \left[\left(\frac{k_{SC}}{\theta} \right) \left(\frac{\mu_e}{\mu_w} \right) \right] (M_e)^{-1} \right\}^{-0.40431} : \text{wind - tunnel - roughness - 4 correlation} \quad (32)$$

$$Re_\theta = 45.252 \left\{ \left[\left(\frac{k_{SC}}{\theta} \right) \left(\frac{\mu_e}{\mu_w} \right) \right]^{+1/2} (M_e)^{-1/2} \left(\frac{k_{SC}}{L_{SC}} \right) \right\}^{-0.45061} : \text{multiple - parameter - 5 correlation} \quad (33)$$

It is somewhat surprising that *any* of these formulations produces a good correlation of the data given the origin of the methods. These methods were developed for use with transition data produced by roughness elements or cavities with height or depth scales on the order of the boundary-layer height, whereas the data herein were obtained from scallops with height scales generally much greater than that of the boundary layer.

With additional data, especially for cases with fixed scallop height but varying scallop length, and for cases at higher Reynolds numbers with smaller scallop heights, the correlations could probably be improved and extended to a wider range of conditions. However, even if the correlations could be improved, the general practice for heat-shield design is to make

conservative assumptions as to how early along a trajectory transition occurs, so any correlation would be applied with a significant uncertainty margin. Additionally, the difficulty of accurately predicting in-flight scalloping heights of an F-TPS would also introduce uncertainty and conservatism into the transition prediction problem. Therefore, for the current goal of developing an approximate fidelity correlation for engineering design purposes, these correlations are considered to be sufficient.

Application of Correlations to Wind Tunnel Conditions

As a check on the correlation methods, the heating augmentation bump factors were applied to the smooth-OML heating predictions to generate estimates for the scalloped heating at wind tunnel conditions. Estimates were developed for fully-turbulent flow and for transitional flow using the *multiple-parameter-5* transition correlation. The comparisons between the wind tunnel data and the scallop heating correlations for both transitional and fully-turbulent flow are shown in Figure 88 - Figure 91 for the IRVE Scallop-2.5 model, Figure 92 - Figure 95 for the IRVE Scallop-5 model, Figure 96 - Figure 99 for the IRVE Scallop-10 model, Figure 100 - Figure 103 for the IRVE Scallop-15 model, Figure 104 - Figure 107 for the IRVE Scallop-20 model, and Figure 108 - Figure 111 for the IRVE EDU model.

In these figures, the predicted laminar and turbulent centerline heating distributions from the smooth-OML computations are shown along with the distributions resulting from application of the correlation to the predictions. Both transitional and fully-turbulent scalloping results are shown, as are transitional results with the transition onset location varied by $\pm 20\%$ in order to show the effects of onset location uncertainty on the resulting heating distributions.

The level of agreement between the heating data and the correlations varied both with Reynolds number and angle of attack and was in many cases influenced by the accuracy of the transition onset correlation. Overall, the correlations provided at least a qualitative estimate of the transition onset location and heating augmentation due to scalloping for all cases.

For the IRVE Scallop-2.5 geometry (Figure 88 - Figure 91), fully-turbulent heating occurred only on the leeward side at the two highest Reynolds numbers for nonzero angles of attack. For these cases, the fully-turbulent correlation levels agreed well with data from the turbulent region. The transitional correlation onset predictions generally did not agree well with the measured leeward side onset locations, which is not surprising considering the scatter in the small scallop height IRVE Scallop-2.5 transition data. The correlation did not predict transition on the windward side, nor was windward side transition observed in the data.

For the IRVE Scallop-5 geometry (Figure 92 - Figure 95), fully-turbulent leeward side heating levels were measured for the $\alpha = 6$ deg case at the two highest Reynolds numbers and for $\alpha = 12$ deg and 18 deg at all Reynolds numbers. For these cases, the heating correlation values were in good agreement with the measured scallop peak heating levels and the transition onset locations were approximately predicted for most cases. On the windward side, only borderline transitional flow was achieved for a few $\alpha = 6$ deg cases and the transition correlation prediction was in approximate agreement with the data.

For the IRVE Scallop-10 geometry (Figure 96 - Figure 99), the leeward side flow was almost entirely turbulent for most cases and the fully-turbulent correlation levels were in good agreement with the data except for underprediction at some of the lower Reynolds number

conditions. The windward side was transitional/turbulent for most cases except at $\alpha = 18$ deg and the correlation heating levels and transition locations were in good agreement.

For the IRVE Scallop-15 and IRVE Scallop-20 geometries (Figure 100 - Figure 103 and Figure 104 - Figure 107), both the leeward side and windward side flow were almost entirely turbulent for all conditions. For most cases, correlations generally agreed with the measured heating levels and onset locations, although for a few cases at lower Reynolds numbers the measured heating exceeded the turbulent correlation levels.

Finally, for the IRVE EDU geometry (Figure 108 - Figure 111), the flow was almost entirely turbulent on both leeward and windward sides except for the windward side at $\alpha = 18$ deg. Agreement between the correlation heating levels and transition onset locations with the data was not as good as for the axisymmetric scallop geometries. For most conditions, the turbulent heating correlation levels fell below the measured scallop heating peaks and the transition onset correlation locations were downstream of the measured locations.

In general, the transition onset and turbulent heating location correlations approximately reproduced the wind tunnel data on the axisymmetric geometries, although for some cases the measured turbulent heating levels exceeded the correlation values. However, the agreement was less satisfactory for the IRVE EDU geometry. Although the average physical height of the surface deflections (~20 mil) on the IRVE EDU was approximately equal to that of the IRVE Scallop-10 geometry, the measured heating levels were greater than the values predicted by the correlations for most cases. This result suggests that the correlations, which were developed by analysis of data set from the axisymmetric scallop deflection models, may not apply to the three-dimensional, rectangular cavity-like deflections of the IRVE EDU model.

With respect to the use of these correlations for future missions, the underprediction of turbulent heating levels for some of the axisymmetric deflection geometries would indicate that a conservative safety factor (on the order of 10%-20%) should be applied to the scalloped heating environment predictions. Also, the larger disparity between predictions and measurements for some of the nonaxisymmetric IRVE EDU model cases highlights the need for further data on such geometries with flight-like surface deflection patterns.

Application of Correlations to Flight Condition Predictions

In order to estimate the surface deflection effects on the aeroheating environment of the IRVE-3 flight test vehicle, the scallop parameters of the IRVE EDU model were geometrically scaled to the size of the flight vehicle, resulting in a scallop height of ~0.4 in. The transition onset and heating augmentation correlations were then applied to smooth-wall CFD solutions generated along the IRVE-3 trajectory (Ref. 5). For reference, the predicted smooth-wall laminar heating on the nose of the IRVE-3 vehicle is shown as a function of time in Figure 112 along with the flight dynamic pressure. Free stream conditions along the flight trajectory are listed in Table 7.

The scallop-augmented heating levels based on the correlations are shown for each trajectory point in Figure 113 - Figure 116. Heating distributions are presented in nondimensional terms as h/h_{ref} , where h_{ref} is the maximum, smooth-wall, laminar value predicted on the aeroshell for that trajectory point. Each figure includes the original smooth-wall laminar and turbulent heating distributions as well as the scallop-augmented values for both transitional and fully-turbulent

flow. Note that the augmented heating values at the nose should be disregarded as this part of the aeroshell was a solid piece of metal over which the F-TPS was applied (see Figure 1) and thus it did not scallop in flight. The angle of attack varied from ~ 5 deg to 15 deg through the flight, at which conditions transition and augmented turbulent heating were predicted on the leeward side of the vehicle for $t > 667$ sec. On the windward side, transition was predicted only for $t > 675$ sec, which was approximately the nose peak-heating point on the trajectory.

These results suggest that the leeward side flank turbulent heating levels could have exceeded the laminar, smooth levels on the nose for $t > 681$ sec. This result is notable because the predicted laminar heating rate at the nose for the peak heating point along the trajectory (~ 677 sec) was the reference point for the F-TPS design. However, these predictions were generated using the scaled IRVE EDU model deflection heights throughout the trajectory, even though that geometry represents only the estimated maximum deflection that would occur at the peak dynamic pressure point. Thus, these predictions provided a worst-case estimate of heating levels. Furthermore, even if the leeward side flank heating did exceed the nose heating level at later times in the trajectory, this would have occurred well after the peak heating time, when the overall heating levels would have been much lower than at peak heating. The success of the IRVE-3 flight test would indicate that excessive scalloping and the corresponding heating augmentation did not occur during the flight. Thus, the results from the scalloping correlations should be regarded as a conservative estimate for flight heating levels rather than an accurate reconstruction of the actual aeroheating environment.

Summary and Conclusions

A wind tunnel test program was conducted at the NASA Langley Research Center to obtain experimental data on the effects of flexible thermal protection system deflections on the aeroheating environment of a Hypersonic Inflatable Aerodynamic Decelerator aeroshell. Boundary-layer transition and global surface heating data measurements were performed in the 20-Inch Mach 6 Air Tunnel using phosphor thermography on multiple geometries similar to that of the IRVE flight test program. Testing was performed on rigid, ceramic wind tunnel models with various surface-scalloping patterns that simulated a range of potential in-flight HIAD F-TPS deflections. A complimentary CFD study was also performed to generate smooth-wall laminar and turbulent heating predictions at the wind tunnel test conditions in order to compare predictions with measurements and to provide flow-field information for use in correlating the data.

Scalloping of the F-TPS was found to promote early boundary-layer transition and to produce augmented heating levels for both laminar and turbulent flow. Scalloping effects on the leeward side flank of the geometries were more severe than on the windward side and in some cases the leeward side, scallop-augmented heating was equal to, or greater than, that at the nose tip. However, the nose radius for the IRVE-3 vehicle (as well as those of the wind tunnel models) was specifically designed to be sharper than that of a normal operational vehicle in order to produce higher heating levels as a test of the F-TPS performance in flight. Thus, the level of leeward side flank heating relative to that of the nose could be even higher for a more conventional fight vehicle geometry with a blunter nose and consequently lower nose heating.

The wind tunnel data and the predicted smooth-wall, laminar boundary-layer conditions were used to develop correlations for transition onset and heating augmentation due to the effects of

F-TPS scalloping. Several general forms of transition correlations based on different parameters were considered and a best-fit correlation was determined for each. A correlation for the heating augmentation due to scalloping was developed that provides bump-factors for both laminar and turbulent flow. These bump-factors can be used as multipliers to smooth-wall laminar heating predictions, which along with the transition onset correlation, allows for estimation of transitional/turbulent heating levels as a function of scallop height.

The correlations were used to both reproduce the wind tunnel results and to assess the scalloping effects on heating along the IRVE-3 trajectory. For the wind tunnel conditions, the correlations produced at least qualitative agreement with all the axisymmetric-deflection geometry data. Scallop-augmented turbulent heating levels were underpredicted for some of the larger deflection cases, indicating that a conservative safety margin would be required for application of these correlations to future vehicle designs. However, excessive conservatism should be avoided because the agreement was better for the smaller deflection cases, which better represent a flight vehicle design, than for the larger deflection cases.

Larger differences between predictions and measurements were observed for the nonaxisymmetric deflections on the IRVE EDU geometry. This geometry included surface deflections due to both the structural toroids and the tension ties, which created more three-dimensional “cavity-like” surface features rather than the axisymmetric scallops of the other geometries. Further data on such deflection patterns will be required to develop better correlations for surface deflection effects on flight-like geometries.

The transition onset and heating correlations were applied to the IRVE-3 trajectory to generate estimates for the flight environment. For some cases, these correlations produced heating levels on the leeward side flank of the vehicle that were greater than those at the nose, which was the design point (at the peak heating trajectory point) for the vehicle’s F-TPS. However, the analysis was performed using the IRVE EDU geometry deflections (scaled to flight vehicle size) throughout the trajectory. Thus, this was a worst-case analysis because those deflections were based on estimated conditions at peak dynamic pressure, which occurs well after the peak heating point. Also, since the highest relative leeward side heating augmentation occurred at times well after the trajectory peak-heating point, the actual magnitude of the leeward side heating, while higher than that at the nose at the specific trajectory point, was still lower than that at the nose at the peak heating point on the trajectory.

In addition to its use in developing the transition onset and heating correlations presented herein, the data set provides a quantitative, global heating data set at well-defined test conditions for the development and/or validation of high-fidelity computational models. In particular, the axisymmetric deflection models (IRVE Scallop-2.5 through IRVE Scallop-20) are based on simple parametric geometries that can easily be reproduced and used for flow field simulations. Validation of flow-field modeling capabilities for such axisymmetric geometries should be a first step, followed by application to three-dimensional deflection cases such as the IRVE EDU model.

References

1. Rohrschneider, R. R. and Braun, R. D., “Survey of Ballute Technology for Aerocapture,” *Journal of Spacecraft and Rockets*, Vol. 44, No. 1, January–February 2007, pp.10–23.

2. Hughes, S. J., Cheatwood, F. M., Dillman, R. A., Wright, H. S., DelCorso, J. A. and Calomino, A. M., "Hypersonic Inflatable Aerodynamic Decelerator (HIAD) Technology Development Overview," AIAA Paper 2011-2524, 21st AIAA Aerodynamic Decelerator Systems Technology Conference and Seminar, Dublin, Ireland, May 23–26, 2011.
3. Hughes, S. J., Dillman, R. A., Starr, B. R., Stephan, R. A., Lindell, M. C., Player, C. J. and Cheatwood, F. M., "Inflatable Re-entry Vehicle Experiment (IRVE) Design Overview," AIAA Paper 2005-1636, 18th Aerodynamic Decelerator Systems Technology Conference and Seminar, Munich, Germany, May 25 2005.
4. O'Keefe, S. A. and Bose, D. M., "IRVE-II Post-Flight Trajectory Reconstruction," AIAA Paper 2010-7515, AIAA Atmospheric Flight Mechanics Conference, Toronto, Ontario Canada, August 2–5, 2010.
5. Olds, A. D., Beck, R. E., Bose, D. M., White, J. P., Edquist, K. T., Hollis, B. R., Lindell, M. C., Cheatwood, F. C., Gsell, V. T. and Bowden, E. L., "IRVE-3 Post-Flight Reconstruction," AIAA Paper 2013-1390, AIAA Aerodynamic Decelerator Systems Conference, Daytona Beach, FL, March 25–28, 2013.
6. Buck, G. M., "Rapid Model Fabrication and Testing for Aerospace Vehicles," AIAA Paper 2000-0826, 38th AIAA Aerospace Sciences Meeting and Exhibit, Reno, NV, January 10–13, 2000.
7. Jurewicz, D., Brown, G., Gilles, B., Lichodziejewski, L., Kelly, C., Tutt, B. and Hughes, S., "Design and Development of Inflatable Aeroshell Structure for IRVE-3," AIAA Paper 2011-2522, 21st AIAA Aerodynamic Decelerator Systems Technology Conference and Seminar, Dublin, Ireland, May 23–26, 2011.
8. Lichodziejewski, L., Kelley, C., Tutt, B., Jurewicz, D., Brown, G., Gilles, B., Barber, D., Dillman, R., and Player, C., "Design and Testing of the Inflatable Aeroshell for the IRVE-3 Flight Experiment," AIAA 2012-1515, 53rd AIAA/ASME/ASCE/AHS/ASC Structures, Structural Dynamics and Materials Conference, Honolulu, HI, April 23–26, 2012.
9. Hollis, B. R., Berger, K. T., Berry, S. A., Brauckmann, G. J., et al, "Entry, Descent, and Landing Aerothermodynamics: NASA Langley Experimental Capabilities and Contributions," AIAA Paper 2014-1154, AIAA 52nd Aerospace Science Meeting, National Harbor, MD, January 13–17, 2014.
10. Berger, K., Rufer, S., Hollingsworth, K. and Wright, S., "NASA Langley Aerothermodynamic Laboratory: Hypersonic Testing Capabilities," AIAA Paper 2015-1337, 53rd AIAA Aerospace Sciences Meeting, Kissimmee, FL, January 5–9, 2015.
11. Fay, J. A., and Riddell, F. R., "Theory of Stagnation Point Heat Transfer in Dissociated Air," *Journal of Aeronautical Sciences*, Vol. 25, No. 2., February 1958, pp. 73–85.
12. Buck, G. M., "Surface Temperature/Heat Transfer Measurement Using a Quantitative Phosphor Thermography System," AIAA Paper 91-0064, 29th Aerospace Sciences Meeting, Reno, NV, January 7–10, 1991.
13. Merski, N. R., "Global Aeroheating Wind-Tunnel Measurements Using Improved Two-Color Phosphor Thermography Methods," *Journal of Spacecraft and Rockets*, Vol. 36, No. 2, March-April 1999, pp. 160–170.
14. Gnoffo, P. A., "An Upwind-Biased, Point-Implicit Algorithm for Viscous, Compressible Perfect-Gas Flows," NASA TP-2953, February 1990.
15. Mazaheri, A., Gnoffo, P. A., Johnston, C. O., and Kleb, B., "LAURA User's Manual: 5.5-65135," NASA TM-2013-217800, February 2011.

16. Hollis, B. R., "Blunt-Body Entry Vehicle Aerothermodynamics: Transition and Turbulent Heating," *Journal of Spacecraft and Rockets*, Vol. 49, No. 3, May–June 2012, pp. 435-449.
17. Jackson, M. D., "Passive Nosedip Technology (PANT) Program. Volume 15: Roughness Induced Transition on Blunt Axisymmetric Bodies – Data Report," Space and Missile Systems Organization TR-74- 86-Vol-XV, April 1974.
18. Reda, D. C., "Correlation of Nosedip Boundary-Layer Transition Measured in Ballistics-Range Experiments," *AIAA Journal*, Vol. 19, No. 3, March 1981, pp. 329–339.
19. Wilder, M. C., Reda, D. C., and Prabhu, D. K., "Transition Experiments on Blunt Bodies with Roughness in Hypersonic Free Flight in Carbon Dioxide," *AIAA Paper 2015-1738*, 53rd AIAA Aerospace Sciences Meeting, Kissimmee, FL, 2015.
20. Batt, R. G. and Legner, H. H., "A Review of Roughness-Induced Nosedip Transition," *AIAA Journal*, Vol. 21, No. 1, January 1983, pp. 7–22.

Table 1. Geometry Information.

Geometry	R_B (m)	R_B (in)	R_N (m)	R_N (in)	R_N/R_B	R_S (m)	R_S (in)	R_S/R_B
IRVE-3 flight vehicle	1.5000	59.055	0.190500	7.500	0.127	0.0508000	2.00000	0.03390
IRVE EDU model	0.0762	3.000	0.009677	0.3810	0.127	0.0025832	0.10170	0.03390
IRVE Scallop-0 model	0.0762	3.000	0.009677	0.3810	0.125	0.0025832	0.10170	0.03390
IRVE Scallop-2.5 model	0.0762	3.000	0.009525	0.3750	0.125	0.0023813	0.09375	0.03125
IRVE Scallop-5 model	0.0762	3.000	0.009525	0.3750	0.125	0.0023813	0.09375	0.03125
IRVE Scallop-10 model	0.0762	3.000	0.009525	0.3750	0.125	0.0023813	0.09375	0.03125
IRVE Scallop-15 model	0.0762	3.000	0.009525	0.3750	0.125	0.0023813	0.09375	0.03125
IRVE Scallop-20 model	0.0762	3.000	0.009525	0.3750	0.125	0.0023813	0.09375	0.03125

Table 2. Parametric Model Information.

Geometry	R_T (in)	R_{SC} (in)	β_{SC} (°)	L_{SC} (in)	k_{SC} (mil)	L_{SC}/k_{SC}
IRVE Scallop-2.5	0.25	5.48140	2.5	0.50	5.45502	91.65870
IRVE Scallop-5	0.25	2.61843	5.0	0.50	10.91524	45.80753
IRVE Scallop-10	0.25	1.18969	10	0.50	21.87217	22.86010
IRVE Scallop-15	0.25	0.71593	15	0.50	32.91312	15.19151
IRVE Scallop-20	0.25	0.48095	20	0.50	44.08175	11.34256
IRVE EDU (average)	N/A	N/A	N/A	~0.50	20	~25
IRVE EDU (maximum)	N/A	N/A	N/A	~0.50	30	~16.7

Table 3. Test 6979, 20-Inch Mach 6 Air Tunnel Conditions.

Run	Model	α (deg)	Re_∞ (1/ft)	M_∞	T_∞ (K)	ρ_∞ (kg/m ³)	U_∞ (m/s)	ΔH_{tot} (J/kg)	h_{FR} (kg/m ² · s)
80	IRVE Scallop-0	0	2.10E+06	5.96	61.9	3.25E-02	939.5	2.03E+05	5.01E-01
81	IRVE Scallop-0	0	3.03E+06	5.99	62.5	4.71E-02	948.7	2.12E+05	6.11E-01
82	IRVE Scallop-0	0	3.88E+06	6.01	63.3	6.05E-02	957.2	2.21E+05	7.00E-01
83	IRVE Scallop-0	0	6.63E+06	6.04	62.6	1.02E-01	954.6	2.17E+05	9.10E-01
84	IRVE Scallop-0	0	8.34E+06	6.03	58.6	1.25E-01	918.1	1.79E+05	9.64E-01
70	IRVE Scallop-0	6	2.10E+06	5.96	61.9	3.25E-02	939.5	2.03E+05	5.01E-01
72	IRVE Scallop-0	6	3.03E+06	5.99	62.5	4.71E-02	948.7	2.12E+05	6.11E-01
71	IRVE Scallop-0	6	3.88E+06	6.01	63.3	6.05E-02	957.2	2.21E+05	7.00E-01
73	IRVE Scallop-0	6	6.63E+06	6.04	62.6	1.02E-01	954.6	2.17E+05	9.10E-01
74	IRVE Scallop-0	6	8.34E+06	6.03	58.6	1.25E-01	918.1	1.79E+05	9.64E-01
103	IRVE Scallop-0	12	2.10E+06	5.96	61.9	3.25E-02	939.5	2.03E+05	5.01E-01
104	IRVE Scallop-0	12	3.03E+06	5.99	62.5	4.71E-02	948.7	2.12E+05	6.11E-01
105	IRVE Scallop-0	12	3.88E+06	6.01	63.3	6.05E-02	957.2	2.21E+05	7.00E-01
106	IRVE Scallop-0	12	6.63E+06	6.04	62.6	1.02E-01	954.6	2.17E+05	9.10E-01
107	IRVE Scallop-0	12	8.34E+06	6.03	58.6	1.25E-01	918.1	1.79E+05	9.64E-01
161	IRVE Scallop-0	18	2.10E+06	5.96	61.9	3.25E-02	939.5	2.03E+05	5.01E-01
162	IRVE Scallop-0	18	3.03E+06	5.99	62.5	4.71E-02	948.7	2.12E+05	6.11E-01
163	IRVE Scallop-0	18	3.88E+06	6.01	63.3	6.05E-02	957.2	2.21E+05	7.00E-01
164	IRVE Scallop-0	18	6.63E+06	6.04	62.6	1.02E-01	954.6	2.17E+05	9.10E-01
165	IRVE Scallop-0	18	8.34E+06	6.03	58.6	1.25E-01	918.1	1.79E+05	9.64E-01
36	IRVE EDU	0	2.10E+06	5.96	61.9	3.25E-02	939.5	2.03E+05	5.01E-01
39	IRVE EDU	0	3.03E+06	5.99	62.5	4.71E-02	948.7	2.12E+05	6.11E-01
40	IRVE EDU	0	3.88E+06	6.01	63.3	6.05E-02	957.2	2.21E+05	7.00E-01
41	IRVE EDU	0	6.63E+06	6.04	62.6	1.02E-01	954.6	2.17E+05	9.10E-01
42	IRVE EDU	0	8.34E+06	6.03	58.6	1.25E-01	918.1	1.79E+05	9.64E-01
122	IRVE EDU	6	2.10E+06	5.96	61.9	3.25E-02	939.5	2.03E+05	5.01E-01
120	IRVE EDU	6	3.03E+06	5.99	62.5	4.71E-02	948.7	2.12E+05	6.11E-01
119	IRVE EDU	6	3.88E+06	6.01	63.3	6.05E-02	957.2	2.21E+05	7.00E-01
123	IRVE EDU	6	6.63E+06	6.04	62.6	1.02E-01	954.6	2.17E+05	9.10E-01
124	IRVE EDU	6	6.63E+06	6.04	62.6	1.02E-01	954.6	2.17E+05	9.10E-01
125	IRVE EDU	6	8.34E+06	6.03	58.6	1.25E-01	918.1	1.79E+05	9.64E-01
113	IRVE EDU	12	2.10E+06	5.96	61.9	3.25E-02	939.5	2.03E+05	5.01E-01
114	IRVE EDU	12	3.03E+06	5.99	62.5	4.71E-02	948.7	2.12E+05	6.11E-01
115	IRVE EDU	12	3.88E+06	6.01	63.3	6.05E-02	957.2	2.21E+05	7.00E-01
117	IRVE EDU	12	6.63E+06	6.04	62.6	1.02E-01	954.6	2.17E+05	9.10E-01
118	IRVE EDU	12	8.34E+06	6.03	58.6	1.25E-01	918.1	1.79E+05	9.64E-01
137	IRVE EDU	18	2.10E+06	5.96	61.9	3.25E-02	939.5	2.03E+05	5.01E-01
138	IRVE EDU	18	3.03E+06	5.99	62.5	4.71E-02	948.7	2.12E+05	6.11E-01
136	IRVE EDU	18	3.88E+06	6.01	63.3	6.05E-02	957.2	2.21E+05	7.00E-01
139	IRVE EDU	18	6.63E+06	6.04	62.6	1.02E-01	954.6	2.17E+05	9.10E-01
140	IRVE EDU	18	8.34E+06	6.03	58.6	1.25E-01	918.1	1.79E+05	9.64E-01
8	IRVE Scallop-2.5	0	2.10E+06	5.96	61.9	3.25E-02	939.5	2.03E+05	5.01E-01
7	IRVE Scallop-2.5	0	3.88E+06	6.01	63.3	6.05E-02	957.2	2.21E+05	6.11E-01
6	IRVE Scallop-2.5	0	3.88E+06	6.01	63.3	6.05E-02	957.2	2.21E+05	7.00E-01
9	IRVE Scallop-2.5	0	6.63E+06	6.04	62.6	1.02E-01	954.6	2.17E+05	9.10E-01
10	IRVE Scallop-2.5	0	8.34E+06	6.03	58.6	1.25E-01	918.1	1.79E+05	9.64E-01
56	IRVE Scallop-2.5	6	2.10E+06	5.96	61.9	3.25E-02	939.5	2.03E+05	5.01E-01
57	IRVE Scallop-2.5	6	3.03E+06	5.99	62.5	4.71E-02	948.7	2.12E+05	6.11E-01
55	IRVE Scallop-2.5	6	3.88E+06	6.01	63.3	6.05E-02	957.2	2.21E+05	7.00E-01
58	IRVE Scallop-2.5	6	6.63E+06	6.04	62.6	1.02E-01	954.6	2.17E+05	9.10E-01
59	IRVE Scallop-2.5	6	8.34E+06	6.03	58.6	1.25E-01	918.1	1.79E+05	9.64E-01
93	IRVE Scallop-2.5	12	2.10E+06	5.96	61.9	3.25E-02	939.5	2.03E+05	5.01E-01
94	IRVE Scallop-2.5	12	3.03E+06	5.99	62.5	4.71E-02	948.7	2.12E+05	6.11E-01
92	IRVE Scallop-2.5	12	3.88E+06	6.01	63.3	6.05E-02	957.2	2.21E+05	7.00E-01
95	IRVE Scallop-2.5	12	6.63E+06	6.04	62.6	1.02E-01	954.6	2.17E+05	9.10E-01
96	IRVE Scallop-2.5	12	8.34E+06	6.03	58.6	1.25E-01	918.1	1.79E+05	9.64E-01
157	IRVE Scallop-2.5	18	2.10E+06	5.96	61.9	3.25E-02	939.5	2.03E+05	5.01E-01
158	IRVE Scallop-2.5	18	3.03E+06	5.99	62.5	4.71E-02	948.7	2.12E+05	6.11E-01

Table 3 (continued). Test 6979, 20-Inch Mach 6 Air Tunnel Conditions.

Run	Model	α (deg)	Re_∞ (1/ft)	M_∞	T_∞ (K)	ρ_∞ (kg/m ³)	U_∞ (m/s)	ΔH_{tot} (J/kg)	h_{FR} (kg/m ² · s)
159	IRVE Scallop-2.5	18	6.63E+06	6.04	62.6	1.02E-01	954.6	2.17E+05	9.10E-01
160	IRVE Scallop-2.5	18	8.34E+06	6.03	58.6	1.25E-01	918.1	1.79E+05	9.64E-01
13	IRVE Scallop-5	0	2.10E+06	5.96	61.9	3.25E-02	939.5	2.03E+05	5.01E-01
12	IRVE Scallop-5	0	3.03E+06	5.99	62.5	4.71E-02	948.7	2.12E+05	6.11E-01
11	IRVE Scallop-5	0	3.88E+06	6.01	63.3	6.05E-02	957.2	2.21E+05	7.00E-01
14	IRVE Scallop-5	0	6.63E+06	6.04	62.6	1.02E-01	954.6	2.17E+05	9.10E-01
15	IRVE Scallop-5	0	8.34E+06	6.03	58.6	1.25E-01	918.1	1.79E+05	9.64E-01
65	IRVE Scallop-5	6	2.10E+06	5.96	61.9	3.25E-02	939.5	2.03E+05	5.01E-01
66	IRVE Scallop-5	6	3.03E+06	5.99	62.5	4.71E-02	948.7	2.12E+05	6.11E-01
67	IRVE Scallop-5	6	3.88E+06	6.01	63.3	6.05E-02	957.2	2.21E+05	7.00E-01
68	IRVE Scallop-5	6	6.63E+06	6.04	62.6	1.02E-01	954.6	2.17E+05	9.10E-01
69	IRVE Scallop-5	6	8.34E+06	6.03	58.6	1.25E-01	918.1	1.79E+05	9.64E-01
185	IRVE Scallop-5	12	2.10E+06	5.96	61.9	3.25E-02	939.5	2.03E+05	5.01E-01
186	IRVE Scallop-5	12	3.03E+06	5.99	62.5	4.71E-02	948.7	2.12E+05	6.11E-01
187	IRVE Scallop-5	12	3.88E+06	6.01	63.3	6.05E-02	957.2	2.21E+05	7.00E-01
188	IRVE Scallop-5	12	6.63E+06	6.04	62.6	1.02E-01	954.6	2.17E+05	9.10E-01
189	IRVE Scallop-5	12	8.34E+06	6.03	58.6	1.25E-01	918.1	1.79E+05	9.64E-01
152	IRVE Scallop-5	18	2.10E+06	5.96	61.9	3.25E-02	939.5	2.03E+05	5.01E-01
153	IRVE Scallop-5	18	3.03E+06	5.99	62.5	4.71E-02	948.7	2.12E+05	6.11E-01
151	IRVE Scallop-5	18	3.88E+06	6.01	63.3	6.05E-02	957.2	2.21E+05	7.00E-01
154	IRVE Scallop-5	18	6.63E+06	6.04	62.6	1.02E-01	954.6	2.17E+05	9.10E-01
155	IRVE Scallop-5	18	8.34E+06	6.03	58.6	1.25E-01	918.1	1.79E+05	9.64E-01
16	IRVE Scallop-10	0	2.10E+06	5.96	61.9	3.25E-02	939.5	2.03E+05	5.01E-01
17	IRVE Scallop-10	0	3.03E+06	5.99	62.5	4.71E-02	948.7	2.12E+05	6.11E-01
18	IRVE Scallop-10	0	3.88E+06	6.01	63.3	6.05E-02	957.2	2.21E+05	7.00E-01
19	IRVE Scallop-10	0	6.63E+06	6.04	62.6	1.02E-01	954.6	2.17E+05	9.10E-01
20	IRVE Scallop-10	0	8.34E+06	6.03	58.6	1.25E-01	918.1	1.79E+05	9.64E-01
50	IRVE Scallop-10	6	2.10E+06	5.96	61.9	3.25E-02	939.5	2.03E+05	5.01E-01
51	IRVE Scallop-10	6	3.03E+06	5.99	62.5	4.71E-02	948.7	2.12E+05	6.11E-01
52	IRVE Scallop-10	6	3.88E+06	6.01	63.3	6.05E-02	957.2	2.21E+05	7.00E-01
53	IRVE Scallop-10	6	6.63E+06	6.04	62.6	1.02E-01	954.6	2.17E+05	9.10E-01
54	IRVE Scallop-10	6	8.34E+06	6.03	58.6	1.25E-01	918.1	1.79E+05	9.64E-01
98	IRVE Scallop-10	12	2.10E+06	5.96	61.9	3.25E-02	939.5	2.03E+05	5.01E-01
99	IRVE Scallop-10	12	3.03E+06	5.99	62.5	4.71E-02	948.7	2.12E+05	6.11E-01
100	IRVE Scallop-10	12	3.88E+06	6.01	63.3	6.05E-02	957.2	2.21E+05	7.00E-01
101	IRVE Scallop-10	12	6.63E+06	6.04	62.6	1.02E-01	954.6	2.17E+05	9.10E-01
102	IRVE Scallop-10	12	8.34E+06	6.03	58.6	1.25E-01	918.1	1.79E+05	9.64E-01
146	IRVE Scallop-10	18	2.10E+06	5.96	61.9	3.25E-02	939.5	2.03E+05	5.01E-01
147	IRVE Scallop-10	18	3.03E+06	5.99	62.5	4.71E-02	948.7	2.12E+05	6.11E-01
148	IRVE Scallop-10	18	3.88E+06	6.01	63.3	6.05E-02	957.2	2.21E+05	7.00E-01
149	IRVE Scallop-10	18	6.63E+06	6.04	62.6	1.02E-01	954.6	2.17E+05	9.10E-01
150	IRVE Scallop-10	18	8.34E+06	6.03	58.6	1.25E-01	918.1	1.79E+05	9.64E-01
22	IRVE Scallop-15	0	2.10E+06	5.96	61.9	3.25E-02	939.5	2.03E+05	5.01E-01
23	IRVE Scallop-15	0	3.03E+06	5.99	62.5	4.71E-02	948.7	2.12E+05	6.11E-01
21	IRVE Scallop-15	0	3.88E+06	6.01	63.3	6.05E-02	957.2	2.21E+05	7.00E-01
24	IRVE Scallop-15	0	6.63E+06	6.04	62.6	1.02E-01	954.6	2.17E+05	9.10E-01
25	IRVE Scallop-15	0	8.34E+06	6.03	58.6	1.25E-01	918.1	1.79E+05	9.64E-01
126	IRVE Scallop-15	6	2.10E+06	5.96	61.9	3.25E-02	939.5	2.03E+05	5.01E-01
127	IRVE Scallop-15	6	3.03E+06	5.99	62.5	4.71E-02	948.7	2.12E+05	6.11E-01
128	IRVE Scallop-15	6	3.88E+06	6.01	63.3	6.05E-02	957.2	2.21E+05	7.00E-01
129	IRVE Scallop-15	6	6.63E+06	6.04	62.6	1.02E-01	954.6	2.17E+05	9.10E-01
130	IRVE Scallop-15	6	8.34E+06	6.03	58.6	1.25E-01	918.1	1.79E+05	9.64E-01
166	IRVE Scallop-15	12	2.10E+06	5.96	61.9	3.25E-02	939.5	2.03E+05	5.01E-01
167	IRVE Scallop-15	12	3.03E+06	5.99	62.5	4.71E-02	948.7	2.12E+05	6.11E-01
168	IRVE Scallop-15	12	3.88E+06	6.01	63.3	6.05E-02	957.2	2.21E+05	7.00E-01
169	IRVE Scallop-15	12	6.63E+06	6.04	62.6	1.02E-01	954.6	2.17E+05	9.10E-01
170	IRVE Scallop-15	12	8.34E+06	6.03	58.6	1.25E-01	918.1	1.79E+05	9.64E-01

Table 3 (concluded). Test 6979, 20-Inch Mach 6 Air Tunnel Conditions.

Run	Model	α (deg)	Re_∞ (1/ft)	M_∞	T_∞ (K)	ρ_∞ (kg/m ³)	U_∞ (m/s)	ΔH_{tot} (J/kg)	h_{FR} (kg/m ² · s)
131	IRVE Scallop-15	18	2.10E+06	5.96	61.9	3.25E-02	939.5	2.03E+05	5.01E-01
132	IRVE Scallop-15	18	3.03E+06	5.99	62.5	4.71E-02	948.7	2.12E+05	6.11E-01
133	IRVE Scallop-15	18	3.88E+06	6.01	63.3	6.05E-02	957.2	2.21E+05	7.00E-01
134	IRVE Scallop-15	18	6.63E+06	6.04	62.6	1.02E-01	954.6	2.17E+05	9.10E-01
135	IRVE Scallop-15	18	8.34E+06	6.03	58.6	1.25E-01	918.1	1.79E+05	9.64E-01
26	IRVE Scallop-20	0	2.10E+06	5.96	61.9	3.25E-02	939.5	2.03E+05	5.01E-01
27	IRVE Scallop-20	0	3.03E+06	5.99	62.5	4.71E-02	948.7	2.12E+05	6.11E-01
28	IRVE Scallop-20	0	3.88E+06	6.01	63.3	6.05E-02	957.2	2.21E+05	7.00E-01
29	IRVE Scallop-20	0	6.63E+06	6.04	62.6	1.02E-01	954.6	2.17E+05	9.10E-01
30	IRVE Scallop-20	0	8.34E+06	6.03	58.6	1.25E-01	918.1	1.79E+05	9.64E-01
45	IRVE Scallop-20	6	2.10E+06	5.96	61.9	3.25E-02	939.5	2.03E+05	5.01E-01
46	IRVE Scallop-20	6	3.03E+06	5.99	62.5	4.71E-02	948.7	2.12E+05	6.11E-01
47	IRVE Scallop-20	6	3.88E+06	6.01	63.3	6.05E-02	957.2	2.21E+05	7.00E-01
48	IRVE Scallop-20	6	6.63E+06	6.04	62.6	1.02E-01	954.6	2.17E+05	9.10E-01
49	IRVE Scallop-20	6	8.34E+06	6.03	58.6	1.25E-01	918.1	1.79E+05	9.64E-01
87	IRVE Scallop-20	12	2.10E+06	5.96	61.9	3.25E-02	939.5	2.03E+05	5.01E-01
89	IRVE Scallop-20	12	3.03E+06	5.99	62.5	4.71E-02	948.7	2.12E+05	6.11E-01
88	IRVE Scallop-20	12	3.88E+06	6.01	63.3	6.05E-02	957.2	2.21E+05	7.00E-01
90	IRVE Scallop-20	12	6.63E+06	6.04	62.6	1.02E-01	954.6	2.17E+05	9.10E-01
91	IRVE Scallop-20	12	8.34E+06	6.03	58.6	1.25E-01	918.1	1.79E+05	9.64E-01
141	IRVE Scallop-20	18	2.10E+06	5.96	61.9	3.25E-02	939.5	2.03E+05	5.01E-01
142	IRVE Scallop-20	18	3.03E+06	5.99	62.5	4.71E-02	948.7	2.12E+05	6.11E-01
143	IRVE Scallop-20	18	3.88E+06	6.01	63.3	6.05E-02	957.2	2.21E+05	7.00E-01
144	IRVE Scallop-20	18	6.63E+06	6.04	62.6	1.02E-01	954.6	2.17E+05	9.10E-01
145	IRVE Scallop-20	18	8.34E+06	6.03	58.6	1.25E-01	918.1	1.79E+05	9.64E-01

Table 4. Curve Fit Information for Scallop Parameter Correlation Form.

$x \equiv (M_e)^\beta \left(\frac{k_{SC}}{L_{SC}} \right)$	β	region	C_{TR}	D_{TR}	R
Scallop-parameter-1	0	leeward side	6.6565	-0.7961	0.93358
		windward side	3.1205	-0.9869	0.90463
		combined	5.0127	-0.8689	0.92805
Scallop-parameter-2	+1/2	leeward side	5.7587	-0.7741	0.89416
		windward side	3.1025	-0.9869	0.90463
		combined	6.3861	-0.6858	0.7865
Scallop-parameter-3	-1	combined	16.398	-0.54117	0.89839
		leeward side	23.773	-0.57793	0.94399
		combined	23.927	-0.42899	0.90692
Scallop-parameter-4	-1/2	leeward side	11.615	-0.67549	0.92747
		windward side	10.596	-0.78522	0.94067
		combined	12.212	-0.66482	0.93462

Table 5. Curve Fit Information for Wind Tunnel Roughness Correlation Form.

$x \equiv \left[\left(\frac{k_{SC}}{\theta} \right) \left(\frac{\mu_e}{\mu_w} \right) \right] (M_e)^\beta$	β	region	C_{TR}	D_{TR}	R
Wind-tunnel-roughness-0	0	leeward side	621.89	-0.7	0.82572
		windward side	561.57	-0.7	0.73625
		combined	612.96	-0.7	0.84065
Wind-tunnel-roughness-1	0	leeward side	385.49	-0.47775	0.91479
		windward side	364.80	-0.58884	0.72662
		combined	357.15	-0.49610	0.88058
Wind-tunnel-roughness-2	+1/2	leeward side	340.51	-0.48004	0.88240
		windward side	173.81	-0.48283	0.52287
		combined	211.31	-0.39149	0.73845
Wind-tunnel-roughness-3	-1/2	combined	385.32	-0.44159	0.92340
		leeward side	422.99	-0.51548	0.79459
		combined	408.34	-0.47486	0.91789
Wind-tunnel-roughness-4	-1	leeward side	359.16	-0.39267	0.91623
		windward side	410.57	-0.42942	0.82165
		combined	371.48	-0.40431	0.91985

Table 6. Curve Fit Information for Multiple Parameter Correlation Form.

$x \equiv \left[\left(\frac{k_{SC}}{\theta} \right) \left(\frac{\mu_e}{\mu_w} \right) \right]^\alpha (M_e)^\beta \left(\frac{k_{SC}}{L_{SC}} \right)^\gamma$	α	β	γ	region	C_{TR}	D_{TR}	R
Multiple-parameter-1	+1	-1/2	+1	leeward side	91.421	-0.30073	0.95205
				windward side	82.670	-0.37416	0.87975
				combined	87.371	-0.32486	0.94525
Multiple-parameter-2	+1	-1/2	+1/2	leeward side	164.67	-0.36049	0.94466
				windward side	167.79	-0.55108	0.85517
				combined	164.60	-0.38879	0.93284
Multiple-parameter-3	+1/2	-1/2	+1/2	leeward side	97.599	-0.56044	0.94091
				windward side	99.959	-0.65795	0.89074
				combined	96.688	-0.58791	0.94843
Multiple-parameter-4	+1/2	-1	+1/2	combined	107.17	-0.47342	0.92956
				leeward side	126.81	-0.51358	0.89717
				combined	108.60	-0.45869	0.93226
Multiple-parameter-5	+1/2	-1/2	+1	leeward side	47.945	-0.42497	0.95357
				windward side	41.821	-0.51116	0.90704
				combined	45.252	-0.45061	0.95189

Table 7. IRVE-3 trajectory parameters.

Time (sec)	T_{∞} (K)	q_{∞} (Pa)	ρ_{∞} (kg/m³)	U_{∞} (m/s)	α (deg)	M_{∞}	Re_{∞} (1/ft)
664.85	194.60	2.951E+01	7.977E-06	2.720E+03	7.30	9.70	1.671E+03
667.00	200.90	7.634E+01	2.034E-05	2.740E+03	8.17	9.62	4.176E+03
669.20	211.90	1.924E+02	5.076E-05	2.754E+03	7.41	9.41	1.001E+04
671.30	226.07	4.500E+02	1.189E-04	2.752E+03	6.71	9.10	2.220E+04
672.40	232.20	7.224E+02	1.926E-04	2.739E+03	7.98	8.94	3.502E+04
673.50	242.10	1.055E+03	2.863E-04	2.715E+03	8.02	8.68	4.987E+04
674.55	250.60	1.448E+03	4.036E-04	2.678E+03	8.22	8.42	6.745E+04
675.65	258.08	1.973E+03	5.732E-04	2.624E+03	7.36	8.12	9.165E+04
676.70	262.48	2.607E+03	8.019E-04	2.550E+03	8.46	7.83	1.229E+05
677.80	266.22	3.386E+03	1.131E-03	2.447E+03	9.33	7.46	1.645E+05
678.90	266.25	4.153E+03	1.550E-03	2.315E+03	10.06	7.06	2.133E+05
679.95	265.96	4.798E+03	2.043E-03	2.168E+03	10.76	6.61	2.634E+05
681.05	261.20	5.537E+03	2.797E-03	1.990E+03	11.79	6.12	3.359E+05
682.10	256.80	5.939E+03	3.661E-03	1.801E+03	12.77	5.59	4.035E+05
683.20	252.70	6.043E+03	4.727E-03	1.599E+03	13.86	5.00	4.684E+05
684.30	248.40	5.777E+03	5.916E-03	1.397E+03	13.50	4.41	5.195E+05
685.35	245.60	5.261E+03	7.086E-03	1.219E+03	13.60	3.87	5.476E+05
687.50	243.10	3.791E+03	9.139E-03	9.108E+02	13.51	2.91	5.323E+05
689.70	239.83	2.637E+03	1.149E-02	6.777E+02	11.18	2.18	5.032E+05
691.85	237.45	1.844E+03	1.357E-02	5.212E+02	11.49	1.68	4.612E+05

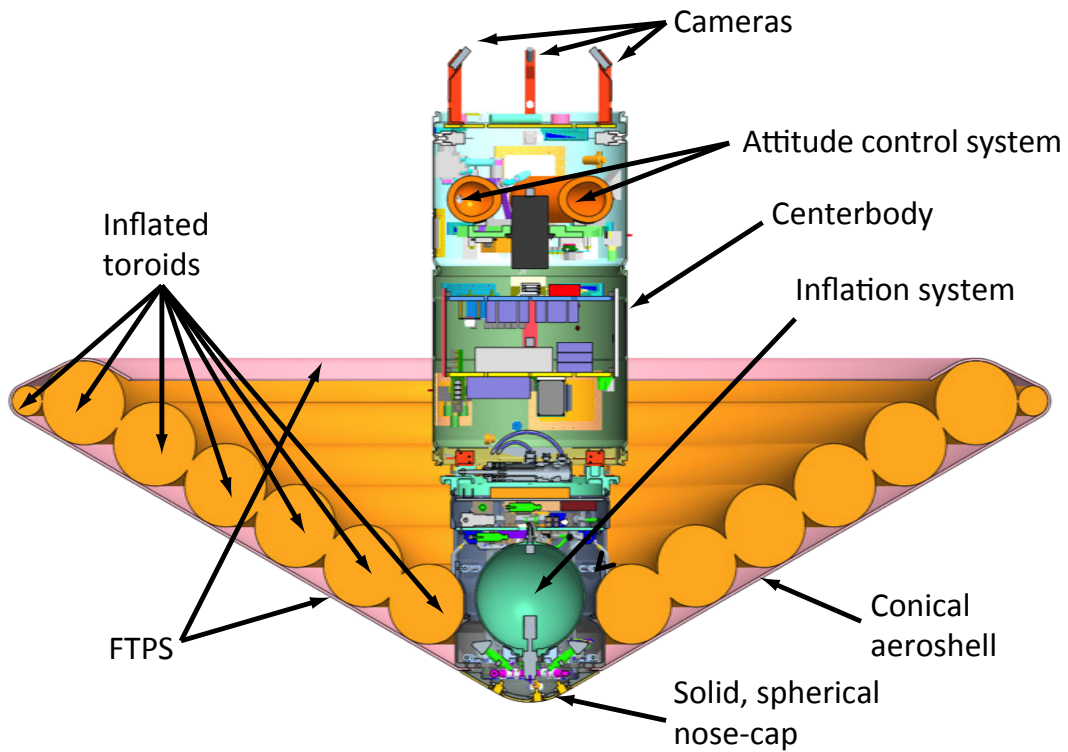


Figure 1. IRVE-3 Flight Vehicle Cross Section.

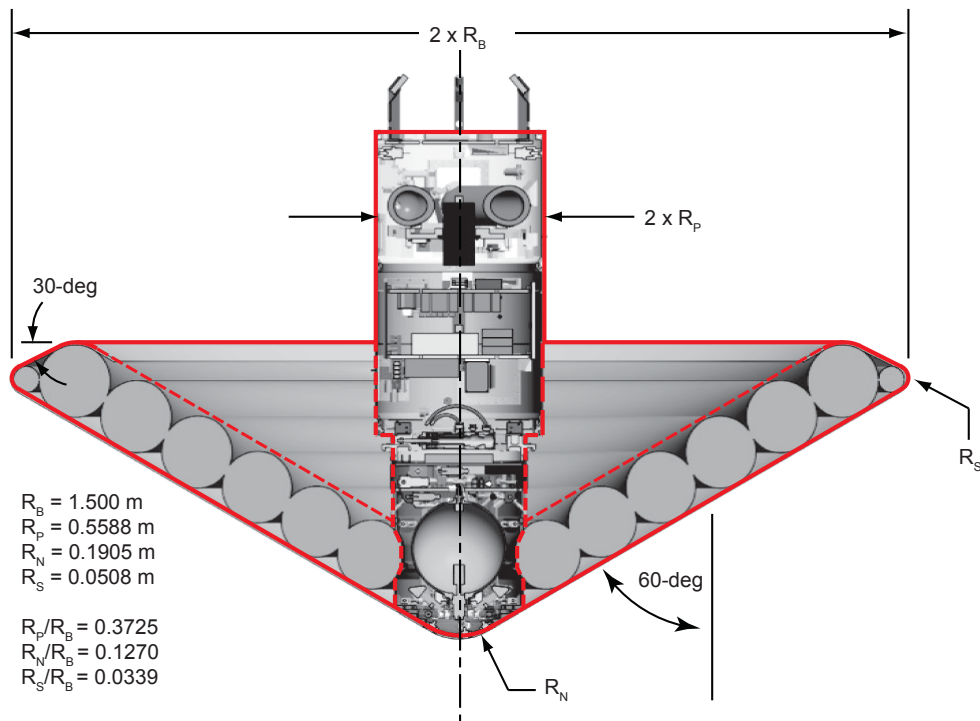


Figure 2. IRVE-3 Flight Vehicle Geometry.



Figure 3. Underlying Structure of IRVE EDU Test Article without F-TPS.



Figure 4. Inflated IRVE EDU Test Article at Static Atmospheric Conditions.

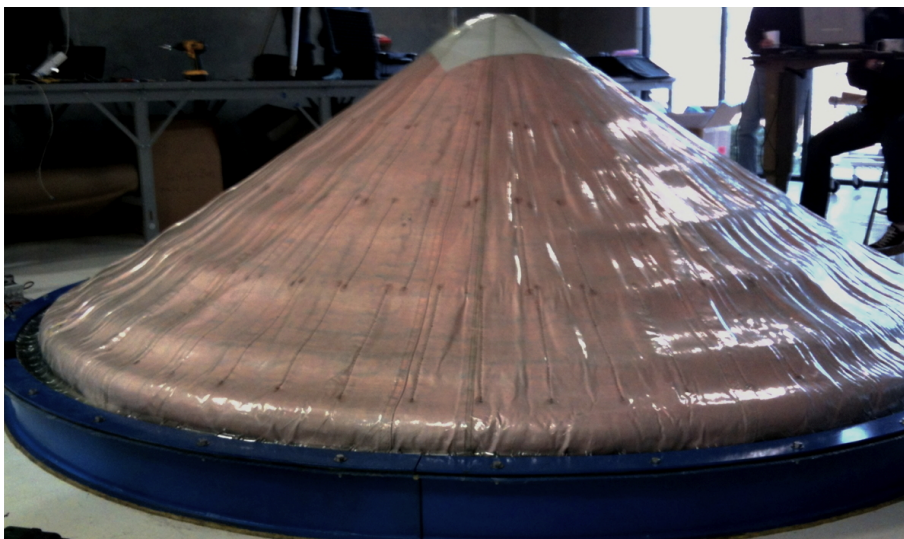


Figure 5. Inflated IRVE EDU Test Article Under Pressure Loading.

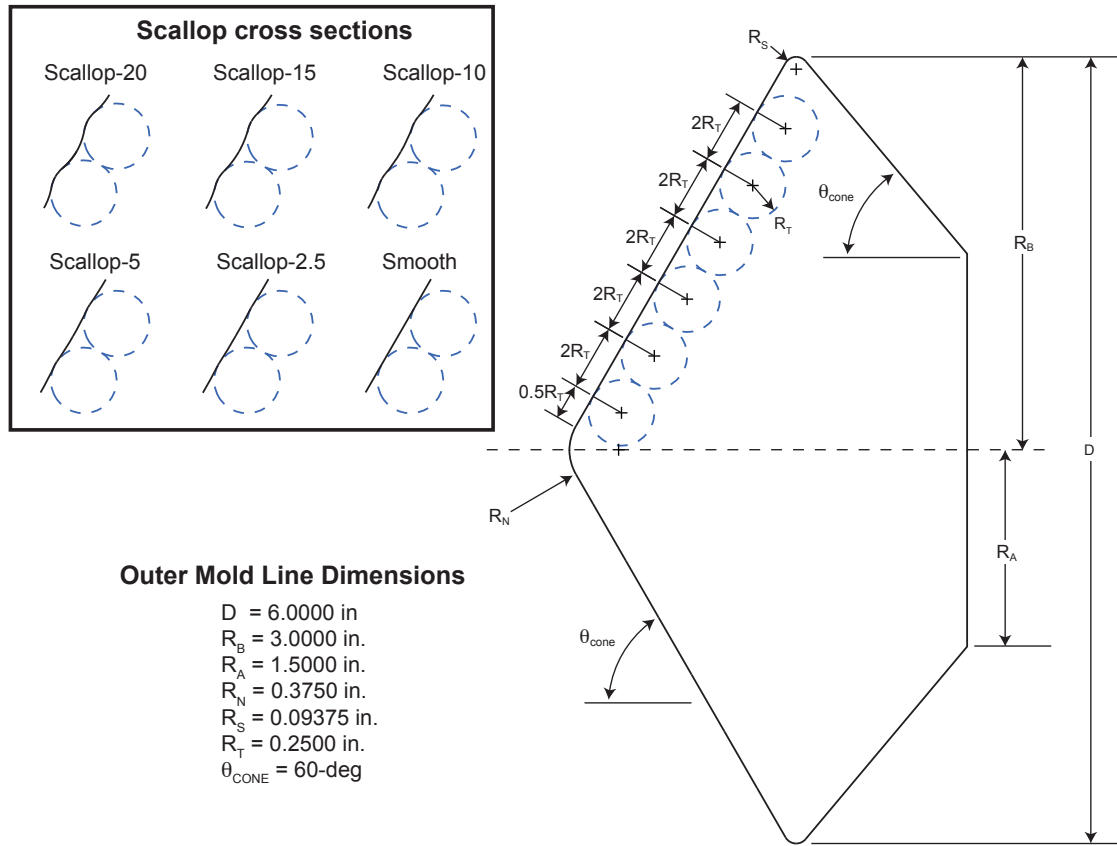


Figure 6. Parametric Scallop Model Outer Mold Line Dimensions.

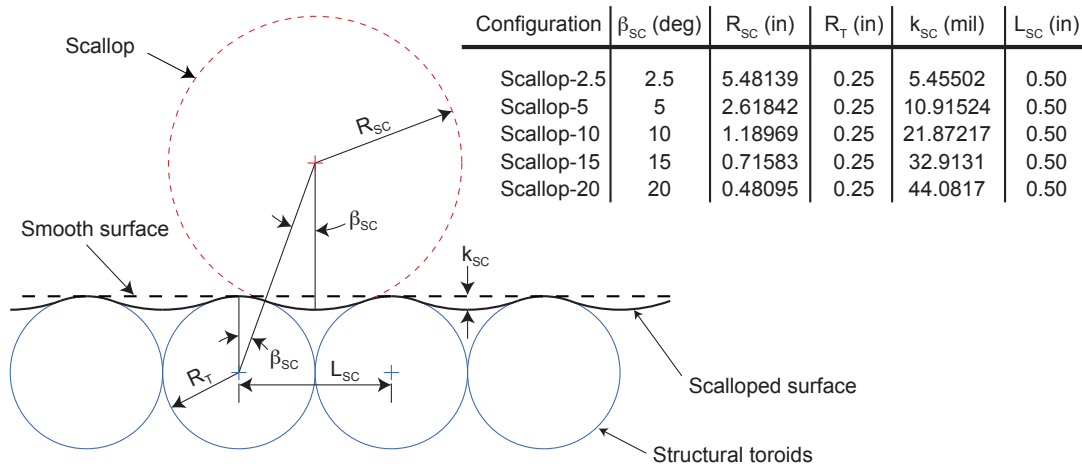


Figure 7. Parametric Scallop Details.



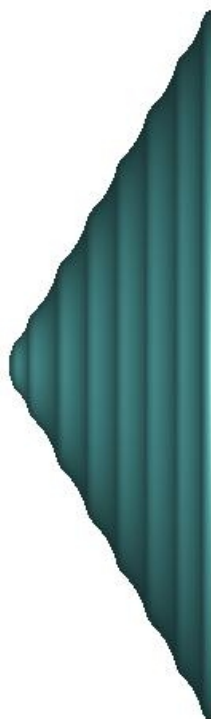
IRVE Scallop-2.5



IRVE Scallop-5



IRVE Scallop-10



IRVE Scallop-15



IRVE Scallop-20



IRVE EDU

Figure 8. Renderings of IRVE Parametric Scallop Model Surfaces.

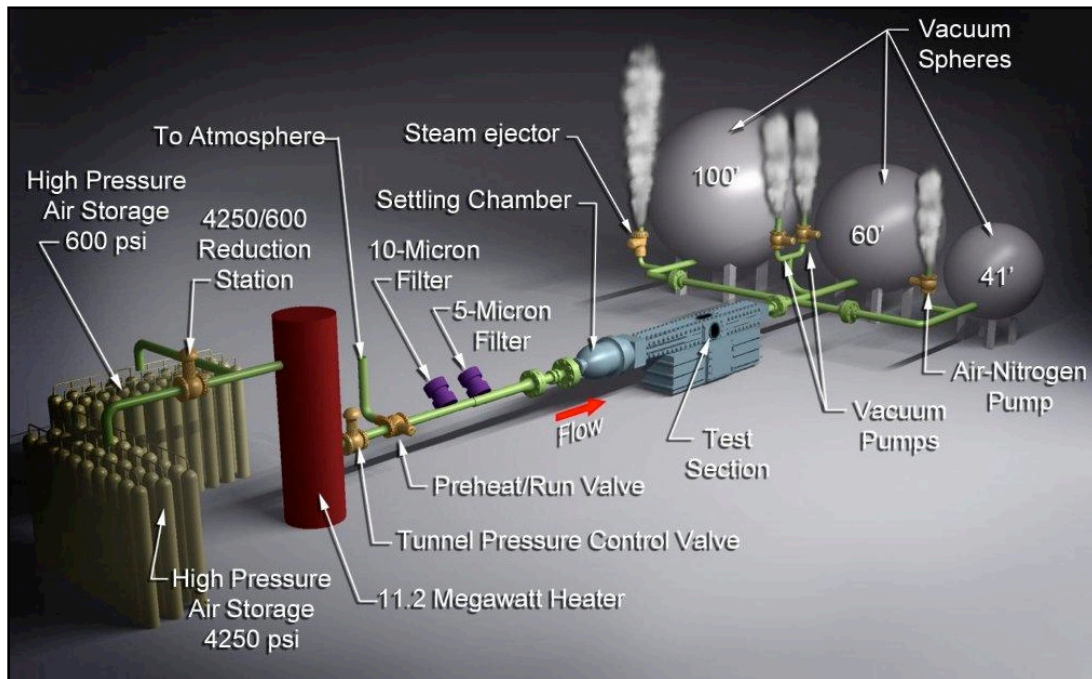


Figure 9. Schematic of LaRC 20-Inch Mach 6 Air Tunnel.

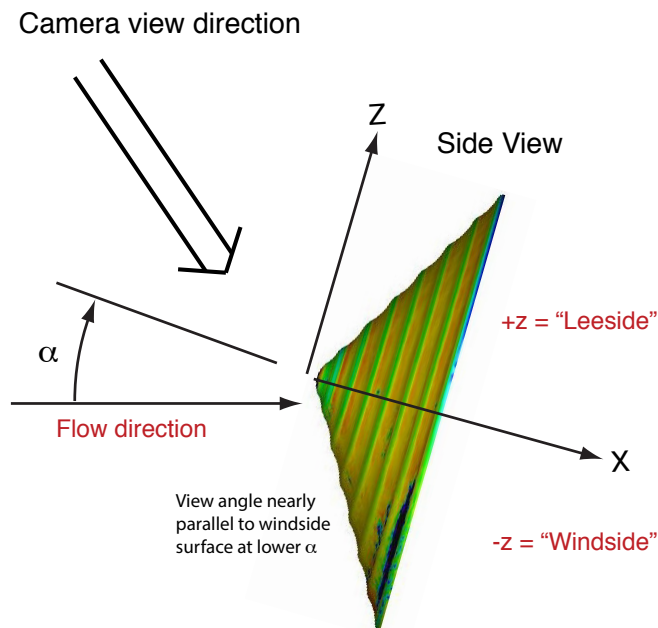
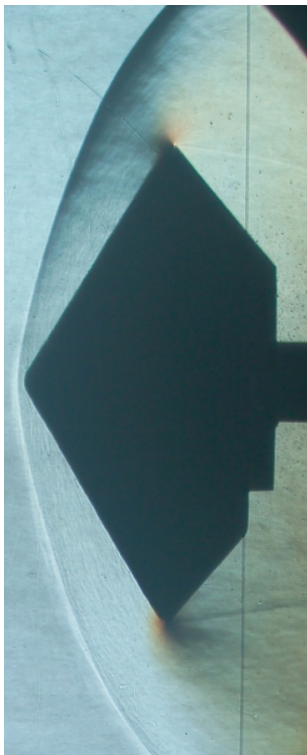


Figure 10. Camera View Direction and Coordinate System Nomenclature.



IRVE Scallop-2.5



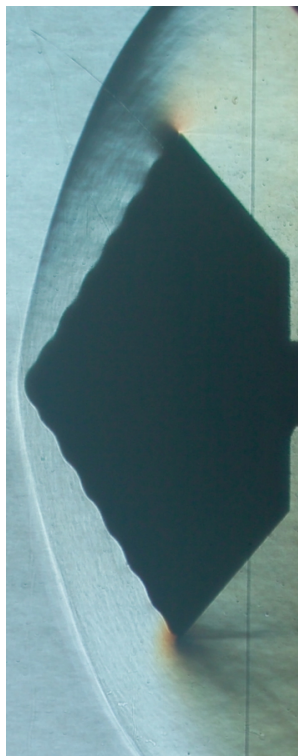
IRVE Scallop-5



IRVE Scallop-10



IRVE Scallop-15



IRVE Scallop-20



IRVE EDU

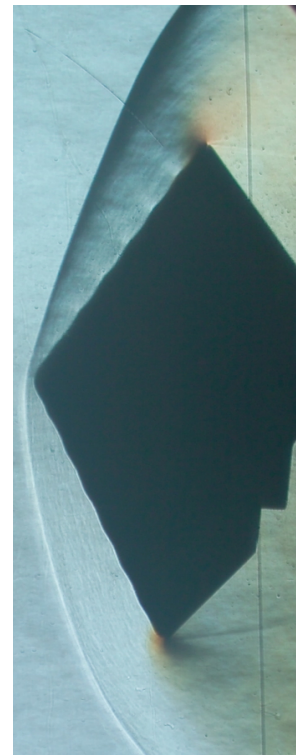
Figure 11. Schlieren Images, $\alpha = 0$ -deg.



IRVE Scallop-2.5



IRVE Scallop-5



IRVE Scallop-10



IRVE Scallop-15

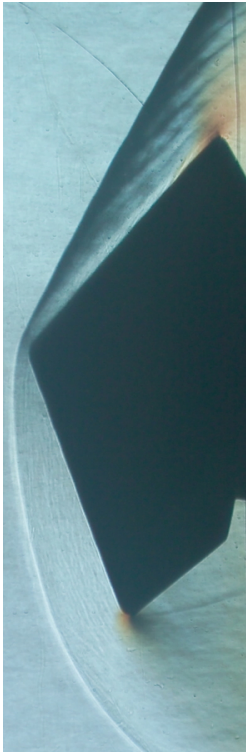


IRVE Scallop-20



IRVE EDU

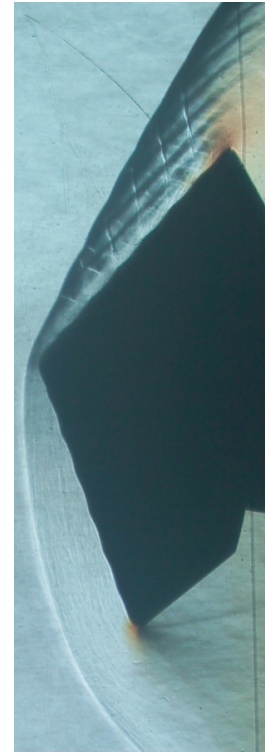
Figure 12. Schlieren Images, $\alpha = 6\text{-deg}$.



IRVE Scallop-2.5



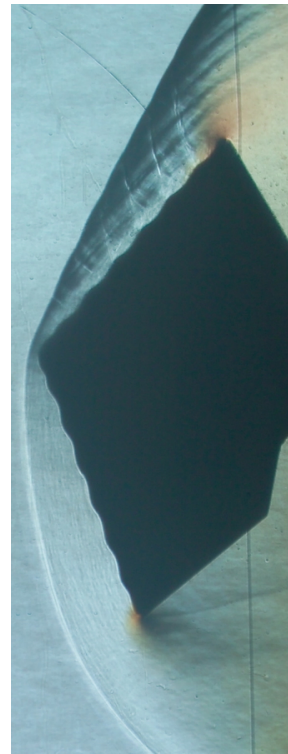
IRVE Scallop-5



IRVE Scallop-10



IRVE Scallop-15



IRVE Scallop-20



IRVE EDU

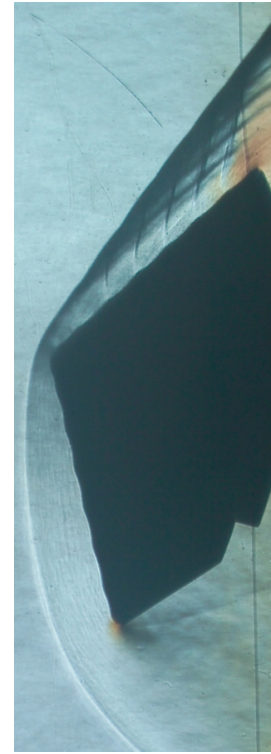
Figure 13. Schlieren Images, $\alpha = 12$ -deg.



IRVE Scallop-2.5



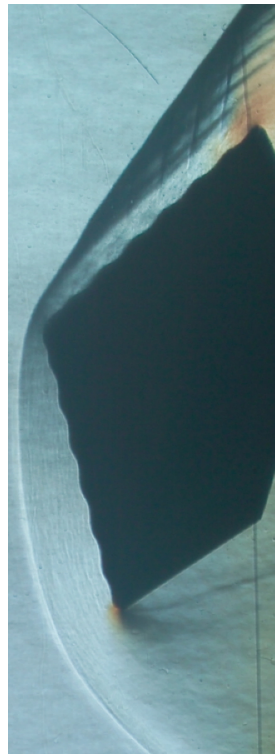
IRVE Scallop-5



IRVE Scallop-10



IRVE Scallop-15



IRVE Scallop-20



IRVE EDU

Figure 14. Schlieren Images, $\alpha = 18$ -deg.

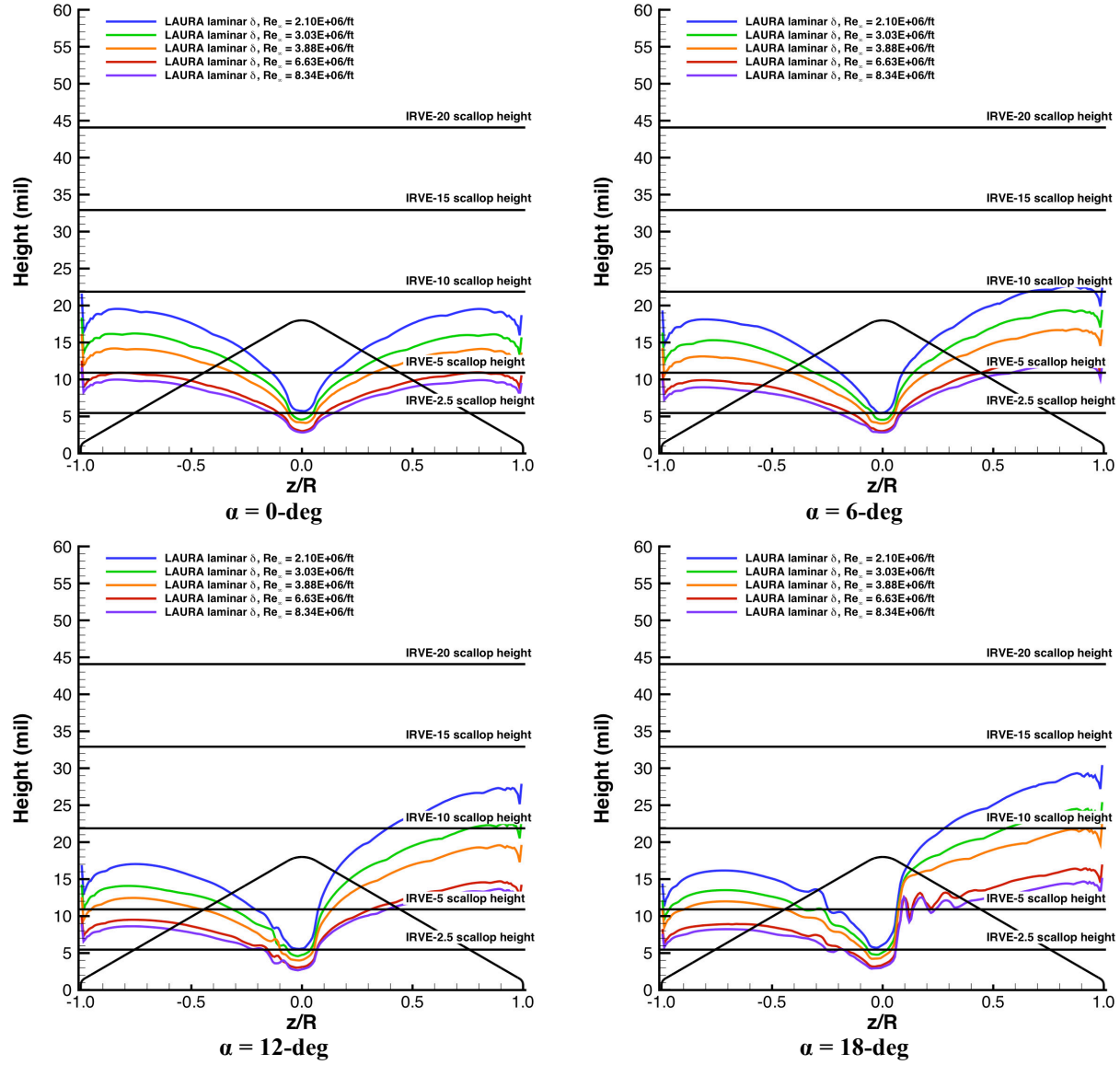


Figure 15. Comparison of Scallop Heights and Smooth-Wall Boundary Layer Heights.

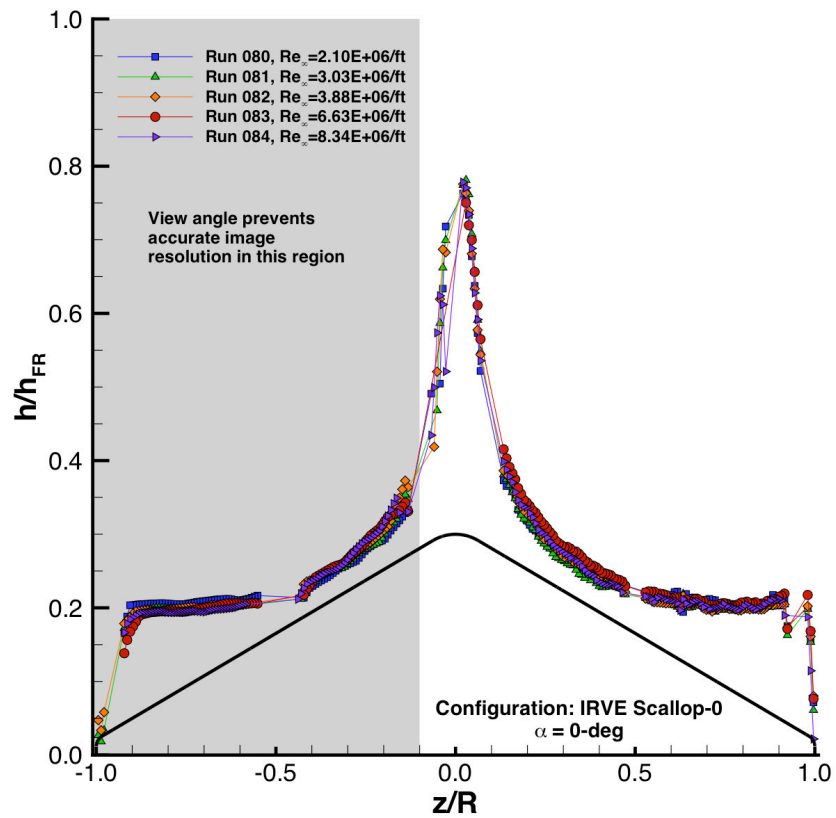
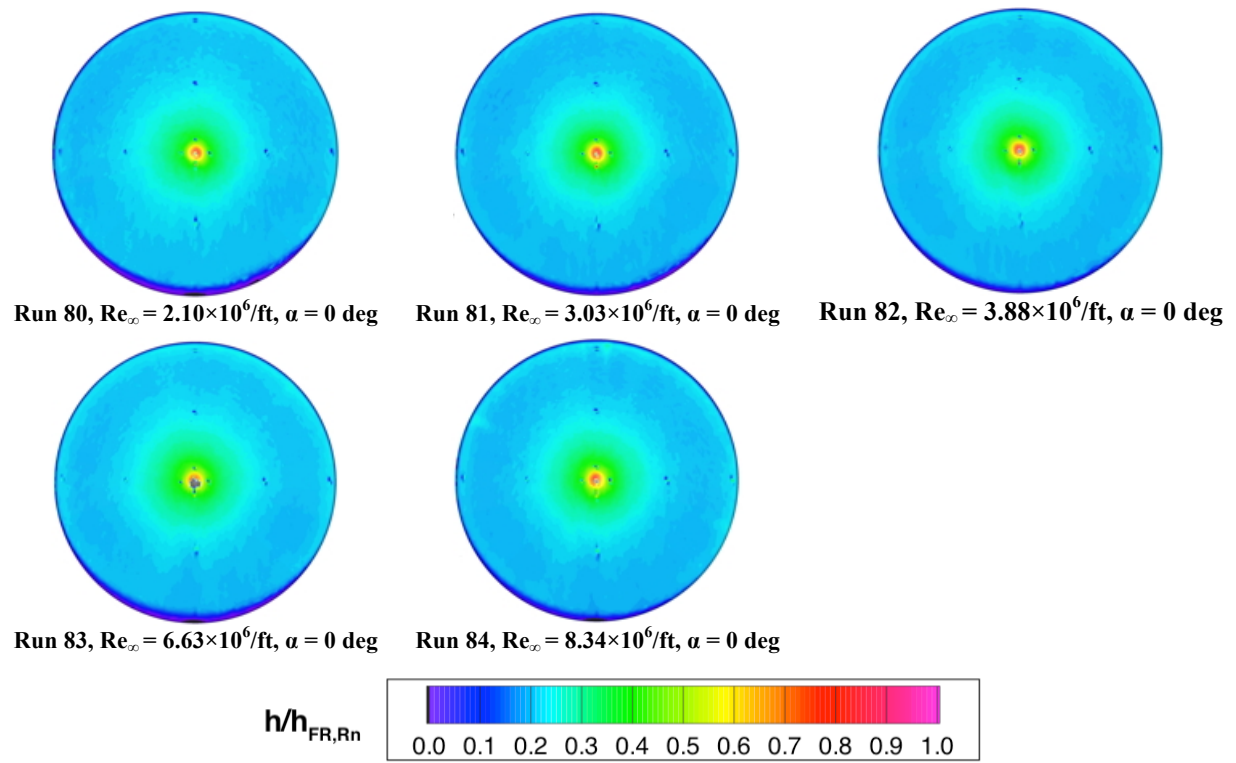


Figure 16. IRVE Scallop-0 Model, Reynolds Number Effects at $\alpha = 0 \text{ deg}$.

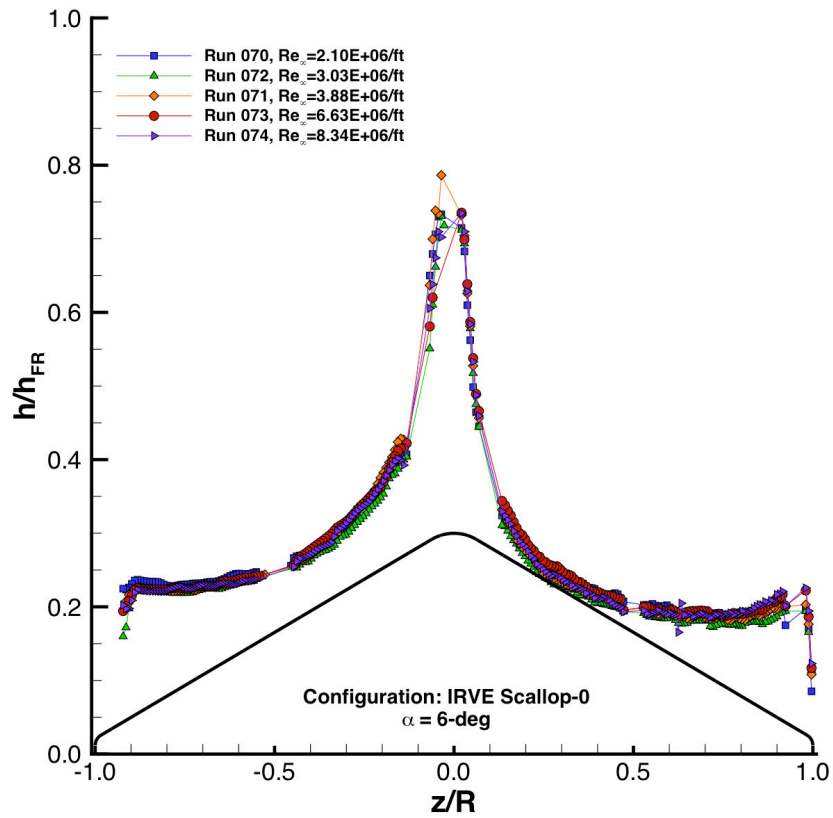
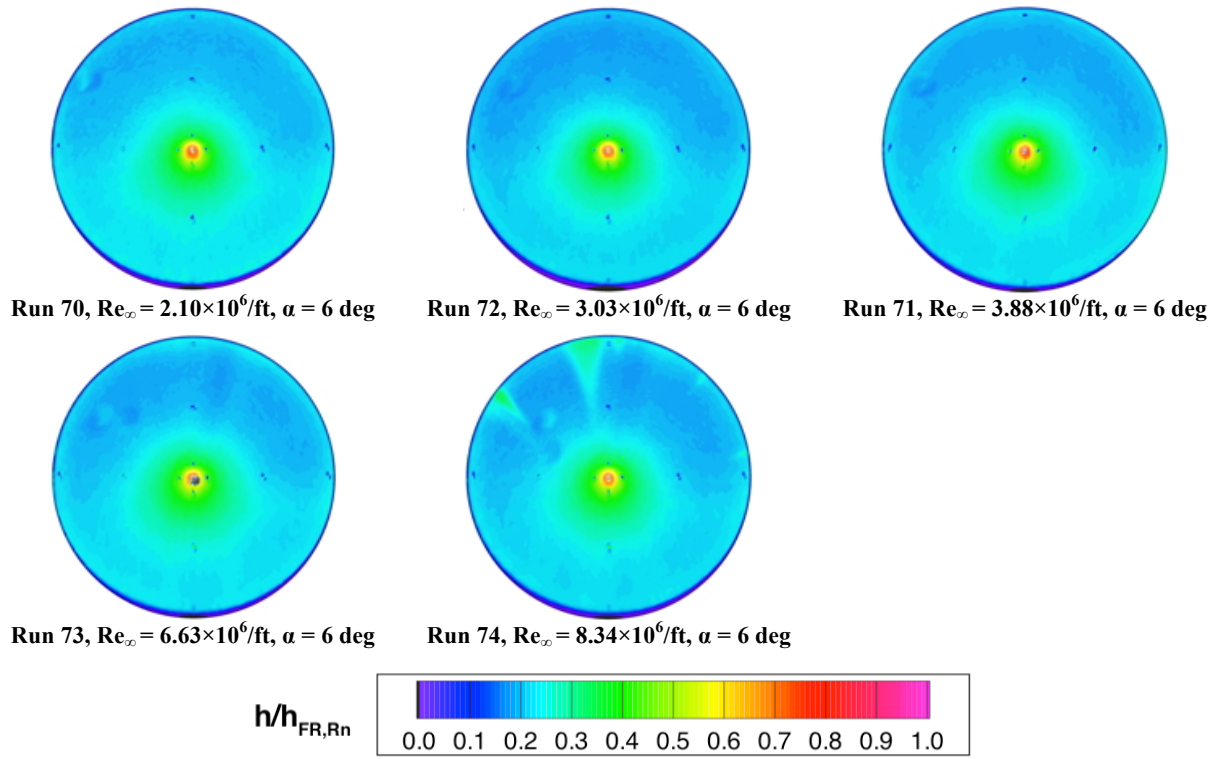


Figure 17. IRVE Scallop-0 Model, Reynolds Number Effects at $\alpha = 6$ deg.

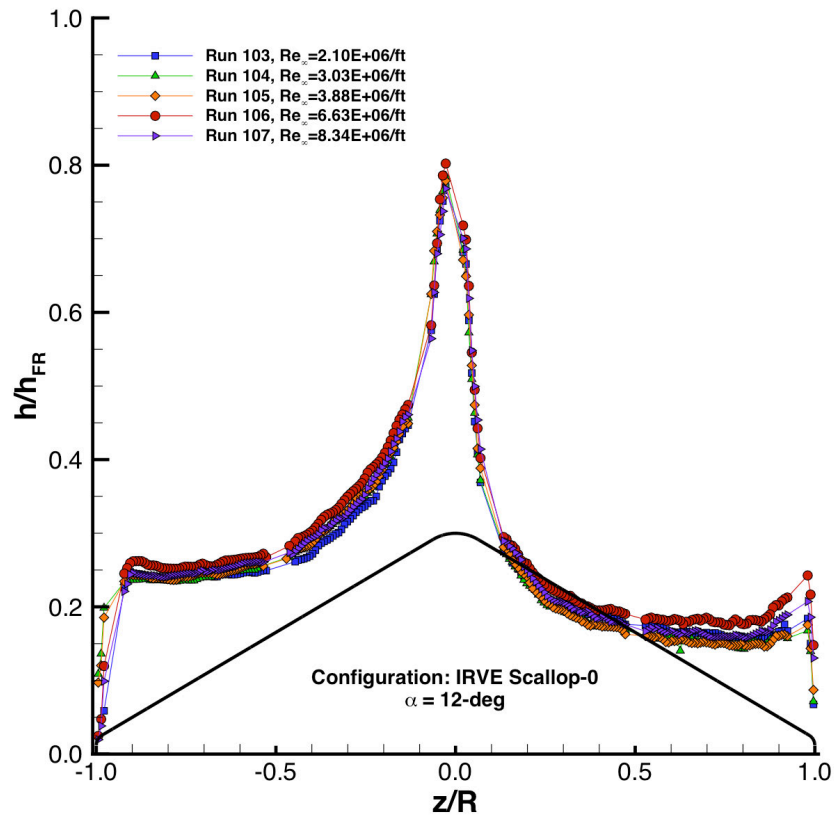
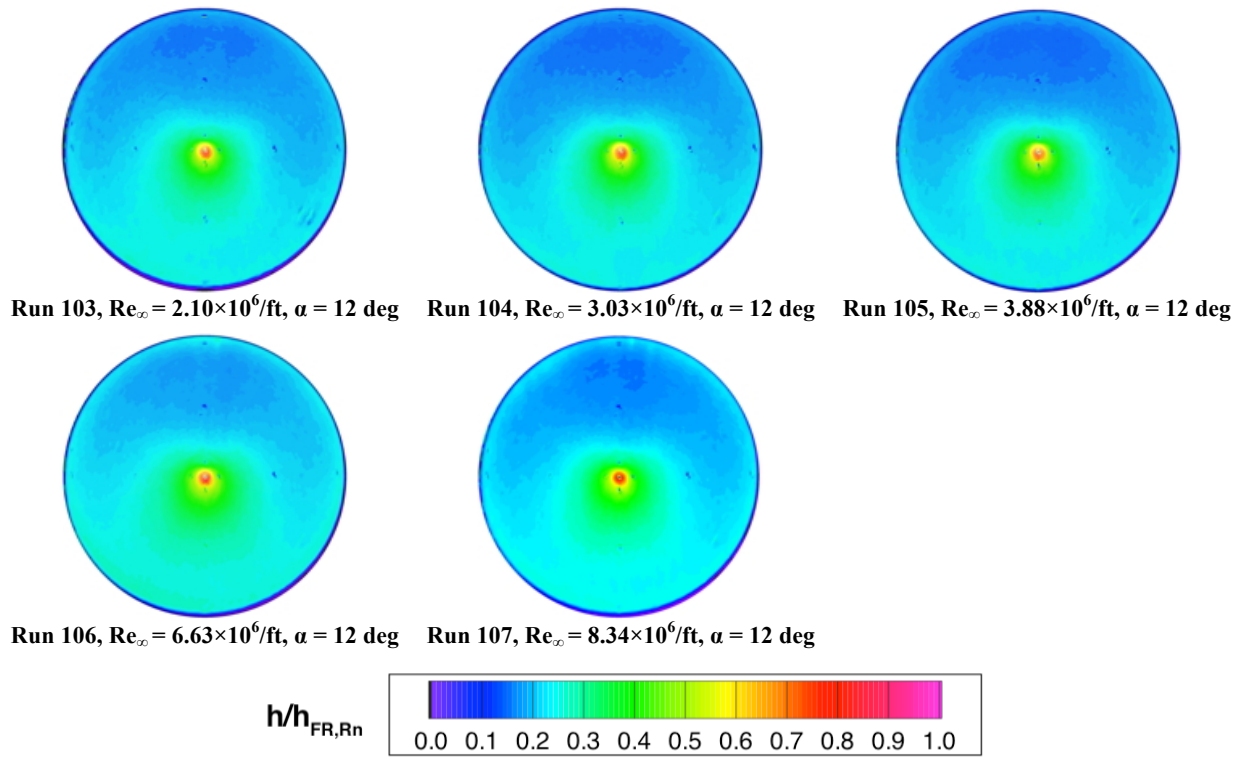


Figure 18. IRVE Scallop-0 Model, Reynolds Number Effects at $\alpha = 12$ deg.

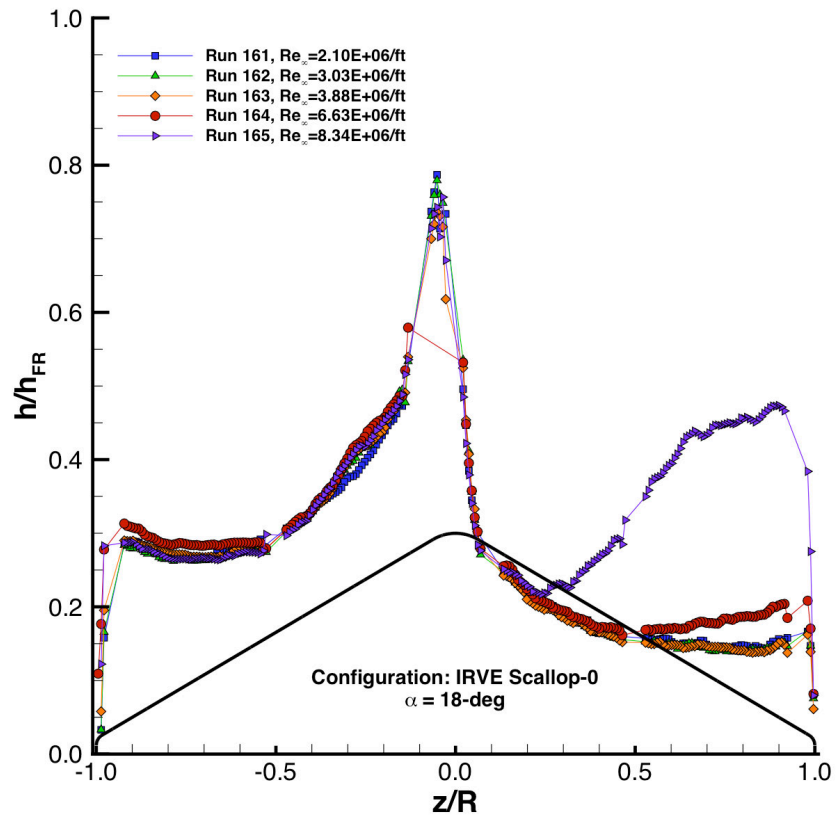
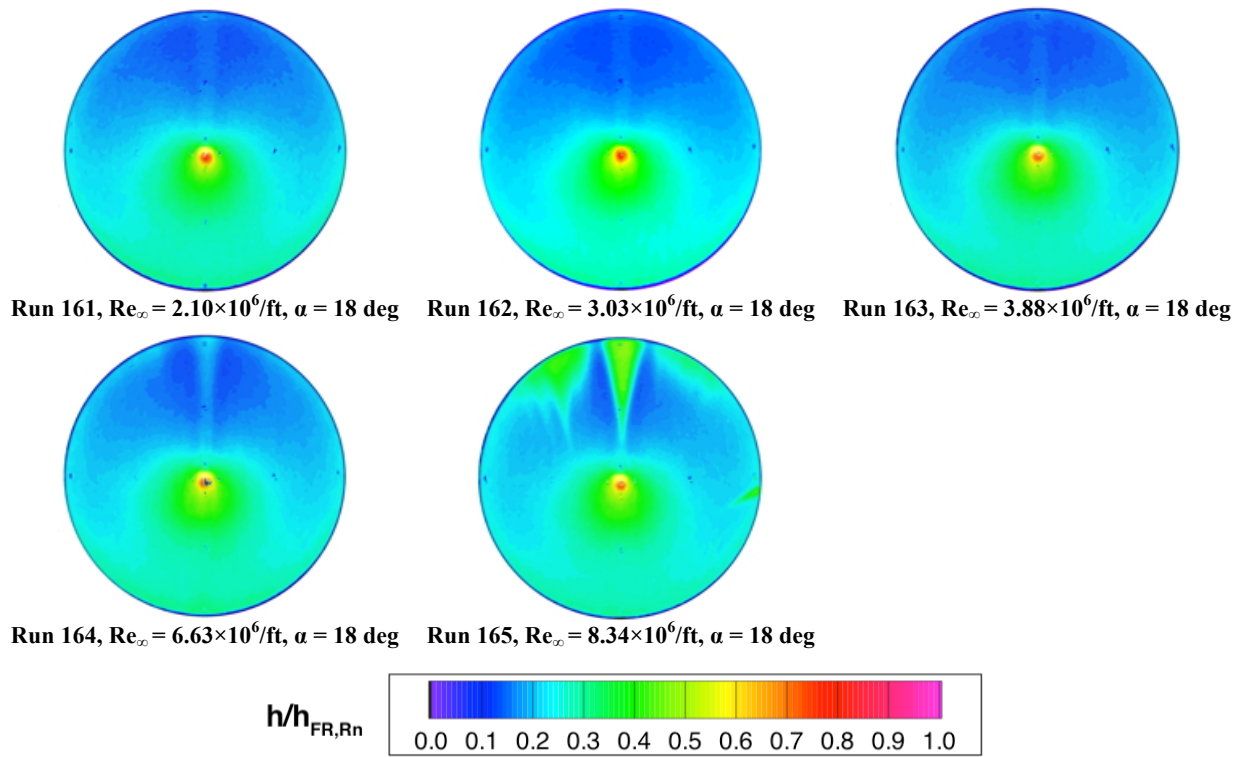


Figure 19. IRVE Scallop-0 Model, Reynolds Number Effects at $\alpha = 18 \text{ deg}$.

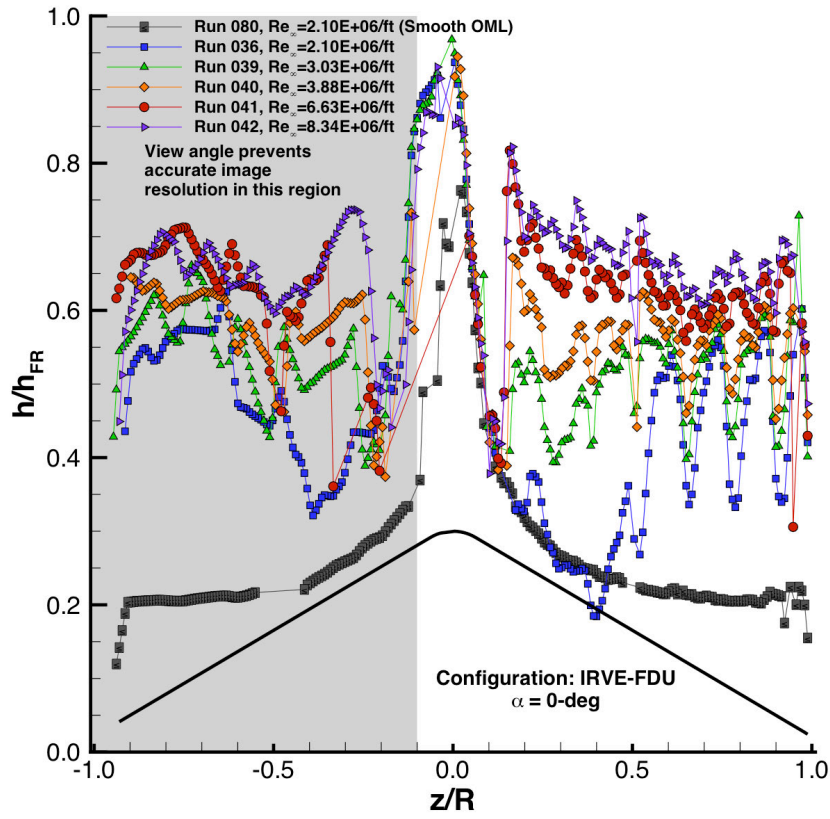
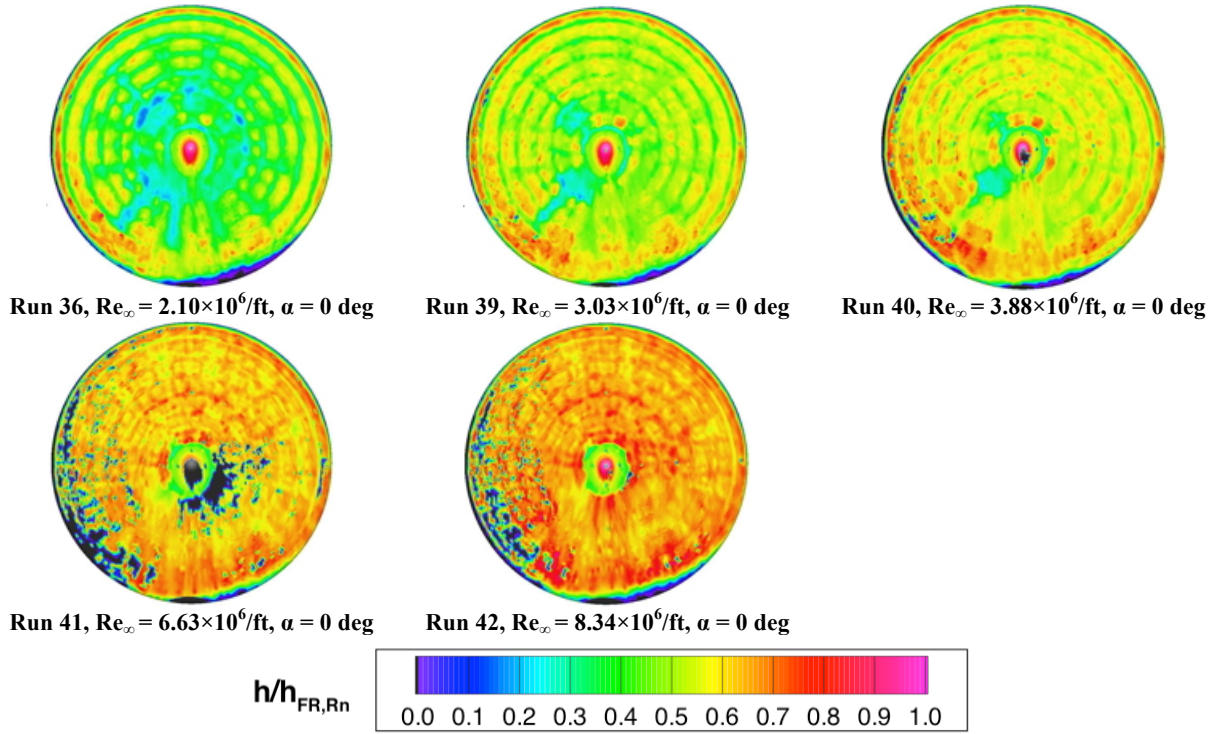


Figure 20. IRVE EDU Model, Reynolds Number Effects at $\alpha = 0$ deg.

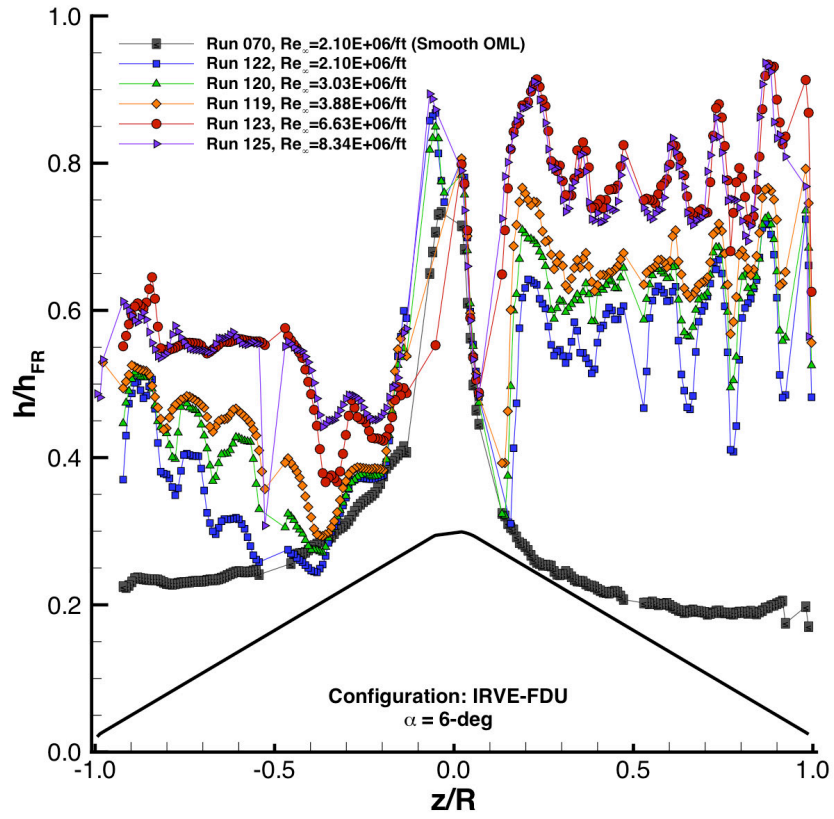
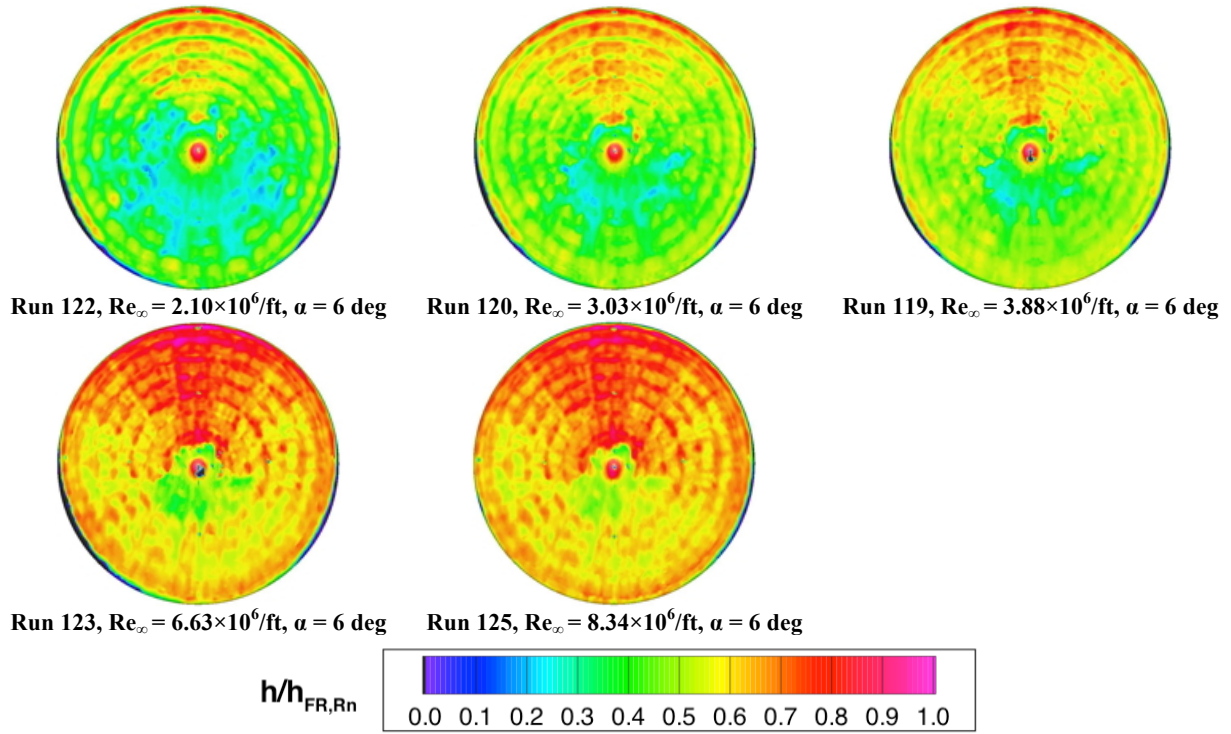


Figure 21. IRVE EDU Model, Reynolds Number Effects at $\alpha = 6$ deg.

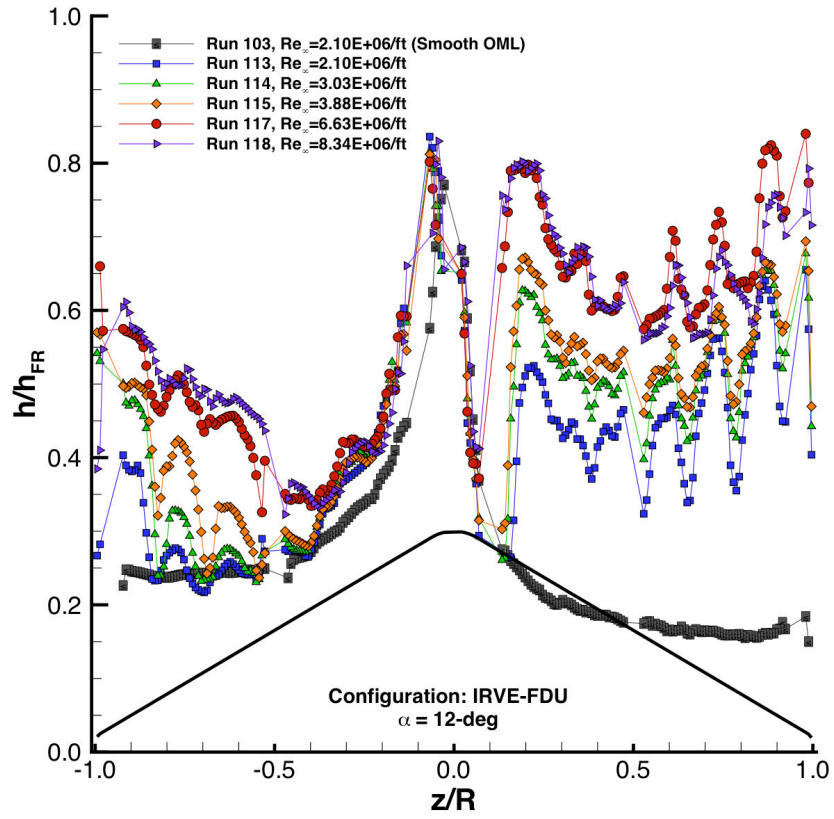
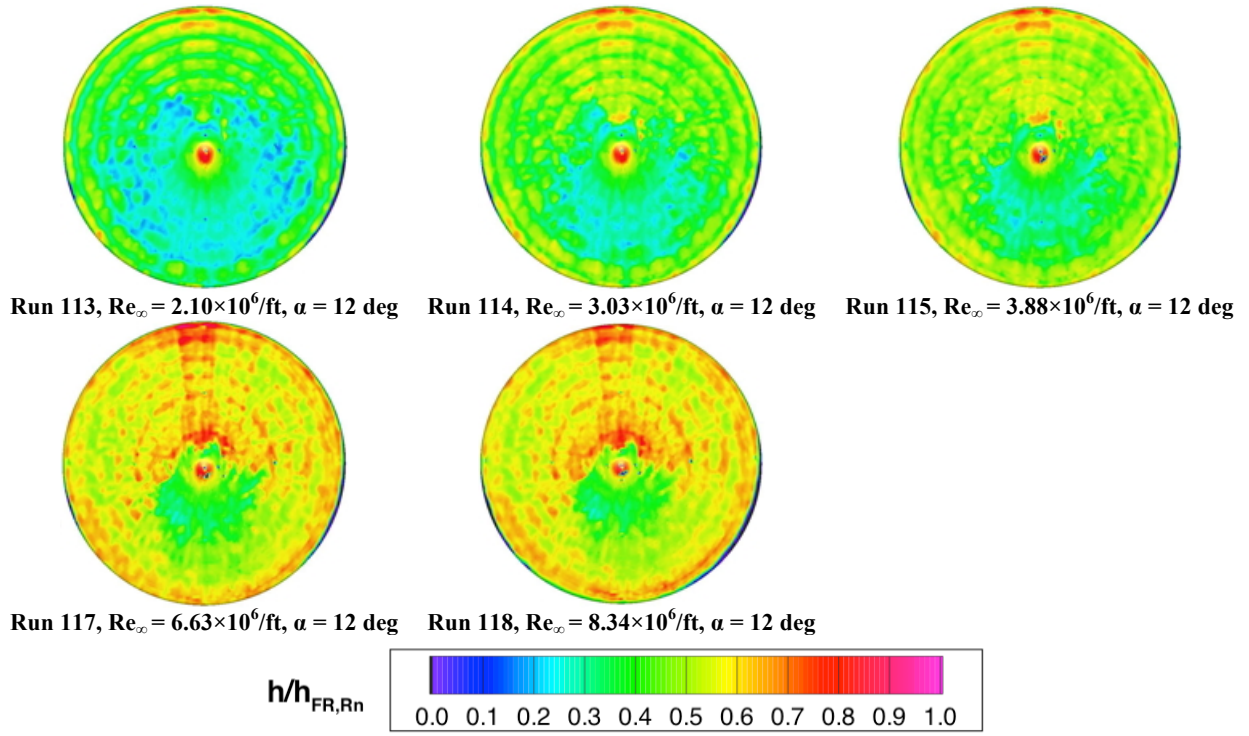


Figure 22. IRVE EDU Model, Reynolds Number Effects at $\alpha = 12 \text{ deg}$.

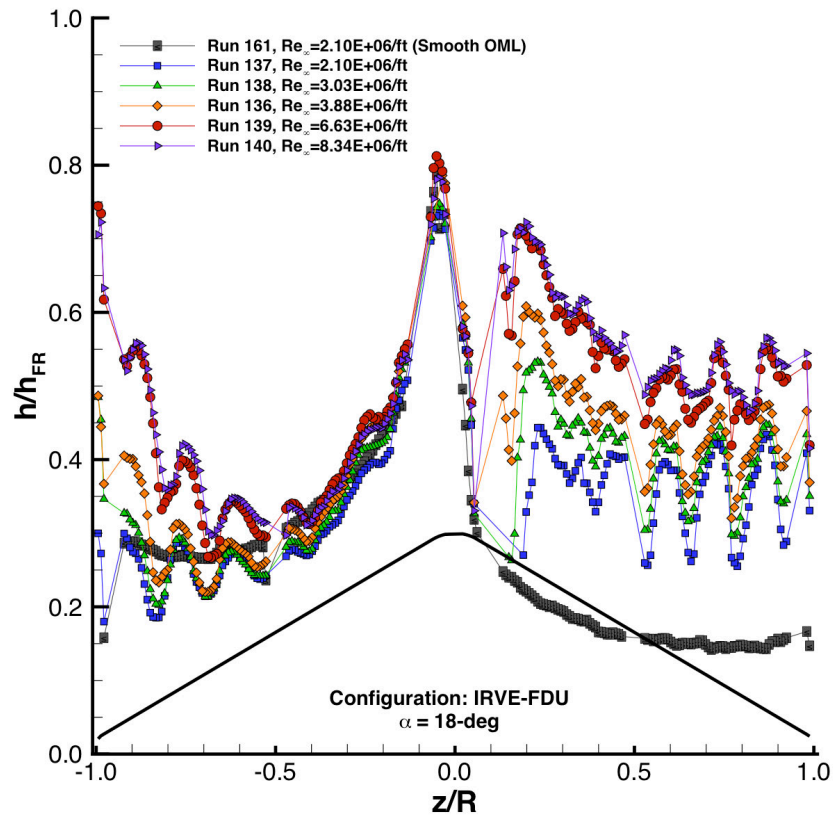
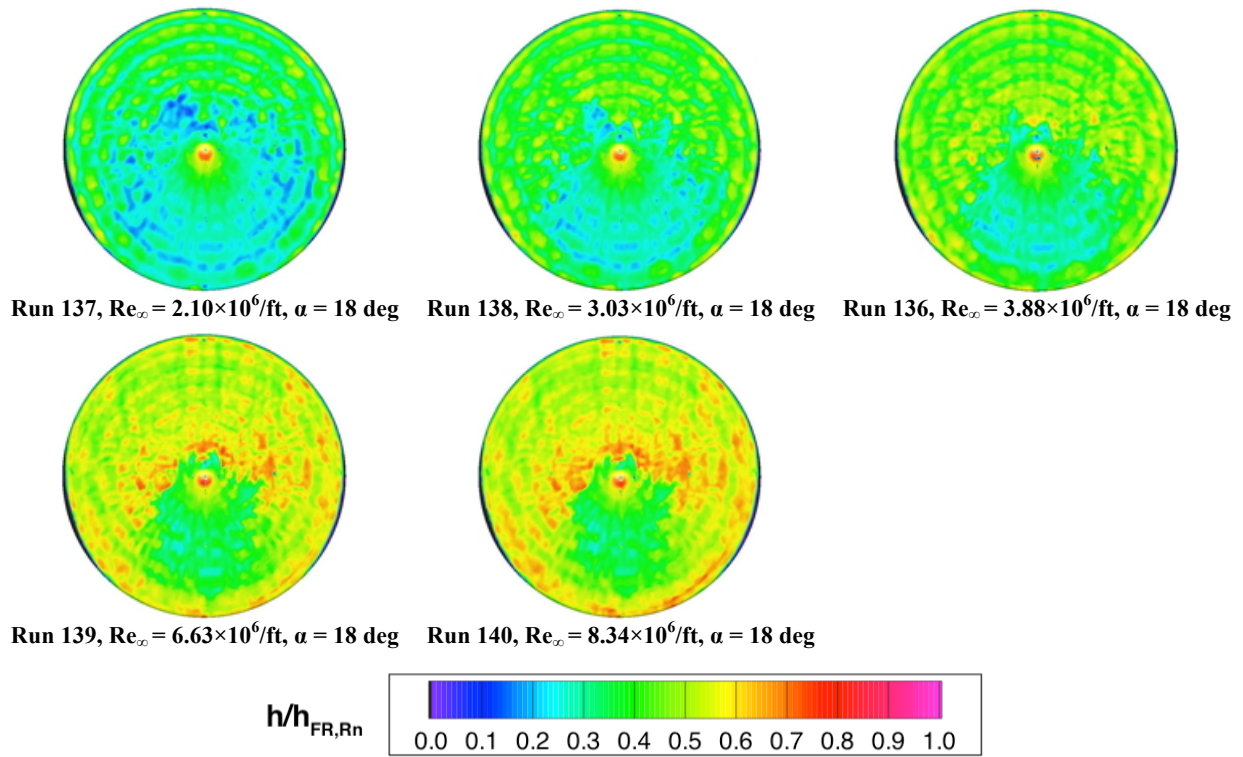


Figure 23. IRVE EDU Model, Reynolds Number Effects at $\alpha = 18$ deg.

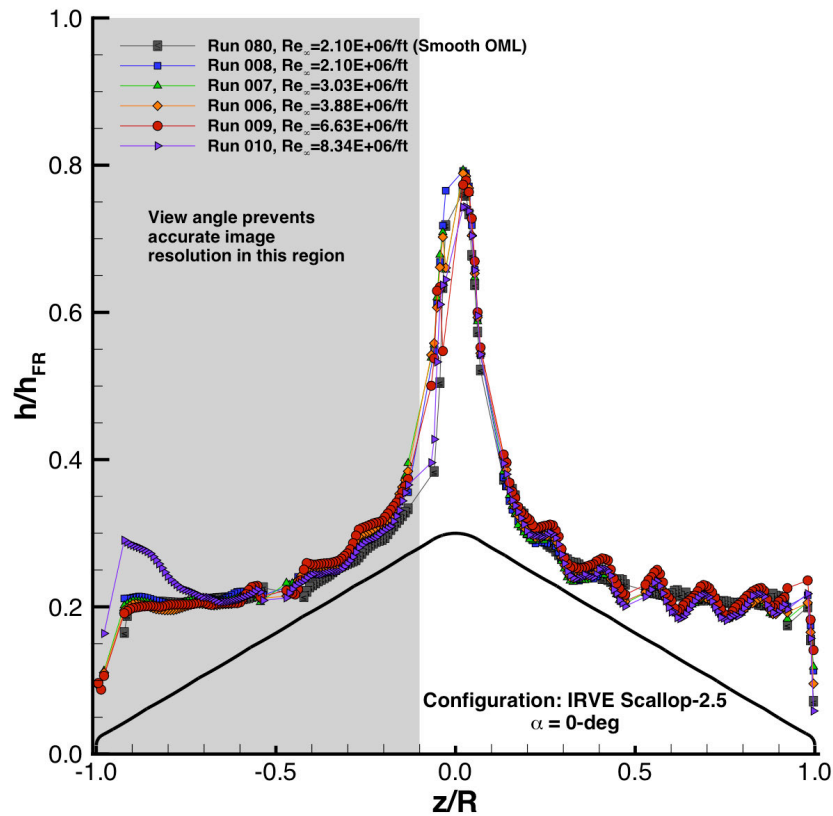
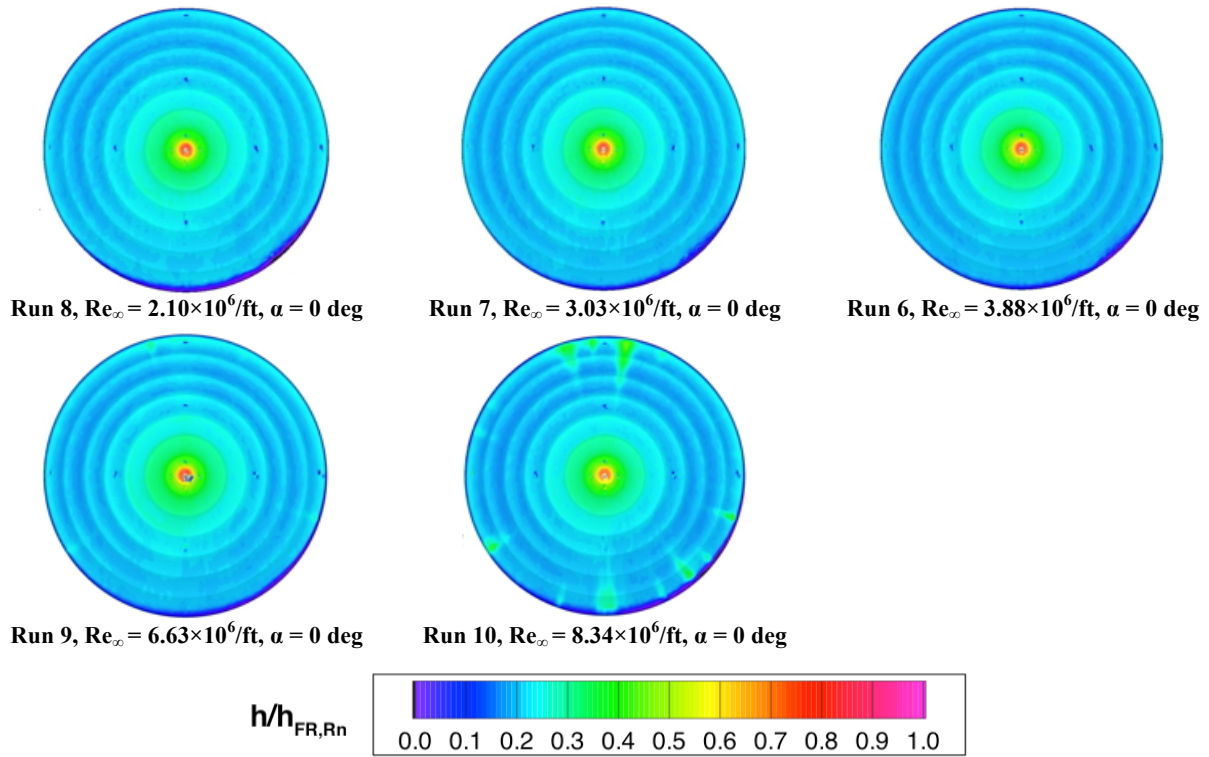


Figure 24. IRVE Scallop-2.5 Model, Reynolds Number Effects at $\alpha = 0$ deg.

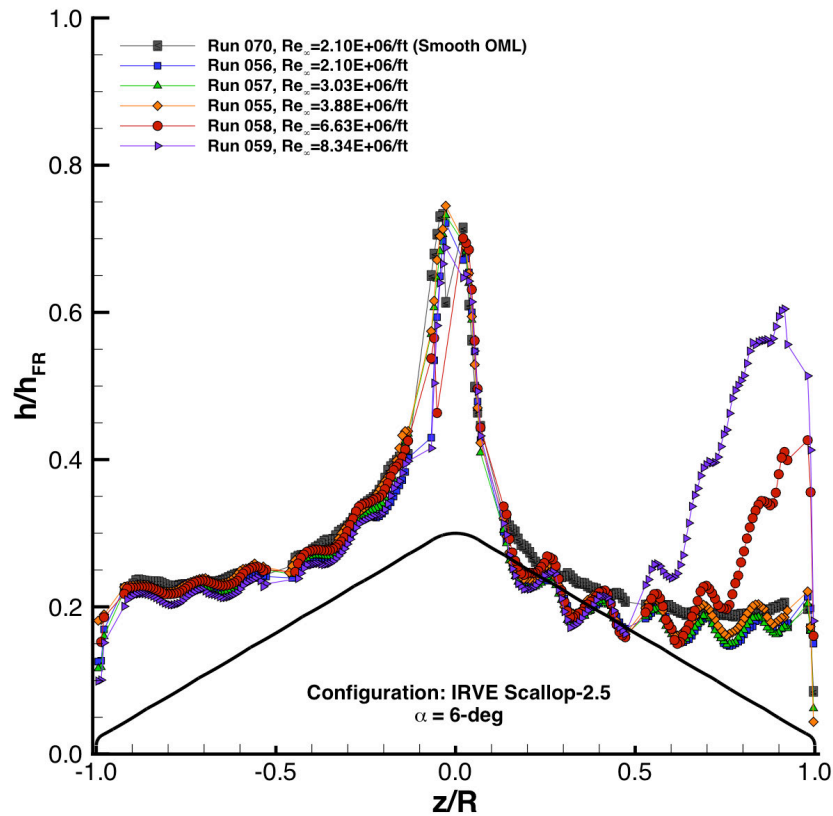
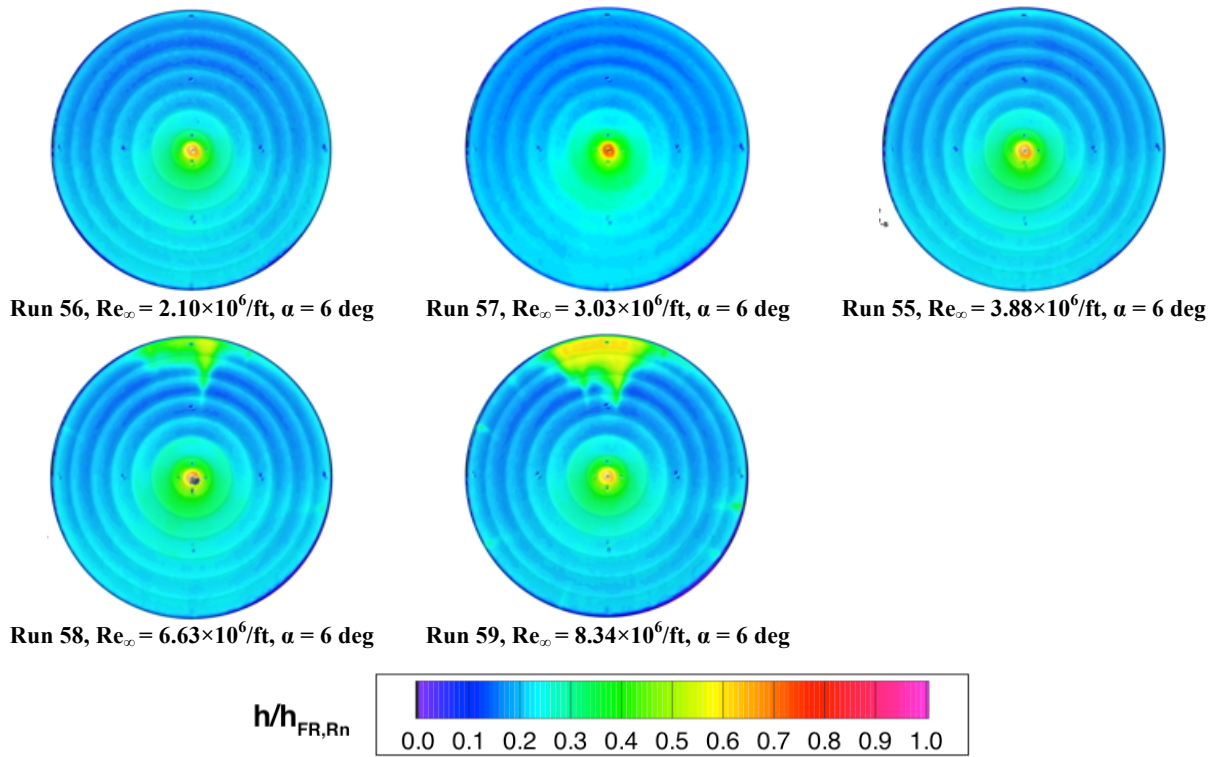


Figure 25. IRVE Scallop-2.5 Model, Reynolds Number Effects at $\alpha = 6$ deg.

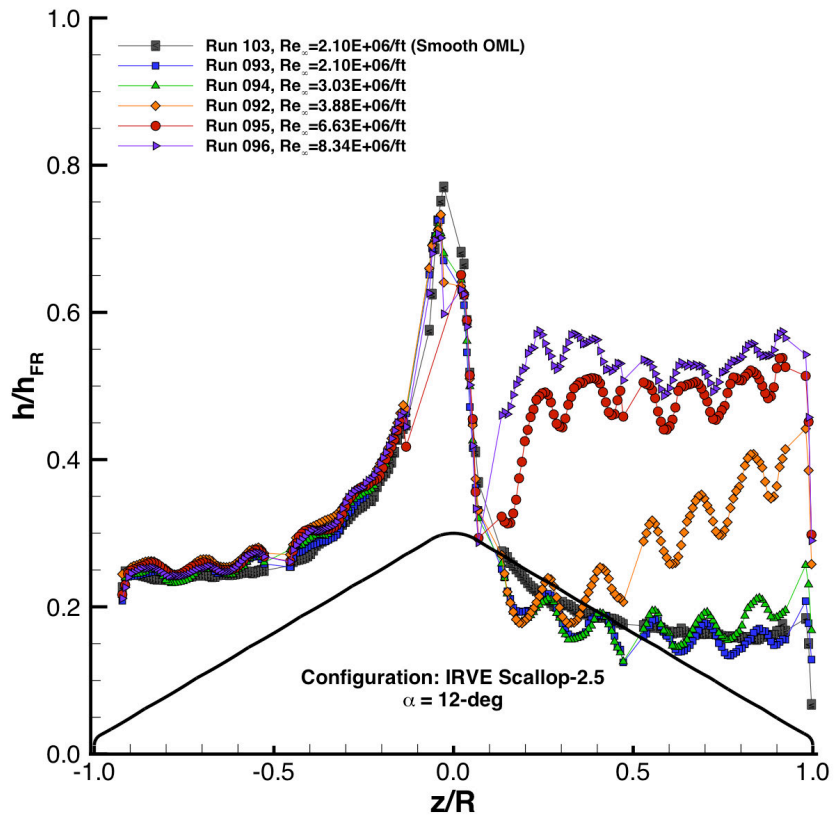
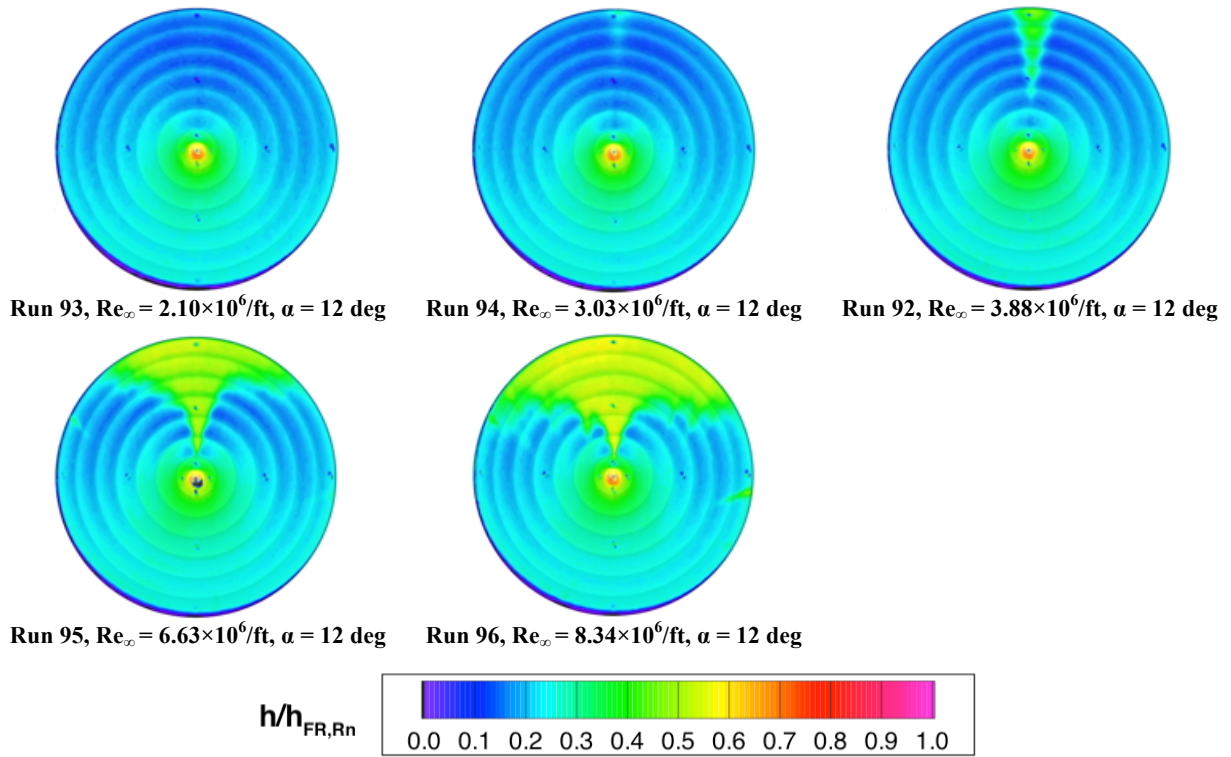


Figure 26. IRVE Scallop-2.5 Model, Reynolds Number Effects at $\alpha = 12$ deg.

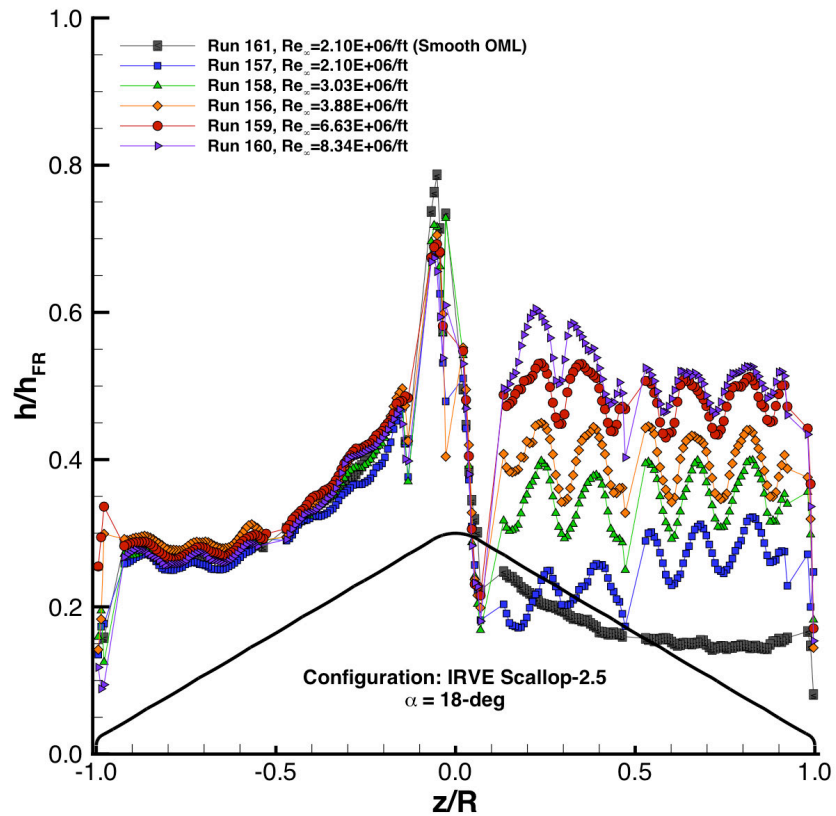
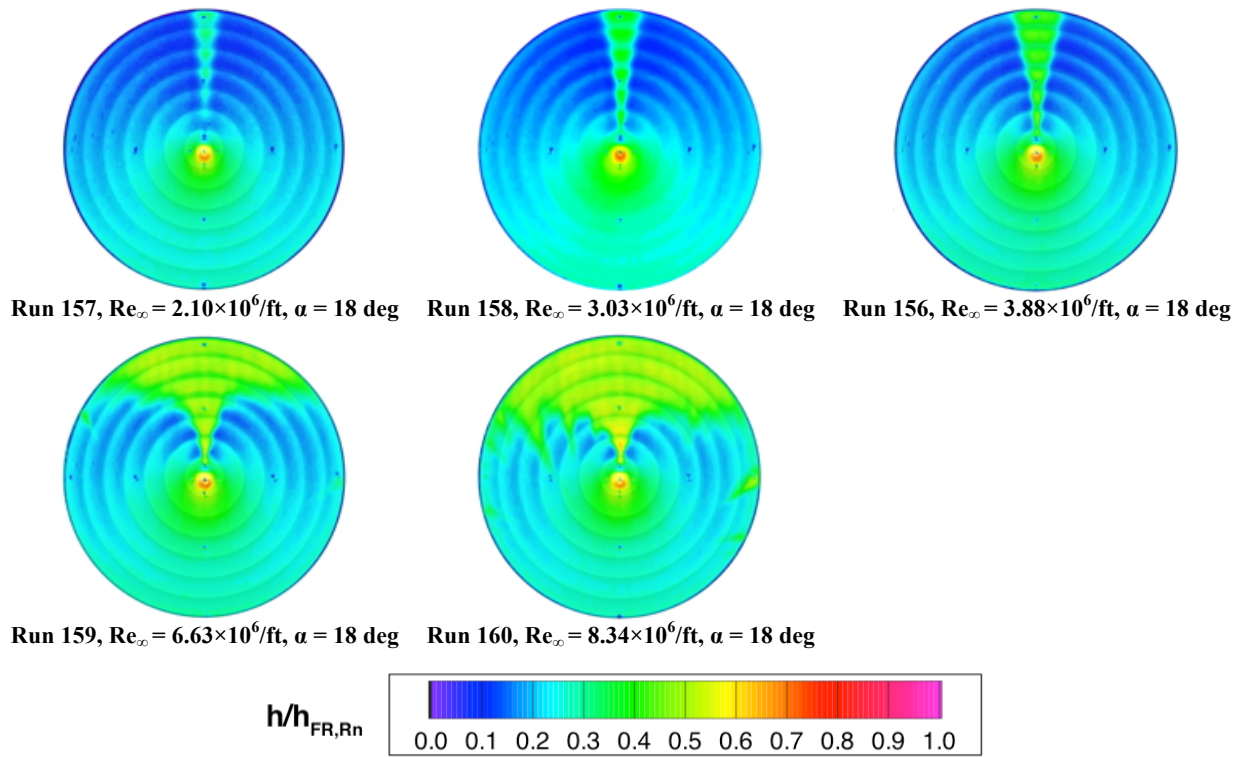


Figure 27. IRVE Scallop-2.5 Model, Reynolds Number Effects at $\alpha = 18^\circ$.

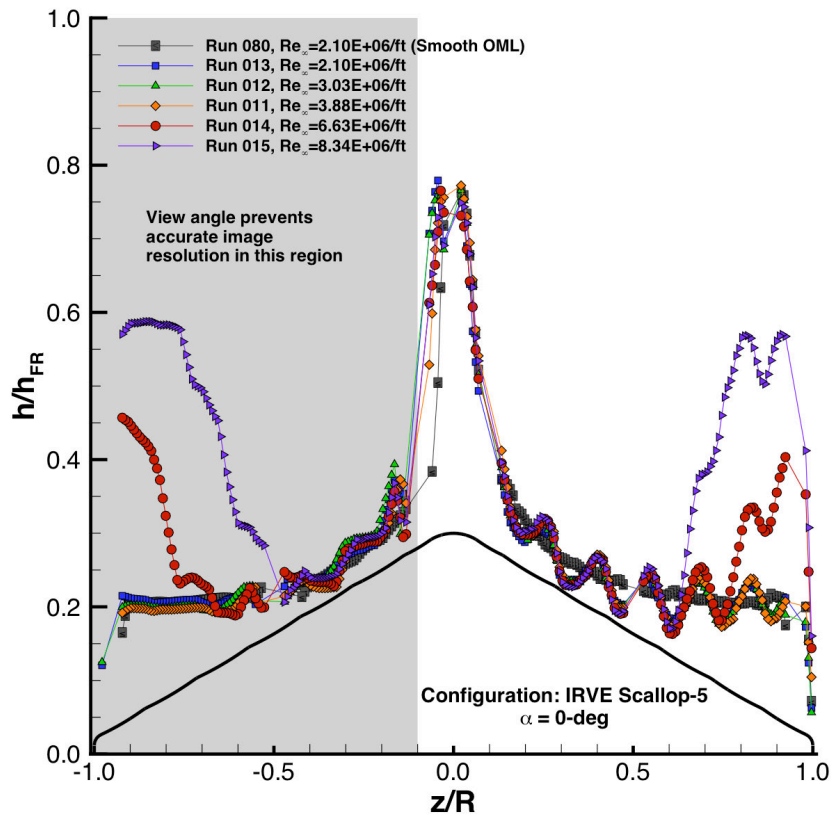
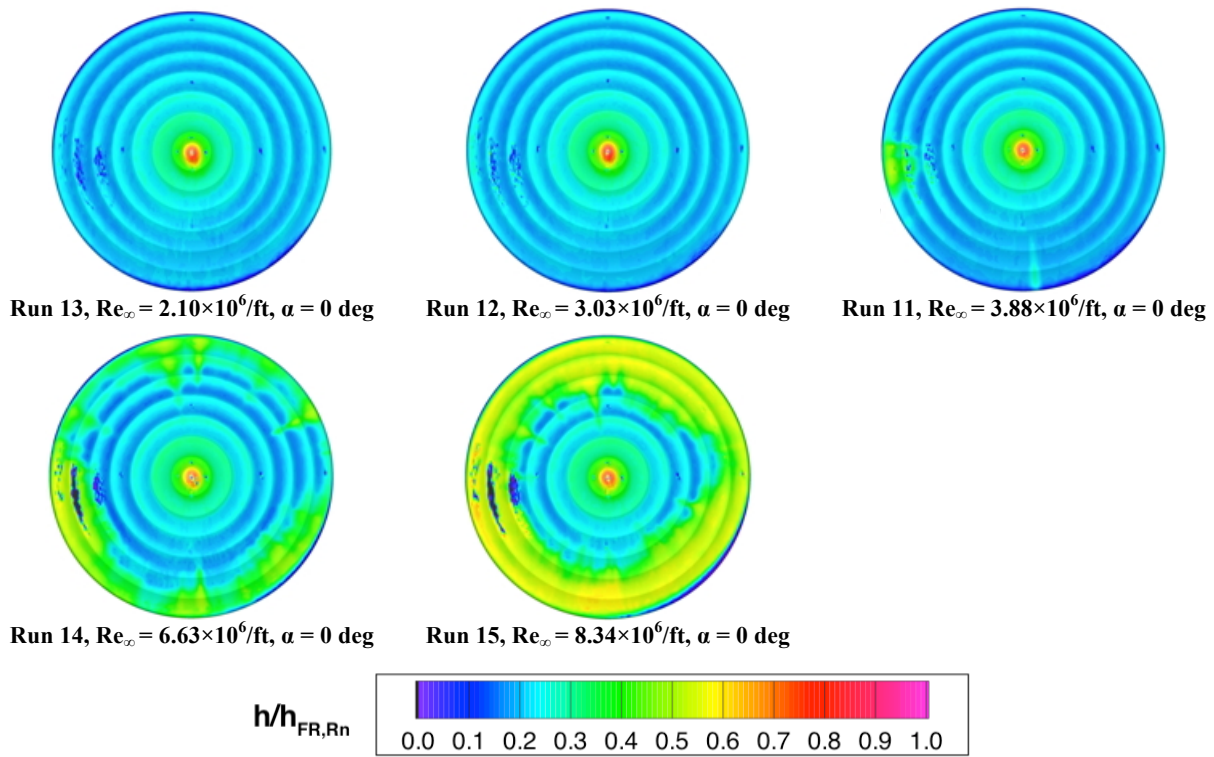


Figure 28. IRVE Scallop-5 Model, Reynolds Number Effects at $\alpha = 0$ deg.

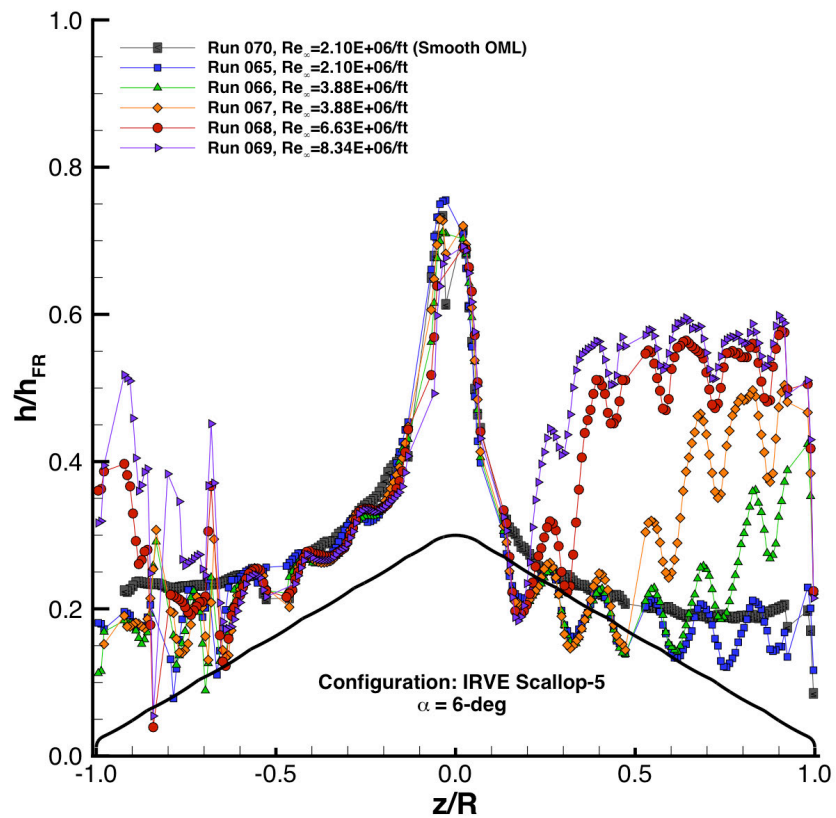
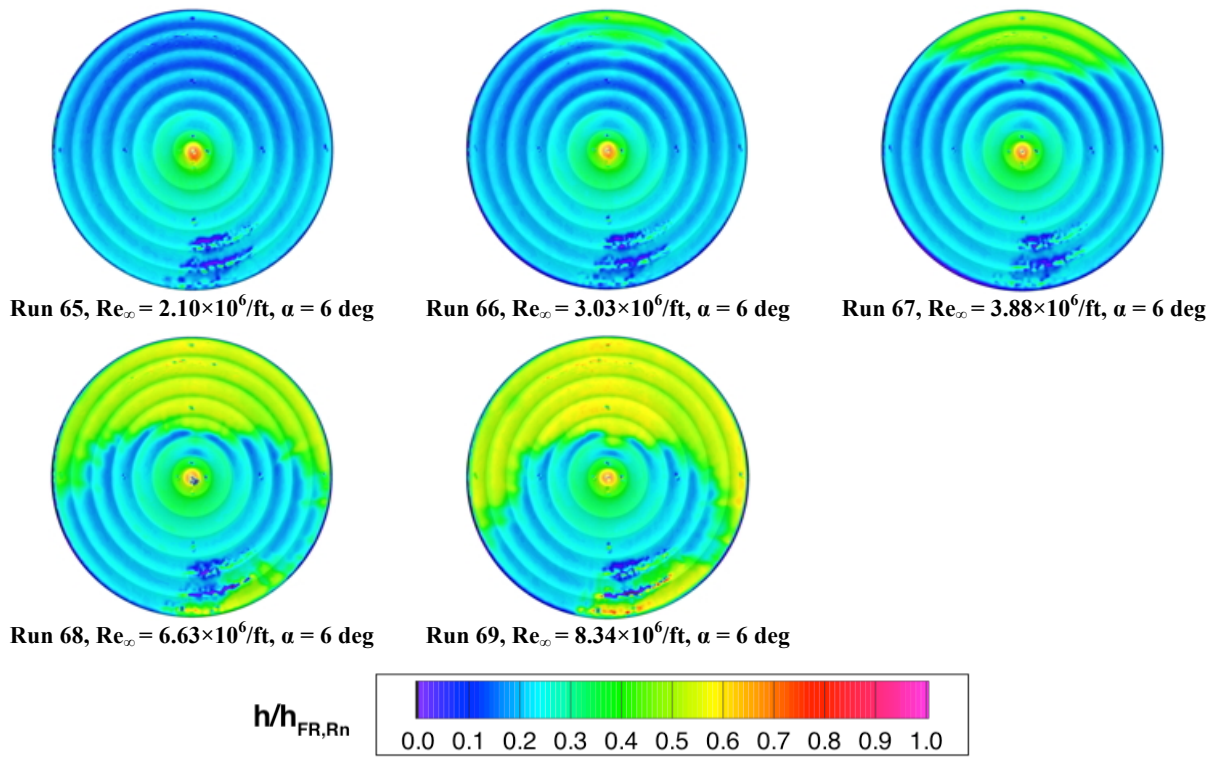


Figure 29. IRVE Scallop-5 Model, Reynolds Number Effects at $\alpha = 6$ deg.

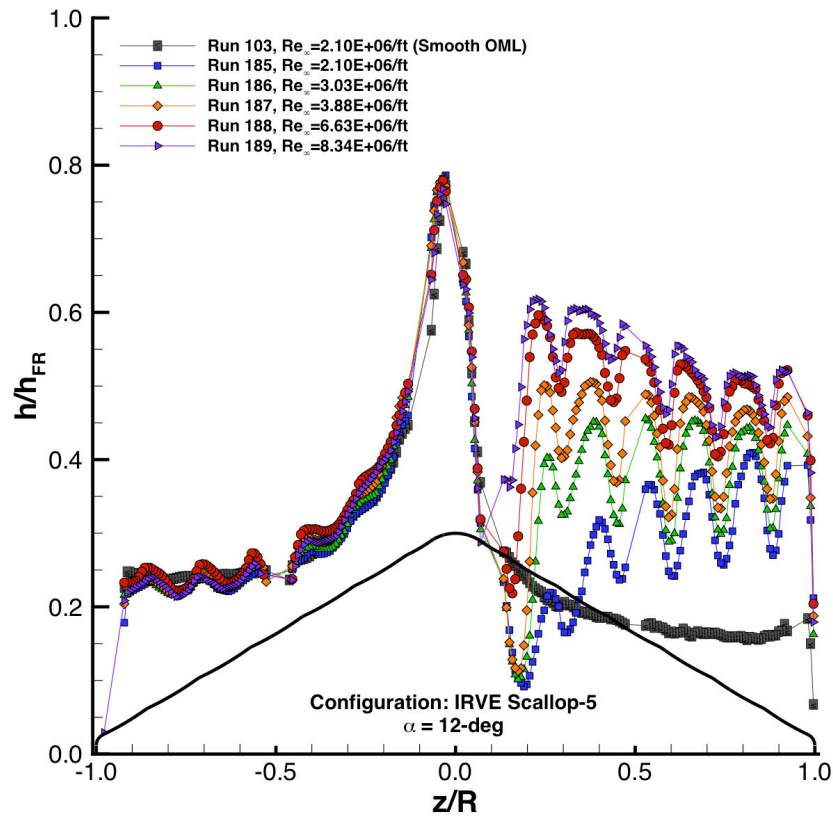
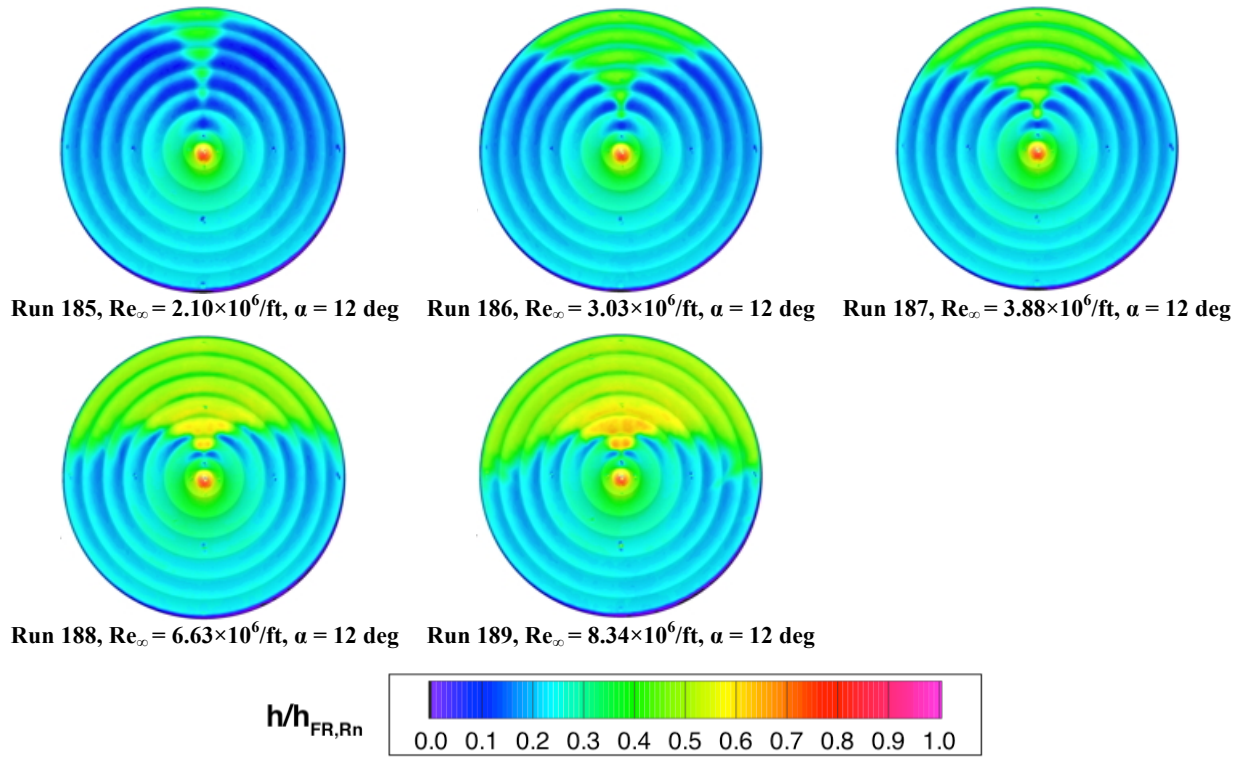


Figure 30. IRVE Scallop-5 Model, Reynolds Number Effects at $\alpha = 12 \text{ deg}$.

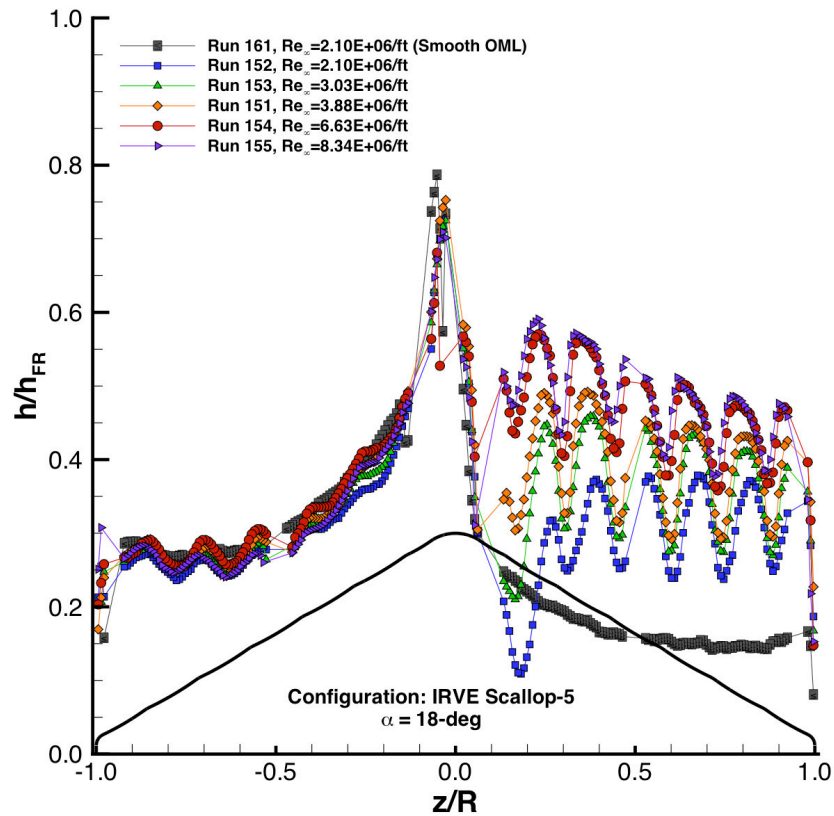
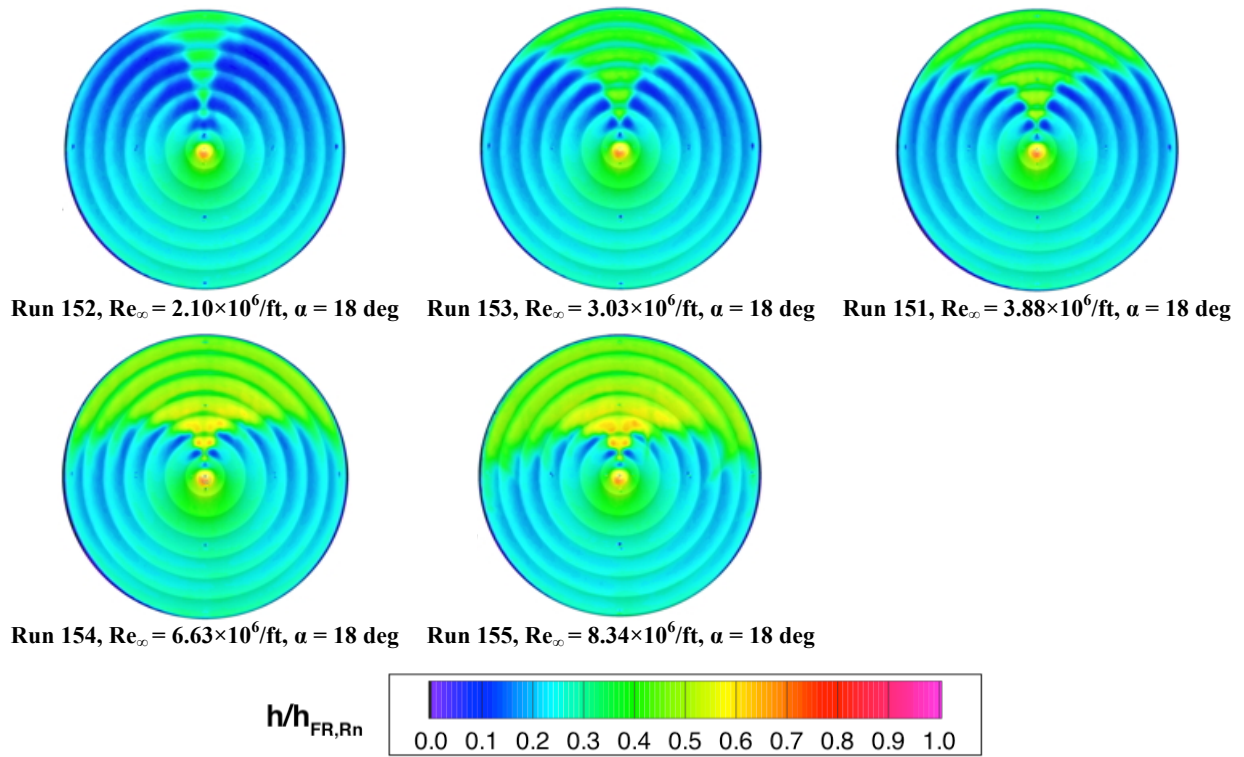


Figure 31. IRVE Scallop-5 Model, Reynolds Number Effects at $\alpha = 18$ deg.

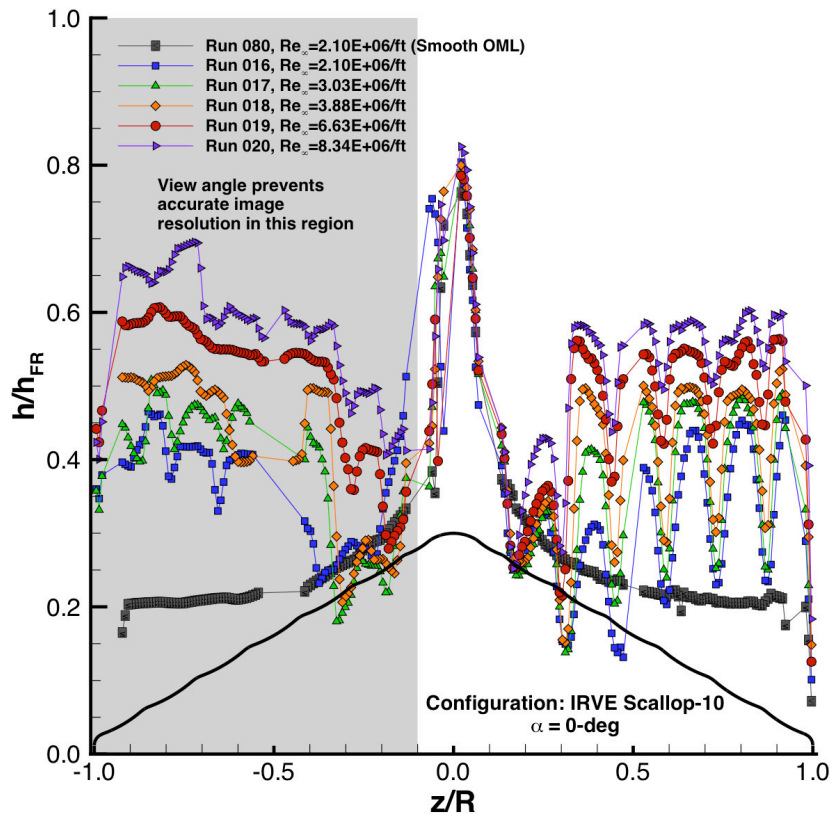
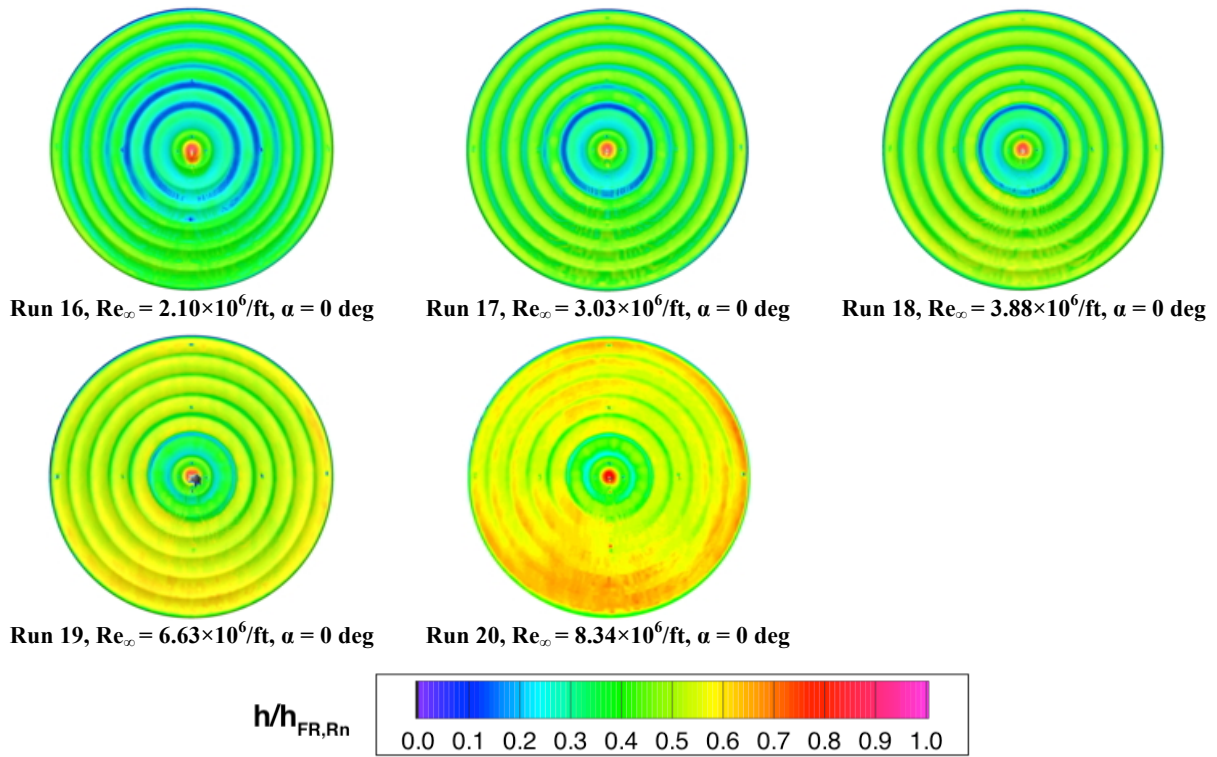


Figure 32. IRVE Scallop-10 Model, Reynolds Number Effects at $\alpha = 0^\circ$.

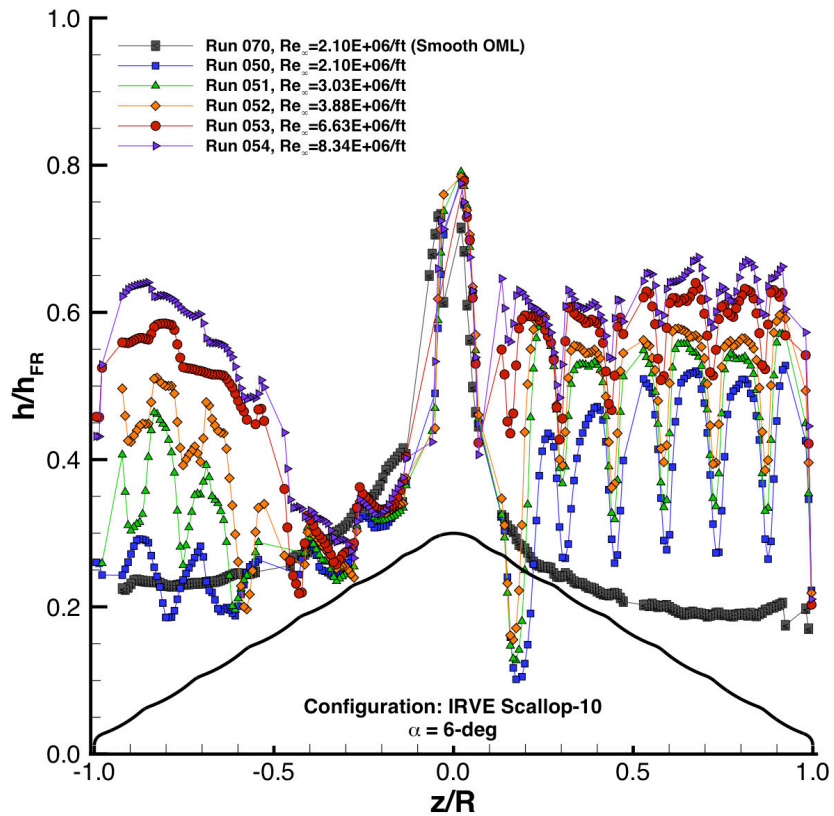
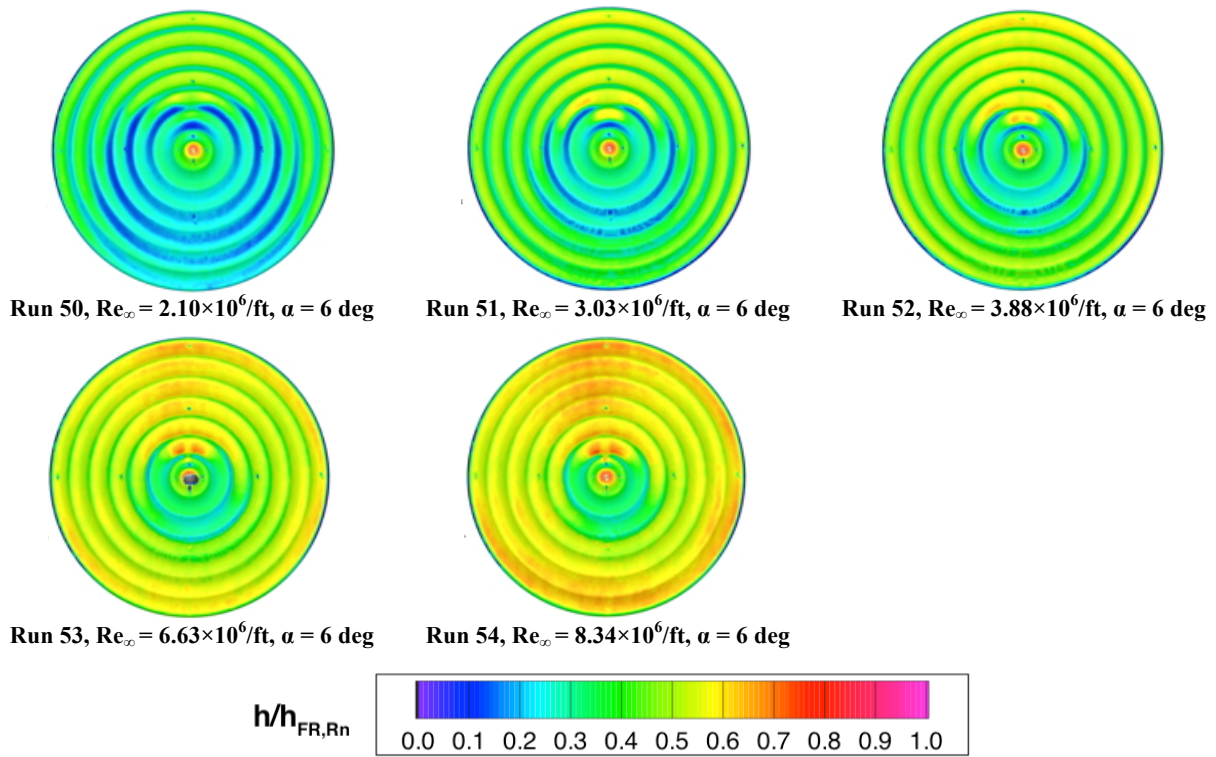


Figure 33. IRVE Scallop-10 Model, Reynolds Number Effects at $\alpha = 6$ deg.

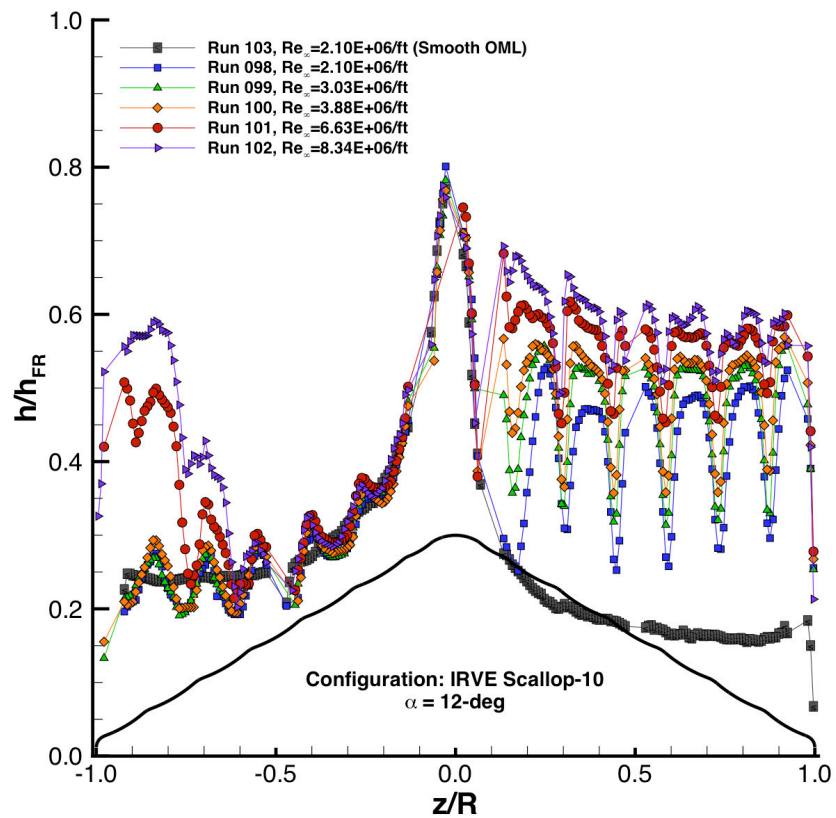
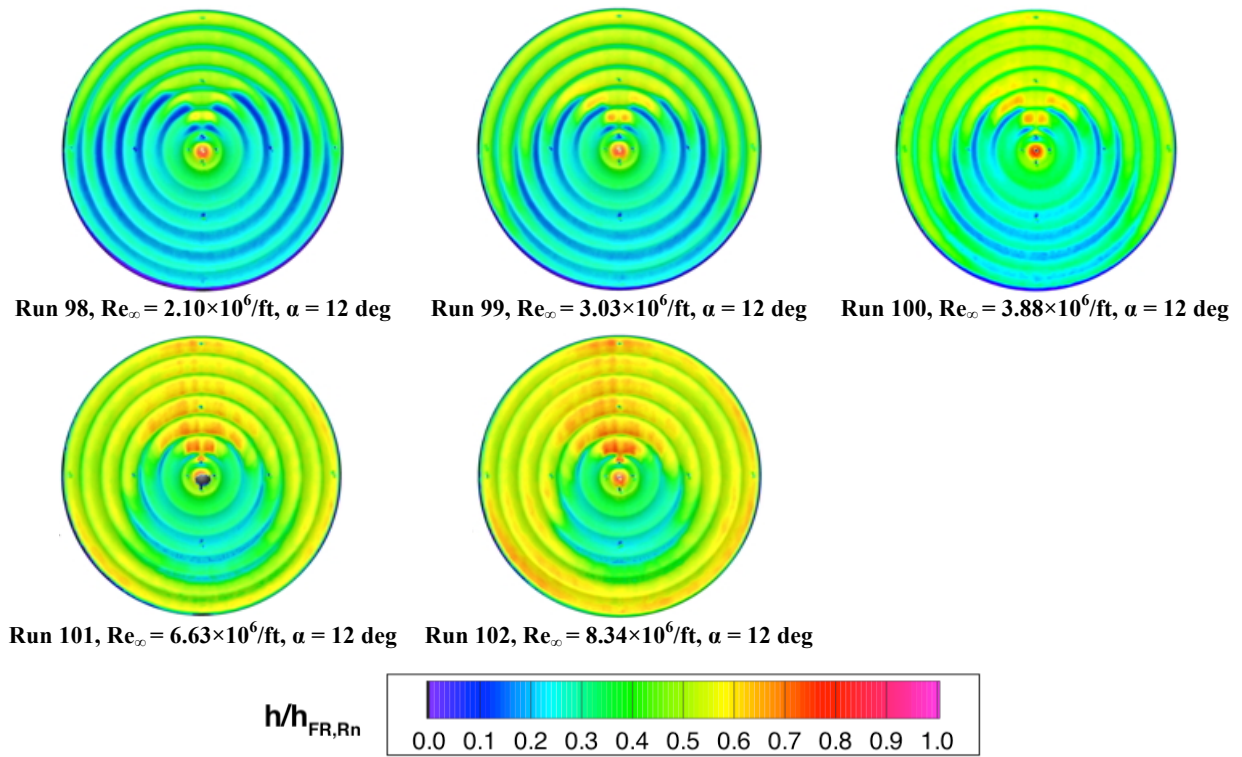


Figure 34. IRVE Scallop-10 Model, Reynolds Number Effects at $\alpha = 12$ deg.

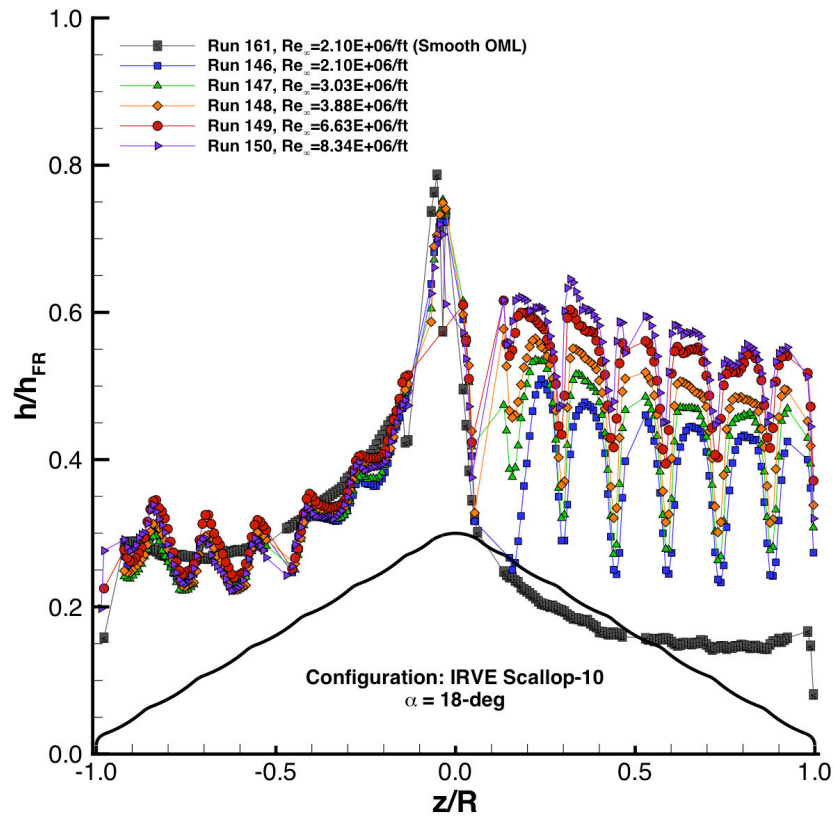
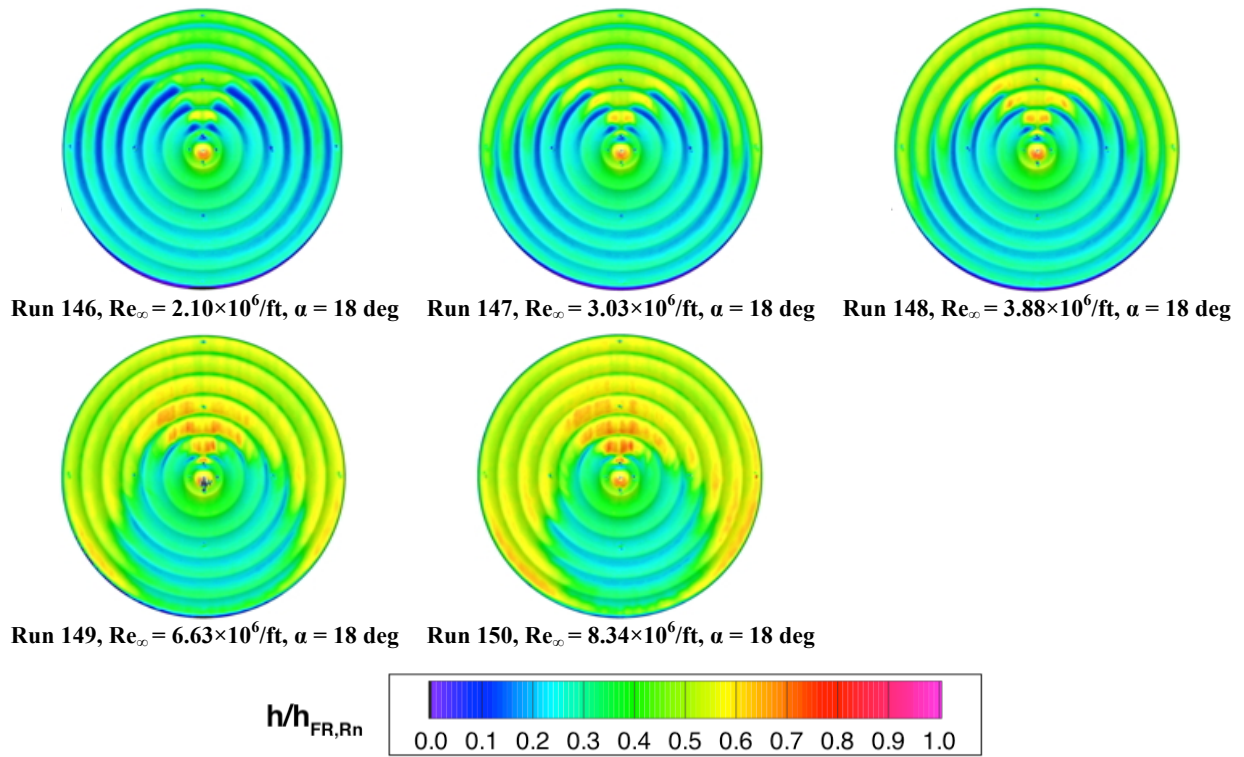


Figure 35. IRVE Scallop-10 Model, Reynolds Number Effects at $\alpha = 18 \text{ deg}$.

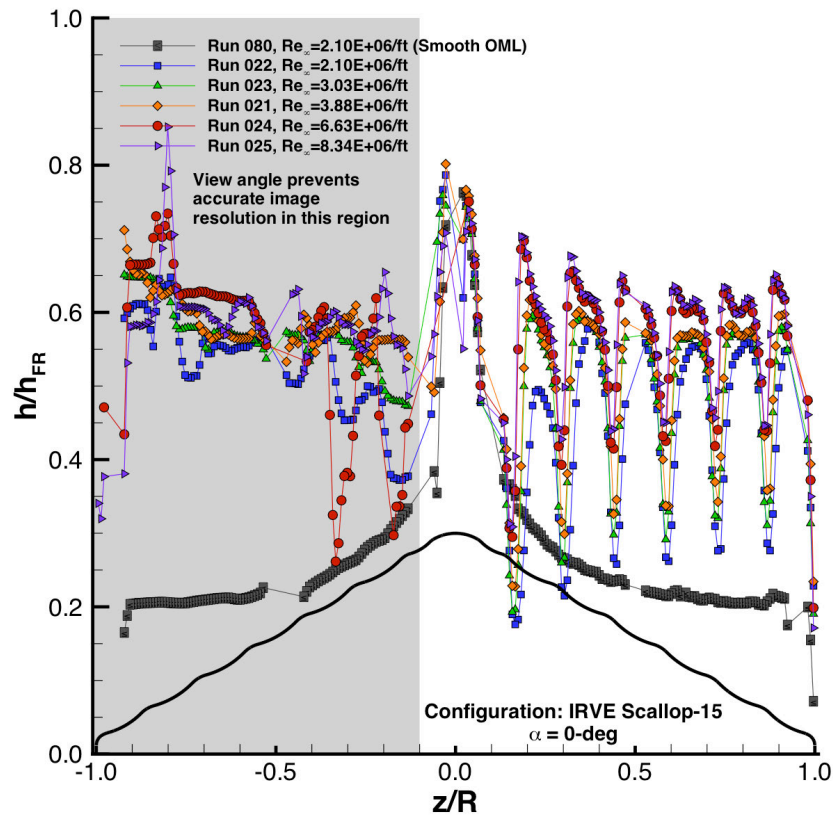
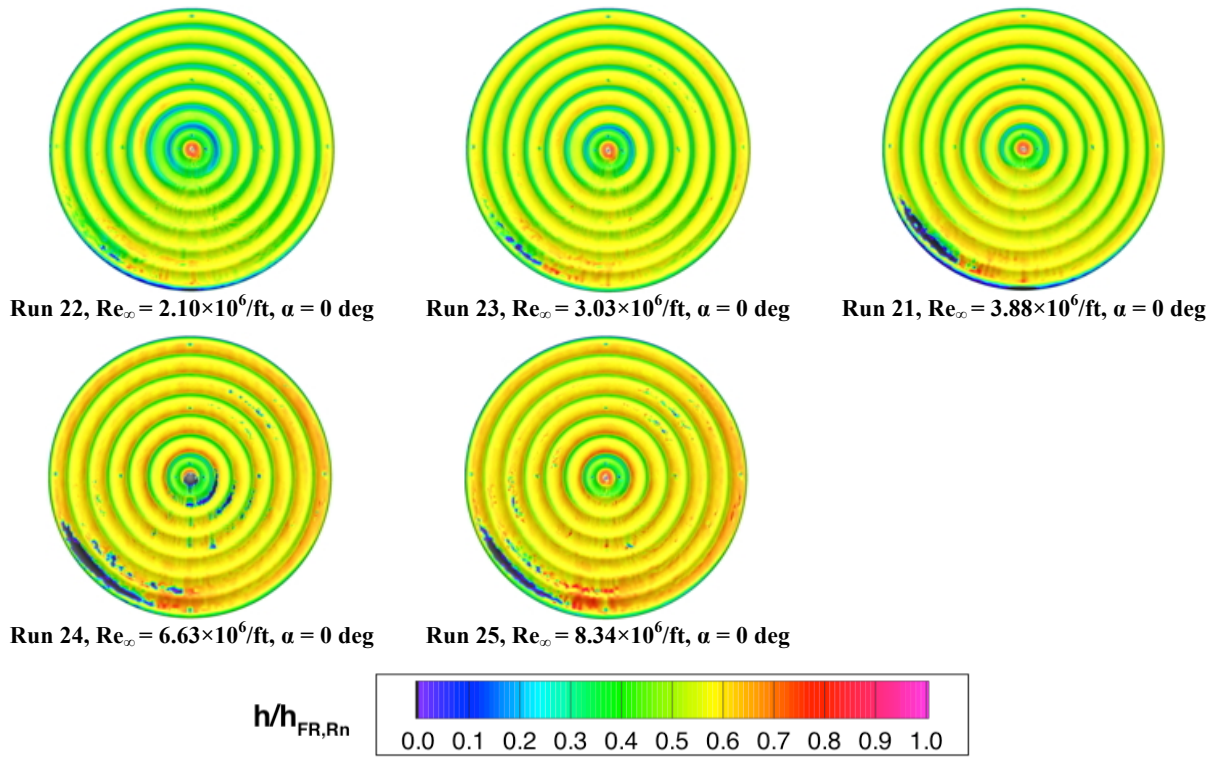


Figure 36. IRVE Scallop-15 Model, Reynolds Number Effects at $\alpha = 0$ deg.

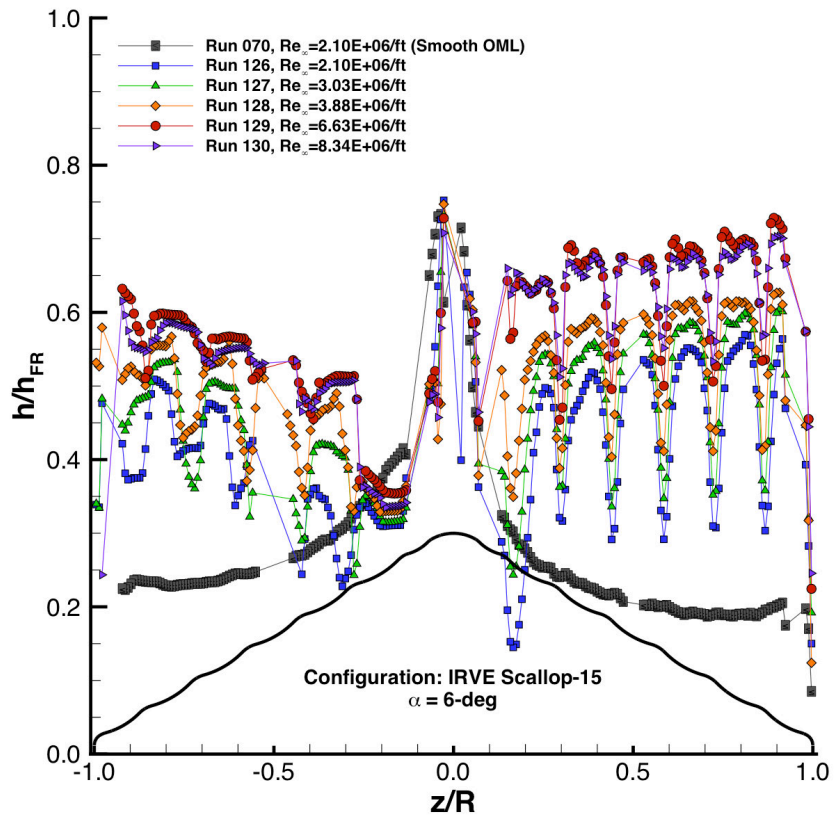
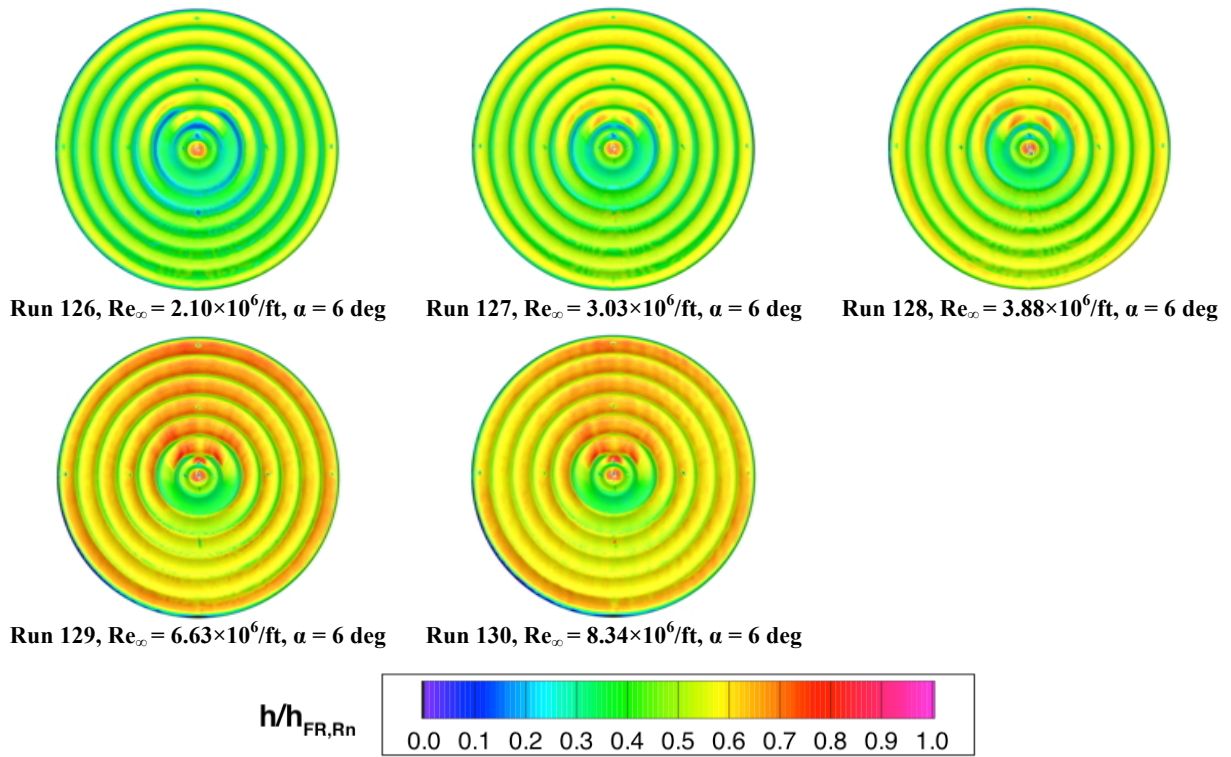


Figure 37. IRVE Scallop-15 Model, Reynolds Number Effects at $\alpha = 6 \text{ deg}$.

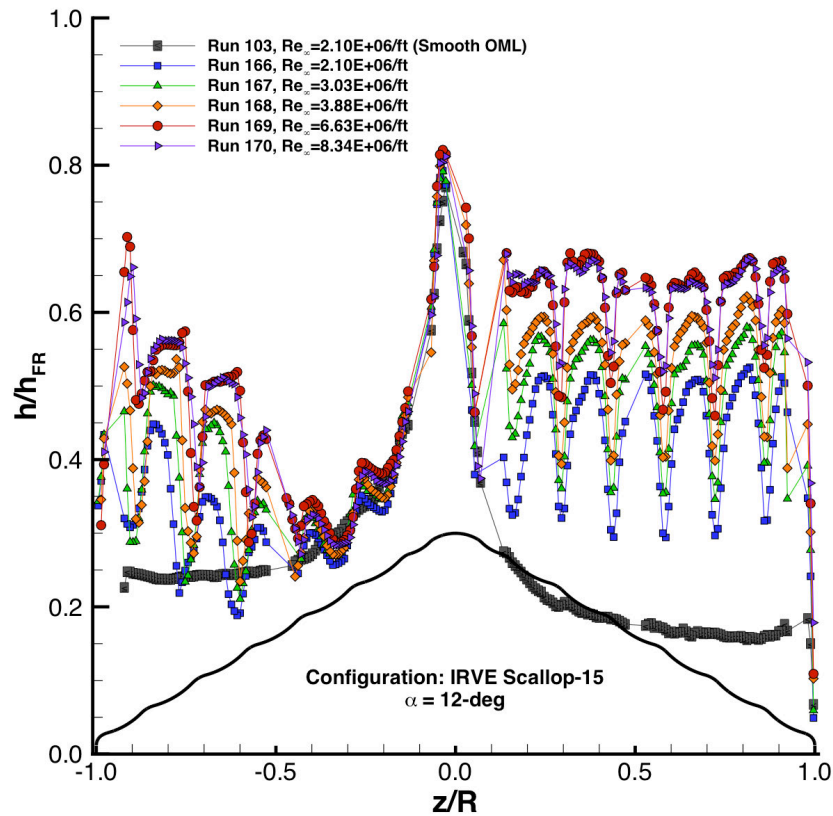
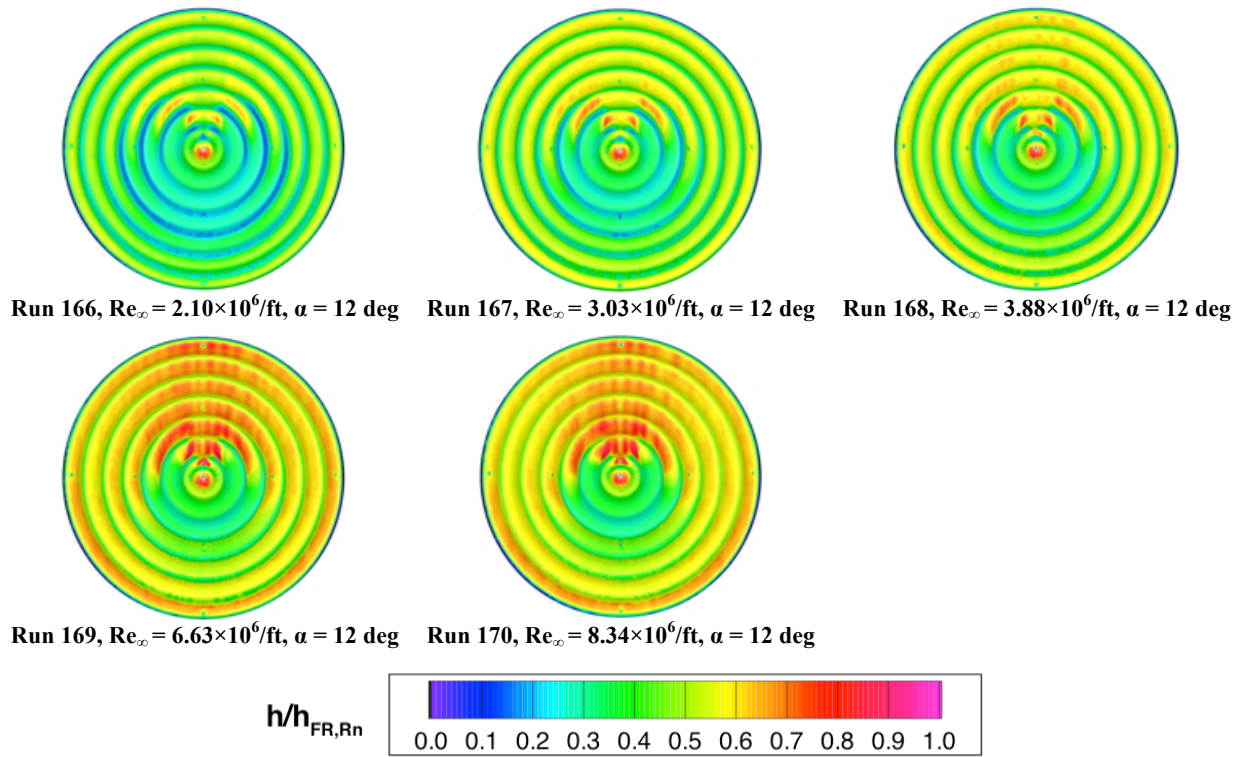


Figure 38. IRVE Scallop-15 Model, Reynolds Number Effects at $\alpha = 12 \text{ deg}$.

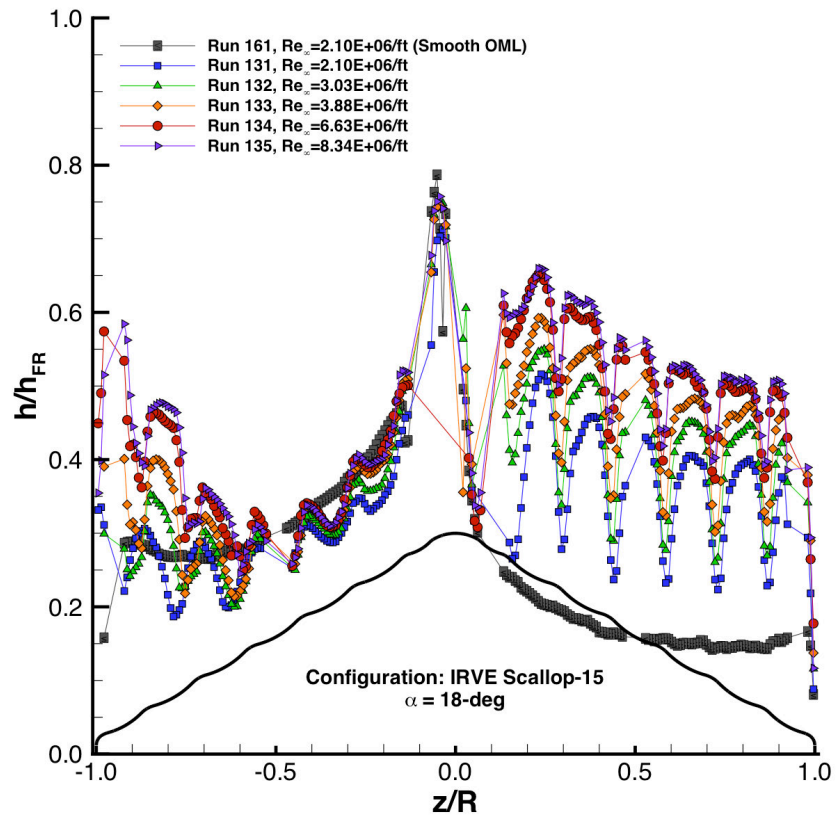
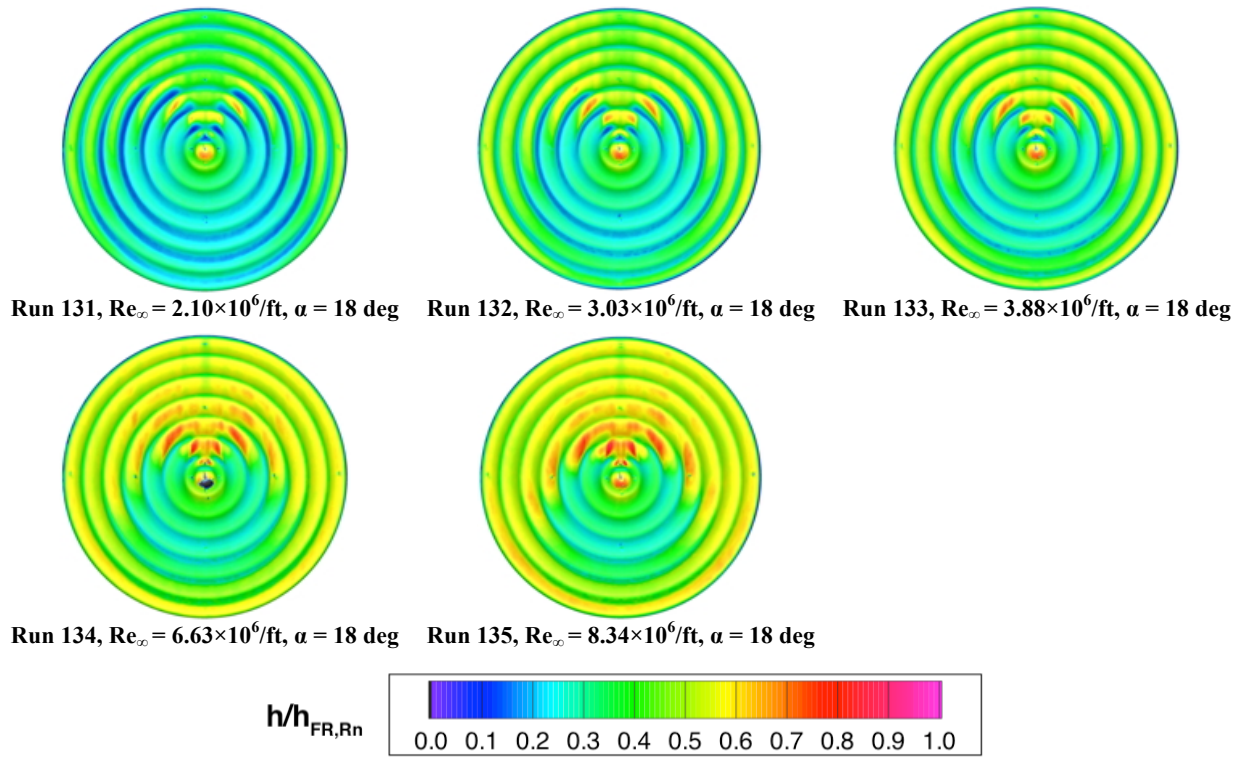


Figure 39. IRVE Scallop-15 Model, Reynolds Number Effects at $\alpha = 18$ deg.

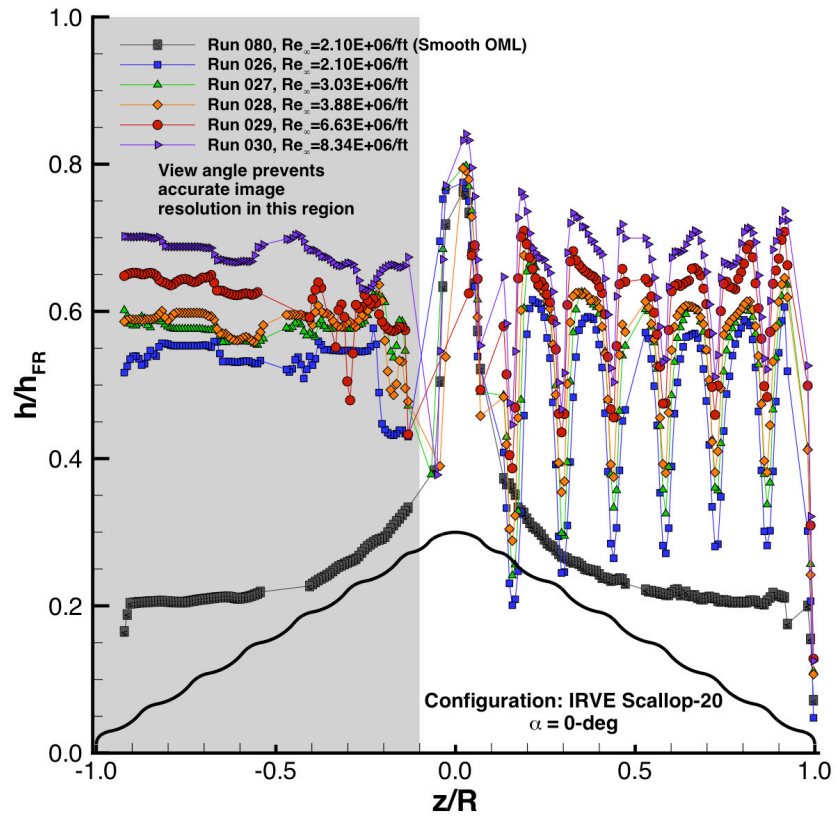
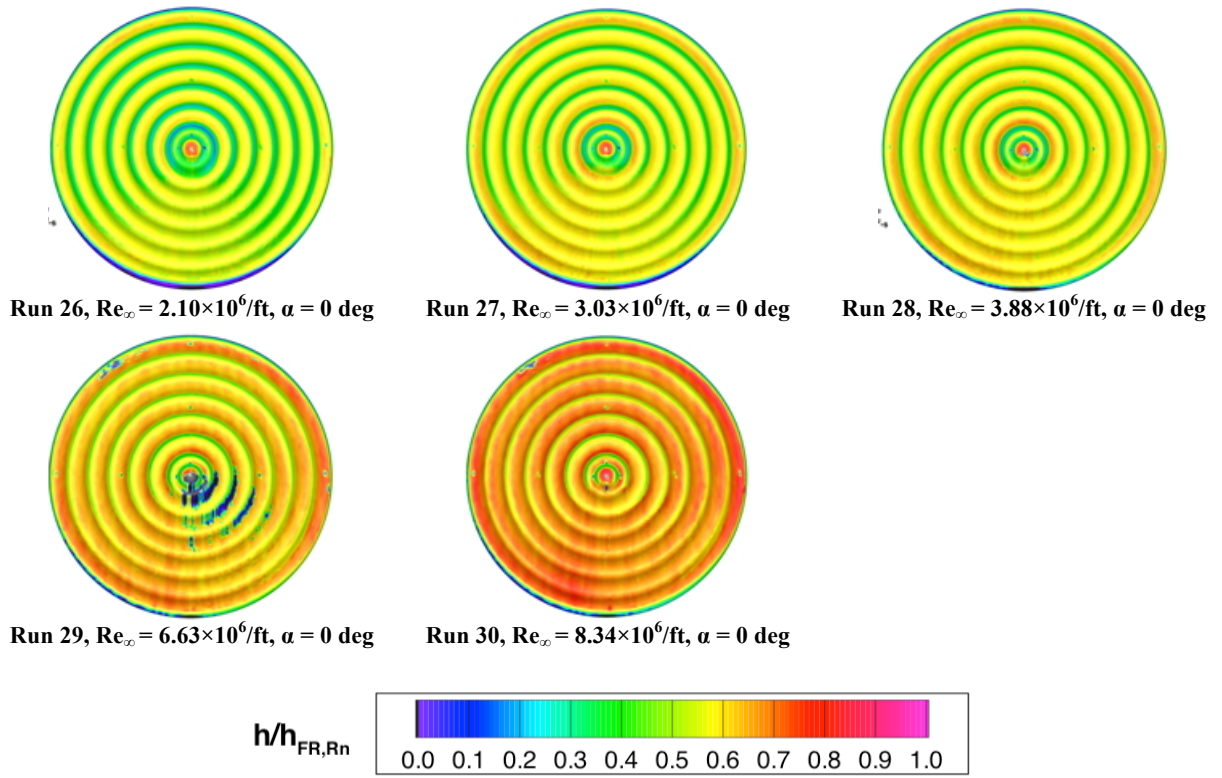


Figure 40. IRVE Scallop-20 Model, Reynolds Number Effects at $\alpha = 0^\circ$.

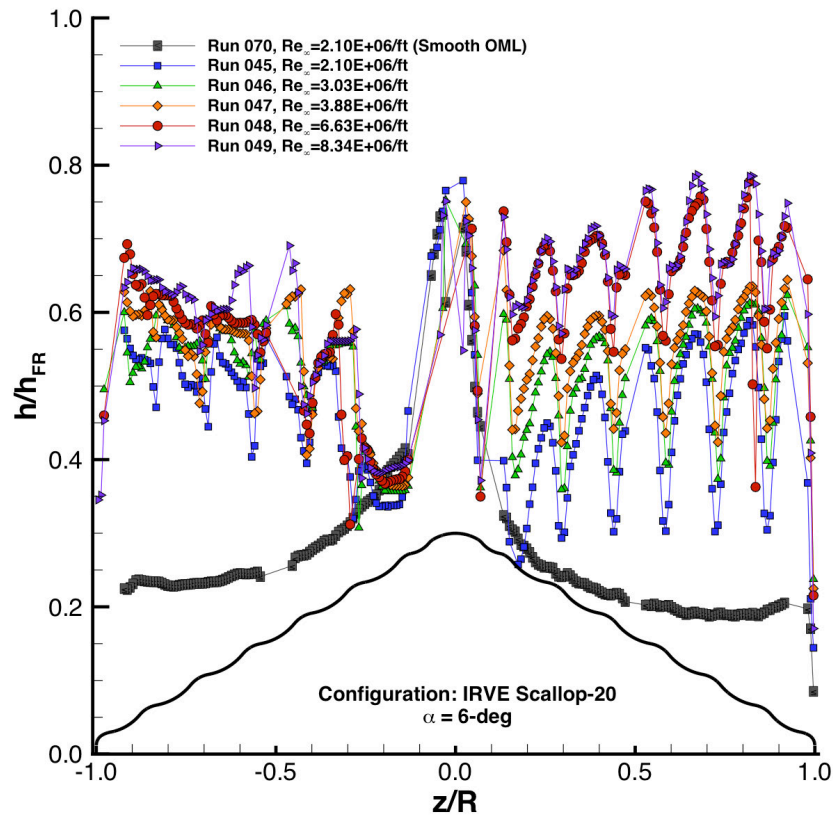
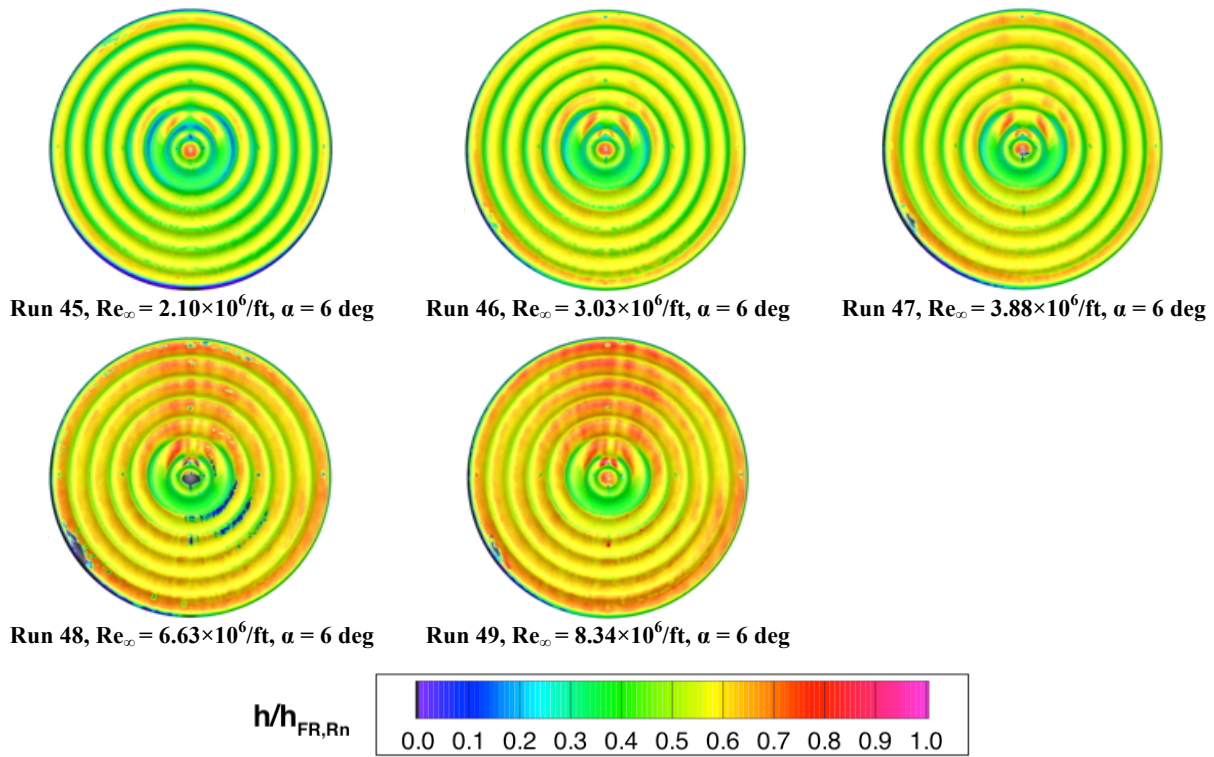


Figure 41. IRVE Scallop-20 Model, Reynolds Number Effects at $\alpha = 6$ deg.

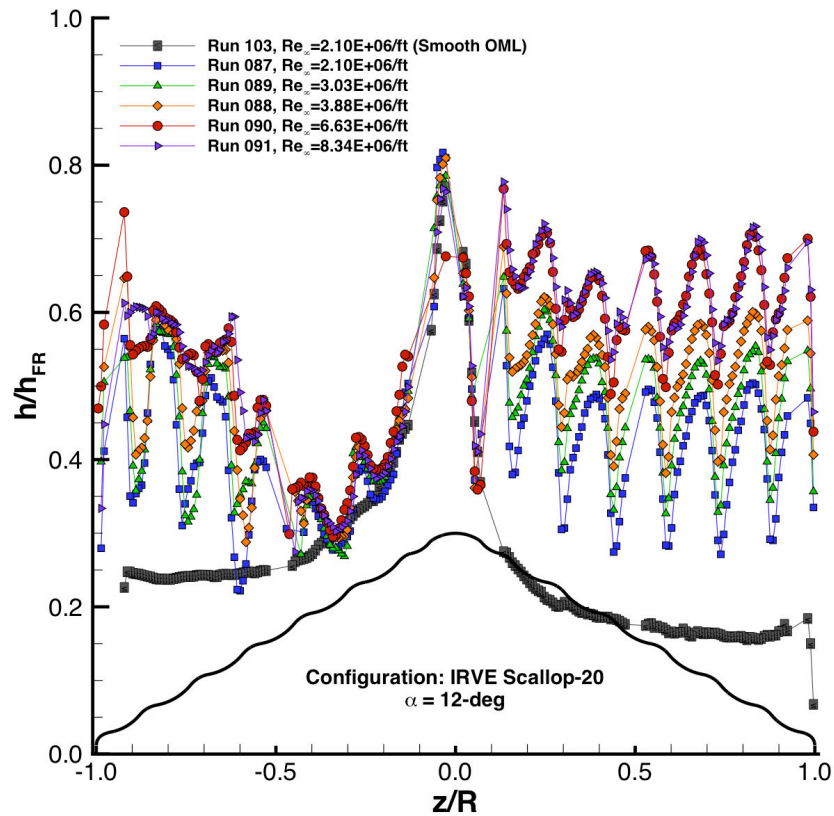
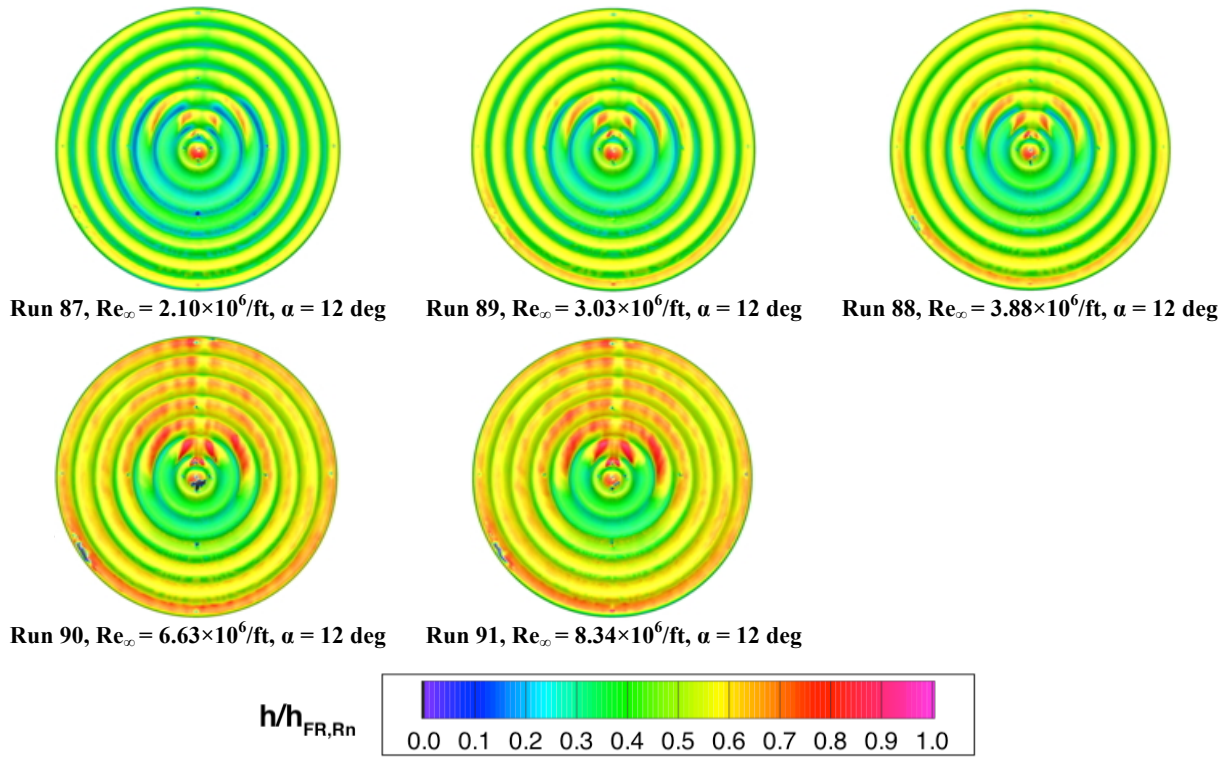


Figure 42. IRVE Scallop-20 Model, Reynolds Number Effects at $\alpha = 12$ deg.

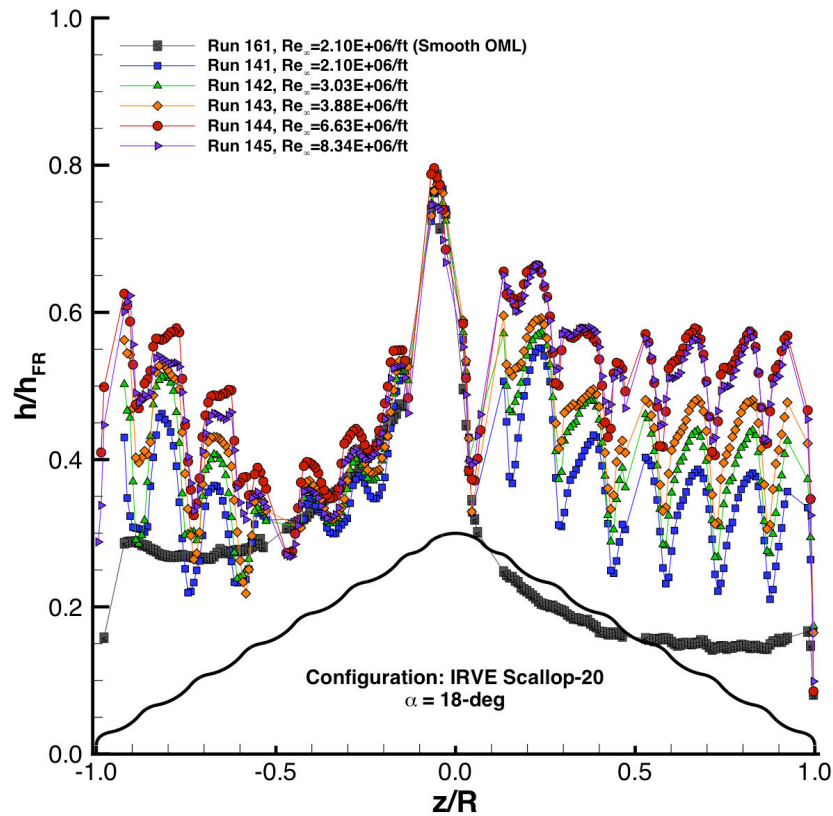
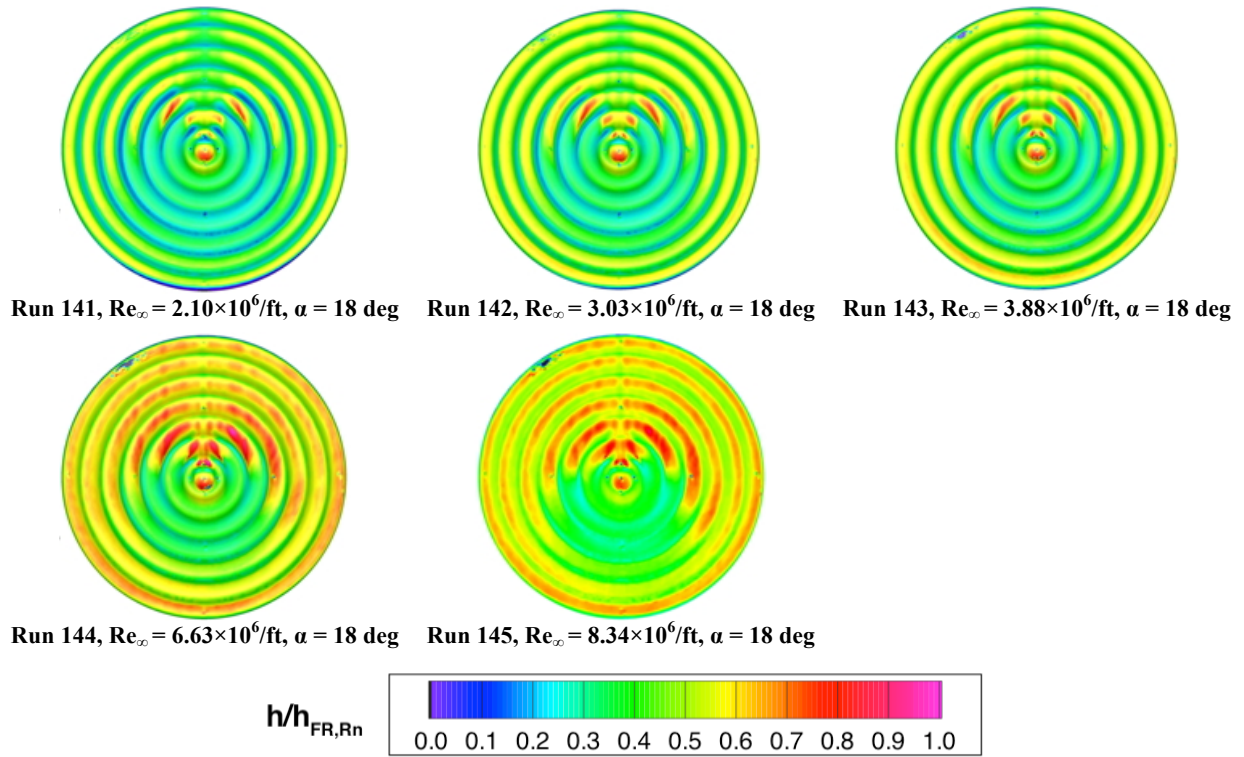


Figure 43. IRVE Scallop-20 Model, Reynolds Number Effects at $\alpha = 18 \text{ deg}$.

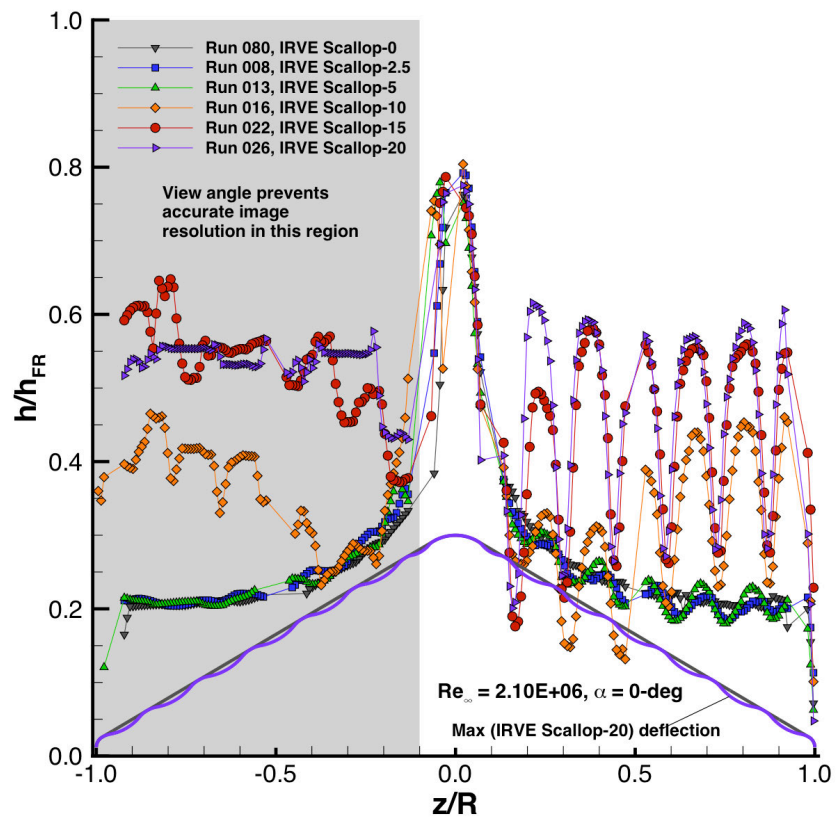
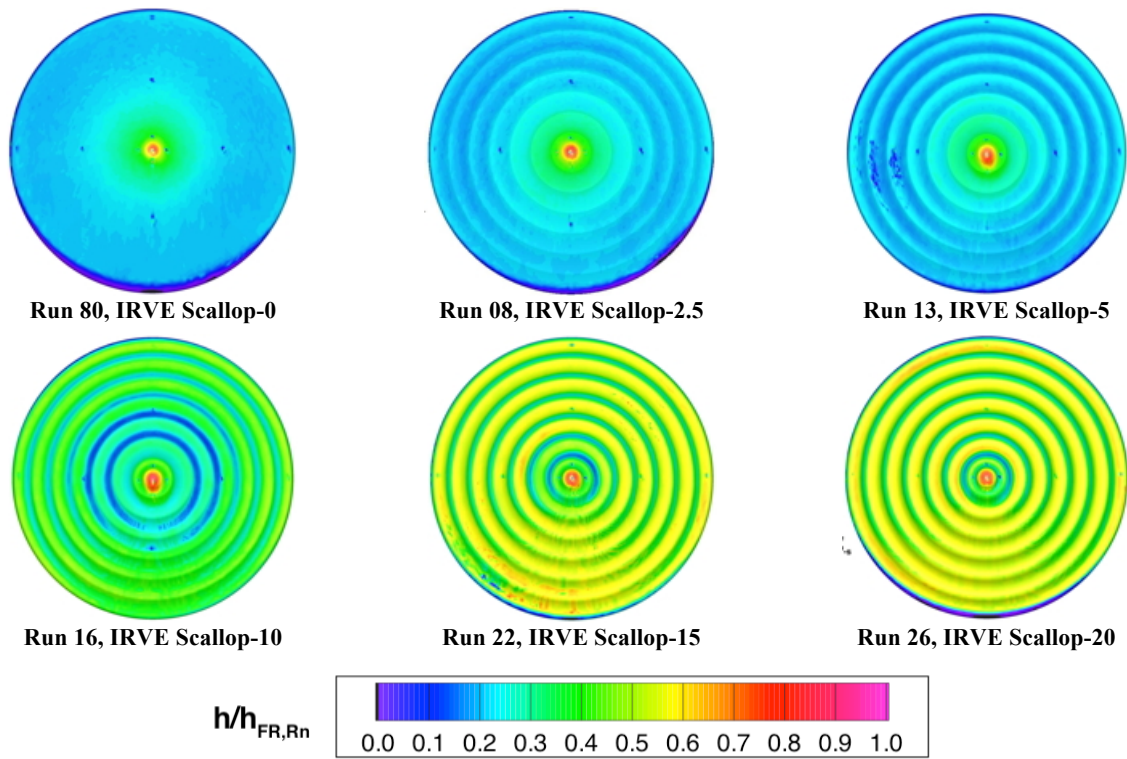


Figure 44. Configuration Effects at $Re_{\infty} = 2.10 \times 10^6/\text{ft}$, $\alpha = 0$ deg.

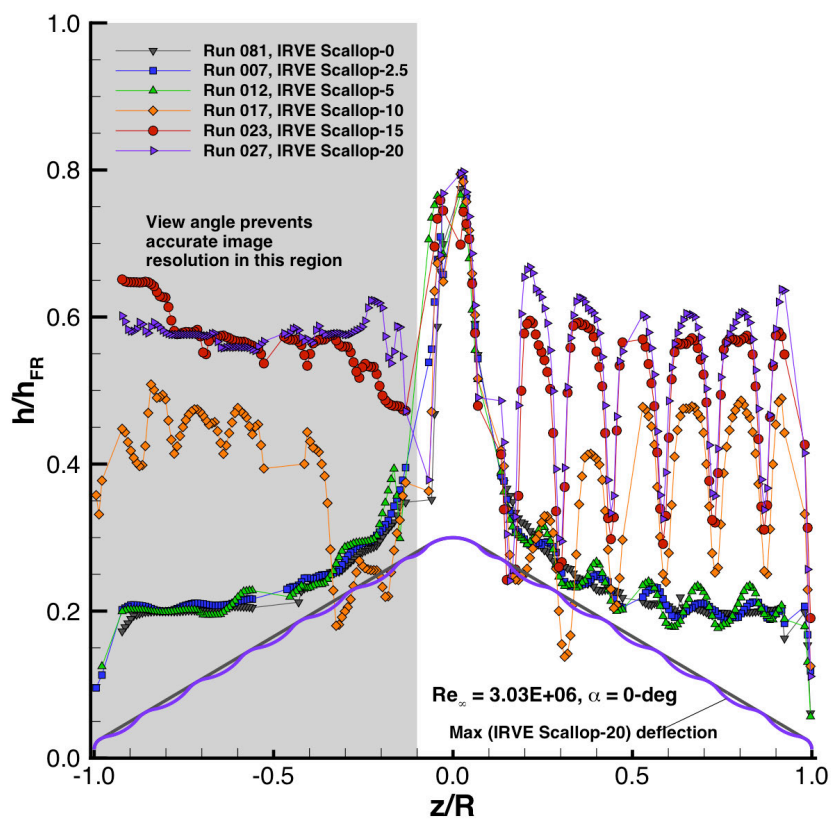
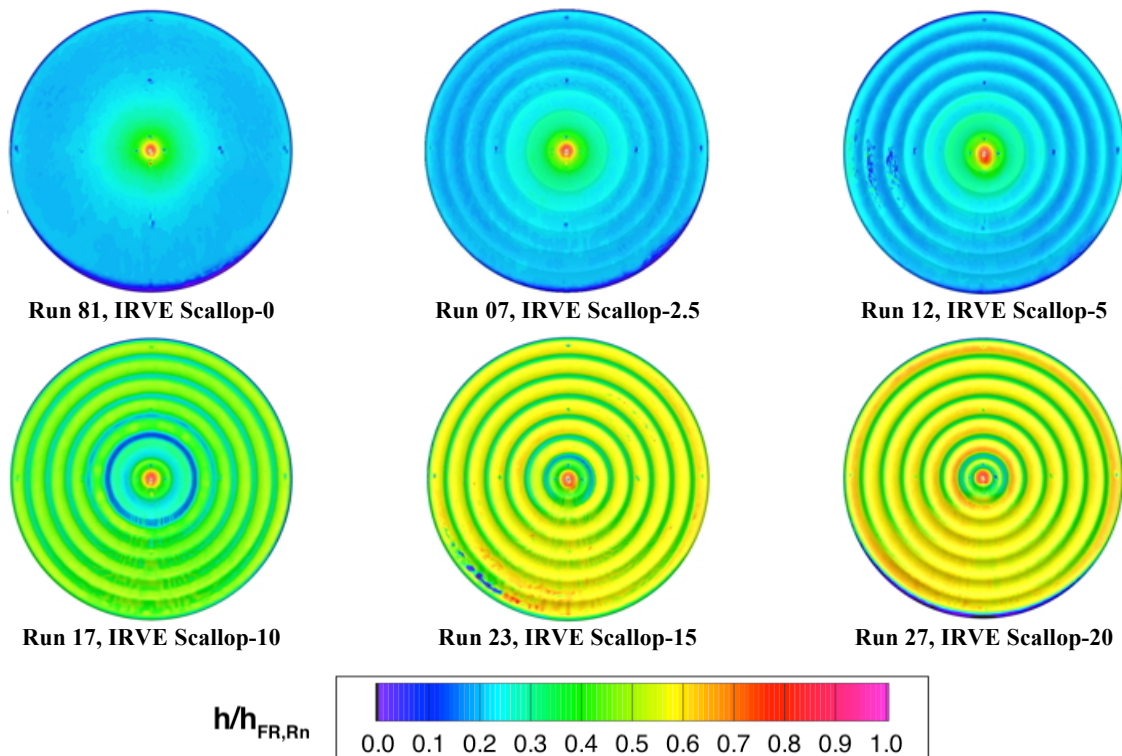


Figure 45. Configuration Effects at $Re_{\infty} = 3.03 \times 10^6/\text{ft}$, $\alpha = 0$ deg.

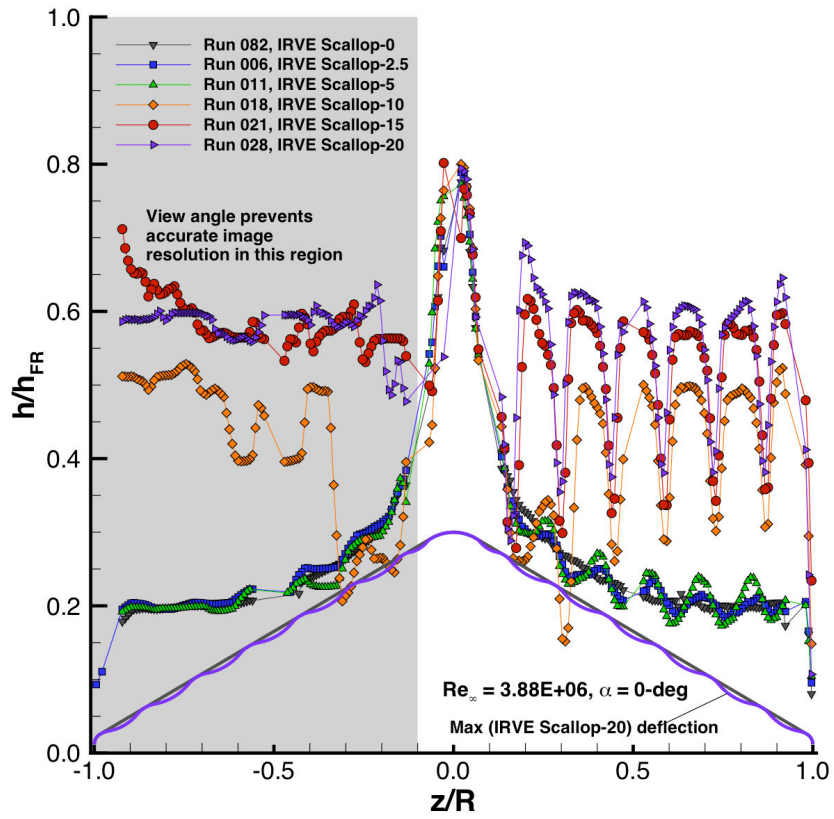
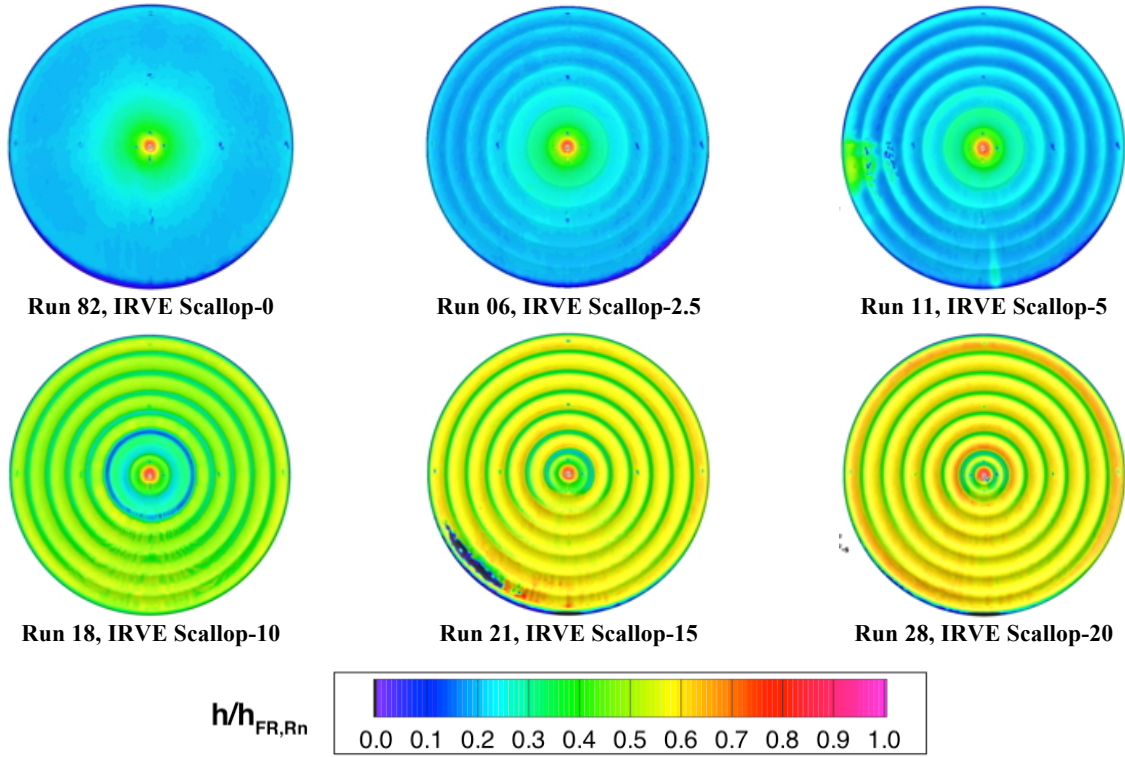


Figure 46. Configuration Effects at $Re_{\infty} = 3.88 \times 10^6/\text{ft}$, $\alpha = 0$ deg.

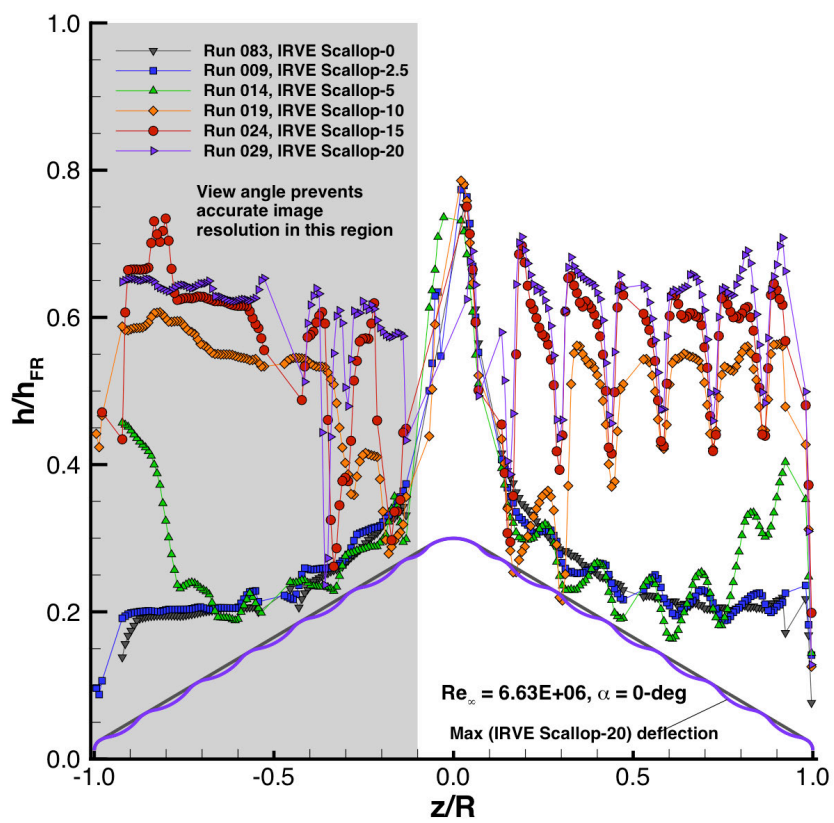
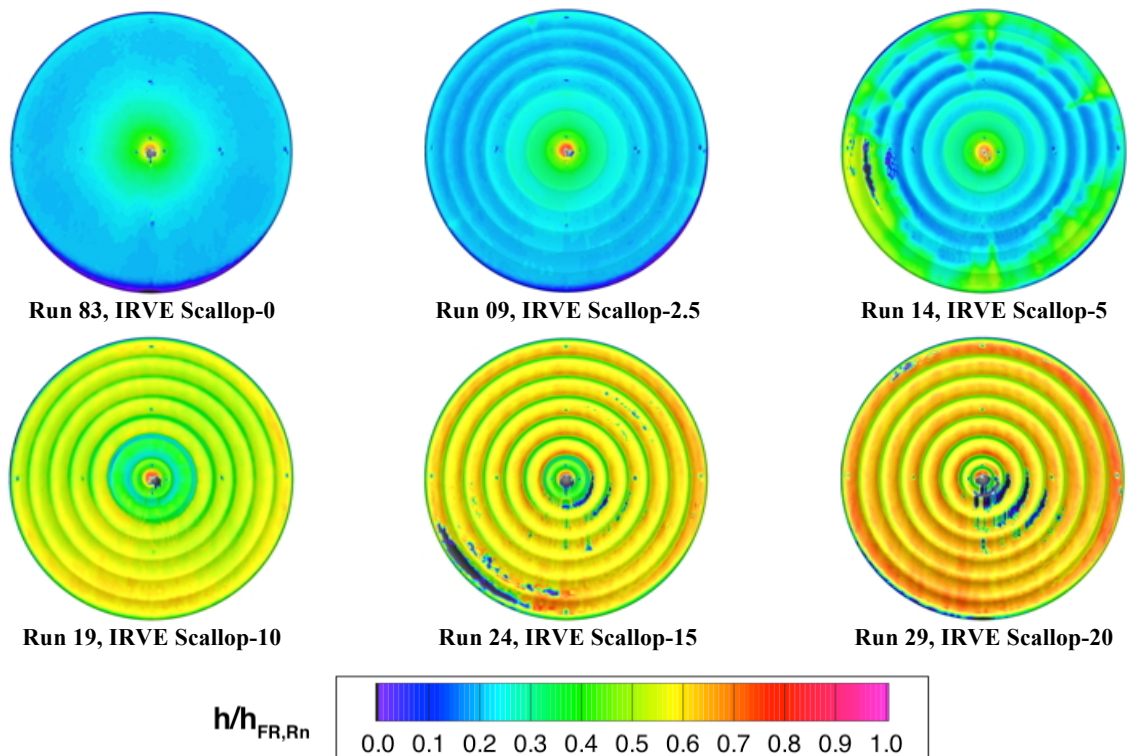


Figure 47. Configuration Effects at $Re_{\infty} = 6.63 \times 10^6 / ft$, $\alpha = 0$ deg.

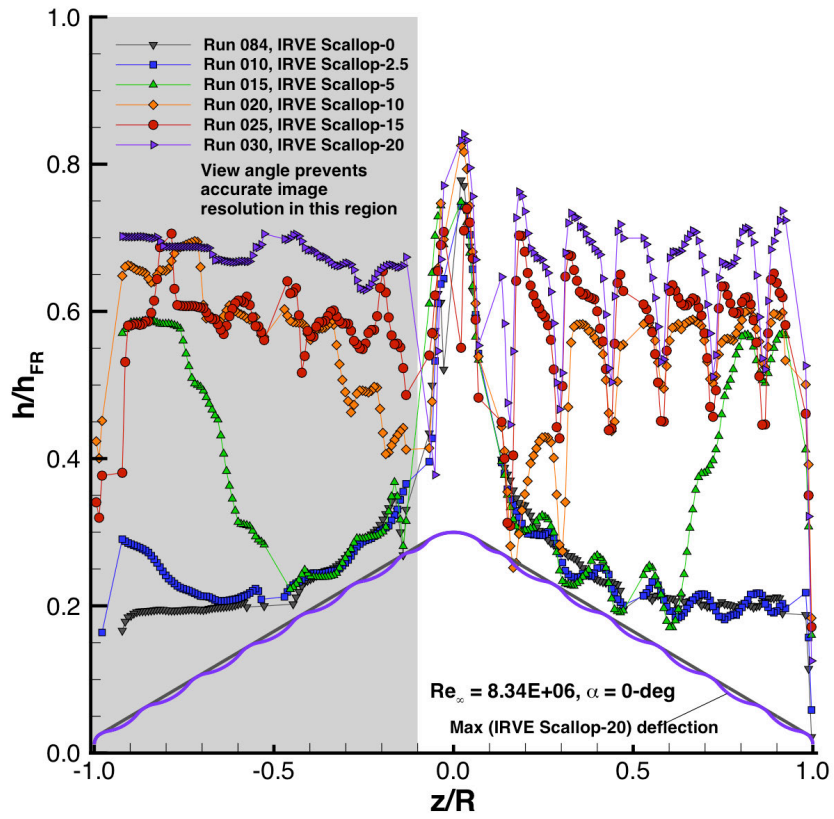
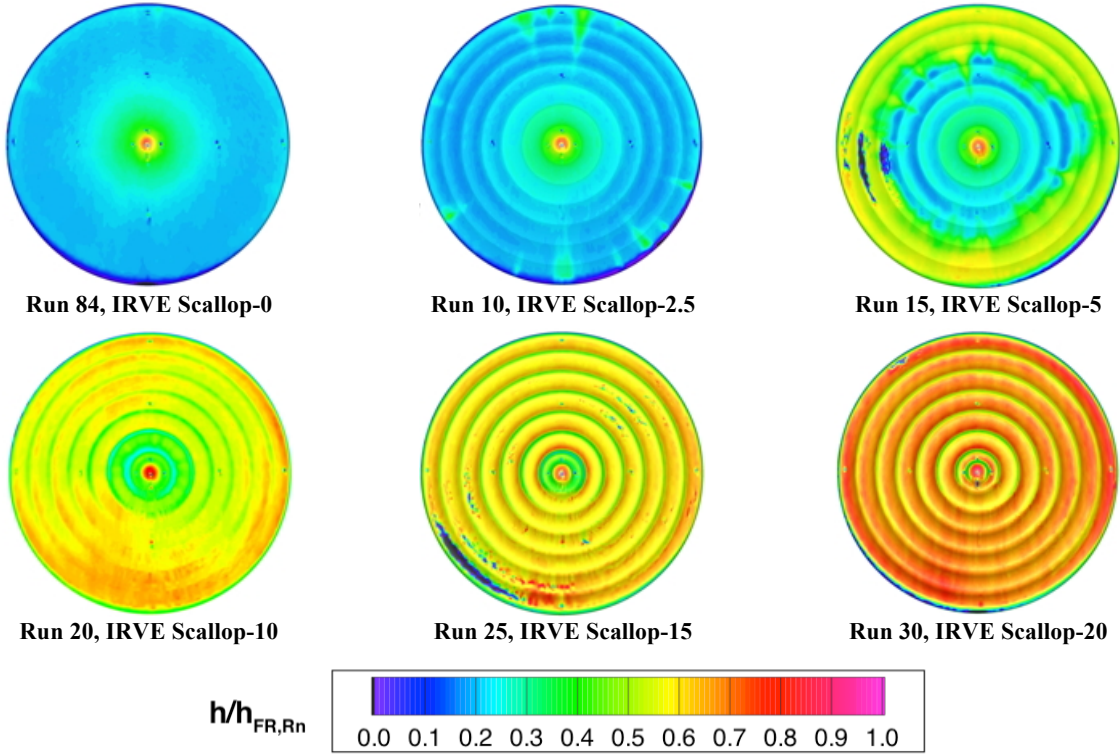


Figure 48. Configuration Effects at $Re_{\infty} = 8.34 \times 10^6/\text{ft}$, $\alpha = 0$ deg.

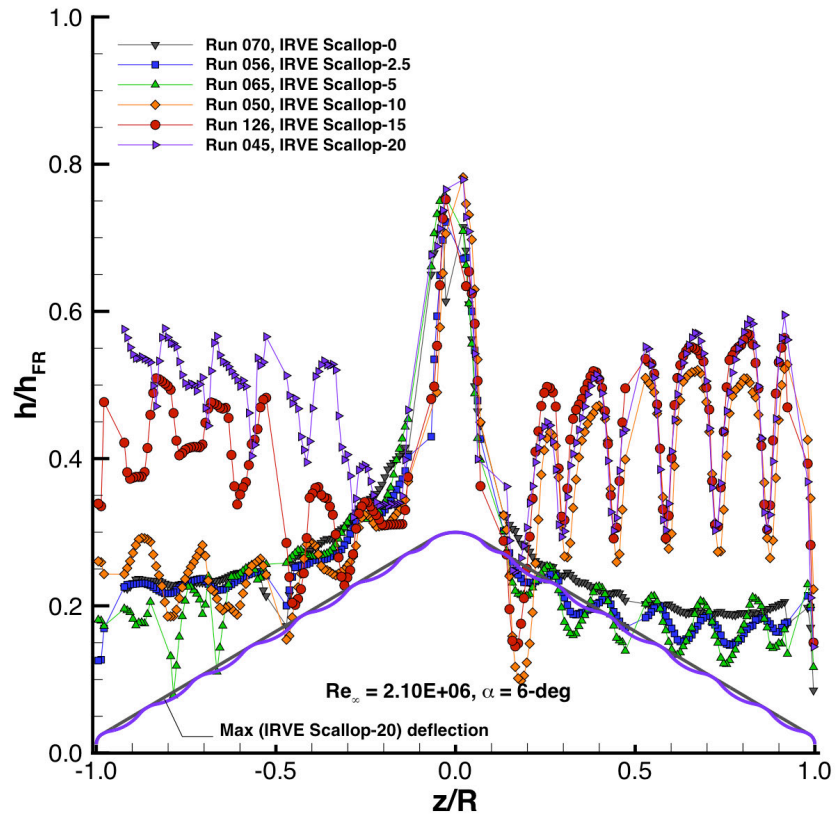
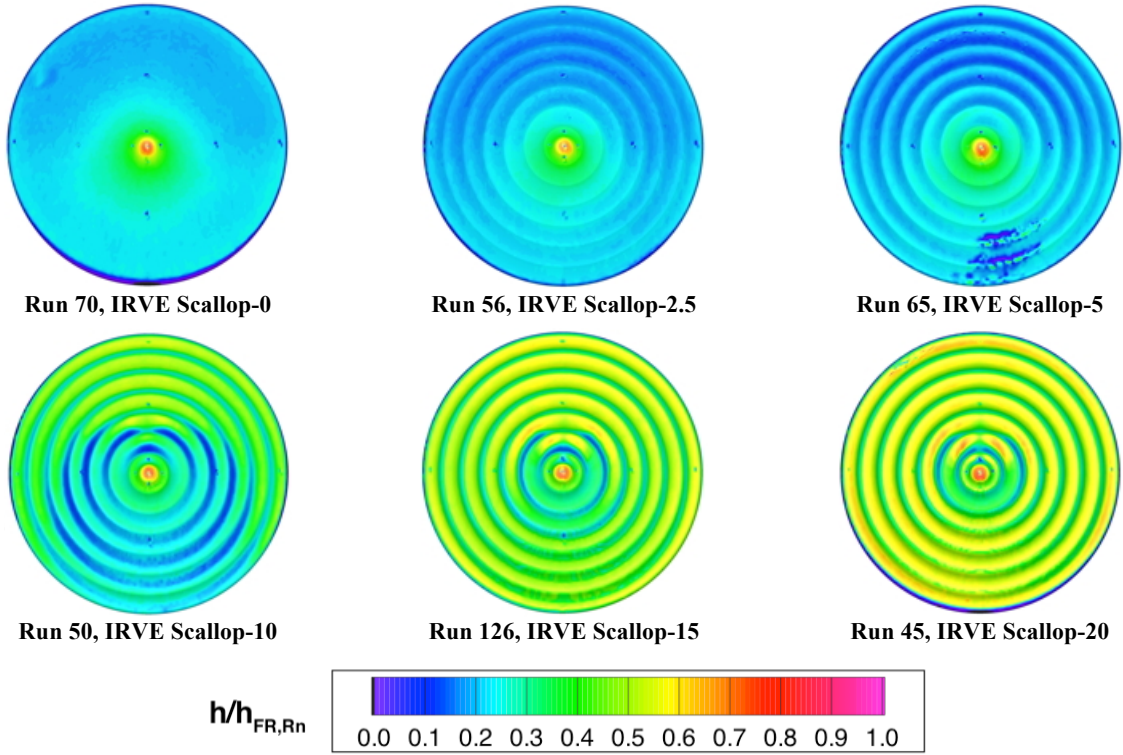


Figure 49. Configuration Effects at $Re_{\infty} = 2.10 \times 10^6 / ft$, $\alpha = 6$ deg.

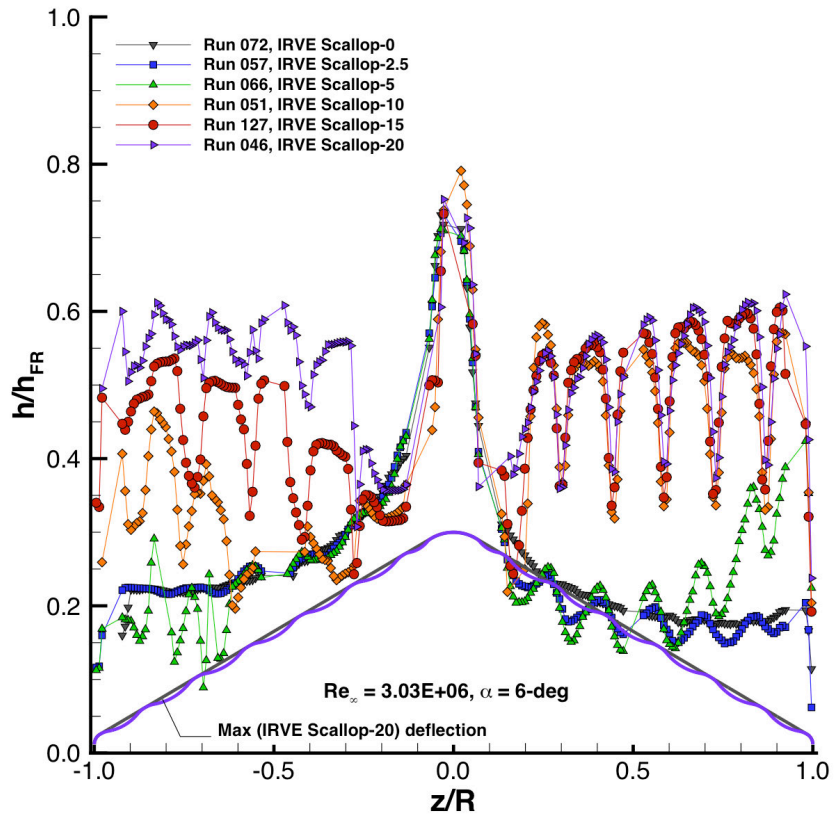
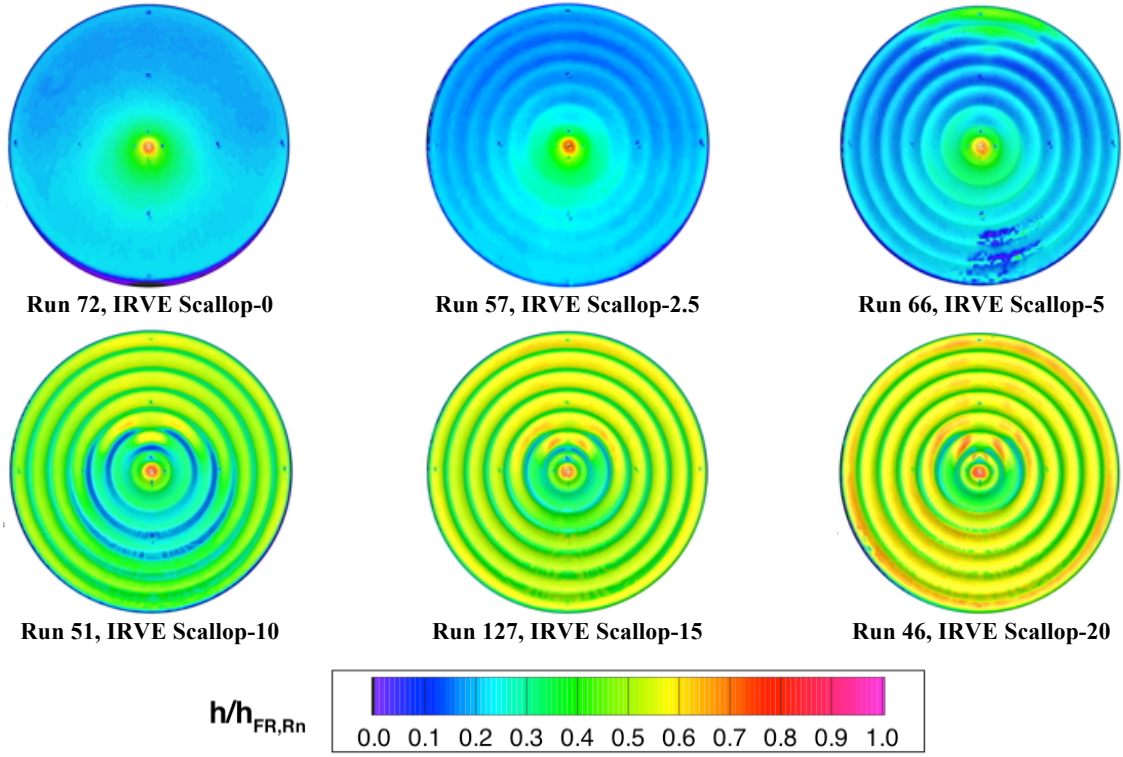


Figure 50. Configuration Effects at $Re_{\infty} = 3.03 \times 10^6/\text{ft}$, $\alpha = 6$ deg.

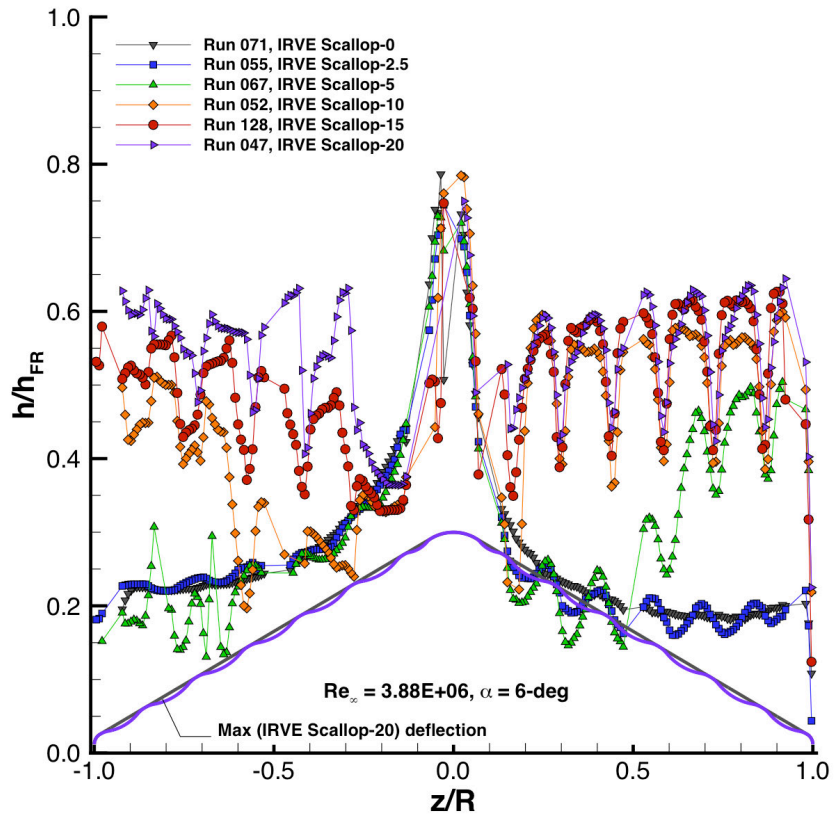
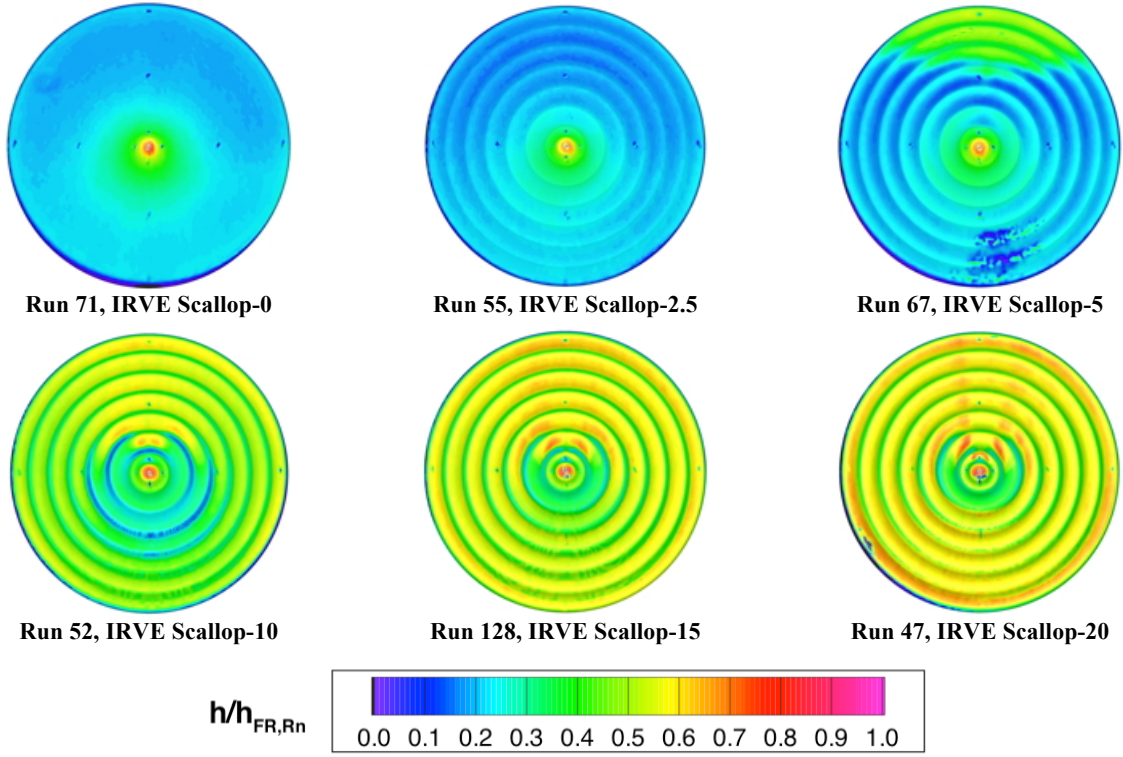


Figure 51. Configuration Effects at $Re_{\infty} = 3.88 \times 10^6/\text{ft}$, $\alpha = 6$ deg.

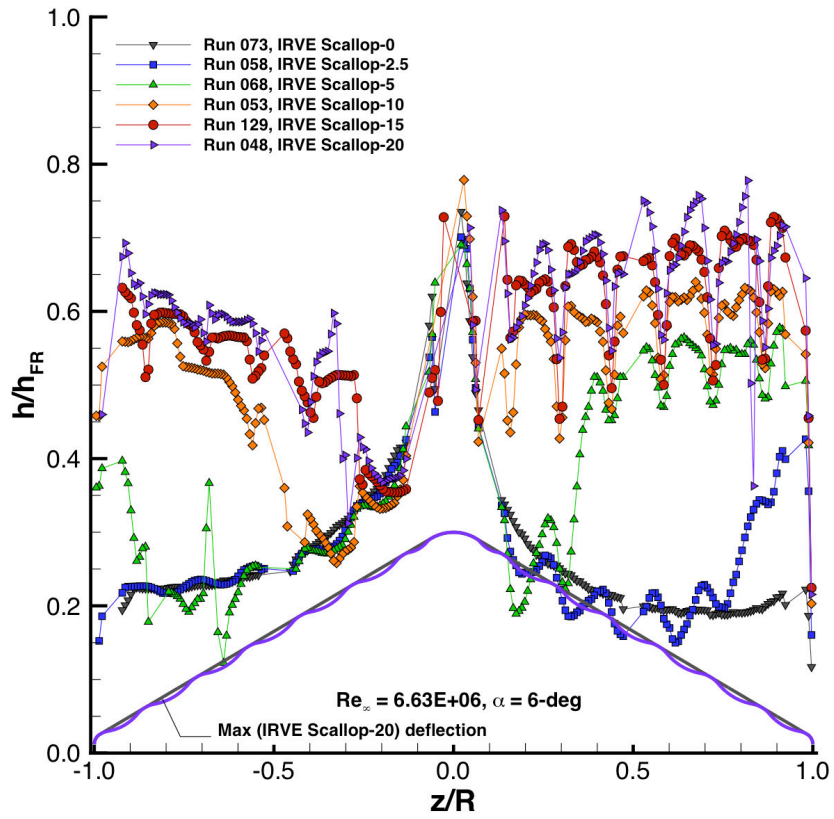
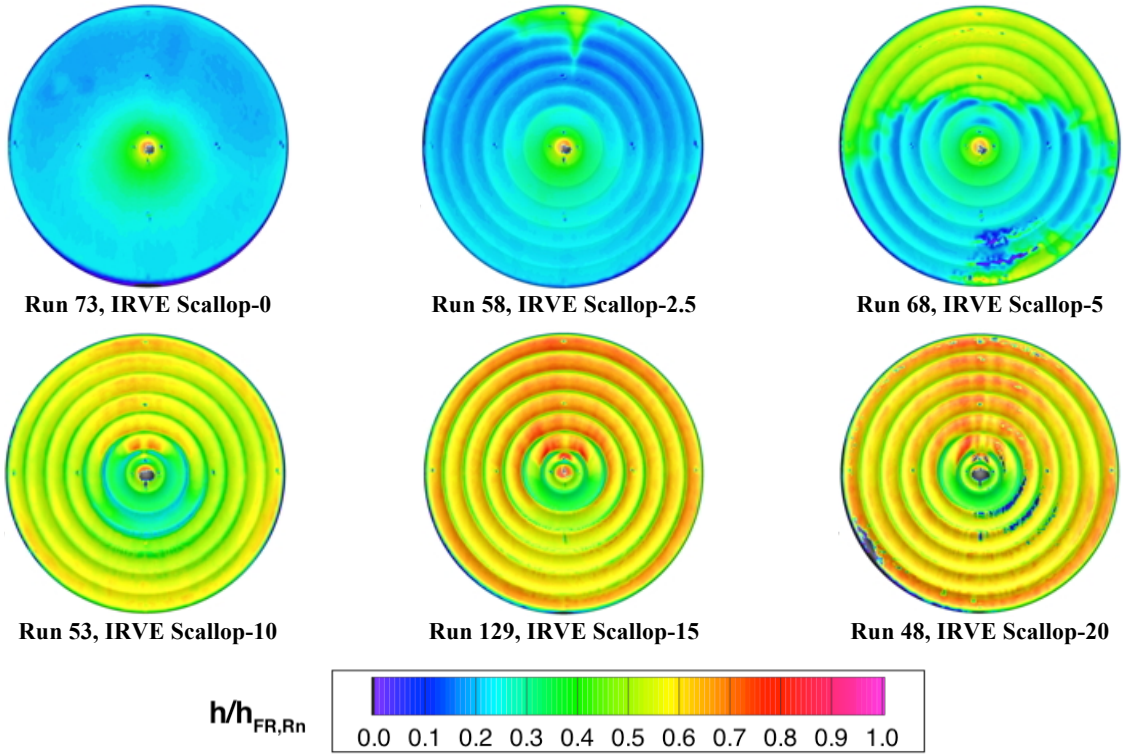


Figure 52. Configuration Effects at $Re_{\infty} = 6.63 \times 10^6/\text{ft}$, $\alpha = 6$ deg.

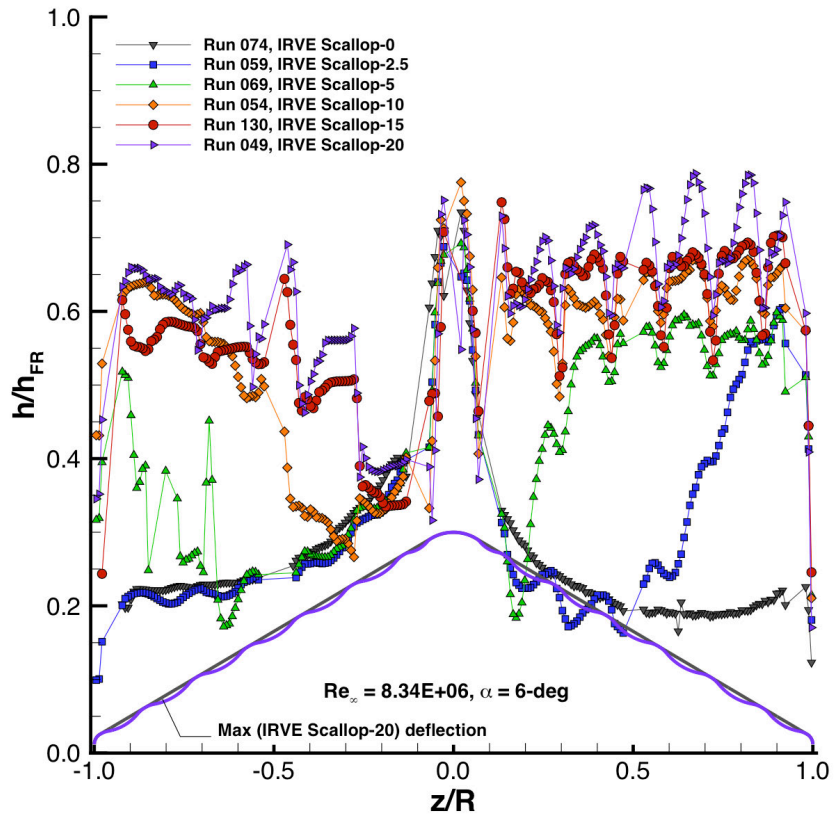
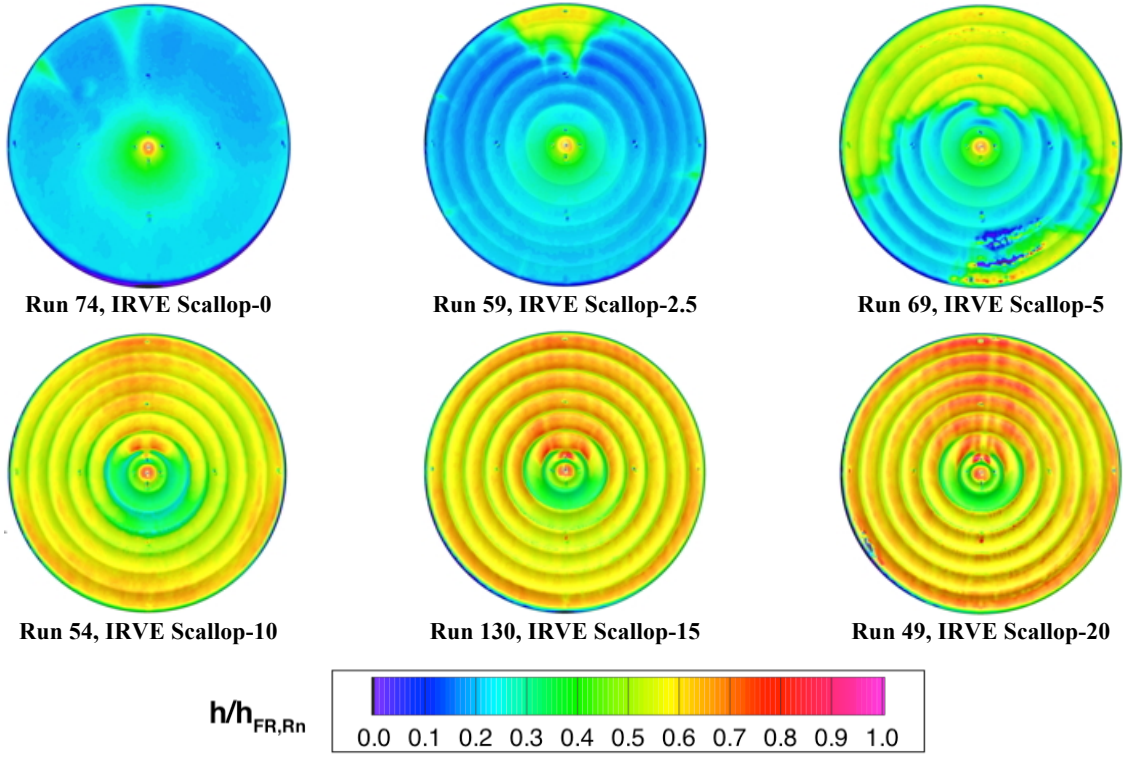


Figure 53. Configuration Effects at $Re_{\infty} = 8.34 \times 10^6/\text{ft}$, $\alpha = 6$ deg.

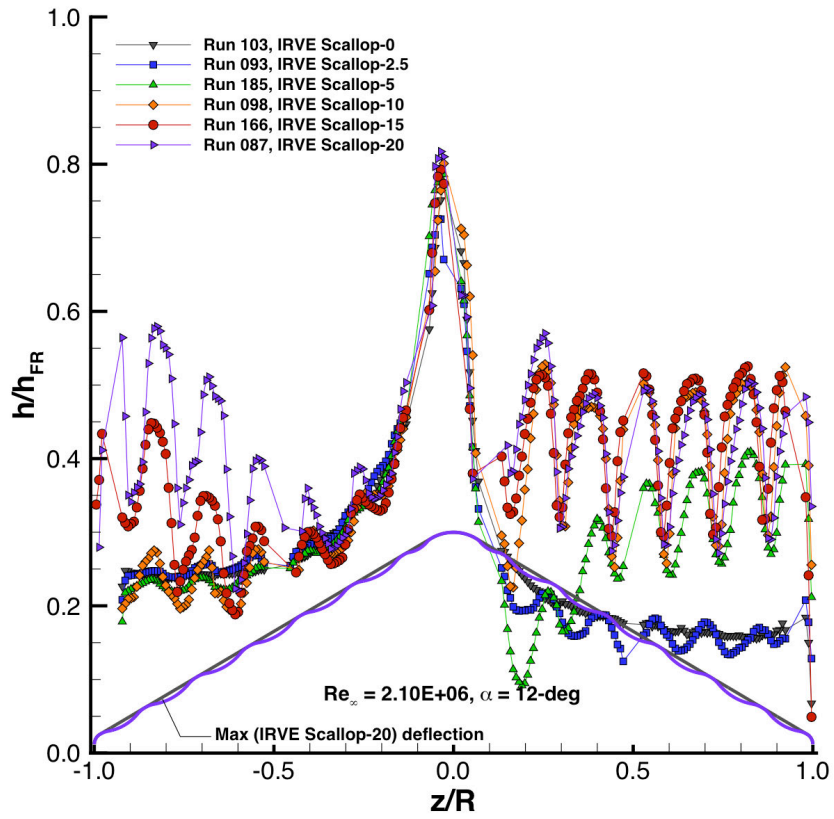
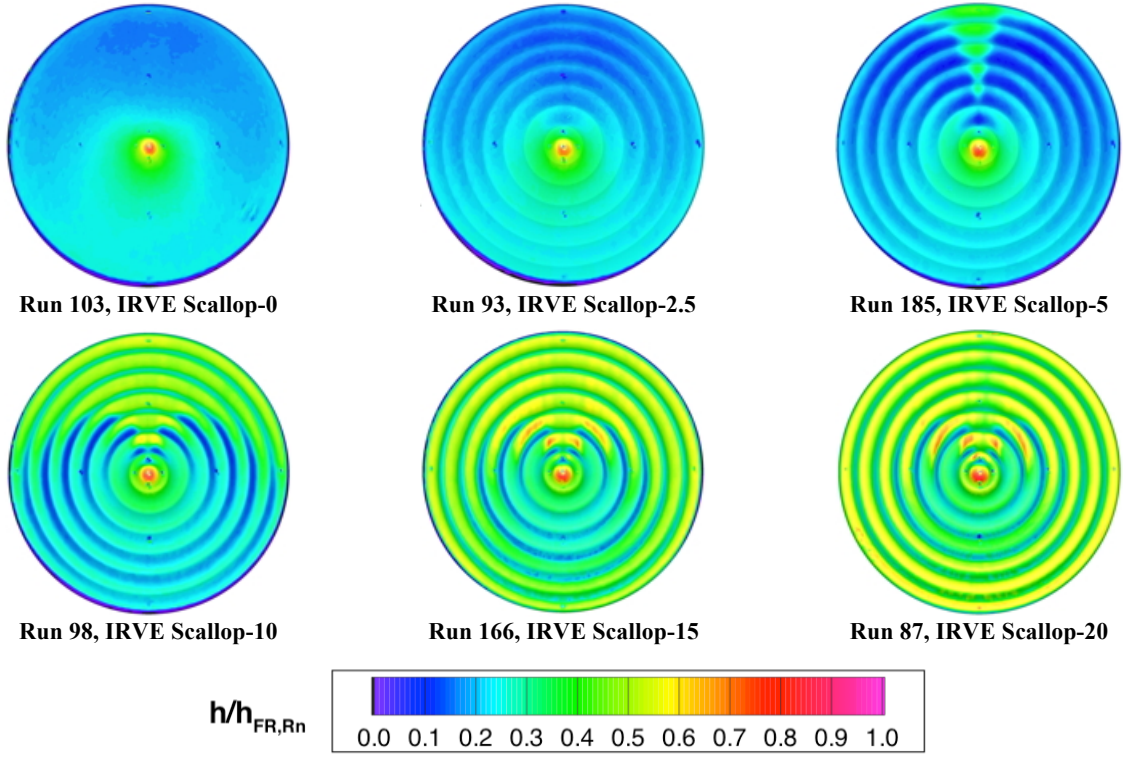


Figure 54. Configuration Effects at $Re_{\infty} = 2.10 \times 10^6/\text{ft}$, $\alpha = 12$ deg.

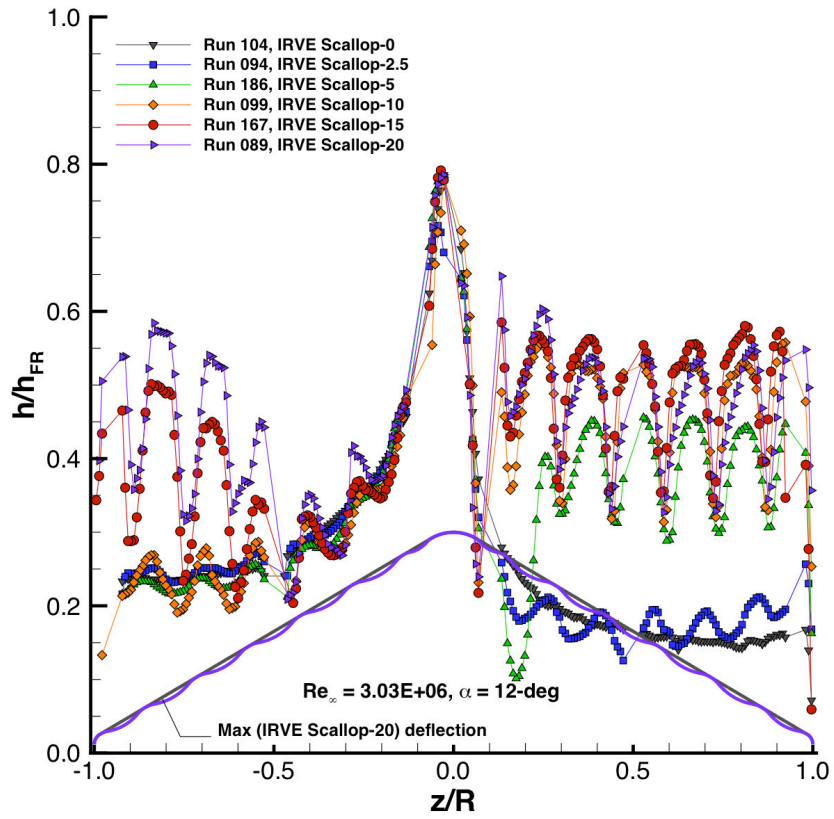
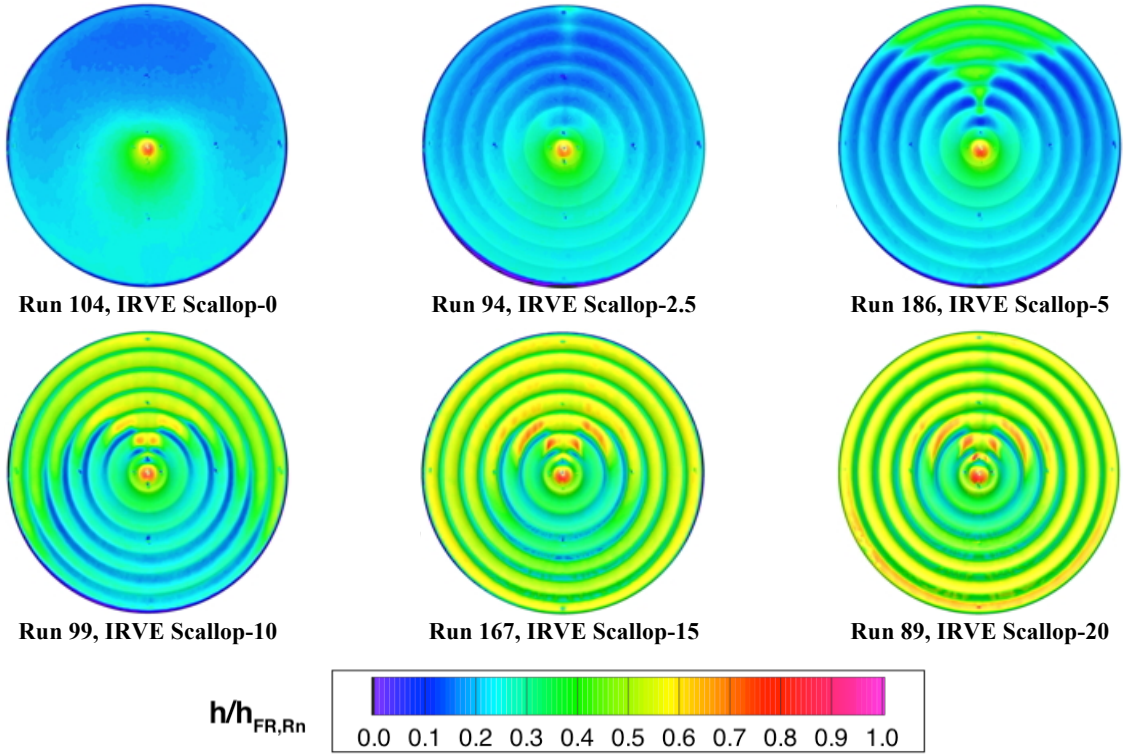


Figure 55. Configuration Effects at $Re_{\infty} = 3.03 \times 10^6/\text{ft}$, $\alpha = 12$ deg.

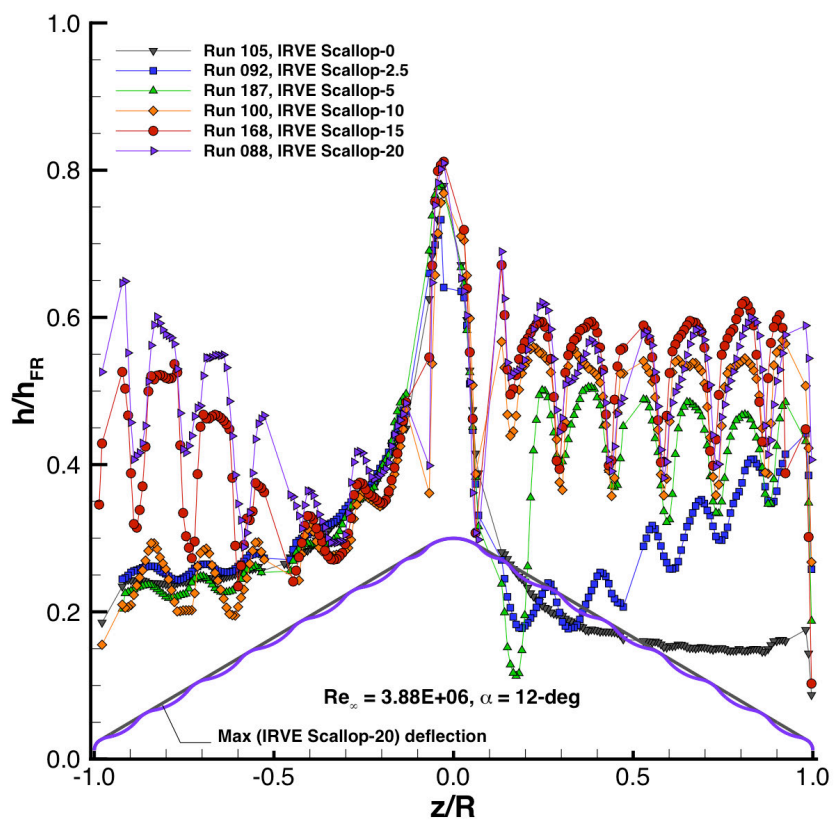
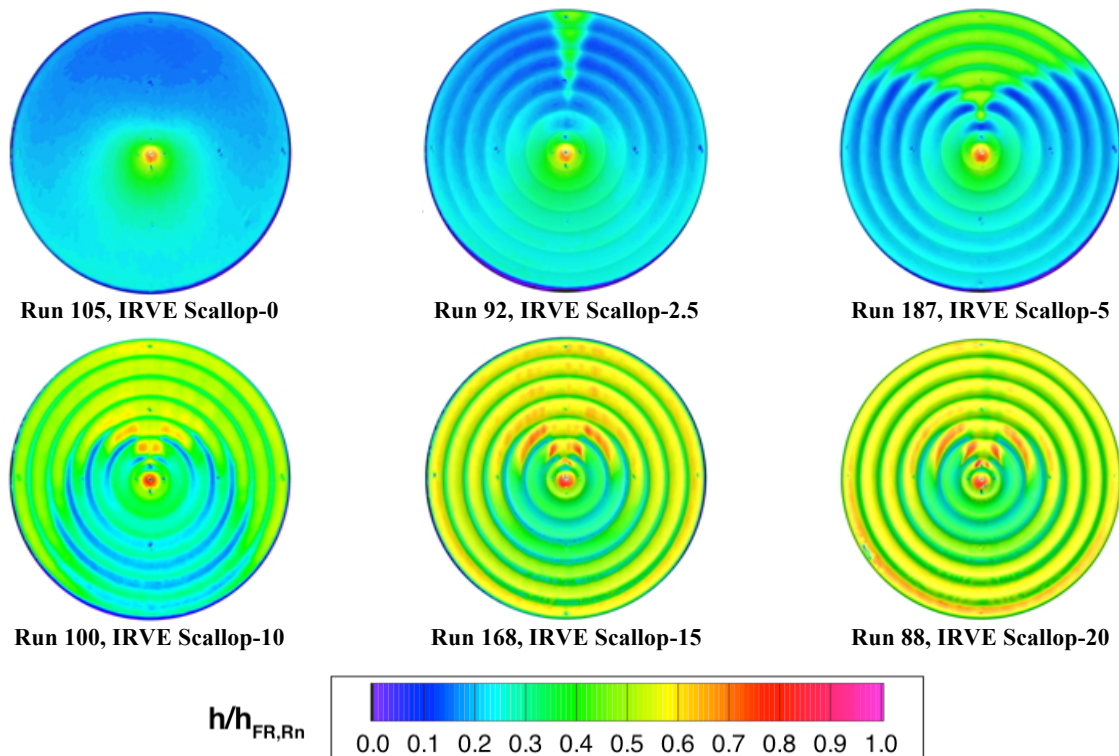


Figure 56. Configuration Effects at $Re_\infty = 3.88 \times 10^6/\text{ft}$, $\alpha = 12$ deg.

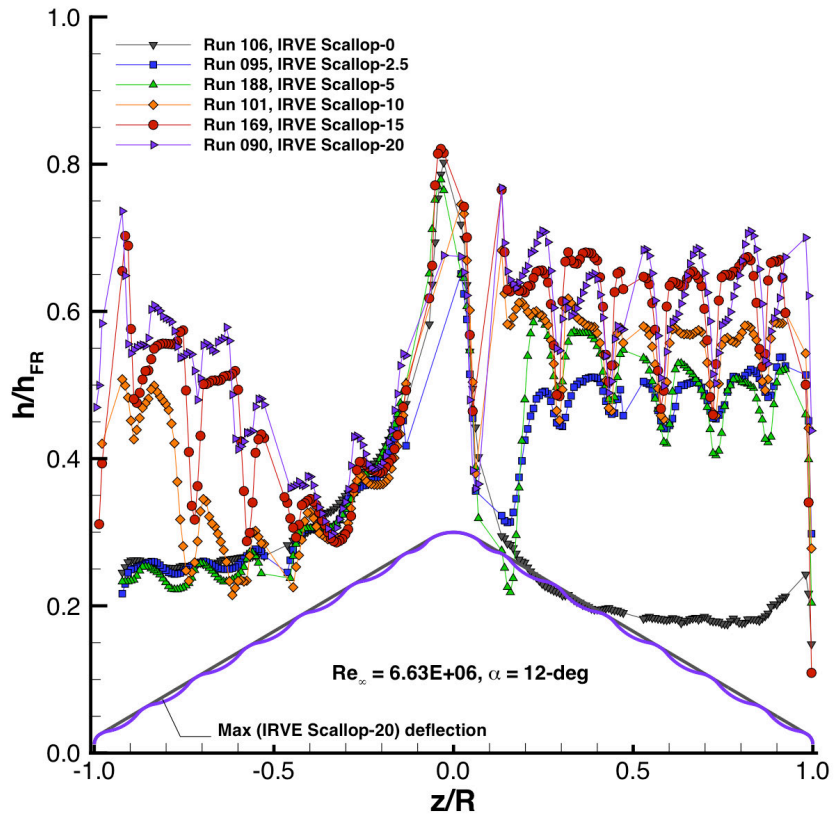
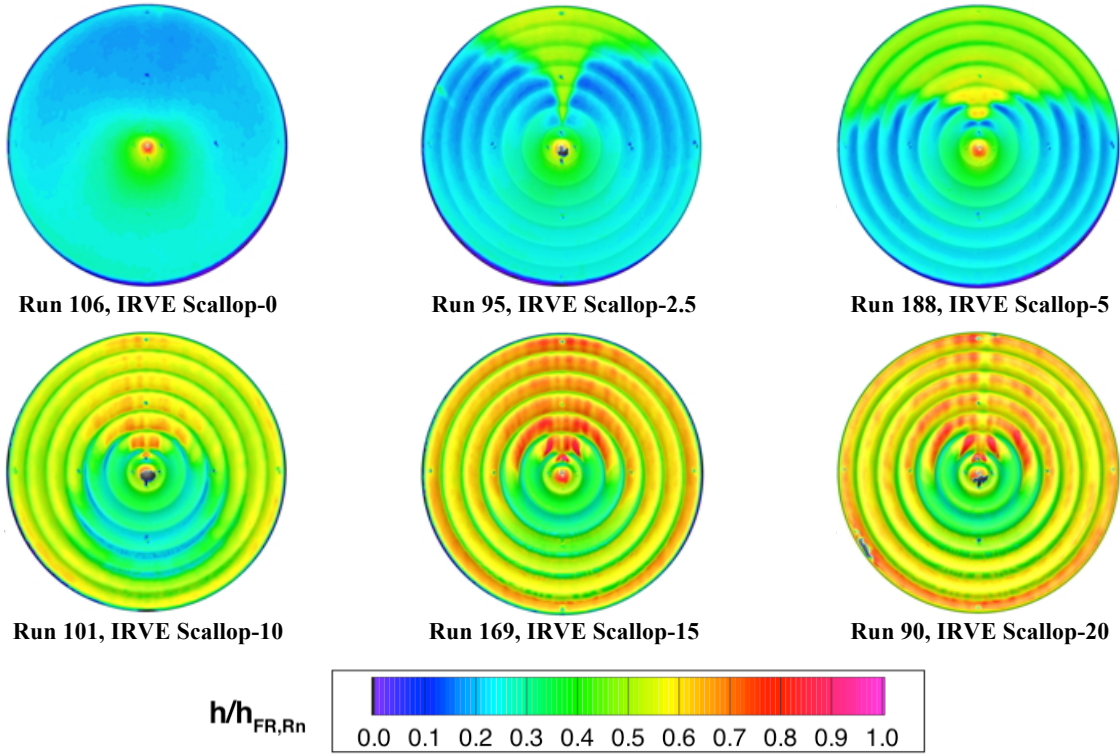


Figure 57. Configuration Effects at $Re_{\infty} = 6.63 \times 10^6/\text{ft}$, $\alpha = 12$ deg.

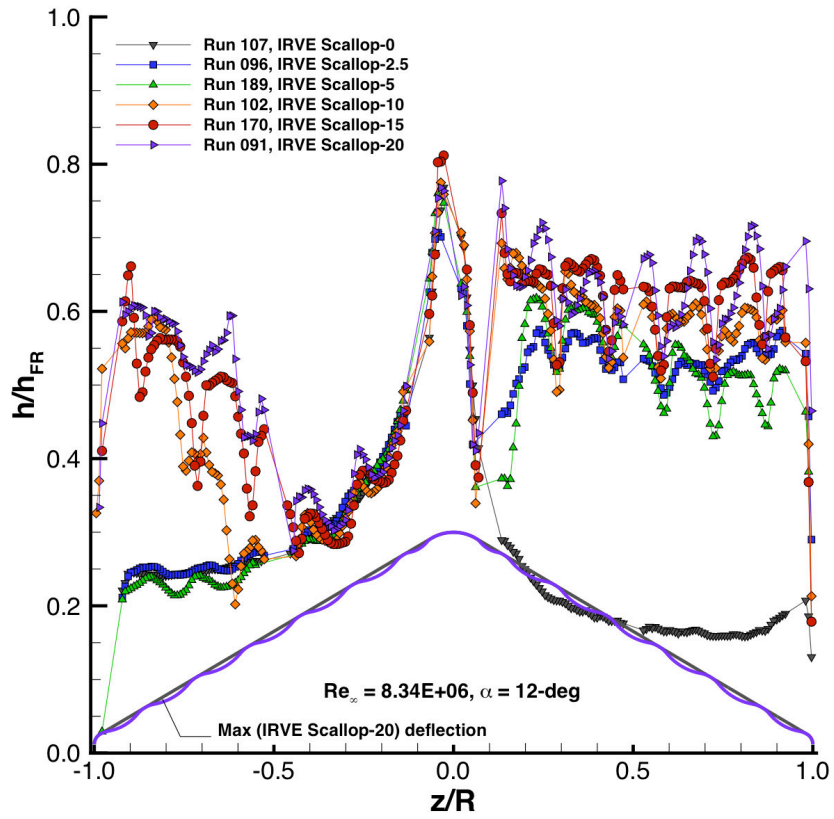
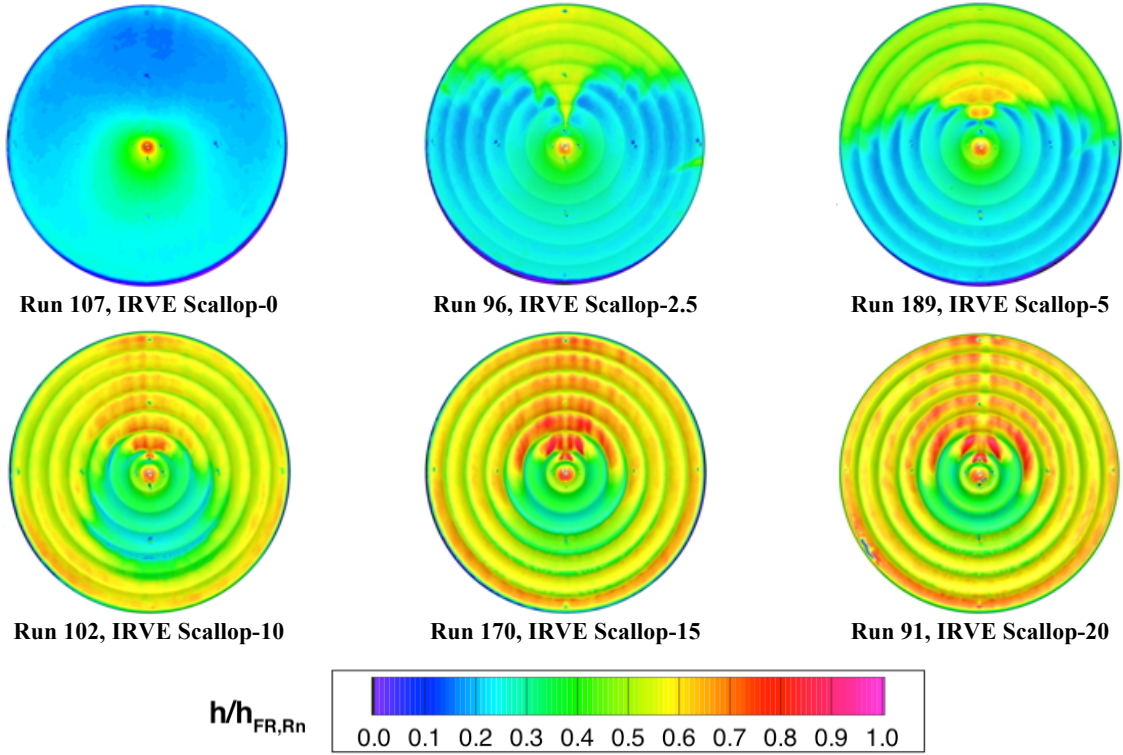


Figure 58. Configuration Effects at $Re_{\infty} = 8.34 \times 10^6/\text{ft}$, $\alpha = 12$ deg.

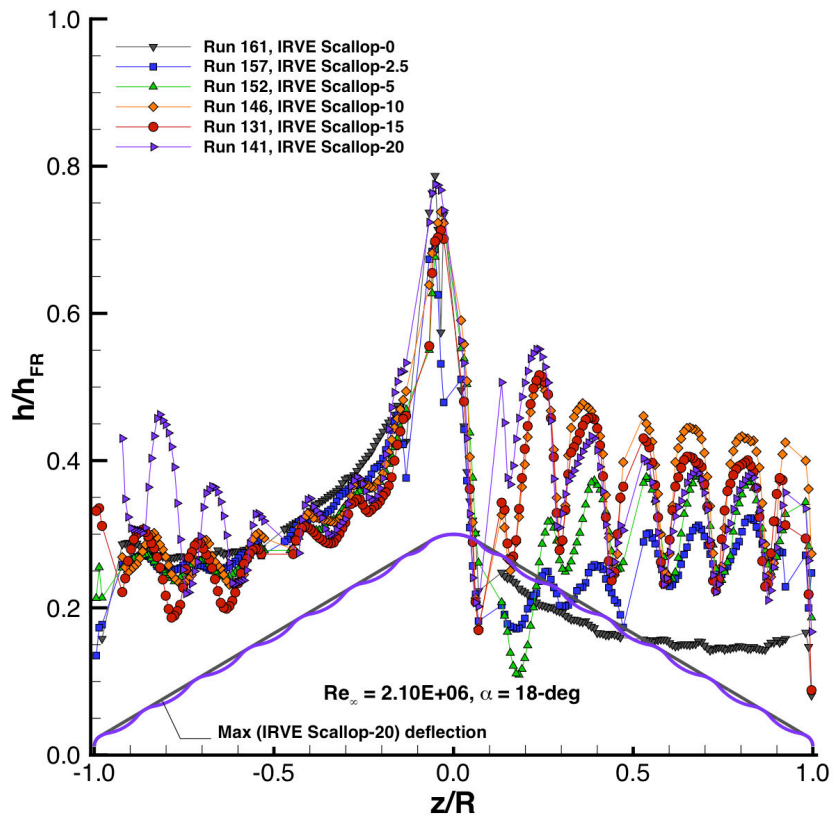
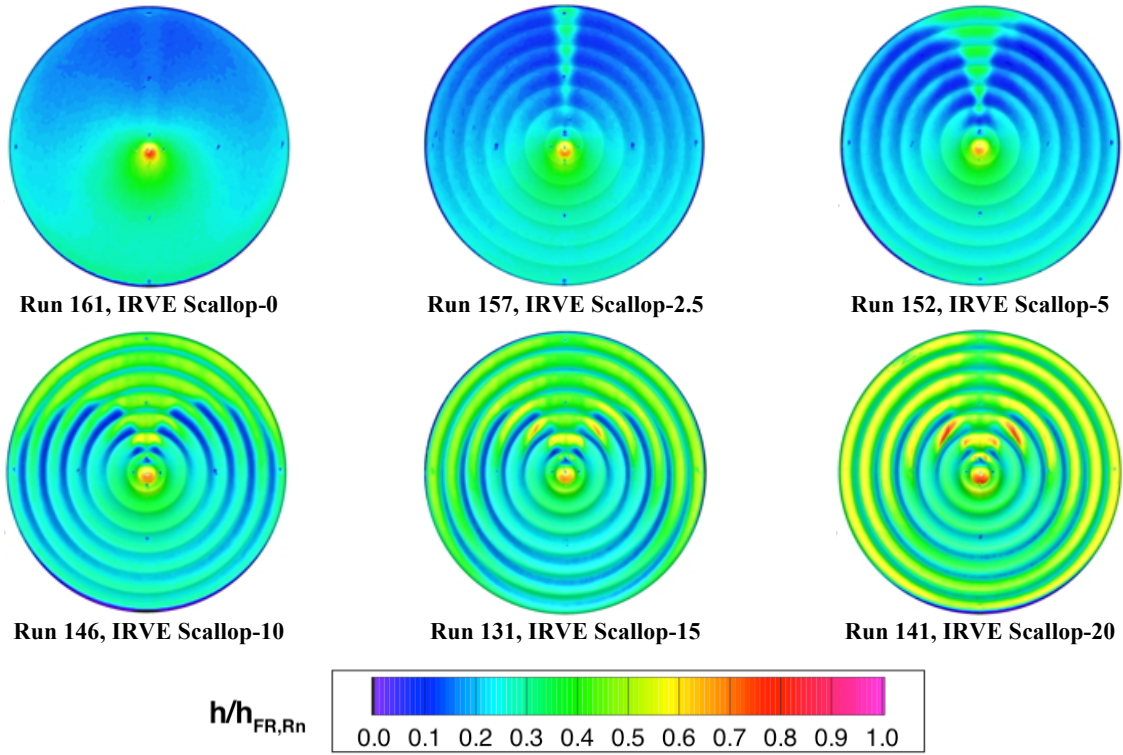


Figure 59. Configuration Effects at $Re_{\infty} = 2.10 \times 10^6/\text{ft}$, $\alpha = 18$ deg.

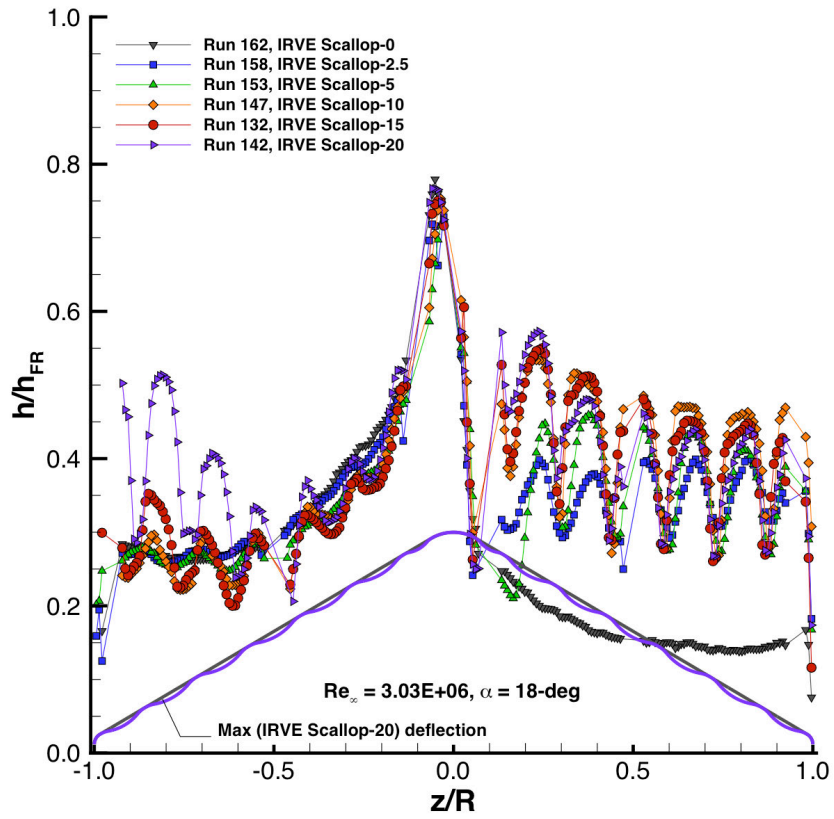
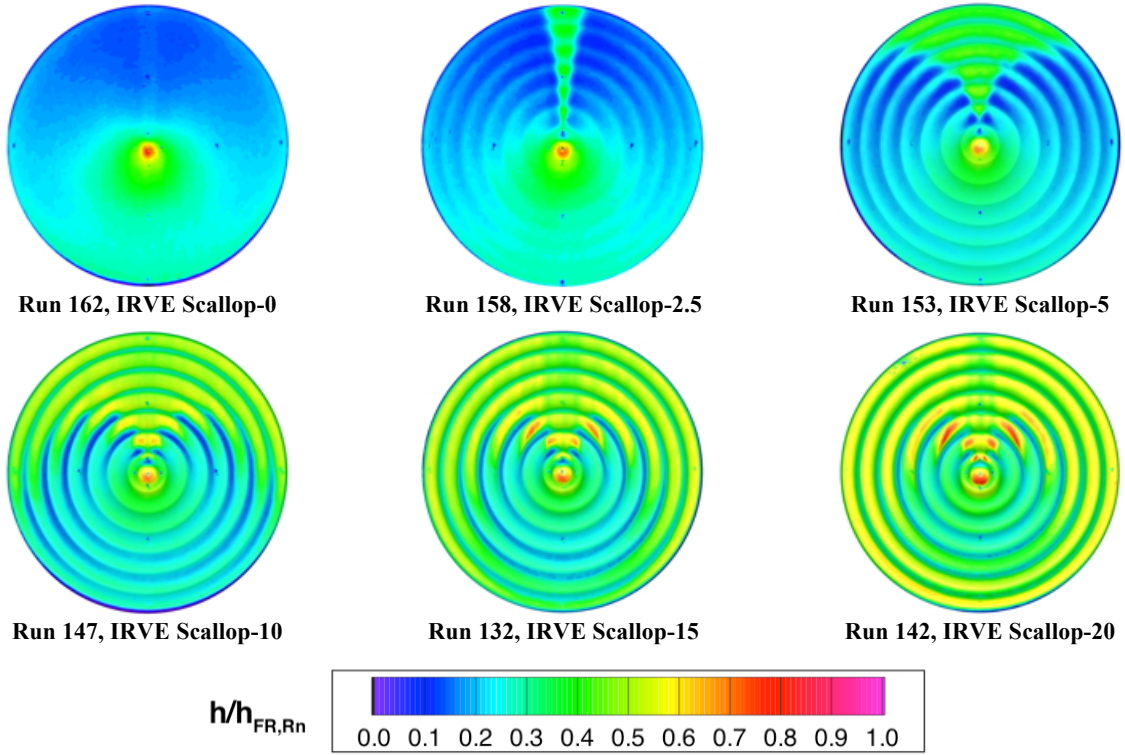


Figure 60. Configuration Effects at $Re_{\infty} = 3.03 \times 10^6/\text{ft}$, $\alpha = 18$ deg.

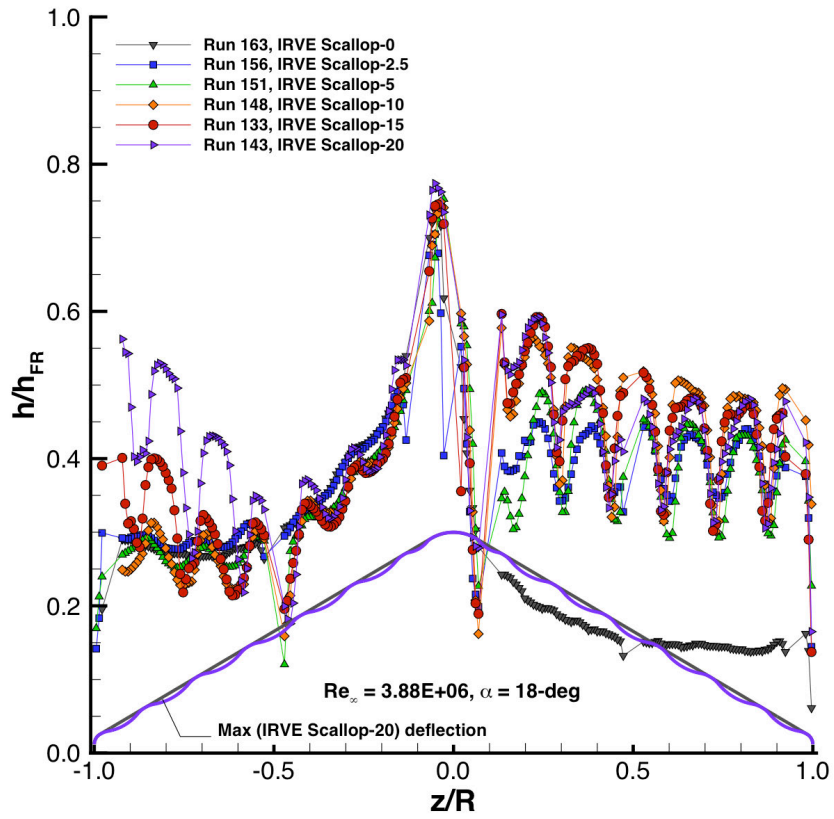
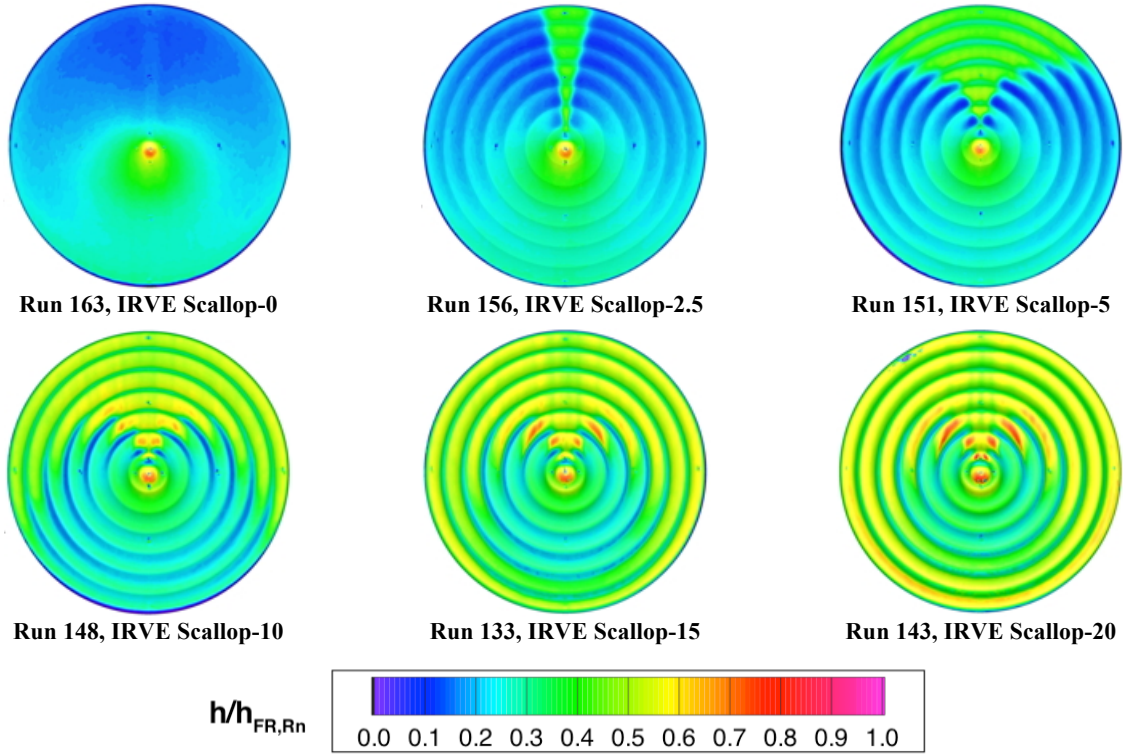


Figure 61. Configuration Effects at $Re_{\infty} = 3.88 \times 10^6/\text{ft}$, $\alpha = 18$ deg.

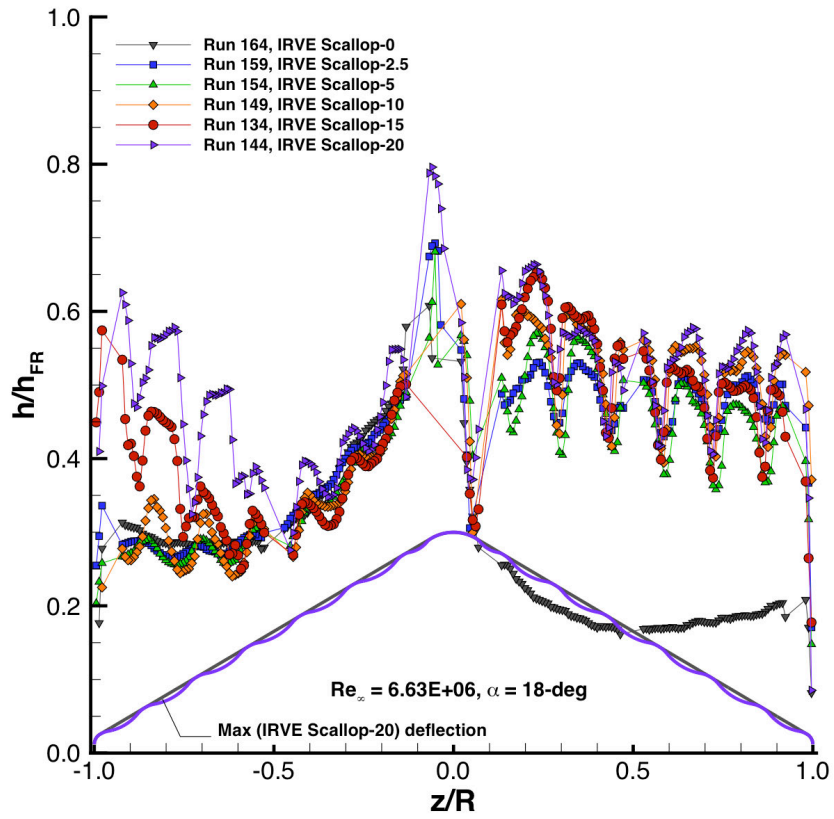
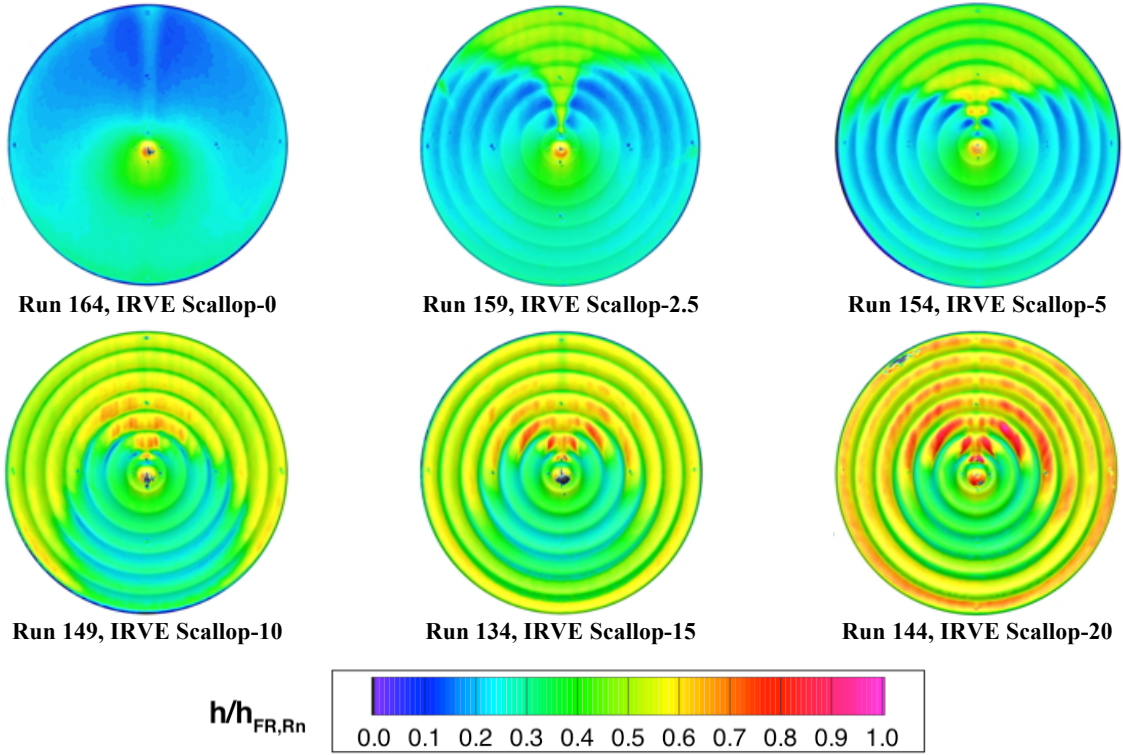


Figure 62. Configuration Effects at $Re_{\infty} = 6.63 \times 10^6/\text{ft}$, $\alpha = 18$ deg.

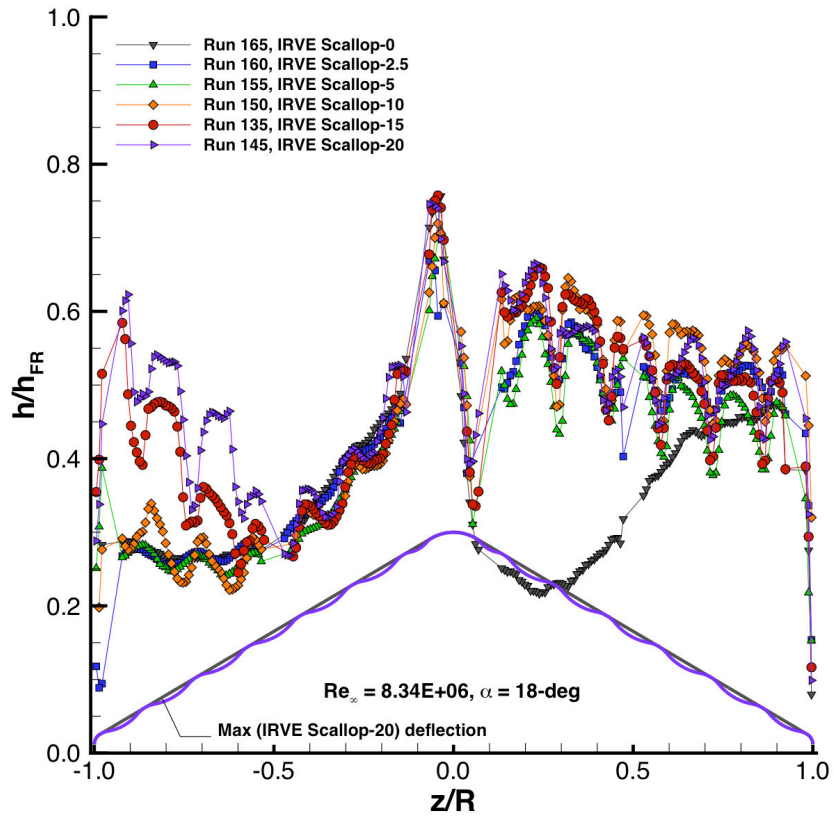
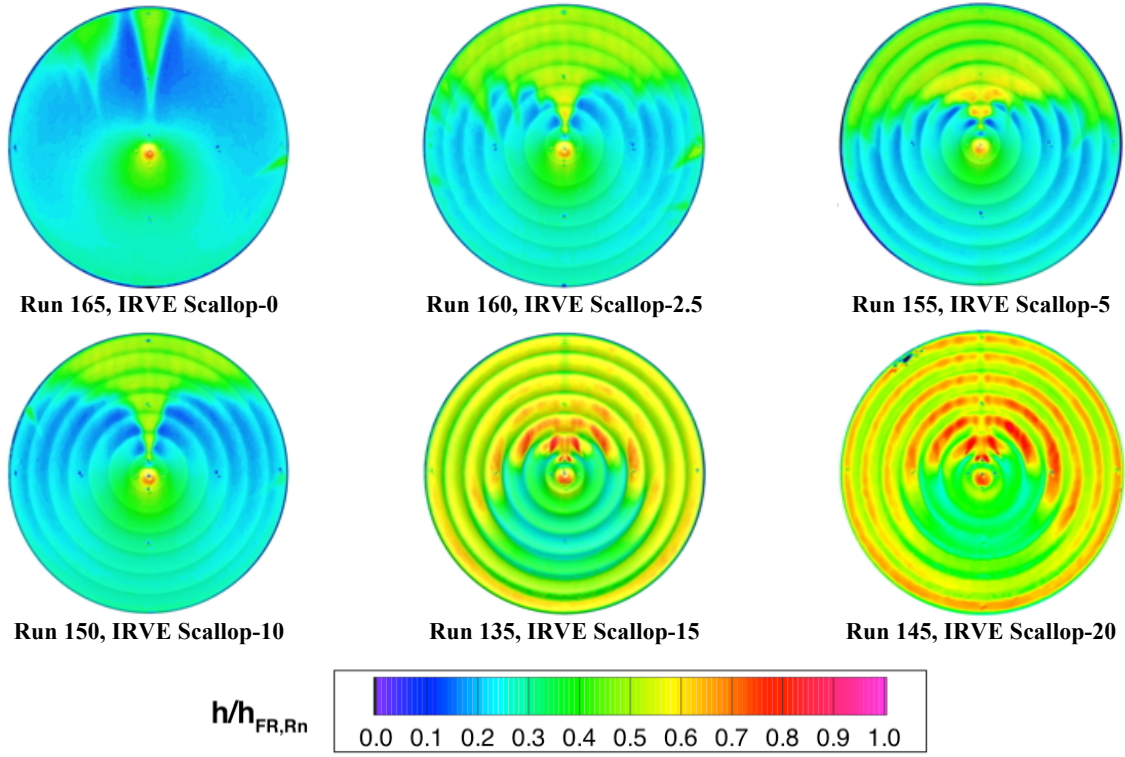


Figure 63. Configuration Effects at $Re_{\infty} = 8.34 \times 10^6/\text{ft}$, $\alpha = 18$ deg.

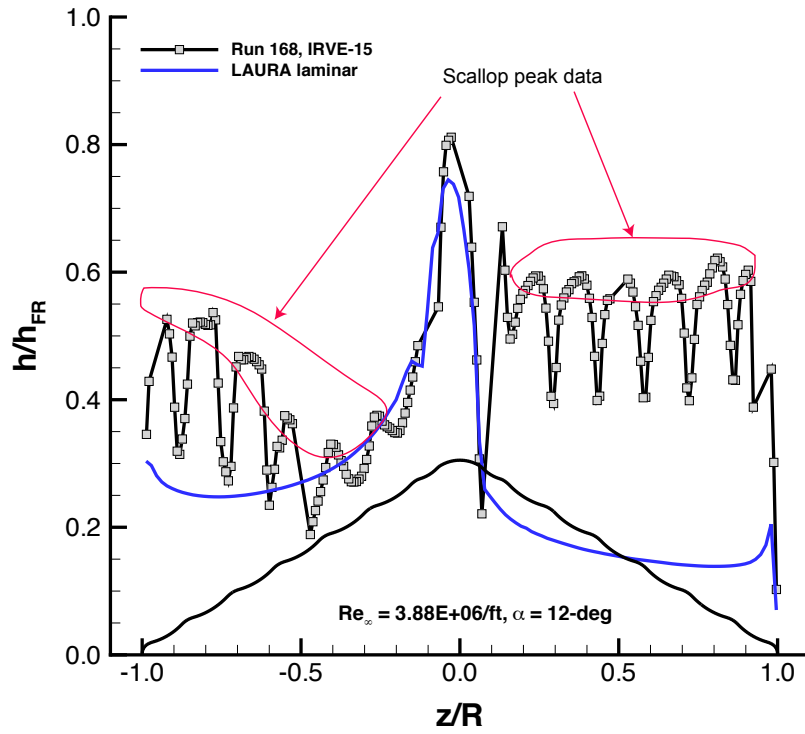


Figure 64. Illustration of Scallop Peak Heating Data used for Correlation.

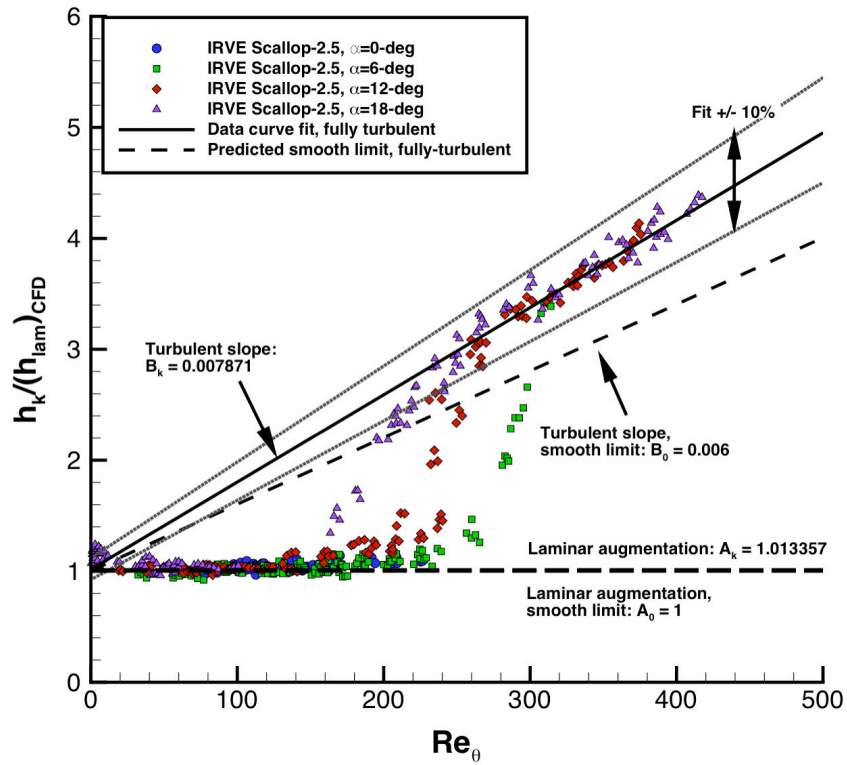


Figure 65. Turbulent Correlation for IRVE Scallop-2.5 Data.

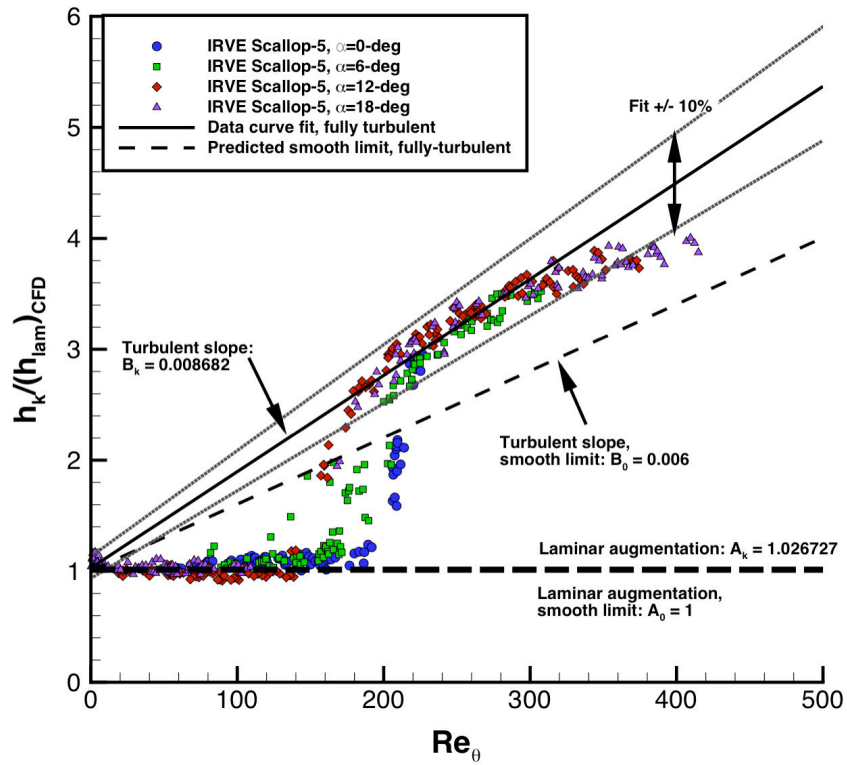


Figure 66. Turbulent Correlation for IRVE Scallop-5 Data.

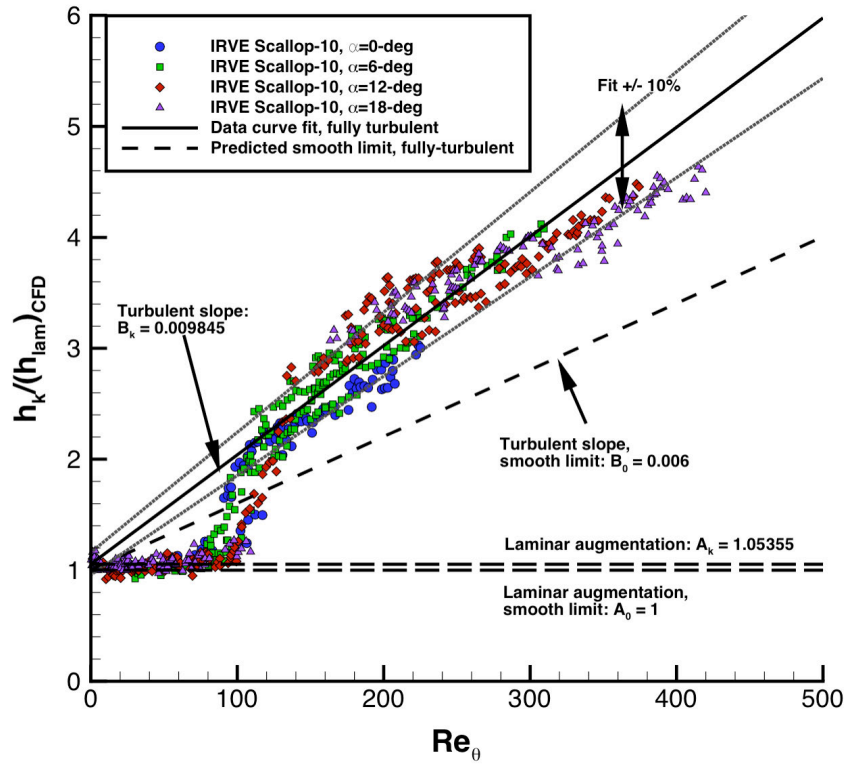


Figure 67. Turbulent Correlation for IRVE Scallop-10 Data.

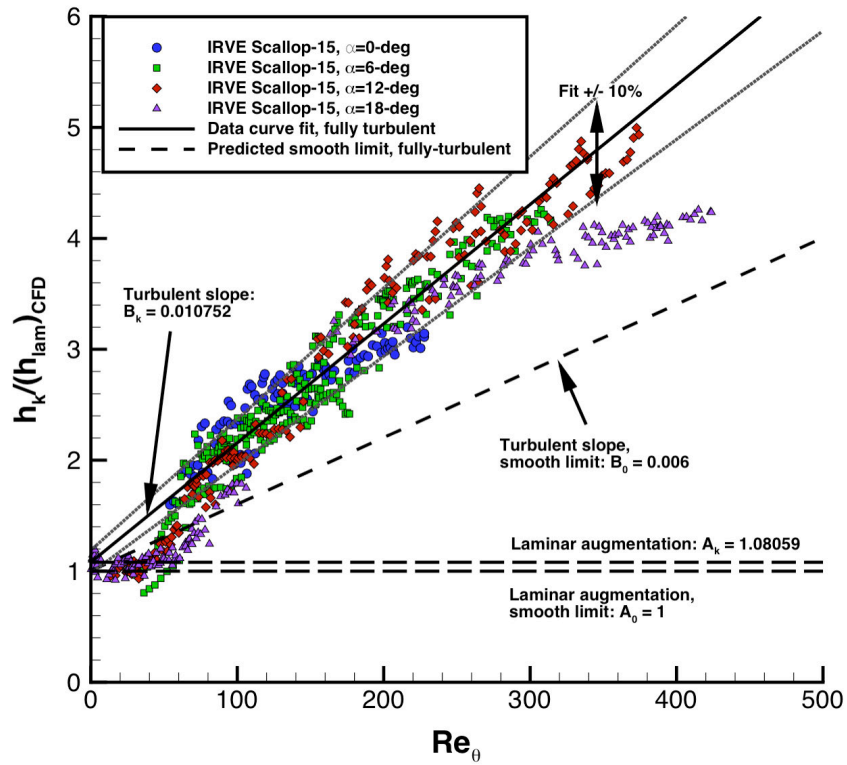


Figure 68. Turbulent Correlation for IRVE Scallop-15 Data.

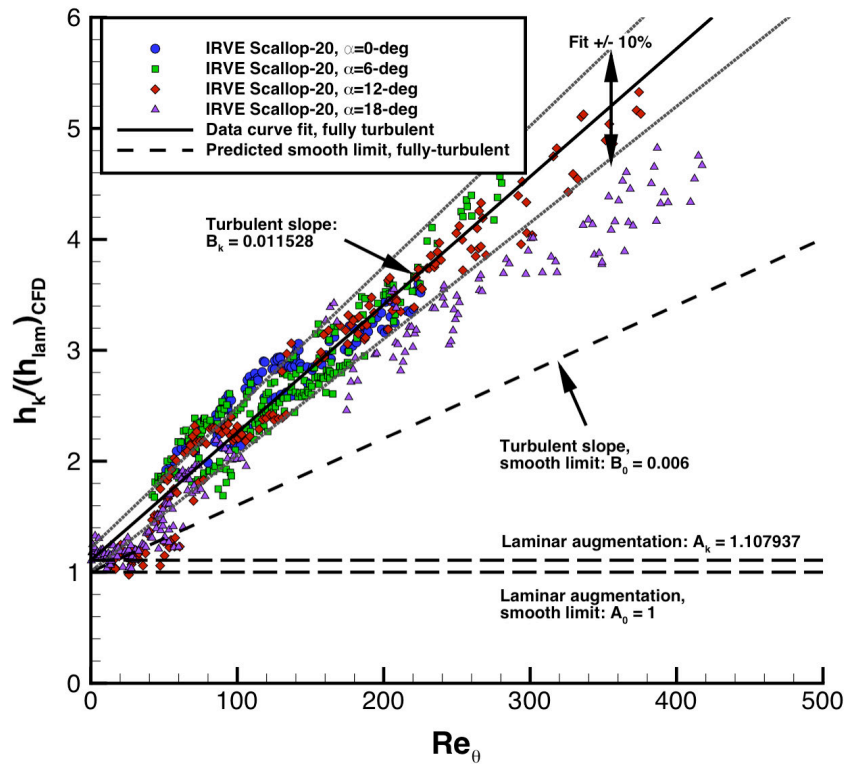


Figure 69. Turbulent Correlation for IRVE Scallop-20 Data.

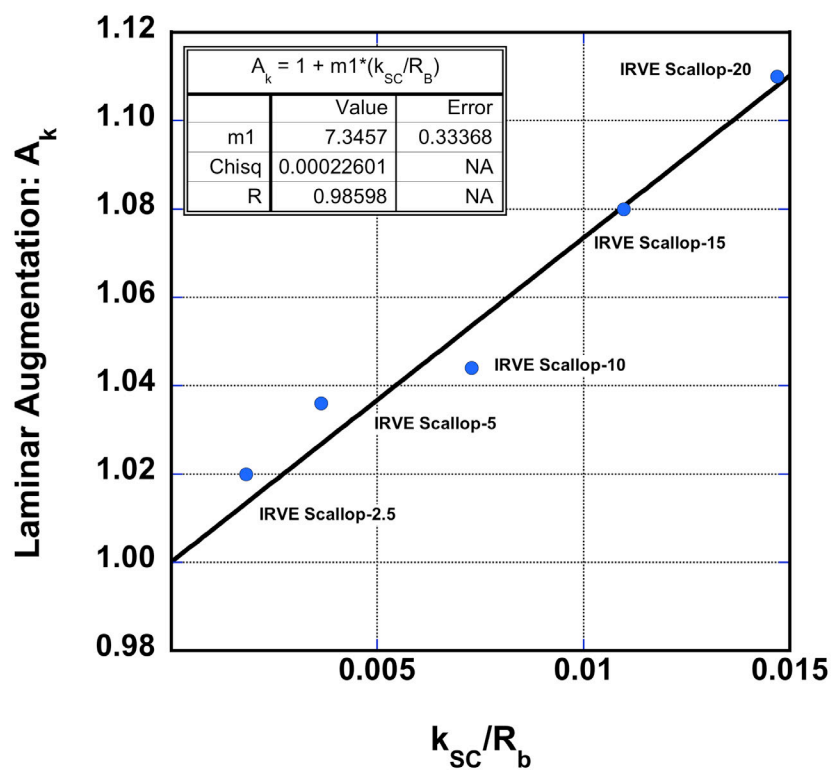


Figure 70. Curve Fit for Laminar Augmentation.

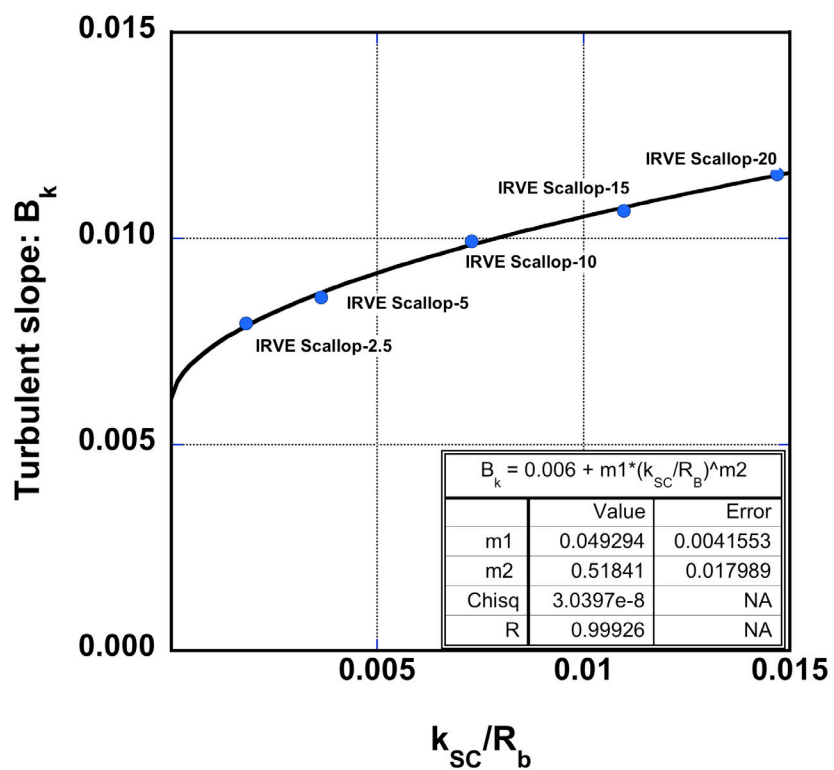


Figure 71. Curve Fit for Turbulent Slope.

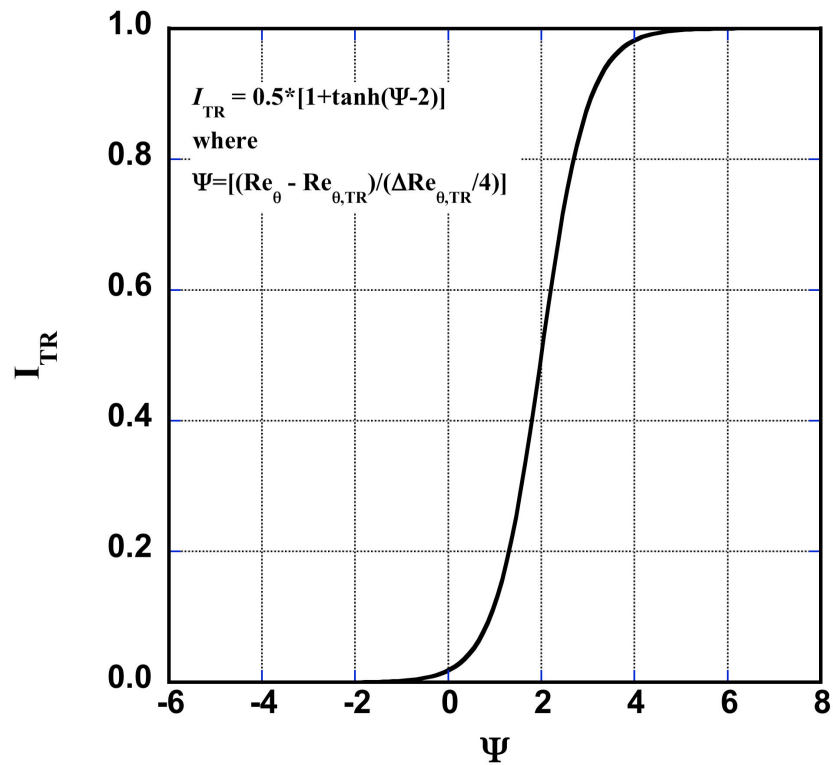


Figure 72. Transition Intermittency Function.

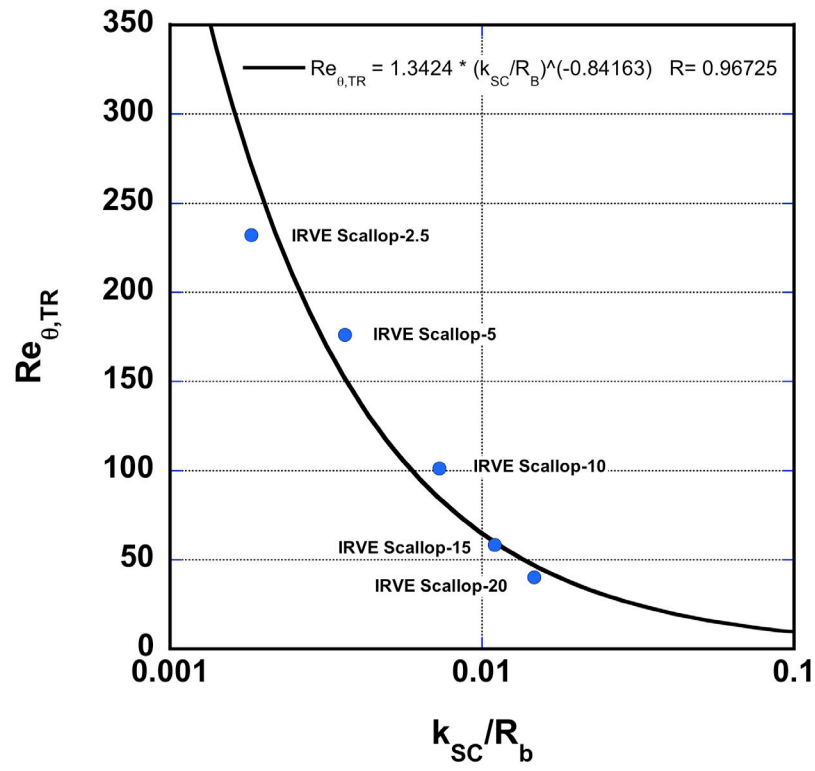


Figure 73. Curve Fit for Simple Transition Onset Model.

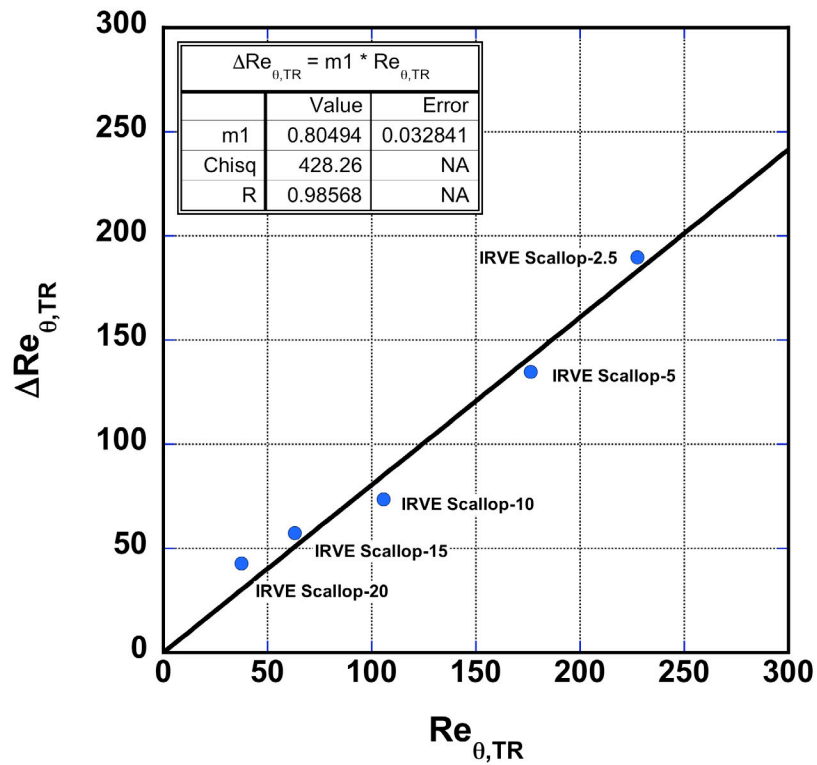


Figure 74. Curve Fit for Transition Length.

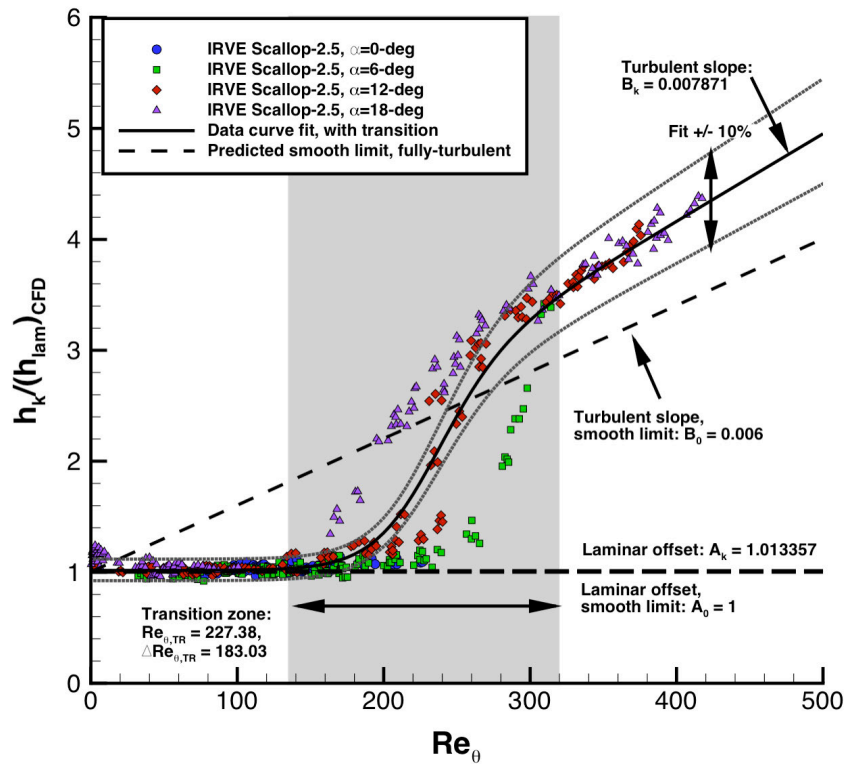


Figure 75. Transitional Correlation for IRVE Scallop-2.5 Data.

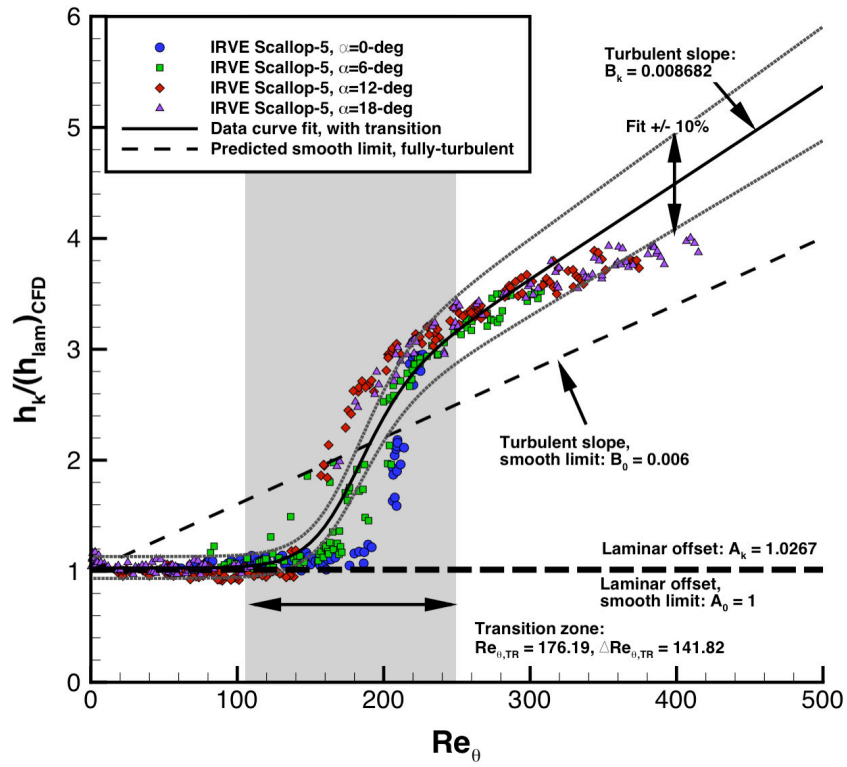


Figure 76. Transitional Correlation for IRVE Scallop-5 Data.

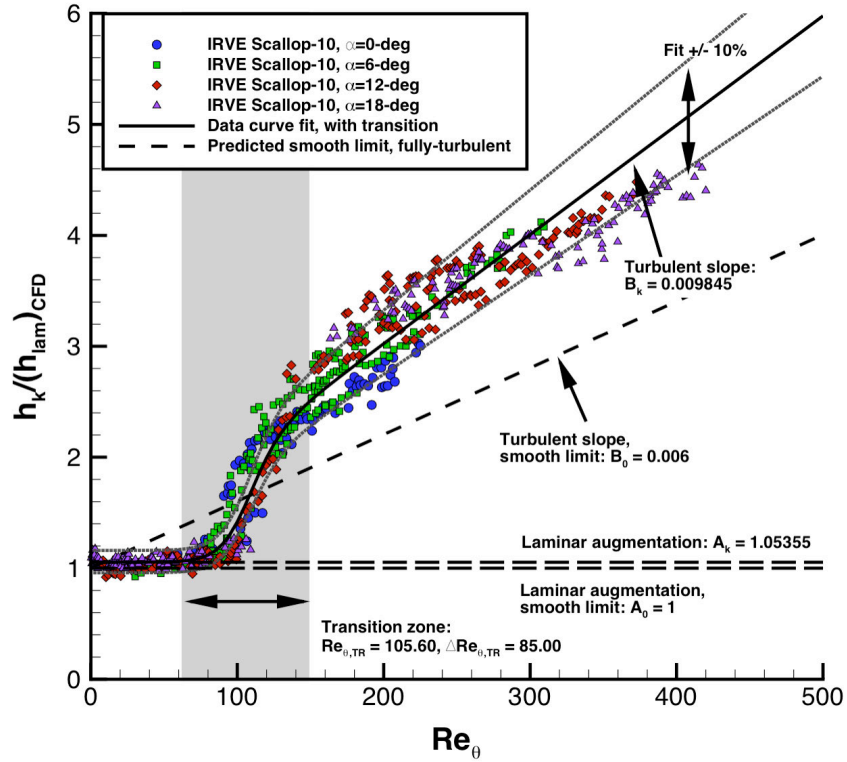


Figure 77. Transitional Correlation for IRVE Scallop-10 Data.

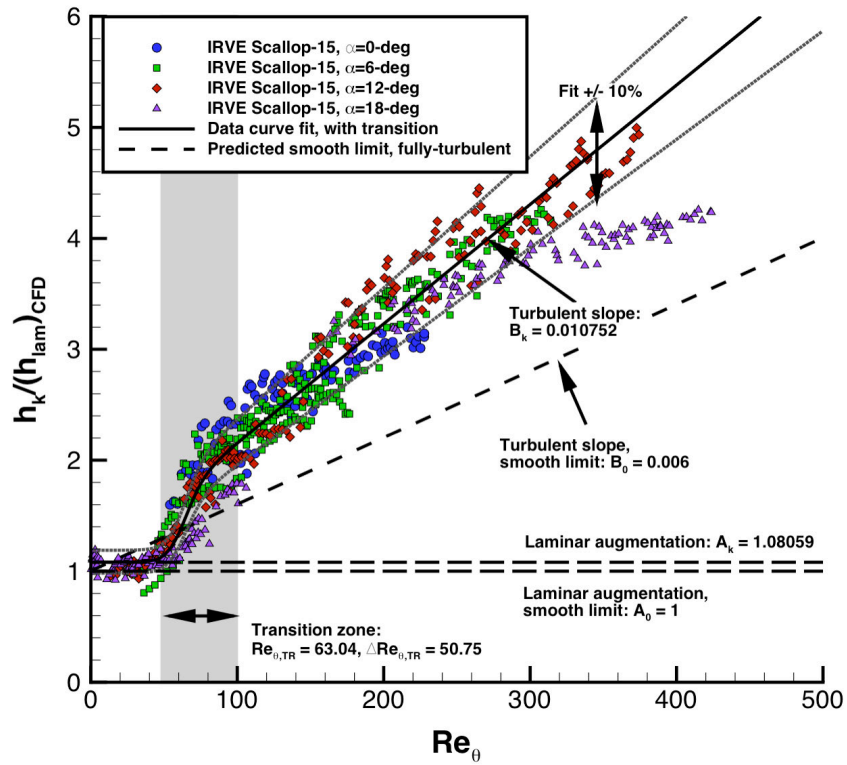


Figure 78. Transitional Correlation for IRVE Scallop-15 Data.

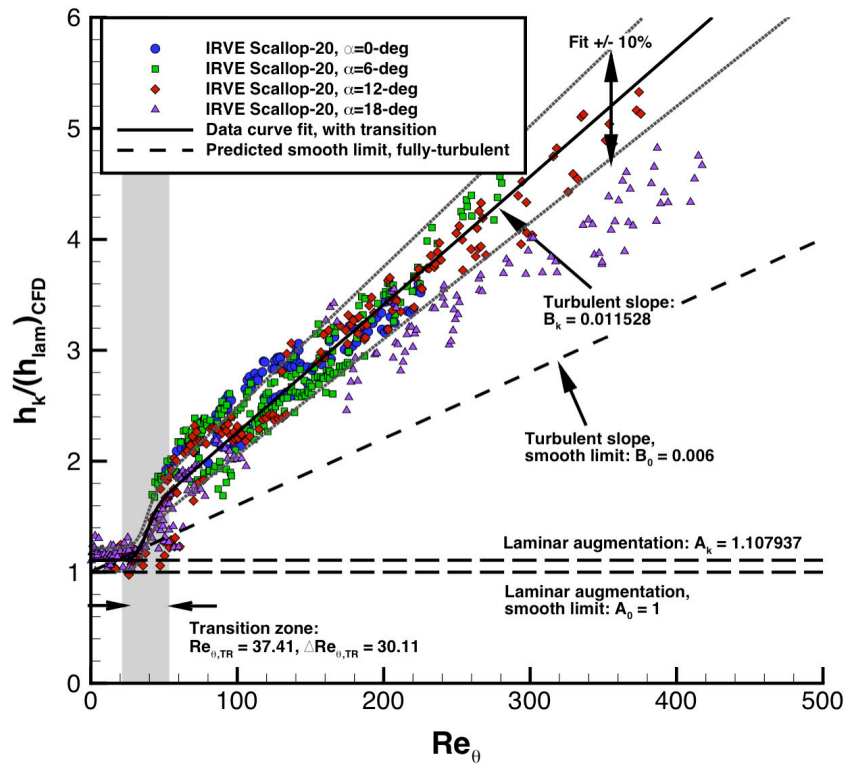


Figure 79. Transitional Correlation for IRVE Scallop-20 Data.

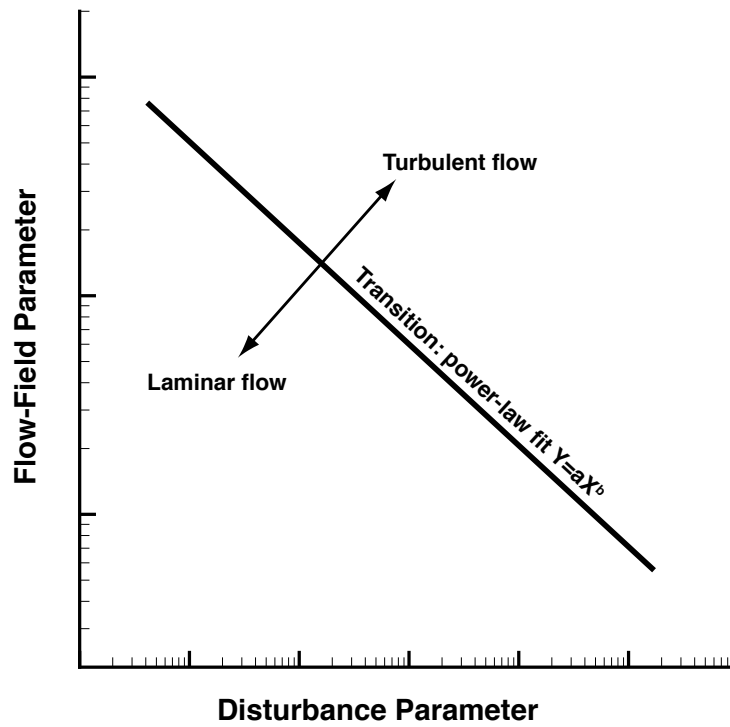


Figure 80. Transition Correlation Form.

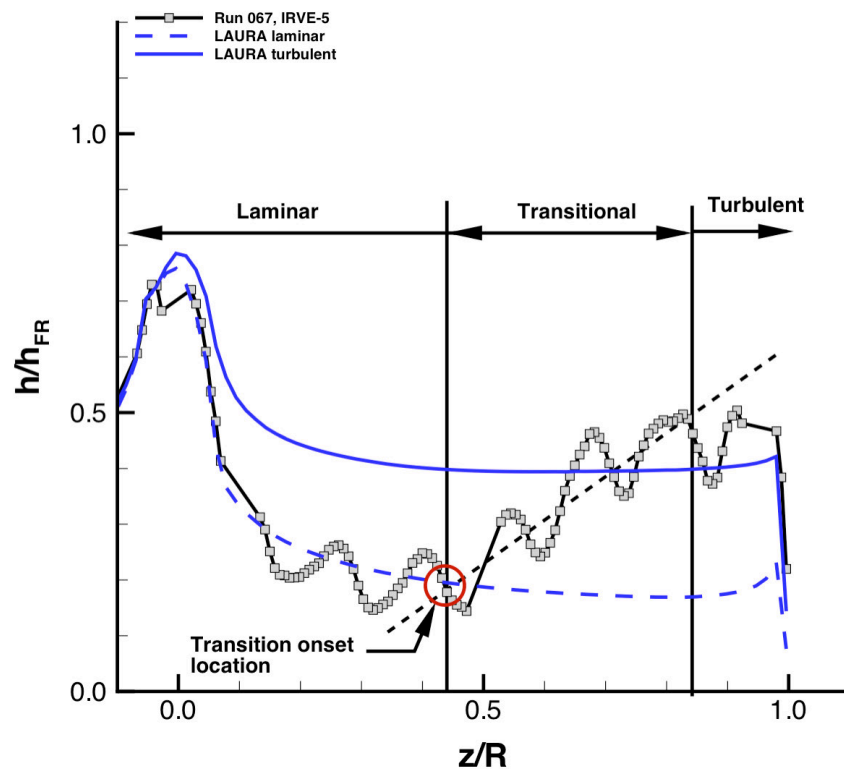


Figure 81. Tangent-Slope-Intercept Identification of Transition Onset.

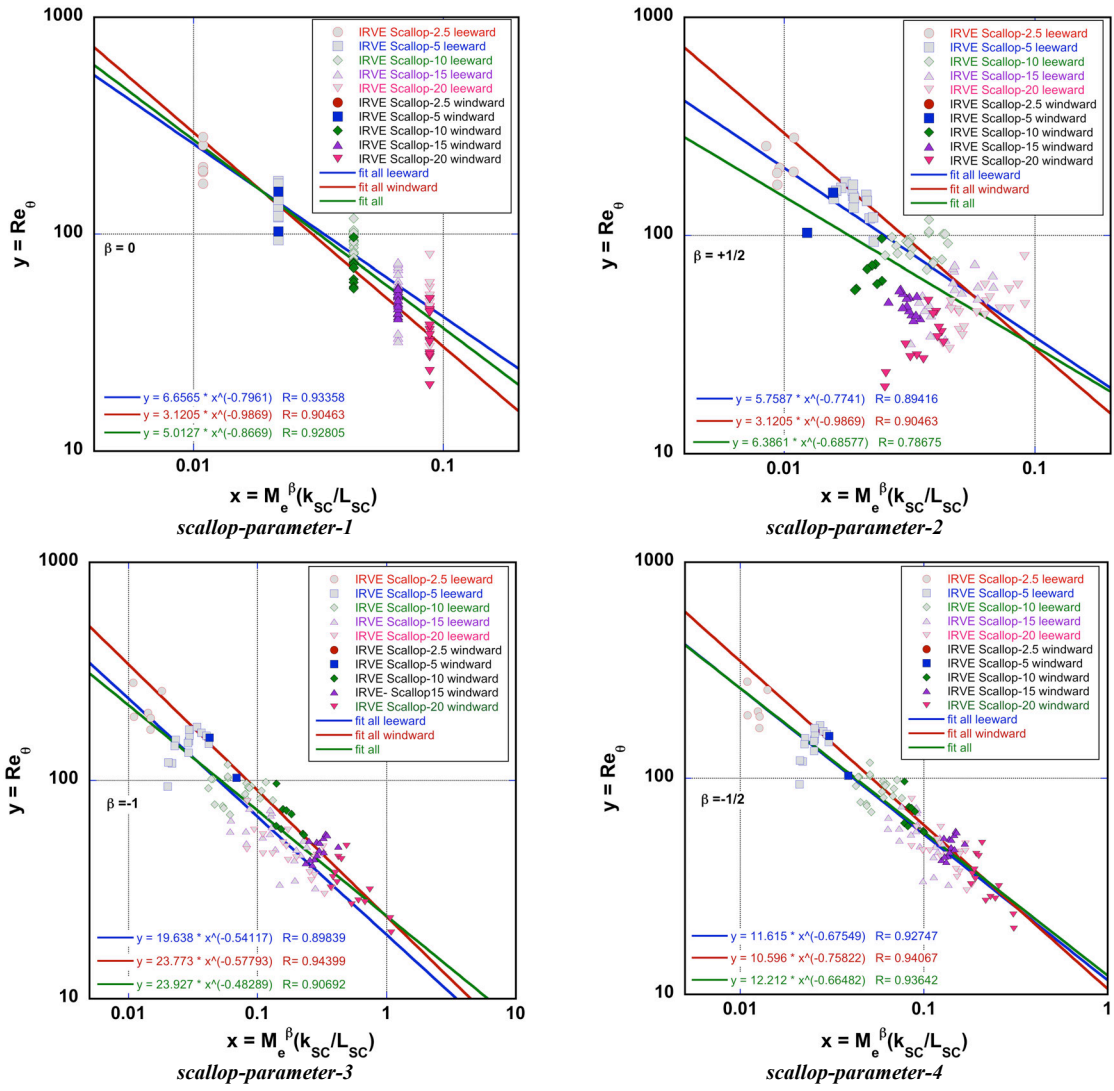


Figure 82. Scallop-Parameter Correlation Variations.

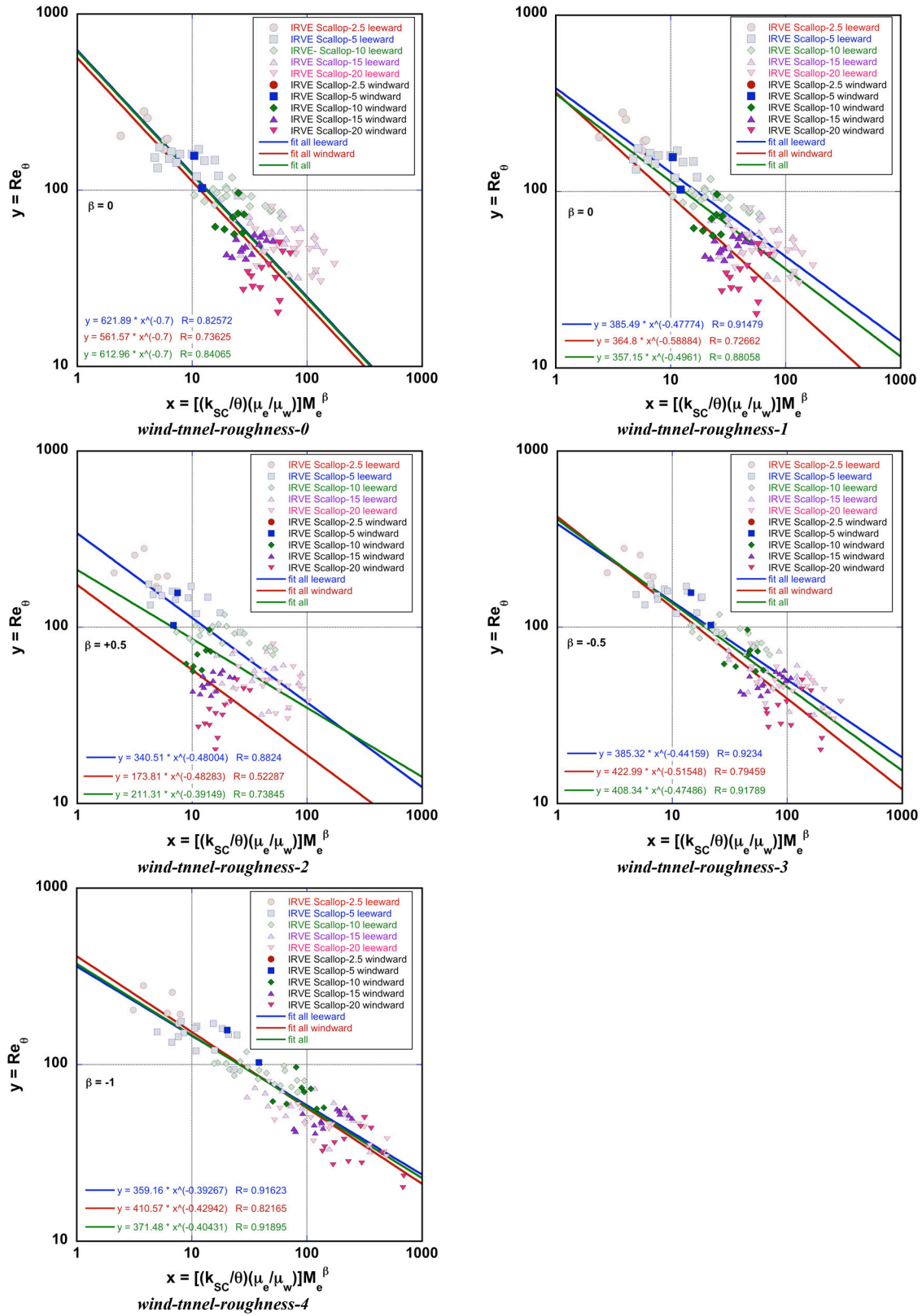


Figure 83. Wind-Tunnel-Roughness Correlation Variations.

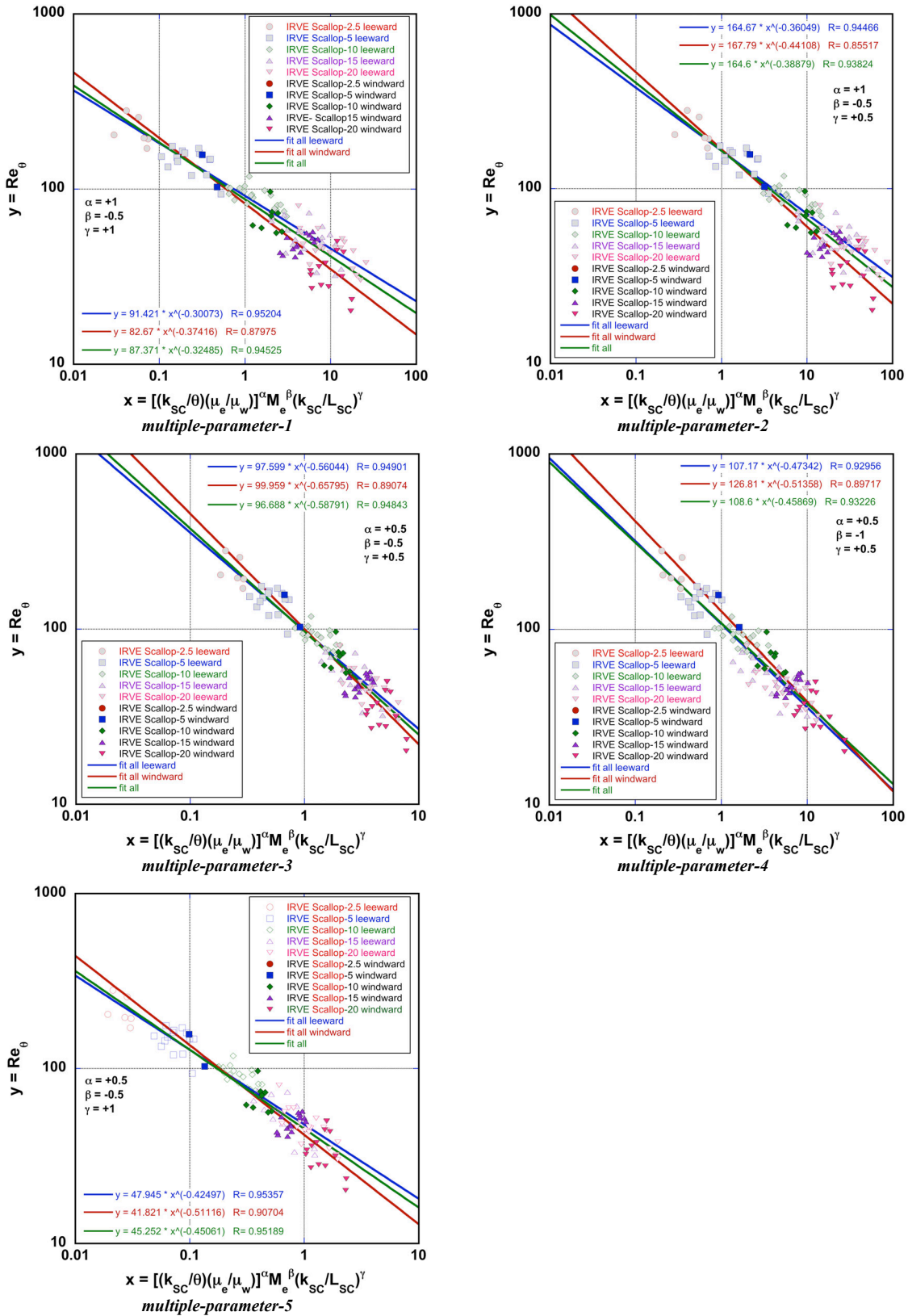


Figure 84. Multiple-Parameter Correlation Variations.

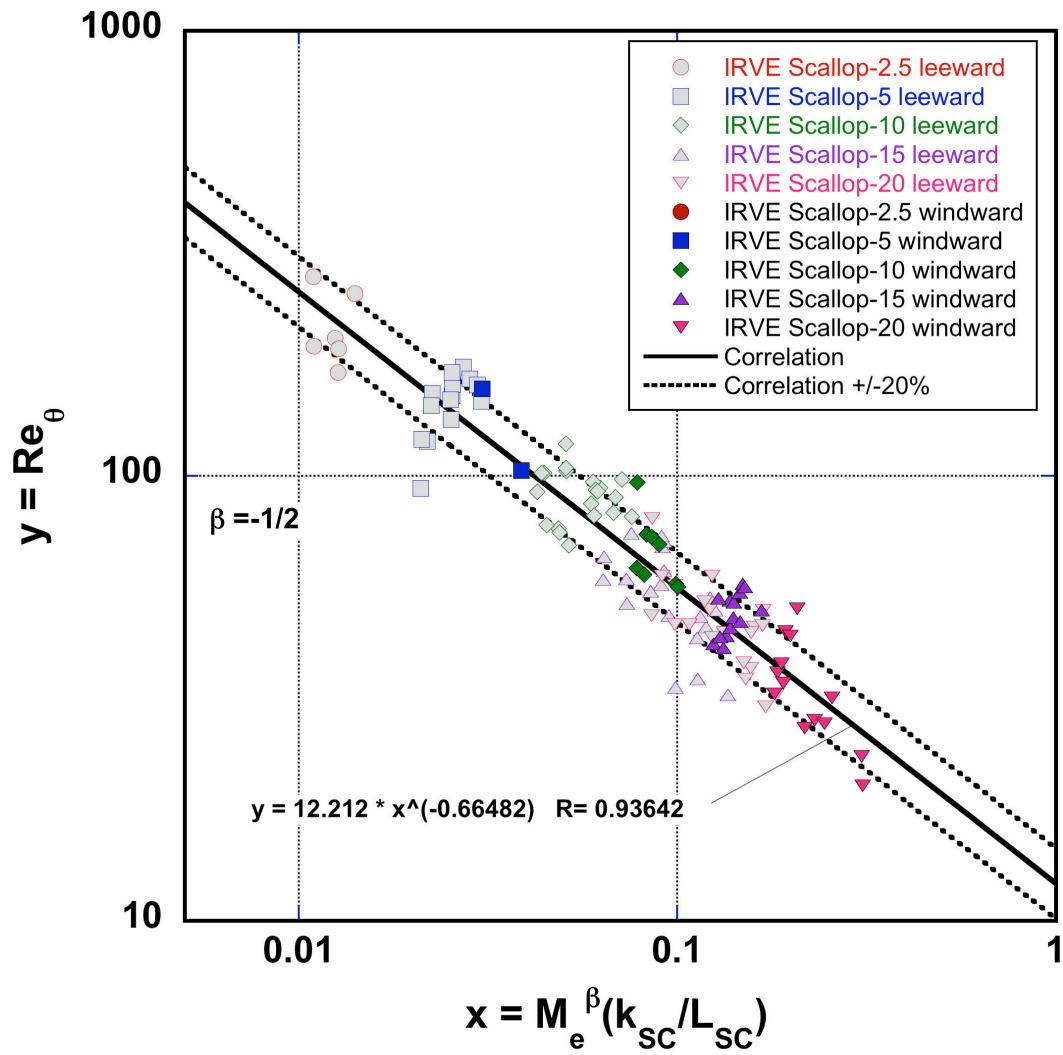


Figure 85. Scallop-Parameter-4 Combined Correlation with Uncertainties.

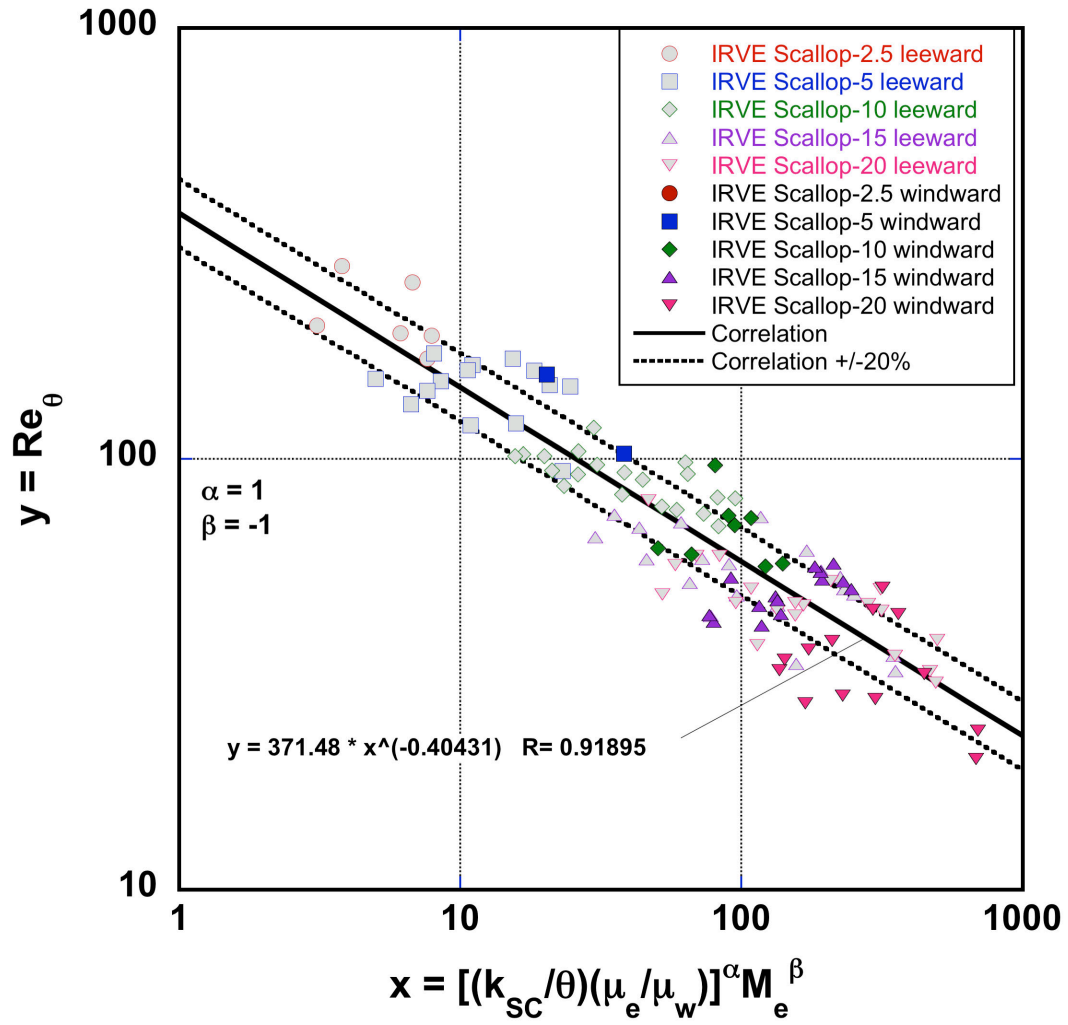


Figure 86. Wind-Tunnel-Roughness-4 Combined Correlation with Uncertainties.

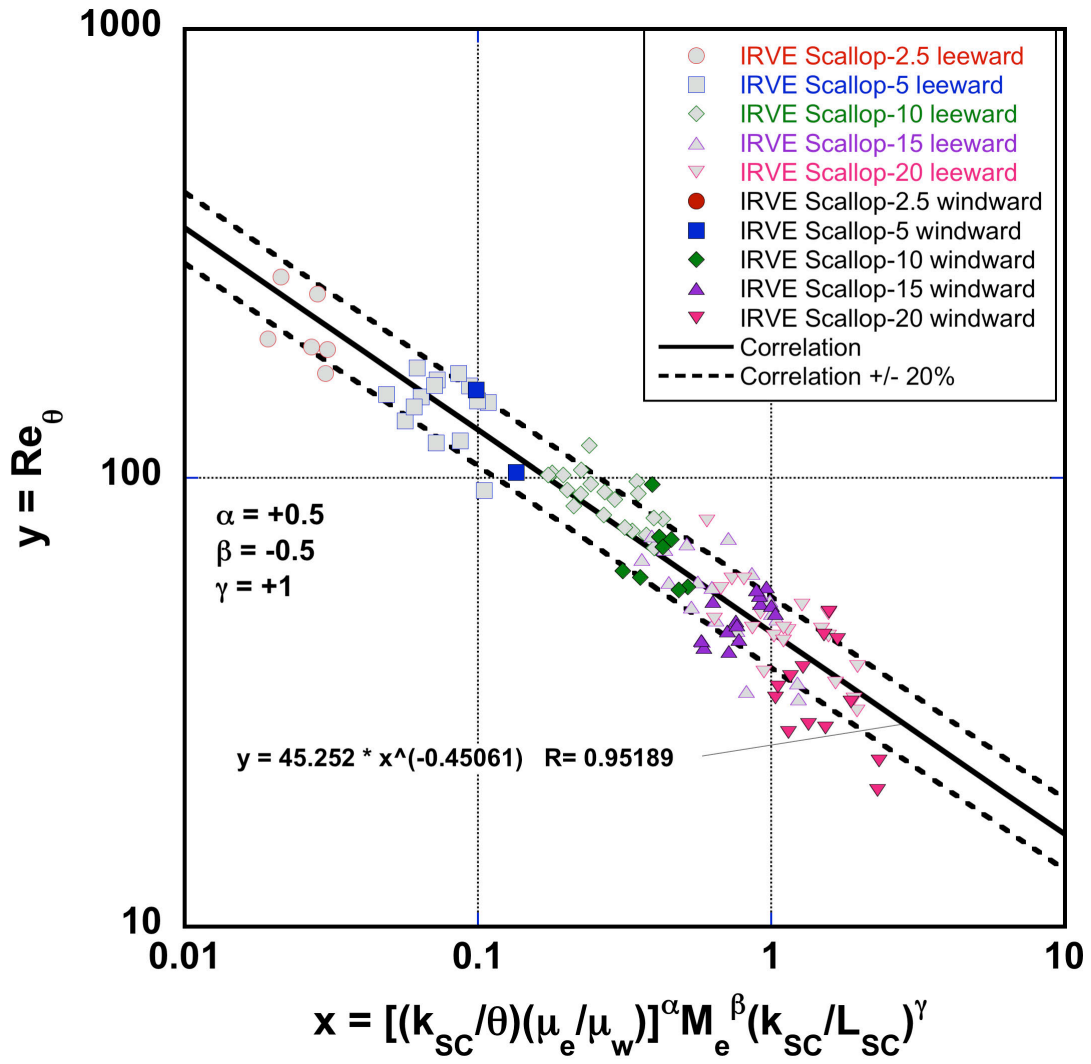


Figure 87. Multiple-Parameter-5 Combined Correlation with Uncertainties.

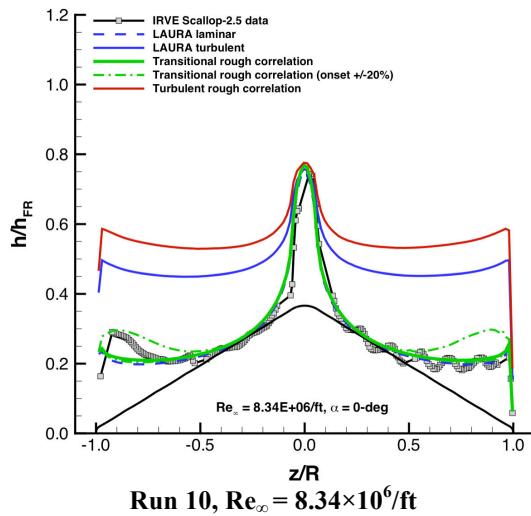
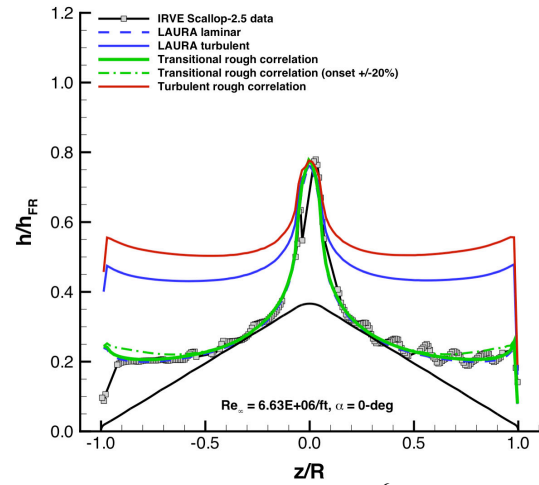
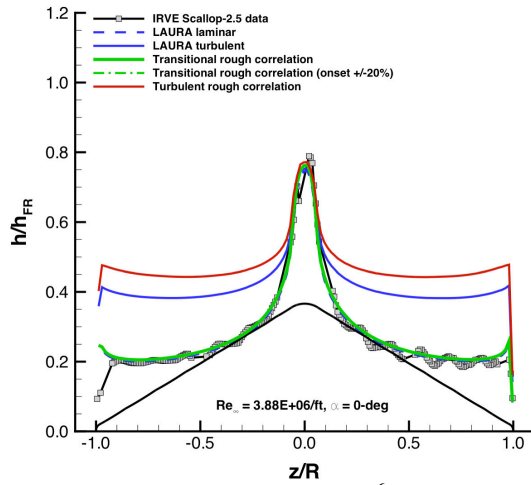
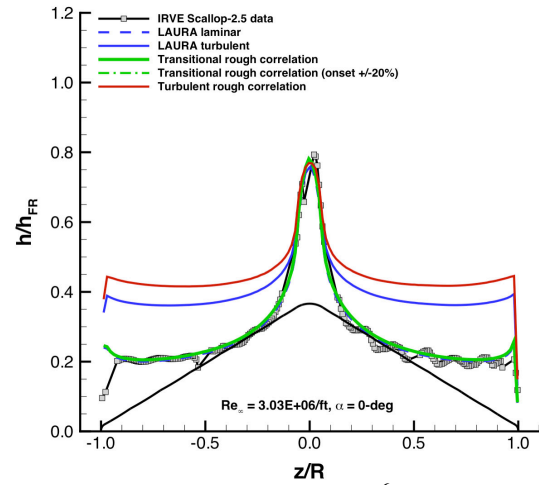
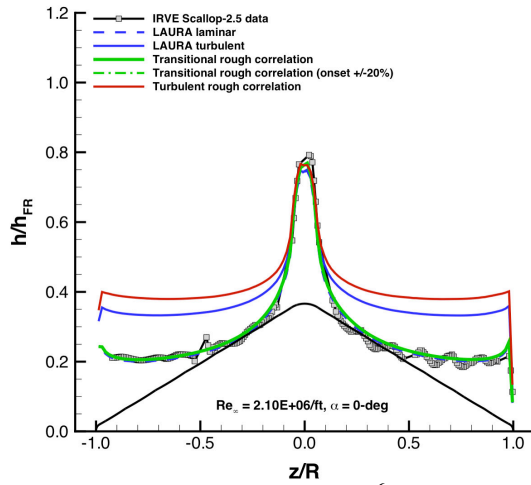


Figure 88. Correlation Comparison with IRVE Scallop-2.5 Model Data, $\alpha = 0$ deg.

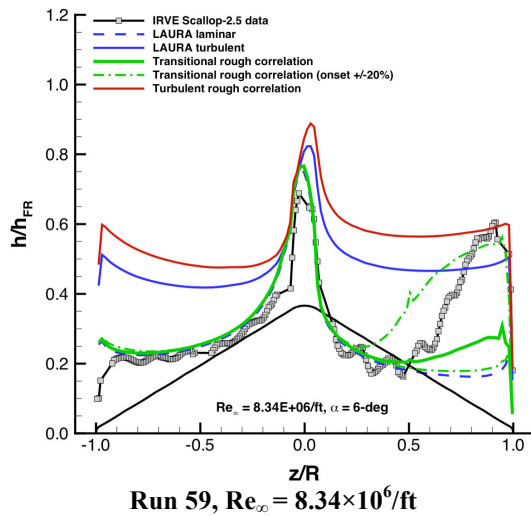
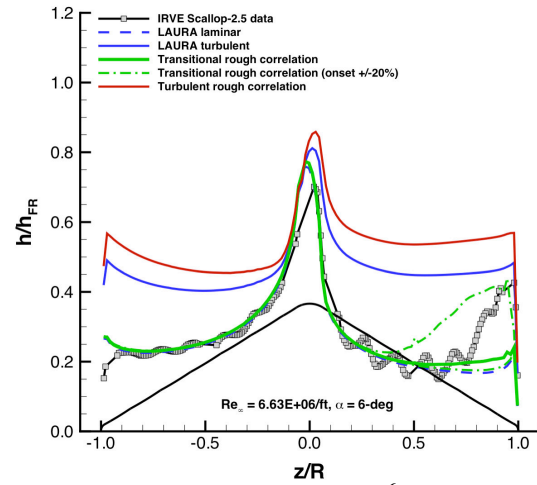
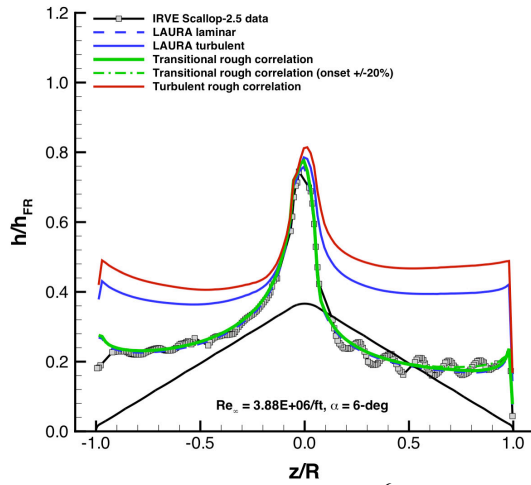
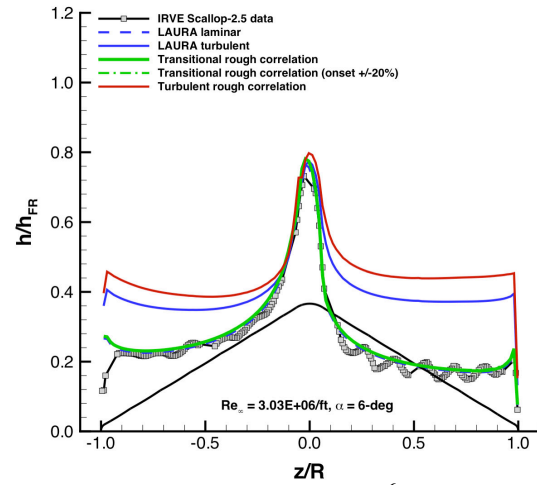
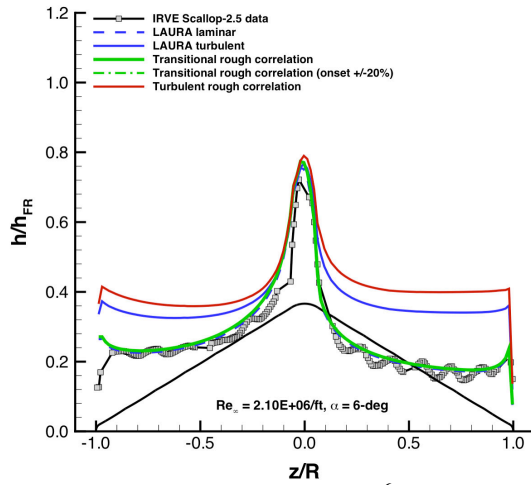


Figure 89. Correlation Comparison with IRVE Scallop-2.5 Model Data, $\alpha = 6$ deg.

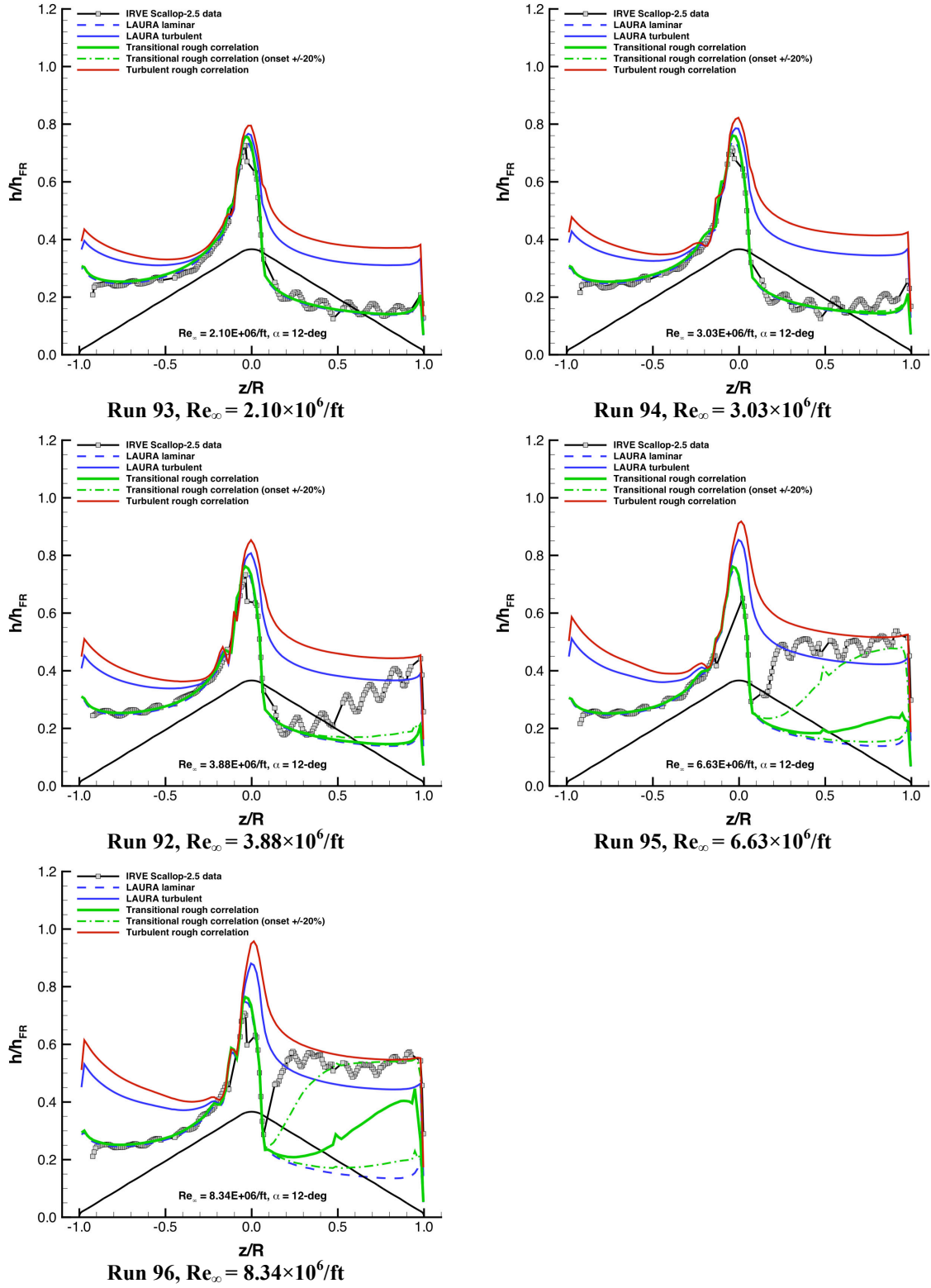


Figure 90. Correlation Comparison with IRVE Scallop-2.5 Model Data, $\alpha = 12^\circ$.

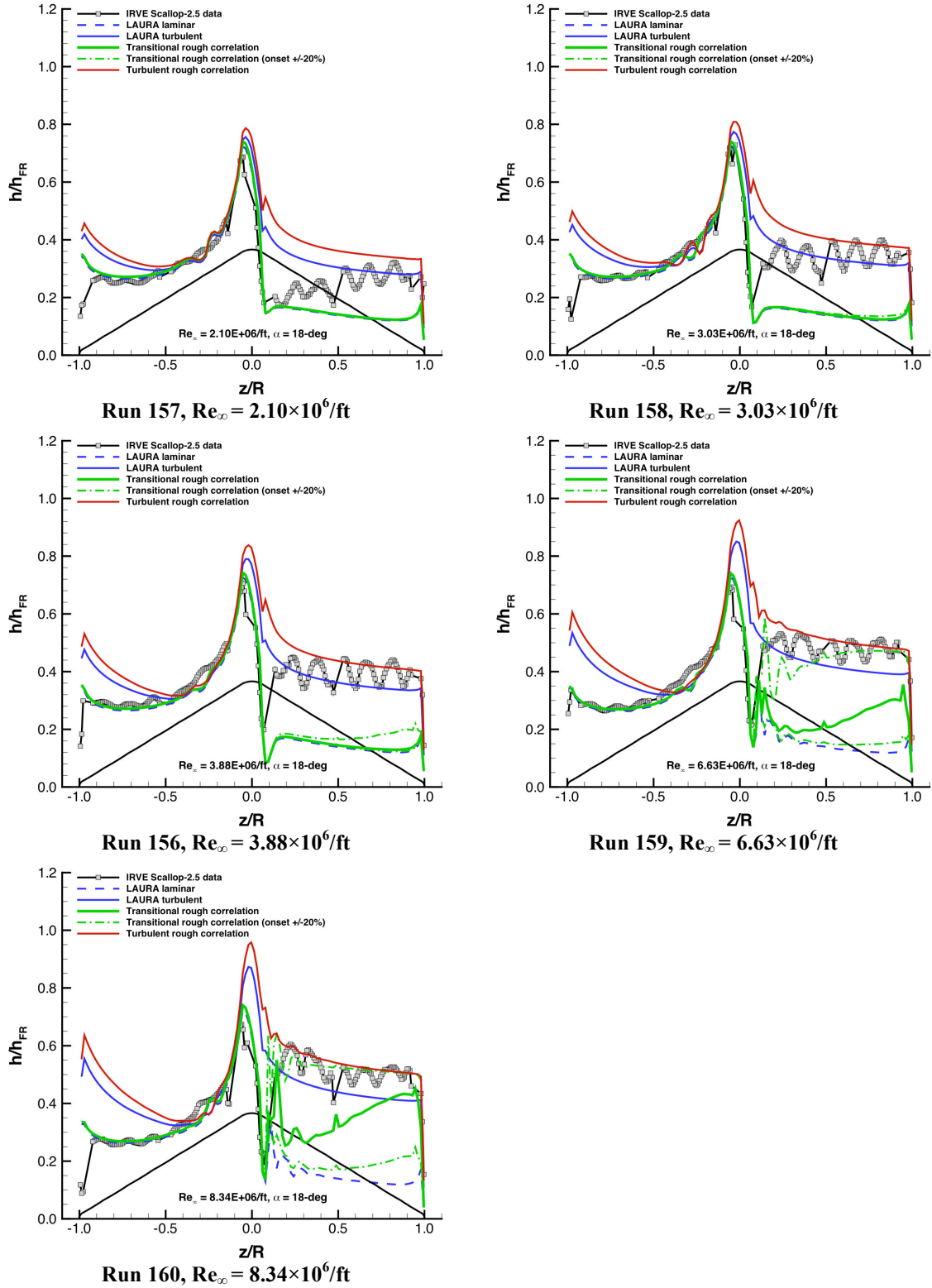
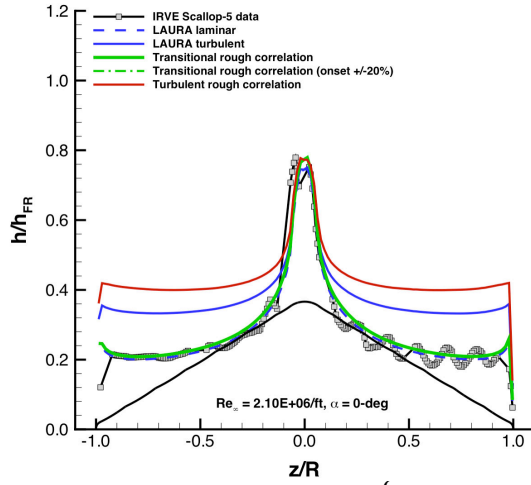
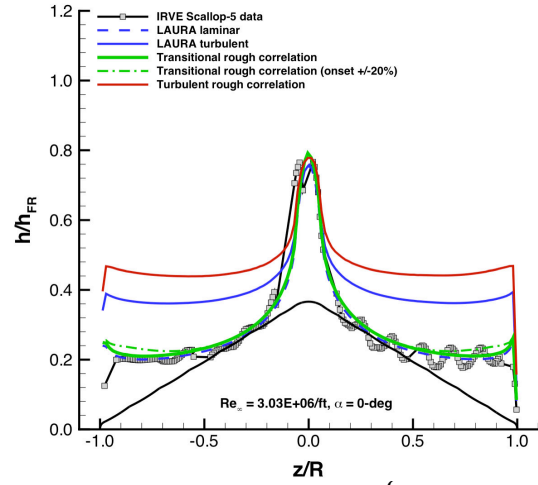


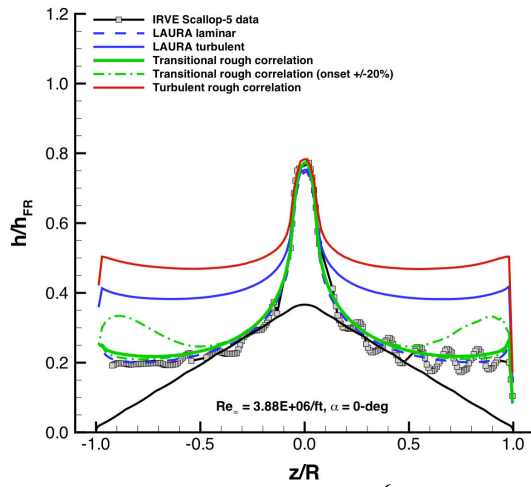
Figure 91. Correlation Comparison with IRVE Scallop-2.5 Model Data, $\alpha = 18^\circ$.



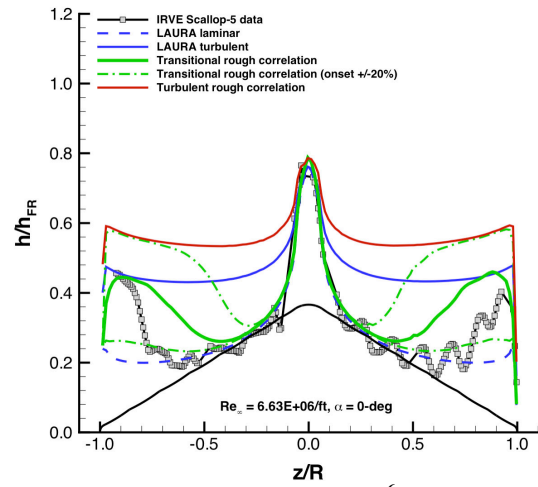
Run 13, $Re_\infty = 2.10 \times 10^6/ft$



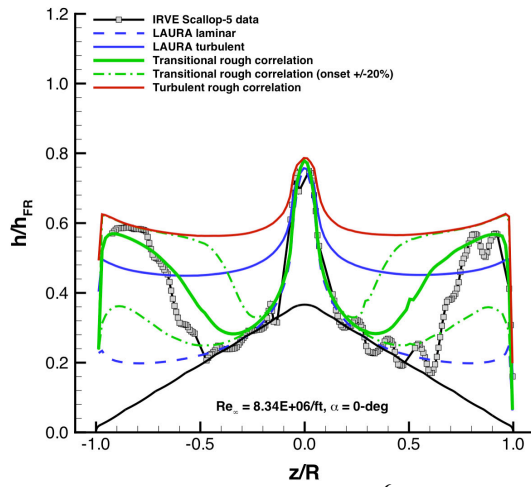
Run 12, $Re_\infty = 3.03 \times 10^6/ft$



Run 11, $Re_\infty = 3.88 \times 10^6/ft$

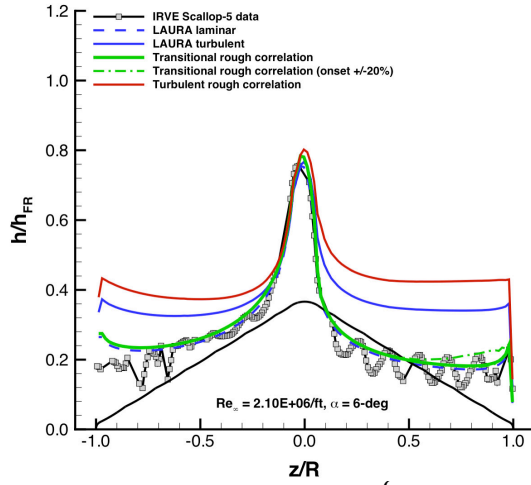


Run 14, $Re_\infty = 6.63 \times 10^6/ft$

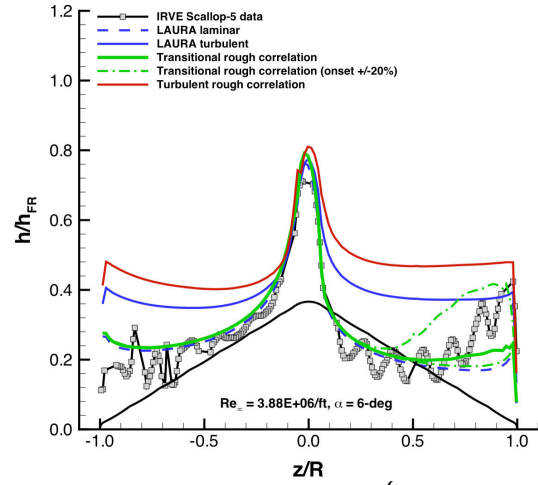


Run 15, $Re_\infty = 8.34 \times 10^6/ft$

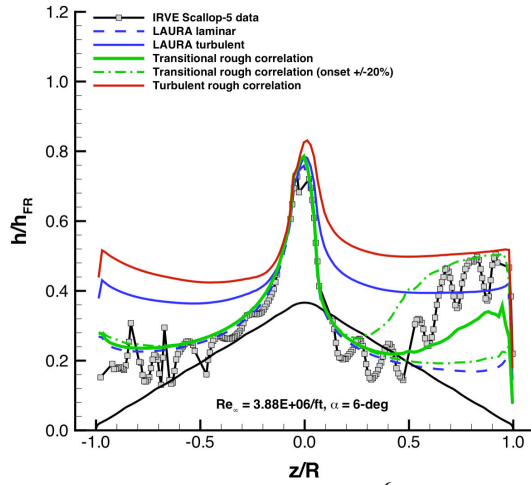
Figure 92. Correlation Comparison with IRVE Scallop-5 Model Data, $\alpha = 0$ deg.



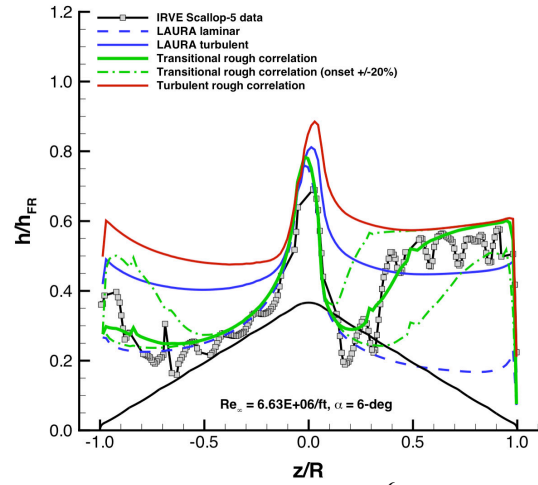
Run 65, $Re_{\infty} = 2.10 \times 10^6/ft$



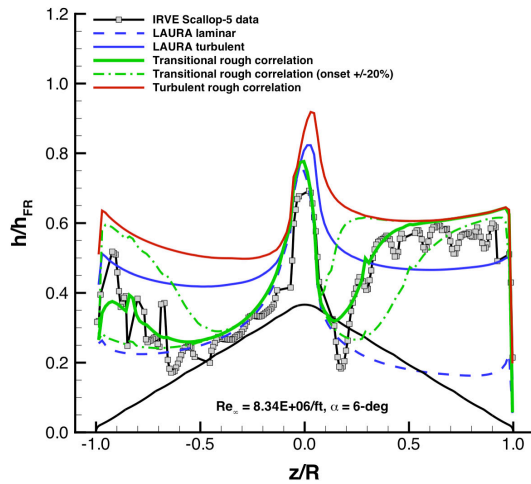
Run 66, $Re_{\infty} = 3.03 \times 10^6/ft$



Run 67, $Re_{\infty} = 3.88 \times 10^6/ft$



Run 68, $Re_{\infty} = 6.63 \times 10^6/ft$



Run 69, $Re_{\infty} = 8.34 \times 10^6/ft$

Figure 93. Correlation Comparison with IRVE Scallop-5 Model Data, $\alpha = 6$ deg.

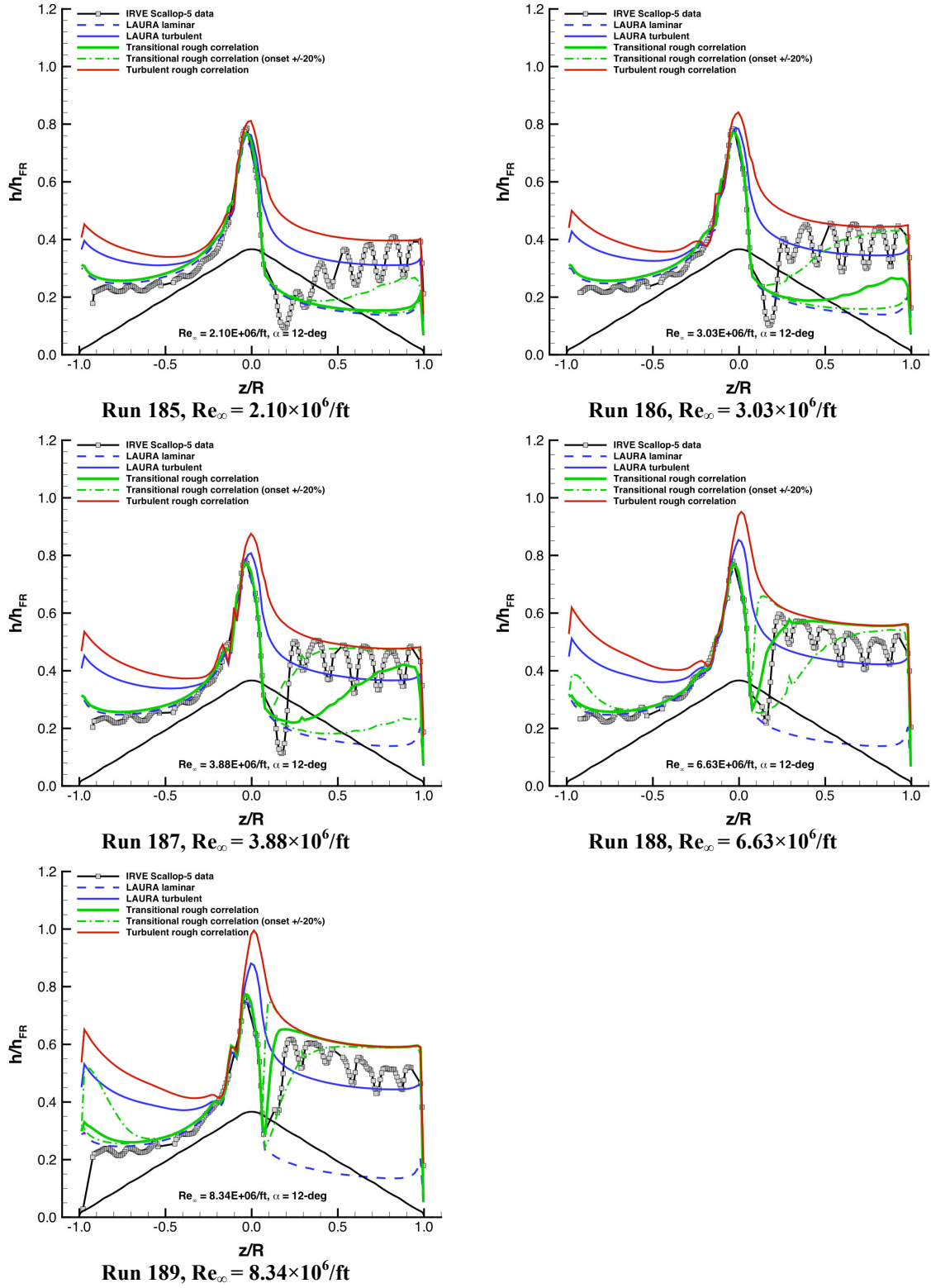


Figure 94. Correlation Comparison with IRVE Scallop-5 Model Data, $\alpha = 12$ deg.

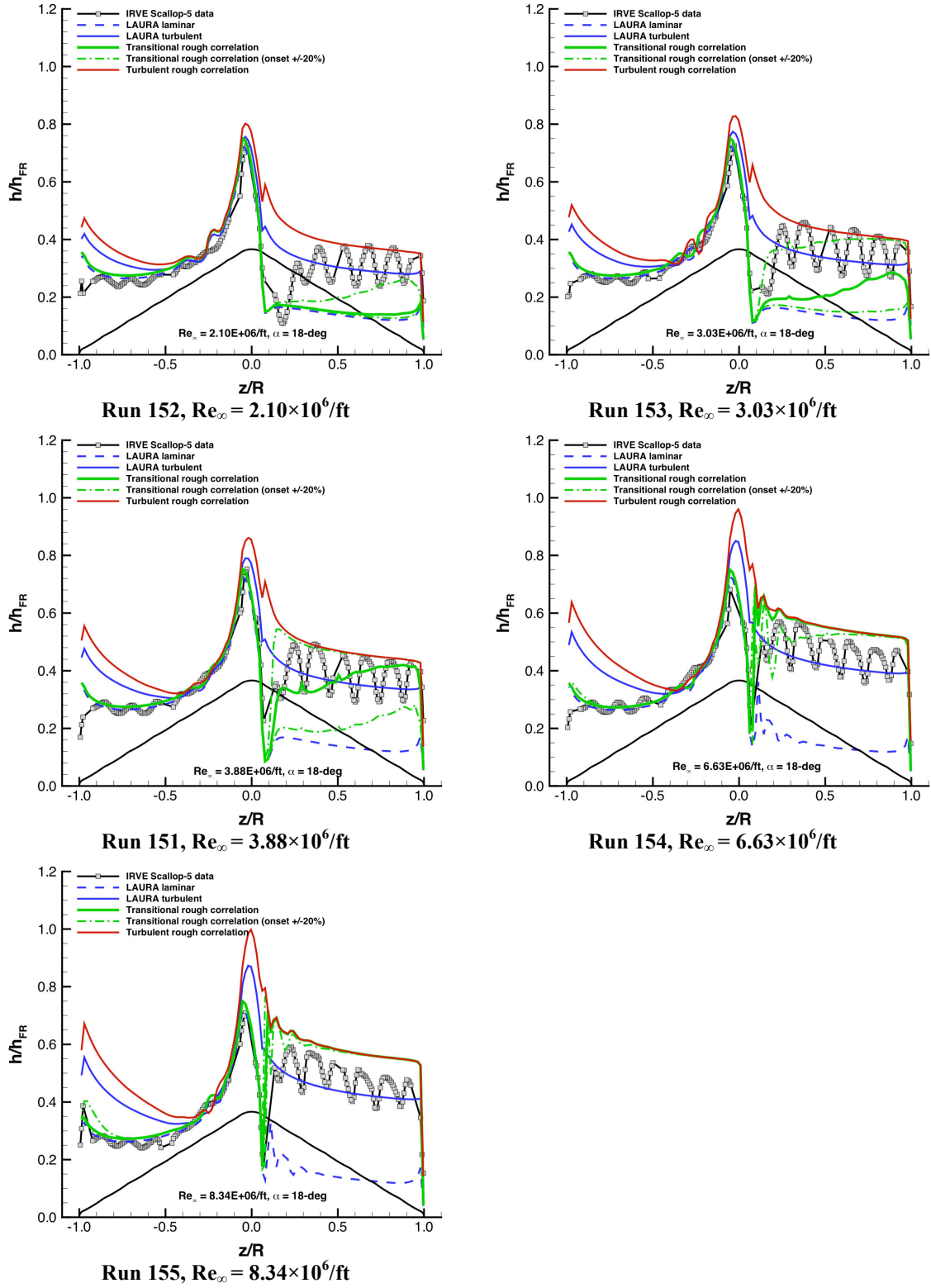


Figure 95. Correlation Comparison with IRVE Scallop-5 Model Data, $\alpha = 18$ deg.

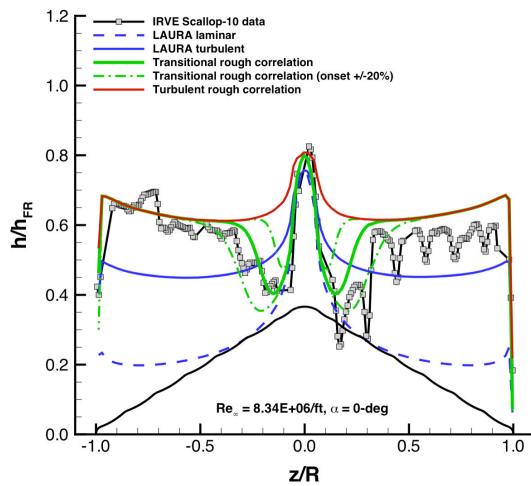
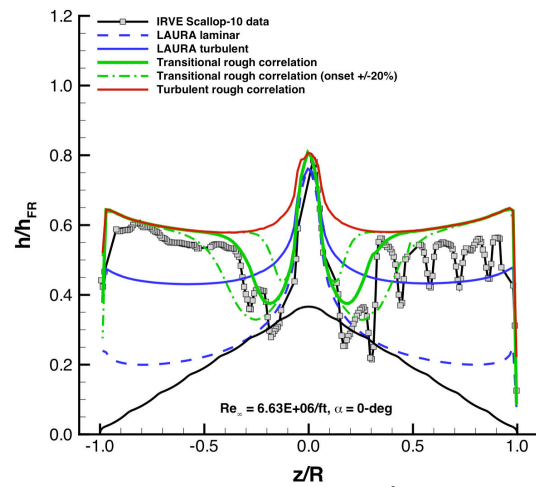
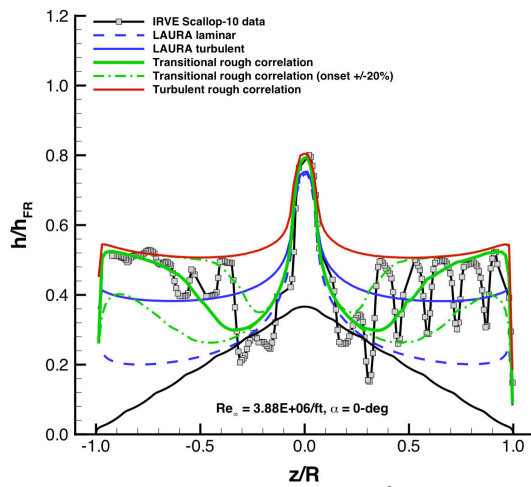
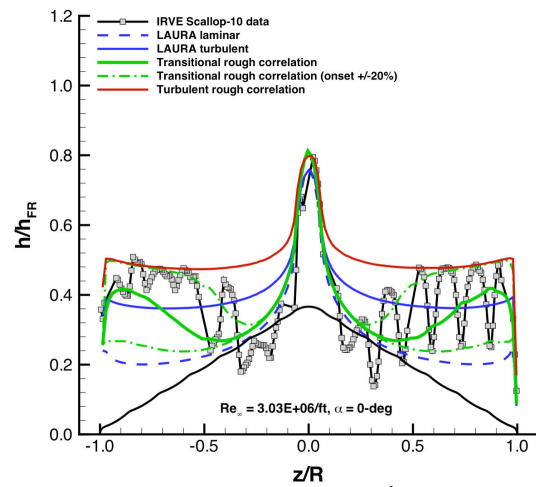
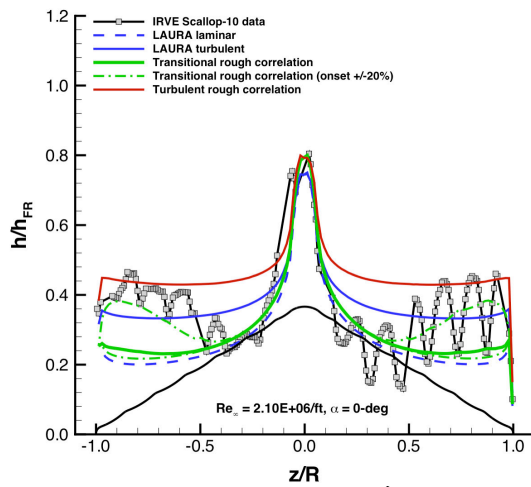
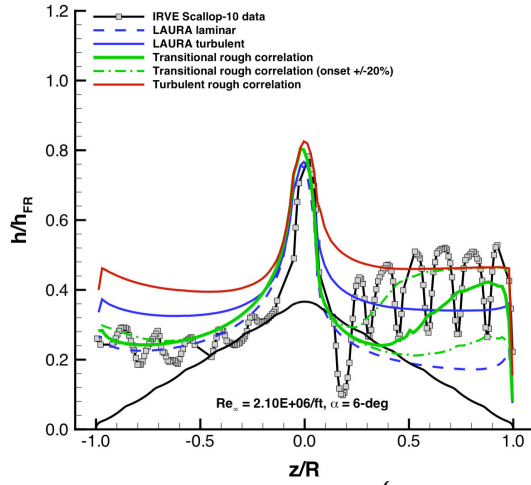
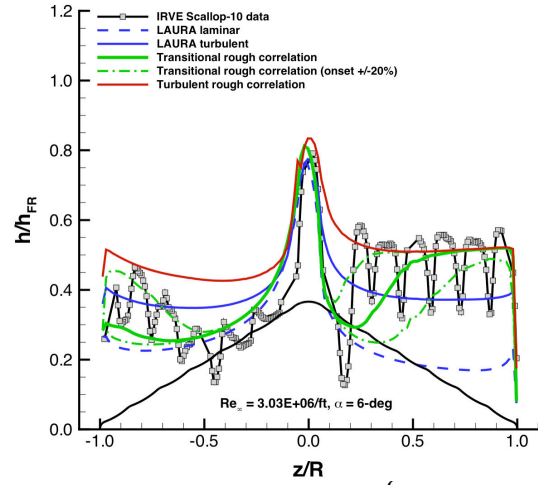


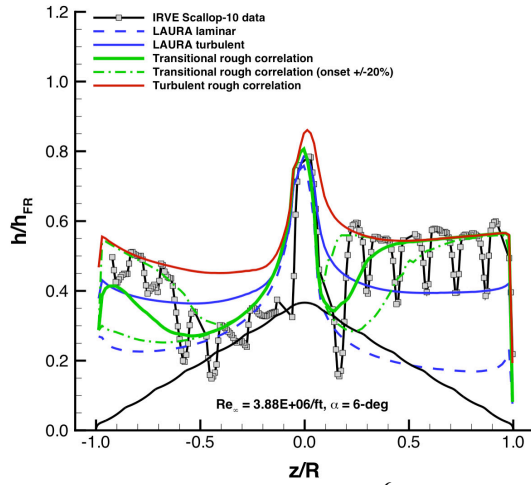
Figure 96. Correlation Comparison with IRVE Scallop-10 Model Data, $\alpha = 0$ deg.



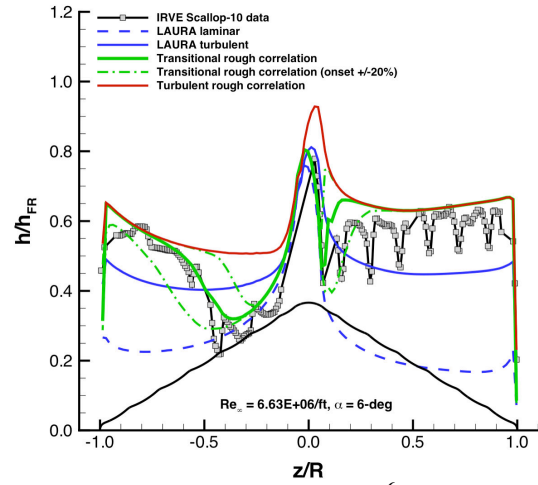
Run 50, $Re_{\infty} = 2.10 \times 10^6/ft$



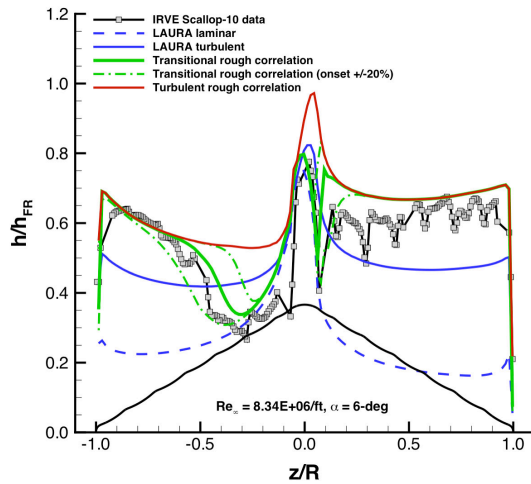
Run 51, $Re_{\infty} = 3.03 \times 10^6/ft$



Run 52, $Re_{\infty} = 3.88 \times 10^6/ft$

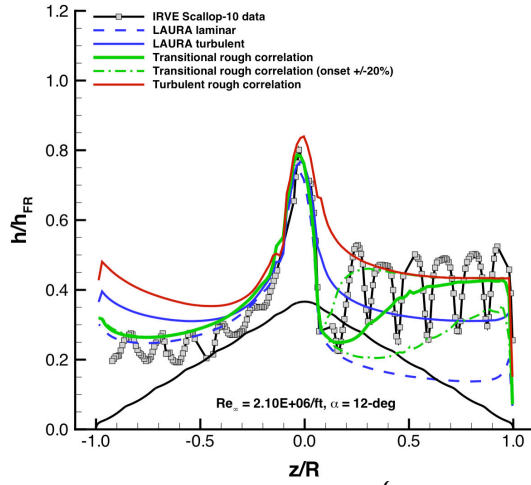


Run 53, $Re_{\infty} = 6.63 \times 10^6/ft$

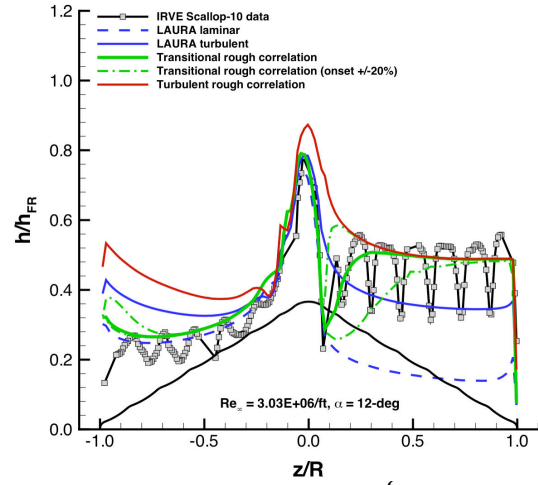


Run 54, $Re_{\infty} = 8.34 \times 10^6/ft$

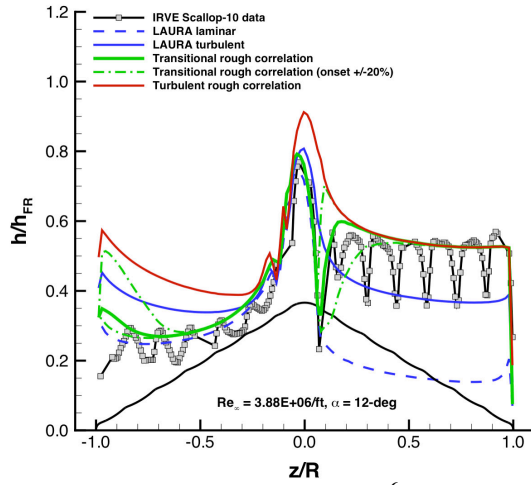
Figure 97. Correlation Comparison with IRVE Scallop-10 Model Data, $\alpha = 6$ deg.



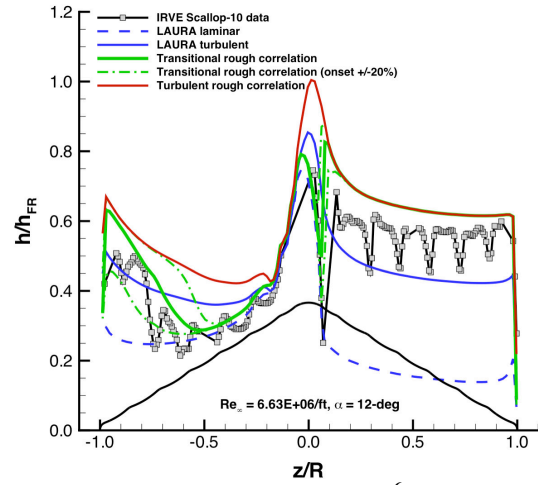
Run 98, $Re_{\infty} = 2.10 \times 10^6/ft$



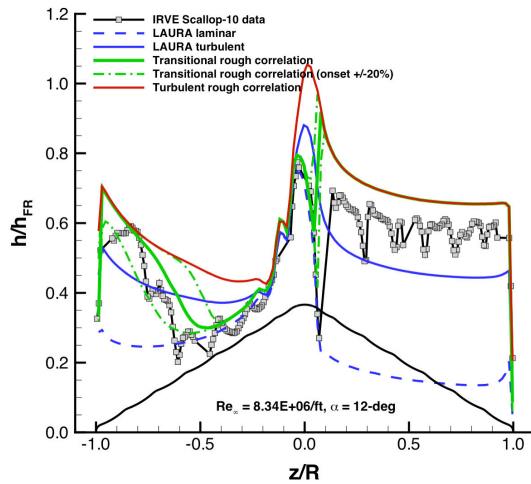
Run 99, $Re_{\infty} = 3.03 \times 10^6/ft$



Run 100, $Re_{\infty} = 3.88 \times 10^6/ft$



Run 101, $Re_{\infty} = 6.63 \times 10^6/ft$



Run 102, $Re_{\infty} = 8.34 \times 10^6/ft$

Figure 98. Correlation Comparison with IRVE Scallop-10 Model Data, $\alpha = 12$ deg.

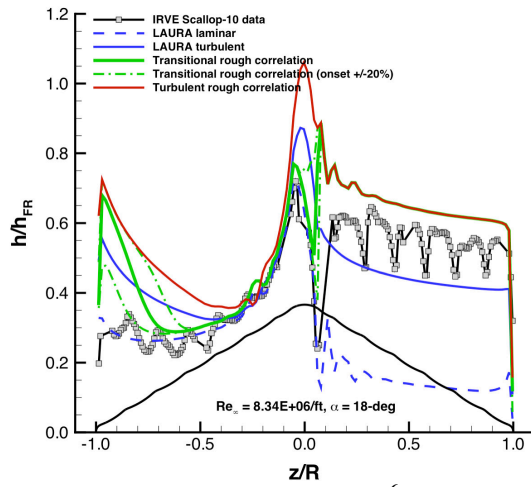
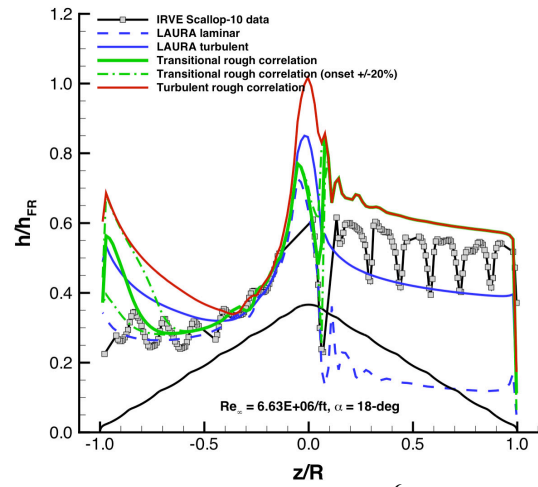
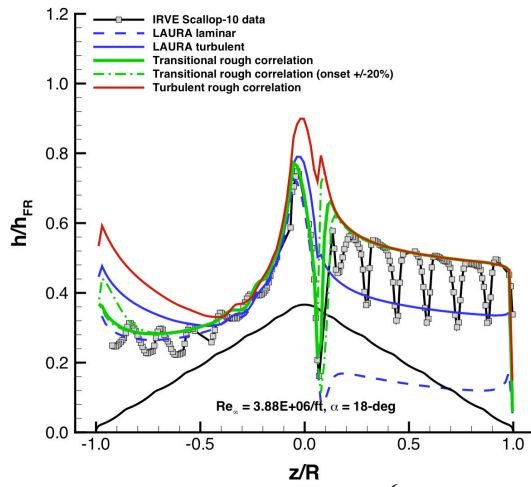
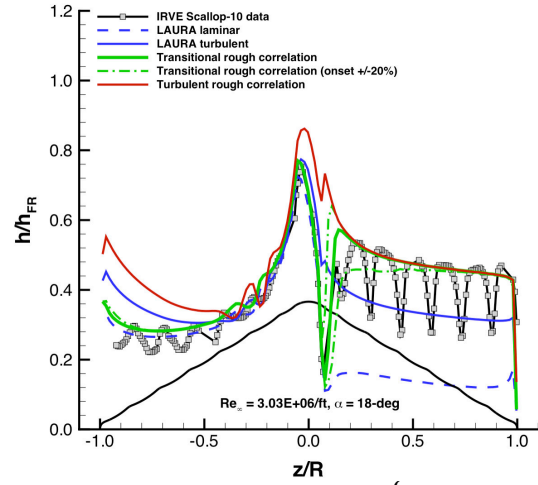
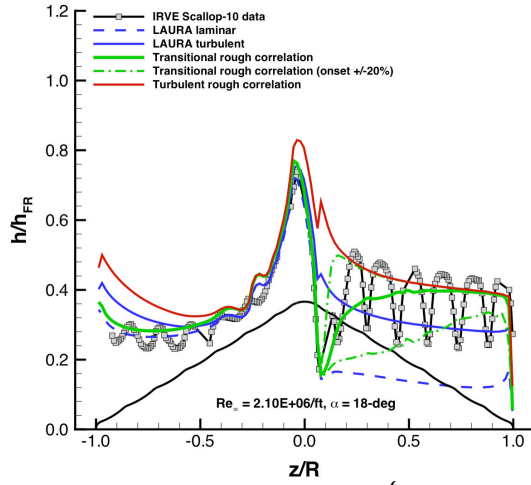


Figure 99. Correlation Comparison with IRVE Scallop-10 Model Data, $\alpha = 18$ deg.

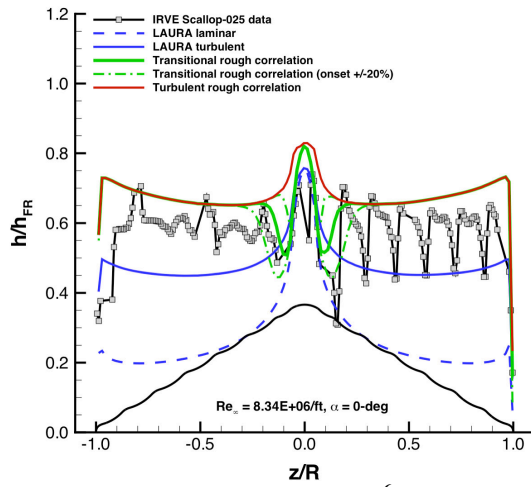
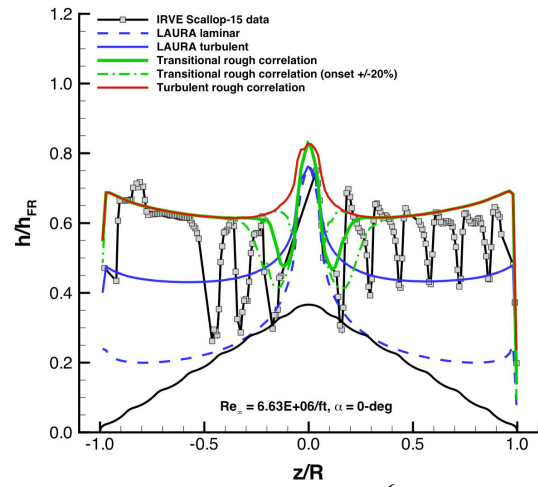
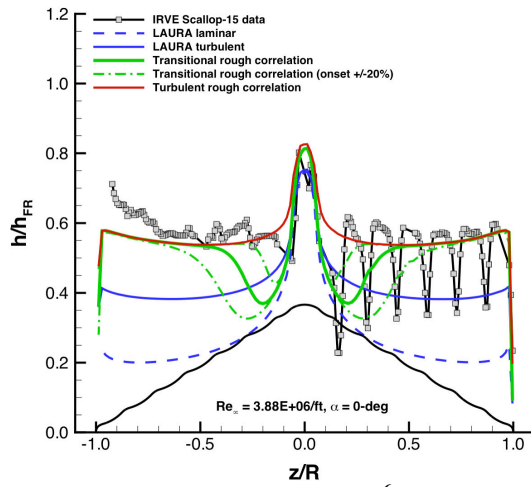
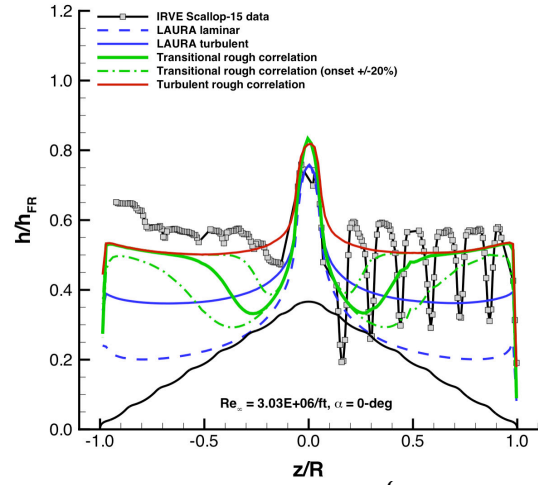
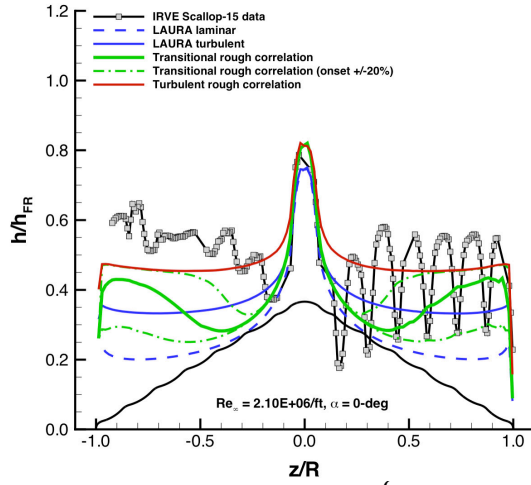


Figure 100. Correlation Comparison with IRVE Scallop-15 Model Data, $\alpha = 0$ deg.

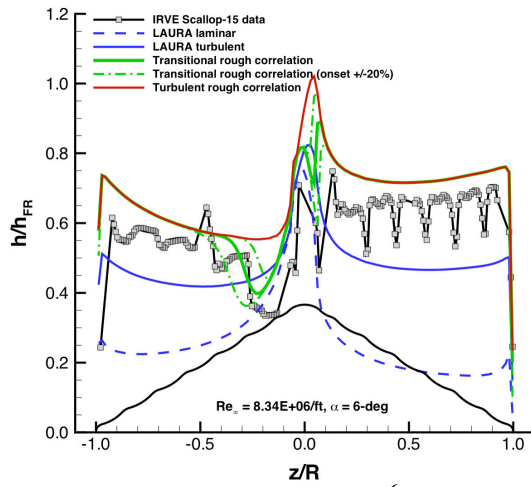
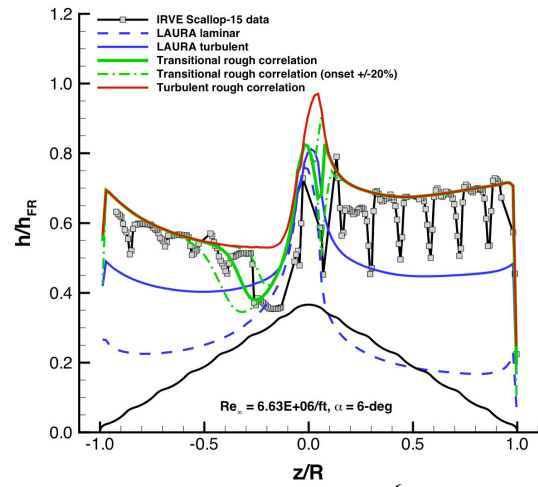
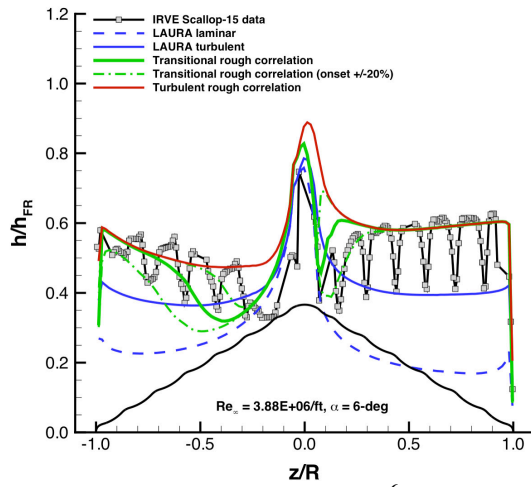
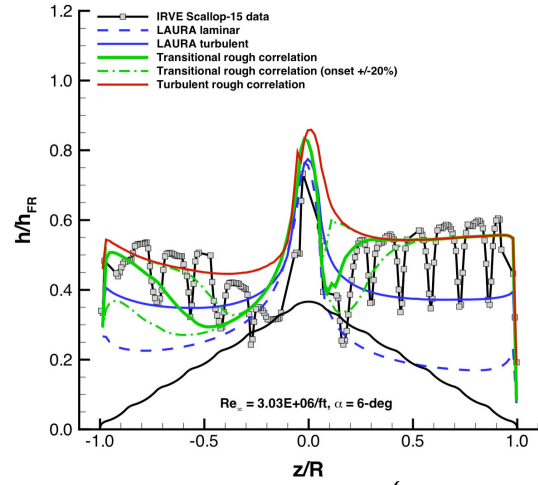
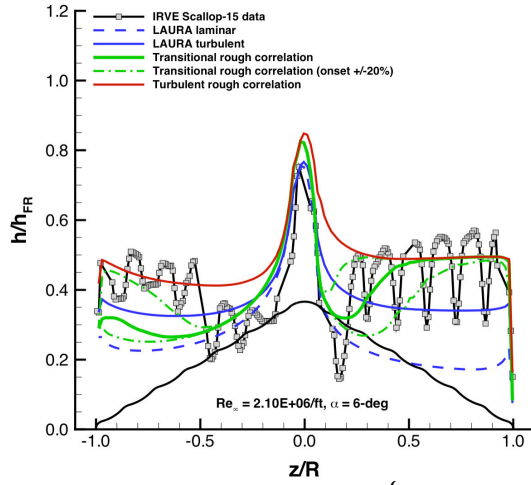


Figure 101. Correlation Comparison with IRVE Scallop-15 Model Data, $\alpha = 6\text{ deg}$.

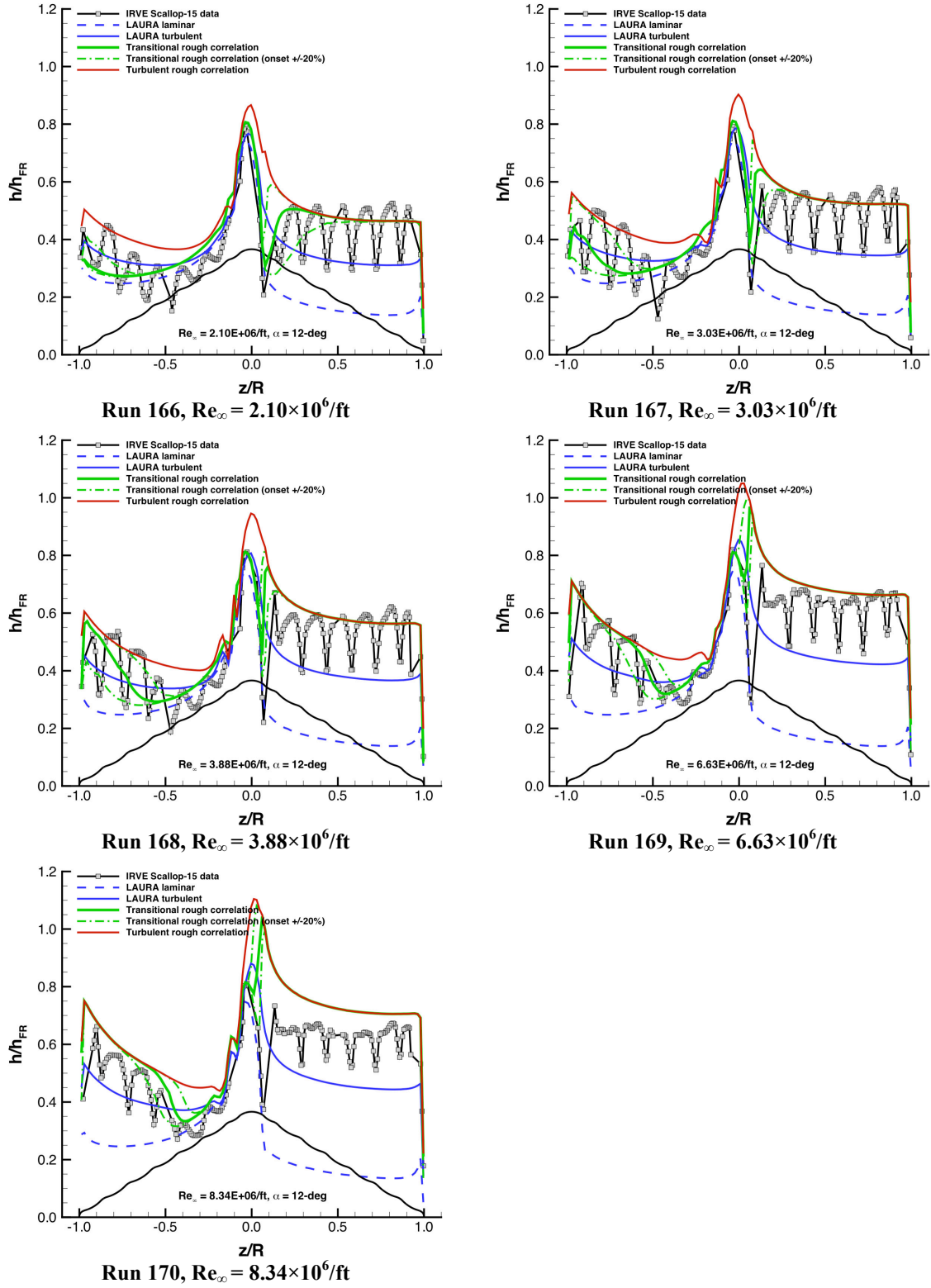


Figure 102. Correlation Comparison with IRVE Scallop-15 Model Data, $\alpha = 12$ deg.

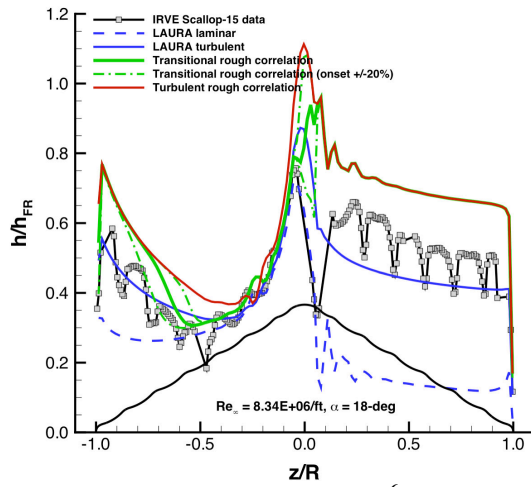
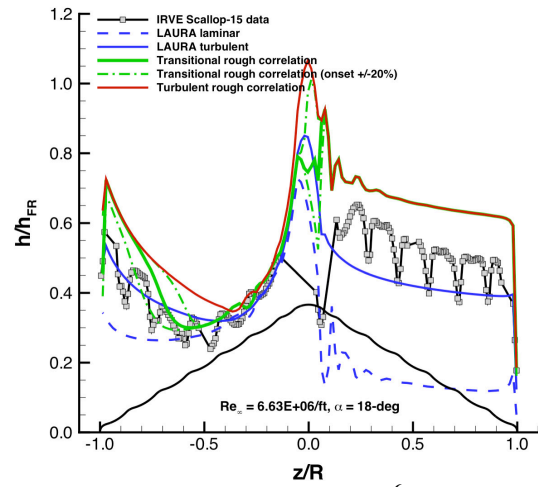
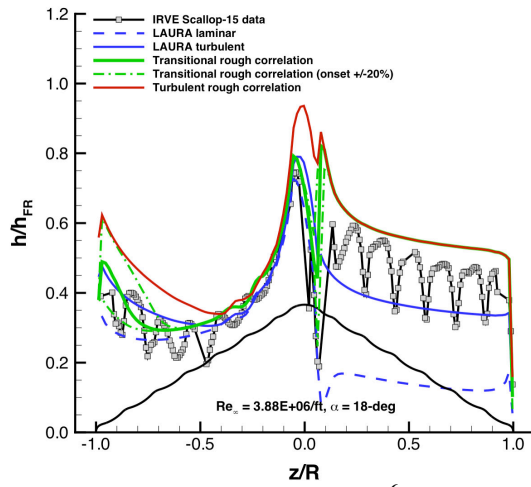
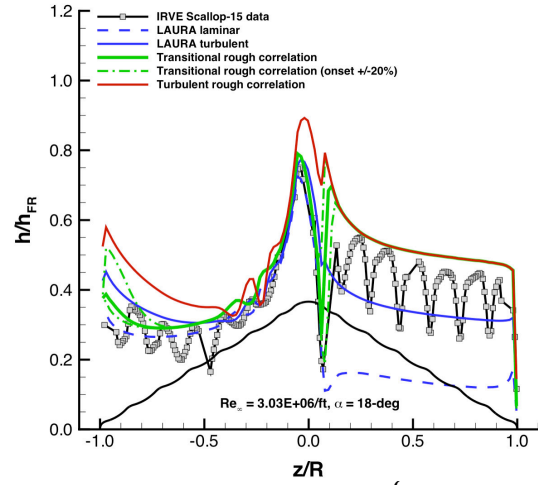
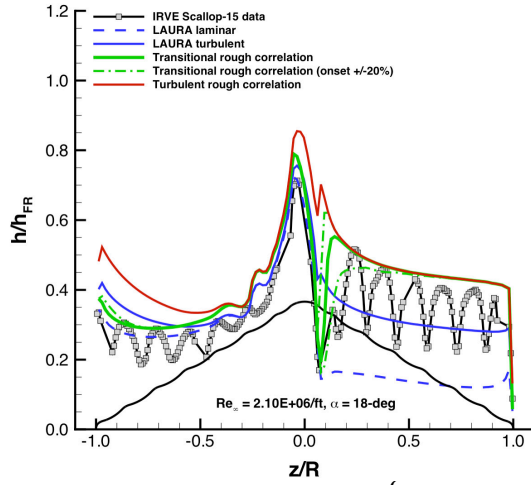


Figure 103. Correlation Comparison with IRVE Scallop-15 Model Data, $\alpha = 18$ deg.

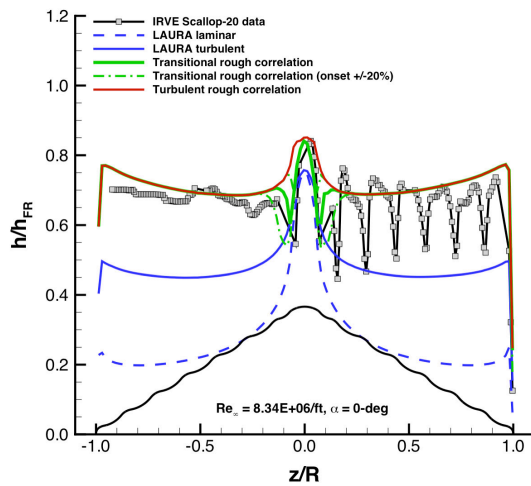
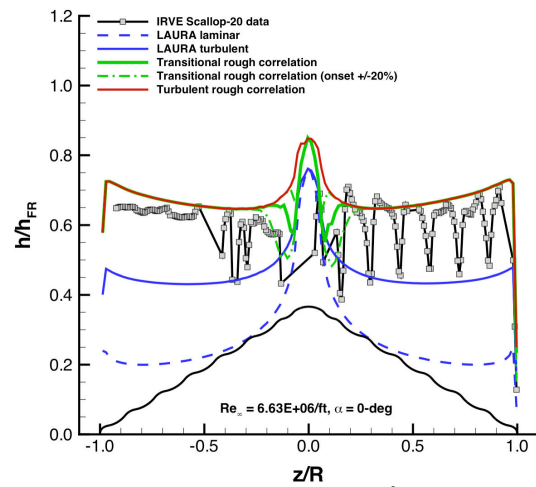
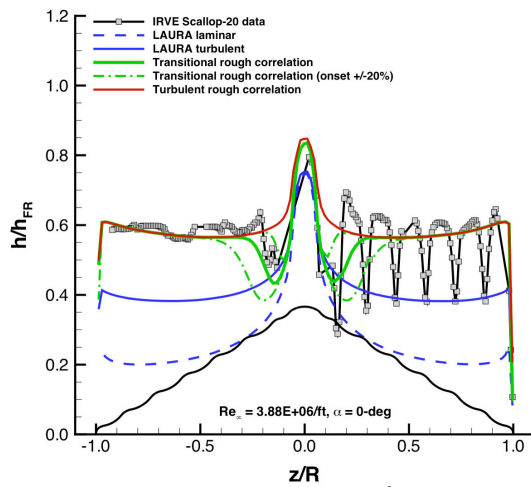
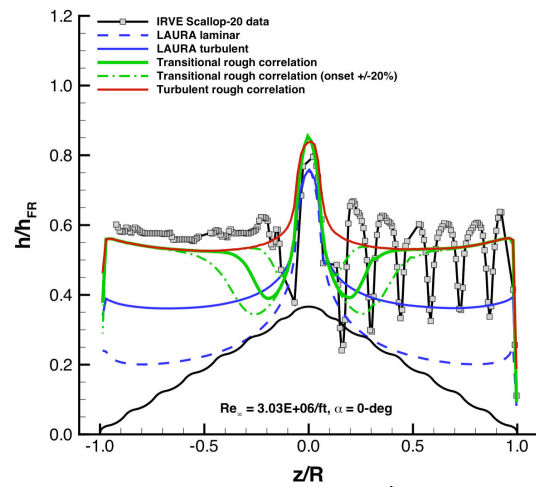
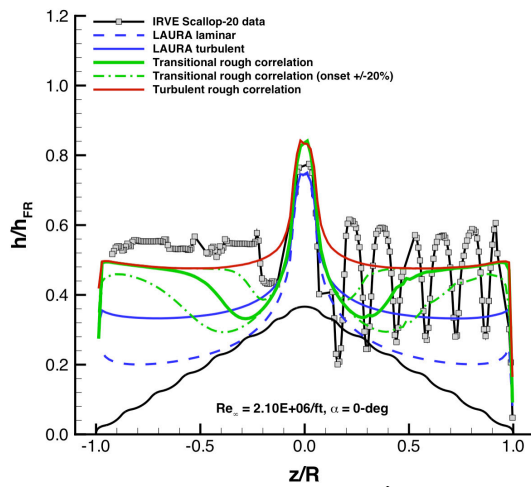


Figure 104. Correlation Comparison with IRVE Scallop-20 Model Data, $\alpha = 0$ deg.

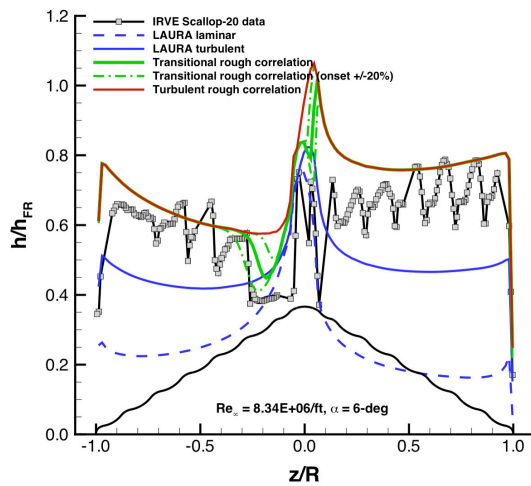
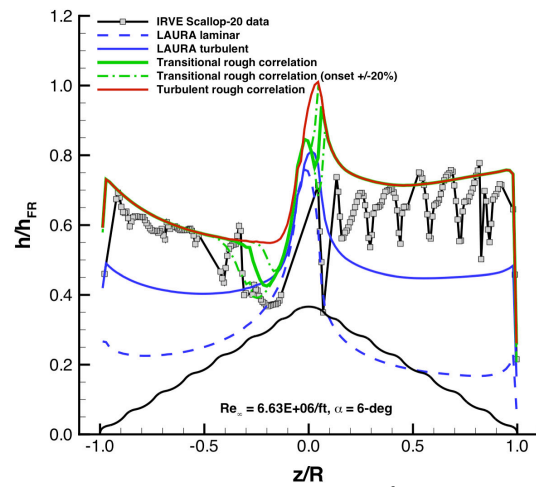
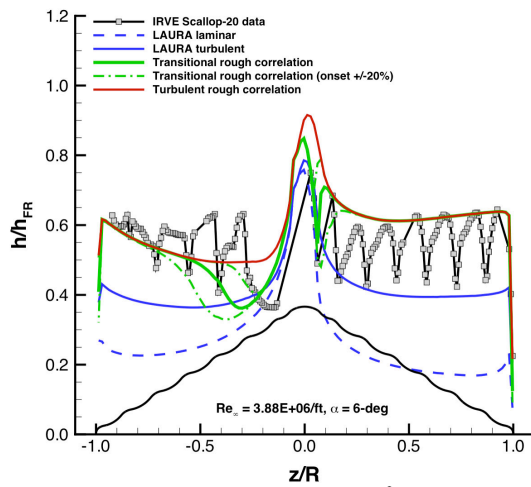
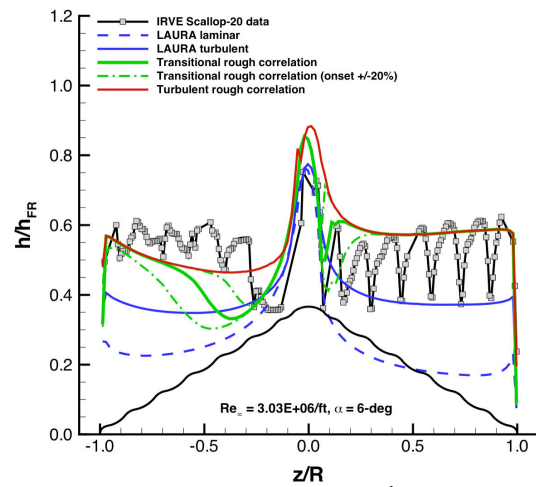
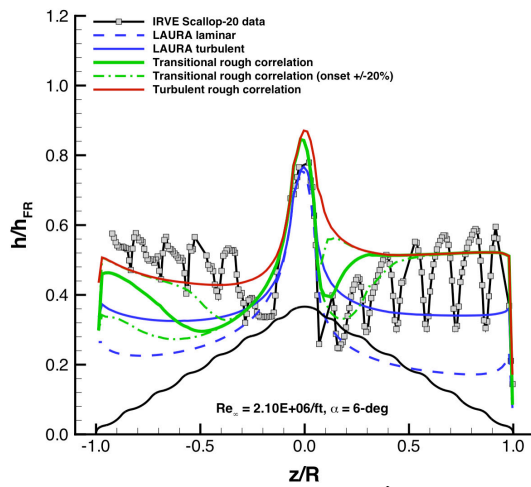


Figure 105. Correlation Comparison with IRVE Scallop-20 Model Data, $\alpha = 6$ deg.

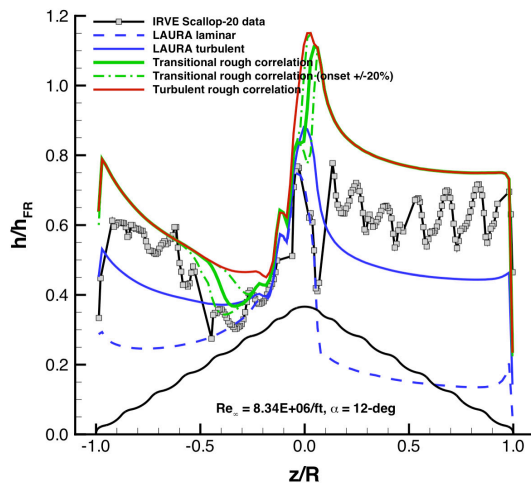
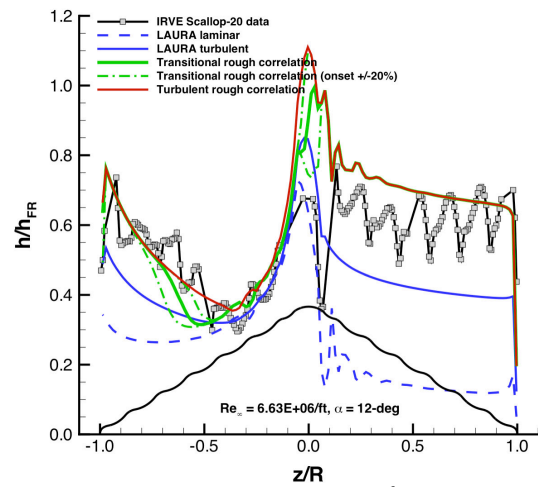
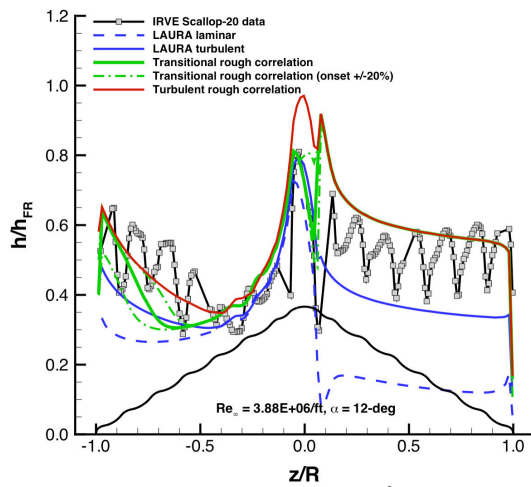
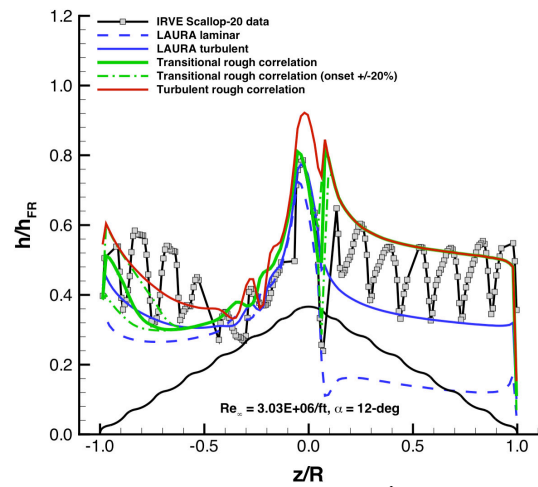
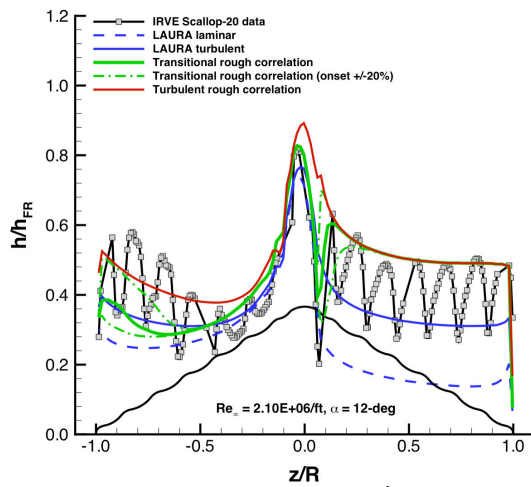


Figure 106. Correlation Comparison with IRVE Scallop-20 Model Data, $\alpha = 12$ deg.

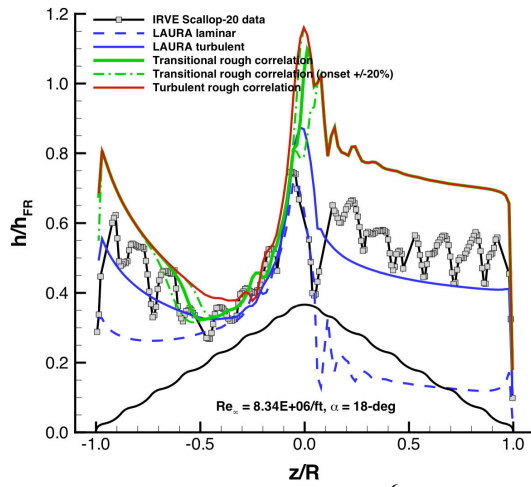
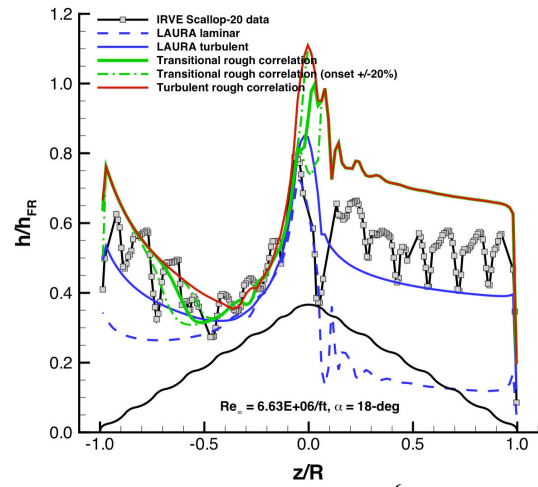
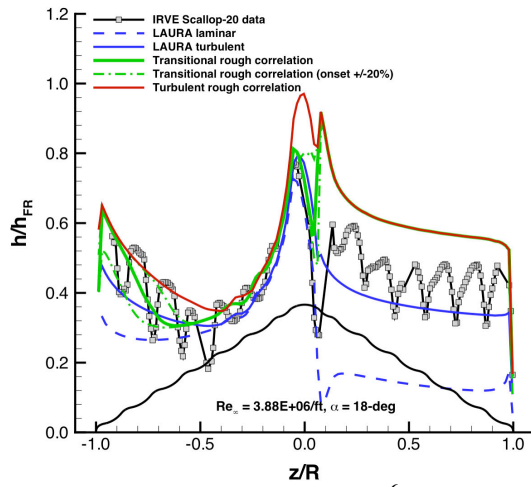
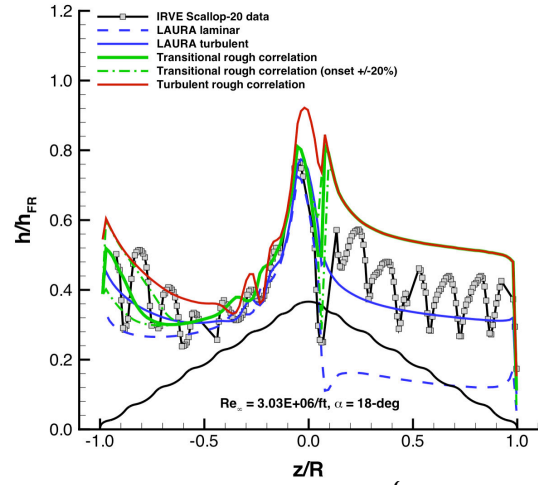
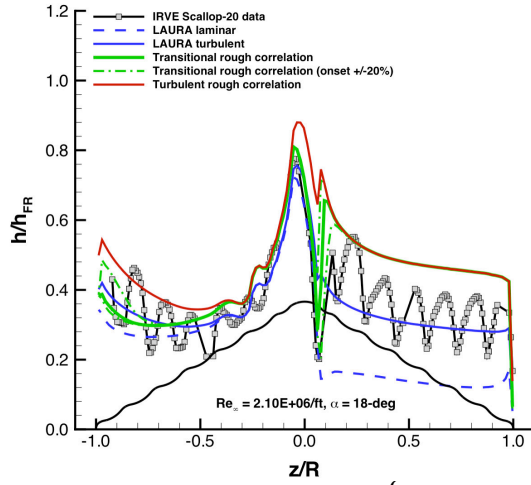


Figure 107. Correlation Comparison with IRVE Scallop-20 Model Data, $\alpha = 18$ deg.

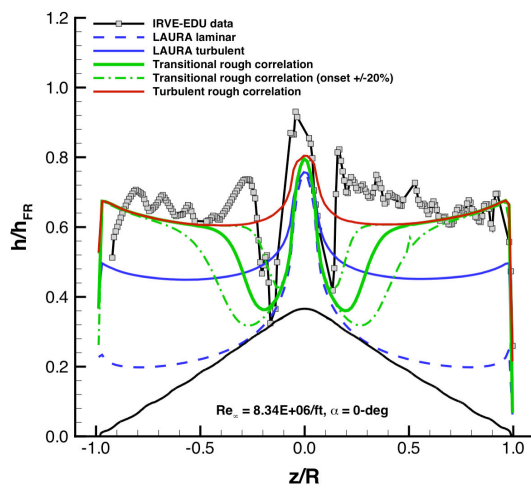
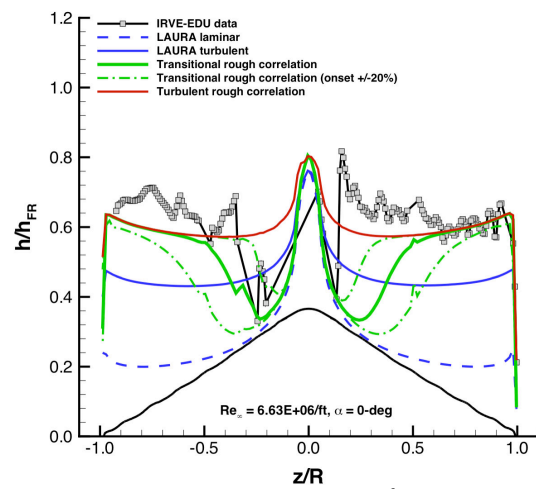
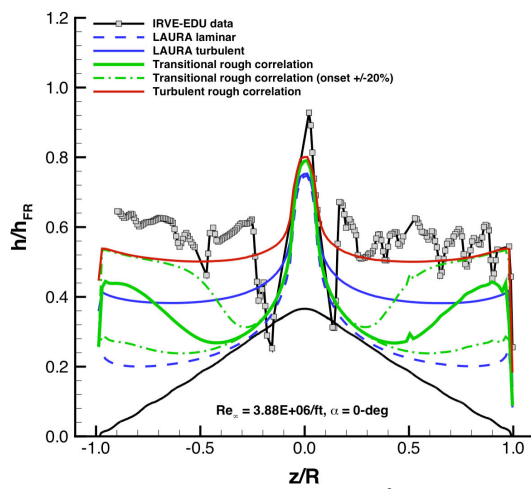
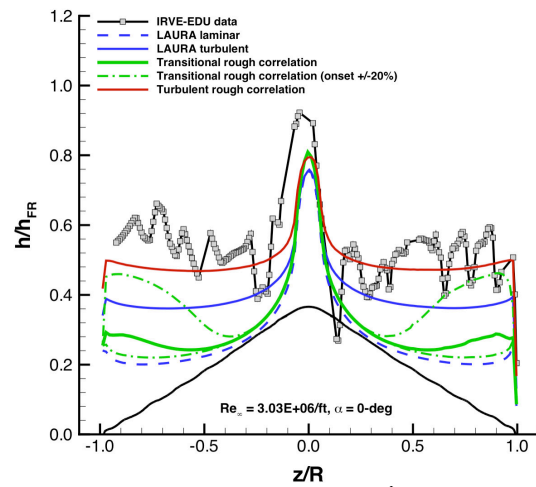
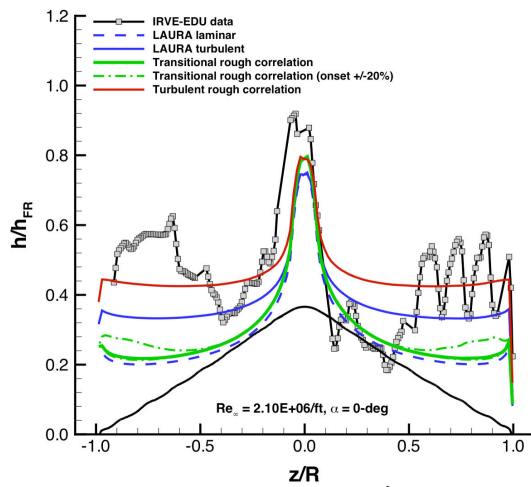


Figure 108. Correlation Comparison with IRVE EDU Model Data, $\alpha = 0$ deg.

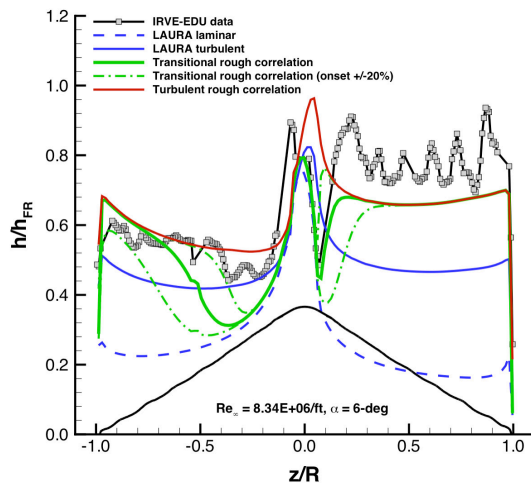
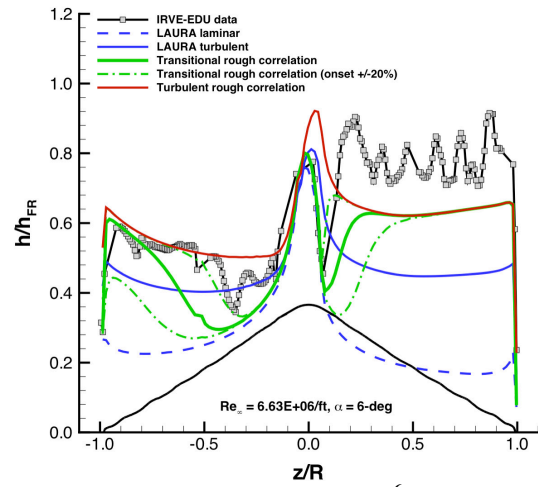
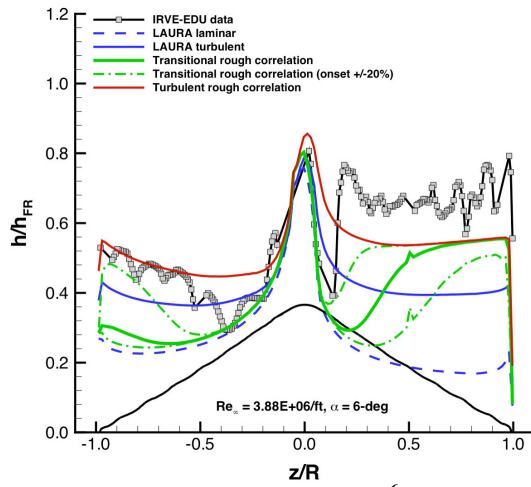
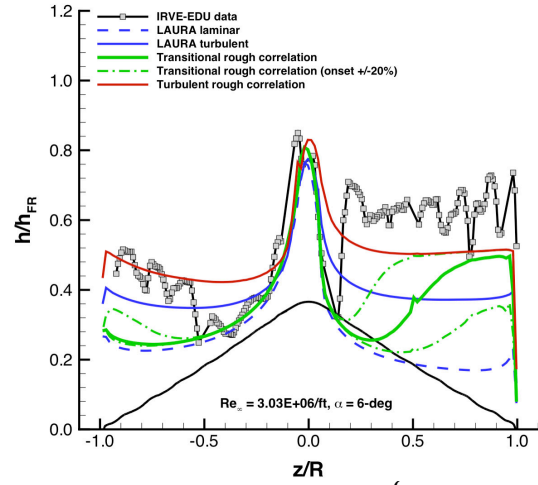
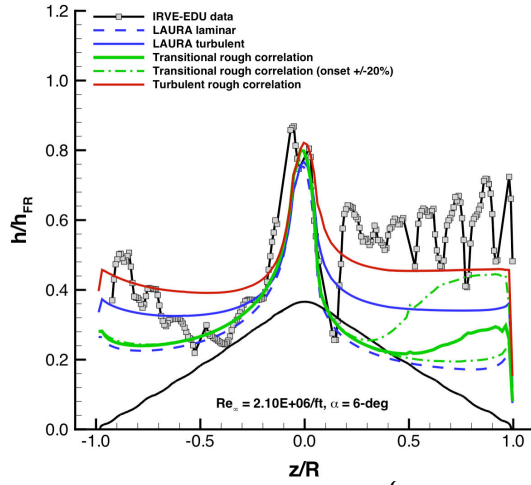
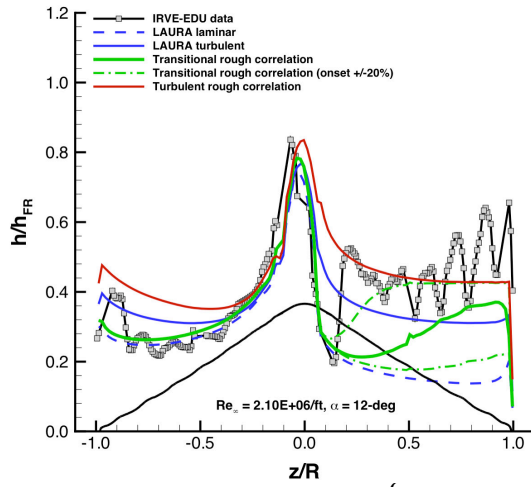
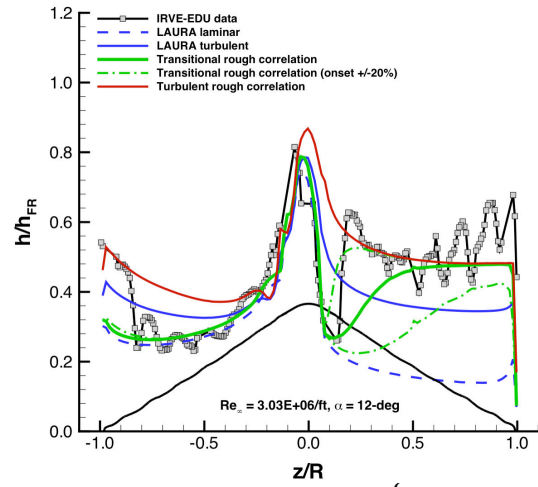


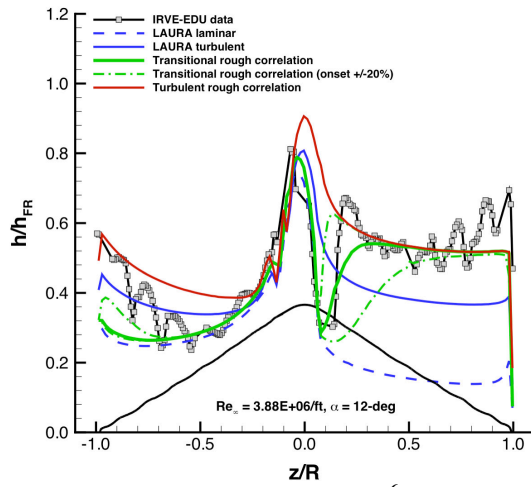
Figure 109. Correlation Comparison with IRVE EDU Model Data, $\alpha = 6\text{ deg}$.



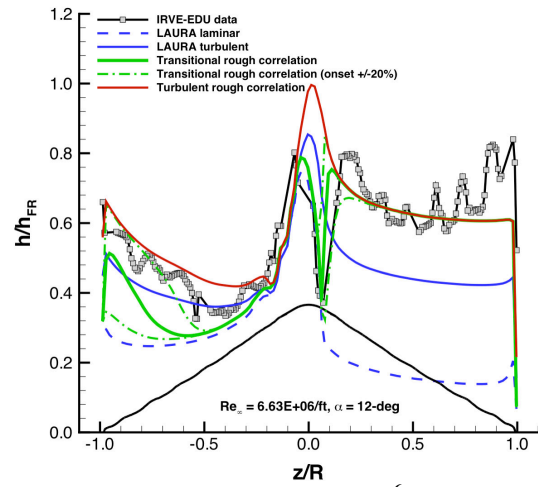
Run 113, $Re_{\infty} = 2.10 \times 10^6/ft$



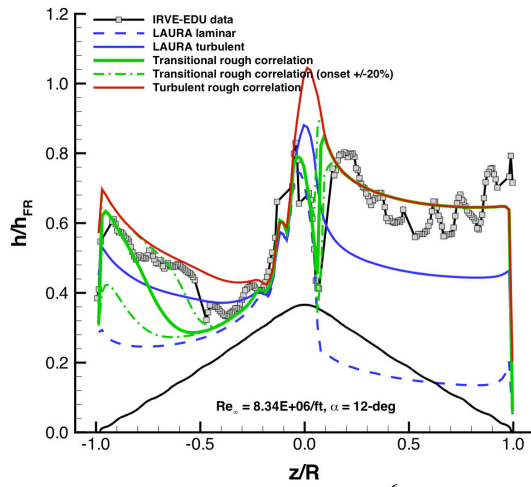
Run 114, $Re_{\infty} = 3.03 \times 10^6/ft$



Run 115, $Re_{\infty} = 3.88 \times 10^6/ft$



Run 117, $Re_{\infty} = 6.63 \times 10^6/ft$



Run 118, $Re_{\infty} = 8.34 \times 10^6/ft$

Figure 110. Correlation Comparison with IRVE EDU Model Data, $\alpha = 12$ deg.

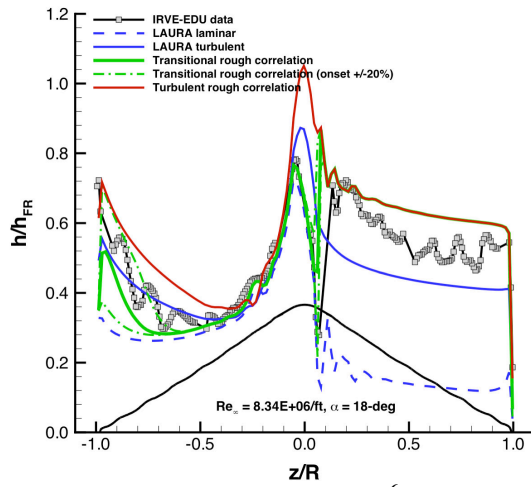
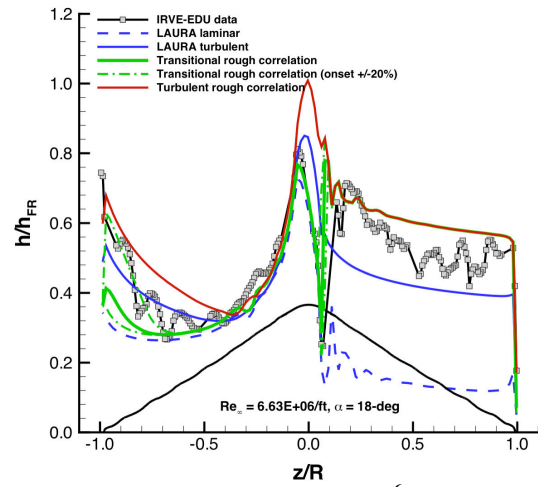
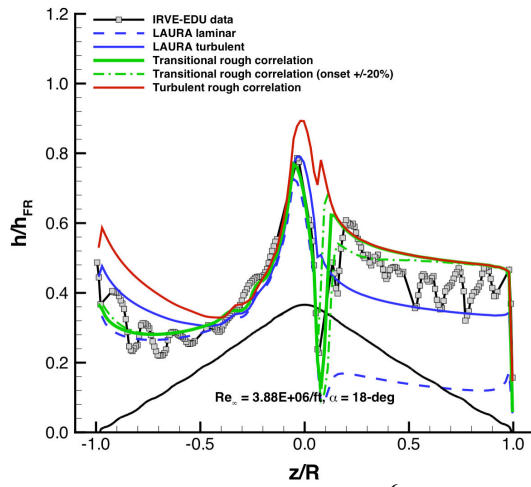
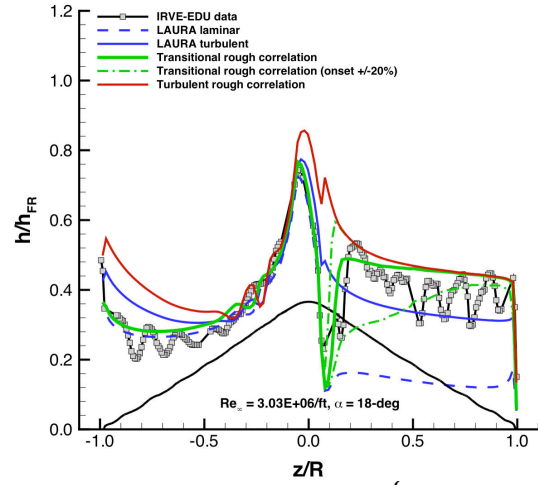
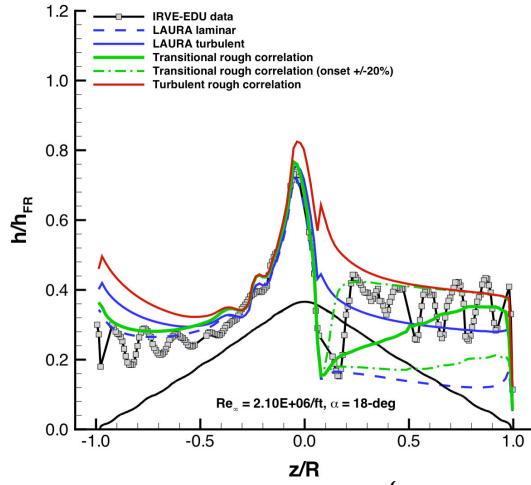


Figure 111. Correlation Comparison with IRVE EDU Model Data, $\alpha = 18$ deg.

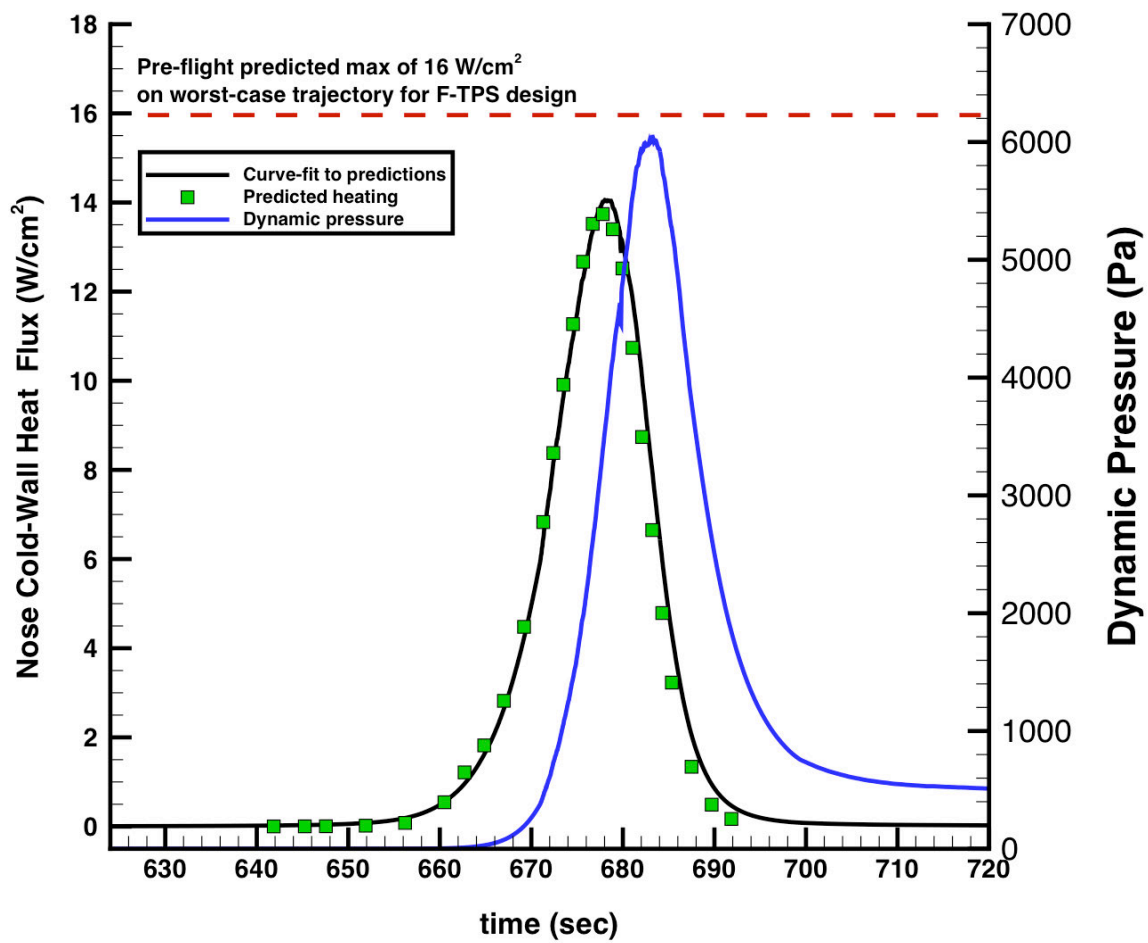


Figure 112. IRVE-3 Flight Trajectory Heating and Pressure.

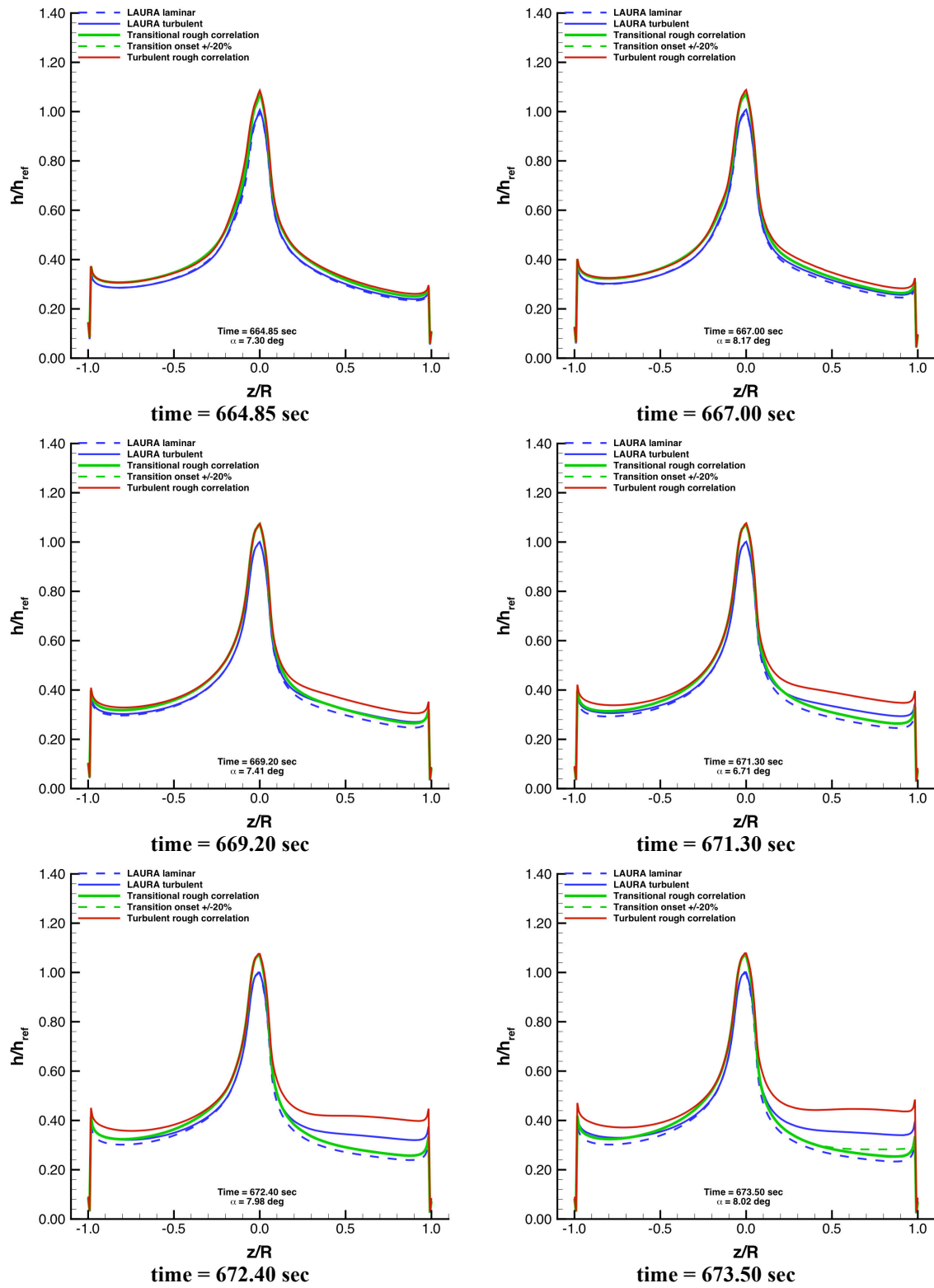


Figure 113. Correlation Applied to IRVE-3 Flight Trajectory – $t = 664.85 \text{ sec} - 673.50 \text{ sec}$.

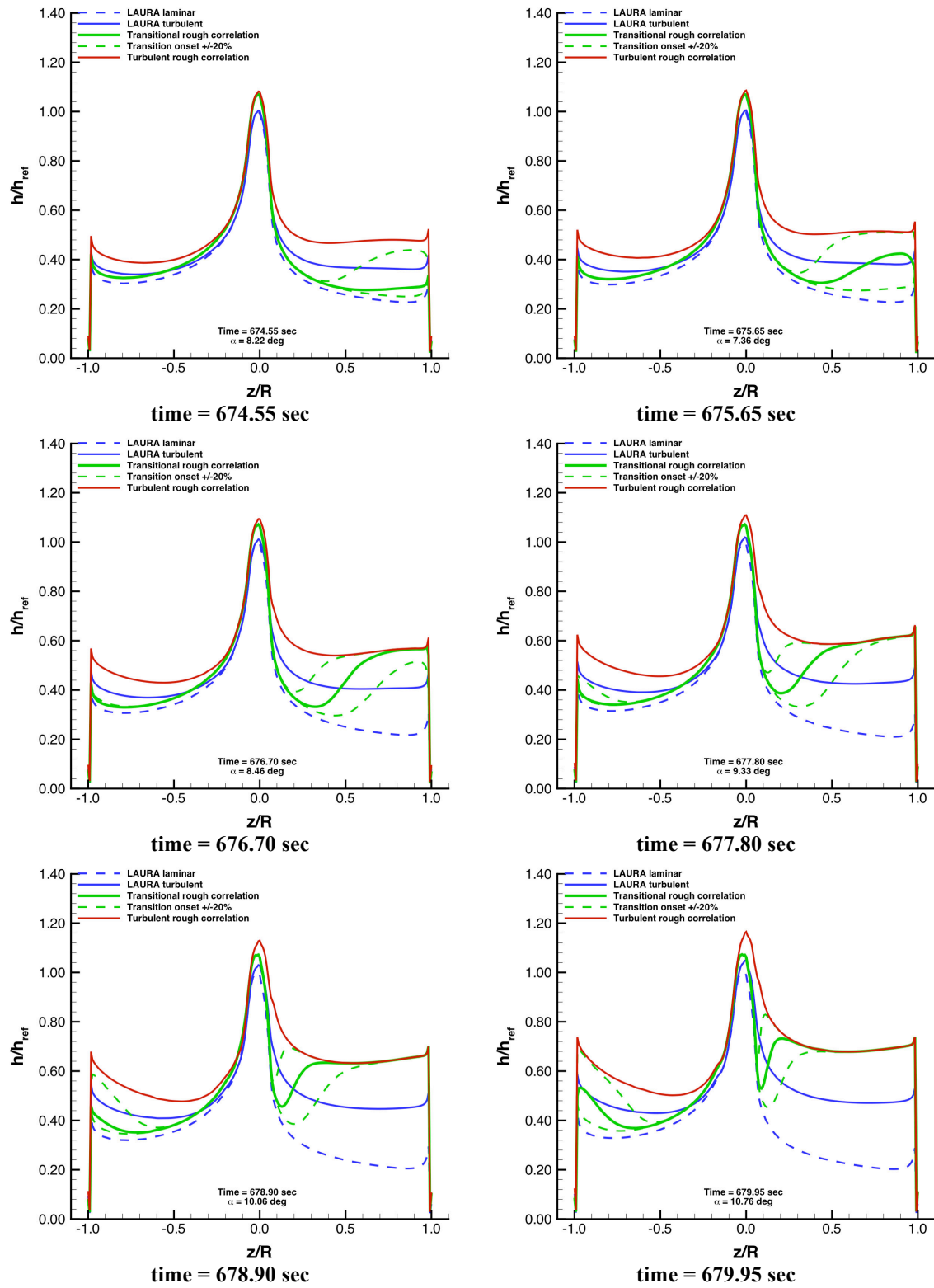


Figure 114. Correlation Applied to IRVE-3 Flight Trajectory – $t = 674.55 \text{ sec} - 679.95 \text{ sec}$.

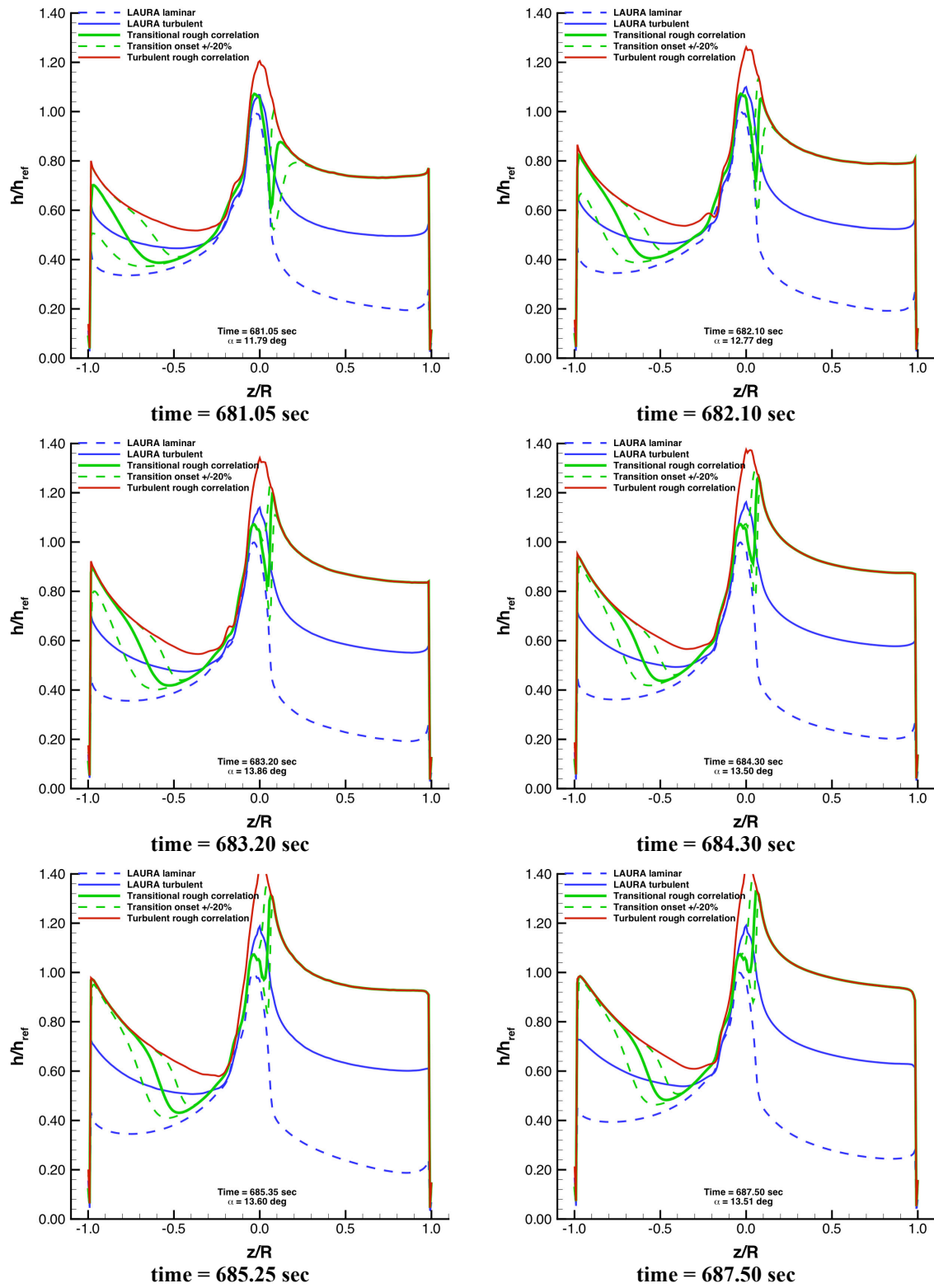


Figure 115. Correlation Applied to IRVE-3 Flight Trajectory – $t = 681.05$ sec – 687.50 sec.

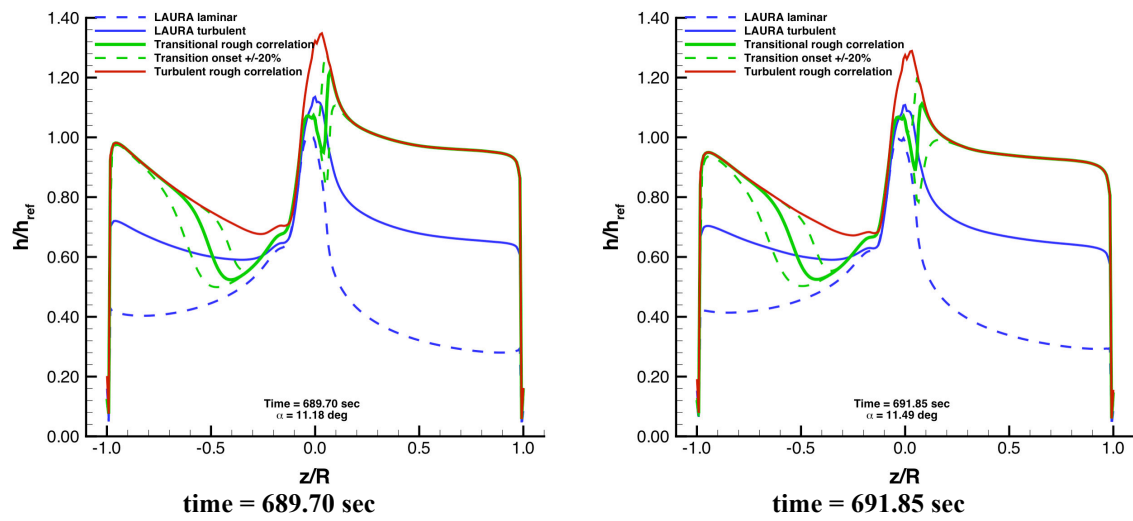


Figure 116. Correlation Applied to IRVE-3 Flight Trajectory – $t = 689.70 \text{ sec} - 691.85 \text{ sec}$.

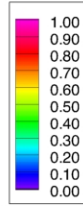
Appendix A. Global Heating Images

Global heating images from Test 6970 in the 20-Inch Mach 6 Air Tunnel are presented in this appendix in Figure 117 - Figure 256. The images are ordered first by model, then by angle-of-attack, then by Reynolds numbers.

Configuration: IRVE-Smooth
D = 6.0 in. / 0.1524 m
R_{nose} = 0.375 in. / 0.00953 m

LaRC 20-Inch Mach 6 Air Tunnel
Test 6979, Run 080

$h/h_{FR,Rn}$



$Re_\infty = 2.10E+06$ /ft
 $Re_\infty = 6.89E+06$ /m
 $\alpha = 0\text{-deg}$
 $U_\infty = 939.5$ m/s
 $\rho_\infty = 3.25E-02$
 $T_\infty = 61.9$ K
 $H_{Total} - H_{300K} = 2.03E+05$
 $q_{FR,Rn} = 1.02E+05$ W/m²
 $h_{FR,Rn} = 5.01E-01$ kg/m²·s

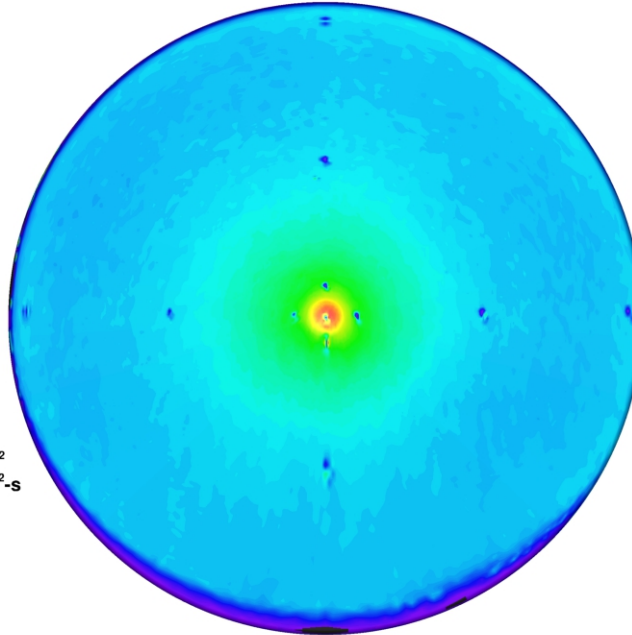
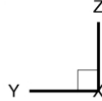
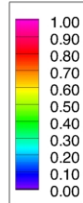


Figure 117. IRVE Scallop-0 Model, Run 80: $\alpha = 0$ deg, $Re_\infty = 2.10 \times 10^6$ /ft.

Configuration: IRVE-Smooth
D = 6.0 in. / 0.1524 m
R_{nose} = 0.375 in. / 0.00953 m

LaRC 20-Inch Mach 6 Air Tunnel
Test 6979, Run 081

$h/h_{FR,Rn}$



$Re_\infty = 3.03E+06$ /ft
 $Re_\infty = 9.95E+06$ /m
 $\alpha = 0\text{-deg}$
 $U_\infty = 948.7$ m/s
 $\rho_\infty = 4.71E-02$
 $T_\infty = 62.5$ K
 $H_{Total} - H_{300K} = 2.12E+05$
 $q_{FR,Rn} = 1.30E+05$ W/m²
 $h_{FR,Rn} = 6.11E-01$ kg/m²·s

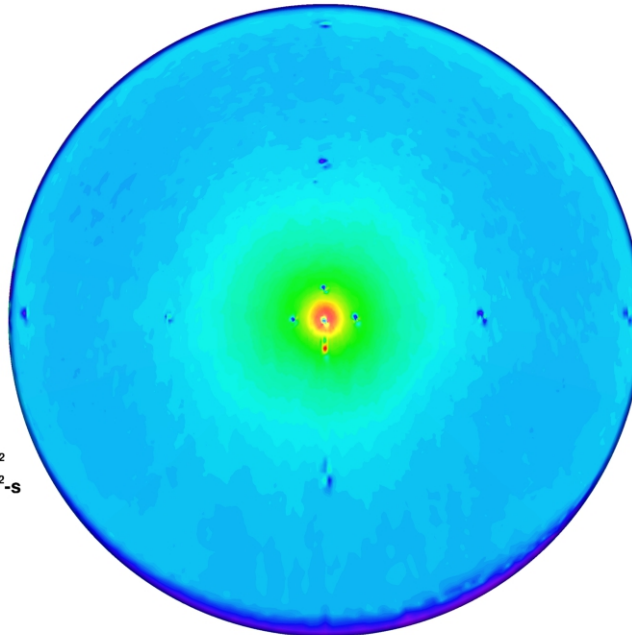
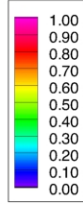


Figure 118. IRVE Scallop-0 Model, Run 81: $\alpha = 0$ deg, $Re_\infty = 3.03 \times 10^6$ /ft.

Configuration: IRVE-Smooth
D = 6.0 in. / 0.1524 m
R_{nose} = 0.375 in. / 0.00953 m

LaRC 20-Inch Mach 6 Air Tunnel
Test 6979, Run 082

$h/h_{FR,Rn}$



$Re_\infty = 3.88E+06$ /ft
 $Re_\infty = 1.28E+07$ /m
 $\alpha = 0\text{-deg}$
 $U_\infty = 957.2$ m/s
 $\rho_\infty = 6.05E-02$
 $T_\infty = 63.3$ K
 $H_{Total} - H_{300K} = 2.21E+05$
 $q_{FR,Rn} = 1.55E+05$ W/m²
 $h_{FR,Rn} = 7.00E-01$ kg/m²-s

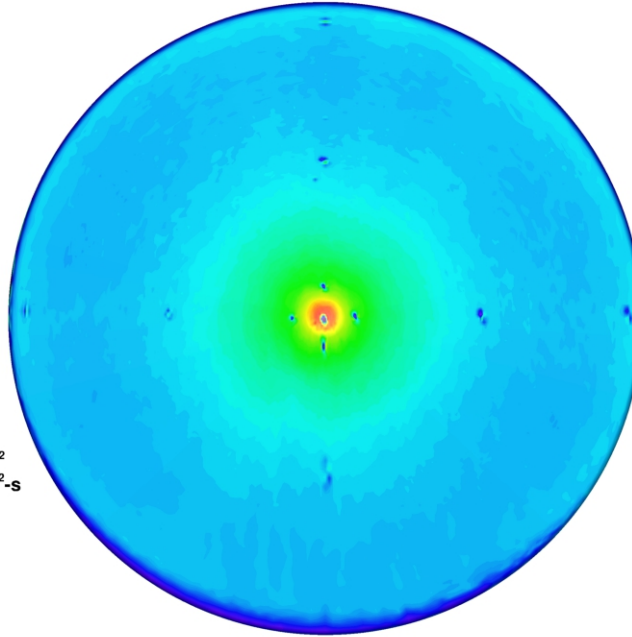
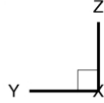
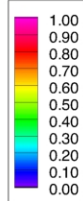


Figure 119. IRVE Scallop-0 Model, Run 82: $\alpha = 0$ deg, $Re_\infty = 3.88 \times 10^6$ /ft.

Configuration: IRVE-Smooth
D = 6.0 in. / 0.1524 m
R_{nose} = 0.375 in. / 0.00953 m

LaRC 20-Inch Mach 6 Air Tunnel
Test 6979, Run 083

$h/h_{FR,Rn}$



$Re_\infty = 6.63E+06$ /ft
 $Re_\infty = 2.18E+07$ /m
 $\alpha = 0\text{-deg}$
 $U_\infty = 954.6$ m/s
 $\rho_\infty = 1.02E-01$
 $T_\infty = 62.6$ K
 $H_{Total} - H_{300K} = 2.17E+05$
 $q_{FR,Rn} = 1.98E+05$ W/m²
 $h_{FR,Rn} = 9.10E-01$ kg/m²-s

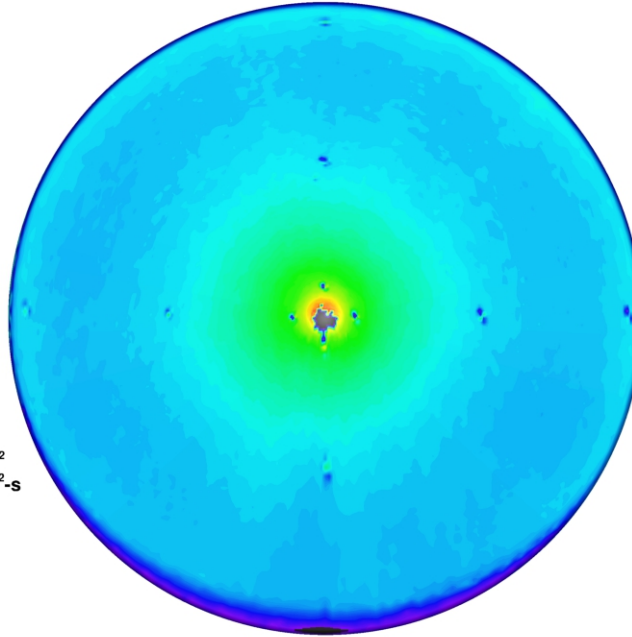
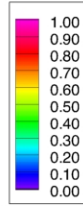


Figure 120. IRVE Scallop-0 Model, Run 83: $\alpha = 0$ deg, $Re_\infty = 6.63 \times 10^6$ /ft.

Configuration: IRVE-Smooth
D = 6.0 in. / 0.1524 m
R_{nose} = 0.375 in. / 0.00953 m

LaRC 20-Inch Mach 6 Air Tunnel
Test 6979, Run 084

$h/h_{FR,Rn}$



$Re_\infty = 8.34E+06$ /ft
 $Re_\infty = 2.74E+07$ /m
 $\alpha = 0\text{-deg}$
 $U_\infty = 918.1$ m/s
 $\rho_\infty = 1.25E-01$
 $T_\infty = 58.6$ K
 $H_{Total} - H_{300K} = 1.79E+05$
 $q_{FR,Rn} = 1.73E+05$ W/m²
 $h_{FR,Rn} = 9.64E-01$ kg/m²-s

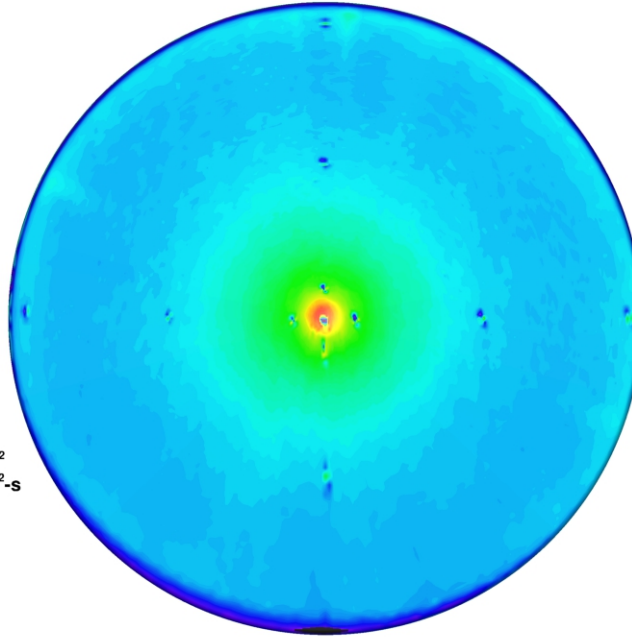
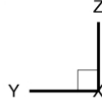
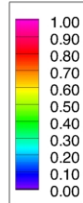


Figure 121. IRVE Scallop-0 Model, Run 84: $\alpha = 0$ deg, $Re_\infty = 8.33 \times 10^6$ /ft.

Configuration: IRVE-Smooth
D = 6.0 in. / 0.1524 m
R_{nose} = 0.375 in. / 0.00953 m

LaRC 20-Inch Mach 6 Air Tunnel
Test 6979, Run 070

$h/h_{FR,Rn}$



$Re_\infty = 2.10E+06$ /ft
 $Re_\infty = 6.89E+06$ /m
 $\alpha = 6\text{-deg}$
 $U_\infty = 939.5$ m/s
 $\rho_\infty = 3.25E-02$
 $T_\infty = 61.9$ K
 $H_{Total} - H_{300K} = 2.03E+05$
 $q_{FR,Rn} = 1.02E+05$ W/m²
 $h_{FR,Rn} = 5.01E-01$ kg/m²-s

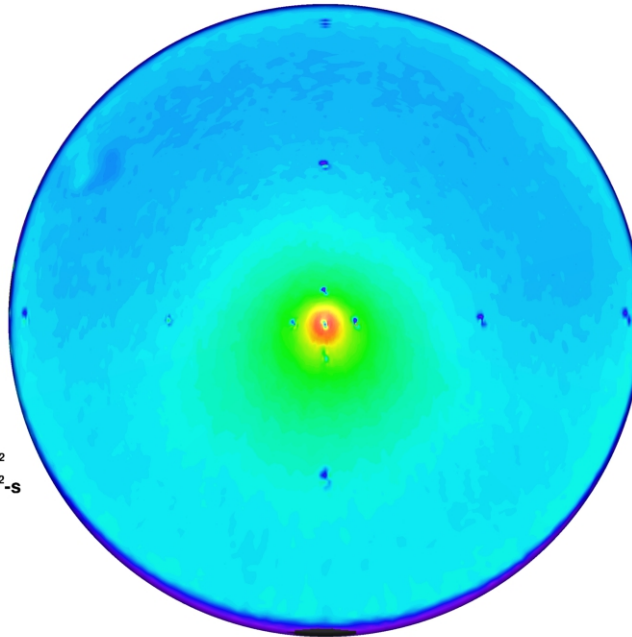
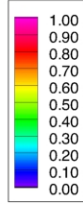


Figure 122. IRVE Scallop-0 Model, Run 70: $\alpha = 6$ deg, $Re_\infty = 2.10 \times 10^6$ /ft.

Configuration: IRVE-Smooth
D = 6.0 in. / 0.1524 m
R_{nose} = 0.375 in. / 0.00953 m

LaRC 20-Inch Mach 6 Air Tunnel
Test 6979, Run 072

$h/h_{FR,Rn}$



$Re_\infty = 3.03E+06$ /ft
 $Re_\infty = 9.95E+06$ /m
 $\alpha = 6\text{-deg}$
 $U_\infty = 948.7$ m/s
 $\rho_\infty = 4.71E-02$
 $T_\infty = 62.5$ K
 $H_{Total} - H_{300K} = 2.12E+05$
 $q_{FR,Rn} = 1.30E+05$ W/m²
 $h_{FR,Rn} = 6.11E-01$ kg/m²·s

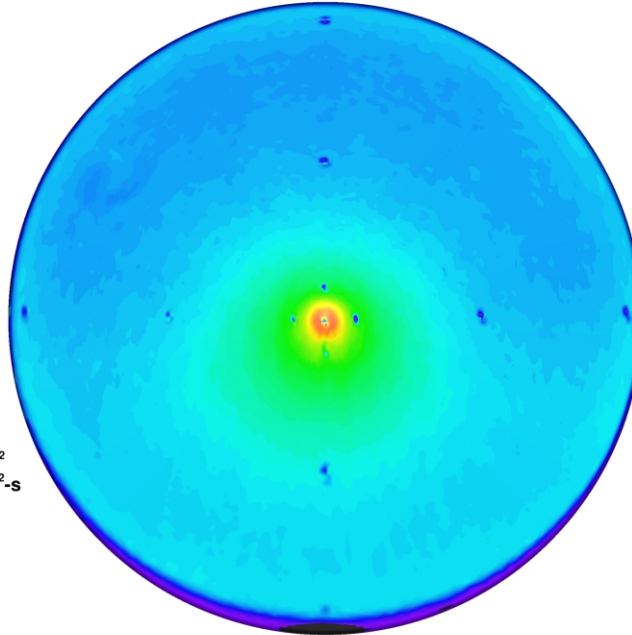
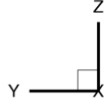
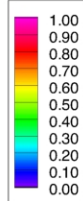


Figure 123. IRVE Scallop-0 Model, Run 72: $\alpha = 6$ deg, $Re_\infty = 3.03 \times 10^6$ /ft.

Configuration: IRVE-Smooth
D = 6.0 in. / 0.1524 m
R_{nose} = 0.375 in. / 0.00953 m

LaRC 20-Inch Mach 6 Air Tunnel
Test 6979, Run 071

$h/h_{FR,Rn}$



$Re_\infty = 3.88E+06$ /ft
 $Re_\infty = 1.28E+07$ /m
 $\alpha = 6\text{-deg}$
 $U_\infty = 957.2$ m/s
 $\rho_\infty = 6.05E-02$
 $T_\infty = 63.3$ K
 $H_{Total} - H_{300K} = 2.21E+05$
 $q_{FR,Rn} = 1.55E+05$ W/m²
 $h_{FR,Rn} = 7.00E-01$ kg/m²·s

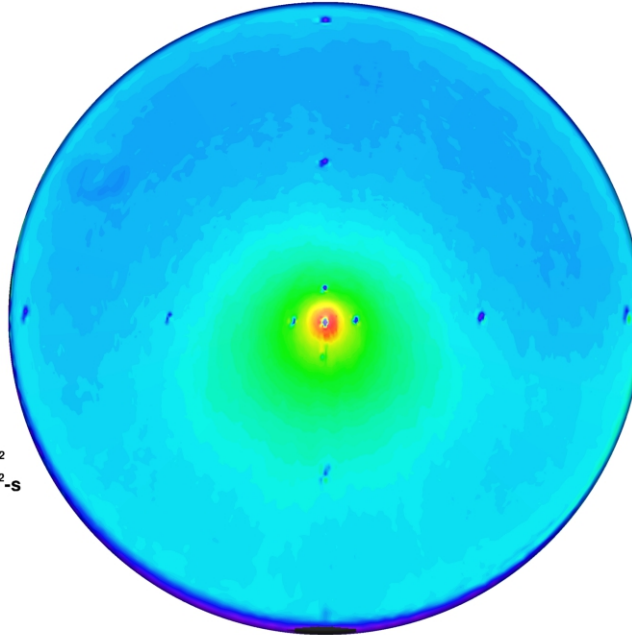
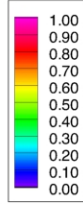


Figure 124. IRVE Scallop-0 Model, Run 71: $\alpha = 6$ deg, $Re_\infty = 3.88 \times 10^6$ /ft.

Configuration: IRVE-Smooth
D = 6.0 in. / 0.1524 m
R_{nose} = 0.375 in. / 0.00953 m

LaRC 20-Inch Mach 6 Air Tunnel
Test 6979, Run 073

$h/h_{FR,Rn}$



$Re_{\infty} = 6.63E+06$ /ft
 $Re_{\infty} = 2.18E+07$ /m
 $\alpha = 6\text{-deg}$
 $U_{\infty} = 954.6$ m/s
 $\rho_{\infty} = 1.02E-01$
 $T_{\infty} = 62.6$ K
 $H_{Total} - H_{300K} = 2.17E+05$
 $q_{FR,Rn} = 1.98E+05$ W/m²
 $h_{FR,Rn} = 9.10E-01$ kg/m²-s

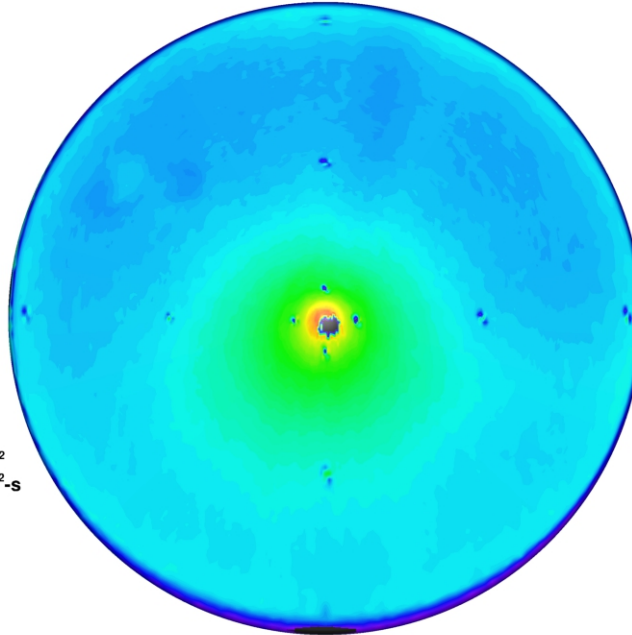
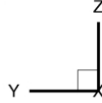
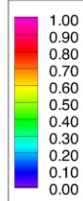


Figure 125. IRVE Scallop-0 Model, Run 73: $\alpha = 6$ deg, $Re_{\infty} = 6.63 \times 10^6$ /ft.

Configuration: IRVE-Smooth
D = 6.0 in. / 0.1524 m
R_{nose} = 0.375 in. / 0.00953 m

LaRC 20-Inch Mach 6 Air Tunnel
Test 6979, Run 074

$h/h_{FR,Rn}$



$Re_{\infty} = 8.34E+06$ /ft
 $Re_{\infty} = 2.74E+07$ /m
 $\alpha = 6\text{-deg}$
 $U_{\infty} = 918.1$ m/s
 $\rho_{\infty} = 1.25E-01$
 $T_{\infty} = 58.6$ K
 $H_{Total} - H_{300K} = 1.79E+05$
 $q_{FR,Rn} = 1.73E+05$ W/m²
 $h_{FR,Rn} = 9.64E-01$ kg/m²-s

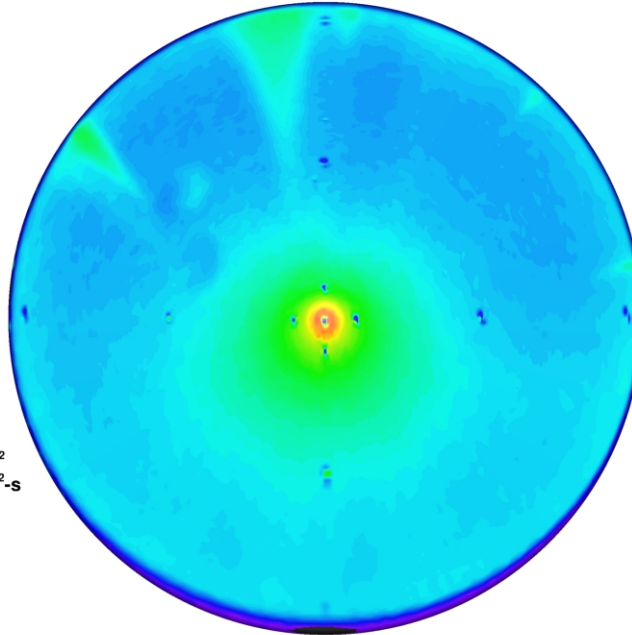
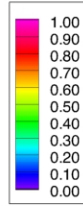


Figure 126. IRVE Scallop-0 Model, Run 74: $\alpha = 6$ deg, $Re_{\infty} = 8.33 \times 10^6$ /ft.

Configuration: IRVE-Smooth
D = 6.0 in. / 0.1524 m
R_{nose} = 0.375 in. / 0.00953 m

LaRC 20-Inch Mach 6 Air Tunnel
Test 6979, Run 103

$h/h_{FR,Rn}$



$Re_\infty = 2.10E+06$ /ft
 $Re_\infty = 6.89E+06$ /m
 $\alpha = 12\text{-deg}$
 $U_\infty = 939.5$ m/s
 $\rho_\infty = 3.25E-02$
 $T_\infty = 61.9$ K
 $H_{Total} - H_{300K} = 2.03E+05$
 $q_{FR,Rn} = 1.02E+05$ W/m²
 $h_{FR,Rn} = 5.01E-01$ kg/m²·s

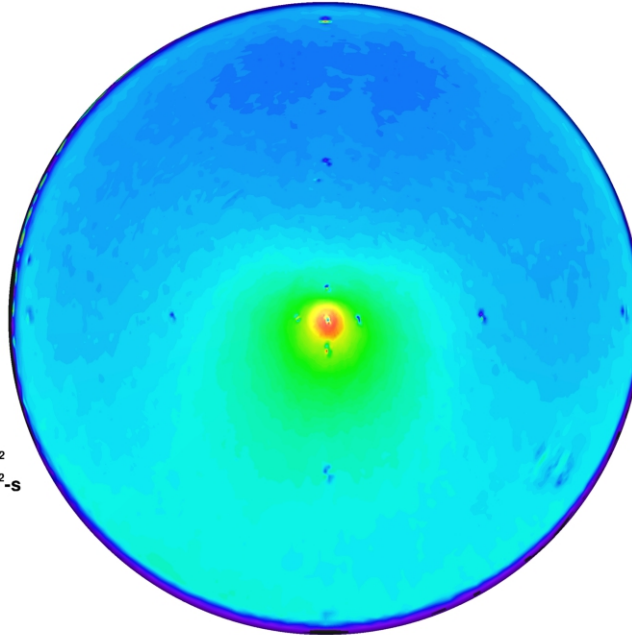
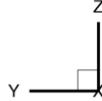
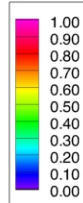


Figure 127. IRVE Scallop-0 Model, Run 103: $\alpha = 12$ deg, $Re_\infty = 2.10 \times 10^6$ /ft.

Configuration: IRVE-Smooth
D = 6.0 in. / 0.1524 m
R_{nose} = 0.375 in. / 0.00953 m

LaRC 20-Inch Mach 6 Air Tunnel
Test 6979, Run 104

$h/h_{FR,Rn}$



$Re_\infty = 3.03E+06$ /ft
 $Re_\infty = 9.95E+06$ /m
 $\alpha = 12\text{-deg}$
 $U_\infty = 948.7$ m/s
 $\rho_\infty = 4.71E-02$
 $T_\infty = 62.5$ K
 $H_{Total} - H_{300K} = 2.12E+05$
 $q_{FR,Rn} = 1.30E+05$ W/m²
 $h_{FR,Rn} = 6.11E-01$ kg/m²·s

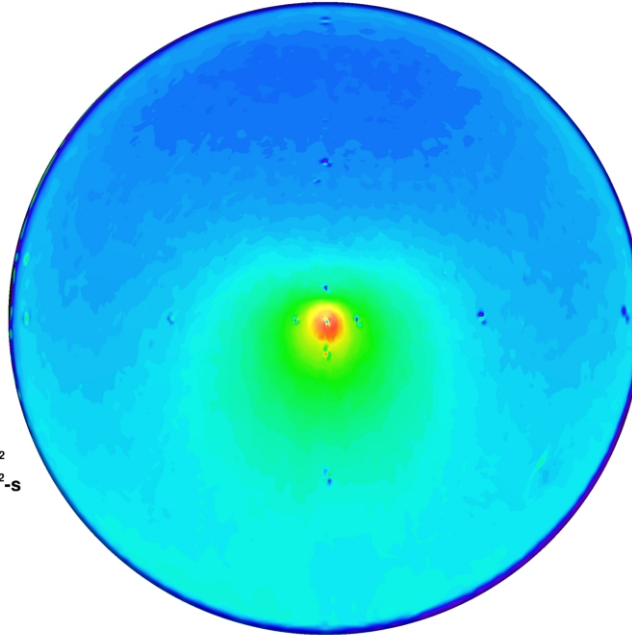
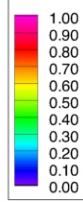


Figure 128. IRVE Scallop-0 Model, Run 104: $\alpha = 12$ deg, $Re_\infty = 3.03 \times 10^6$ /ft.

Configuration: IRVE-Smooth
D = 6.0 in. / 0.1524 m
R_{nose} = 0.375 in. / 0.00953 m

LaRC 20-Inch Mach 6 Air Tunnel
Test 6979, Run 105

$h/h_{FR,Rn}$



$Re_\infty = 3.88E+06$ /ft
 $Re_\infty = 1.28E+07$ /m
 $\alpha = 12\text{-deg}$
 $U_\infty = 957.2$ m/s
 $\rho_\infty = 6.05E-02$
 $T_\infty = 63.3$ K
 $H_{Total} - H_{300K} = 2.21E+05$
 $q_{FR,Rn} = 1.55E+05$ W/m²
 $h_{FR,Rn} = 7.00E-01$ kg/m²·s

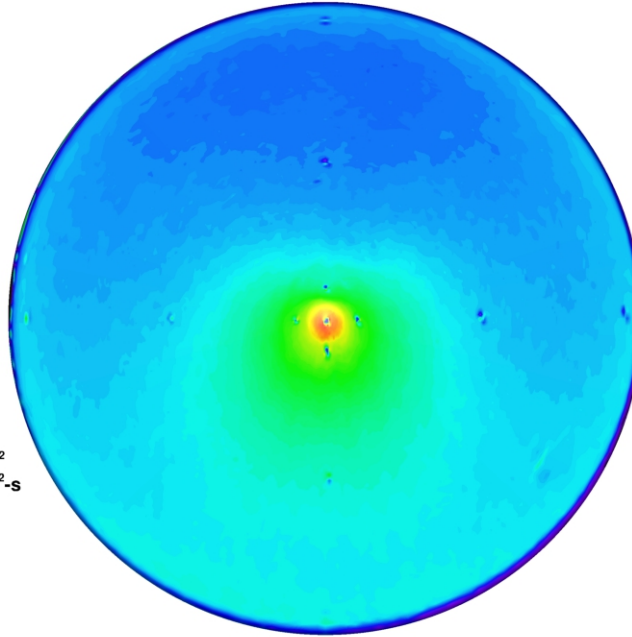
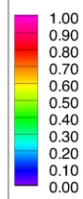


Figure 129. IRVE Scallop-0 Model, Run 105: $\alpha = 12$ deg, $Re_\infty = 3.88 \times 10^6$ /ft.

Configuration: IRVE-Smooth
D = 6.0 in. / 0.1524 m
R_{nose} = 0.375 in. / 0.00953 m

LaRC 20-Inch Mach 6 Air Tunnel
Test 6979, Run 106

$h/h_{FR,Rn}$



$Re_\infty = 6.63E+06$ /ft
 $Re_\infty = 2.18E+07$ /m
 $\alpha = 12\text{-deg}$
 $U_\infty = 954.6$ m/s
 $\rho_\infty = 1.02E-01$
 $T_\infty = 62.6$ K
 $H_{Total} - H_{300K} = 2.17E+05$
 $q_{FR,Rn} = 1.98E+05$ W/m²
 $h_{FR,Rn} = 9.10E-01$ kg/m²·s

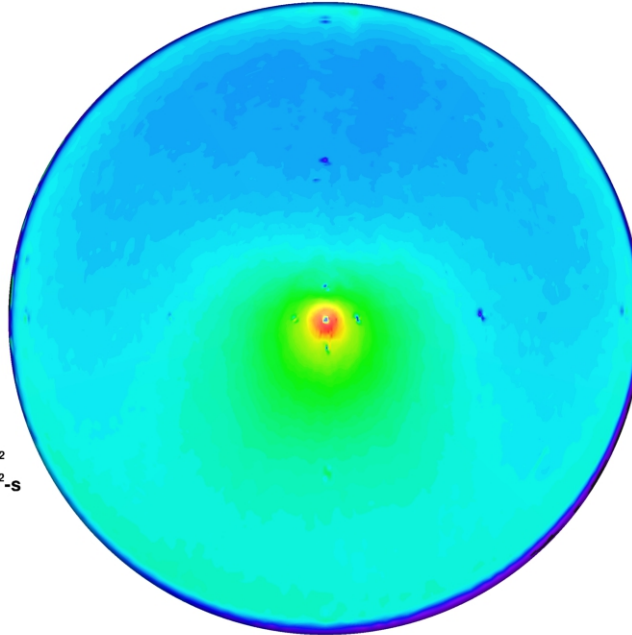
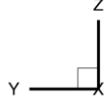
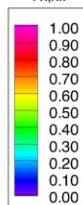


Figure 130. IRVE Scallop-0 Model, Run 106: $\alpha = 12$ deg, $Re_\infty = 6.63 \times 10^6$ /ft.

Configuration: IRVE-Smooth
 $D = 6.0 \text{ in.} / 0.1524 \text{ m}$
 $R_{\text{nose}} = 0.375 \text{ in.} / 0.00953 \text{ m}$

IRVE Deflected OML Study
 LaRC 20-Inch Mach 6 Air Tunnel
 Test 6979, Run 107

$h/h_{FR,Rn}$



$Re_{\infty} = 8.34E+06 \text{ /ft}$
 $Re_{\infty} = 2.74E+07 \text{ /m}$
 $\alpha = 12\text{-deg}$
 $U_{\infty} = 918.1 \text{ m/s}$
 $\rho_{\infty} = 1.25E-01$
 $T_{\infty} = 58.6 \text{ K}$
 $H_{\text{Total}} - H_{300K} = 1.79E+05$
 $q_{FR,Rn} = 1.73E+05 \text{ W/m}^2$
 $h_{FR,Rn} = 9.64E-01 \text{ kg/m}^2\cdot\text{s}$

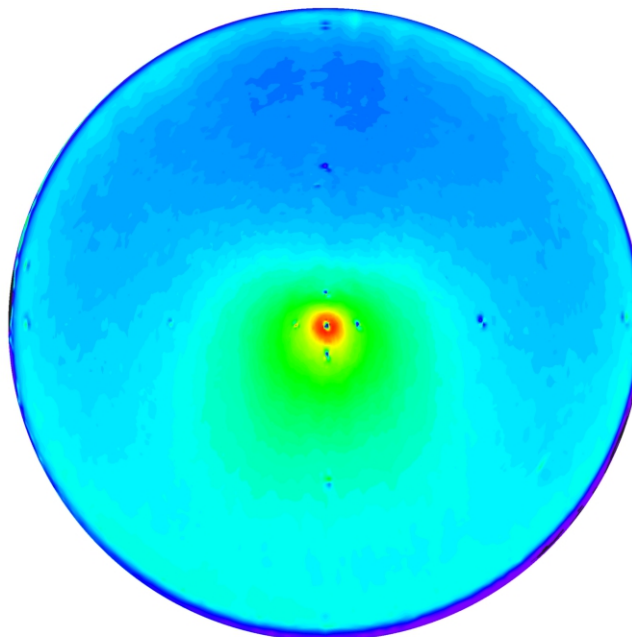
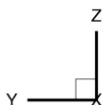
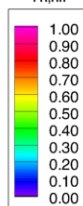


Figure 131. IRVE Scallop-0 Model, Run 107: $\alpha = 12 \text{ deg}$, $Re_{\infty} = 8.33 \times 10^6 \text{ /ft}$.

Configuration: IRVE-Smooth
 $D = 6.0 \text{ in.} / 0.1524 \text{ m}$
 $R_{\text{nose}} = 0.375 \text{ in.} / 0.00953 \text{ m}$

LaRC 20-Inch Mach 6 Air Tunnel
 Test 6979, Run 161

$h/h_{FR,Rn}$



$Re_{\infty} = 2.10E+06 \text{ /ft}$
 $Re_{\infty} = 6.89E+06 \text{ /m}$
 $\alpha = 18\text{-deg}$
 $U_{\infty} = 939.5 \text{ m/s}$
 $\rho_{\infty} = 3.25E-02$
 $T_{\infty} = 61.9 \text{ K}$
 $H_{\text{Total}} - H_{300K} = 2.03E+05$
 $q_{FR,Rn} = 1.02E+05 \text{ W/m}^2$
 $h_{FR,Rn} = 5.01E-01 \text{ kg/m}^2\cdot\text{s}$

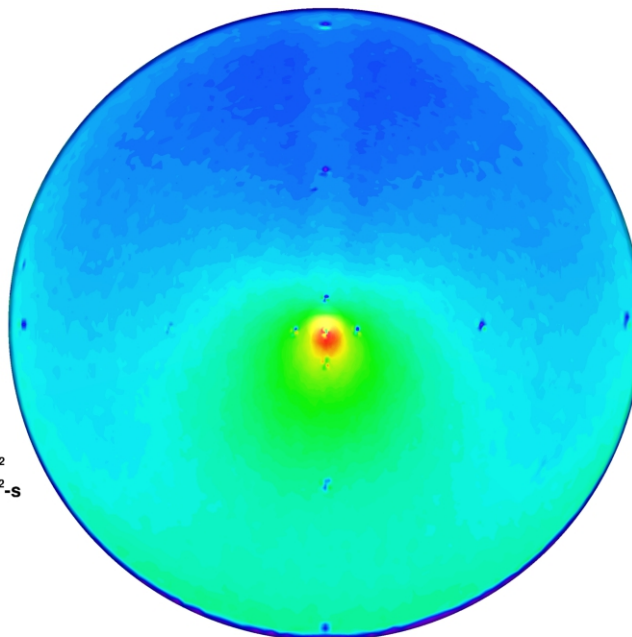
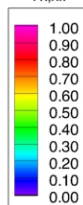


Figure 132. IRVE Scallop-0 Model, Run 161: $\alpha = 18 \text{ deg}$, $Re_{\infty} = 2.10 \times 10^6 \text{ /ft}$.

Configuration: IRVE-Smooth
 $D = 6.0 \text{ in.} / 0.1524 \text{ m}$
 $R_{\text{nose}} = 0.375 \text{ in.} / 0.00953 \text{ m}$

IRVE Deflected OML Study
 LaRC 20-Inch Mach 6 Air Tunnel
 Test 6979, Run 162

$h/h_{FR,Rn}$



$Re_{\infty} = 3.03E+06 / \text{ft}$
 $Re_{\infty} = 9.95E+06 / \text{m}$
 $\alpha = 18\text{-deg}$
 $U_{\infty} = 948.7 \text{ m/s}$
 $\rho_{\infty} = 4.71E-02$
 $T_{\infty} = 62.5 \text{ K}$
 $H_{\text{Total}} - H_{300K} = 2.12E+05$
 $q_{FR,Rn} = 1.30E+05 \text{ W/m}^2$
 $h_{FR,Rn} = 6.11E-01 \text{ kg/m}^2\text{-s}$

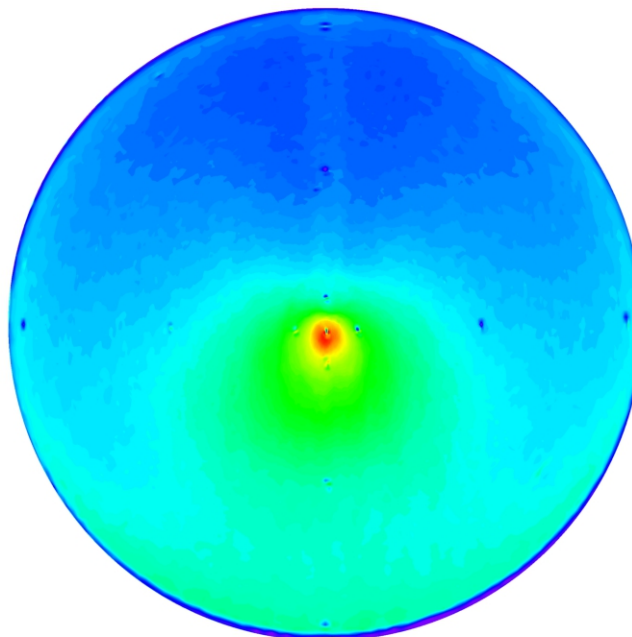
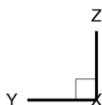
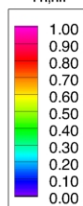


Figure 133. IRVE Scallop-0 Model, Run 162: $\alpha = 18 \text{ deg}$, $Re_{\infty} = 3.03 \times 10^6 / \text{ft}$.

Configuration: IRVE-Smooth
 $D = 6.0 \text{ in.} / 0.1524 \text{ m}$
 $R_{\text{nose}} = 0.375 \text{ in.} / 0.00953 \text{ m}$

LaRC 20-Inch Mach 6 Air Tunnel
 Test 6979, Run 163

$h/h_{FR,Rn}$



$Re_{\infty} = 3.88E+06 / \text{ft}$
 $Re_{\infty} = 1.28E+07 / \text{m}$
 $\alpha = 18\text{-deg}$
 $U_{\infty} = 957.2 \text{ m/s}$
 $\rho_{\infty} = 6.05E-02$
 $T_{\infty} = 63.3 \text{ K}$
 $H_{\text{Total}} - H_{300K} = 2.21E+05$
 $q_{FR,Rn} = 1.55E+05 \text{ W/m}^2$
 $h_{FR,Rn} = 7.00E-01 \text{ kg/m}^2\text{-s}$

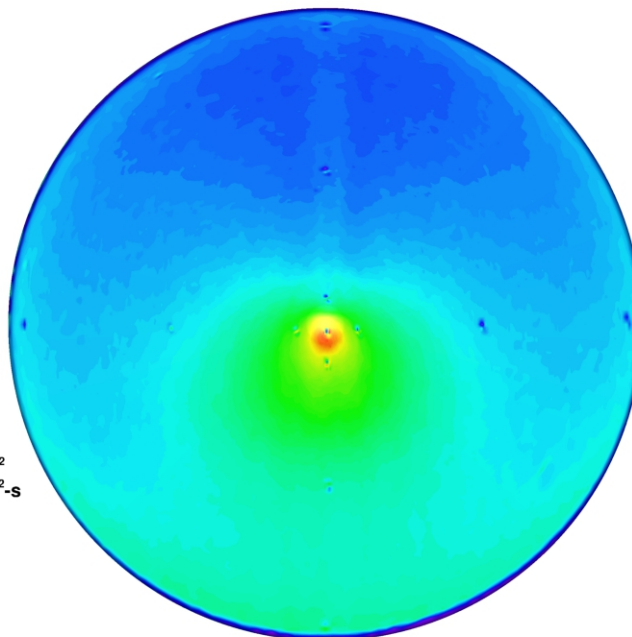
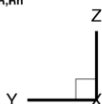
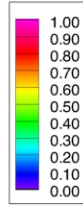


Figure 134. IRVE Scallop-0 Model, Run 163: $\alpha = 18 \text{ deg}$, $Re_{\infty} = 3.88 \times 10^6 / \text{ft}$.

Configuration: IRVE-Smooth
D = 6.0 in. / 0.1524 m
R_{nose} = 0.375 in. / 0.00953 m

LaRC 20-Inch Mach 6 Air Tunnel
Test 6979, Run 164

$h/h_{FR,Rn}$



$Re_\infty = 6.63E+06$ /ft
 $Re_\infty = 2.18E+07$ /m
 $\alpha = 18\text{-deg}$
 $U_\infty = 954.6$ m/s
 $\rho_\infty = 1.02E-01$
 $T_\infty = 62.6$ K
 $H_{Total} - H_{300K} = 2.17E+05$
 $q_{FR,Rn} = 1.98E+05$ W/m²
 $h_{FR,Rn} = 9.10E-01$ kg/m²-s

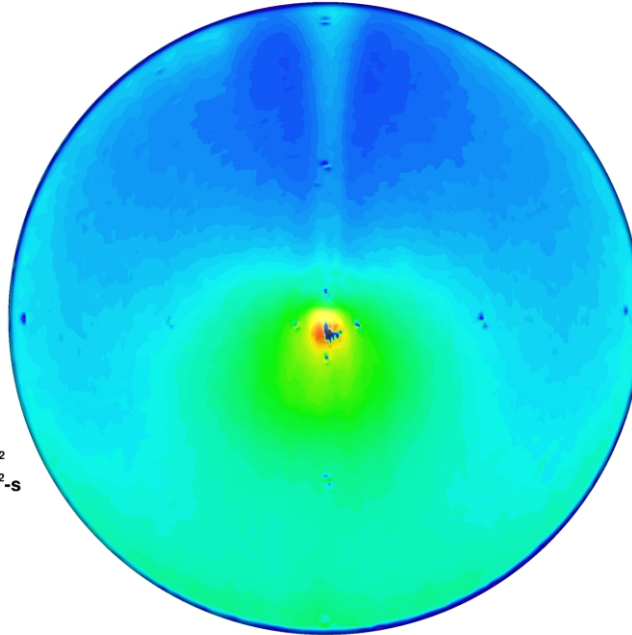
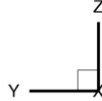
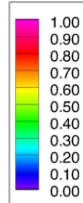


Figure 135. IRVE Scallop-0 Model, Run 164: $\alpha = 18$ deg, $Re_\infty = 6.63 \times 10^6$ /ft.

Configuration: IRVE-Smooth
D = 6.0 in. / 0.1524 m
R_{nose} = 0.375 in. / 0.00953 m

LaRC 20-Inch Mach 6 Air Tunnel
Test 6979, Run 165

$h/h_{FR,Rn}$



$Re_\infty = 8.34E+06$ /ft
 $Re_\infty = 2.74E+07$ /m
 $\alpha = 18\text{-deg}$
 $U_\infty = 918.1$ m/s
 $\rho_\infty = 1.25E-01$
 $T_\infty = 58.6$ K
 $H_{Total} - H_{300K} = 1.79E+05$
 $q_{FR,Rn} = 1.73E+05$ W/m²
 $h_{FR,Rn} = 9.64E-01$ kg/m²-s

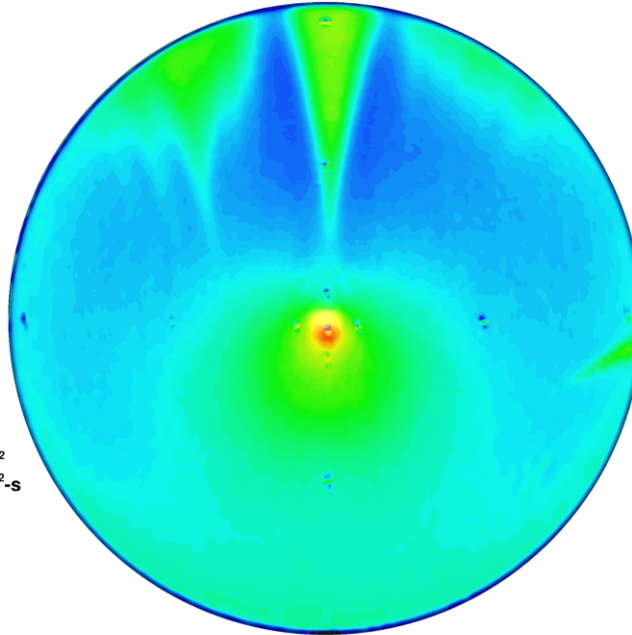
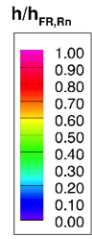


Figure 136. IRVE Scallop-0 Model, Run 165: $\alpha = 18$ deg, $Re_\infty = 8.33 \times 10^6$ /ft.

Configuration: IRVE-EDU
D = 6.0 in. / 0.1524 m
R_{nose} = 0.375 in. / 0.009525 m

LaRC 20-Inch Mach 6 Air Tunnel
Test 6979, Run 036



Re_∞ = 2.10E+06 /ft
Re_∞ = 6.89E+06 /m
α = 0-deg
U_∞ = 939.5 m/s
ρ_∞ = 3.25E-02
T_∞ = 61.9 K
H_{Total} - H_{300K} = 2.03E+05
q_{FR,Rn} = 1.02E+05 W/m²
h_{FR,Rn} = 5.01E-01 kg/m²·s

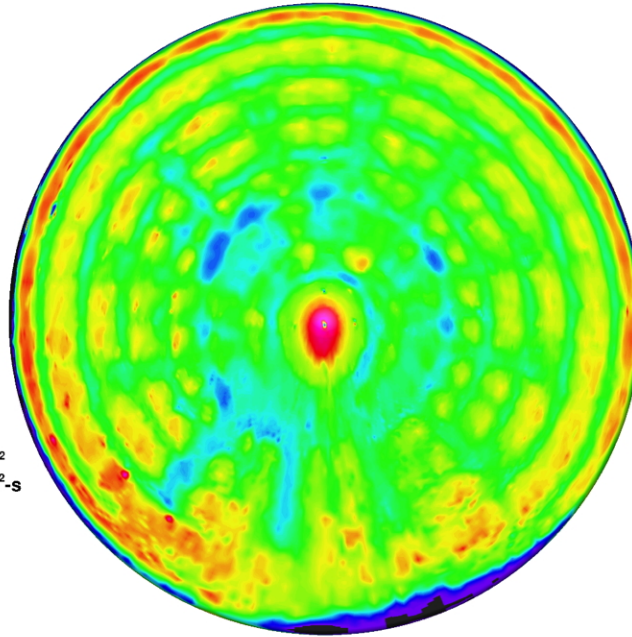
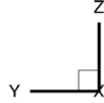
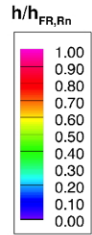


Figure 137. IRVE EDU Model, Run 36: α = 0 deg, Re_∞ = 2.10×10⁶/ft.

Configuration: IRVE-EDU
D = 6.0 in. / 0.1524 m
R_{nose} = 0.375 in. / 0.009525 m

LaRC 20-Inch Mach 6 Air Tunnel
Test 6979, Run 039



Re_∞ = 3.03E+06 /ft
Re_∞ = 9.95E+06 /m
α = 0-deg
U_∞ = 948.7 m/s
ρ_∞ = 4.71E-02
T_∞ = 62.5 K
H_{Total} - H_{300K} = 2.12E+05
q_{FR,Rn} = 1.30E+05 W/m²
h_{FR,Rn} = 6.11E-01 kg/m²·s

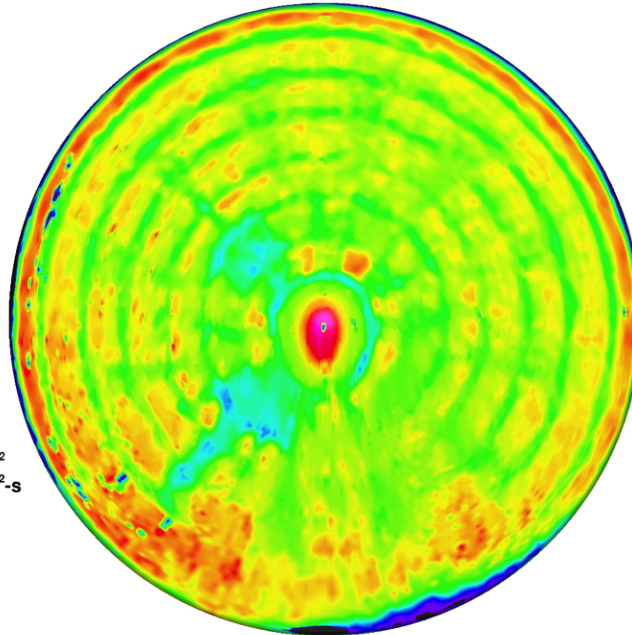
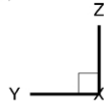
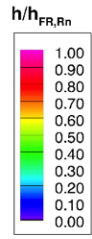


Figure 138. IRVE EDU Model, Run 39: α = 0 deg, Re_∞ = 3.03×10⁶/ft.

Configuration: IRVE-EDU
D = 6.0 in. / 0.1524 m
R_{nose} = 0.375 in. / 0.009525 m

LaRC 20-Inch Mach 6 Air Tunnel
Test 6979, Run 040



Re_∞ = 3.88E+06 /ft
Re_∞ = 1.28E+07 /m
α = 0-deg
U_∞ = 957.2 m/s
ρ_∞ = 6.05E-02
T_∞ = 63.3 K
H_{Total} - H_{300K} = 2.21E+05
q_{FR,Rn} = 1.55E+05 W/m²
h_{FR,Rn} = 7.00E-01 kg/m²-s

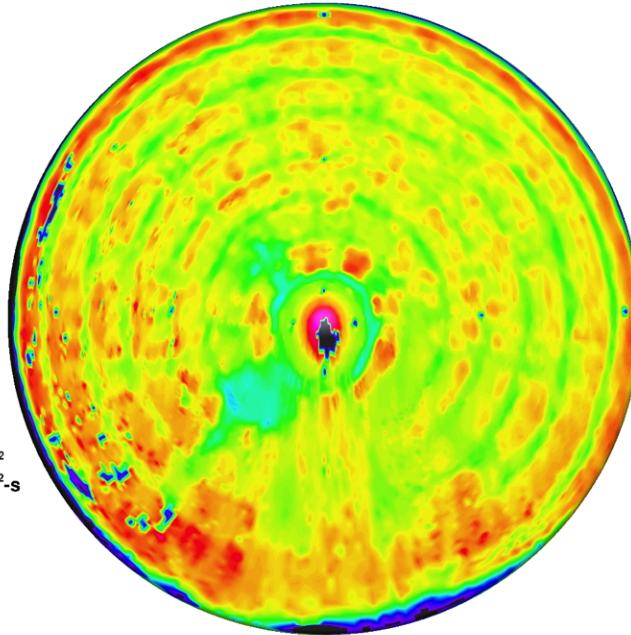
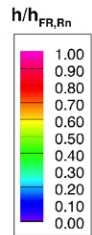


Figure 139. IRVE EDU Model, Run 40: α = 0 deg, Re_∞ = 3.88×10⁶/ft.

Configuration: IRVE-EDU
D = 6.0 in. / 0.1524 m
R_{nose} = 0.375 in. / 0.009525 m

LaRC 20-Inch Mach 6 Air Tunnel
Test 6979, Run 041



Re_∞ = 6.63E+06 /ft
Re_∞ = 2.18E+07 /m
α = 0-deg
U_∞ = 954.6 m/s
ρ_∞ = 1.02E-01
T_∞ = 62.6 K
H_{Total} - H_{300K} = 2.17E+05
q_{FR,Rn} = 1.98E+05 W/m²
h_{FR,Rn} = 9.10E-01 kg/m²-s

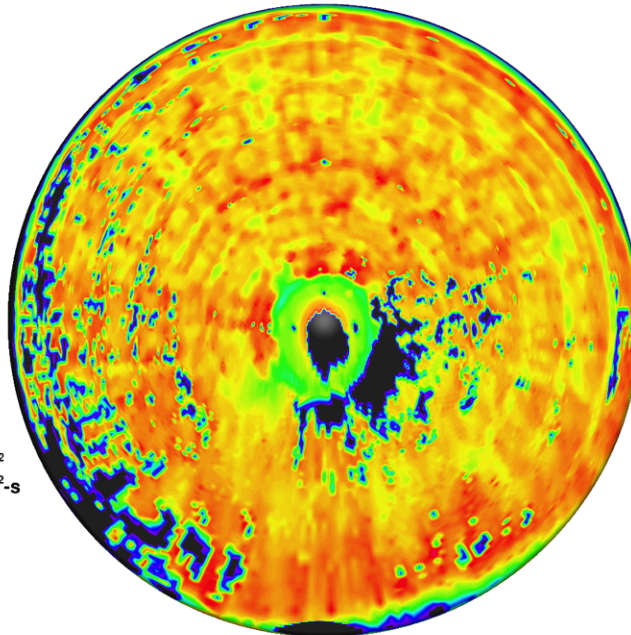
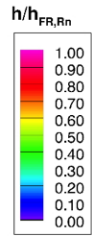


Figure 140. IRVE EDU Model, Run 41: α = 0 deg, Re_∞ = 6.63×10⁶/ft.

Configuration: IRVE-EDU
D = 6.0 in. / 0.1524 m
R_{nose} = 0.375 in. / 0.009525 m

LaRC 20-Inch Mach 6 Air Tunnel
Test 6979, Run 042



Re_∞ = 8.34E+06 /ft
Re_∞ = 2.74E+07 /m
α = 0-deg
U_∞ = 918.1 m/s
ρ_∞ = 1.25E-01
T_∞ = 58.6 K
H_{Total} - H_{300K} = 1.79E+05
q_{FR,Rn} = 1.73E+05 W/m²
h_{FR,Rn} = 9.64E-01 kg/m²-s

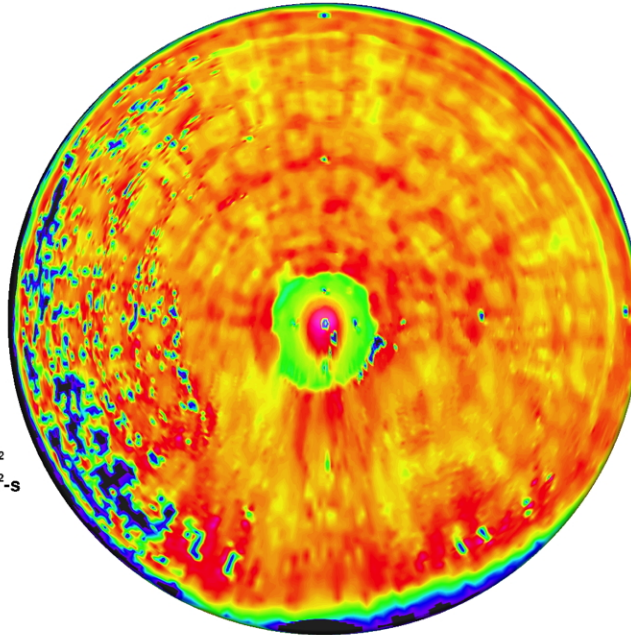
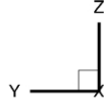
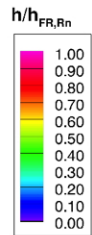


Figure 141. IRVE EDU Model, Run 42: α = 0 deg, Re_∞ = 8.33×10⁶/ft.

Configuration: IRVE-EDU
D = 6.0 in. / 0.1524 m
R_{nose} = 0.375 in. / 0.009525 m

LaRC 20-Inch Mach 6 Air Tunnel
Test 6979, Run 122



Re_∞ = 2.10E+06 /ft
Re_∞ = 6.89E+06 /m
α = 6-deg
U_∞ = 939.5 m/s
ρ_∞ = 3.25E-02
T_∞ = 61.9 K
H_{Total} - H_{300K} = 2.03E+05
q_{FR,Rn} = 1.02E+05 W/m²
h_{FR,Rn} = 5.01E-01 kg/m²-s

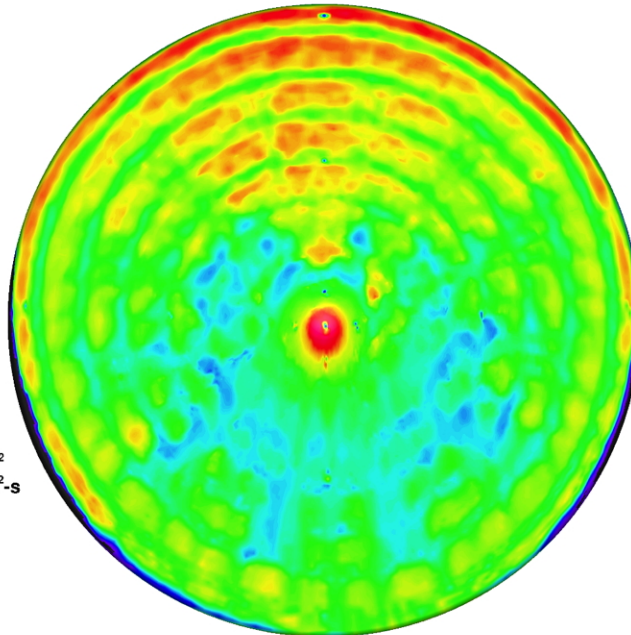
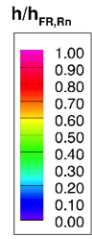


Figure 142. IRVE EDU Model, Run 122: α = 6 deg, Re_∞ = 2.10×10⁶/ft.

Configuration: IRVE-EDU
D = 6.0 in. / 0.1524 m
R_{nose} = 0.375 in. / 0.009525 m

LaRC 20-Inch Mach 6 Air Tunnel
Test 6979, Run 120



$Re_\infty = 3.03E+06$ /ft
 $Re_\infty = 9.95E+06$ /m
 $\alpha = 6\text{-deg}$
 $U_\infty = 948.7$ m/s
 $\rho_\infty = 4.71E-02$
 $T_\infty = 62.5$ K
 $H_{Total} - H_{300K} = 2.12E+05$
 $q_{FR,Rn} = 1.30E+05$ W/m²
 $h_{FR,Rn} = 6.11E-01$ kg/m²·s

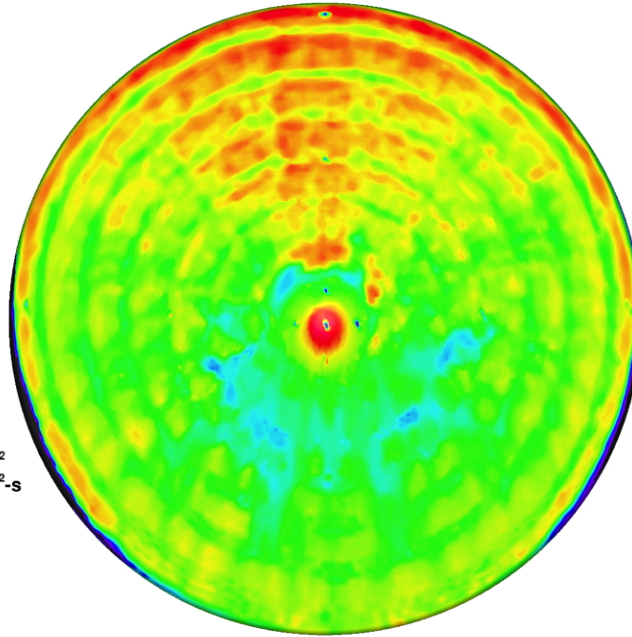
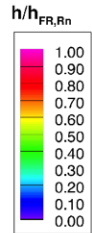


Figure 143. IRVE EDU Model, Run 120: $\alpha = 6$ deg, $Re_\infty = 3.03 \times 10^6$ /ft.

Configuration: IRVE-EDU
D = 6.0 in. / 0.1524 m
R_{nose} = 0.375 in. / 0.009525 m

LaRC 20-Inch Mach 6 Air Tunnel
Test 6979, Run 119



$Re_\infty = 3.88E+06$ /ft
 $Re_\infty = 1.28E+07$ /m
 $\alpha = 6\text{-deg}$
 $U_\infty = 957.2$ m/s
 $\rho_\infty = 6.05E-02$
 $T_\infty = 63.3$ K
 $H_{Total} - H_{300K} = 2.21E+05$
 $q_{FR,Rn} = 1.55E+05$ W/m²
 $h_{FR,Rn} = 7.00E-01$ kg/m²·s

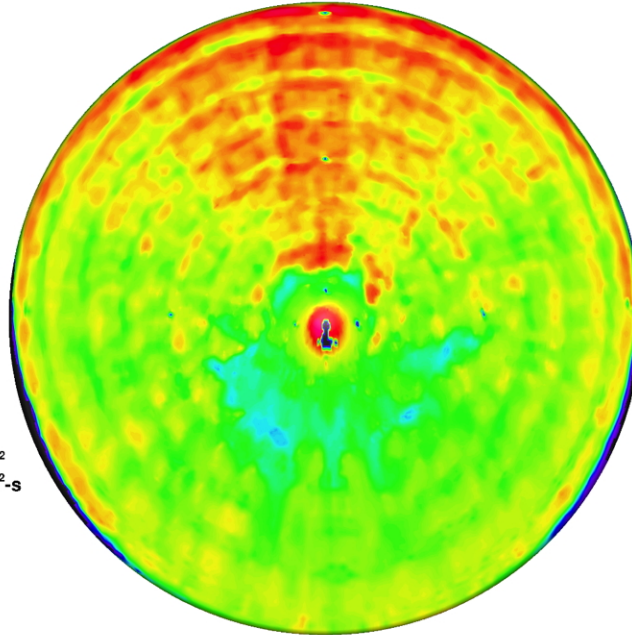
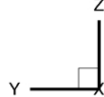
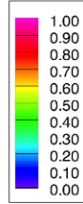


Figure 144. IRVE EDU Model, Run 119: $\alpha = 6$ deg, $Re_\infty = 3.88 \times 10^6$ /ft.

Configuration: IRVE-EDU
D = 6.0 in. / 0.1524 m
R_{nose} = 0.375 in. / 0.009525 m

LaRC 20-Inch Mach 6 Air Tunnel
Test 6979, Run 123

$h/h_{FR,Rn}$



$Re_\infty = 6.63E+06$ /ft
 $Re_\infty = 2.18E+07$ /m
 $\alpha = 6\text{-deg}$
 $U_\infty = 954.6$ m/s
 $\rho_\infty = 1.02E-01$
 $T_\infty = 62.6$ K
 $H_{Total} - H_{300K} = 2.17E+05$
 $q_{FR,Rn} = 1.98E+05$ W/m²
 $h_{FR,Rn} = 9.10E-01$ kg/m²·s

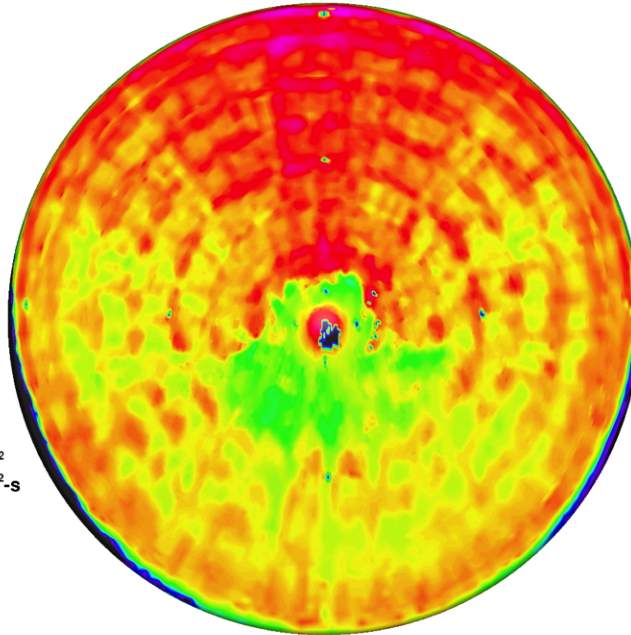
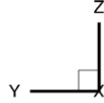
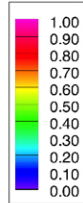


Figure 145. IRVE EDU Model, Run 123: $\alpha = 6$ deg, $Re_\infty = 6.63 \times 10^6$ /ft.

Configuration: IRVE-EDU
D = 6.0 in. / 0.1524 m
R_{nose} = 0.375 in. / 0.009525 m

LaRC 20-Inch Mach 6 Air Tunnel
Test 6979, Run 125

$h/h_{FR,Rn}$



$Re_\infty = 8.34E+06$ /ft
 $Re_\infty = 2.74E+07$ /m
 $\alpha = 6\text{-deg}$
 $U_\infty = 918.1$ m/s
 $\rho_\infty = 1.25E-01$
 $T_\infty = 58.6$ K
 $H_{Total} - H_{300K} = 1.79E+05$
 $q_{FR,Rn} = 1.73E+05$ W/m²
 $h_{FR,Rn} = 9.64E-01$ kg/m²·s

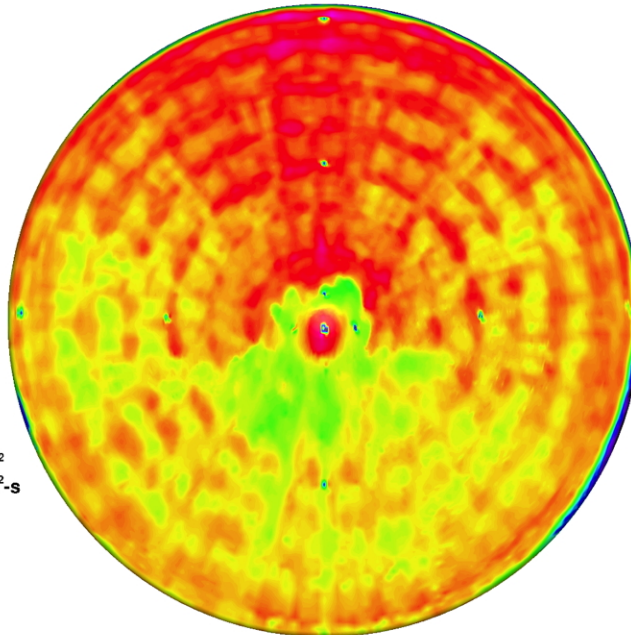
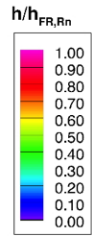


Figure 146. IRVE EDU Model, Run 125: $\alpha = 6$ deg, $Re_\infty = 8.33 \times 10^6$ /ft.

Configuration: IRVE-EDU
D = 6.0 in. / 0.1524 m
R_{nose} = 0.375 in. / 0.009525 m

LaRC 20-Inch Mach 6 Air Tunnel
Test 6979, Run 113



Re_∞ = 2.10E+06 /ft
Re_∞ = 6.89E+06 /m
α = 12-deg
U_∞ = 939.5 m/s
ρ_∞ = 3.25E-02
T_∞ = 61.9 K
H_{Total} - H_{300K} = 2.03E+05
q_{FR,Rn} = 1.02E+05 W/m²
h_{FR,Rn} = 5.01E-01 kg/m²-s

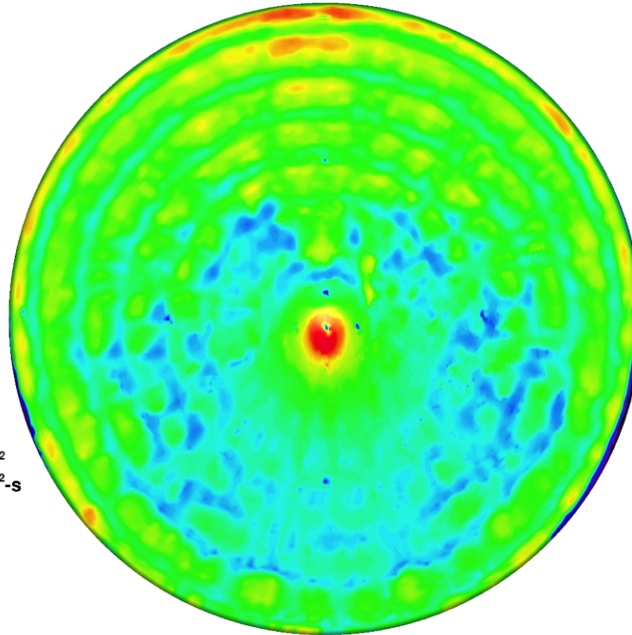
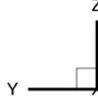
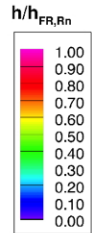


Figure 147. IRVE EDU Model, Run 113: α = 12 deg, Re_∞ = 2.10×10⁶/ft.

Configuration: IRVE-EDU
D = 6.0 in. / 0.1524 m
R_{nose} = 0.375 in. / 0.009525 m

LaRC 20-Inch Mach 6 Air Tunnel
Test 6979, Run 114



Re_∞ = 3.03E+06 /ft
Re_∞ = 9.95E+06 /m
α = 12-deg
U_∞ = 948.7 m/s
ρ_∞ = 4.71E-02
T_∞ = 62.5 K
H_{Total} - H_{300K} = 2.12E+05
q_{FR,Rn} = 1.30E+05 W/m²
h_{FR,Rn} = 6.11E-01 kg/m²-s

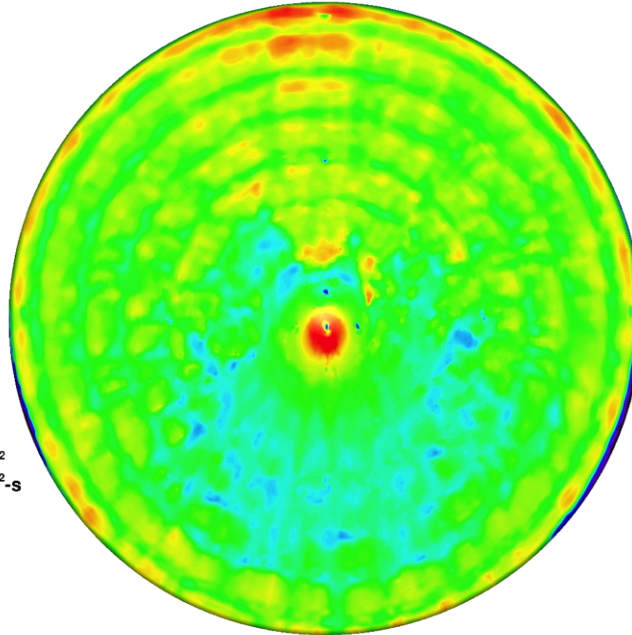
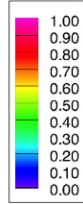


Figure 148. IRVE EDU Model, Run 114: α = 12 deg, Re_∞ = 3.03×10⁶/ft.

Configuration: IRVE-EDU
D = 6.0 in. / 0.1524 m
R_{nose} = 0.375 in. / 0.009525 m

LaRC 20-Inch Mach 6 Air Tunnel
Test 6979, Run 115

$h/h_{FR,Rn}$



$Re_\infty = 3.88E+06$ /ft
 $Re_\infty = 1.28E+07$ /m
 $\alpha = 12\text{-deg}$
 $U_\infty = 957.2$ m/s
 $\rho_\infty = 6.05E-02$
 $T_\infty = 63.3$ K
 $H_{Total} - H_{300K} = 2.21E+05$
 $q_{FR,Rn} = 1.55E+05$ W/m²
 $h_{FR,Rn} = 7.00E-01$ kg/m²-s

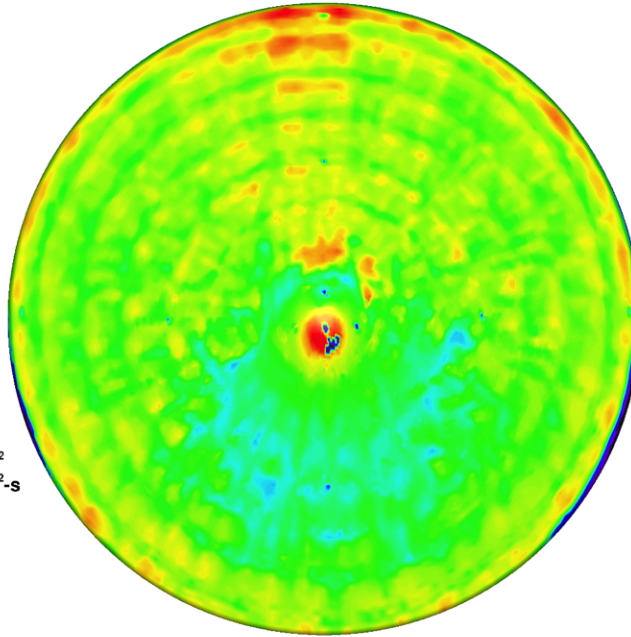
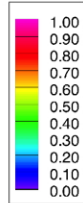


Figure 149. IRVE EDU Model, Run 115: $\alpha = 12$ deg, $Re_\infty = 3.88 \times 10^6$ /ft.

Configuration: IRVE-EDU
D = 6.0 in. / 0.1524 m
R_{nose} = 0.375 in. / 0.009525 m

LaRC 20-Inch Mach 6 Air Tunnel
Test 6979, Run 117

$h/h_{FR,Rn}$



$Re_\infty = 6.63E+06$ /ft
 $Re_\infty = 2.18E+07$ /m
 $\alpha = 12\text{-deg}$
 $U_\infty = 954.6$ m/s
 $\rho_\infty = 1.02E-01$
 $T_\infty = 62.6$ K
 $H_{Total} - H_{300K} = 2.17E+05$
 $q_{FR,Rn} = 1.98E+05$ W/m²
 $h_{FR,Rn} = 9.10E-01$ kg/m²-s

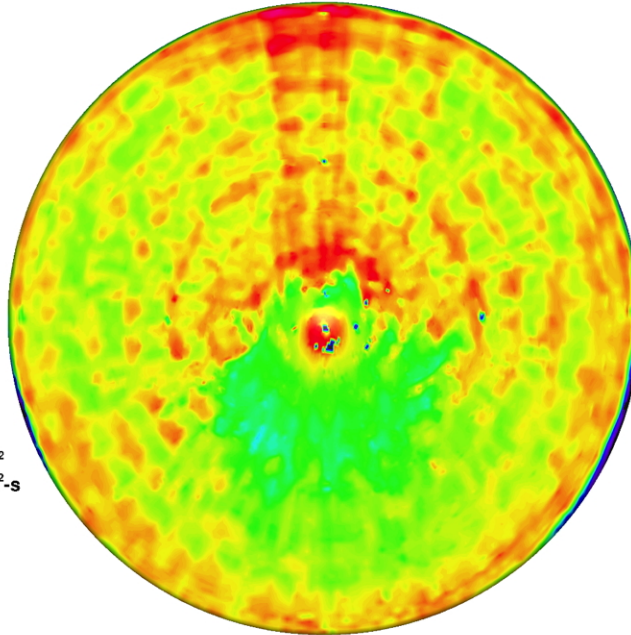
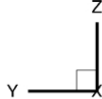
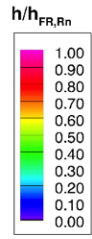


Figure 150. IRVE EDU Model, Run 117: $\alpha = 12$ deg, $Re_\infty = 6.63 \times 10^6$ /ft.

Configuration: IRVE-EDU
D = 6.0 in. / 0.1524 m
R_{nose} = 0.375 in. / 0.009525 m

LaRC 20-Inch Mach 6 Air Tunnel
Test 6979, Run 118



Re_∞ = 8.34E+06 /ft
Re_∞ = 2.74E+07 /m
α = 12-deg
U_∞ = 918.1 m/s
ρ_∞ = 1.25E-01
T_∞ = 58.6 K
H_{Total} - H_{300K} = 1.79E+05
q_{FR,Rn} = 1.73E+05 W/m²
h_{FR,Rn} = 9.64E-01 kg/m²-s

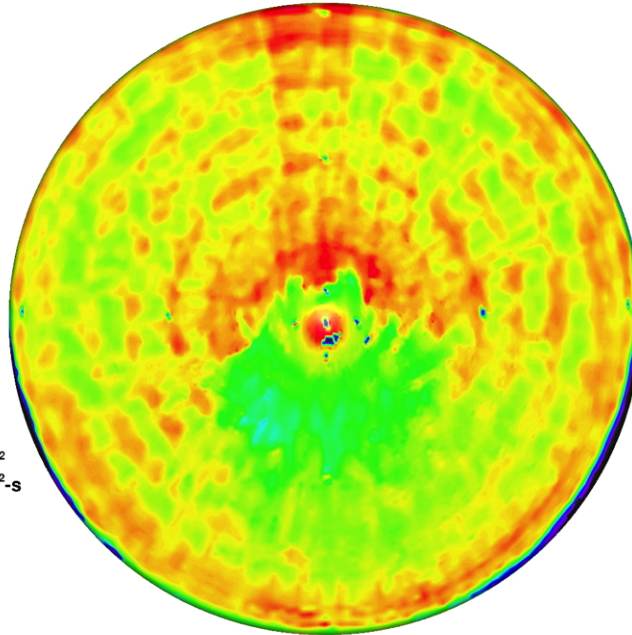
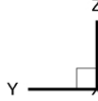
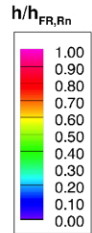


Figure 151. IRVE EDU Model, Run 118: α = 12 deg, Re_∞ = 8.33×10⁶/ft.

Configuration: IRVE-EDU
D = 6.0 in. / 0.1524 m
R_{nose} = 0.375 in. / 0.009525 m

LaRC 20-Inch Mach 6 Air Tunnel
Test 6979, Run 137



Re_∞ = 2.10E+06 /ft
Re_∞ = 6.89E+06 /m
α = 18-deg
U_∞ = 939.5 m/s
ρ_∞ = 3.25E-02
T_∞ = 61.9 K
H_{Total} - H_{300K} = 2.03E+05
q_{FR,Rn} = 1.02E+05 W/m²
h_{FR,Rn} = 5.01E-01 kg/m²-s

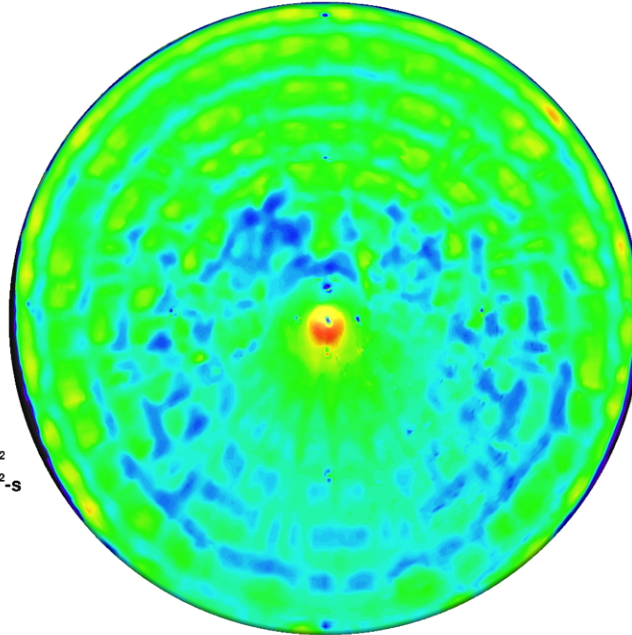
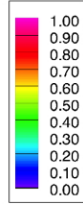


Figure 152. IRVE EDU Model, Run 137: α = 18 deg, Re_∞ = 2.10×10⁶/ft.

Configuration: IRVE-EDU
D = 6.0 in. / 0.1524 m
R_{nose} = 0.375 in. / 0.009525 m

LaRC 20-Inch Mach 6 Air Tunnel
Test 6979, Run 138

$h/h_{FR,Rn}$



$Re_\infty = 3.03E+06$ /ft
 $Re_\infty = 9.95E+06$ /m
 $\alpha = 18\text{-deg}$
 $U_\infty = 948.7$ m/s
 $\rho_\infty = 4.71E-02$
 $T_\infty = 62.5$ K
 $H_{Total} - H_{300K} = 2.12E+05$
 $q_{FR,Rn} = 1.30E+05$ W/m²
 $h_{FR,Rn} = 6.11E-01$ kg/m²·s

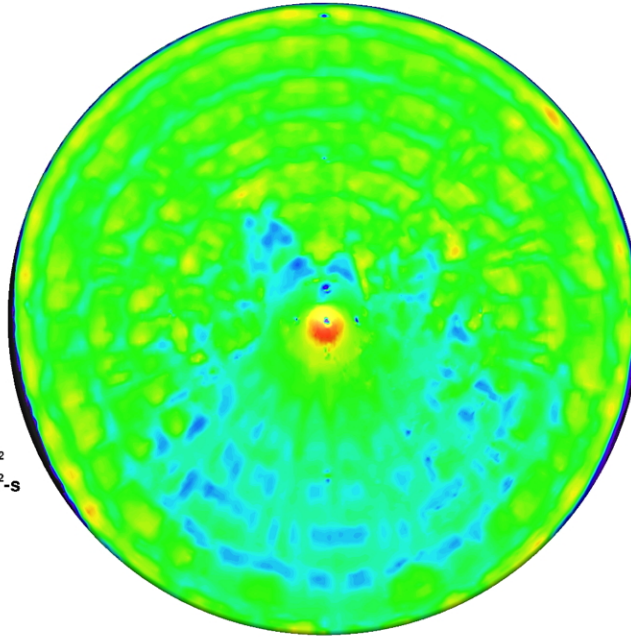
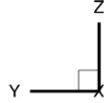
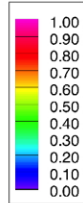


Figure 153. IRVE EDU Model, Run 138: $\alpha = 18$ deg, $Re_\infty = 3.03 \times 10^6$ /ft.

Configuration: IRVE-EDU
D = 6.0 in. / 0.1524 m
R_{nose} = 0.375 in. / 0.009525 m

LaRC 20-Inch Mach 6 Air Tunnel
Test 6979, Run 136

$h/h_{FR,Rn}$



$Re_\infty = 3.88E+06$ /ft
 $Re_\infty = 1.28E+07$ /m
 $\alpha = 18\text{-deg}$
 $U_\infty = 957.2$ m/s
 $\rho_\infty = 6.05E-02$
 $T_\infty = 63.3$ K
 $H_{Total} - H_{300K} = 2.21E+05$
 $q_{FR,Rn} = 1.55E+05$ W/m²
 $h_{FR,Rn} = 7.00E-01$ kg/m²·s

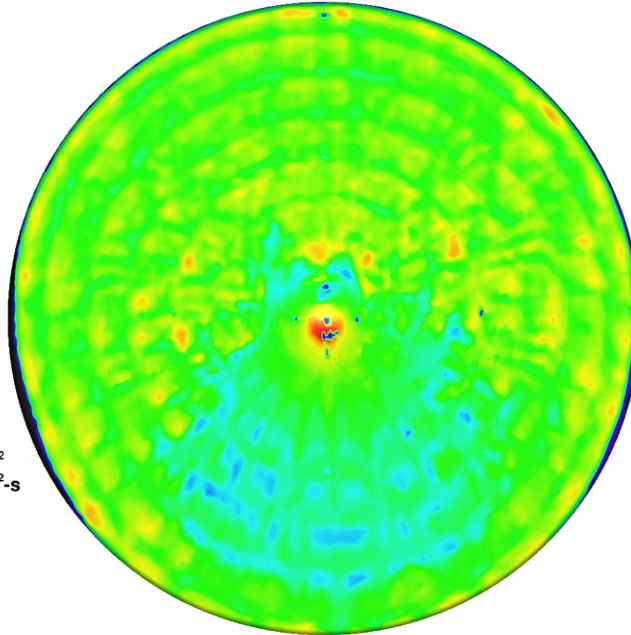
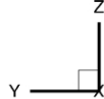
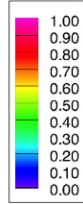


Figure 154. IRVE EDU Model, Run 136: $\alpha = 18$ deg, $Re_\infty = 3.88 \times 10^6$ /ft.

Configuration: IRVE-EDU
D = 6.0 in. / 0.1524 m
R_{nose} = 0.375 in. / 0.009525 m

LaRC 20-Inch Mach 6 Air Tunnel
Test 6979, Run 139

$h/h_{FR,Rn}$



$Re_\infty = 6.63E+06$ /ft
 $Re_\infty = 2.18E+07$ /m
 $\alpha = 18\text{-deg}$
 $U_\infty = 954.6$ m/s
 $\rho_\infty = 1.02E-01$
 $T_\infty = 62.6$ K
 $H_{Total} - H_{300K} = 2.17E+05$
 $q_{FR,Rn} = 1.98E+05$ W/m²
 $h_{FR,Rn} = 9.10E-01$ kg/m²·s

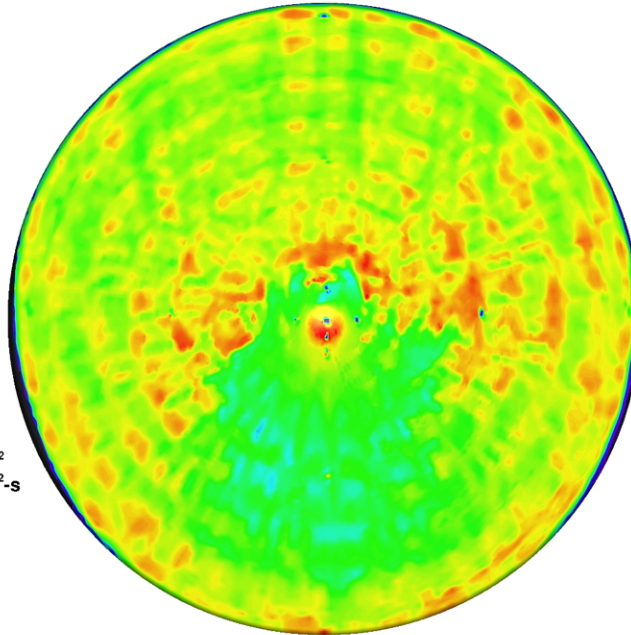
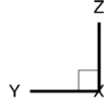
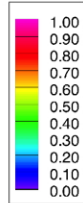


Figure 155. IRVE EDU Model, Run 139: $\alpha = 18$ deg, $Re_\infty = 6.33 \times 10^6$ /ft.

Configuration: IRVE-EDU
D = 6.0 in. / 0.1524 m
R_{nose} = 0.375 in. / 0.009525 m

LaRC 20-Inch Mach 6 Air Tunnel
Test 6979, Run 140

$h/h_{FR,Rn}$



$Re_\infty = 8.34E+06$ /ft
 $Re_\infty = 2.74E+07$ /m
 $\alpha = 18\text{-deg}$
 $U_\infty = 918.1$ m/s
 $\rho_\infty = 1.25E-01$
 $T_\infty = 58.6$ K
 $H_{Total} - H_{300K} = 1.79E+05$
 $q_{FR,Rn} = 1.73E+05$ W/m²
 $h_{FR,Rn} = 9.64E-01$ kg/m²·s

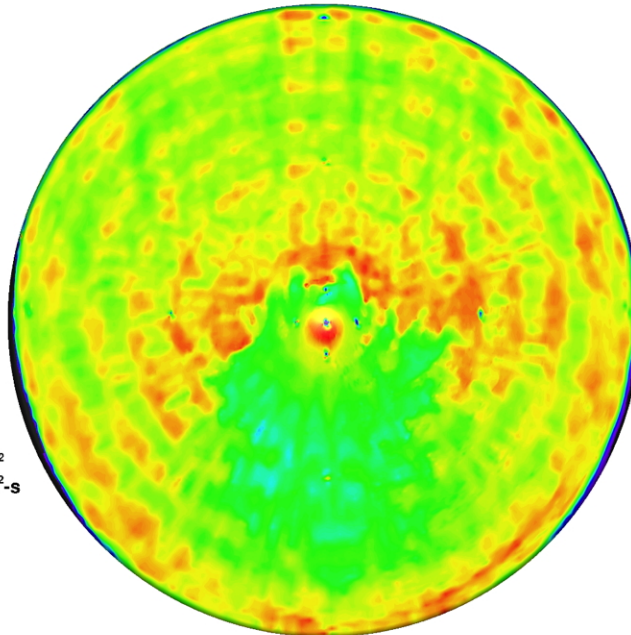
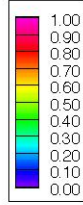


Figure 156. IRVE EDU Model, Run 140: $\alpha = 18$ deg, $Re_\infty = 8.34 \times 10^6$ /ft.

Configuration: IRVE-2.5
D = 6.0 in. / 0.1524 m
R_{nose} = 0.375 in. / 0.00953 m

LaRC 20-Inch Mach 6 Air Tunnel
Test 6979, Run 008

$h/h_{FR,Rn}$



$Re_\infty = 2.10E+06$ /ft
 $Re_\infty = 6.89E+06$ /m
 $\alpha = 0$ -deg
 $U_\infty = 939.5$ m/s
 $\rho_\infty = 3.25E-02$
 $T_\infty = 61.9$ K
 $H_{Total} - H_{300K} = 2.03E+05$
 $q_{FR,Rn} = 1.02E+05$ W/m²
 $h_{FR,Rn} = 5.01E-01$ kg/m²·s

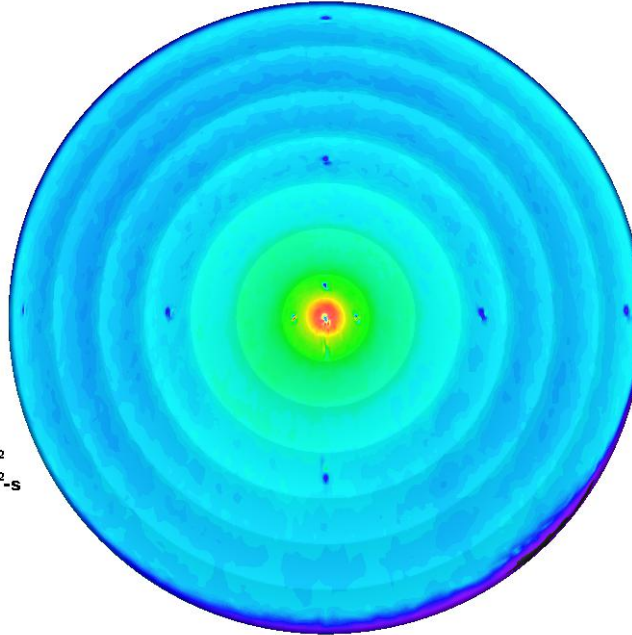
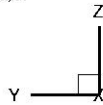
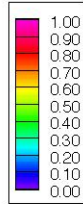


Figure 157. IRVE Scallop-2.5 Model, Run 8: $\alpha = 0$ deg, $Re_\infty = 2.10 \times 10^6$ /ft.

Configuration: IRVE-2.5
D = 6.0 in. / 0.1524 m
R_{nose} = 0.375 in. / 0.00953 m

LaRC 20-Inch Mach 6 Air Tunnel
Test 6979, Run 007

$h/h_{FR,Rn}$



$Re_\infty = 3.03E+06$ /ft
 $Re_\infty = 9.95E+06$ /m
 $\alpha = 0$ -deg
 $U_\infty = 948.7$ m/s
 $\rho_\infty = 4.71E-02$
 $T_\infty = 62.5$ K
 $H_{Total} - H_{300K} = 2.12E+05$
 $q_{FR,Rn} = 1.30E+05$ W/m²
 $h_{FR,Rn} = 6.11E-01$ kg/m²·s

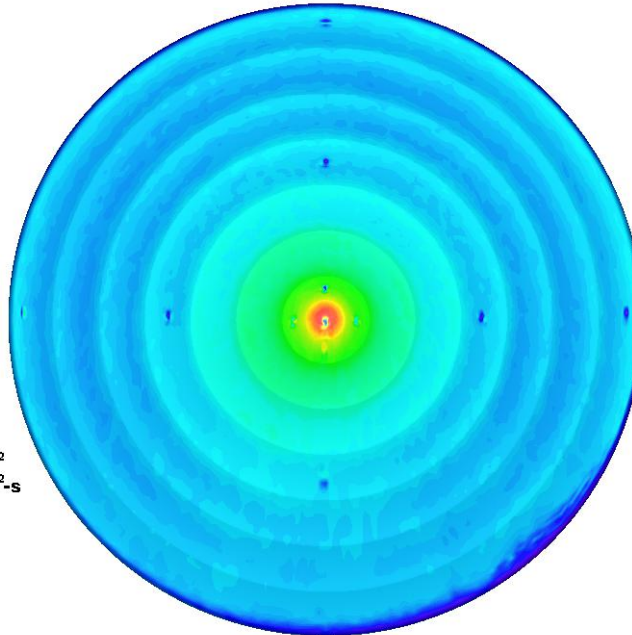
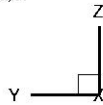
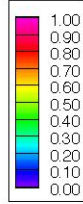


Figure 158. IRVE Scallop-2.5 Model, Run 7: $\alpha = 0$ deg, $Re_\infty = 3.03 \times 10^6$ /ft.

Configuration: IRVE-2.5
D = 6.0 in. / 0.1524 m
R_{nose} = 0.375 in. / 0.00953 m

LaRC 20-Inch Mach 6 Air Tunnel
Test 6979, Run 006

$h/h_{FR,Rn}$



$Re_\infty = 3.88E+06$ /ft
 $Re_\infty = 1.28E+07$ /m
 $\alpha = 0$ -deg
 $U_\infty = 957.2$ m/s
 $\rho_\infty = 6.05E-02$
 $T_\infty = 63.3$ K
 $H_{Total} - H_{300K} = 2.21E+05$
 $q_{FR,Rn} = 1.55E+05$ W/m²
 $h_{FR,Rn} = 7.00E-01$ kg/m²-s

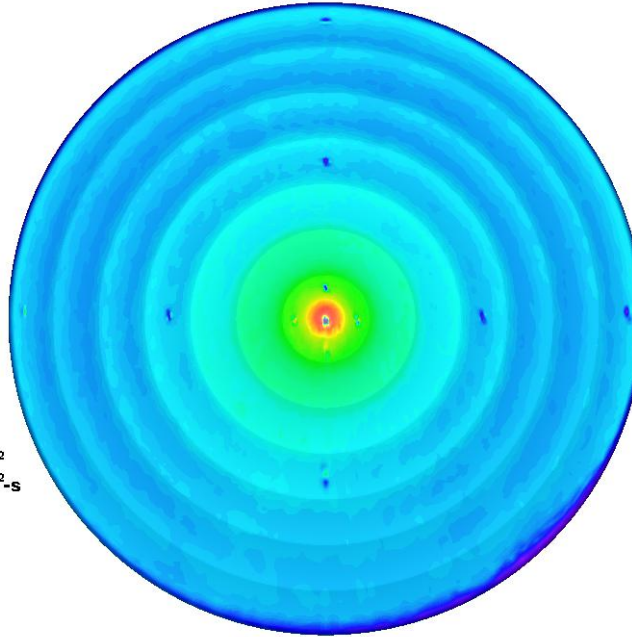
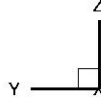
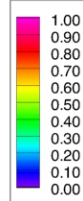


Figure 159. IRVE Scallop-2.5 Model, Run 6: $\alpha = 0$ deg, $Re_\infty = 3.88 \times 10^6$ /ft.

Configuration: IRVE-2.5
D = 6.0 in. / 0.1524 m
R_{nose} = 0.375 in. / 0.00953 m

LaRC 20-Inch Mach 6 Air Tunnel
Test 6979, Run 009

$h/h_{FR,Rn}$



$Re_\infty = 6.63E+06$ /ft
 $Re_\infty = 2.18E+07$ /m
 $\alpha = 0$ -deg
 $U_\infty = 954.6$ m/s
 $\rho_\infty = 1.02E-01$
 $T_\infty = 62.6$ K
 $H_{Total} - H_{300K} = 2.17E+05$
 $q_{FR,Rn} = 1.98E+05$ W/m²
 $h_{FR,Rn} = 9.10E-01$ kg/m²-s

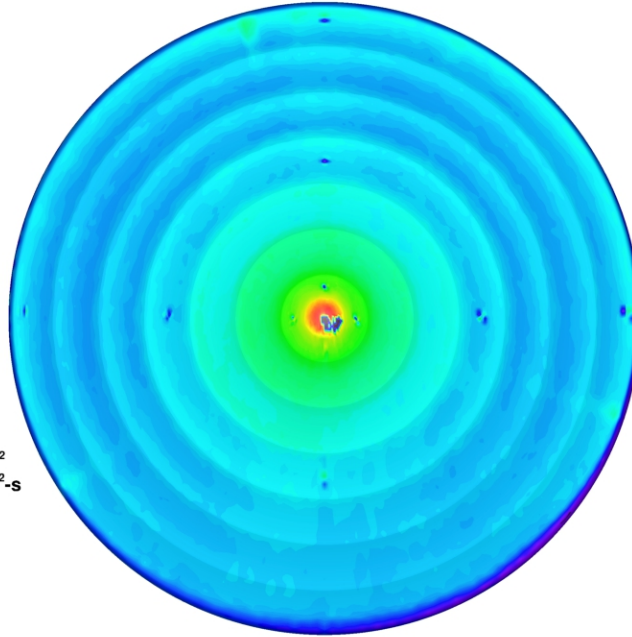
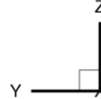
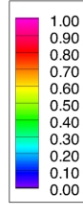


Figure 160. IRVE Scallop-2.5 Model, Run 9: $\alpha = 0$ deg, $Re_\infty = 6.63 \times 10^6$ /ft.

Configuration: IRVE-2.5
D = 6.0 in. / 0.1524 m
R_{nose} = 0.375 in. / 0.00953 m

LaRC 20-Inch Mach 6 Air Tunnel
Test 6979, Run 010

$h/h_{FR,Rn}$



$Re_\infty = 8.34E+06$ /ft
 $Re_\infty = 2.74E+07$ /m
 $\alpha = 0\text{-deg}$
 $U_\infty = 918.1$ m/s
 $\rho_\infty = 1.25E-01$
 $T_\infty = 58.6$ K
 $H_{Total} - H_{300K} = 1.79E+05$
 $q_{FR,Rn} = 1.73E+05$ W/m²
 $h_{FR,Rn} = 9.64E-01$ kg/m²-s

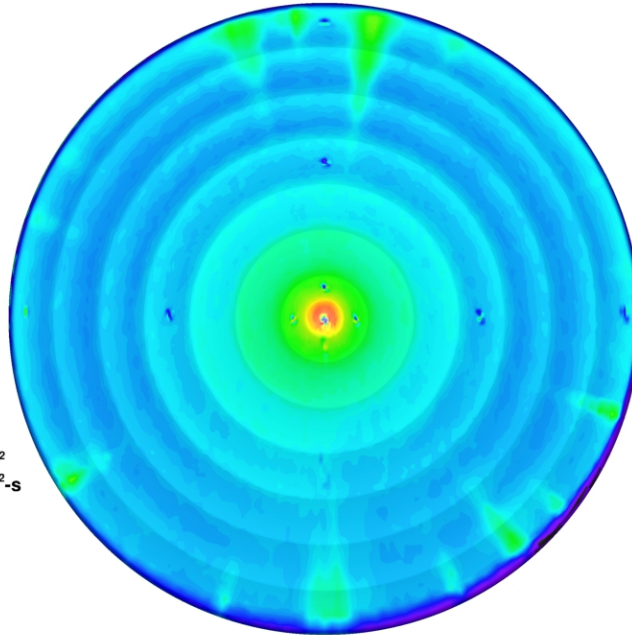
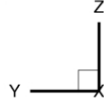
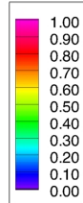


Figure 161. IRVE Scallop-2.5 Model, Run 10: $\alpha = 0$ deg, $Re_\infty = 8.33 \times 10^6$ /ft.

Configuration: IRVE-2.5
D = 6.0 in. / 0.1524 m
R_{nose} = 0.375 in. / 0.00953 m

LaRC 20-Inch Mach 6 Air Tunnel
Test 6979, Run 056

$h/h_{FR,Rn}$



$Re_\infty = 2.10E+06$ /ft
 $Re_\infty = 6.89E+06$ /m
 $\alpha = 6\text{-deg}$
 $U_\infty = 939.5$ m/s
 $\rho_\infty = 3.25E-02$
 $T_\infty = 61.9$ K
 $H_{Total} - H_{300K} = 2.03E+05$
 $q_{FR,Rn} = 1.02E+05$ W/m²
 $h_{FR,Rn} = 5.01E-01$ kg/m²-s

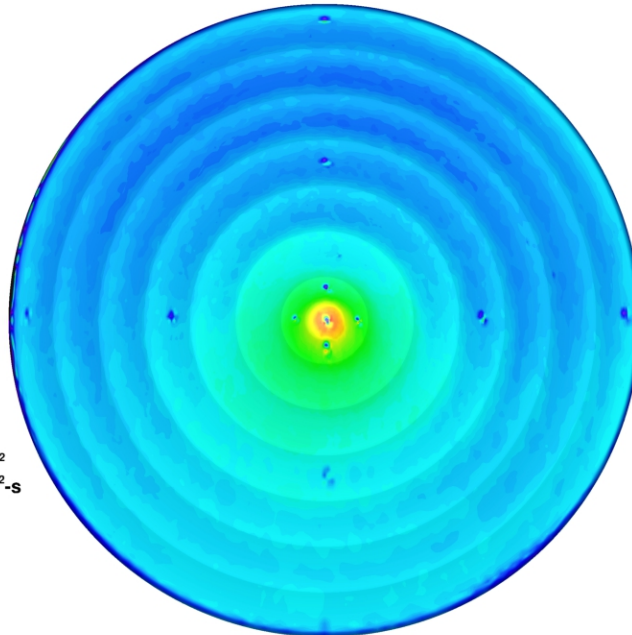
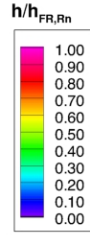


Figure 162. IRVE Scallop-2.5 Model, Run 56: $\alpha = 6$ deg, $Re_\infty = 2.10 \times 10^6$ /ft.

Configuration: IRVE-2.5
D = 6.0 in. / 0.1524 m
R_{nose} = 0.375 in. / 0.00953 m

IRVE Deflected OML Study
LaRC 20-Inch Mach 6 Air Tunnel
Test 6979, Run 057



Re_∞ = 3.03E+06 /ft
Re_∞ = 9.95E+06 /m
α = 6-deg
U_∞ = 948.7 m/s
ρ_∞ = 4.71E-02
T_∞ = 62.5 K
H_{Total}-H_{300K} = 2.12E+05
q_{FR,Rn} = 1.30E+05 W/m²
h_{FR,Rn} = 6.11E-01 kg/m²-s

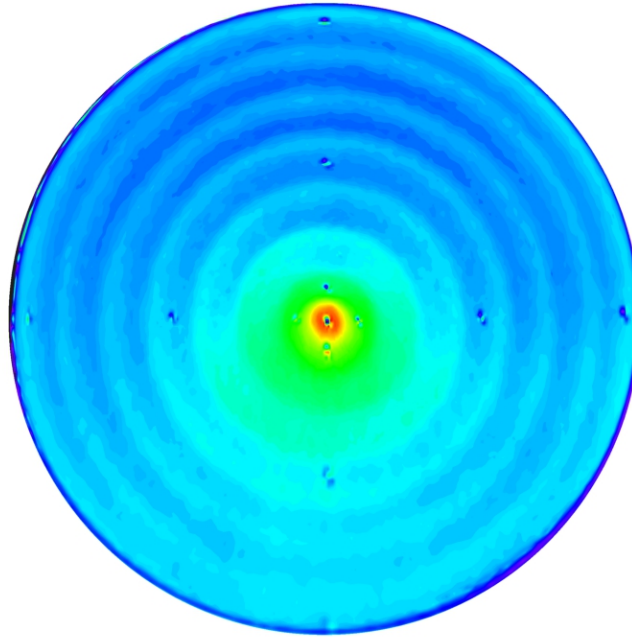
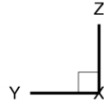
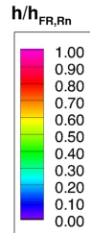


Figure 163. IRVE Scallop-2.5 Model, Run 57: α = 6 deg, Re_∞ = 3.03×10⁶/ft.

Configuration: IRVE-2.5
D = 6.0 in. / 0.1524 m
R_{nose} = 0.375 in. / 0.00953 m

LaRC 20-Inch Mach 6 Air Tunnel
Test 6979, Run 055



Re_∞ = 3.88E+06 /ft
Re_∞ = 1.28E+07 /m
α = 6-deg
U_∞ = 957.2 m/s
ρ_∞ = 6.05E-02
T_∞ = 63.3 K
H_{Total}-H_{300K} = 2.21E+05
q_{FR,Rn} = 1.55E+05 W/m²
h_{FR,Rn} = 7.00E-01 kg/m²-s

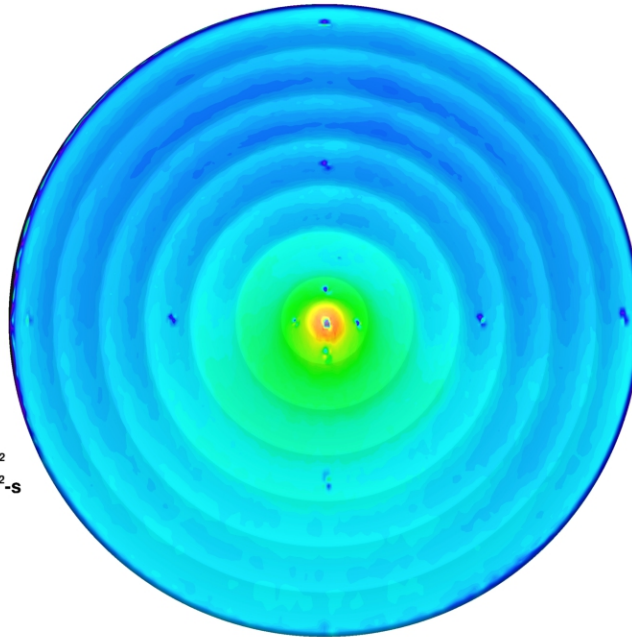
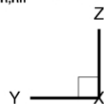
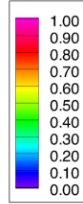


Figure 164. IRVE Scallop-2.5 Model, Run 55: α = 6 deg, Re_∞ = 3.88×10⁶/ft.

Configuration: IRVE-2.5
D = 6.0 in. / 0.1524 m
R_{nose} = 0.375 in. / 0.00953 m

LaRC 20-Inch Mach 6 Air Tunnel
Test 6979, Run 058

$h/h_{FR,Rn}$



$Re_{\infty} = 6.63E+06$ /ft
 $Re_{\infty} = 2.18E+07$ /m
 $\alpha = 6\text{-deg}$
 $U_{\infty} = 954.6$ m/s
 $\rho_{\infty} = 1.02E-01$
 $T_{\infty} = 62.6$ K
 $H_{Total} - H_{300K} = 2.17E+05$
 $q_{FR,Rn} = 1.98E+05$ W/m²
 $h_{FR,Rn} = 9.10E-01$ kg/m²-s

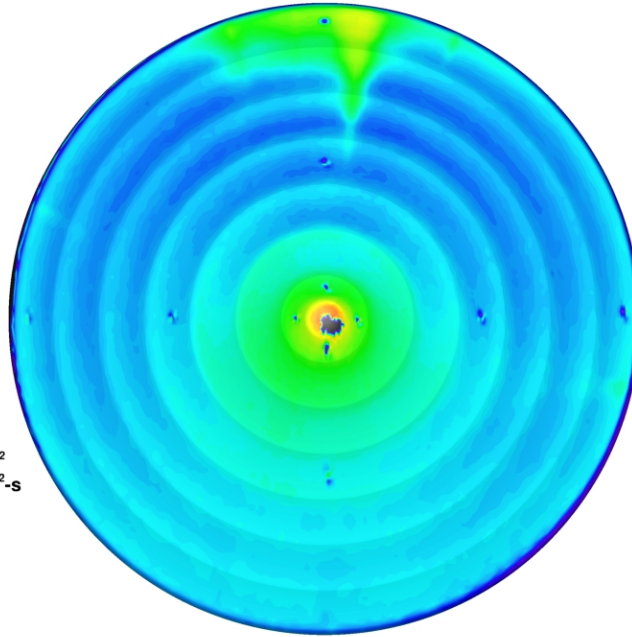
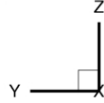
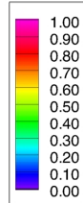


Figure 165. IRVE Scallop-2.5 Model, Run 58: $\alpha = 6$ deg, $Re_{\infty} = 6.63 \times 10^6$ /ft.

Configuration: IRVE-2.5
D = 6.0 in. / 0.1524 m
R_{nose} = 0.375 in. / 0.00953 m

LaRC 20-Inch Mach 6 Air Tunnel
Test 6979, Run 059

$h/h_{FR,Rn}$



$Re_{\infty} = 8.34E+06$ /ft
 $Re_{\infty} = 2.74E+07$ /m
 $\alpha = 6\text{-deg}$
 $U_{\infty} = 918.1$ m/s
 $\rho_{\infty} = 1.25E-01$
 $T_{\infty} = 58.6$ K
 $H_{Total} - H_{300K} = 1.79E+05$
 $q_{FR,Rn} = 1.73E+05$ W/m²
 $h_{FR,Rn} = 9.64E-01$ kg/m²-s

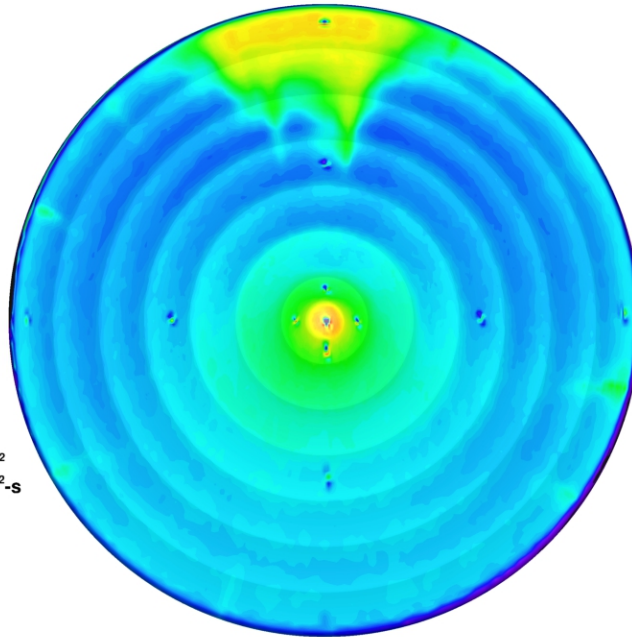
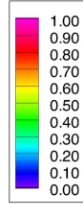


Figure 166. IRVE Scallop-2.5 Model, Run 59: $\alpha = 6$ deg, $Re_{\infty} = 8.33 \times 10^6$ /ft.

Configuration: IRVE-2.5
D = 6.0 in. / 0.1524 m
R_{nose} = 0.375 in. / 0.00953 m

LaRC 20-Inch Mach 6 Air Tunnel
Test 6979, Run 093

$h/h_{FR,Rn}$



$Re_\infty = 2.10E+06$ /ft
 $Re_\infty = 6.89E+06$ /m
 $\alpha = 12\text{-deg}$
 $U_\infty = 939.5$ m/s
 $\rho_\infty = 3.25E-02$
 $T_\infty = 61.9$ K
 $H_{Total} - H_{300K} = 2.03E+05$
 $q_{FR,Rn} = 1.02E+05$ W/m²
 $h_{FR,Rn} = 5.01E-01$ kg/m²-s

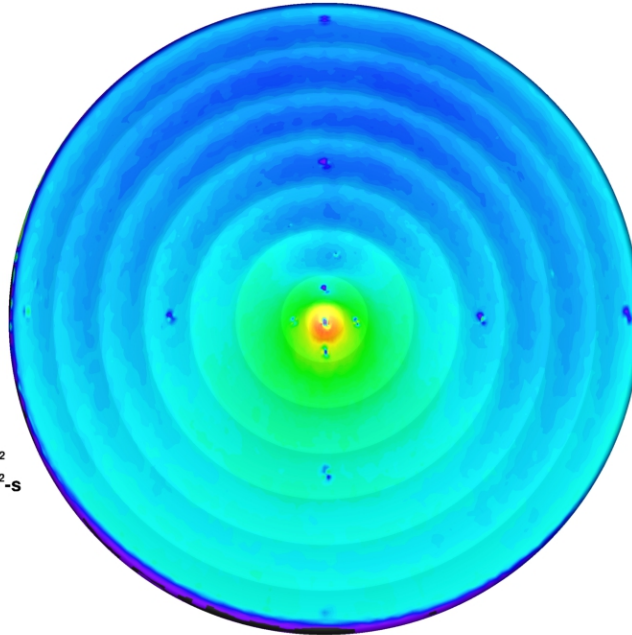
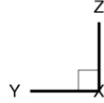
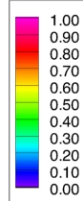


Figure 167. IRVE Scallop-2.5 Model, Run 93: $\alpha = 12$ deg, $Re_\infty = 2.10 \times 10^6$ /ft.

Configuration: IRVE-2.5
D = 6.0 in. / 0.1524 m
R_{nose} = 0.375 in. / 0.00953 m

LaRC 20-Inch Mach 6 Air Tunnel
Test 6979, Run 094

$h/h_{FR,Rn}$



$Re_\infty = 3.03E+06$ /ft
 $Re_\infty = 9.95E+06$ /m
 $\alpha = 12\text{-deg}$
 $U_\infty = 948.7$ m/s
 $\rho_\infty = 4.71E-02$
 $T_\infty = 62.5$ K
 $H_{Total} - H_{300K} = 2.12E+05$
 $q_{FR,Rn} = 1.30E+05$ W/m²
 $h_{FR,Rn} = 6.11E-01$ kg/m²-s

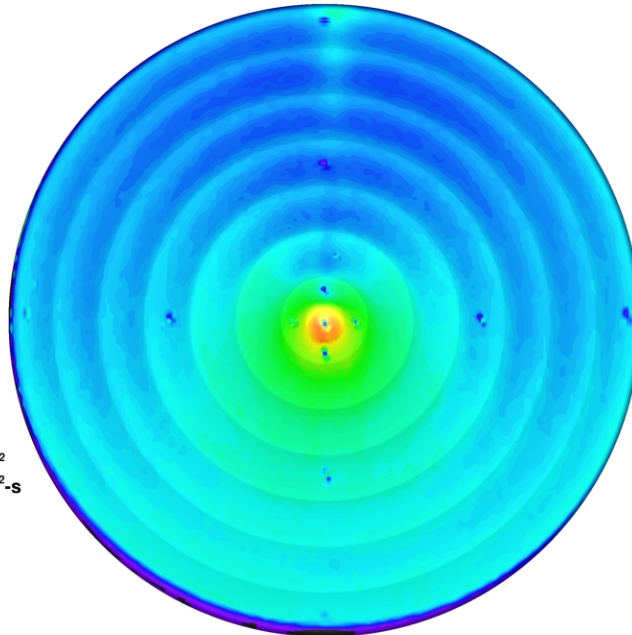
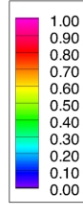


Figure 168. IRVE Scallop-2.5 Model, Run 94: $\alpha = 12$ deg, $Re_\infty = 3.03 \times 10^6$ /ft.

Configuration: IRVE-2.5
D = 6.0 in. / 0.1524 m
R_{nose} = 0.375 in. / 0.00953 m

LaRC 20-Inch Mach 6 Air Tunnel
Test 6979, Run 092

$h/h_{FR,Rn}$



$Re_\infty = 3.88E+06$ /ft
 $Re_\infty = 1.28E+07$ /m
 $\alpha = 12\text{-deg}$
 $U_\infty = 957.2$ m/s
 $\rho_\infty = 6.05E-02$
 $T_\infty = 63.3$ K
 $H_{Total} - H_{300K} = 2.21E+05$
 $q_{FR,Rn} = 1.55E+05$ W/m²
 $h_{FR,Rn} = 7.00E-01$ kg/m²-s

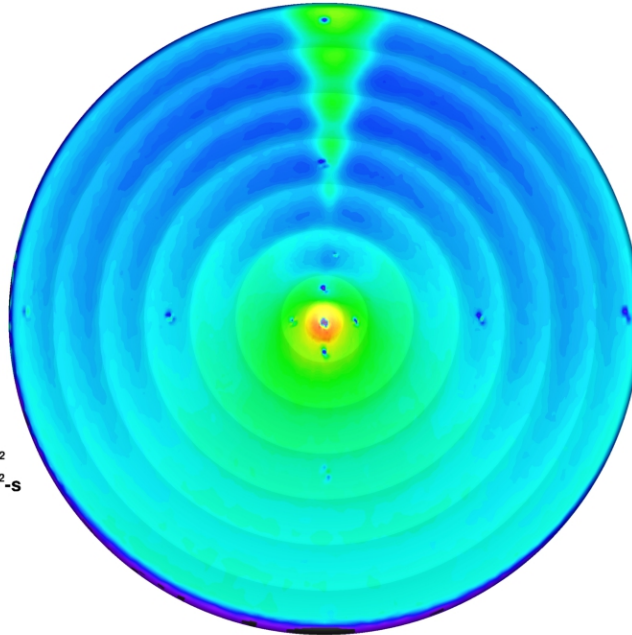
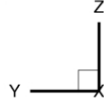
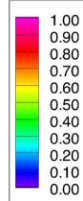


Figure 169. IRVE Scallop-2.5 Model, Run 92: $\alpha = 12$ deg, $Re_\infty = 3.88 \times 10^6$ /ft.

Configuration: IRVE-2.5
D = 6.0 in. / 0.1524 m
R_{nose} = 0.375 in. / 0.00953 m

LaRC 20-Inch Mach 6 Air Tunnel
Test 6979, Run 095

$h/h_{FR,Rn}$



$Re_\infty = 6.63E+06$ /ft
 $Re_\infty = 2.18E+07$ /m
 $\alpha = 12\text{-deg}$
 $U_\infty = 954.6$ m/s
 $\rho_\infty = 1.02E-01$
 $T_\infty = 62.6$ K
 $H_{Total} - H_{300K} = 2.17E+05$
 $q_{FR,Rn} = 1.98E+05$ W/m²
 $h_{FR,Rn} = 9.10E-01$ kg/m²-s

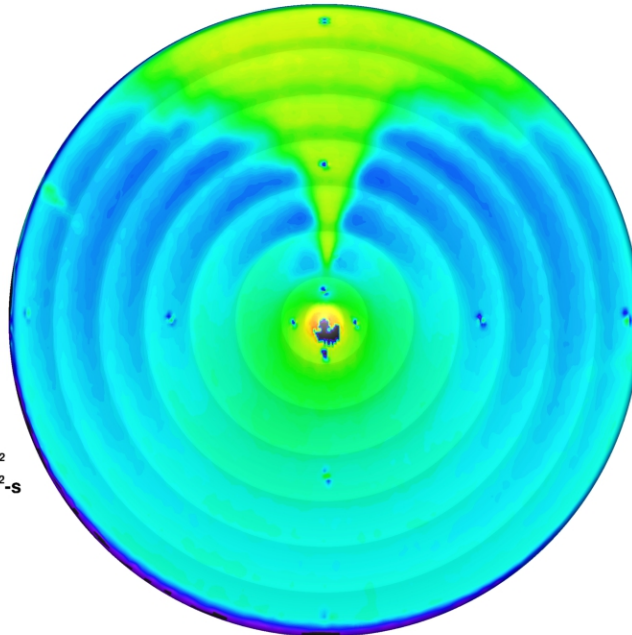
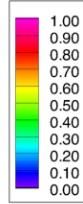


Figure 170. IRVE Scallop-2.5 Model, Run 95: $\alpha = 12$ deg, $Re_\infty = 6.63 \times 10^6$ /ft.

Configuration: IRVE-2.5
D = 6.0 in. / 0.1524 m
R_{nose} = 0.375 in. / 0.00953 m

LaRC 20-Inch Mach 6 Air Tunnel
Test 6979, Run 096

$h/h_{FR,Rn}$



$Re_\infty = 8.34E+06$ /ft
 $Re_\infty = 2.74E+07$ /m
 $\alpha = 12$ -deg
 $U_\infty = 918.1$ m/s
 $\rho_\infty = 1.25E-01$
 $T_\infty = 58.6$ K
 $H_{Total} - H_{300K} = 1.79E+05$
 $q_{FR,Rn} = 1.73E+05$ W/m²
 $h_{FR,Rn} = 9.64E-01$ kg/m²-s

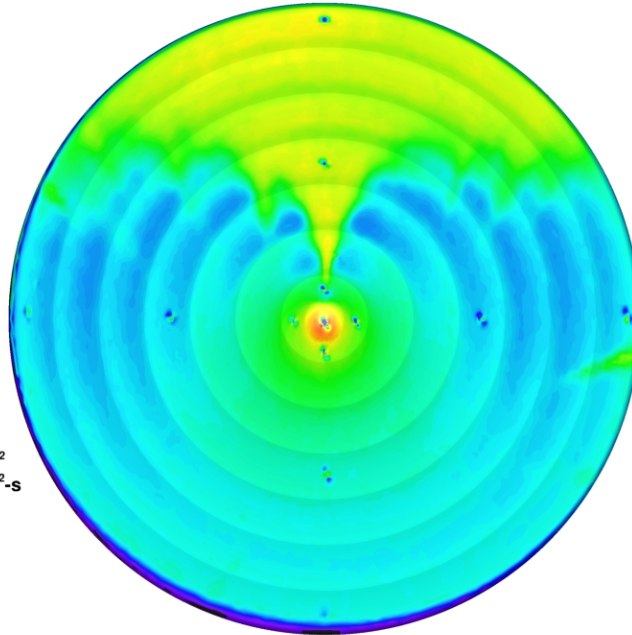
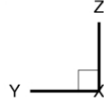
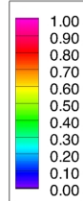


Figure 171. IRVE Scallop-2.5 Model, Run 96: $\alpha = 12$ deg, $Re_\infty = 8.33 \times 10^6$ /ft.

Configuration: IRVE-2.5
D = 6.0 in. / 0.1524 m
R_{nose} = 0.375 in. / 0.00953 m

LaRC 20-Inch Mach 6 Air Tunnel
Test 6979, Run 157

$h/h_{FR,Rn}$



$Re_\infty = 2.10E+06$ /ft
 $Re_\infty = 6.89E+06$ /m
 $\alpha = 18$ -deg
 $U_\infty = 939.5$ m/s
 $\rho_\infty = 3.25E-02$
 $T_\infty = 61.9$ K
 $H_{Total} - H_{300K} = 2.03E+05$
 $q_{FR,Rn} = 1.02E+05$ W/m²
 $h_{FR,Rn} = 5.01E-01$ kg/m²-s

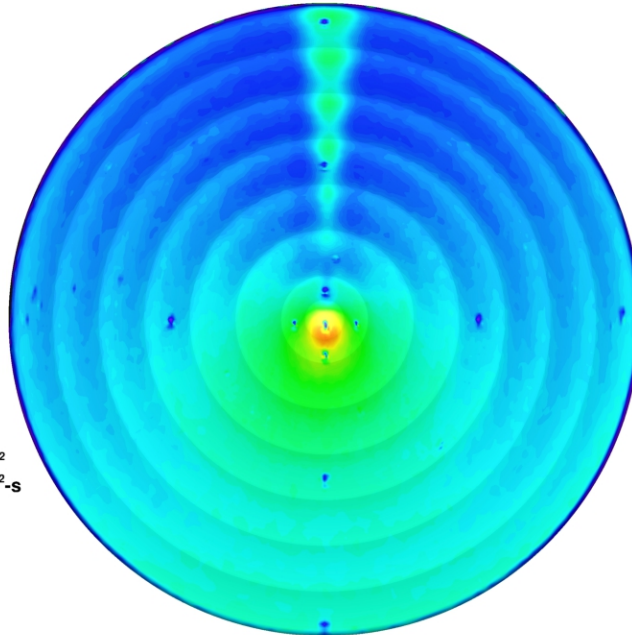
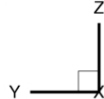
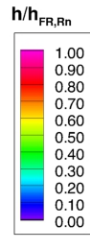


Figure 172. IRVE Scallop-2.5 Model, Run 157: $\alpha = 18$ deg, $Re_\infty = 2.10 \times 10^6$ /ft.

Configuration: IRVE-2.5
D = 6.0 in. / 0.1524 m
R_{nose} = 0.375 in. / 0.00953 m

IRVE Deflected OML Study
LaRC 20-Inch Mach 6 Air Tunnel
Test 6979, Run 158



Re_∞ = 3.03E+06 /ft
Re_∞ = 9.95E+06 /m
α = 18-deg
U_∞ = 948.7 m/s
ρ_∞ = 4.71E-02
T_∞ = 62.5 K
H_{Total} - H_{300K} = 2.12E+05
q_{FR,Rn} = 1.30E+05 W/m²
h_{FR,Rn} = 6.11E-01 kg/m²-s

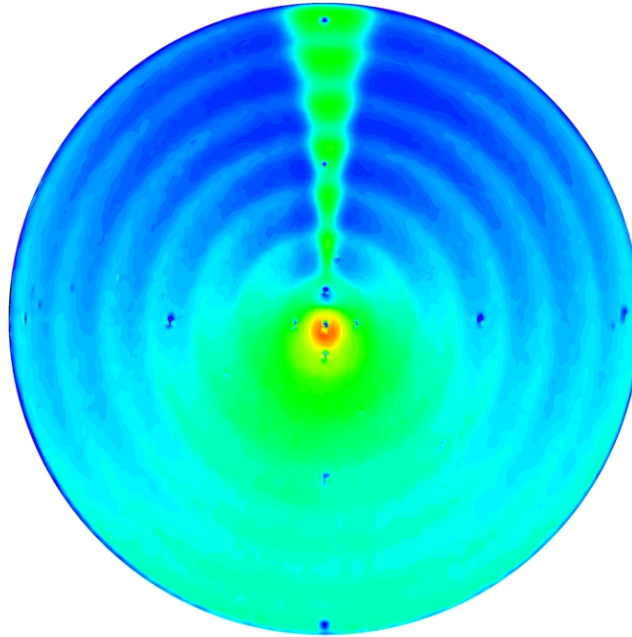
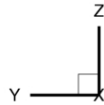
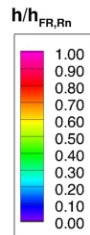


Figure 173. IRVE Scallop-2.5 Model, Run 158: α = 18 deg, Re_∞ = 3.03×10⁶/ft.

Configuration: IRVE-2.5
D = 6.0 in. / 0.1524 m
R_{nose} = 0.375 in. / 0.00953 m

LaRC 20-Inch Mach 6 Air Tunnel
Test 6979, Run 156



Re_∞ = 3.88E+06 /ft
Re_∞ = 1.28E+07 /m
α = 18-deg
U_∞ = 957.2 m/s
ρ_∞ = 6.05E-02
T_∞ = 63.3 K
H_{Total} - H_{300K} = 2.21E+05
q_{FR,Rn} = 1.55E+05 W/m²
h_{FR,Rn} = 7.00E-01 kg/m²-s

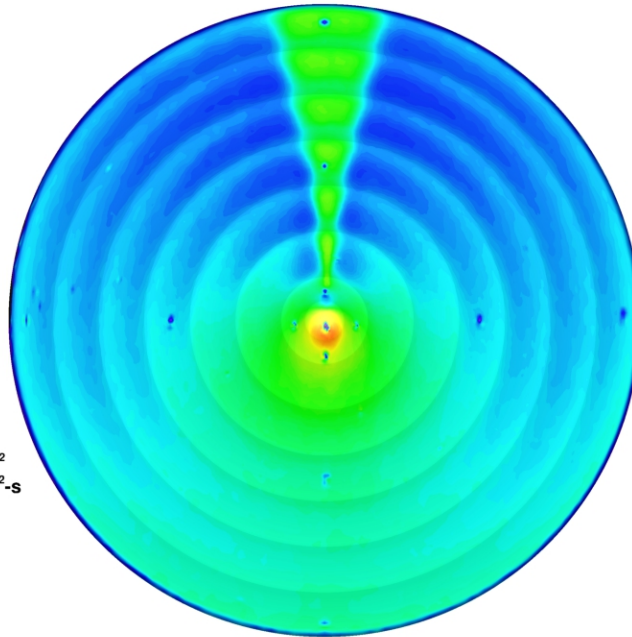
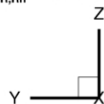
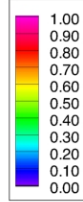


Figure 174. IRVE Scallop-2.5 Model, Run 156: α = 18 deg, Re_∞ = 3.88×10⁶/ft.

Configuration: IRVE-2.5
D = 6.0 in. / 0.1524 m
R_{nose} = 0.375 in. / 0.00953 m

LaRC 20-Inch Mach 6 Air Tunnel
Test 6979, Run 159

$h/h_{FR,Rn}$



$Re_\infty = 6.63E+06$ /ft
 $Re_\infty = 2.18E+07$ /m
 $\alpha = 18\text{-deg}$
 $U_\infty = 954.6$ m/s
 $\rho_\infty = 1.02E-01$
 $T_\infty = 62.6$ K
 $H_{Total} - H_{300K} = 2.17E+05$
 $q_{FR,Rn} = 1.98E+05$ W/m²
 $h_{FR,Rn} = 9.10E-01$ kg/m²-s

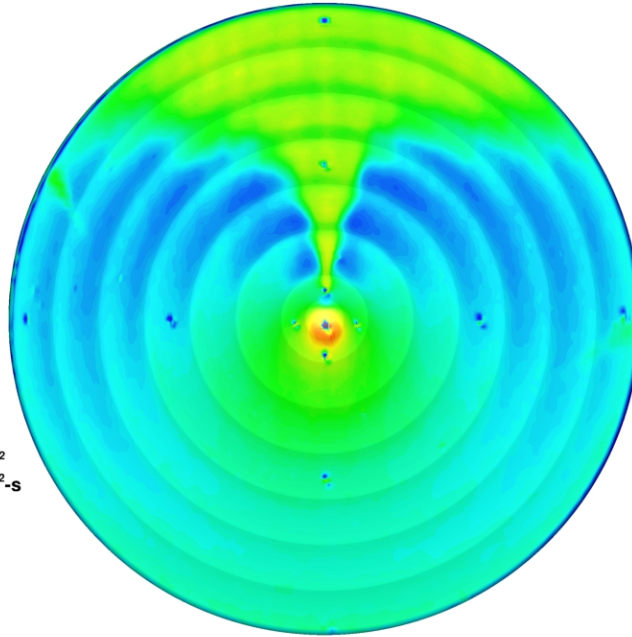
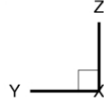
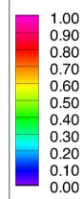


Figure 175. IRVE Scallop-2.5 Model, Run 159: $\alpha = 18$ deg, $Re_\infty = 6.63 \times 10^6$ /ft.

Configuration: IRVE-2.5
D = 6.0 in. / 0.1524 m
R_{nose} = 0.375 in. / 0.00953 m

LaRC 20-Inch Mach 6 Air Tunnel
Test 6979, Run 160

$h/h_{FR,Rn}$



$Re_\infty = 8.34E+06$ /ft
 $Re_\infty = 2.74E+07$ /m
 $\alpha = 18\text{-deg}$
 $U_\infty = 918.1$ m/s
 $\rho_\infty = 1.25E-01$
 $T_\infty = 58.6$ K
 $H_{Total} - H_{300K} = 1.79E+05$
 $q_{FR,Rn} = 1.73E+05$ W/m²
 $h_{FR,Rn} = 9.64E-01$ kg/m²-s

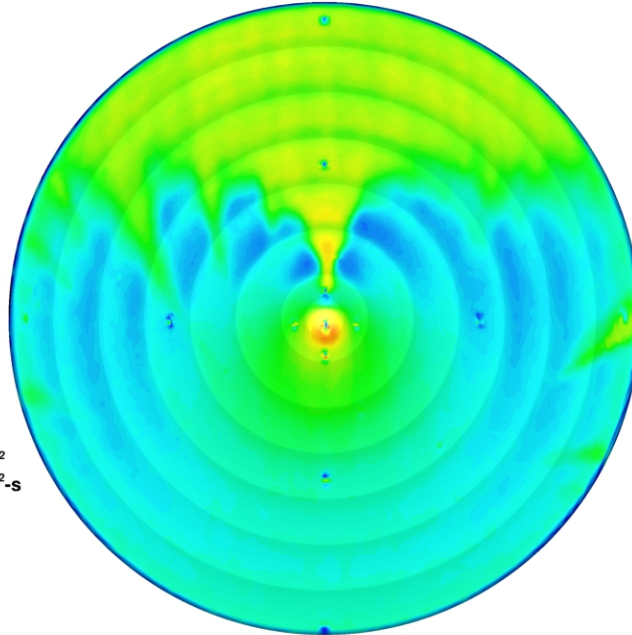
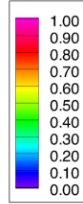


Figure 176. IRVE Scallop-2.5 Model, Run 160: $\alpha = 18$ deg, $Re_\infty = 8.33 \times 10^6$ /ft.

Configuration: IRVE-5
D = 6.0 in. / 0.1524 m
R_{nose} = 0.375 in. / 0.00953 m

LaRC 20-Inch Mach 6 Air Tunnel
Test 6979, Run 013

$h/h_{FR,Rn}$



$Re_\infty = 2.10E+06$ /ft
 $Re_\infty = 6.89E+06$ /m
 $\alpha = 0\text{-deg}$
 $U_\infty = 939.5$ m/s
 $\rho_\infty = 3.25E-02$
 $T_\infty = 61.9$ K
 $H_{Total} - H_{300K} = 2.03E+05$
 $q_{FR,Rn} = 1.02E+05$ W/m²
 $h_{FR,Rn} = 5.01E-01$ kg/m²-s

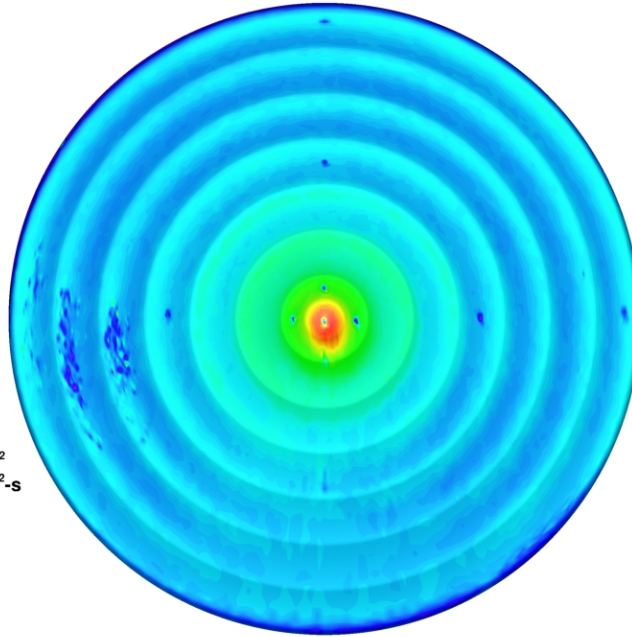
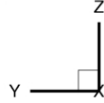
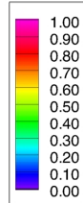


Figure 177. IRVE Scallop-5 Model, Run 13: $\alpha = 0$ deg, $Re_\infty = 2.10 \times 10^6$ /ft.

Configuration: IRVE-5
D = 6.0 in. / 0.1524 m
R_{nose} = 0.375 in. / 0.00953 m

LaRC 20-Inch Mach 6 Air Tunnel
Test 6979, Run 012

$h/h_{FR,Rn}$



$Re_\infty = 3.03E+06$ /ft
 $Re_\infty = 9.95E+06$ /m
 $\alpha = 0\text{-deg}$
 $U_\infty = 948.7$ m/s
 $\rho_\infty = 4.71E-02$
 $T_\infty = 62.5$ K
 $H_{Total} - H_{300K} = 2.12E+05$
 $q_{FR,Rn} = 1.30E+05$ W/m²
 $h_{FR,Rn} = 6.11E-01$ kg/m²-s

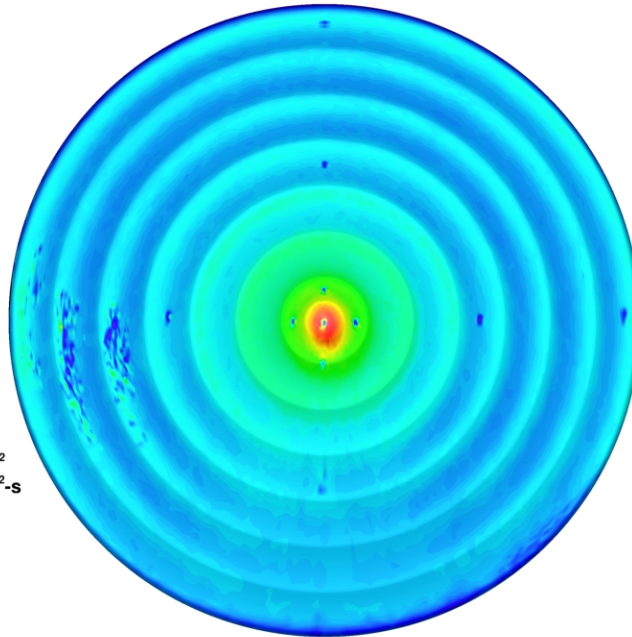
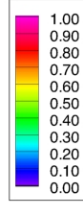


Figure 178. IRVE Scallop-5 Model, Run 12: $\alpha = 0$ deg, $Re_\infty = 3.03 \times 10^6$ /ft.

Configuration: IRVE-5
D = 6.0 in. / 0.1524 m
R_{nose} = 0.375 in. / 0.00953 m

LaRC 20-Inch Mach 6 Air Tunnel
Test 6979, Run 011

$h/h_{FR,Rn}$



$Re_\infty = 3.88E+06$ /ft
 $Re_\infty = 1.28E+07$ /m
 $\alpha = 0$ -deg
 $U_\infty = 957.2$ m/s
 $\rho_\infty = 6.05E-02$
 $T_\infty = 63.3$ K
 $H_{Total} - H_{300K} = 2.21E+05$
 $q_{FR,Rn} = 1.55E+05$ W/m²
 $h_{FR,Rn} = 7.00E-01$ kg/m²-s

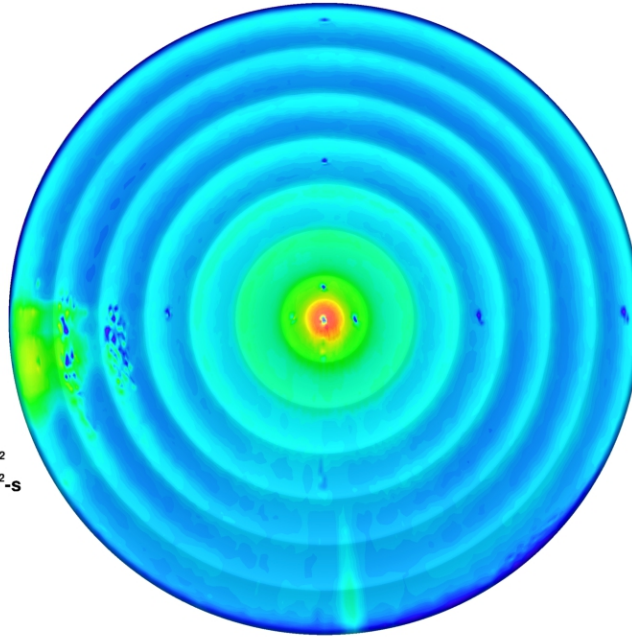
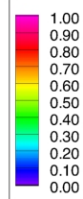


Figure 179. IRVE Scallop-5 Model, Run 11: $\alpha = 0$ deg, $Re_\infty = 3.88 \times 10^6$ /ft.

Configuration: IRVE-5
D = 6.0 in. / 0.1524 m
R_{nose} = 0.375 in. / 0.00953 m

LaRC 20-Inch Mach 6 Air Tunnel
Test 6979, Run 014

$h/h_{FR,Rn}$



$Re_\infty = 6.63E+06$ /ft
 $Re_\infty = 2.18E+07$ /m
 $\alpha = 0$ -deg
 $U_\infty = 954.6$ m/s
 $\rho_\infty = 1.02E-01$
 $T_\infty = 62.6$ K
 $H_{Total} - H_{300K} = 2.17E+05$
 $q_{FR,Rn} = 1.98E+05$ W/m²
 $h_{FR,Rn} = 9.10E-01$ kg/m²-s

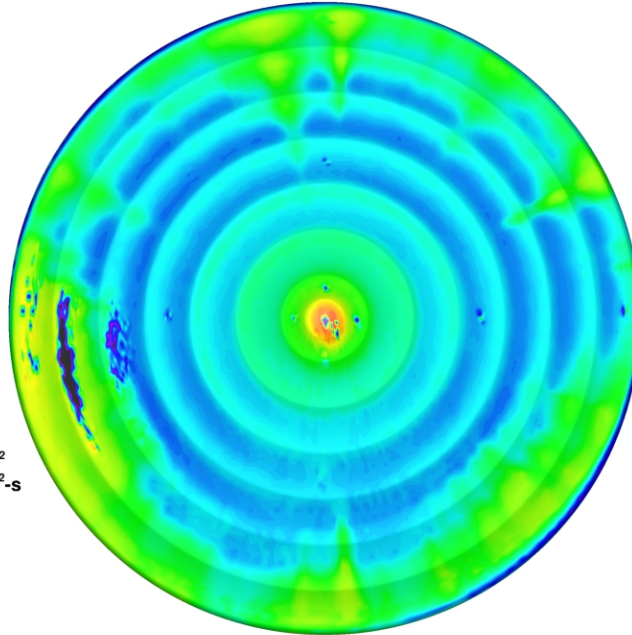
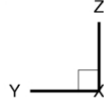
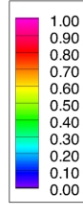


Figure 180. IRVE Scallop-5 Model, Run 14: $\alpha = 0$ deg, $Re_\infty = 6.63 \times 10^6$ /ft.

Configuration: IRVE-5
D = 6.0 in. / 0.1524 m
R_{nose} = 0.375 in. / 0.00953 m

LaRC 20-Inch Mach 6 Air Tunnel
Test 6979, Run 015

$h/h_{FR,Rn}$



$Re_\infty = 8.34E+06$ /ft
 $Re_\infty = 2.74E+07$ /m
 $\alpha = 0\text{-deg}$
 $U_\infty = 918.1$ m/s
 $\rho_\infty = 1.25E-01$
 $T_\infty = 58.6$ K
 $H_{Total} - H_{300K} = 1.79E+05$
 $q_{FR,Rn} = 1.73E+05$ W/m²
 $h_{FR,Rn} = 9.64E-01$ kg/m²-s

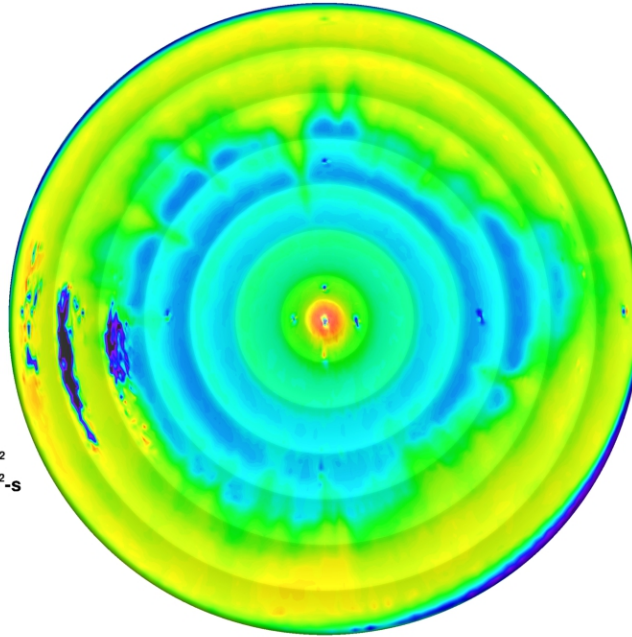
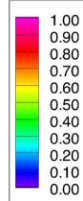


Figure 181. IRVE Scallop-5 Model, Run 15: $\alpha = 0$ deg, $Re_\infty = 8.33 \times 10^6$ /ft.

Configuration: IRVE-5
D = 6.0 in. / 0.1524 m
R_{nose} = 0.375 in. / 0.00953 m

LaRC 20-Inch Mach 6 Air Tunnel
Test 6979, Run 065

$h/h_{FR,Rn}$



$Re_\infty = 2.10E+06$ /ft
 $Re_\infty = 6.89E+06$ /m
 $\alpha = 6\text{-deg}$
 $U_\infty = 939.5$ m/s
 $\rho_\infty = 3.25E-02$
 $T_\infty = 61.9$ K
 $H_{Total} - H_{300K} = 2.03E+05$
 $q_{FR,Rn} = 1.02E+05$ W/m²
 $h_{FR,Rn} = 5.01E-01$ kg/m²-s

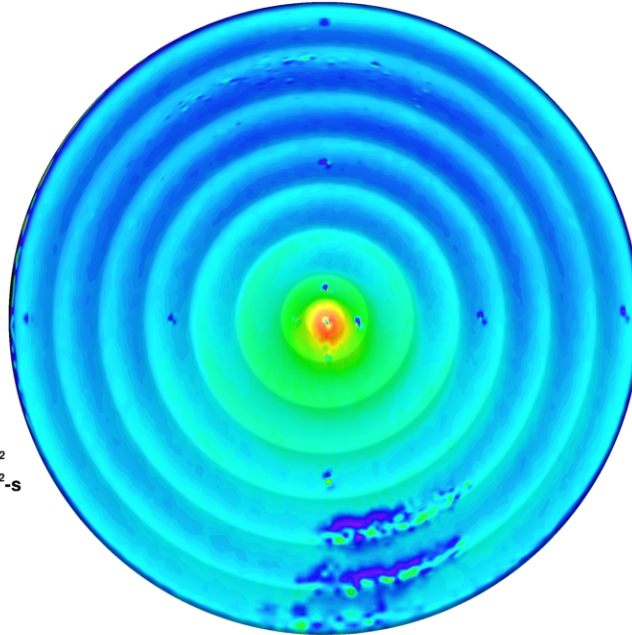
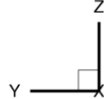
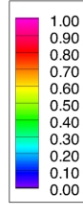


Figure 182. IRVE Scallop-5 Model, Run 65: $\alpha = 6$ deg, $Re_\infty = 2.10 \times 10^6$ /ft.

Configuration: IRVE-5
D = 6.0 in. / 0.1524 m
R_{nose} = 0.375 in. / 0.00953 m

LaRC 20-Inch Mach 6 Air Tunnel
Test 6979, Run 066

$h/h_{FR,Rn}$



$Re_\infty = 3.88E+06$ /ft
 $Re_\infty = 1.28E+07$ /m
 $\alpha = 6\text{-deg}$
 $U_\infty = 957.2$ m/s
 $\rho_\infty = 6.05E-02$
 $T_\infty = 63.3$ K
 $H_{Total} - H_{300K} = 2.21E+05$
 $q_{FR,Rn} = 1.55E+05$ W/m²
 $h_{FR,Rn} = 7.00E-01$ kg/m²-s

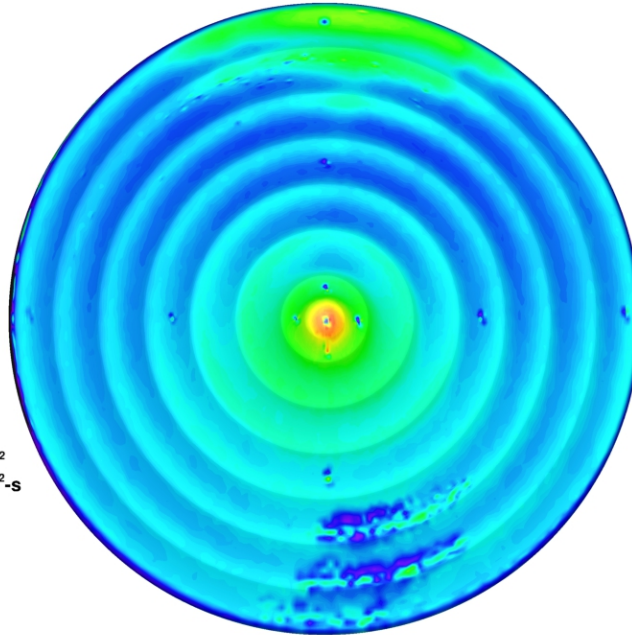
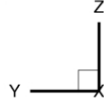
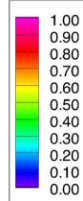


Figure 183. IRVE Scallop-5 Model, Run 66: $\alpha = 6$ deg, $Re_\infty = 3.03 \times 10^6$ /ft.

Configuration: IRVE-5
D = 6.0 in. / 0.1524 m
R_{nose} = 0.375 in. / 0.00953 m

LaRC 20-Inch Mach 6 Air Tunnel
Test 6979, Run 067

$h/h_{FR,Rn}$



$Re_\infty = 3.88E+06$ /ft
 $Re_\infty = 1.28E+07$ /m
 $\alpha = 6\text{-deg}$
 $U_\infty = 957.2$ m/s
 $\rho_\infty = 6.05E-02$
 $T_\infty = 63.3$ K
 $H_{Total} - H_{300K} = 2.21E+05$
 $q_{FR,Rn} = 1.55E+05$ W/m²
 $h_{FR,Rn} = 7.00E-01$ kg/m²-s

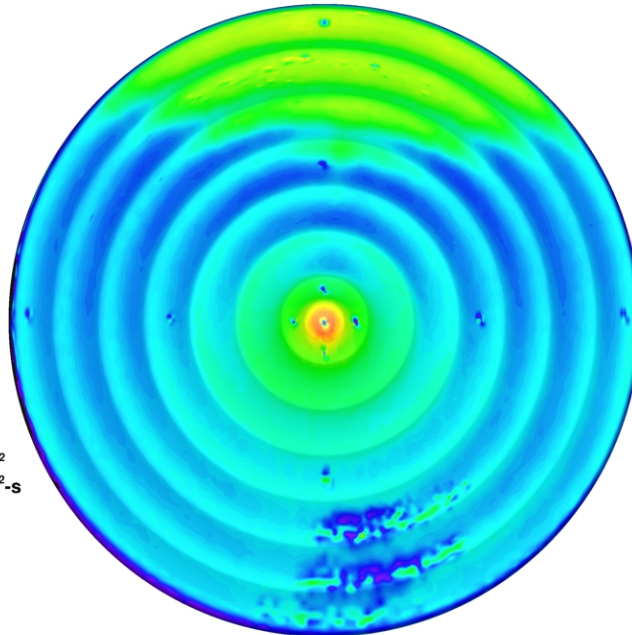
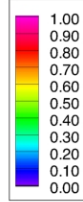


Figure 184. IRVE Scallop-5 Model, Run 67: $\alpha = 6$ deg, $Re_\infty = 3.88 \times 10^6$ /ft.

Configuration: IRVE-5
D = 6.0 in. / 0.1524 m
R_{nose} = 0.375 in. / 0.00953 m

LaRC 20-Inch Mach 6 Air Tunnel
Test 6979, Run 068

$h/h_{FR,Rn}$



$Re_\infty = 6.63E+06$ /ft
 $Re_\infty = 2.18E+07$ /m
 $\alpha = 6\text{-deg}$
 $U_\infty = 954.6$ m/s
 $\rho_\infty = 1.02E-01$
 $T_\infty = 62.6$ K
 $H_{Total} - H_{300K} = 2.17E+05$
 $q_{FR,Rn} = 1.98E+05$ W/m²
 $h_{FR,Rn} = 9.10E-01$ kg/m²-s

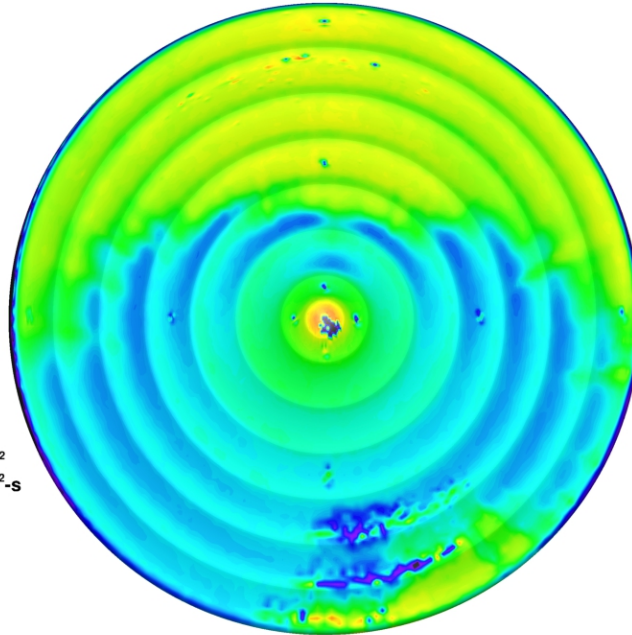
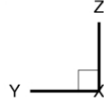
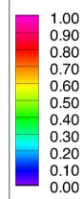


Figure 185. IRVE Scallop-5 Model, Run 68: $\alpha = 6$ deg, $Re_\infty = 6.63 \times 10^6$ /ft.

Configuration: IRVE-5
D = 6.0 in. / 0.1524 m
R_{nose} = 0.375 in. / 0.00953 m

LaRC 20-Inch Mach 6 Air Tunnel
Test 6979, Run 069

$h/h_{FR,Rn}$



$Re_\infty = 8.34E+06$ /ft
 $Re_\infty = 2.74E+07$ /m
 $\alpha = 6\text{-deg}$
 $U_\infty = 918.1$ m/s
 $\rho_\infty = 1.25E-01$
 $T_\infty = 58.6$ K
 $H_{Total} - H_{300K} = 1.79E+05$
 $q_{FR,Rn} = 1.73E+05$ W/m²
 $h_{FR,Rn} = 9.64E-01$ kg/m²-s

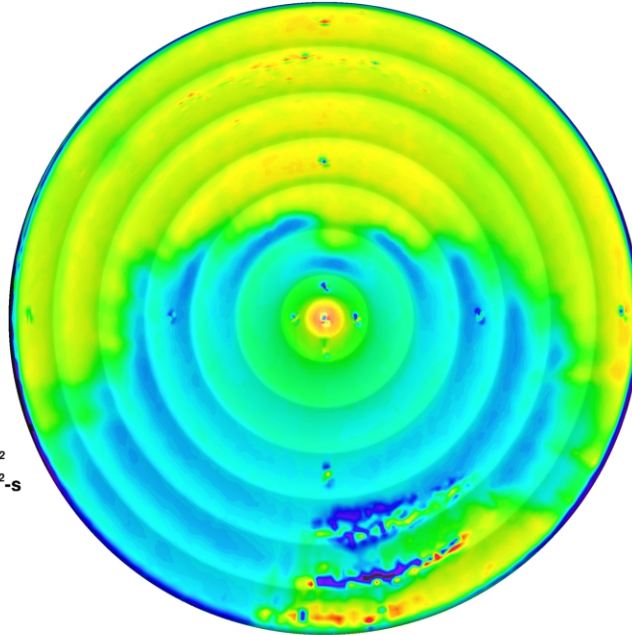
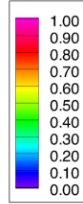


Figure 186. IRVE Scallop-5 Model, Run 69: $\alpha = 6$ deg, $Re_\infty = 8.33 \times 10^6$ /ft.

Configuration: IRVE-5
D = 6.0 in. / 0.1524 m
R_{nose} = 0.375 in. / 0.00953 m

LaRC 20-Inch Mach 6 Air Tunnel
Test 6979, Run 185

$h/h_{FR,Rn}$



$Re_\infty = 2.10E+06$ /ft
 $Re_\infty = 6.89E+06$ /m
 $\alpha = 12$ -deg
 $U_\infty = 939.5$ m/s
 $\rho_\infty = 3.25E-02$
 $T_\infty = 61.9$ K
 $H_{Total} - H_{300K} = 2.03E+05$
 $q_{FR,Rn} = 1.02E+05$ W/m²
 $h_{FR,Rn} = 5.01E-01$ kg/m²-s

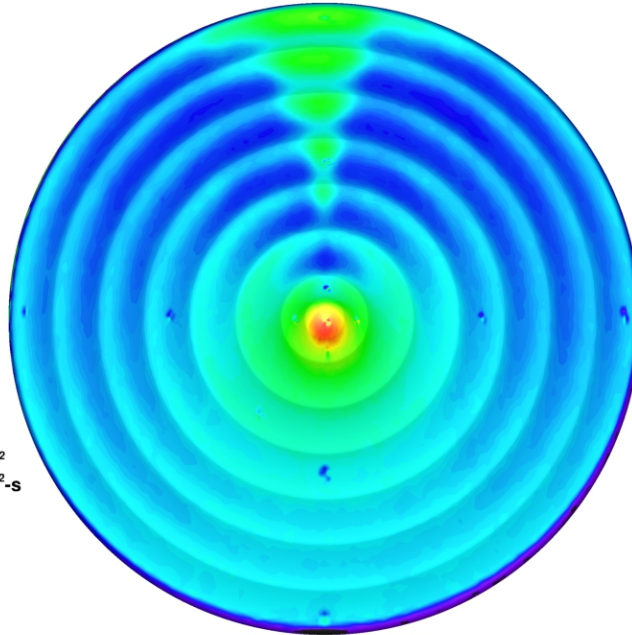
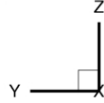
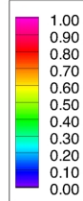


Figure 187. IRVE Scallop-5 Model, Run 185: $\alpha = 12$ deg, $Re_\infty = 2.10 \times 10^6$ /ft.

Configuration: IRVE-5
D = 6.0 in. / 0.1524 m
R_{nose} = 0.375 in. / 0.00953 m

LaRC 20-Inch Mach 6 Air Tunnel
Test 6979, Run 186

$h/h_{FR,Rn}$



$Re_\infty = 3.03E+06$ /ft
 $Re_\infty = 9.95E+06$ /m
 $\alpha = 12$ -deg
 $U_\infty = 948.7$ m/s
 $\rho_\infty = 4.71E-02$
 $T_\infty = 62.5$ K
 $H_{Total} - H_{300K} = 2.12E+05$
 $q_{FR,Rn} = 1.30E+05$ W/m²
 $h_{FR,Rn} = 6.11E-01$ kg/m²-s

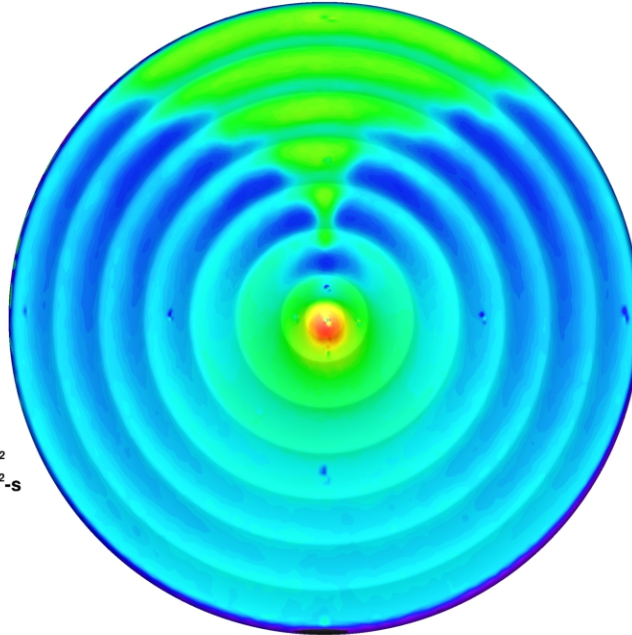
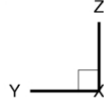
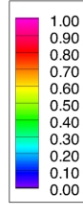


Figure 188. IRVE Scallop-5 Model, Run 186: $\alpha = 12$ deg, $Re_\infty = 3.03 \times 10^6$ /ft.

Configuration: IRVE-5
D = 6.0 in. / 0.1524 m
R_{nose} = 0.375 in. / 0.00953 m

LaRC 20-Inch Mach 6 Air Tunnel
Test 6979, Run 187

$h/h_{FR,Rn}$



$Re_\infty = 3.88E+06$ /ft
 $Re_\infty = 1.28E+07$ /m
 $\alpha = 12\text{-deg}$
 $U_\infty = 957.2$ m/s
 $\rho_\infty = 6.05E-02$
 $T_\infty = 63.3$ K
 $H_{Total} - H_{300K} = 2.21E+05$
 $q_{FR,Rn} = 1.55E+05$ W/m²
 $h_{FR,Rn} = 7.00E-01$ kg/m²-s

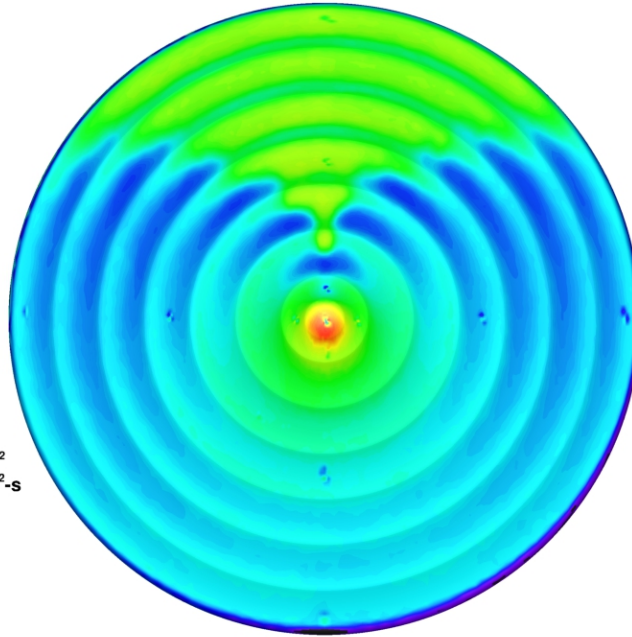
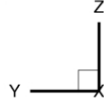
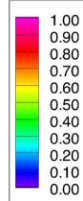


Figure 189. IRVE Scallop-5 Model, Run 187: $\alpha = 12$ deg, $Re_\infty = 3.88 \times 10^6$ /ft.

Configuration: IRVE-5
D = 6.0 in. / 0.1524 m
R_{nose} = 0.375 in. / 0.00953 m

LaRC 20-Inch Mach 6 Air Tunnel
Test 6979, Run 188

$h/h_{FR,Rn}$



$Re_\infty = 6.63E+06$ /ft
 $Re_\infty = 2.18E+07$ /m
 $\alpha = 12\text{-deg}$
 $U_\infty = 954.6$ m/s
 $\rho_\infty = 1.02E-01$
 $T_\infty = 62.6$ K
 $H_{Total} - H_{300K} = 2.17E+05$
 $q_{FR,Rn} = 1.98E+05$ W/m²
 $h_{FR,Rn} = 9.10E-01$ kg/m²-s

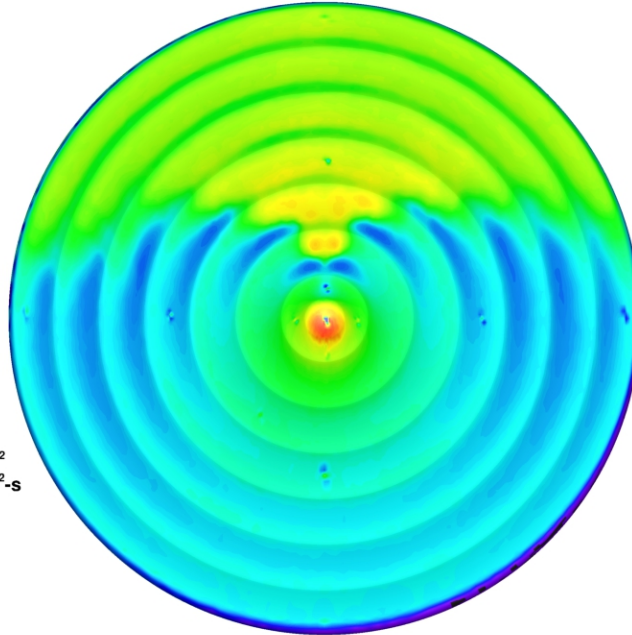
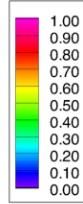


Figure 190. IRVE Scallop-5 Model, Run 188: $\alpha = 12$ deg, $Re_\infty = 6.63 \times 10^6$ /ft.

Configuration: IRVE-5
D = 6.0 in. / 0.1524 m
R_{nose} = 0.375 in. / 0.00953 m

LaRC 20-Inch Mach 6 Air Tunnel
Test 6979, Run 189

$h/h_{FR,Rn}$



$Re_\infty = 8.34E+06$ /ft
 $Re_\infty = 2.74E+07$ /m
 $\alpha = 12\text{-deg}$
 $U_\infty = 918.1$ m/s
 $\rho_\infty = 1.25E-01$
 $T_\infty = 58.6$ K
 $H_{Total} - H_{300K} = 1.79E+05$
 $q_{FR,Rn} = 1.73E+05$ W/m²
 $h_{FR,Rn} = 9.64E-01$ kg/m²-s

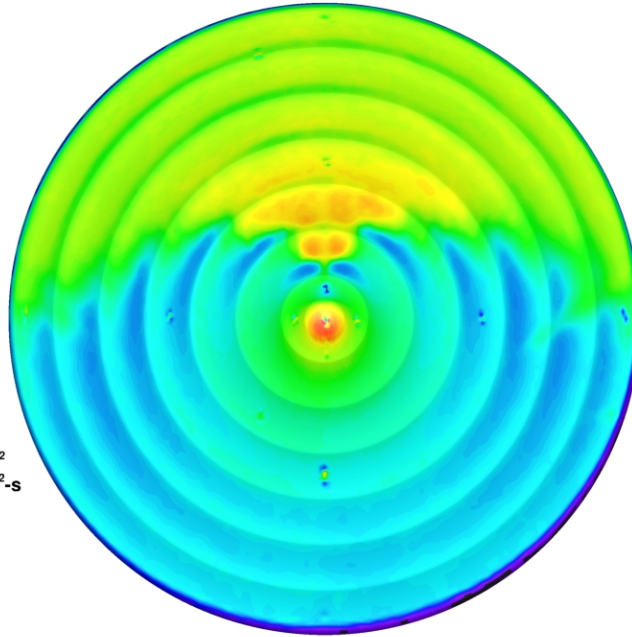
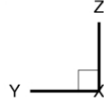
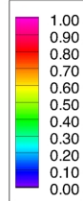


Figure 191. IRVE Scallop-5 Model, Run 189: $\alpha = 12$ deg, $Re_\infty = 8.33 \times 10^6$ /ft.

Configuration: IRVE-5
D = 6.0 in. / 0.1524 m
R_{nose} = 0.375 in. / 0.00953 m

LaRC 20-Inch Mach 6 Air Tunnel
Test 6979, Run 152

$h/h_{FR,Rn}$



$Re_\infty = 2.10E+06$ /ft
 $Re_\infty = 6.89E+06$ /m
 $\alpha = 18\text{-deg}$
 $U_\infty = 939.5$ m/s
 $\rho_\infty = 3.25E-02$
 $T_\infty = 61.9$ K
 $H_{Total} - H_{300K} = 2.03E+05$
 $q_{FR,Rn} = 1.02E+05$ W/m²
 $h_{FR,Rn} = 5.01E-01$ kg/m²-s

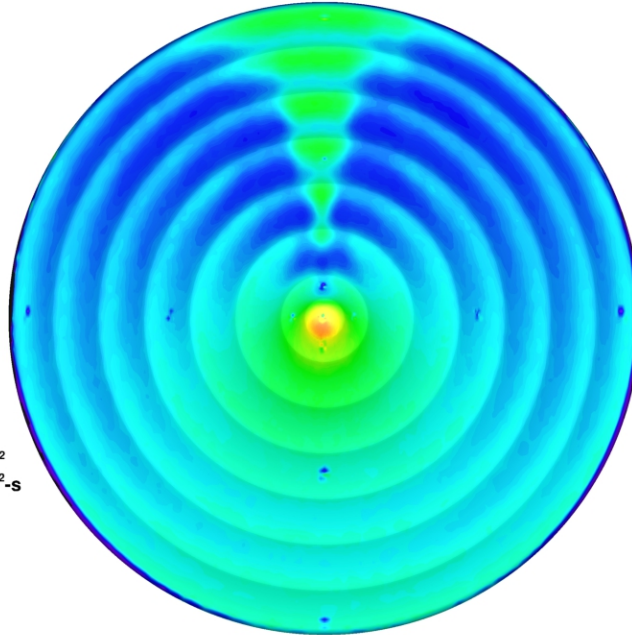
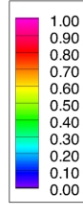


Figure 192. IRVE Scallop-5 Model, Run 152: $\alpha = 18$ deg, $Re_\infty = 2.10 \times 10^6$ /ft.

Configuration: IRVE-5
D = 6.0 in. / 0.1524 m
R_{nose} = 0.375 in. / 0.00953 m

LaRC 20-Inch Mach 6 Air Tunnel
Test 6979, Run 153

$h/h_{FR,Rn}$



$Re_\infty = 3.03E+06$ /ft
 $Re_\infty = 9.95E+06$ /m
 $\alpha = 18\text{-deg}$
 $U_\infty = 948.7$ m/s
 $\rho_\infty = 4.71E-02$
 $T_\infty = 62.5$ K
 $H_{Total} - H_{300K} = 2.12E+05$
 $q_{FR,Rn} = 1.30E+05$ W/m²
 $h_{FR,Rn} = 6.11E-01$ kg/m²-s

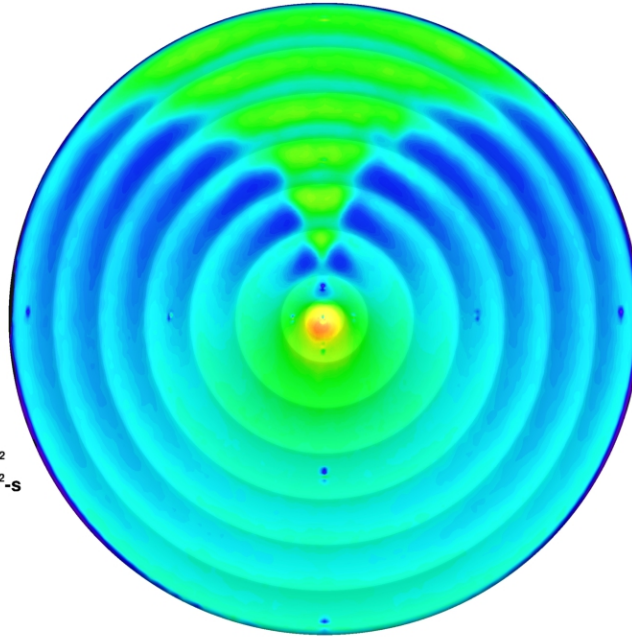
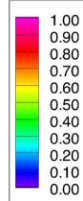


Figure 193. IRVE Scallop-5 Model, Run 153: $\alpha = 18$ deg, $Re_\infty = 3.03 \times 10^6$ /ft.

Configuration: IRVE-5
D = 6.0 in. / 0.1524 m
R_{nose} = 0.375 in. / 0.00953 m

LaRC 20-Inch Mach 6 Air Tunnel
Test 6979, Run 151

$h/h_{FR,Rn}$



$Re_\infty = 3.88E+06$ /ft
 $Re_\infty = 1.28E+07$ /m
 $\alpha = 18\text{-deg}$
 $U_\infty = 957.2$ m/s
 $\rho_\infty = 6.05E-02$
 $T_\infty = 63.3$ K
 $H_{Total} - H_{300K} = 2.21E+05$
 $q_{FR,Rn} = 1.55E+05$ W/m²
 $h_{FR,Rn} = 7.00E-01$ kg/m²-s

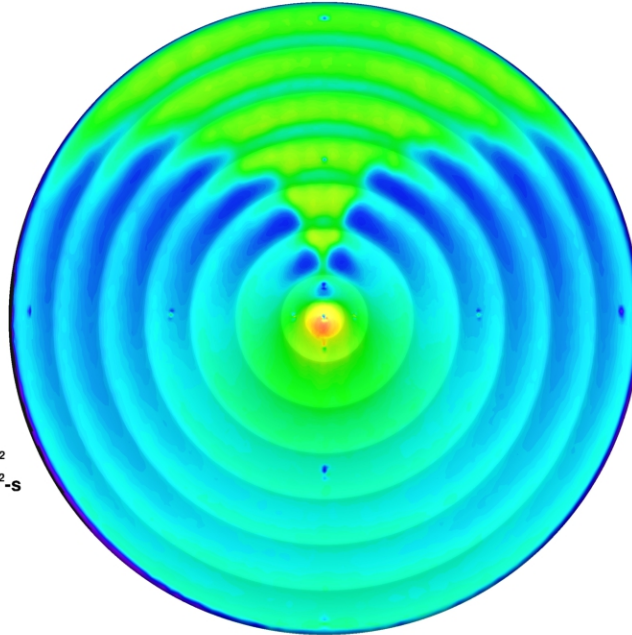
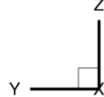
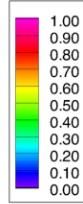


Figure 194. IRVE Scallop-5 Model, Run 151: $\alpha = 18$ deg, $Re_\infty = 3.88 \times 10^6$ /ft.

Configuration: IRVE-5
D = 6.0 in. / 0.1524 m
R_{nose} = 0.375 in. / 0.00953 m

LaRC 20-Inch Mach 6 Air Tunnel
Test 6979, Run 154

$h/h_{FR,Rn}$



$Re_\infty = 6.63E+06$ /ft
 $Re_\infty = 2.18E+07$ /m
 $\alpha = 18\text{-deg}$
 $U_\infty = 954.6$ m/s
 $\rho_\infty = 1.02E-01$
 $T_\infty = 62.6$ K
 $H_{Total} - H_{300K} = 2.17E+05$
 $q_{FR,Rn} = 1.98E+05$ W/m²
 $h_{FR,Rn} = 9.10E-01$ kg/m²-s

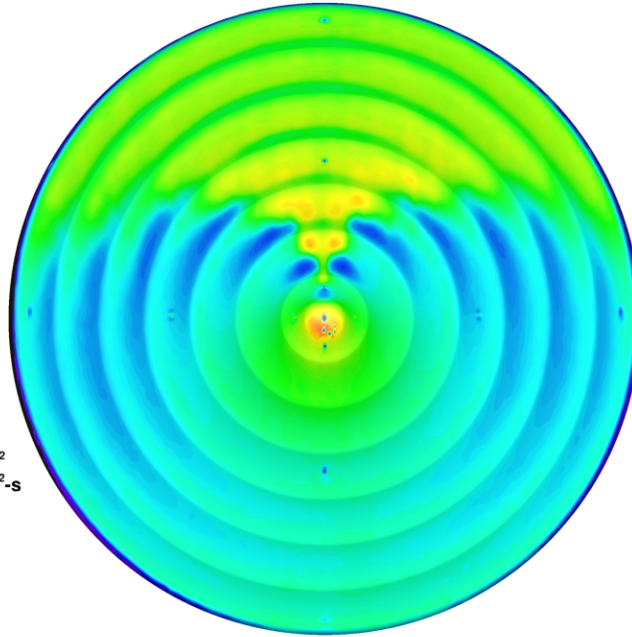
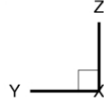
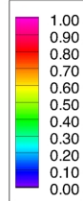


Figure 195. IRVE Scallop-5 Model, Run 154: $\alpha = 18$ deg, $Re_\infty = 6.63 \times 10^6$ /ft.

Configuration: IRVE-5
D = 6.0 in. / 0.1524 m
R_{nose} = 0.375 in. / 0.00953 m

LaRC 20-Inch Mach 6 Air Tunnel
Test 6979, Run 155

$h/h_{FR,Rn}$



$Re_\infty = 8.34E+06$ /ft
 $Re_\infty = 2.74E+07$ /m
 $\alpha = 18\text{-deg}$
 $U_\infty = 918.1$ m/s
 $\rho_\infty = 1.25E-01$
 $T_\infty = 58.6$ K
 $H_{Total} - H_{300K} = 1.79E+05$
 $q_{FR,Rn} = 1.73E+05$ W/m²
 $h_{FR,Rn} = 9.64E-01$ kg/m²-s

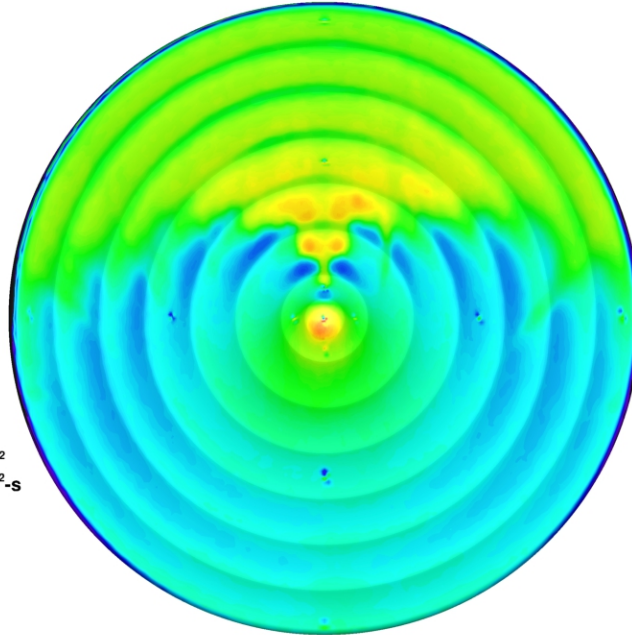
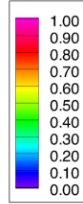


Figure 196. IRVE Scallop-5 Model, Run 155: $\alpha = 18$ deg, $Re_\infty = 8.33 \times 10^6$ /ft.

Configuration: IRVE-10
D = 6.0 in. / 0.1524 m
R_{nose} = 0.375 in. / 0.00953 m

LaRC 20-Inch Mach 6 Air Tunnel
Test 6979, Run 016

$h/h_{FR,Rn}$



$Re_\infty = 2.10E+06$ /ft
 $Re_\infty = 6.89E+06$ /m
 $\alpha = 0\text{-deg}$
 $U_\infty = 939.5$ m/s
 $\rho_\infty = 3.25E-02$
 $T_\infty = 61.9$ K
 $H_{Total} - H_{300K} = 2.03E+05$
 $q_{FR,Rn} = 1.02E+05$ W/m²
 $h_{FR,Rn} = 5.01E-01$ kg/m²-s

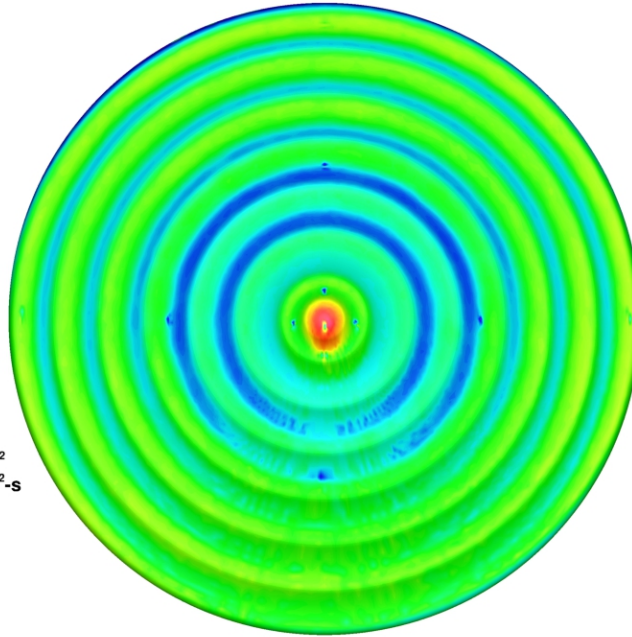
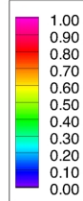


Figure 197. IRVE Scallop-10 Model, Run 16: $\alpha = 0$ deg, $Re_\infty = 2.10 \times 10^6$ /ft.

Configuration: IRVE-10
D = 6.0 in. / 0.1524 m
R_{nose} = 0.375 in. / 0.00953 m

LaRC 20-Inch Mach 6 Air Tunnel
Test 6979, Run 017

$h/h_{FR,Rn}$



$Re_\infty = 3.03E+06$ /ft
 $Re_\infty = 9.95E+06$ /m
 $\alpha = 0\text{-deg}$
 $U_\infty = 948.7$ m/s
 $\rho_\infty = 4.71E-02$
 $T_\infty = 62.5$ K
 $H_{Total} - H_{300K} = 2.12E+05$
 $q_{FR,Rn} = 1.30E+05$ W/m²
 $h_{FR,Rn} = 6.11E-01$ kg/m²-s

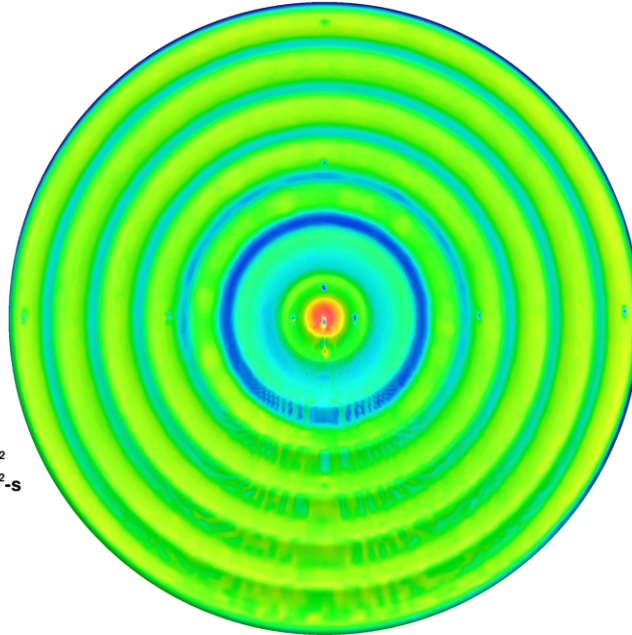
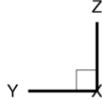
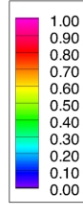


Figure 198. IRVE Scallop-10 Model, Run 17: $\alpha = 0$ deg, $Re_\infty = 3.03 \times 10^6$ /ft.

Configuration: IRVE-10
D = 6.0 in. / 0.1524 m
R_{nose} = 0.375 in. / 0.00953 m

LaRC 20-Inch Mach 6 Air Tunnel
Test 6979, Run 018

$h/h_{FR,Rn}$



$Re_\infty = 3.88E+06$ /ft
 $Re_\infty = 1.28E+07$ /m
 $\alpha = 0$ -deg
 $U_\infty = 957.2$ m/s
 $\rho_\infty = 6.05E-02$
 $T_\infty = 63.3$ K
 $H_{Total} - H_{300K} = 2.21E+05$
 $q_{FR,Rn} = 1.55E+05$ W/m²
 $h_{FR,Rn} = 7.00E-01$ kg/m²-s

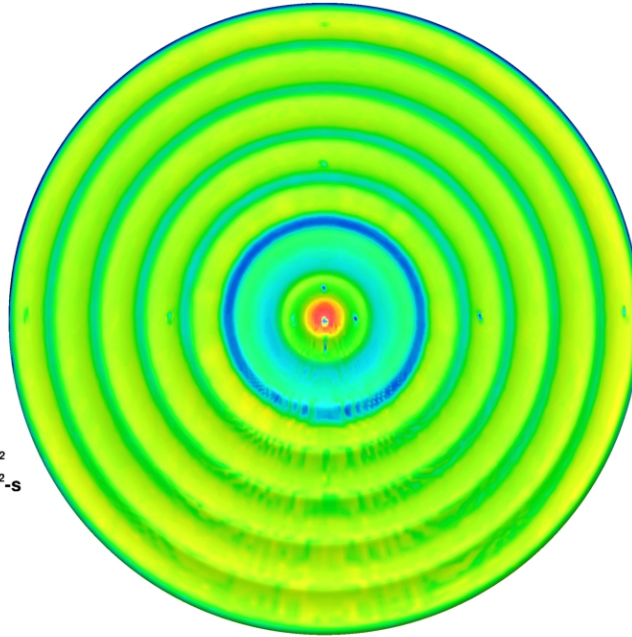
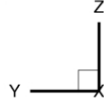
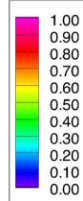


Figure 199. IRVE Scallop-10 Model, Run 18: $\alpha = 0$ deg, $Re_\infty = 3.88 \times 10^6$ /ft.

Configuration: IRVE-10
D = 6.0 in. / 0.1524 m
R_{nose} = 0.375 in. / 0.00953 m

LaRC 20-Inch Mach 6 Air Tunnel
Test 6979, Run 019

$h/h_{FR,Rn}$



$Re_\infty = 6.63E+06$ /ft
 $Re_\infty = 2.18E+07$ /m
 $\alpha = 0$ -deg
 $U_\infty = 954.6$ m/s
 $\rho_\infty = 1.02E-01$
 $T_\infty = 62.6$ K
 $H_{Total} - H_{300K} = 2.17E+05$
 $q_{FR,Rn} = 1.98E+05$ W/m²
 $h_{FR,Rn} = 9.10E-01$ kg/m²-s

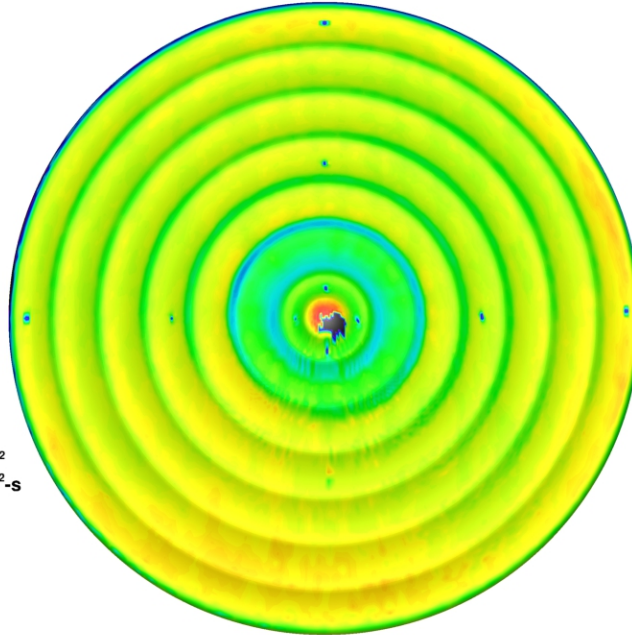
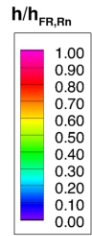


Figure 200. IRVE Scallop-10 Model, Run 19: $\alpha = 0$ deg, $Re_\infty = 6.63 \times 10^6$ /ft.

Configuration: IRVE-10
D = 6.0 in. / 0.1524 m
R_{nose} = 0.375 in. / 0.00953 m

IRVE Deflected OML Study
LaRC 20-Inch Mach 6 Air Tunnel
Test 6979, Run 020



Re_∞ = 8.34E+06 /ft
Re_∞ = 2.74E+07 /m
α = 0-deg
U_∞ = 918.1 m/s
ρ_∞ = 1.25E-01
T_∞ = 58.6 K
H_{Total} - H_{300K} = 1.79E+05
q_{FR,Rn} = 1.73E+05 W/m²
h_{FR,Rn} = 9.64E-01 kg/m²-s

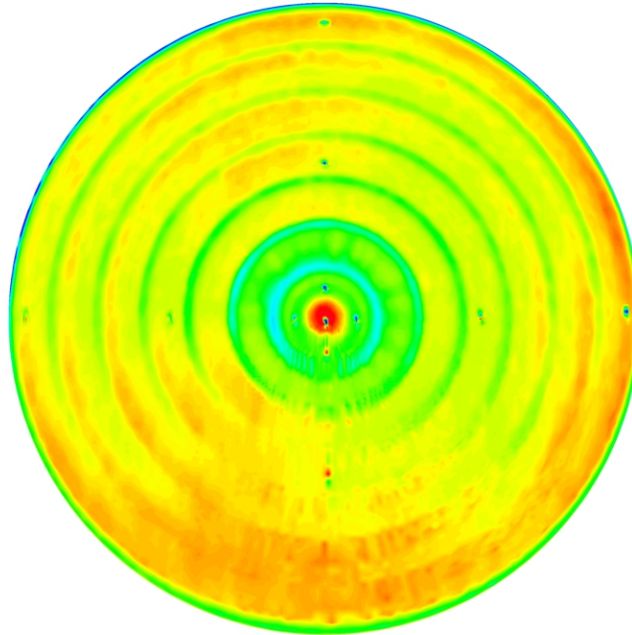
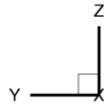
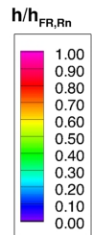


Figure 201. IRVE Scallop-10 Model, Run 20: α = 0 deg, Re_∞ = 8.33×10⁶/ft.

Configuration: IRVE-10
D = 6.0 in. / 0.1524 m
R_{nose} = 0.375 in. / 0.00953 m

LaRC 20-Inch Mach 6 Air Tunnel
Test 6979, Run 050



Re_∞ = 2.10E+06 /ft
Re_∞ = 6.89E+06 /m
α = 6-deg
U_∞ = 939.5 m/s
ρ_∞ = 3.25E-02
T_∞ = 61.9 K
H_{Total} - H_{300K} = 2.03E+05
q_{FR,Rn} = 1.02E+05 W/m²
h_{FR,Rn} = 5.01E-01 kg/m²-s

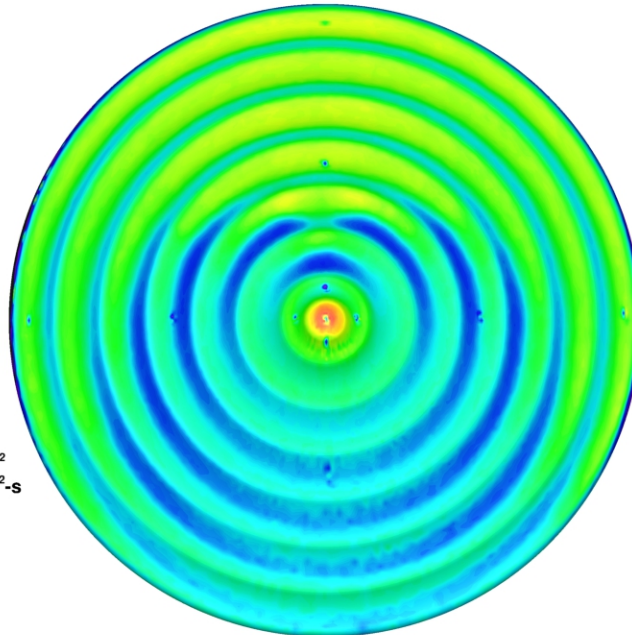
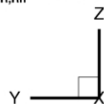
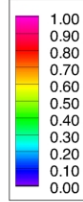


Figure 202. IRVE Scallop-10 Model, Run 50: α = 6 deg, Re_∞ = 2.10×10⁶/ft.

Configuration: IRVE-10
D = 6.0 in. / 0.1524 m
R_{nose} = 0.375 in. / 0.00953 m

LaRC 20-Inch Mach 6 Air Tunnel
Test 6979, Run 051

$h/h_{FR,Rn}$



$Re_\infty = 3.03E+06$ /ft
 $Re_\infty = 9.95E+06$ /m
 $\alpha = 6\text{-deg}$
 $U_\infty = 948.7$ m/s
 $\rho_\infty = 4.71E-02$
 $T_\infty = 62.5$ K
 $H_{Total} - H_{300K} = 2.12E+05$
 $q_{FR,Rn} = 1.30E+05$ W/m²
 $h_{FR,Rn} = 6.11E-01$ kg/m²-s

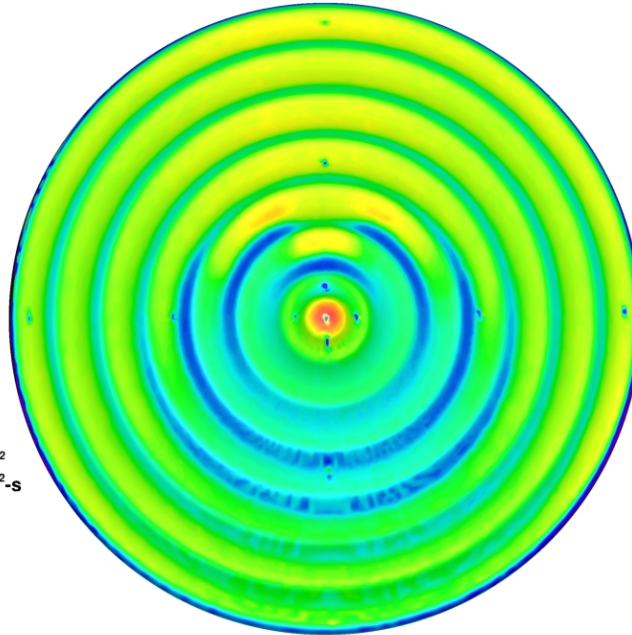
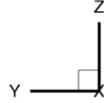
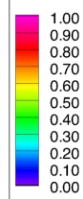


Figure 203. IRVE Scallop-10 Model, Run 51: $\alpha = 6$ deg, $Re_\infty = 3.03 \times 10^6$ /ft.

Configuration: IRVE-10
D = 6.0 in. / 0.1524 m
R_{nose} = 0.375 in. / 0.00953 m

LaRC 20-Inch Mach 6 Air Tunnel
Test 6979, Run 052

$h/h_{FR,Rn}$



$Re_\infty = 3.88E+06$ /ft
 $Re_\infty = 1.28E+07$ /m
 $\alpha = 6\text{-deg}$
 $U_\infty = 957.2$ m/s
 $\rho_\infty = 6.05E-02$
 $T_\infty = 63.3$ K
 $H_{Total} - H_{300K} = 2.21E+05$
 $q_{FR,Rn} = 1.55E+05$ W/m²
 $h_{FR,Rn} = 7.00E-01$ kg/m²-s

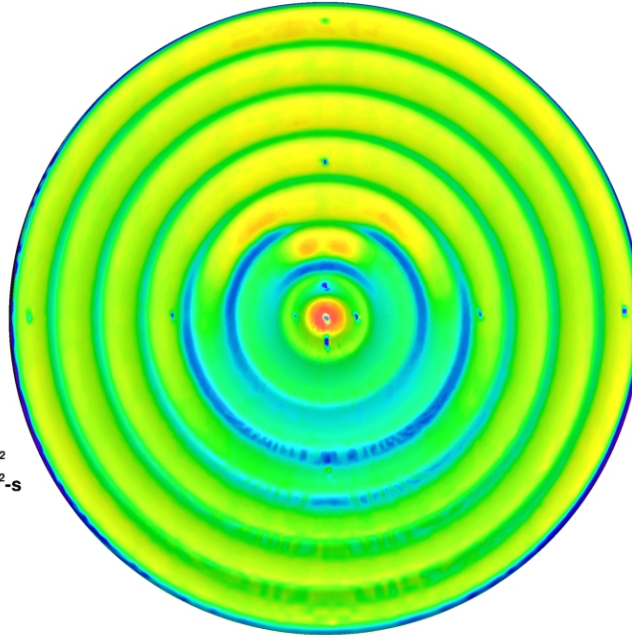
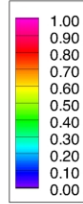


Figure 204. IRVE Scallop-10 Model, Run 52: $\alpha = 6$ deg, $Re_\infty = 3.88 \times 10^6$ /ft.

Configuration: IRVE-10
D = 6.0 in. / 0.1524 m
R_{nose} = 0.375 in. / 0.00953 m

LaRC 20-Inch Mach 6 Air Tunnel
Test 6979, Run 053

$h/h_{FR,Rn}$



$Re_\infty = 6.63E+06$ /ft
 $Re_\infty = 2.18E+07$ /m
 $\alpha = 6\text{-deg}$
 $U_\infty = 954.6$ m/s
 $\rho_\infty = 1.02E-01$
 $T_\infty = 62.6$ K
 $H_{Total} - H_{300K} = 2.17E+05$
 $q_{FR,Rn} = 1.98E+05$ W/m²
 $h_{FR,Rn} = 9.10E-01$ kg/m²-s

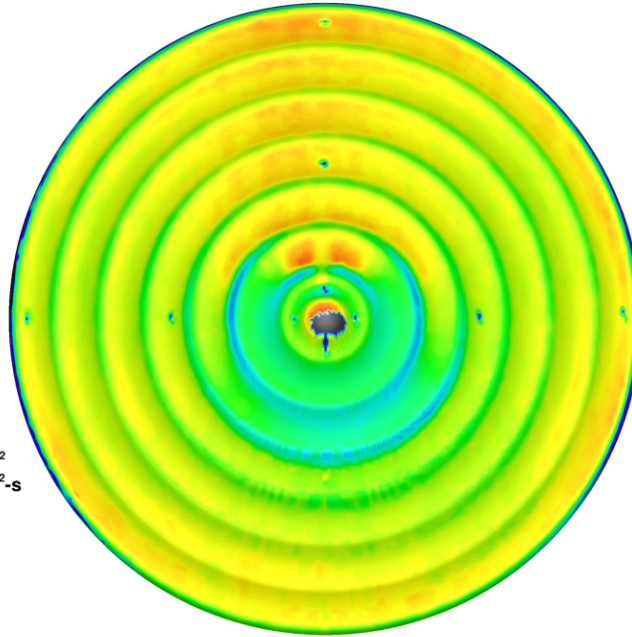
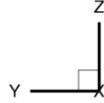
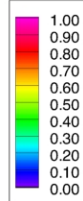


Figure 205. IRVE Scallop-10 Model, Run 53: $\alpha = 6$ deg, $Re_\infty = 6.63 \times 10^6$ /ft.

Configuration: IRVE-10
D = 6.0 in. / 0.1524 m
R_{nose} = 0.375 in. / 0.00953 m

LaRC 20-Inch Mach 6 Air Tunnel
Test 6979, Run 054

$h/h_{FR,Rn}$



$Re_\infty = 8.34E+06$ /ft
 $Re_\infty = 2.74E+07$ /m
 $\alpha = 6\text{-deg}$
 $U_\infty = 918.1$ m/s
 $\rho_\infty = 1.25E-01$
 $T_\infty = 58.6$ K
 $H_{Total} - H_{300K} = 1.79E+05$
 $q_{FR,Rn} = 1.73E+05$ W/m²
 $h_{FR,Rn} = 9.64E-01$ kg/m²-s

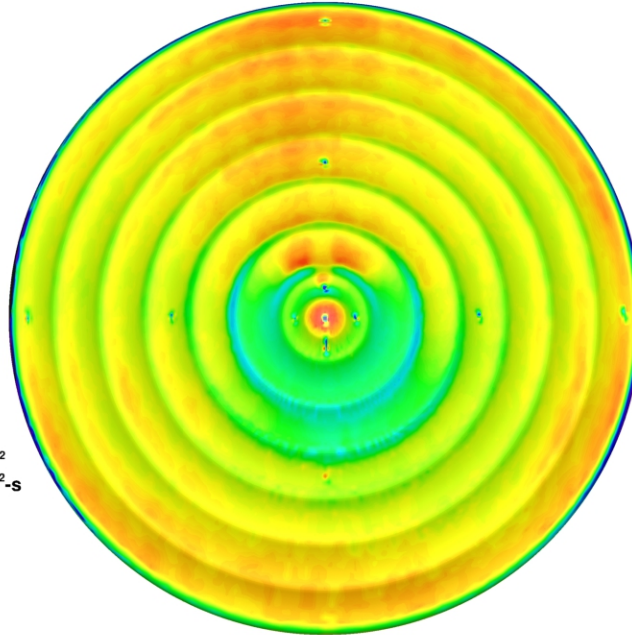
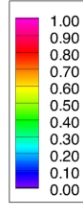


Figure 206. IRVE Scallop-10 Model, Run 54: $\alpha = 6$ deg, $Re_\infty = 8.33 \times 10^6$ /ft.

Configuration: IRVE-10
D = 6.0 in. / 0.1524 m
R_{nose} = 0.375 in. / 0.00953 m

LaRC 20-Inch Mach 6 Air Tunnel
Test 6979, Run 098

$h/h_{FR,Rn}$



$Re_\infty = 2.10E+06$ /ft
 $Re_\infty = 6.89E+06$ /m
 $\alpha = 12$ -deg
 $U_\infty = 939.5$ m/s
 $\rho_\infty = 3.25E-02$
 $T_\infty = 61.9$ K
 $H_{Total} - H_{300K} = 2.03E+05$
 $q_{FR,Rn} = 1.02E+05$ W/m²
 $h_{FR,Rn} = 5.01E-01$ kg/m²-s

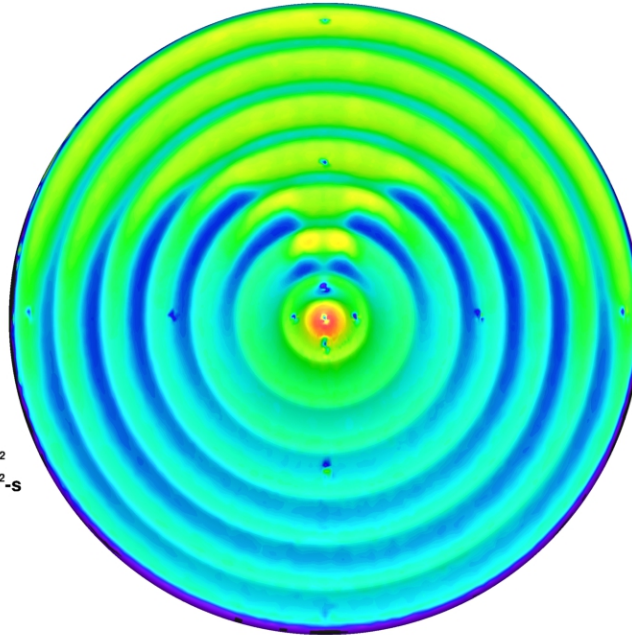
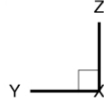
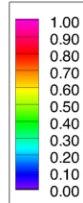


Figure 207. IRVE Scallop-10 Model, Run 98: $\alpha = 12$ deg, $Re_\infty = 2.10 \times 10^6$ /ft.

Configuration: IRVE-10
D = 6.0 in. / 0.1524 m
R_{nose} = 0.375 in. / 0.00953 m

LaRC 20-Inch Mach 6 Air Tunnel
Test 6979, Run 099

$h/h_{FR,Rn}$



$Re_\infty = 3.03E+06$ /ft
 $Re_\infty = 9.95E+06$ /m
 $\alpha = 12$ -deg
 $U_\infty = 948.7$ m/s
 $\rho_\infty = 4.71E-02$
 $T_\infty = 62.5$ K
 $H_{Total} - H_{300K} = 2.12E+05$
 $q_{FR,Rn} = 1.30E+05$ W/m²
 $h_{FR,Rn} = 6.11E-01$ kg/m²-s

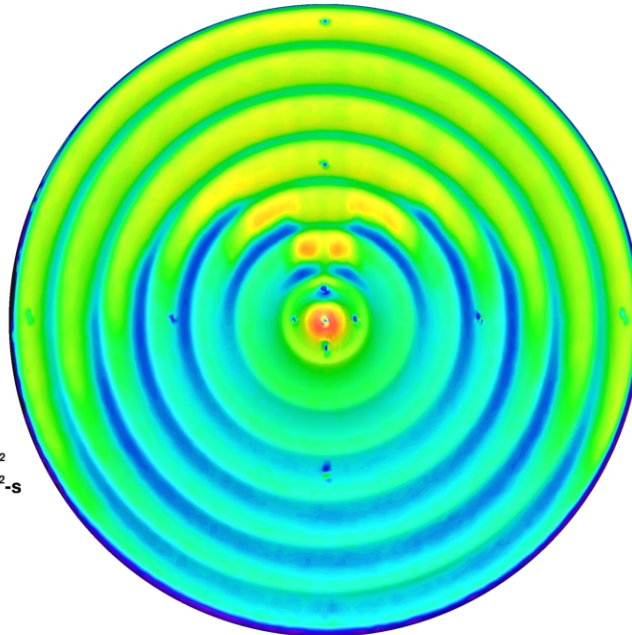
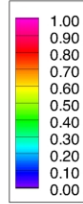


Figure 208. IRVE Scallop-10 Model, Run 99: $\alpha = 12$ deg, $Re_\infty = 3.03 \times 10^6$ /ft.

Configuration: IRVE-10
D = 6.0 in. / 0.1524 m
R_{nose} = 0.375 in. / 0.00953 m

IRVE Deflected OML Study
LaRC 20-Inch Mach 6 Air Tunnel
Test 6979, Run 100

$h/h_{FR,Rn}$



$Re_\infty = 3.88E+06$ /ft
 $Re_\infty = 1.28E+07$ /m
 $\alpha = 12\text{-deg}$
 $U_\infty = 957.2$ m/s
 $\rho_\infty = 6.05E-02$
 $T_\infty = 63.3$ K
 $H_{Total} - H_{300K} = 2.21E+05$
 $q_{FR,Rn} = 1.55E+05$ W/m²
 $h_{FR,Rn} = 7.00E-01$ kg/m²-s

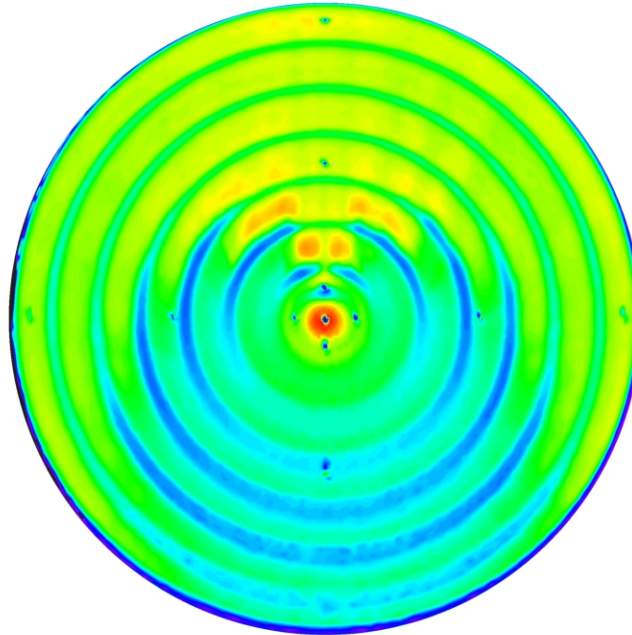
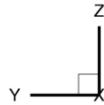
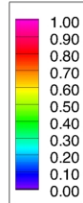


Figure 209. IRVE Scallop-10 Model, Run 100: $\alpha = 12$ deg, $Re_\infty = 3.88 \times 10^6$ /ft.

Configuration: IRVE-10
D = 6.0 in. / 0.1524 m
R_{nose} = 0.375 in. / 0.00953 m

LaRC 20-Inch Mach 6 Air Tunnel
Test 6979, Run 101

$h/h_{FR,Rn}$



$Re_\infty = 6.63E+06$ /ft
 $Re_\infty = 2.18E+07$ /m
 $\alpha = 12\text{-deg}$
 $U_\infty = 954.6$ m/s
 $\rho_\infty = 1.02E-01$
 $T_\infty = 62.6$ K
 $H_{Total} - H_{300K} = 2.17E+05$
 $q_{FR,Rn} = 1.98E+05$ W/m²
 $h_{FR,Rn} = 9.10E-01$ kg/m²-s

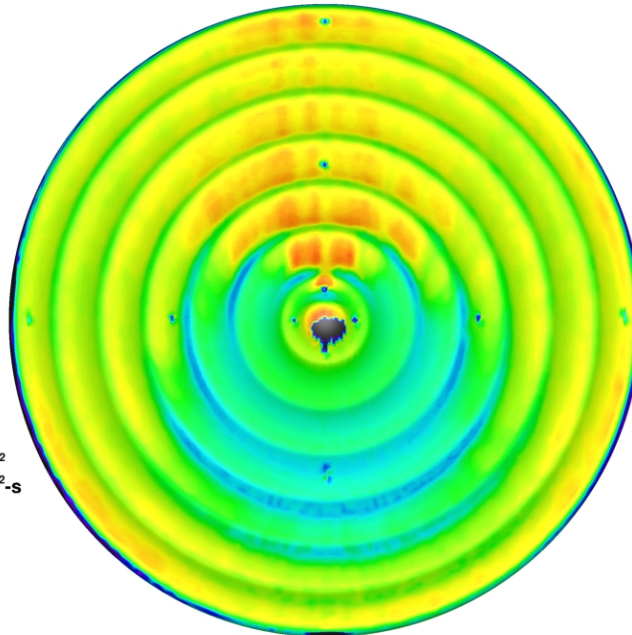
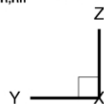
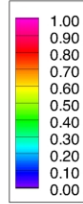


Figure 210. IRVE Scallop-10 Model, Run 101: $\alpha = 12$ deg, $Re_\infty = 6.63 \times 10^6$ /ft.

Configuration: IRVE-10
D = 6.0 in. / 0.1524 m
R_{nose} = 0.375 in. / 0.00953 m

LaRC 20-Inch Mach 6 Air Tunnel
Test 6979, Run 102

$h/h_{FR,Rn}$



$Re_\infty = 8.34E+06$ /ft
 $Re_\infty = 2.74E+07$ /m
 $\alpha = 12\text{-deg}$
 $U_\infty = 918.1$ m/s
 $\rho_\infty = 1.25E-01$
 $T_\infty = 58.6$ K
 $H_{Total} - H_{300K} = 1.79E+05$
 $q_{FR,Rn} = 1.73E+05$ W/m²
 $h_{FR,Rn} = 9.64E-01$ kg/m²-s

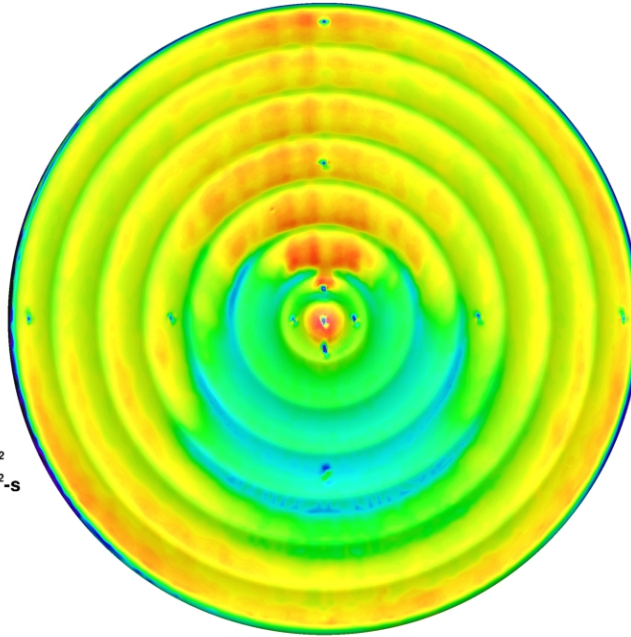
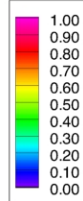


Figure 211. IRVE Scallop-10 Model, Run 102: $\alpha = 12$ deg, $Re_\infty = 8.33 \times 10^6$ /ft.

Configuration: IRVE-10
D = 6.0 in. / 0.1524 m
R_{nose} = 0.375 in. / 0.00953 m

LaRC 20-Inch Mach 6 Air Tunnel
Test 6979, Run 146

$h/h_{FR,Rn}$



$Re_\infty = 2.10E+06$ /ft
 $Re_\infty = 6.89E+06$ /m
 $\alpha = 18\text{-deg}$
 $U_\infty = 939.5$ m/s
 $\rho_\infty = 3.25E-02$
 $T_\infty = 61.9$ K
 $H_{Total} - H_{300K} = 2.03E+05$
 $q_{FR,Rn} = 1.02E+05$ W/m²
 $h_{FR,Rn} = 5.01E-01$ kg/m²-s

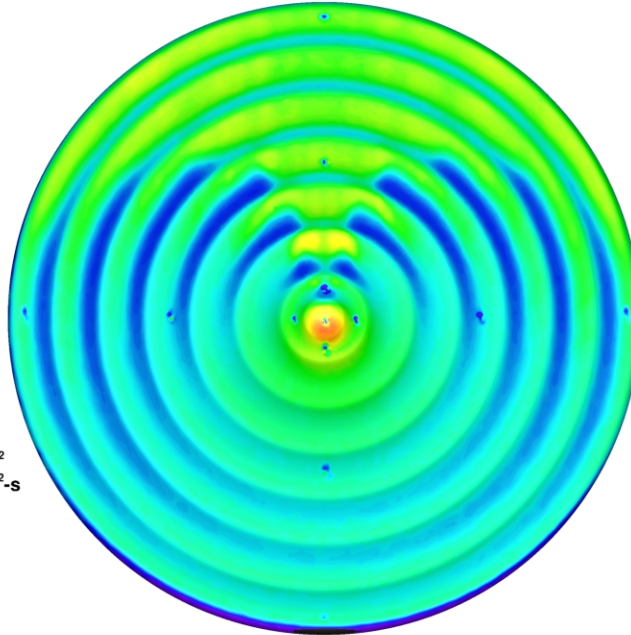
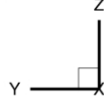
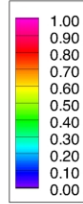


Figure 212. IRVE Scallop-10 Model, Run 146: $\alpha = 18$ deg, $Re_\infty = 2.10 \times 10^6$ /ft.

Configuration: IRVE-10
D = 6.0 in. / 0.1524 m
R_{nose} = 0.375 in. / 0.00953 m

LaRC 20-Inch Mach 6 Air Tunnel
Test 6979, Run 147

$h/h_{FR,Rn}$



$Re_\infty = 3.03E+06$ /ft
 $Re_\infty = 9.95E+06$ /m
 $\alpha = 18\text{-deg}$
 $U_\infty = 948.7$ m/s
 $\rho_\infty = 4.71E-02$
 $T_\infty = 62.5$ K
 $H_{Total} - H_{300K} = 2.12E+05$
 $q_{FR,Rn} = 1.30E+05$ W/m²
 $h_{FR,Rn} = 6.11E-01$ kg/m²·s

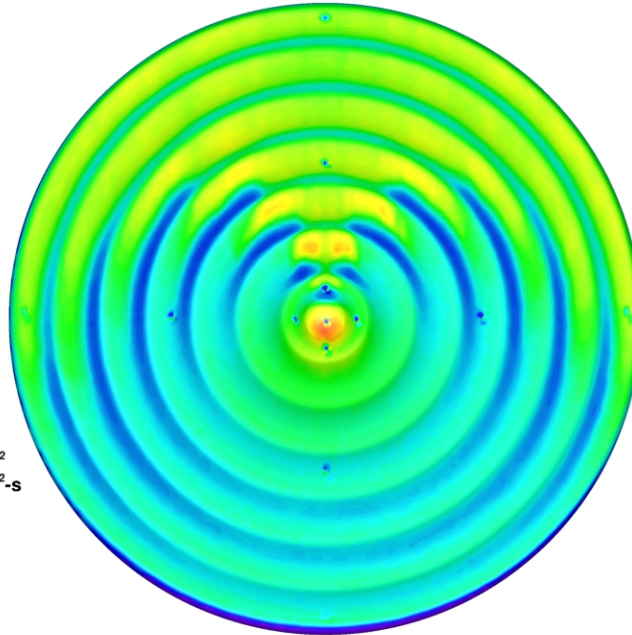
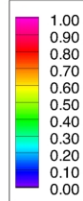


Figure 213. IRVE Scallop-10 Model, Run 147: $\alpha = 18$ deg, $Re_\infty = 3.03 \times 10^6$ /ft.

Configuration: IRVE-10
D = 6.0 in. / 0.1524 m
R_{nose} = 0.375 in. / 0.00953 m

LaRC 20-Inch Mach 6 Air Tunnel
Test 6979, Run 148

$h/h_{FR,Rn}$



$Re_\infty = 3.88E+06$ /ft
 $Re_\infty = 1.28E+07$ /m
 $\alpha = 18\text{-deg}$
 $U_\infty = 957.2$ m/s
 $\rho_\infty = 6.05E-02$
 $T_\infty = 63.3$ K
 $H_{Total} - H_{300K} = 2.21E+05$
 $q_{FR,Rn} = 1.55E+05$ W/m²
 $h_{FR,Rn} = 7.00E-01$ kg/m²·s

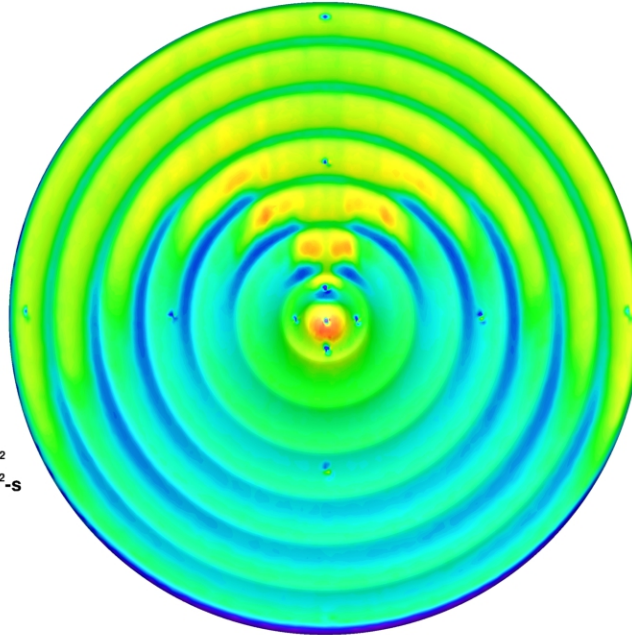
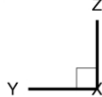
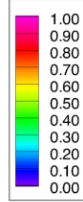


Figure 214. IRVE Scallop-10 Model, Run 148: $\alpha = 18$ deg, $Re_\infty = 3.88 \times 10^6$ /ft.

Configuration: IRVE-10
D = 6.0 in. / 0.1524 m
R_{nose} = 0.375 in. / 0.00953 m

LaRC 20-Inch Mach 6 Air Tunnel
Test 6979, Run 149

$h/h_{FR,Rn}$



$Re_\infty = 6.63E+06$ /ft
 $Re_\infty = 2.18E+07$ /m
 $\alpha = 18\text{-deg}$
 $U_\infty = 954.6$ m/s
 $\rho_\infty = 1.02E-01$
 $T_\infty = 62.6$ K
 $H_{Total} - H_{300K} = 2.17E+05$
 $q_{FR,Rn} = 1.98E+05$ W/m²
 $h_{FR,Rn} = 9.10E-01$ kg/m²-s

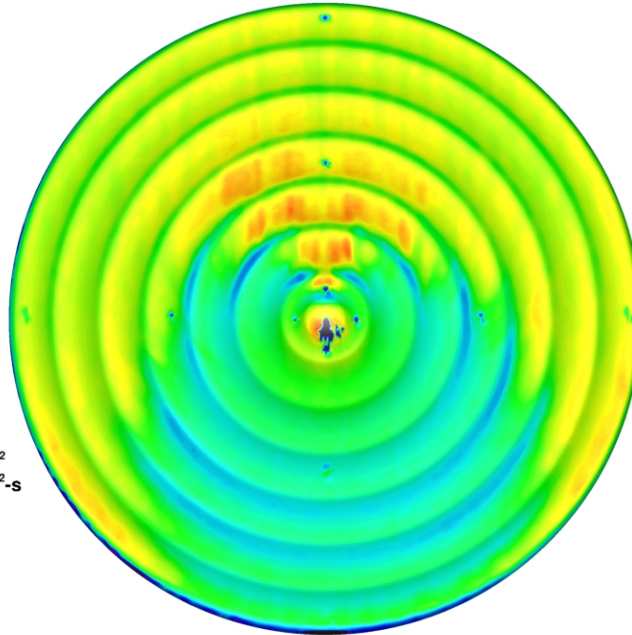
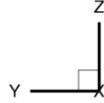
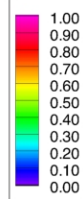


Figure 215. IRVE Scallop-10 Model, Run 149: $\alpha = 18$ deg, $Re_\infty = 6.63 \times 10^6$ /ft.

Configuration: IRVE-10
D = 6.0 in. / 0.1524 m
R_{nose} = 0.375 in. / 0.00953 m

LaRC 20-Inch Mach 6 Air Tunnel
Test 6979, Run 150

$h/h_{FR,Rn}$



$Re_\infty = 8.34E+06$ /ft
 $Re_\infty = 2.74E+07$ /m
 $\alpha = 18\text{-deg}$
 $U_\infty = 918.1$ m/s
 $\rho_\infty = 1.25E-01$
 $T_\infty = 58.6$ K
 $H_{Total} - H_{300K} = 1.79E+05$
 $q_{FR,Rn} = 1.73E+05$ W/m²
 $h_{FR,Rn} = 9.64E-01$ kg/m²-s

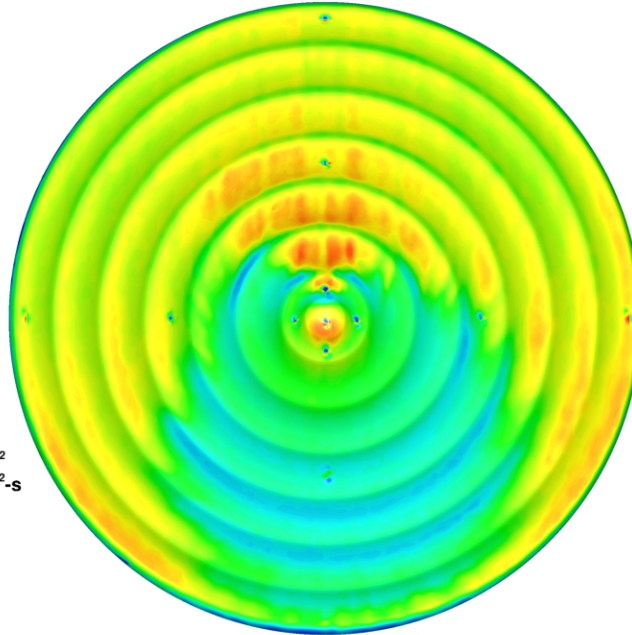
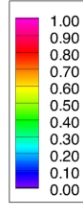


Figure 216. IRVE Scallop-10 Model, Run 150: $\alpha = 18$ deg, $Re_\infty = 8.33 \times 10^6$ /ft.

Configuration: IRVE-15
D = 6.0 in. / 0.1524 m
R_{nose} = 0.375 in. / 0.00953 m

LaRC 20-Inch Mach 6 Air Tunnel
Test 6979, Run 022

$h/h_{FR,Rn}$



$Re_\infty = 2.10E+06$ /ft
 $Re_\infty = 6.89E+06$ /m
 $\alpha = 0$ -deg
 $U_\infty = 939.5$ m/s
 $\rho_\infty = 3.25E-02$
 $T_\infty = 61.9$ K
 $H_{Total} - H_{300K} = 2.03E+05$
 $q_{FR,Rn} = 1.02E+05$ W/m²
 $h_{FR,Rn} = 5.01E-01$ kg/m²-s

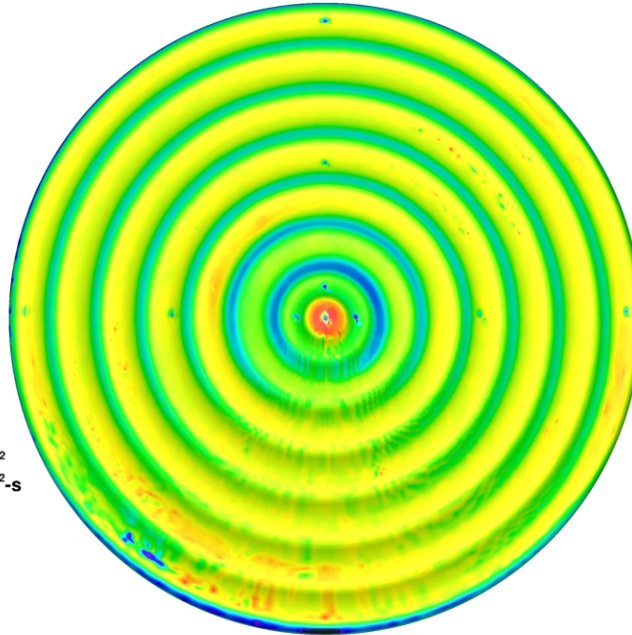
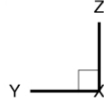
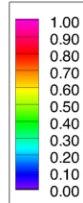


Figure 217. IRVE Scallop-15 Model, Run 22: $\alpha = 0$ deg, $Re_\infty = 2.10 \times 10^6$ /ft.

Configuration: IRVE-15
D = 6.0 in. / 0.1524 m
R_{nose} = 0.375 in. / 0.00953 m

LaRC 20-Inch Mach 6 Air Tunnel
Test 6979, Run 023

$h/h_{FR,Rn}$



$Re_\infty = 3.03E+06$ /ft
 $Re_\infty = 9.95E+06$ /m
 $\alpha = 0$ -deg
 $U_\infty = 948.7$ m/s
 $\rho_\infty = 4.71E-02$
 $T_\infty = 62.5$ K
 $H_{Total} - H_{300K} = 2.12E+05$
 $q_{FR,Rn} = 1.30E+05$ W/m²
 $h_{FR,Rn} = 6.11E-01$ kg/m²-s

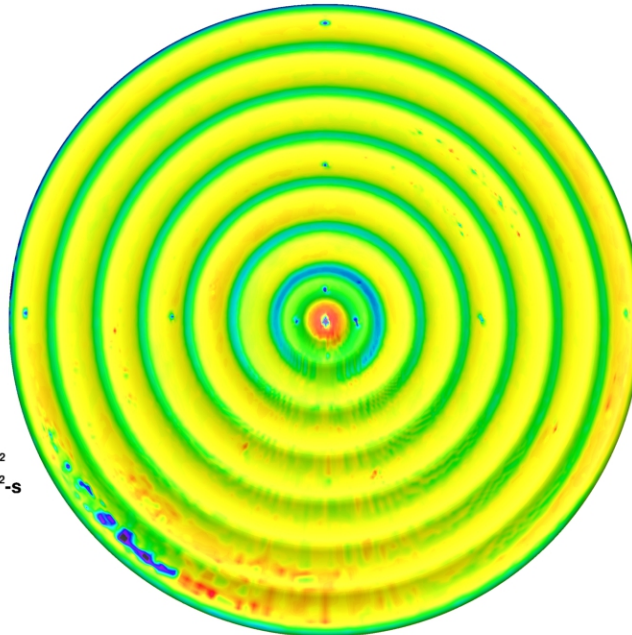
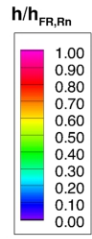


Figure 218. IRVE Scallop-15 Model, Run 23: $\alpha = 0$ deg, $Re_\infty = 3.03 \times 10^6$ /ft.

Configuration: IRVE-15
D = 6.0 in. / 0.1524 m
R_{nose} = 0.375 in. / 0.00953 m

LaRC 20-Inch Mach 6 Air Tunnel
Test 6979, Run 021



Re_∞ = 3.88E+06 /ft
Re_∞ = 1.28E+07 /m
α = 0-deg
U_∞ = 957.2 m/s
ρ_∞ = 6.05E-02
T_∞ = 63.3 K
H_{Total} - H_{300K} = 2.21E+05
q_{FR,Rn} = 1.55E+05 W/m²
h_{FR,Rn} = 7.00E-01 kg/m²-s

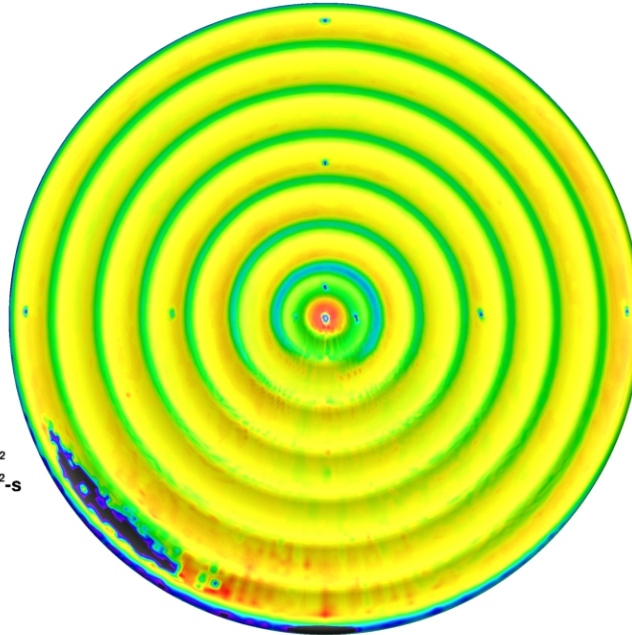
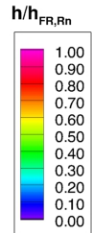


Figure 219. IRVE Scallop-15 Model, Run 21: α = 0 deg, Re_∞ = 3.88×10⁶/ft.

Configuration: IRVE-15
D = 6.0 in. / 0.1524 m
R_{nose} = 0.375 in. / 0.00953 m

LaRC 20-Inch Mach 6 Air Tunnel
Test 6979, Run 024



Re_∞ = 6.63E+06 /ft
Re_∞ = 2.18E+07 /m
α = 0-deg
U_∞ = 954.6 m/s
ρ_∞ = 1.02E-01
T_∞ = 62.6 K
H_{Total} - H_{300K} = 2.17E+05
q_{FR,Rn} = 1.98E+05 W/m²
h_{FR,Rn} = 9.10E-01 kg/m²-s

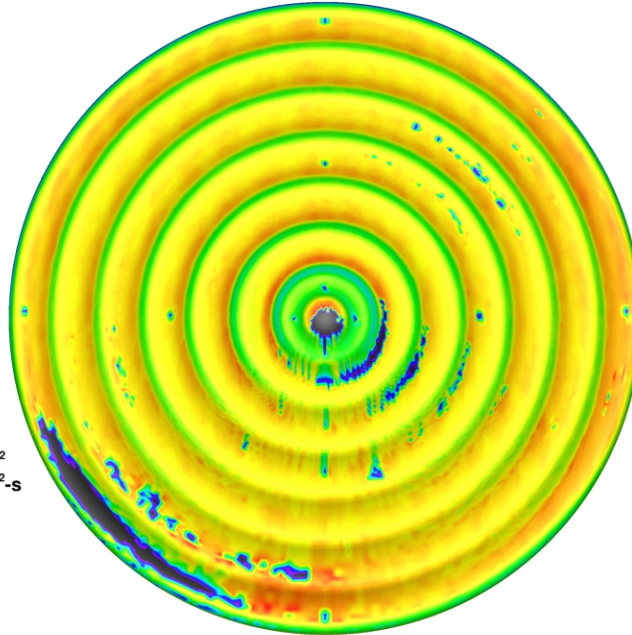
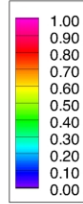


Figure 220. IRVE Scallop-15 Model, Run 24: α = 0 deg, Re_∞ = 6.63×10⁶/ft.

Configuration: IRVE-15
D = 6.0 in. / 0.1524 m
R_{nose} = 0.375 in. / 0.00953 m

LaRC 20-Inch Mach 6 Air Tunnel
Test 6979, Run 025

$h/h_{FR,Rn}$



$Re_\infty = 8.34E+06$ /ft
 $Re_\infty = 2.74E+07$ /m
 $\alpha = 0\text{-deg}$
 $U_\infty = 918.1$ m/s
 $\rho_\infty = 1.25E-01$
 $T_\infty = 58.6$ K
 $H_{Total} - H_{300K} = 1.79E+05$
 $q_{FR,Rn} = 1.73E+05$ W/m²
 $h_{FR,Rn} = 9.64E-01$ kg/m²-s

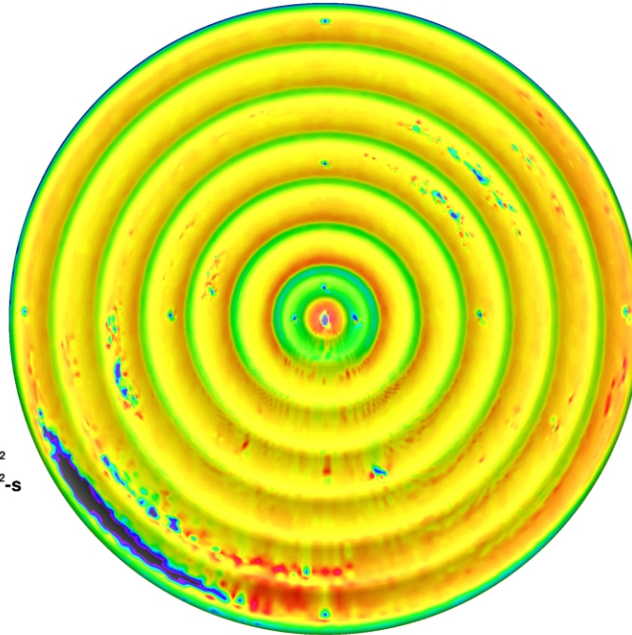
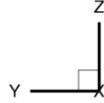
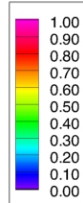


Figure 221. IRVE Scallop-15 Model, Run 25: $\alpha = 0$ deg, $Re_\infty = 8.33 \times 10^6$ /ft.

Configuration: IRVE-15
D = 6.0 in. / 0.1524 m
R_{nose} = 0.375 in. / 0.00953 m

LaRC 20-Inch Mach 6 Air Tunnel
Test 6979, Run 126

$h/h_{FR,Rn}$



$Re_\infty = 2.10E+06$ /ft
 $Re_\infty = 6.89E+06$ /m
 $\alpha = 6\text{-deg}$
 $U_\infty = 939.5$ m/s
 $\rho_\infty = 3.25E-02$
 $T_\infty = 61.9$ K
 $H_{Total} - H_{300K} = 2.03E+05$
 $q_{FR,Rn} = 1.02E+05$ W/m²
 $h_{FR,Rn} = 5.01E-01$ kg/m²-s

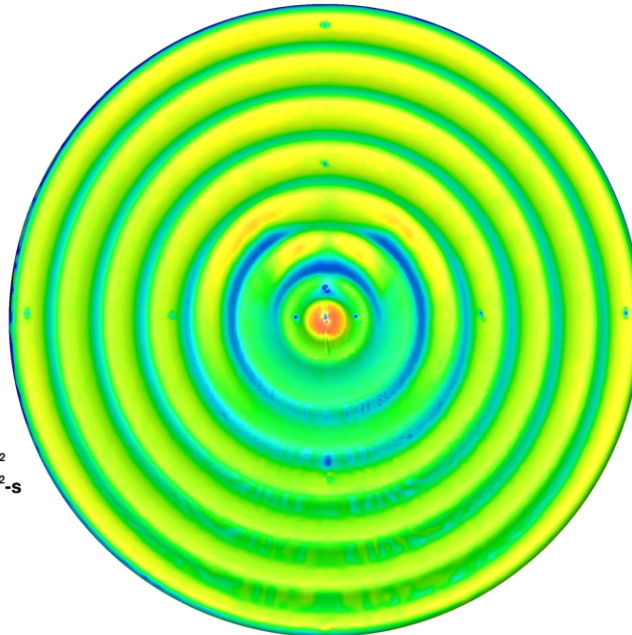
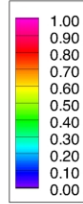


Figure 222. IRVE Scallop-15 Model, Run 126: $\alpha = 6$ deg, $Re_\infty = 2.10 \times 10^6$ /ft.

Configuration: IRVE-15
D = 6.0 in. / 0.1524 m
R_{nose} = 0.375 in. / 0.00953 m

LaRC 20-Inch Mach 6 Air Tunnel
Test 6979, Run 127

$h/h_{FR,Rn}$



$Re_\infty = 3.03E+06$ /ft
 $Re_\infty = 9.95E+06$ /m
 $\alpha = 6\text{-deg}$
 $U_\infty = 948.7$ m/s
 $\rho_\infty = 4.71E-02$
 $T_\infty = 62.5$ K
 $H_{Total} - H_{300K} = 2.12E+05$
 $q_{FR,Rn} = 1.30E+05$ W/m²
 $h_{FR,Rn} = 6.11E-01$ kg/m²-s

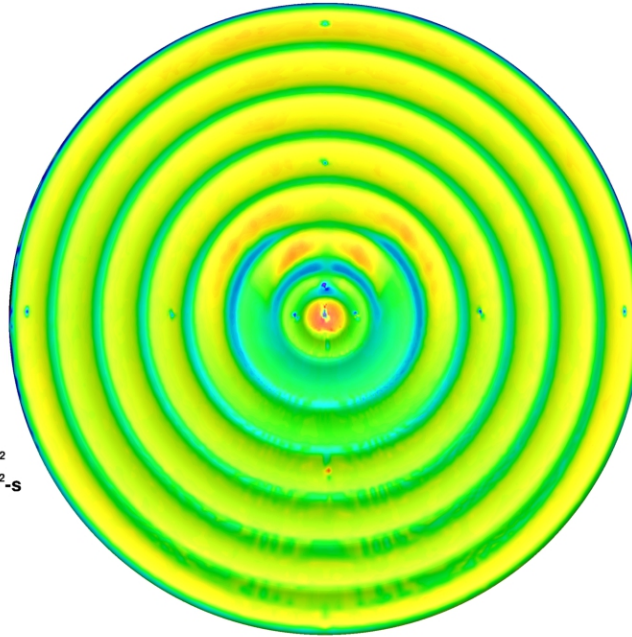
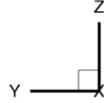
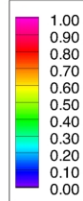


Figure 223. IRVE Scallop-15 Model, Run 127: $\alpha = 6$ deg, $Re_\infty = 3.03 \times 10^6$ /ft.

Configuration: IRVE-15
D = 6.0 in. / 0.1524 m
R_{nose} = 0.375 in. / 0.00953 m

LaRC 20-Inch Mach 6 Air Tunnel
Test 6979, Run 128

$h/h_{FR,Rn}$



$Re_\infty = 3.88E+06$ /ft
 $Re_\infty = 1.28E+07$ /m
 $\alpha = 6\text{-deg}$
 $U_\infty = 957.2$ m/s
 $\rho_\infty = 6.05E-02$
 $T_\infty = 63.3$ K
 $H_{Total} - H_{300K} = 2.21E+05$
 $q_{FR,Rn} = 1.55E+05$ W/m²
 $h_{FR,Rn} = 7.00E-01$ kg/m²-s

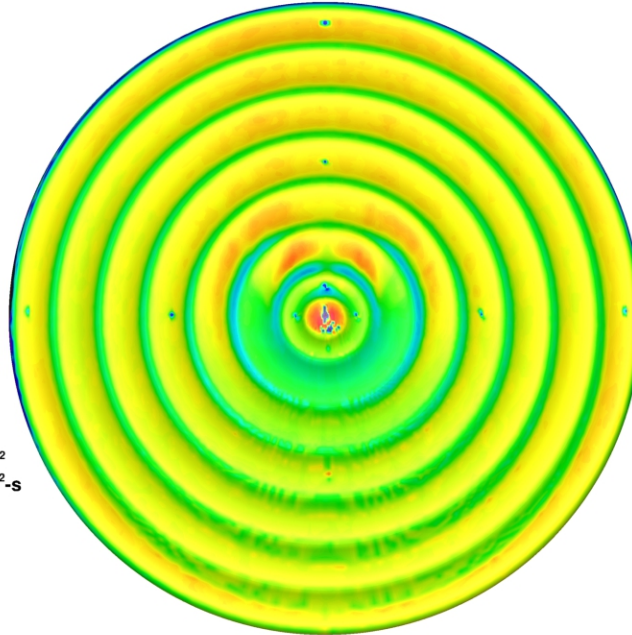
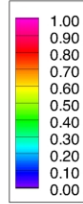


Figure 224. IRVE Scallop-15 Model, Run 128: $\alpha = 6$ deg, $Re_\infty = 3.88 \times 10^6$ /ft.

Configuration: IRVE-15
D = 6.0 in. / 0.1524 m
R_{nose} = 0.375 in. / 0.00953 m

LaRC 20-Inch Mach 6 Air Tunnel
Test 6979, Run 129

$h/h_{FR,Rn}$



$Re_\infty = 6.63E+06$ /ft
 $Re_\infty = 2.18E+07$ /m
 $\alpha = 6\text{-deg}$
 $U_\infty = 954.6$ m/s
 $\rho_\infty = 1.02E-01$
 $T_\infty = 62.6$ K
 $H_{Total} - H_{300K} = 2.17E+05$
 $q_{FR,Rn} = 1.98E+05$ W/m²
 $h_{FR,Rn} = 9.10E-01$ kg/m²-s

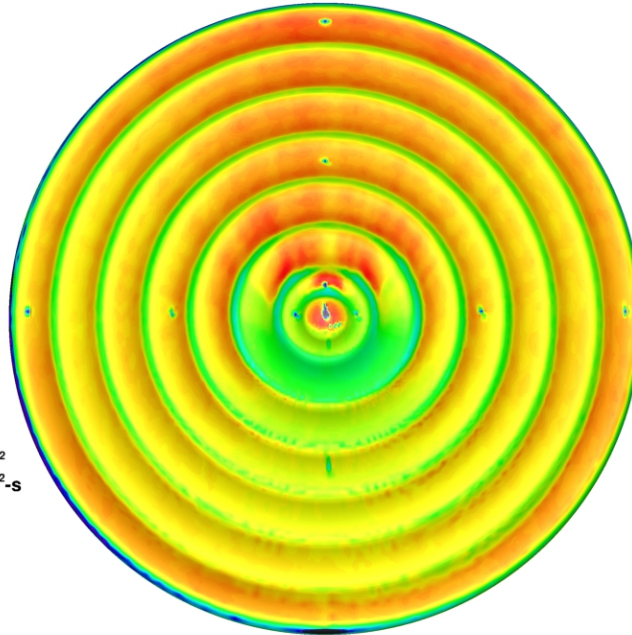
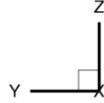
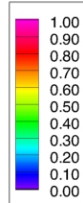


Figure 225. IRVE Scallop-15 Model, Run 129: $\alpha = 6$ deg, $Re_\infty = 6.63 \times 10^6$ /ft.

Configuration: IRVE-15
D = 6.0 in. / 0.1524 m
R_{nose} = 0.375 in. / 0.00953 m

LaRC 20-Inch Mach 6 Air Tunnel
Test 6979, Run 130

$h/h_{FR,Rn}$



$Re_\infty = 8.34E+06$ /ft
 $Re_\infty = 2.74E+07$ /m
 $\alpha = 6\text{-deg}$
 $U_\infty = 918.1$ m/s
 $\rho_\infty = 1.25E-01$
 $T_\infty = 58.6$ K
 $H_{Total} - H_{300K} = 1.79E+05$
 $q_{FR,Rn} = 1.73E+05$ W/m²
 $h_{FR,Rn} = 9.64E-01$ kg/m²-s

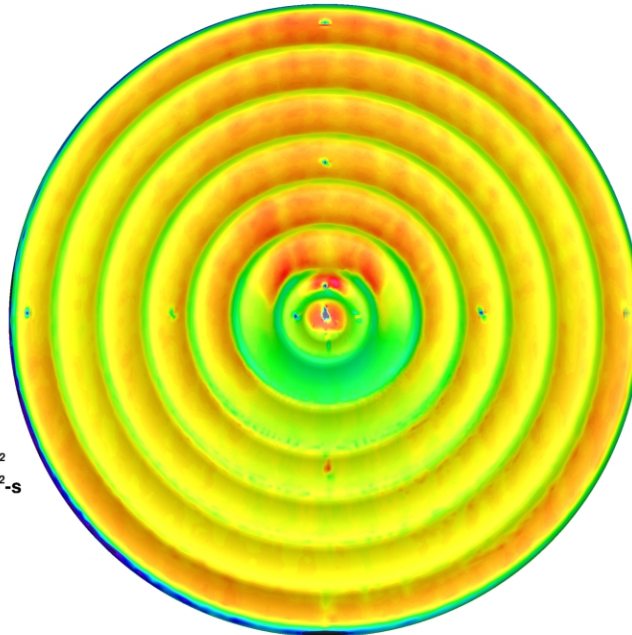
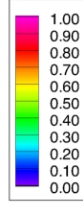


Figure 226. IRVE Scallop-15 Model, Run 130: $\alpha = 6$ deg, $Re_\infty = 8.33 \times 10^6$ /ft.

Configuration: IRVE-15
D = 6.0 in. / 0.1524 m
R_{nose} = 0.375 in. / 0.00953 m

LaRC 20-Inch Mach 6 Air Tunnel
Test 6979, Run 166

$h/h_{FR,Rn}$



$Re_\infty = 2.10E+06$ /ft
 $Re_\infty = 6.89E+06$ /m
 $\alpha = 12\text{-deg}$
 $U_\infty = 939.5$ m/s
 $\rho_\infty = 3.25E-02$
 $T_\infty = 61.9$ K
 $H_{Total} - H_{300K} = 2.03E+05$
 $q_{FR,Rn} = 1.02E+05$ W/m²
 $h_{FR,Rn} = 5.01E-01$ kg/m²·s

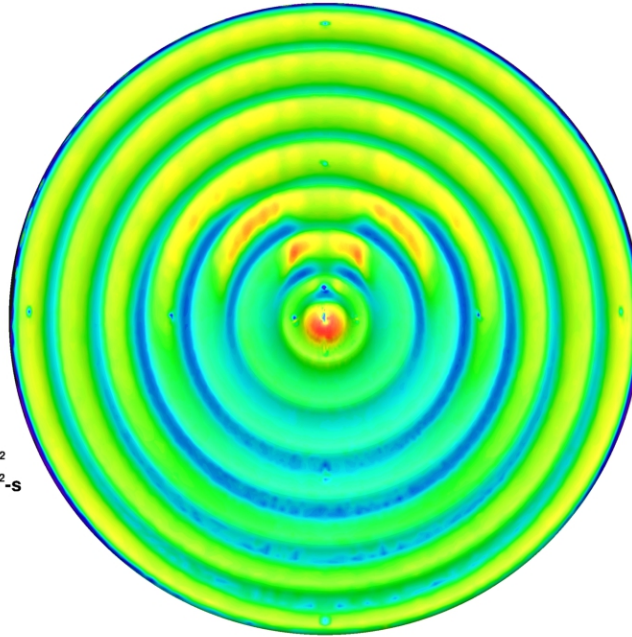
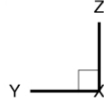
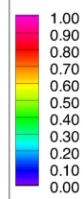


Figure 227. IRVE Scallop-15 Model, Run 166: $\alpha = 12$ deg, $Re_\infty = 2.10 \times 10^6$ /ft.

Configuration: IRVE-15
D = 6.0 in. / 0.1524 m
R_{nose} = 0.375 in. / 0.00953 m

LaRC 20-Inch Mach 6 Air Tunnel
Test 6979, Run 167

$h/h_{FR,Rn}$



$Re_\infty = 3.03E+06$ /ft
 $Re_\infty = 9.95E+06$ /m
 $\alpha = 12\text{-deg}$
 $U_\infty = 948.7$ m/s
 $\rho_\infty = 4.71E-02$
 $T_\infty = 62.5$ K
 $H_{Total} - H_{300K} = 2.12E+05$
 $q_{FR,Rn} = 1.30E+05$ W/m²
 $h_{FR,Rn} = 6.11E-01$ kg/m²·s

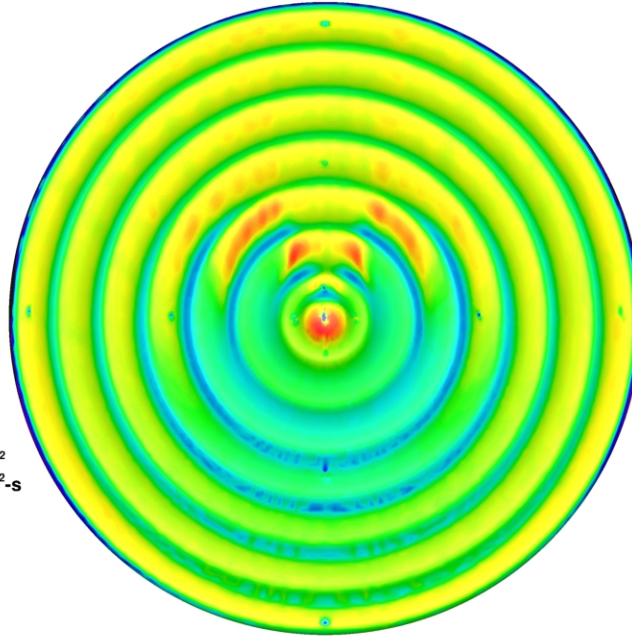
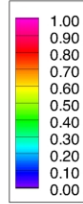


Figure 228. IRVE Scallop-15 Model, Run 167: $\alpha = 12$ deg, $Re_\infty = 3.03 \times 10^6$ /ft.

Configuration: IRVE-15
D = 6.0 in. / 0.1524 m
R_{nose} = 0.375 in. / 0.00953 m

LaRC 20-Inch Mach 6 Air Tunnel
Test 6979, Run 168

$h/h_{FR,Rn}$



$Re_\infty = 3.88E+06$ /ft
 $Re_\infty = 1.28E+07$ /m
 $\alpha = 12\text{-deg}$
 $U_\infty = 957.2$ m/s
 $\rho_\infty = 6.05E-02$
 $T_\infty = 63.3$ K
 $H_{Total} - H_{300K} = 2.21E+05$
 $q_{FR,Rn} = 1.55E+05$ W/m²
 $h_{FR,Rn} = 7.00E-01$ kg/m²-s

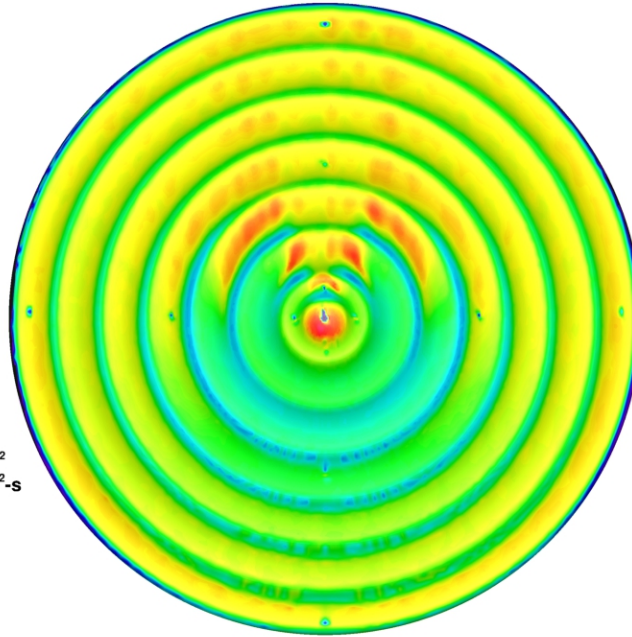
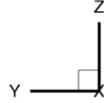
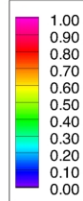


Figure 229. IRVE Scallop-15 Model, Run 168: $\alpha = 12$ deg, $Re_\infty = 3.88 \times 10^6$ /ft.

Configuration: IRVE-15
D = 6.0 in. / 0.1524 m
R_{nose} = 0.375 in. / 0.00953 m

LaRC 20-Inch Mach 6 Air Tunnel
Test 6979, Run 169

$h/h_{FR,Rn}$



$Re_\infty = 6.63E+06$ /ft
 $Re_\infty = 2.18E+07$ /m
 $\alpha = 12\text{-deg}$
 $U_\infty = 954.6$ m/s
 $\rho_\infty = 1.02E-01$
 $T_\infty = 62.6$ K
 $H_{Total} - H_{300K} = 2.17E+05$
 $q_{FR,Rn} = 1.98E+05$ W/m²
 $h_{FR,Rn} = 9.10E-01$ kg/m²-s

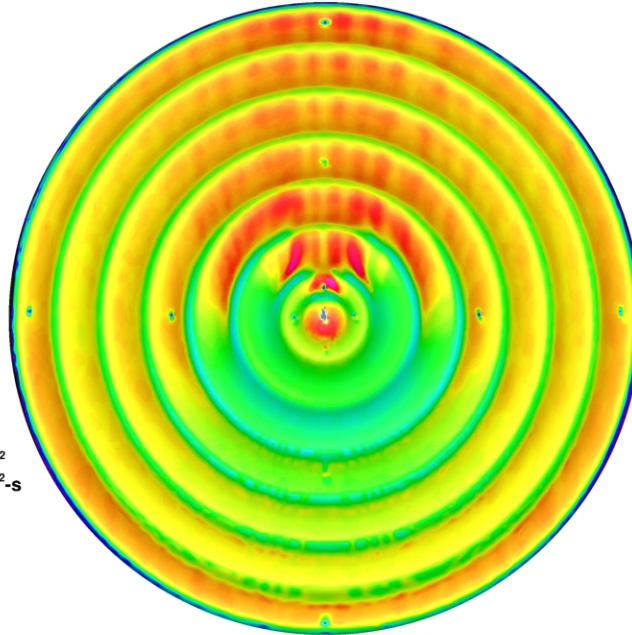
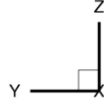
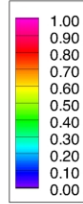


Figure 230. IRVE Scallop-15 Model, Run 169: $\alpha = 12$ deg, $Re_\infty = 6.63 \times 10^6$ /ft.

Configuration: IRVE-15
D = 6.0 in. / 0.1524 m
R_{nose} = 0.375 in. / 0.00953 m

LaRC 20-Inch Mach 6 Air Tunnel
Test 6979, Run 170

$h/h_{FR,Rn}$



$Re_\infty = 8.34E+06$ /ft
 $Re_\infty = 2.74E+07$ /m
 $\alpha = 12\text{-deg}$
 $U_\infty = 918.1$ m/s
 $\rho_\infty = 1.25E-01$
 $T_\infty = 58.6$ K
 $H_{Total} - H_{300K} = 1.79E+05$
 $q_{FR,Rn} = 1.73E+05$ W/m²
 $h_{FR,Rn} = 9.64E-01$ kg/m²-s

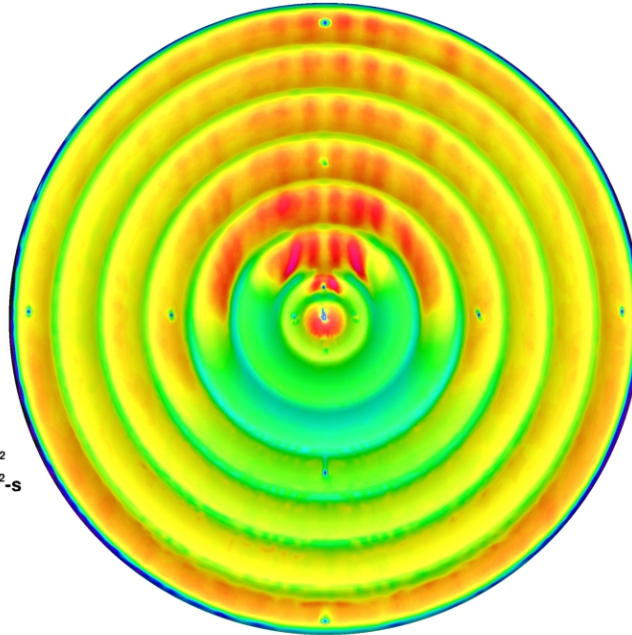
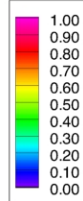


Figure 231. IRVE Scallop-15 Model, Run 170: $\alpha = 12$ deg, $Re_\infty = 8.33 \times 10^6$ /ft.

Configuration: IRVE-15
D = 6.0 in. / 0.1524 m
R_{nose} = 0.375 in. / 0.00953 m

LaRC 20-Inch Mach 6 Air Tunnel
Test 6979, Run 131

$h/h_{FR,Rn}$



$Re_\infty = 2.10E+06$ /ft
 $Re_\infty = 6.89E+06$ /m
 $\alpha = 18\text{-deg}$
 $U_\infty = 939.5$ m/s
 $\rho_\infty = 3.25E-02$
 $T_\infty = 61.9$ K
 $H_{Total} - H_{300K} = 2.03E+05$
 $q_{FR,Rn} = 1.02E+05$ W/m²
 $h_{FR,Rn} = 5.01E-01$ kg/m²-s

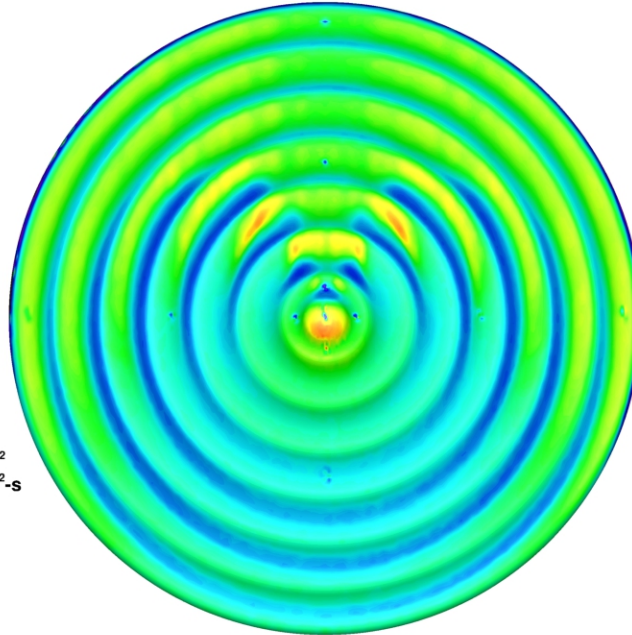
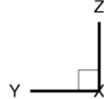
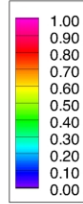


Figure 232. IRVE Scallop-15 Model, Run 131: $\alpha = 18$ deg, $Re_\infty = 2.10 \times 10^6$ /ft.

Configuration: IRVE-15
D = 6.0 in. / 0.1524 m
R_{nose} = 0.375 in. / 0.00953 m

LaRC 20-Inch Mach 6 Air Tunnel
Test 6979, Run 132

$h/h_{FR,Rn}$



$Re_\infty = 3.03E+06$ /ft
 $Re_\infty = 9.95E+06$ /m
 $\alpha = 18\text{-deg}$
 $U_\infty = 948.7$ m/s
 $\rho_\infty = 4.71E-02$
 $T_\infty = 62.5$ K
 $H_{Total} - H_{300K} = 2.12E+05$
 $q_{FR,Rn} = 1.30E+05$ W/m²
 $h_{FR,Rn} = 6.11E-01$ kg/m²-s

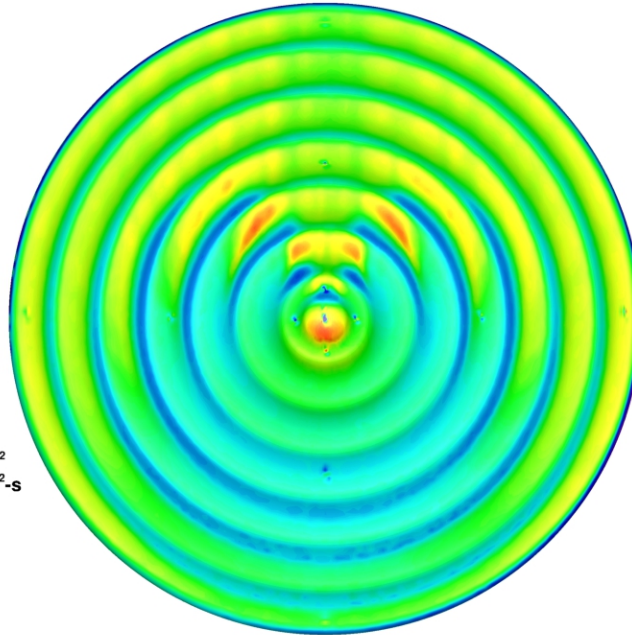
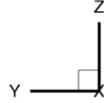
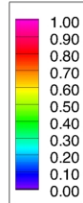


Figure 233. IRVE Scallop-15 Model, Run 132: $\alpha = 18$ deg, $Re_\infty = 3.03 \times 10^6$ /ft.

Configuration: IRVE-15
D = 6.0 in. / 0.1524 m
R_{nose} = 0.375 in. / 0.00953 m

LaRC 20-Inch Mach 6 Air Tunnel
Test 6979, Run 133

$h/h_{FR,Rn}$



$Re_\infty = 3.88E+06$ /ft
 $Re_\infty = 1.28E+07$ /m
 $\alpha = 18\text{-deg}$
 $U_\infty = 957.2$ m/s
 $\rho_\infty = 6.05E-02$
 $T_\infty = 63.3$ K
 $H_{Total} - H_{300K} = 2.21E+05$
 $q_{FR,Rn} = 1.55E+05$ W/m²
 $h_{FR,Rn} = 7.00E-01$ kg/m²-s

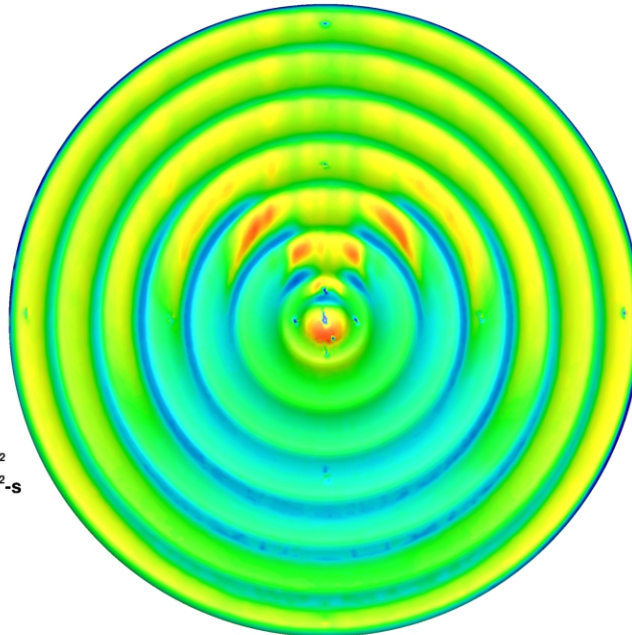
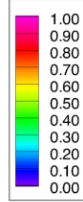


Figure 234. IRVE Scallop-15 Model, Run 133: $\alpha = 18$ deg, $Re_\infty = 3.88 \times 10^6$ /ft.

Configuration: IRVE-15
D = 6.0 in. / 0.1524 m
R_{nose} = 0.375 in. / 0.00953 m

LaRC 20-Inch Mach 6 Air Tunnel
Test 6979, Run 134

$h/h_{FR,Rn}$



$Re_\infty = 6.63E+06$ /ft
 $Re_\infty = 2.18E+07$ /m
 $\alpha = 18\text{-deg}$
 $U_\infty = 954.6$ m/s
 $\rho_\infty = 1.02E-01$
 $T_\infty = 62.6$ K
 $H_{Total} - H_{300K} = 2.17E+05$
 $q_{FR,Rn} = 1.98E+05$ W/m²
 $h_{FR,Rn} = 9.10E-01$ kg/m²-s

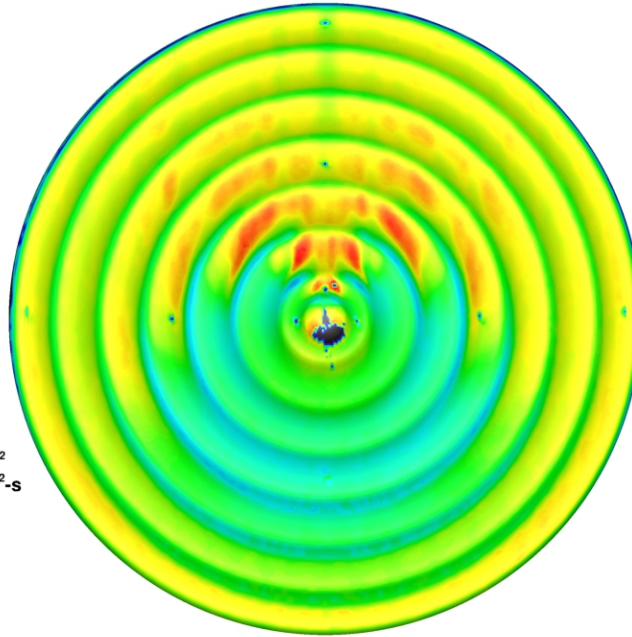
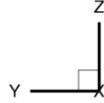
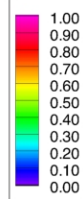


Figure 235. IRVE Scallop-15 Model, Run 134: $\alpha = 18$ deg, $Re_\infty = 6.63 \times 10^6$ /ft.

Configuration: IRVE-15
D = 6.0 in. / 0.1524 m
R_{nose} = 0.375 in. / 0.00953 m

LaRC 20-Inch Mach 6 Air Tunnel
Test 6979, Run 135

$h/h_{FR,Rn}$



$Re_\infty = 8.34E+06$ /ft
 $Re_\infty = 2.74E+07$ /m
 $\alpha = 18\text{-deg}$
 $U_\infty = 918.1$ m/s
 $\rho_\infty = 1.25E-01$
 $T_\infty = 58.6$ K
 $H_{Total} - H_{300K} = 1.79E+05$
 $q_{FR,Rn} = 1.73E+05$ W/m²
 $h_{FR,Rn} = 9.64E-01$ kg/m²-s

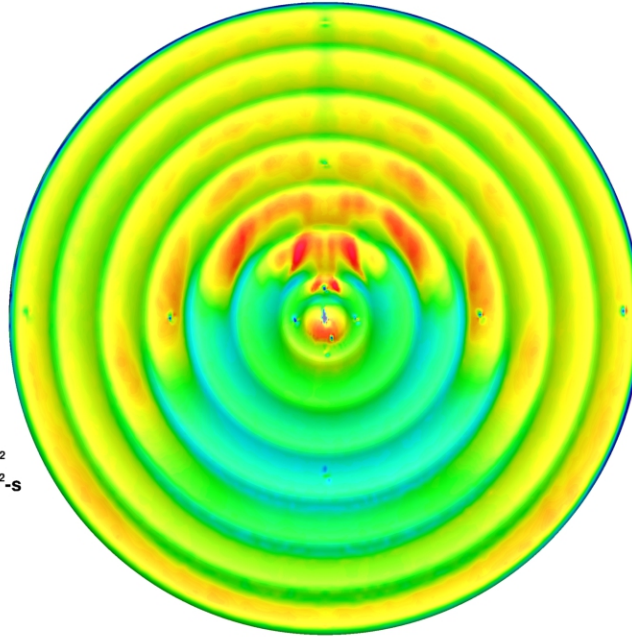
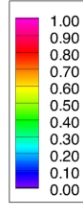


Figure 236. IRVE Scallop-15 Model, Run 135: $\alpha = 18$ deg, $Re_\infty = 8.33 \times 10^6$ /ft.

Configuration: IRVE-20
D = 6.0 in. / 0.1524 m
R_{nose} = 0.375 in. / 0.00953 m

LaRC 20-Inch Mach 6 Air Tunnel
Test 6979, Run 026

$h/h_{FR,Rn}$



$Re_\infty = 2.10E+06$ /ft
 $Re_\infty = 6.89E+06$ /m
 $\alpha = 0\text{-deg}$
 $U_\infty = 939.5$ m/s
 $\rho_\infty = 3.25E-02$
 $T_\infty = 61.9$ K
 $H_{Total} - H_{300K} = 2.03E+05$
 $q_{FR,Rn} = 1.02E+05$ W/m²
 $h_{FR,Rn} = 5.01E-01$ kg/m²-s

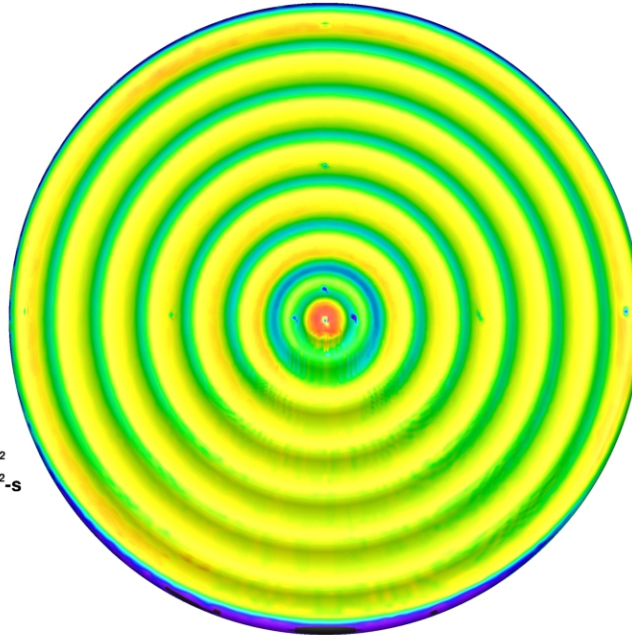
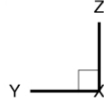
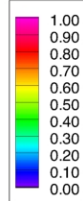


Figure 237. IRVE Scallop-20 Model, Run 26: $\alpha = 0$ deg, $Re_\infty = 2.10 \times 10^6$ /ft.

Configuration: IRVE-20
D = 6.0 in. / 0.1524 m
R_{nose} = 0.375 in. / 0.00953 m

LaRC 20-Inch Mach 6 Air Tunnel
Test 6979, Run 027

$h/h_{FR,Rn}$



$Re_\infty = 3.03E+06$ /ft
 $Re_\infty = 9.95E+06$ /m
 $\alpha = 0\text{-deg}$
 $U_\infty = 948.7$ m/s
 $\rho_\infty = 4.71E-02$
 $T_\infty = 62.5$ K
 $H_{Total} - H_{300K} = 2.12E+05$
 $q_{FR,Rn} = 1.30E+05$ W/m²
 $h_{FR,Rn} = 6.11E-01$ kg/m²-s

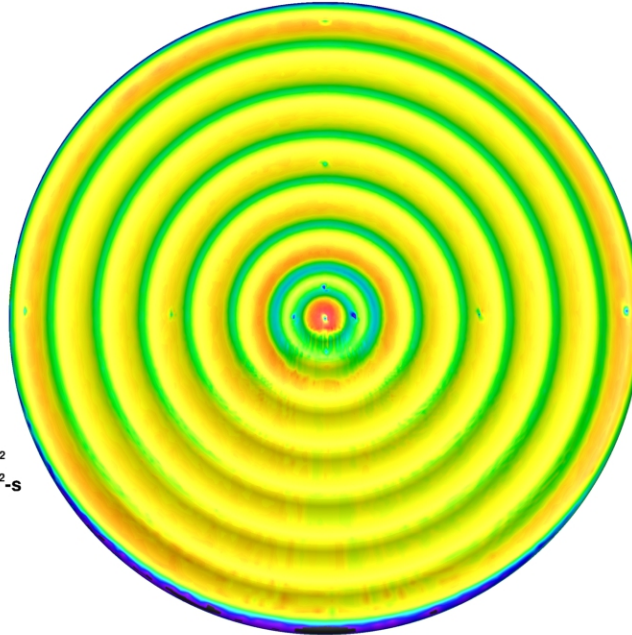
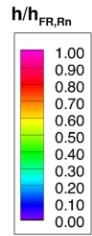


Figure 238. IRVE Scallop-20 Model, Run 27: $\alpha = 0$ deg, $Re_\infty = 3.03 \times 10^6$ /ft.

Configuration: IRVE-20
D = 6.0 in. / 0.1524 m
R_{nose} = 0.375 in. / 0.00953 m

LaRC 20-Inch Mach 6 Air Tunnel
Test 6979, Run 028



$Re_{\infty} = 3.88E+06$ /ft
 $Re_{\infty} = 1.28E+07$ /m
 $\alpha = 0$ -deg
 $U_{\infty} = 957.2$ m/s
 $\rho_{\infty} = 6.05E-02$
 $T_{\infty} = 63.3$ K
 $H_{Total} - H_{300K} = 2.21E+05$
 $q_{FR,Rn} = 1.55E+05$ W/m²
 $h_{FR,Rn} = 7.00E-01$ kg/m²-s

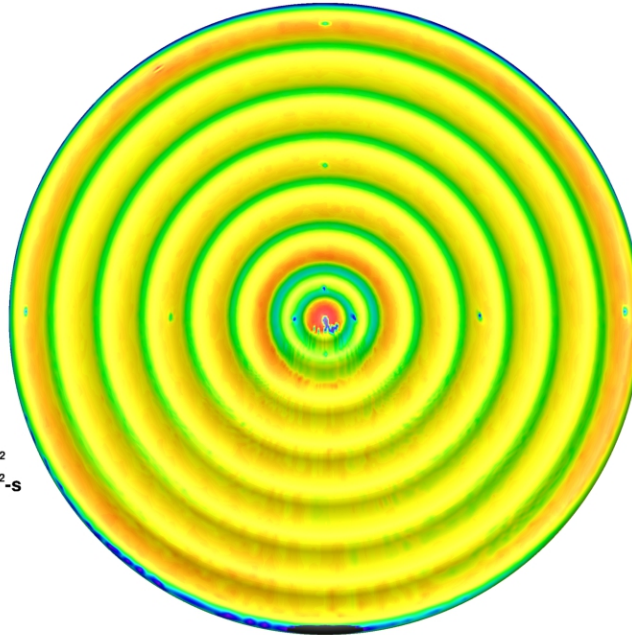
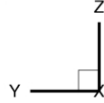
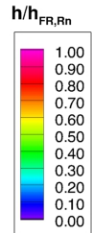


Figure 239. IRVE Scallop-20 Model, Run 28: $\alpha = 0$ deg, $Re_{\infty} = 3.88 \times 10^6$ /ft.

Configuration: IRVE-20
D = 6.0 in. / 0.1524 m
R_{nose} = 0.375 in. / 0.00953 m

LaRC 20-Inch Mach 6 Air Tunnel
Test 6979, Run 029



$Re_{\infty} = 6.63E+06$ /ft
 $Re_{\infty} = 2.18E+07$ /m
 $\alpha = 0$ -deg
 $U_{\infty} = 954.6$ m/s
 $\rho_{\infty} = 1.02E-01$
 $T_{\infty} = 62.6$ K
 $H_{Total} - H_{300K} = 2.17E+05$
 $q_{FR,Rn} = 1.98E+05$ W/m²
 $h_{FR,Rn} = 9.10E-01$ kg/m²-s

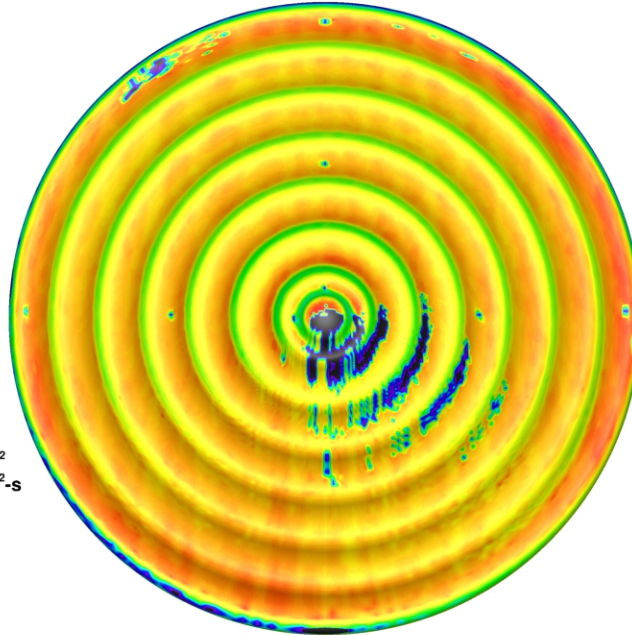
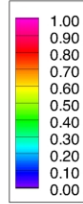


Figure 240. IRVE Scallop-20 Model, Run 29: $\alpha = 0$ deg, $Re_{\infty} = 6.63 \times 10^6$ /ft.

Configuration: IRVE-20
D = 6.0 in. / 0.1524 m
R_{nose} = 0.375 in. / 0.00953 m

LaRC 20-Inch Mach 6 Air Tunnel
Test 6979, Run 030

$h/h_{FR,Rn}$



$Re_\infty = 8.34E+06$ /ft
 $Re_\infty = 2.74E+07$ /m
 $\alpha = 0$ -deg
 $U_\infty = 918.1$ m/s
 $\rho_\infty = 1.25E-01$
 $T_\infty = 58.6$ K
 $H_{Total} - H_{300K} = 1.79E+05$
 $q_{FR,Rn} = 1.73E+05$ W/m²
 $h_{FR,Rn} = 9.64E-01$ kg/m²-s

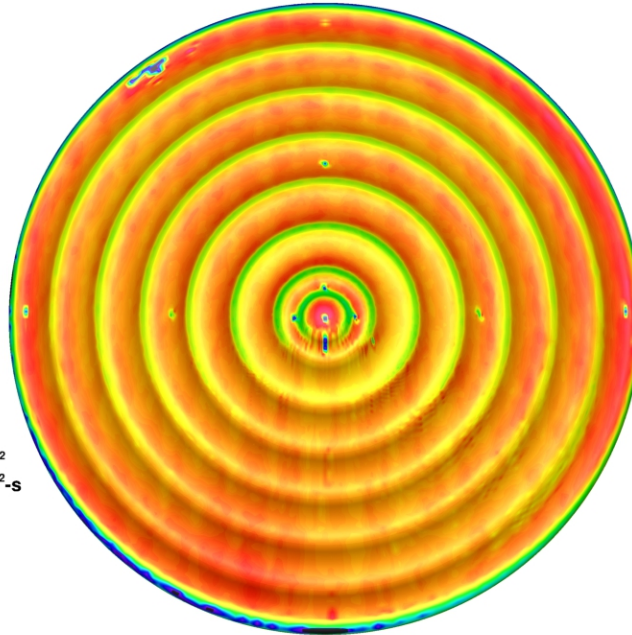
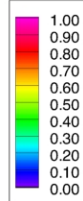


Figure 241. IRVE Scallop-20 Model, Run 30: $\alpha = 0$ deg, $Re_\infty = 8.33 \times 10^6$ /ft.

Configuration: IRVE-20
D = 6.0 in. / 0.1524 m
R_{nose} = 0.375 in. / 0.00953 m

LaRC 20-Inch Mach 6 Air Tunnel
Test 6979, Run 045

$h/h_{FR,Rn}$



$Re_\infty = 2.10E+06$ /ft
 $Re_\infty = 6.89E+06$ /m
 $\alpha = 6$ -deg
 $U_\infty = 939.5$ m/s
 $\rho_\infty = 3.25E-02$
 $T_\infty = 61.9$ K
 $H_{Total} - H_{300K} = 2.03E+05$
 $q_{FR,Rn} = 1.02E+05$ W/m²
 $h_{FR,Rn} = 5.01E-01$ kg/m²-s

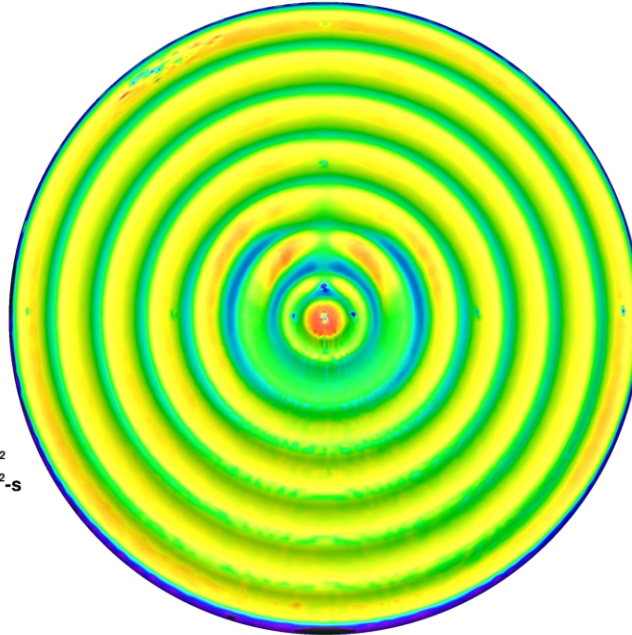
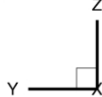
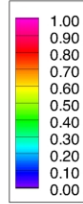


Figure 242. IRVE Scallop-20 Model, Run 45: $\alpha = 6$ deg, $Re_\infty = 2.10 \times 10^6$ /ft.

Configuration: IRVE-20
D = 6.0 in. / 0.1524 m
R_{nose} = 0.375 in. / 0.00953 m

LaRC 20-Inch Mach 6 Air Tunnel
Test 6979, Run 046

$h/h_{FR,Rn}$



$Re_\infty = 3.03E+06$ /ft
 $Re_\infty = 9.95E+06$ /m
 $\alpha = 6\text{-deg}$
 $U_\infty = 948.7$ m/s
 $\rho_\infty = 4.71E-02$
 $T_\infty = 62.5$ K
 $H_{Total} - H_{300K} = 2.12E+05$
 $q_{FR,Rn} = 1.30E+05$ W/m²
 $h_{FR,Rn} = 6.11E-01$ kg/m²-s

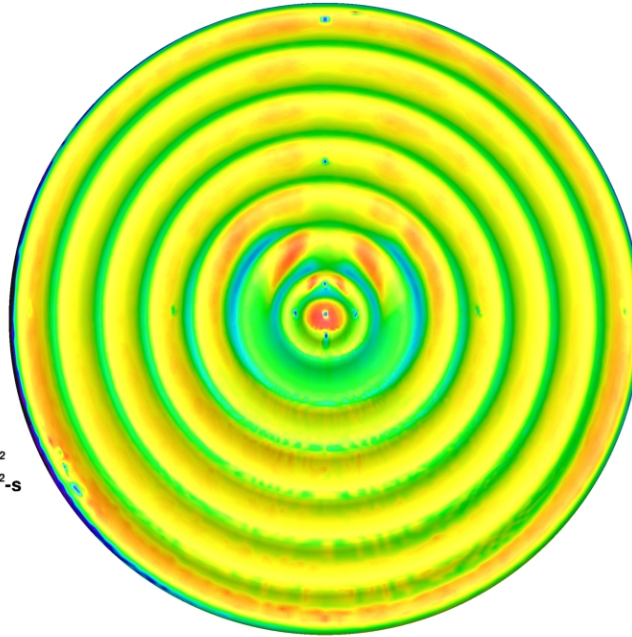
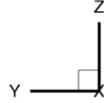
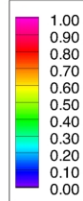


Figure 243. IRVE Scallop-20 Model, Run 46: $\alpha = 6$ deg, $Re_\infty = 3.03 \times 10^6$ /ft.

Configuration: IRVE-20
D = 6.0 in. / 0.1524 m
R_{nose} = 0.375 in. / 0.00953 m

LaRC 20-Inch Mach 6 Air Tunnel
Test 6979, Run 047

$h/h_{FR,Rn}$



$Re_\infty = 3.88E+06$ /ft
 $Re_\infty = 1.28E+07$ /m
 $\alpha = 6\text{-deg}$
 $U_\infty = 957.2$ m/s
 $\rho_\infty = 6.05E-02$
 $T_\infty = 63.3$ K
 $H_{Total} - H_{300K} = 2.21E+05$
 $q_{FR,Rn} = 1.55E+05$ W/m²
 $h_{FR,Rn} = 7.00E-01$ kg/m²-s

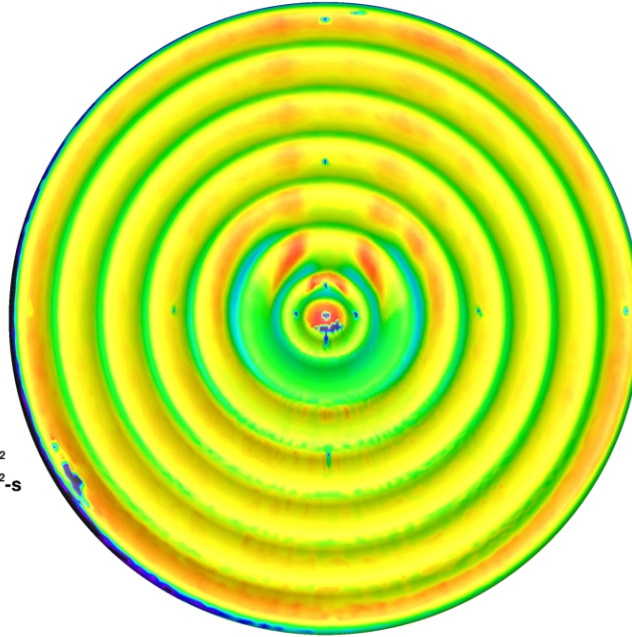
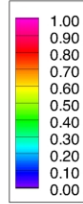


Figure 244. IRVE Scallop-20 Model, Run 47: $\alpha = 6$ deg, $Re_\infty = 3.88 \times 10^6$ /ft.

Configuration: IRVE-20
D = 6.0 in. / 0.1524 m
R_{nose} = 0.375 in. / 0.00953 m

LaRC 20-Inch Mach 6 Air Tunnel
Test 6979, Run 048

$h/h_{FR,Rn}$



$Re_\infty = 6.63E+06$ /ft
 $Re_\infty = 2.18E+07$ /m
 $\alpha = 6\text{-deg}$
 $U_\infty = 954.6$ m/s
 $\rho_\infty = 1.02E-01$
 $T_\infty = 62.6$ K
 $H_{Total} - H_{300K} = 2.17E+05$
 $q_{FR,Rn} = 1.98E+05$ W/m²
 $h_{FR,Rn} = 9.10E-01$ kg/m²-s

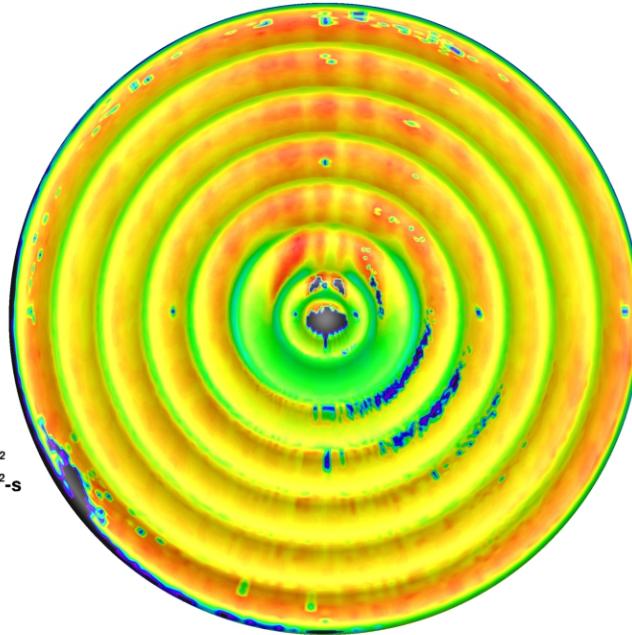
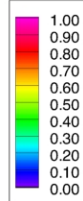


Figure 245. IRVE Scallop-20 Model, Run 48: $\alpha = 6$ deg, $Re_\infty = 6.63 \times 10^6$ /ft.

Configuration: IRVE-20
D = 6.0 in. / 0.1524 m
R_{nose} = 0.375 in. / 0.00953 m

LaRC 20-Inch Mach 6 Air Tunnel
Test 6979, Run 049

$h/h_{FR,Rn}$



$Re_\infty = 8.34E+06$ /ft
 $Re_\infty = 2.74E+07$ /m
 $\alpha = 6\text{-deg}$
 $U_\infty = 918.1$ m/s
 $\rho_\infty = 1.25E-01$
 $T_\infty = 58.6$ K
 $H_{Total} - H_{300K} = 1.79E+05$
 $q_{FR,Rn} = 1.73E+05$ W/m²
 $h_{FR,Rn} = 9.64E-01$ kg/m²-s

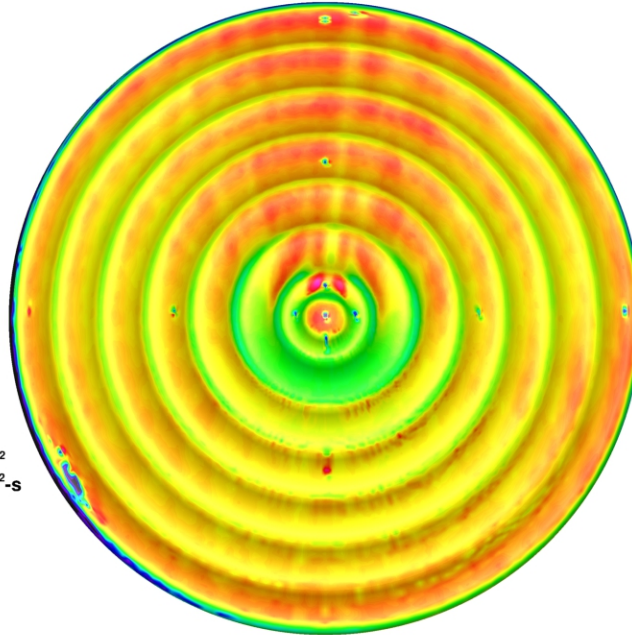
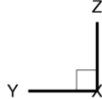
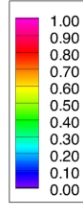


Figure 246. IRVE Scallop-20 Model, Run 49: $\alpha = 6$ deg, $Re_\infty = 8.33 \times 10^6$ /ft.

Configuration: IRVE-20
D = 6.0 in. / 0.1524 m
R_{nose} = 0.375 in. / 0.00953 m

LaRC 20-Inch Mach 6 Air Tunnel
Test 6979, Run 087

$h/h_{FR,Rn}$



$Re_\infty = 2.10E+06$ /ft
 $Re_\infty = 6.89E+06$ /m
 $\alpha = 12$ -deg
 $U_\infty = 939.5$ m/s
 $\rho_\infty = 3.25E-02$
 $T_\infty = 61.9$ K
 $H_{Total} - H_{300K} = 2.03E+05$
 $q_{FR,Rn} = 1.02E+05$ W/m²
 $h_{FR,Rn} = 5.01E-01$ kg/m²-s

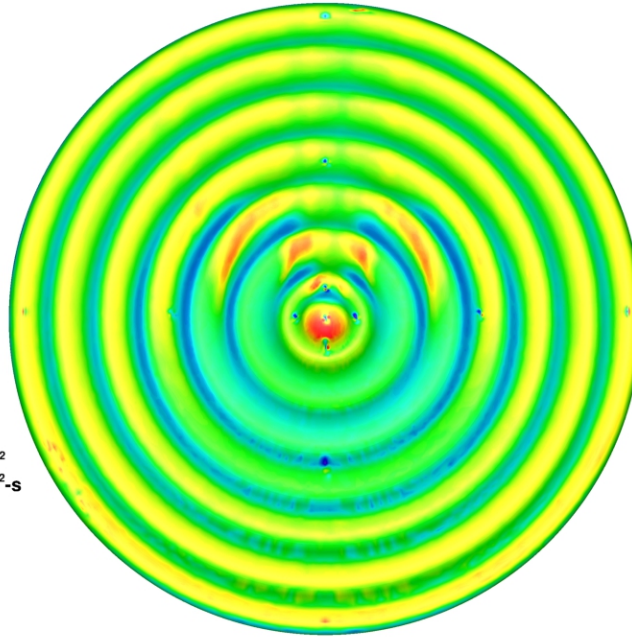
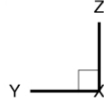
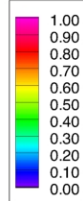


Figure 247. IRVE Scallop-20 Model, Run 87: $\alpha = 12$ deg, $Re_\infty = 2.10 \times 10^6$ /ft.

Configuration: IRVE-20
D = 6.0 in. / 0.1524 m
R_{nose} = 0.375 in. / 0.00953 m

LaRC 20-Inch Mach 6 Air Tunnel
Test 6979, Run 089

$h/h_{FR,Rn}$



$Re_\infty = 3.03E+06$ /ft
 $Re_\infty = 9.95E+06$ /m
 $\alpha = 12$ -deg
 $U_\infty = 948.7$ m/s
 $\rho_\infty = 4.71E-02$
 $T_\infty = 62.5$ K
 $H_{Total} - H_{300K} = 2.12E+05$
 $q_{FR,Rn} = 1.30E+05$ W/m²
 $h_{FR,Rn} = 6.11E-01$ kg/m²-s

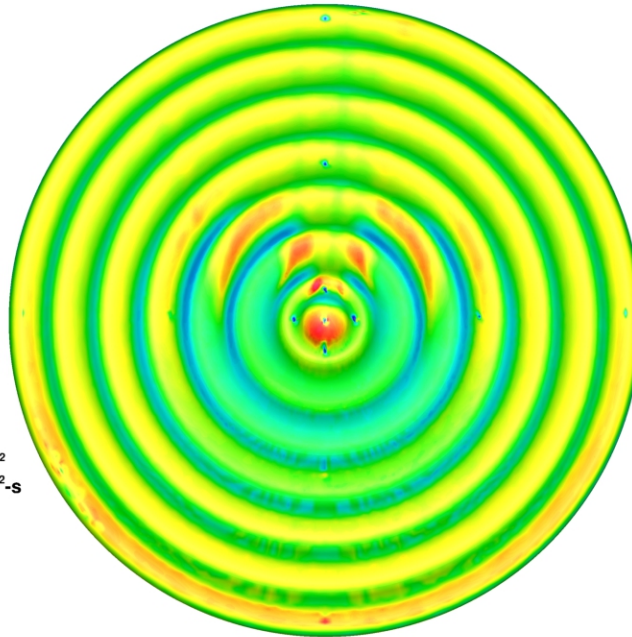
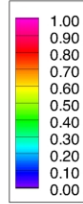


Figure 248. IRVE Scallop-20 Model, Run 89: $\alpha = 12$ deg, $Re_\infty = 3.03 \times 10^6$ /ft.

Configuration: IRVE-20
D = 6.0 in. / 0.1524 m
R_{nose} = 0.375 in. / 0.00953 m

LaRC 20-Inch Mach 6 Air Tunnel
Test 6979, Run 088

$h/h_{FR,Rn}$



$Re_\infty = 3.88E+06$ /ft
 $Re_\infty = 1.28E+07$ /m
 $\alpha = 12\text{-deg}$
 $U_\infty = 957.2$ m/s
 $\rho_\infty = 6.05E-02$
 $T_\infty = 63.3$ K
 $H_{Total} - H_{300K} = 2.21E+05$
 $q_{FR,Rn} = 1.55E+05$ W/m²
 $h_{FR,Rn} = 7.00E-01$ kg/m²-s

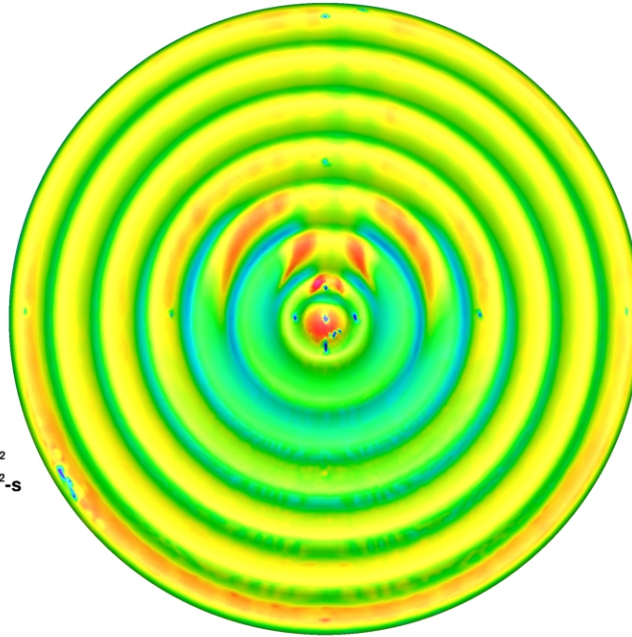
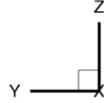
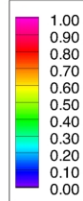


Figure 249. IRVE Scallop-20 Model, Run 88: $\alpha = 12$ deg, $Re_\infty = 3.88 \times 10^6$ /ft.

Configuration: IRVE-20
D = 6.0 in. / 0.1524 m
R_{nose} = 0.375 in. / 0.00953 m

LaRC 20-Inch Mach 6 Air Tunnel
Test 6979, Run 090

$h/h_{FR,Rn}$



$Re_\infty = 6.63E+06$ /ft
 $Re_\infty = 2.18E+07$ /m
 $\alpha = 12\text{-deg}$
 $U_\infty = 954.6$ m/s
 $\rho_\infty = 1.02E-01$
 $T_\infty = 62.6$ K
 $H_{Total} - H_{300K} = 2.17E+05$
 $q_{FR,Rn} = 1.98E+05$ W/m²
 $h_{FR,Rn} = 9.10E-01$ kg/m²-s

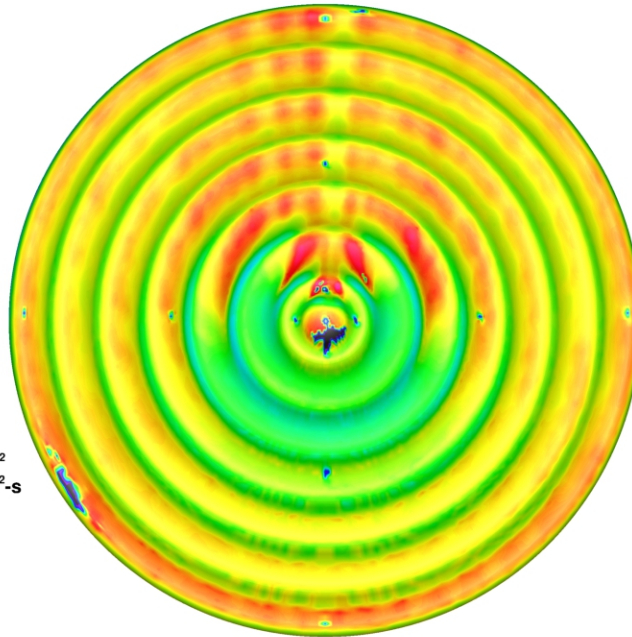
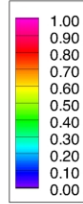


Figure 250. IRVE Scallop-20 Model, Run 90: $\alpha = 12$ deg, $Re_\infty = 6.63 \times 10^6$ /ft.

Configuration: IRVE-20
D = 6.0 in. / 0.1524 m
R_{nose} = 0.375 in. / 0.00953 m

LaRC 20-Inch Mach 6 Air Tunnel
Test 6979, Run 091

$h/h_{FR,Rn}$



$Re_\infty = 8.34E+06$ /ft
 $Re_\infty = 2.74E+07$ /m
 $\alpha = 12\text{-deg}$
 $U_\infty = 918.1$ m/s
 $\rho_\infty = 1.25E-01$
 $T_\infty = 58.6$ K
 $H_{Total} - H_{300K} = 1.79E+05$
 $q_{FR,Rn} = 1.73E+05$ W/m²
 $h_{FR,Rn} = 9.64E-01$ kg/m²-s

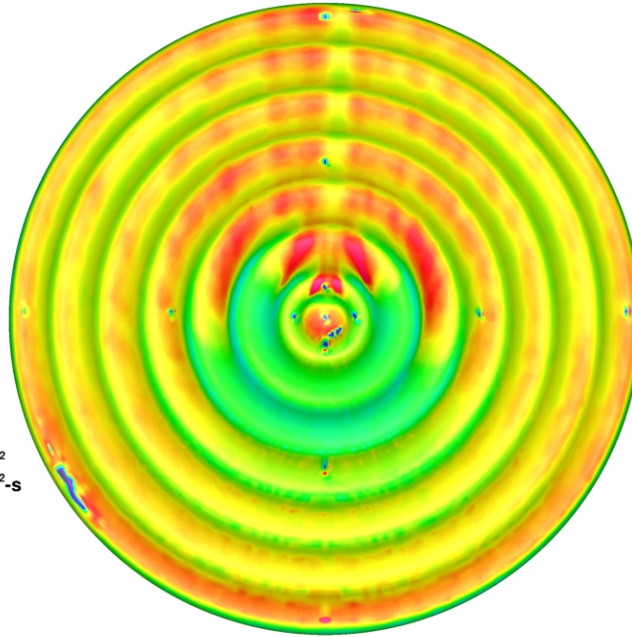
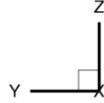
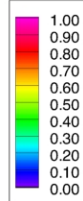


Figure 251. IRVE Scallop-20 Model, Run 91: $\alpha = 12$ deg, $Re_\infty = 8.33 \times 10^6$ /ft.

Configuration: IRVE-20
D = 6.0 in. / 0.1524 m
R_{nose} = 0.375 in. / 0.00953 m

LaRC 20-Inch Mach 6 Air Tunnel
Test 6979, Run 087

$h/h_{FR,Rn}$



$Re_\infty = 2.10E+06$ /ft
 $Re_\infty = 6.89E+06$ /m
 $\alpha = 12\text{-deg}$
 $U_\infty = 939.5$ m/s
 $\rho_\infty = 3.25E-02$
 $T_\infty = 61.9$ K
 $H_{Total} - H_{300K} = 2.03E+05$
 $q_{FR,Rn} = 1.02E+05$ W/m²
 $h_{FR,Rn} = 5.01E-01$ kg/m²-s

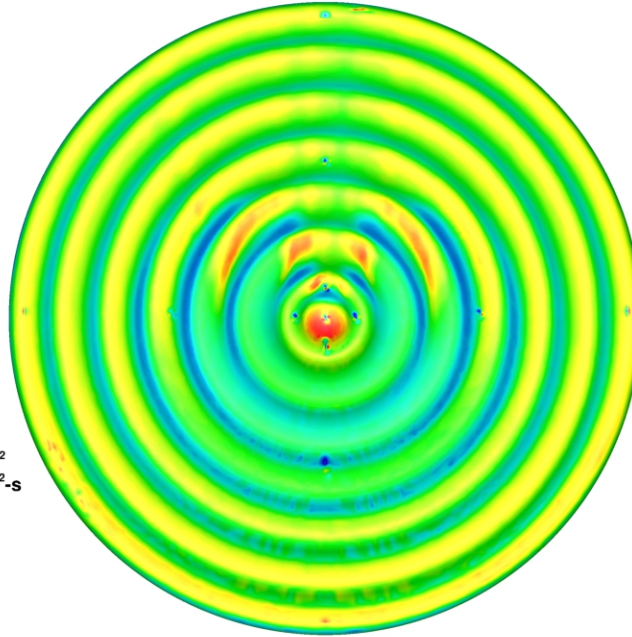
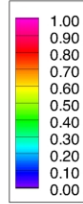


Figure 252. IRVE Scallop-20 Model, Run 141: $\alpha = 18$ deg, $Re_\infty = 2.10 \times 10^6$ /ft.

Configuration: IRVE-20
D = 6.0 in. / 0.1524 m
R_{nose} = 0.375 in. / 0.00953 m

LaRC 20-Inch Mach 6 Air Tunnel
Test 6979, Run 089

$h/h_{FR,Rn}$



$Re_\infty = 3.03E+06$ /ft
 $Re_\infty = 9.95E+06$ /m
 $\alpha = 12$ -deg
 $U_\infty = 948.7$ m/s
 $\rho_\infty = 4.71E-02$
 $T_\infty = 62.5$ K
 $H_{Total} - H_{300K} = 2.12E+05$
 $q_{FR,Rn} = 1.30E+05$ W/m²
 $h_{FR,Rn} = 6.11E-01$ kg/m²-s

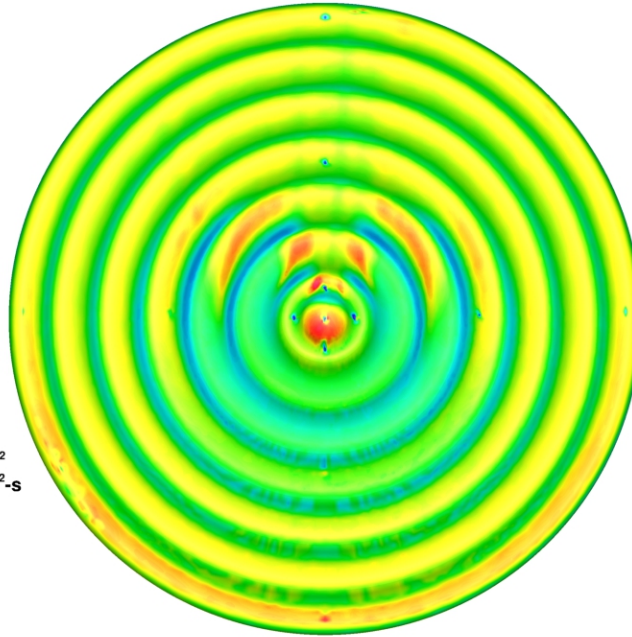
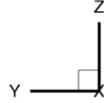
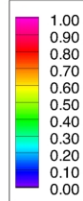


Figure 253. IRVE Scallop-20 Model, Run 142: $\alpha = 18$ deg, $Re_\infty = 3.03 \times 10^6$ /ft.

Configuration: IRVE-20
D = 6.0 in. / 0.1524 m
R_{nose} = 0.375 in. / 0.00953 m

LaRC 20-Inch Mach 6 Air Tunnel
Test 6979, Run 088

$h/h_{FR,Rn}$



$Re_\infty = 3.88E+06$ /ft
 $Re_\infty = 1.28E+07$ /m
 $\alpha = 12$ -deg
 $U_\infty = 957.2$ m/s
 $\rho_\infty = 6.05E-02$
 $T_\infty = 63.3$ K
 $H_{Total} - H_{300K} = 2.21E+05$
 $q_{FR,Rn} = 1.55E+05$ W/m²
 $h_{FR,Rn} = 7.00E-01$ kg/m²-s

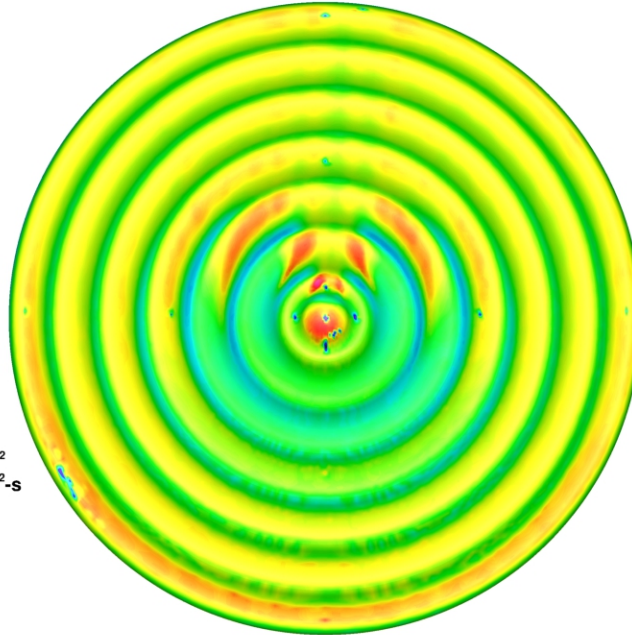
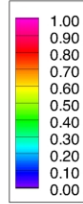


Figure 254. IRVE Scallop-20 Model, Run 143: $\alpha = 18$ deg, $Re_\infty = 3.88 \times 10^6$ /ft.

Configuration: IRVE-20
D = 6.0 in. / 0.1524 m
R_{nose} = 0.375 in. / 0.00953 m

LaRC 20-Inch Mach 6 Air Tunnel
Test 6979, Run 090

$h/h_{FR,Rn}$



$Re_\infty = 6.63E+06$ /ft
 $Re_\infty = 2.18E+07$ /m
 $\alpha = 12$ -deg
 $U_\infty = 954.6$ m/s
 $\rho_\infty = 1.02E-01$
 $T_\infty = 62.6$ K
 $H_{Total} - H_{300K} = 2.17E+05$
 $q_{FR,Rn} = 1.98E+05$ W/m²
 $h_{FR,Rn} = 9.10E-01$ kg/m²-s

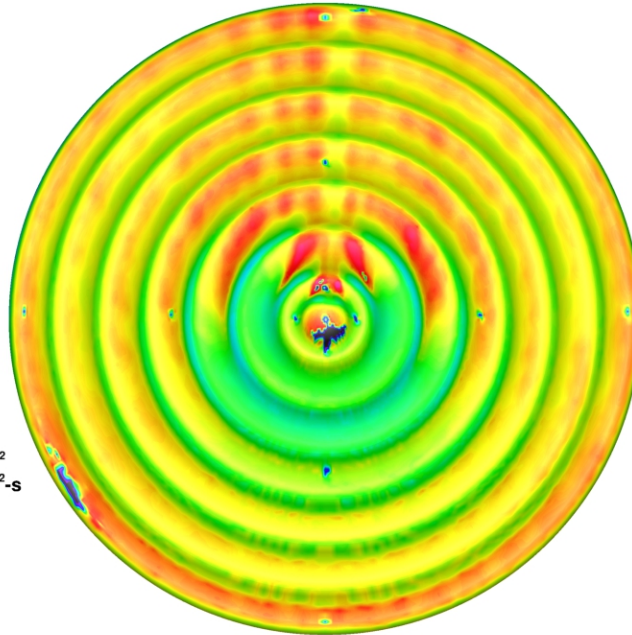
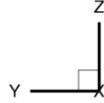
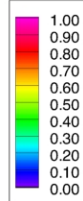


Figure 255. IRVE Scallop-20 Model, Run 144: $\alpha = 18$ deg, $Re_\infty = 6.63 \times 10^6$ /ft.

Configuration: IRVE-20
D = 6.0 in. / 0.1524 m
R_{nose} = 0.375 in. / 0.00953 m

LaRC 20-Inch Mach 6 Air Tunnel
Test 6979, Run 091

$h/h_{FR,Rn}$



$Re_\infty = 8.34E+06$ /ft
 $Re_\infty = 2.74E+07$ /m
 $\alpha = 12$ -deg
 $U_\infty = 918.1$ m/s
 $\rho_\infty = 1.25E-01$
 $T_\infty = 58.6$ K
 $H_{Total} - H_{300K} = 1.79E+05$
 $q_{FR,Rn} = 1.73E+05$ W/m²
 $h_{FR,Rn} = 9.64E-01$ kg/m²-s

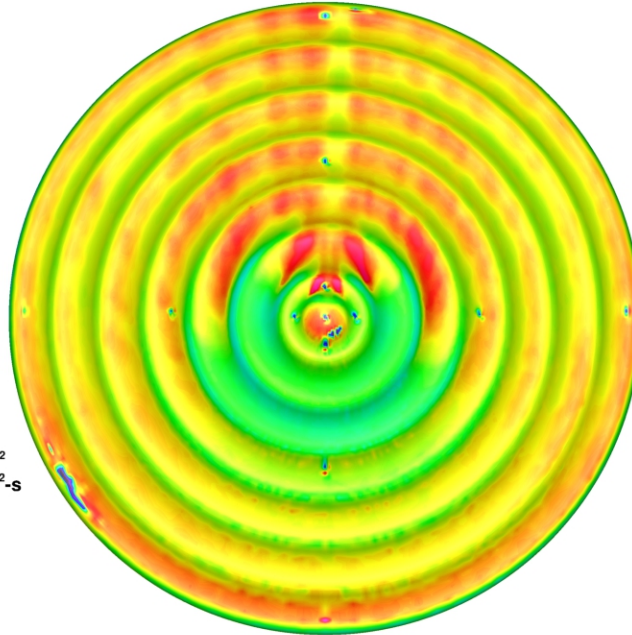
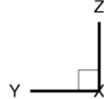


Figure 256. IRVE Scallop-20 Model, Run 145: $\alpha = 18$ deg, $Re_\infty = 8.33 \times 10^6$ /ft.

REPORT DOCUMENTATION PAGE

Form Approved
OMB No. 0704-0188

The public reporting burden for this collection of information is estimated to average 1 hour per response, including the time for reviewing instructions, searching existing data sources, gathering and maintaining the data needed, and completing and reviewing the collection of information. Send comments regarding this burden estimate or any other aspect of this collection of information, including suggestions for reducing the burden, to Department of Defense, Washington Headquarters Services, Directorate for Information Operations and Reports (0704-0188), 1215 Jefferson Davis Highway, Suite 1204, Arlington, VA 22202-4302. Respondents should be aware that notwithstanding any other provision of law, no person shall be subject to any penalty for failing to comply with a collection of information if it does not display a currently valid OMB control number.

PLEASE DO NOT RETURN YOUR FORM TO THE ABOVE ADDRESS.

1. REPORT DATE (DD-MM-YYYY) 01- 03 - 2017			2. REPORT TYPE Technical Memorandum		3. DATES COVERED (From - To)	
4. TITLE AND SUBTITLE Experimental Aeroheating Study of Hypersonic Inflatable Aerodynamic Decelerator (HIAD) Aeroshell with Axisymmetric Surface Deflection Patterns					5a. CONTRACT NUMBER	
					5b. GRANT NUMBER	
					5c. PROGRAM ELEMENT NUMBER	
6. AUTHOR(S) Hollis, Brian R.; Hollingsworth, Kevin E.					5d. PROJECT NUMBER	
					5e. TASK NUMBER	
					5f. WORK UNIT NUMBER 677714.03.01.07	
7. PERFORMING ORGANIZATION NAME(S) AND ADDRESS(ES) NASA Langley Research Center Hampton, VA 23681-2199					8. PERFORMING ORGANIZATION REPORT NUMBER L-20787	
9. SPONSORING/MONITORING AGENCY NAME(S) AND ADDRESS(ES) National Aeronautics and Space Administration Washington, DC 20546-0001					10. SPONSOR/MONITOR'S ACRONYM(S) NASA	
					11. SPONSOR/MONITOR'S REPORT NUMBER(S) NASA-TM-2017-219585	
12. DISTRIBUTION/AVAILABILITY STATEMENT Unclassified - Unlimited Subject Category 34 Availability: NASA STI Program (757) 864-9658						
13. SUPPLEMENTARY NOTES						
14. ABSTRACT A wind tunnel test program was conducted to obtain aeroheating environment data on Hypersonic Inflatable Aerodynamic Decelerator aeroshells with flexible thermal protection systems. Data were obtained on a set of rigid wind tunnel models with surface deflection patterns of various heights that simulated a range of potential in-flight aeroshell deformations. Wind tunnel testing was conducted at Mach 6 at unit Reynolds numbers from 2.1×10 ⁶ /ft to 8.3×10 ⁶ /ft and angles of attack from 0 deg to 18 deg. Boundary-layer transition onset and global surface heating distribution measurements were performed using phosphor thermography and flow field images were obtained through schlieren photography. Surface deflections were found to both promote early transition of the boundary layer and to augment heating levels for both laminar and turbulent flows. A complimentary computational flow field study was also performed to provide heating predictions for comparison with the measurements as well as boundary layer flow field properties for use in correlating the data. Correlations of the wind tunnel data were developed to predict deflection effects on boundary layer transition and surface heating and were applied to both the wind tunnel test conditions and to the trajectory of NASA's successful IRVE-3 flight test.						
15. SUBJECT TERMS EDL; FTPS; HIAD; Aerothermodynamics; Blunt-body; Roughness						
16. SECURITY CLASSIFICATION OF:			17. LIMITATION OF ABSTRACT	18. NUMBER OF PAGES	19a. NAME OF RESPONSIBLE PERSON	
a. REPORT	b. ABSTRACT	c. THIS PAGE			STI Help Desk (email: help@sti.nasa.gov)	
U	U	U	UU	219	19b. TELEPHONE NUMBER (Include area code) (757) 864-9658	